HANDBOOK OF

ADVANCED CERAMICS MACHINING

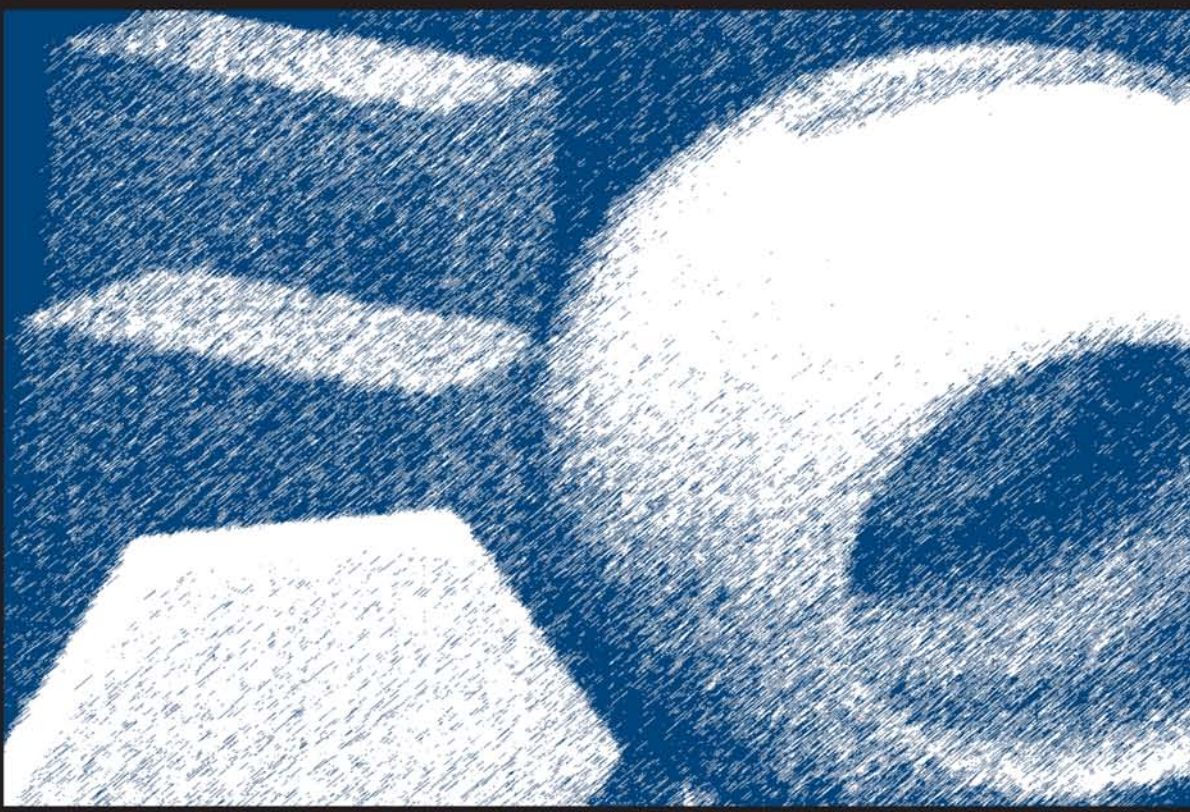

EDITED BY

IOAN D. MARINESCU

CRC Press
Taylor & Francis Group

Handbook of
ADVANCED CERAMICS MACHINING

Handbook of
ADVANCED CERAMICS MACHINING

Edited by
Ioan D. Marinescu

CRC Press
Taylor & Francis Group
Boca Raton London New York

CRC Press is an imprint of the
Taylor & Francis Group, an informa business

CRC Press
Taylor & Francis Group
6000 Broken Sound Parkway NW, Suite 300
Boca Raton, FL 33487-2742

Printed in the United States of America on acid-free paper
10 9 8 7 6 5 4 3 2 1

International Standard Book Number-10: 0-8493-3837-9 (Hardcover)
International Standard Book Number-13: 978-0-8493-3837-3 (Hardcover)

Library of Congress Cataloging-in-Publication Data

Handbook of advanced ceramics machining / edited by Ioan D. Marinescu.
p. cm.
Includes bibliographical references and index.
ISBN-13: 978-0-8493-3837-3 (alk. paper)
ISBN-10: 0-8493-3837-9 (alk. paper)
1. Ceramic materials--Machining--Handbooks, manuals, etc. I. Marinescu, Ioan D. II. Title.

TJ1185.H1565 2006
666'.04--dc22 2006025617

Visit the Taylor & Francis Web site at
http://www.taylorandfrancis.com

and the CRC Press Web site at
http://www.crcpress.com

Preface

Ceramics is one of the primary fields in which improvements in processing and advanced products can be anticipated. Such products have an increased technological knowledge content and have to be manufactured using processing technology that is more advanced and better controlled. Advancements in ceramic machining and manufacturing technology are necessary for the commercialization of new processing technology; these innovations may lead to eliminating expensive steps, improving productivity, and increasing product reliability.

Most of the industrialized countries of the world have invested heavily in the manufacturing (processing) of new ceramic materials, which led to the production of lower-priced ceramics with better properties. This successful development is useful, but is not good enough for the anticipated boom in the ceramic materials industry. The main problem in the use of ceramics is that machining is still very expensive. This prohibits the replacement of metal parts with ceramic parts in nearly all industries in which machined parts are used, such as the automotive, aerospace, and semiconductor industries.

This book presents the latest developments in machining of advanced ceramics. Most of the authors have dedicated their whole lives to the study of ceramic machining and ceramic stock removal mechanisms.

Ductile grinding of ceramics is the focus of Chapter 1 by Professor Eda of Ibaraki University in Japan. His laboratory is well known mainly for new methods and tools for machining of ceramics and other semiconductor materials. Chapter 2 comes from Kumamoto University. Over the years, Professors Yasui and Matsuo developed special techniques for grinding fine ceramics using diamond wheels with coarse grains.

Chapter 3 deals with fundamentals: mechanisms for grinding of ceramics. Professor Malkin, considered a ''guru'' in grinding of ceramics and general grinding, spent many years investigating different aspects of the grinding of ceramics. This chapter is a kind of summary of his findings. Chapter 4 focuses on the correlation between grinding parameters and the strength and depth of mechanical damage. Professor Mayer of the University of Texas spent most of his life investigating these phenomena.

Chapter 5, Chapter 6, Chapter 9, and Chapter 15 present a new technology: electrolytic in-process dressing (ELID) grinding of ceramics, which was developed in Japan by Professor Nakagawa and his student Dr. Ohmori, who is coauthor of three of the chapters dedicated to ELID technologies. The other authors spent long periods of time working with Dr. Ohmori and his

team at the Japan Institute for Physical and Chemical Research (RIKEN) in Tokyo. ELID is one of the most promising technologies for machining of ceramics, especially for high accuracy and mirror-like surfaces. I would like to mention three very young coauthors of these chapters: Dr. Katahira, Dr. Kato, and Dr. Spanu, who finished his doctoral thesis on this subject two years ago. The authors of this chapter represent three generations of researchers working on this promising technology.

Chapter 7 was written by a team from the Precision Micro-Machining Center of the University of Toledo, Ohio. The chapter presents a method that is new and not very familiar to the industry: belt centerless grinding of ceramics materials using special diamond belts. This method is used mainly for high-efficiency grinding applications where the main objective is the stock removal rate and the second objective is the quality of the surface.

Chapter 8 also comes from the Precision Micro-Machining Center and presents a modern technique for monitoring the ceramic lapping process: acoustic emission (AE). AE is well known as a tool to monitor the ceramic grinding process; however, there are only a few studies regarding AE in the lapping process.

Chapter 10 was written by a team of academic and industrial researchers: Mariana Pruteanu, Ion Benea, and myself. The chapter presents a study dealing with the lapping of ceramics with diamond slurry and it emphasizes the differences between mono- and polycrystalline diamond.

Chapter 11 is one of the chapters with emphasis on fundamentals and presents an original model for lapping of ceramics: the double fracture model. I developed this model with my students over the past fifteen years, trying to provide a more complex material removal model in the case of lapping of ceramics (indentation and scratch).

Chapter 12 looks at a method to replace lapping (double lapping) of ceramics with grinding (double grinding) using the same kinematics. Written by Dr. Christian Spanu, Dr. Mike Hitchiner, and myself, this chapter discusses the state of the art for this technology, which is gaining more ground every day.

Chapter 13 focuses on the nanomachining of ceramic materials, mainly through super polishing, a technology developed in principle for the semiconductor industry. The work was done at the Precision Micro-Machining Center and uses a state-of-the-art super-polishing machine with a special technology for AlTiC magnetic heads. The quality of the surface obtained is at the level of 2–5 Å.

Chapter 14 discusses a new technology that has never been used in industry: laser-assisted grinding of ceramics. I developed this technology with Dr. Howes and Dr. Webster at the University of Connecticut in the early 1990s. New developments show that this is a promising technology, which may allow grinding of ceramics with high productivity and high accuracy at the same time.

Chapter 16 and Chapter 17 come from the Fraunhofer Institute of Berlin, one of the best machining laboratories in Germany, with an old tradition in machining of ceramics. Developed by senior Professor Spur and his successor, Professor Uhlmann, one chapter is dedicated to the ultrasonic grinding of ceramics, a technology successfully developed in Berlin; the second is a summary of the findings of the latest research in different grinding methods of ceramic materials.

This book is addressed to a broad category of people: engineers and technicians in industry; students; and researchers and scientists in government research institutions. With new alternative fuels and energy on the horizon, ceramic materials are feasible alternative engine materials, able to work at high temperature with minimum wear.

I would like to thank all my coauthors and contributors for taking the time to prepare the manuscript. I would also like to thank my wife Jocelyn for putting up with my long hours of work and with very short weekends. Without their help and encouragement, this book would not have been possible.

Editor

Ioan D. Marinescu, Ph.D., is a professor of mechanical, industrial, and manufacturing engineering at the University of Toledo in Ohio. He is also the director of the Precision Micro-Machining Center of the College of Engineering of the same university.

Dr. Marinescu is the author of more than 15 books and 300 technical and scientific papers, and lectures and holds workshops in more than 40 countries around the world. He is the president and CEO of Advanced Manufacturing Solutions Co., LLC, a company he founded in 1998.

Contributors

Th. Ardelt Institute for Machine Tools and Factory Management, Technical University of Berlin, Germany

B.P. Bandyopadhyay University of North Dakota, Grand Forks

I. Benea Vice President, Superabrasives of Engis Co., Wheeling, Illinois

R. Coman Precision Micro Machining Center, College of Engineering, University of Toledo, Ohio

N.-A. Daus Institute for Machine Tools and Factory Management, Technical University of Berlin, Germany

G. Dontu Diamond Abrasive Company, New York, New York

H. Eda Saint Gobain Abrasives Company, Romulus, Michigan

M. Hitchiner Saint Gobain Abrasives Company, Romulus, Michigan

S.-E. Holl Institute for Machine Tools and Factory Management, Technical University of Berlin, Germany

T.D. Howes Center for Grinding R&D, University of Connecticut, Storrs

T.W. Hwang Department of Mechanical and Industrial Engineering, University of Massachusetts, Amherst

K. Katahira Materials Fabrication Laboratory, RIKEN, Saitamaken, Japan

T. Kato Materials Fabrication Laboratory, RIKEN, Saitamaken, Japan

J. Laufer Institute for Machine Tools and Factory Management, Technical University of Berlin, Germany

A. Makinouchi Materials Fabrication Laboratory, RIKEN, Saitamaken, Japan

S. Malkin Department of Mechanical and Industrial Engineering, University of Massachusetts, Amherst

I.D. Marinescu Precision Micro Machining Center, College of Engineering, University of Toledo, Ohio

J.E. Mayer, Jr. Texas A&M University, College Station

J. Webster Cool-Grind Technologies LLC, Storrs, Connecticut

H. Ohmori Materials Fabrication Laboratory, RIKEN, Saitamaken, Japan

M. Pruteanu Inasco Inc., Quakertown, Pennsylvania

J. Ramírez-Salas Precision Micro Machining Center, College of Engineering, University of Toledo, Ohio

C.E. Spanu Geiser Tool Company, Ventura, California

G. Spur Institute of Machine Tools and Factory Management, Technical University of Berlin, Germany

E. Uhlmann Institute of Machine Tools and Factory Management, Technical University of Berlin, Germany

D. Wu Precision Micro Machining Center, College of Engineering, University of Toledo, Ohio

H. Yasui Department of Mechanical Engineering and Materials Science, Kumamoto University, Kumamoto, Japan

Contents

1

Ductile Grinding of Ceramics: Machine Tool and Process

H. Eda

CONTENTS

1.1 Ceramics and Metals

Engineering materials are generally referred to as metallic and nonmetallic (ceramics and high polymers) materials, which are further classified as ductile or brittle.[1] As shown in the stress–strain diagram in Figure 1.1, the strain of ductile materials is 100–1000 times larger than that of brittle materials. The following three indexes are often used to characterize the materials.

[|]	Fracture toughness, K_{IC}	Ductile > Brittle
[||]	Weibull coefficient, m	Ductile > Brittle
[|||]	Crack growth rate, n	Ductile < Brittle

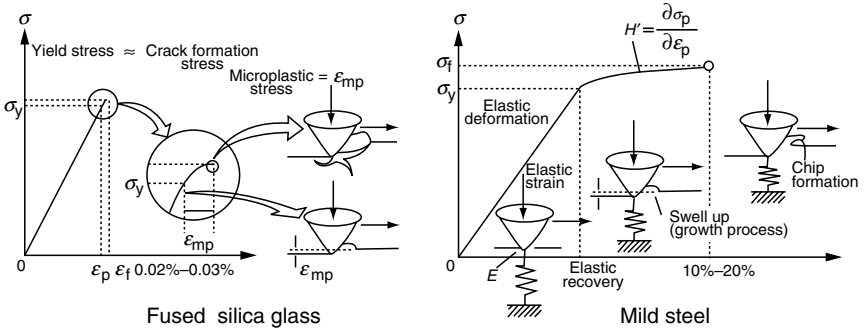

FIGURE 1.1
$\sigma-\varepsilon$ curves of brittle and ductile materials.

Each index for typical metals and ceramics is listed below to compare the brittle materials with the ductile materials.

Index [|] Fracture Toughness

Metals	**Ceramics**
$K_{IC} = 50\ \text{MPa} \cdot \varepsilon\text{m}^{-\frac{1}{2}}$	$K_{IC} = 5\ \text{MPa} \cdot \varepsilon\text{m}^{-\frac{1}{2}}$
$K_{IC} = 10\text{–}100\ \text{MPa} \cdot \varepsilon\text{m}^{-\frac{1}{2}}$	$K_{IC} = 1\text{–}10\ \text{MPa} \cdot \varepsilon\text{m}^{-\frac{1}{2}}$

Using the value of K_{IC}, the tolerable defect size $2C_c$ (the crack length) can be written in the form

$$C_c = \frac{K_{IC}^2}{\pi\sigma^2} \tag{1.1}$$

The K_{IC} here functions as the resistance against the crack growth. Substituting the actual value for the above equation, the tolerable defect size is quantified as

$$2C_c = (3\text{–}13) \times 10^3 \mu\text{m} \qquad | \ 2C_c = 60\text{–}600\ \mu\text{m}$$

Index [||] Weibull Coefficient
According to the Weibull distribution, the fracture probability P_f is expressed by

$$P_f = 1 - \exp\left\{-\left(\frac{\sigma_f - \sigma_u}{\sigma_0}\right)^m\right\} \tag{1.2}$$

where σ_f is the fracture stress, σ_u the guaranteed stress below which P_f is taken as zero, and σ_0 the normalized stress factor.

The shape parameter m is usually called as the Weibull coefficient. A bigger m makes the variance of the material strength smaller.

$$m \approx 50 \qquad | \; m = 5\text{–}20$$

Ceramics normally show about $\pm 25\%$ of the variance.

Index [|||] Crack Growth Rate

$$n = 2\text{–}4 \qquad | \; n = 40\text{–}100$$

The crack growth rate dC/dt can be given by the equation

$$\frac{dC}{dt} = A \cdot K_I^n \tag{1.3}$$

where K_I is the stress intensity factor and A a constant.

In brittle materials, normally there are preexisting cracks or defects or both due to some uncertain factors. The three indexes here indicate that the cracks (or defects) start growing when they reach the tolerable crack size C_C of about 30 μm. As illustrated in Figure 1.2, the crack growth rate greatly depends on the crack size c.

$C \leq 30$ μm	$dC/dt \leq 60$ m/sec
$30 < C \leq 300$ μm	$60 < dC/dt \leq 150$ m/sec
$C > 300$ μm	$150 \ll dC/dt \leq 4000$–6000 m/sec

In the process zone, the tip of the crack develops in zigzag form by selectively inducing the microdefects (or microcracks). The fracture toughness of the material therefore appears to have increased. Generally, the microcracks sized between 30–300 μm grow toward the macrocracks by repeating initiation-propagation cycle to stop. Ultimately, the final crack takes place in a single stroke, as the cracks grow big enough. The growth rate at that moment approaches the self-characterized elastic propagation rate of the material (approximately about 4000–6000 m/sec).

$$\frac{dC}{dt} = \sqrt{\frac{E}{\rho}} \tag{1.4}$$

where E is Young's modulus and ρ the material density.

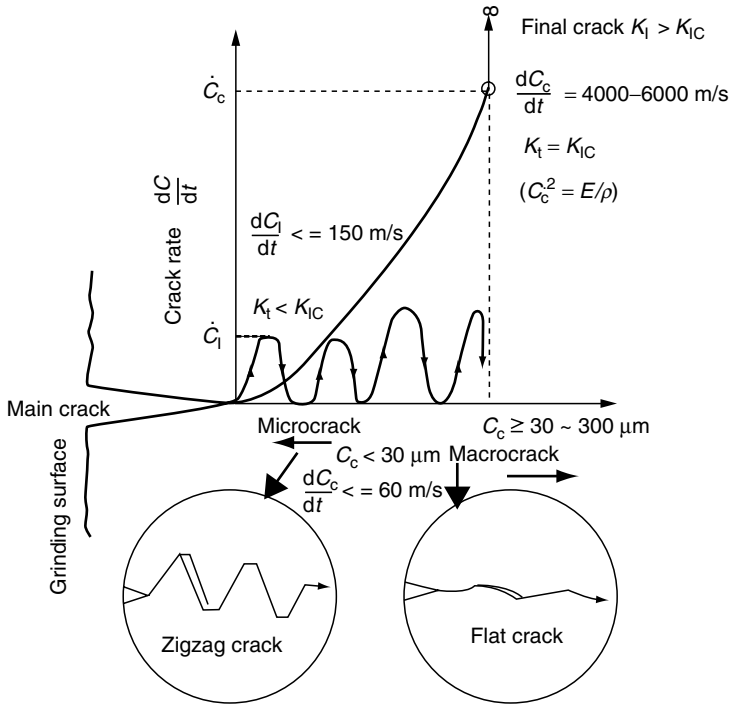

FIGURE 1.2
Micro- and macrocracks.

1.2 Brittle Materials and Grinding

As previously described in the indexes (K_{IC}, m, n), ceramics are ten-fold more sensitive to cracks than metals. As shown in Figure 1.3, for example, the abrasive grain tracks are remaining on the ground surface. The roughness diagram shows that the valleys appearing on ceramics are deeper and denser than those on metals. Comparing the R_y/R_a between ceramics and metals, the values of

$$R_y/R_a = 3\text{–}5 \text{ (average)} \qquad | \; R_y/R_a = 5\text{–}21 \text{ (average)}$$

are about three times different. The valley depth of ceramics is one digit larger than its centerline average roughness. The tip angle 2α of the valley for each material is about

$$2\alpha \approx 134^\circ \qquad | \; 2\alpha \approx 150^\circ\text{–}170^\circ$$

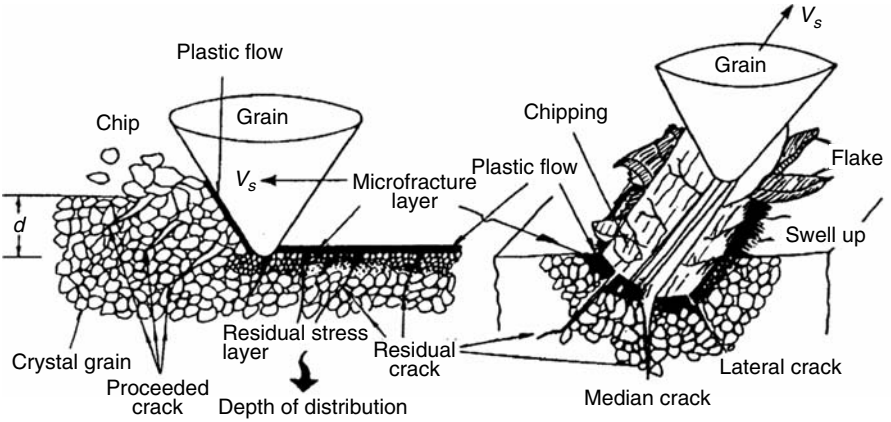

FIGURE 1.3
Ground surface layer by single abrasive grain.

It means that extremely sharp cracks extend deeply into ceramics. It should be further noted that the actual tips of the cracks are often closed and undetectable by normal measuring instruments.

The initial study on the ductile-mode machining of brittle materials was done by Yoshikawa[2] and Taniguchi[3] who have developed the general description for the behavior of brittle materials in the plastic flow zone, by generalizing the microplasticity[4] of Mcmahon, and the elastic/plastic theory of Hill and Hertz.

As shown in Figure 1.1, brittle materials (glass, for example) are subject to plastic flow when the strain ε reaches 0.02%–0.03%. In grinding using diamond abrasives, the deformed area around a single cutting edge scales in 10–20 μm arising from the residual stress on the ground surface. With the first-order approximation, the strain equivalent to 0.02%–0.03% results in a plastic flow zone sized 2–6 nm. Any bigger deformation caused by abrasives potentially risks an initiation of the crack and then transits the machining to the brittle mode.

In other words, the brittle material removal takes place in the ductile mode only when the strain ranges between the starting point of the plastic flow ε_p and the ending point ε_f given in the stress–strain diagram in Figure 1.1. The position and motion of each cutting edge must therefore be precisely controlled so that the grinding pressure (grinding energy) can be constantly constrained within the allowable condition for achieving the ductile-mode grinding.

The description here intends to exemplify the event by generalizing the idea of the stress–strain diagram, but is not precisely correspondent to the thermal and dynamical environments in the actual 3D-grinding zone.

In machining of brittle materials, it is generally known that ductile behavior is achieved when the specific material removal unit is small enough.[5] The critical depth of cut d_c is specified as

$$d_c = 0.15\left(\frac{E}{H}\right)\left(\frac{K_c}{H}\right)^2 \tag{1.5}$$

where E is Young's modulus, H the hardness, and K_c the fracture toughness.

The knowledge accumulated so far can be best summarized by the existence of the brittle–ductile transition. From a new point of view, however, the following achievements further show that brittle–ductile transition is controllable by atmospheric conditions.

Although it was a simulation related to the cutting process, the brittle–ductile transition can be commonly evaluated by the critical depth of cut d_c. Inamura et al.[6] have developed a new simulation technique called renormalized molecular dynamics, which is able to deal with the dynamical phenomenon scaled from nanometer to micrometer. In the simulation, a defectless monocrystalline silicon was cut at the speed of 20 m/sec, the depth of cut of 1 μm, and in an absolute vacuum environment.

As shown in Figure 1.4, the result achieved at the 1 μm depth of cut is quite similar to that achieved at 1 nm, in which no brittle behavior is

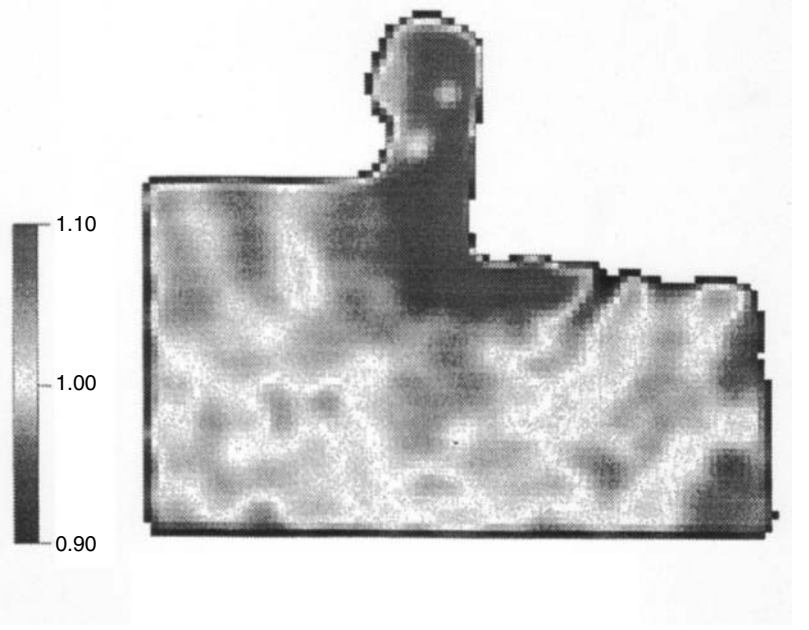

FIGURE 1.4
Cluster density distribution taken as a snapshot during cutting (normalized by the bulk value). Undeformed chip thickness is 1 μm.

observed. The density distribution of the silicon atom becomes higher near the tool (diamond) tip, from where acoustic emission is continuously discharged. At the flank side of the tool, similar to the behavior of cracks, the low-density area undergoes an intermittent cycle of formation and dispersion.

By taking into consideration the atmospheric molecules adsorbed by the contact surfaces of the tool and workpiece, the cutting process has also been simulated at the condition close to a normal atmosphere. The results are shown in Figure 1.5, with (a) for 0.5 μm and (b) for 1.0 μm depth of cut, respectively. It is obvious from Figure 1.5 that silicon behaves as a brittle material. In Figure 1.5b, the cracks in advance of the cutting edge are clearly visible, showing that the material is removed in the brittle mode. In Figure 1.5a, however, there is no advanced crack. It indicates that the cutting process is in the critical state, as it is transited from the ductile mode to the brittle mode.

For such dynamically progressed local cracks, the stress field was further studied from the viewpoint of fracture mechanics. The results based on Figure 1.5b are simulated in Figure 1.6. Figure 1.6 expresses the principal stress: tensile stress in red and compressive stress in blue. The broken line in

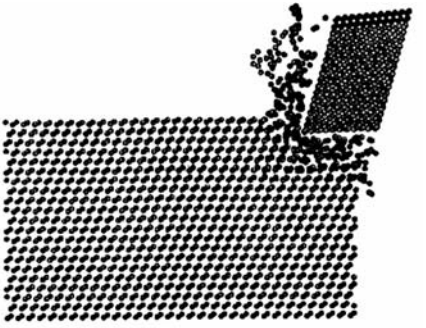

FIGURE 1.5
Result of simulation obtained by taking into account the effect of atmospheric gas.

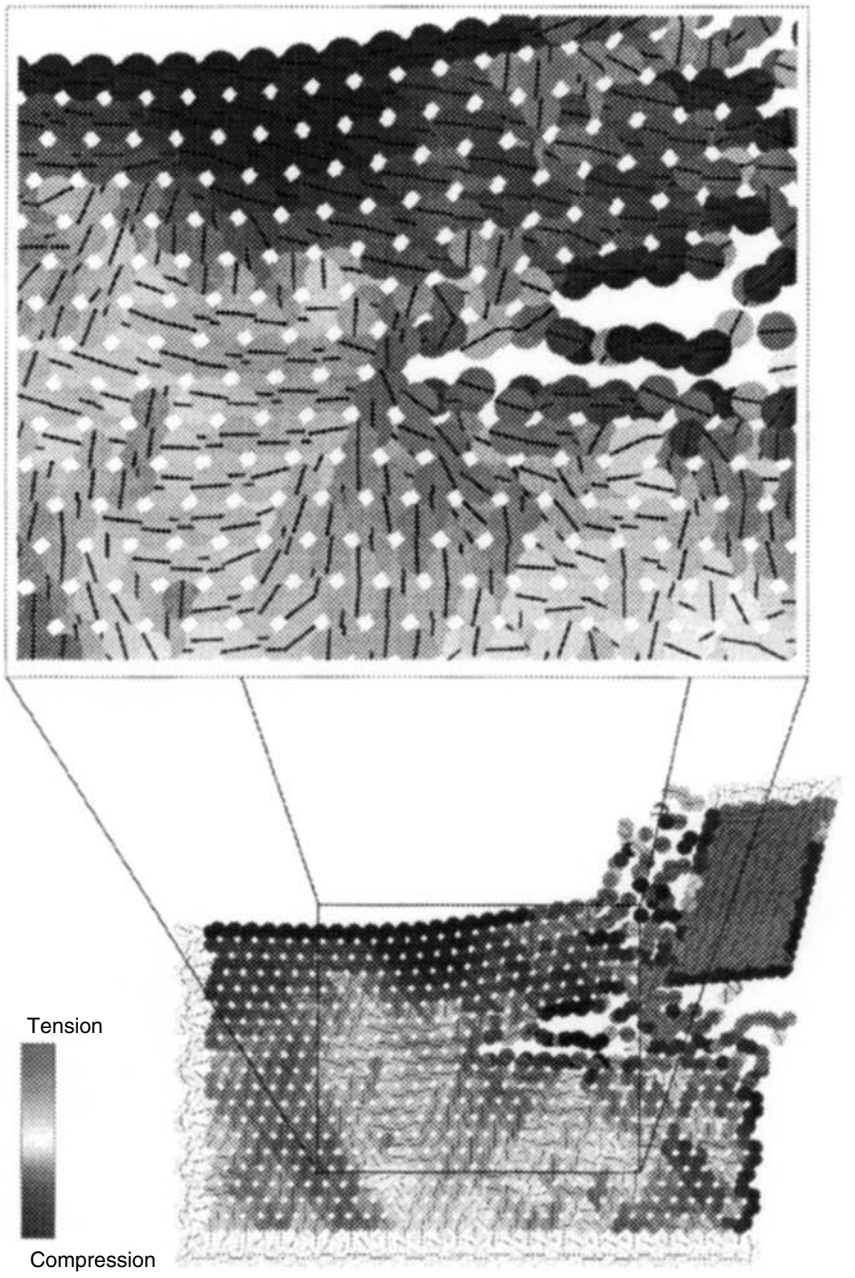

FIGURE 1.6
Stress distribution in the workspace during cutting (undeformed chip thickness is 1 μm).

the scale-up view indicates the direction of the principal stress. The tip of the crack shows that there is tensile-stress concentration affecting the crack at mode I. Moreover, the chip in front is folded upward, which results in an additional tensile stress in the horizontal direction, and thus forms a combined stress field. The crack growth rate is about a quarter of (2200 m/sec) elastic propagation rate, which is expected to be quite reasonable.

From the above results, it can be concluded that the cracks are generated by a sudden liberation of the strain energy, which is stored near the cutting edge. The liberation of the strain energy is normally triggered by the reaction heat of atmosphere (O_2) and the active molecule (Si). That is why no brittle mode occurs at a light cutting where the total strain energy accumulated at the cutting point is too small, and in cutting metals, which take the structure of a face-centered cubic lattice.

The conclusion also reveals whether the growth of preexisting cracks depends on the dimensional relationship between the energy necessary for the new surface generation and the energy that is liberated by the crack generation, and the relationship is decided by the quantity of material removal units. The concept has been supported and proven by Tanaka and Ueguchi through their experimental research on ''Grinding Process in Vacuum Atmosphere.''[7]

1.3 In-Site Observation of Ductile Behavior in Ceramics

In-site observation of ductile behavior in ceramics was first designed by Hatamura et al. They developed a system,[8] as shown in Figure 1.7, consisting of an *X*–*Y*–*Z* stage with a traveling length of 50 μm and resolution of 0.1 nm/pulse, a parallel-plate type of load cell capable of measuring the normal and tangential forces, and a diamond indenter. The physical properties of the test materials are listed in Table 1.1. The diamond indenter is sharply pointed into a nominal angle of 20° between the face and vertical axis and tip radius of 20 nm.

The experiment demonstrated that the normal force applied to the indenter determined the brittle–ductile transition, and that the critical force was almost equivalent to the Knoop hardness of the test material.

1.3.1 Scratch at the Brittle-Mode

The process of indentation-scratching on the TRC 5 glass is shown in Figure 1.8, Figure 1.9, and Figure 1.10. Along the edge of the scratched groove, as shown in Figure 1.9, the chipping caused by lateral cracks is visible. Such cracks undergo a periodical initiation-growth-fracture process, vary the

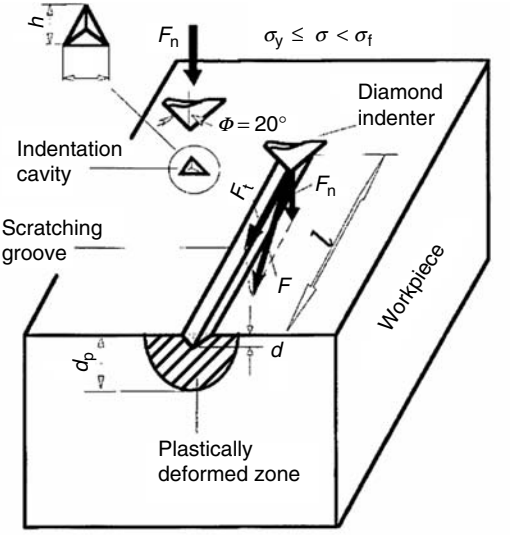

Schematic of scratching test by diamond indenter

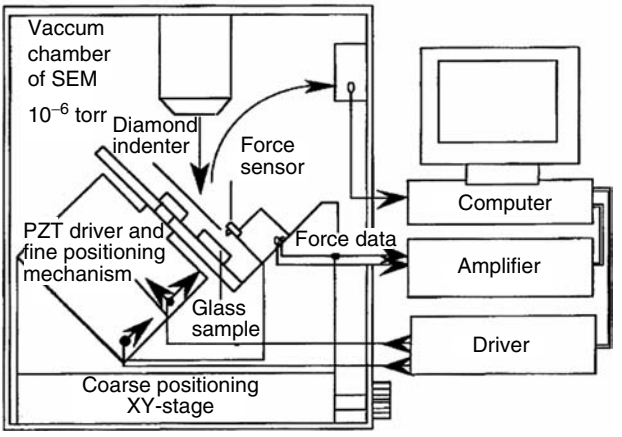

FIGURE 1.7
Schematic of the nanoindentation-scratching apparatus.

normal force and tangential (scratching) force that grants the indenter a stick-slip motion, and leave a serrate shape on the groove.

1.3.2 In-Site Observation of the Ductile Mode

Knowing the indenter geometry, the average pressure P_{tip} on the indenter surface during the scratching is simply given as

TABLE 1.1

Properties of Glasses

Properties	Materials					
	KzF6	F6	BK7	Sk7	GOE91 Glass Ceramic	TRC 5 (Glass II)
Mechanical						
Young's modulus (E) (GPa)	53.1	59.0	80.2	82.2	95.8	108.3
Knoop hardness (H_k) (GPa)	4.44	4.14	5.62	5.32	6.71	8.48
Bulk modulus (K) (GPa)	30.18	35.63	45.74	58.20	64.03	60.30
Yield stress (Y) (GPa)	2.83	1.98	2.63	2.62	3.32	5.02
Modulus of rigidity (G) (GPa)	22	24.1	33.2	32.5	38.3	45.1
Fracture toughness (K_{IC}) (MPa $m^{\frac{1}{2}}$)	0.3	0.38	0.38	0.49	0.39	1.56
Poisson ratio σ	0.27	0.22	0.20	0.26	0.25	0.20
Density ρ (kg m^{-3})	2550	3740	2520	3510	2550	2980
Thermal						
Expansion coefficient (α)	57	96	86	76	47	52
Specific heat (C) (j kg^{-1} k^{-1})	544	524	760	725	880	727
Diffusivity 10^{-9} (D) (m^2 sec^{-1})	503	420	542	421	728	603
Thermal conductivity (k) (wm^{-1} k^{-1})	0.93	0.82	1.04	0.83	1.62	1.31
Yield point (At) (°C)	515	473	624	699	—	961
Chemical						
Water resistance (RW) (p)	6	2	3	2	2	2
Acid resistance (RA) (p)	4	1	1	4	4	1
Weathering resistance (W) (s)	2	2	1	3	1	1
Phosphate resistance (PR)	3.0	1.0	1.0	51.2	1.0	—

$$P_{tip} = \frac{\overline{F}}{d^2} \tag{1.6}$$

where $\overline{F}$ is the average scratching force, and d the depth of indentation.

Constraining the P_{tip} into $\sigma_p \leq P_{tip} < \sigma_f$ in accordance with the condition given in Figure 1.1, the static pressure P_{static} is determined as $P_{plastic} = 8.52$ GPa $= 1.27\, H_k$.

Figure 1.11 shows the GOE91 glass scratched by the diamond indenter. A groove of 2.5 μm is formed. As the scratching proceeds further, as shown Figure 1.12, the chips are visibly generated. Over the scratching process, the normal force F_n and the scratching force F_t applied to the indenter are

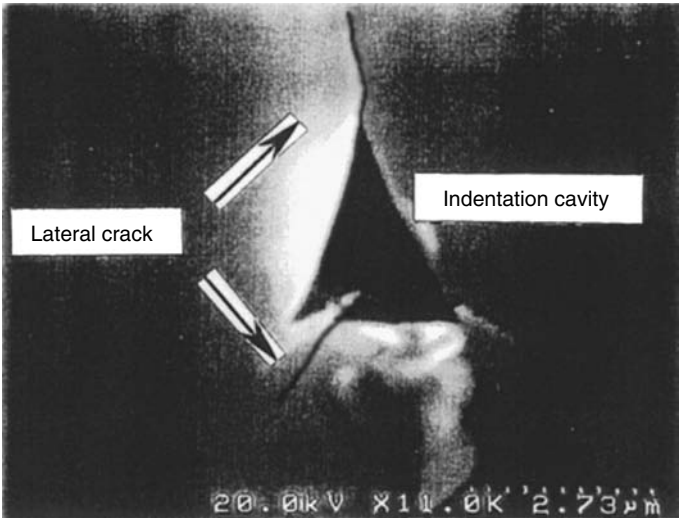

FIGURE 1.8
SEM micrograph of brittle indentation made on surface of TRC 5.

recorded as shown in Figure 1.13. The average dynamic pressure P_{tip} is then equal to 6.69 GPa or 0.99 H_k. The stretching force in Figure 1.13 arrives in a steady state after the plastic stress has been discharged in one stroke at the end of the plastic flow and chip releasing. During the process of chip generation, unlike largely varying force observed in the crack initiation-growth fracture, the force slightly varies from time to time according to the size and shape of the chips. The above-mentioned critical depth-of-cut

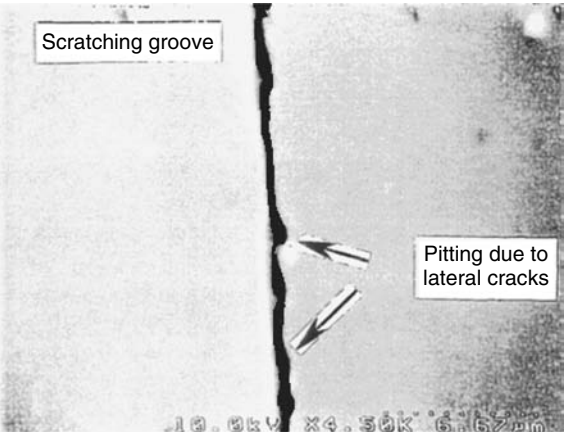

FIGURE 1.9
SEM micrograph of brittle scratch made on surface of TRC 5.

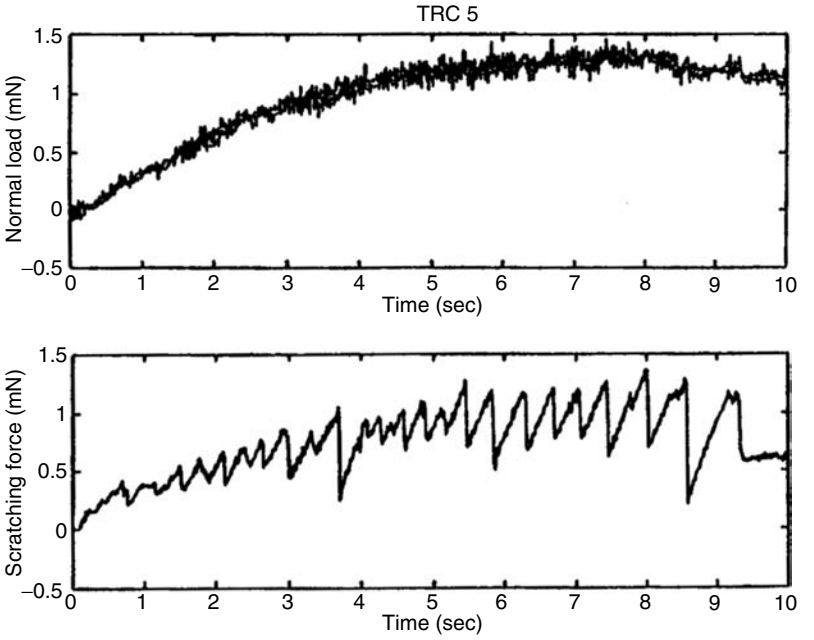

FIGURE 1.10
Force data measured during brittle scratching on surface of TRC 5, where scratching velocity was 5 mm/sec.

d_{cg} is acquired by way of the experiments and is listed in Table 1.2 along with the indentation depth d_{ci}. The relationship between d_{cg} and d_{ci} can be expressed in the form

$$d_{cg} = 7d_{ci} \tag{1.7}$$

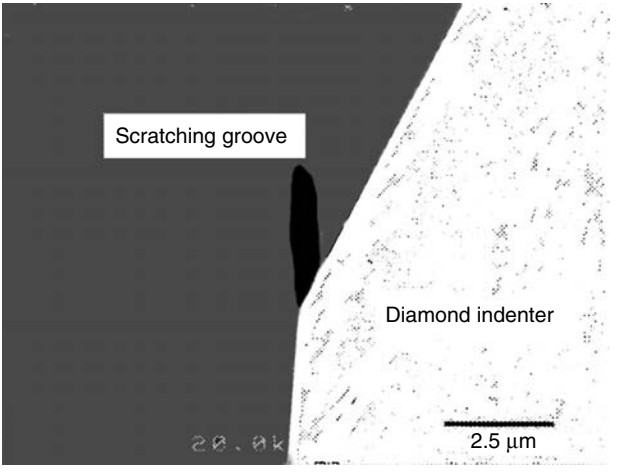

FIGURE 1.11
SEM micrograph of ductile scratching made on surface of GOE91 (in process).

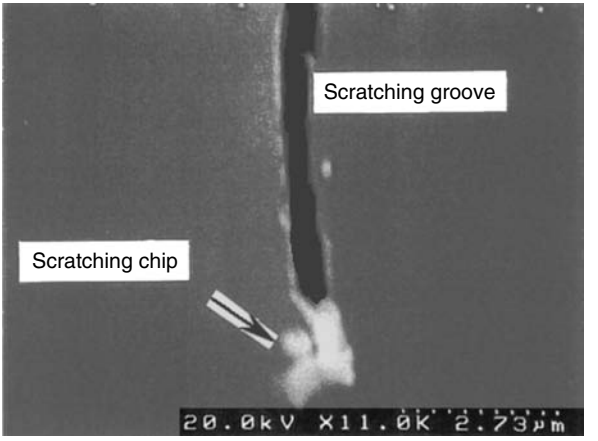

FIGURE 1.12
SEM micrograph of ductile scratching made on surface of GOE91 (after process).

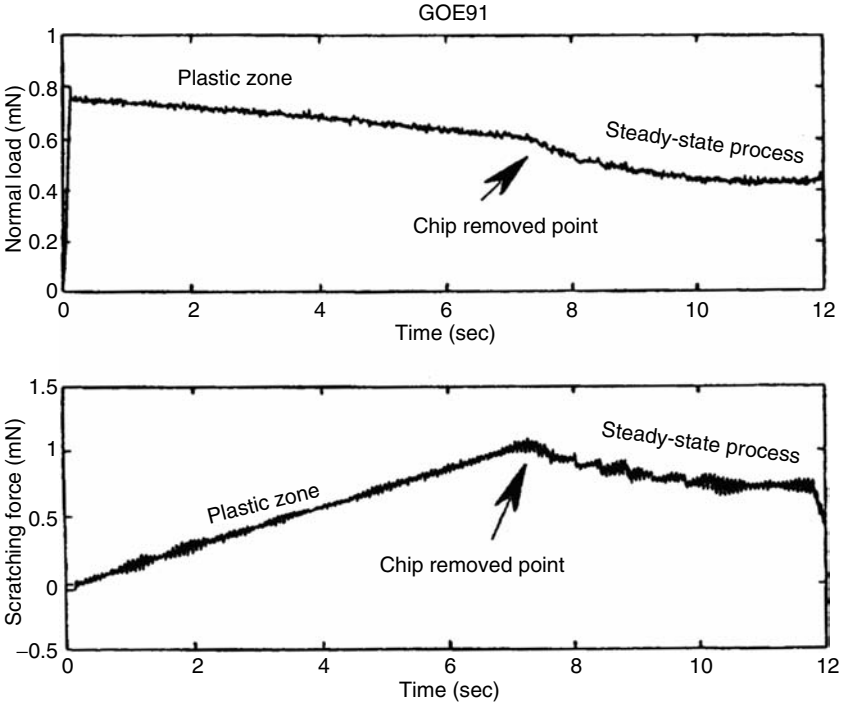

FIGURE 1.13
Force data measured during ductile scratching test on surface of GOE91 (see Figure 1.11).

TABLE 1.2

Estimated Data for Glasses

	Material					
Data	**KzF6**	**BK7**	**F6**	**SK7**	**GOE91**	**TRC 5**
E/H	11.94	14.27	14.25	15.45	14.27	12.77
R (Pa m)	20.1	25.3	35.5	43.3	21.1	28.69
d_{ci} (nm) (Indentation)	8.18	9.78	18.33	19.66	7.23	6.48
d_{cg} (nm) (Grinding)	54.5	65.2	120	131	48.2	43.2

1.4 Ductile-Mode Grinding of Ceramics

The current technology for ductile-mode grinding is indebted to the works mainly by Syn and Taylor[9], Blackley and Scattergood[10], and Bifano and Fawcett.[11] According to the cutting model[10] (Figure 1.14) proposed by Scattergood, ductile-mode machining is realizable when no crack is generated or left in the area below the envelope of y_c. It means that in spite of the occurrence of cracks at the work shoulder zone, the newly generated surface is crack free as long as no crack penetrates into the new surface and the undeformed-chip thickness is controlled to be the critical depth d_c ($=d$) or smaller. The critical condition is determined by the maximum feed rate f_{max}, which is given as

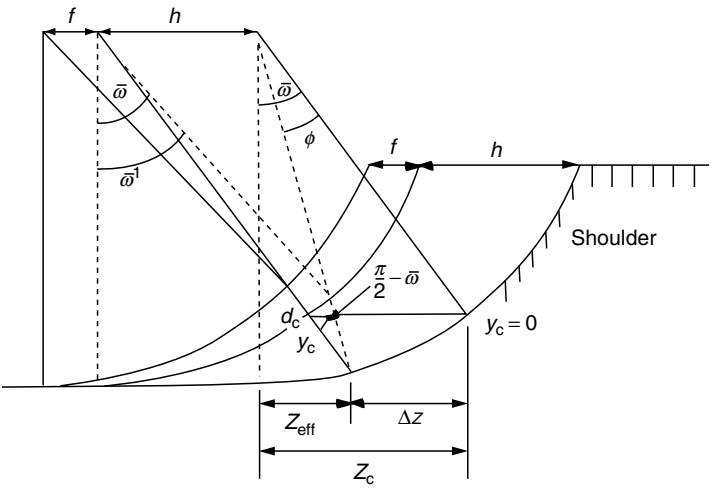

FIGURE 1.14
Geometry used to derive values of d_c and y_c.

$$f_{\max} = \sqrt{R(d_c + y_c) \pm R(d_c + y_c)\sqrt{1 - \left(\frac{d_c}{d_c + y_c}\right)^2}} \tag{1.8}$$

If $(d_c/(d_c + y_c))^2 \ll 1$, the equation is simplified as

$$f_{\max} = d_c\sqrt{\frac{R}{2(d_c + y_c)}} \tag{1.9}$$

This model is useful since it acknowledges the occurrence of the cracks in the cutting zone or the zone to be cut and the effectiveness of reducing the machining energy. However, it is difficult to predict the crack path and to control its growth rate. In the final finishing, the available alternative for feed rate $f_{\max} = d_c$ as if concerning the crack growth and its penetration depth. Eda et al.[12,13] have developed a new ultraprecision machine with an actuator capable of controlling the specific material removal within the condition, $f_{\max} = d_c$, with which the surface roughness of subnanometer was achieved for a wide range of materials.

The grinding energy required for ductile mode is different from that for brittle mode. Based on the concept of the critical depth-of-cut d_c, which has attracted considerable attention so far, a general description has been successfully introduced to express the brittle–ductile relationship.

The total grinding energy E_b required for brittle materials is the sum of the energy for brittle grinding E_f and the energy for ductile grinding E_p. Out of E_b, E_f is expressed as

$$E_f = \left(2\pi C_L \gamma_s + 2C_m \gamma_s + \frac{\pi}{4}\alpha\sigma_p d_p^2\right)L \tag{1.10}$$

where C_L is the lateral crack radius, L the length of C_L cylinder, γ_s the energy for surface generation, C_m the median crack radius, σ_p the yield stress, d_p the diameter of plastic flow zone, and α a constant, whereas E_p is

$$E_p = F_t L \tag{1.11}$$

where F_t is the tangential grinding force and L the grinding length.

Dividing this by the removed volume V_f at the brittle mode or V_p at the ductile mode, the specific grinding energy μ_f and μ_p are given as

$$\mu_f = E_f/V_f = K_f d^{-\frac{4}{3}} + K_p, \tag{1.12}$$

$$\mu_p = E_p/V_p \approx \sigma_Y \approx H = K_p \tag{1.13}$$

As grinding shifts from the brittle mode to the perfect ductile mode, the specific energy for brittle grinding μ_f should agree with the condition $\sigma_p < \sigma < \sigma_f$ shown in Figure 1.1, and the specific energy for ductile grinding μ_p should take a value equivalent to hardness H. If the grinding speed is as

slow as scratching, μ_p should be equal to P_{tip} described in Section 1.3.2. In Figure 1.15, the specific energy μ_p of grinding SiC produced by CVD is plotted against $d^{-\frac{4}{3}}$. The line can be approximately expressed by the equation

$$\mu_p = 535 + 53776 d^{-\frac{4}{3}} (\mathrm{GJ/m^3}) \tag{1.14}$$

Figure 1.16 summarizes the grinding results of six kinds of materials listed in Table 1.1.[14]

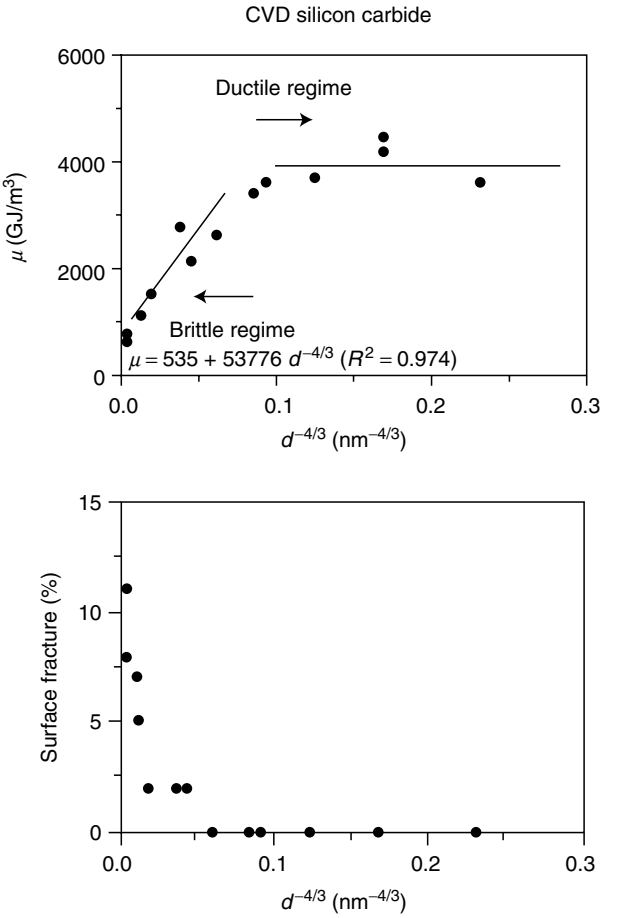

FIGURE 1.15
Specific grinding energy (top) and area percent grinding-induced surface fracture (bottom) vs. the grain depth-of-cut to the −4/3 power for CVD silicon carbide. Tomita, Y. and Eda, H., Development of new bonding materials for fixed abrasive of grinding stone instead of free abrasives processing, *Bull JSPE* (in Japanese), 61, 10 (1995) 1428; Lawn, B.R. and Swain, M.V., Microfracture beneath point indentations in brittle solids, *J Mater Sci*, 10 (1975) 113.

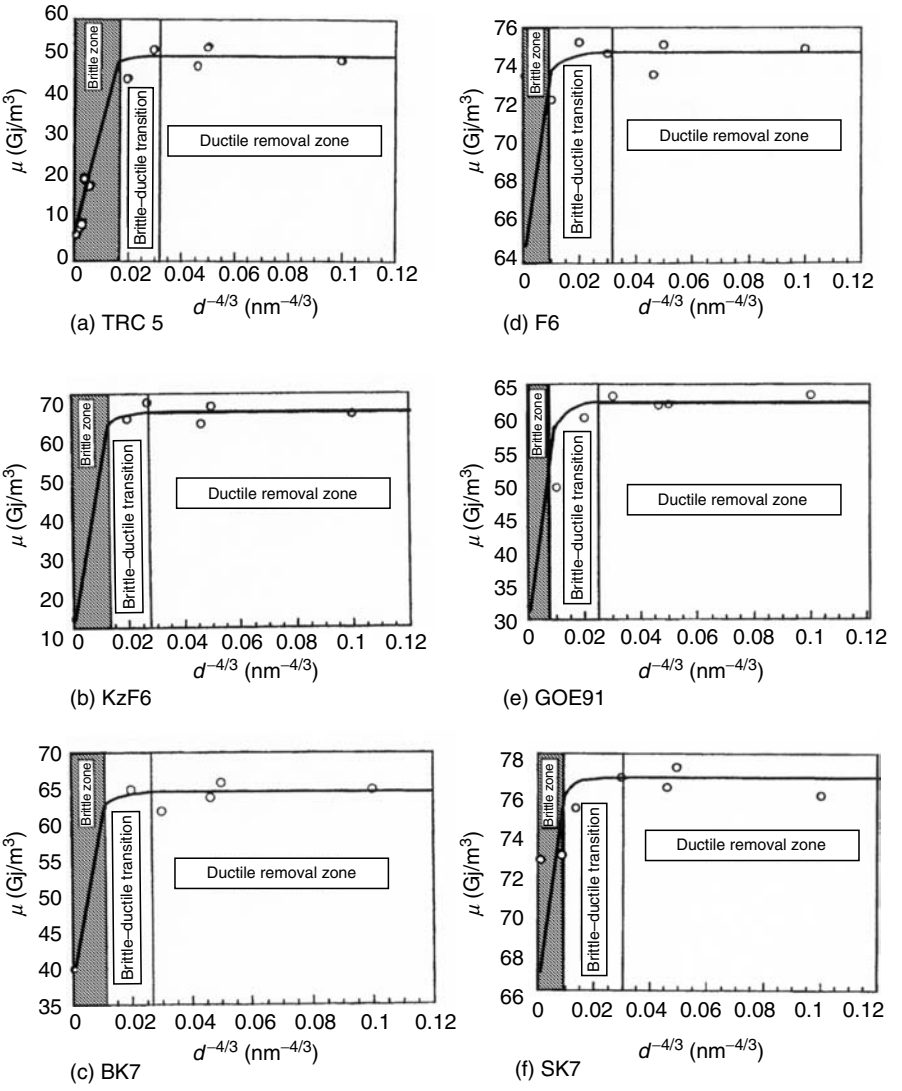

FIGURE 1.16
Specific grinding energy vs. $d^{-4/3}$.

1.5 Machine Tools for Ductile Grinding of Ceramics

1.5.1 Design Criteria of Ductile Microgrinding Machine Tool

Generally, microgrinding is referred to as the material removal rate (MRR) ranging from 0.1 to 0.0001 mm^3/mm sec, which includes the process

normally done by polishing.[17,18] Now, it is possible to reach 10^{-4} mm^3/mm sec or even smaller by using fixed abrasives with sponge bond.[15] In such cases, the in-feed (depth-of-cut) is usually about several 10 nm, the grinding area is 100 mm^2 or smaller, and the grinding force is about several 10 mN.

For studying the grinding temperature, Lawn has conducted a penetration test by applying a constant force against a diamond indenter with the half-nominal angle of 68°. The temperature rise ΔT, including the heat due to plastic flow and the heat due to sliding friction between the abrasive and workpiece, is expressed as

$$\Delta T = \frac{H \cot \theta}{2\pi\rho C_\rho} \tag{1.15}$$

Taking Si as an example, its hardness $H = 10.6$ GPa, density $\rho = 2325$ kg_f/m^3, specific heat $C_\rho = 678$ Nm/kg_f K, and ΔT is assumed to be 433 K. The temperature rises for various ceramics are summarized in Table 1.3.

Going one step ahead, Blok et al. have solved the temperature at the contact area between the wheel and workpiece, by simplifying the grinding process into a rectangular object (wheel) sliding over the workpiece. The following equation is introduced to express the maximum surface temperature.

$$T_{\max} = \frac{2q}{k}\left(\frac{\alpha \cdot l}{V}\right)^{\frac{1}{2}} \tag{1.16}$$

TABLE 1.3

The Estimated Temperature Rises in the Plastic Zone during Indentation Test of Several Brittle Materials

	Estimated Data			
Material	**Hardness (*H*) (GPa)**	**Density (kg m^{-3})**	**Specific Heat (C_ρ) (j kg^{-1} k^{-1})**	**Temperature Rise (*T*) (K)**
KzF6	4.44	2550	544	190.82
BK7	5.62	2520	760	174.95
F6	4.14	3740	524	125.94
GOE91	6.71	2550	880	178.27
SK7	5.32	3510	725	124.64
Glass II; TRC 5	8.48	2980	727	233.36
AL_2O_3	15.2	3710	1050	232.63
ZrO_2	12.8	2530	821	367.40
SiC	10.6	3100	1040	196.02
Si_3N_4	9.2	2500	710	309.01

where q is the thermal heat flux, k the thermal conductivity, α the thermal diffusivity, l the contact length, and V the grinding wheel speed.

When the tangential grinding force $F_t \leq 4$ N, $V \leq 10$ m/sec and $l \approx 0.006$ m, the q $(= Ft \cdot V/l) \leq 10^6$ 10^6 J/m^{2}sec. However, the temperature ΔT is only 2°C, which is much lower than the actual case. Subsequently, the model is rebuilt on the sliding contact by the diamond abrasive alone, excluding the effect of contact between the bond and workpiece. The results are much closer to the actual grinding process. Figure 1.17 shows the grinding temperature calculated using the new equation as below

$$T_{\max} = \frac{3qd^2N^{\frac{1}{2}}}{4\sqrt{2}k} \tag{1.17}$$

where d is the diameter of contact diamond and N the number of diamond abrasive in the contact zone.

The result shows that the temperature at ceramic grinding is much lower than the melting point of the material, and the temperature for diamond oxidation is even lower than 700°C. It is important to note the role played by

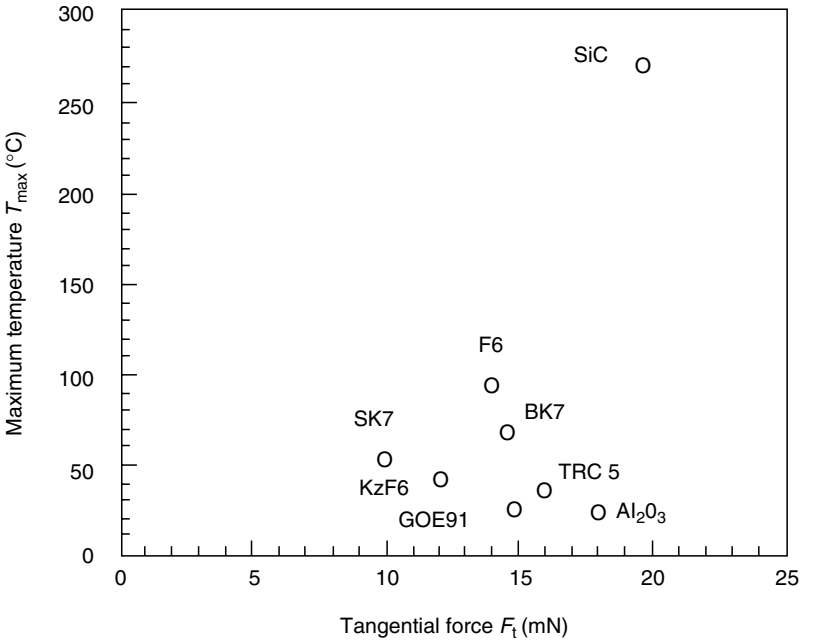

FIGURE 1.17
The estimated maximum surface temperature rise vs. the tangential grinding force for fixed experimental conditions.

trueing. To achieve nanometer accuracy, the grinding wheel must be precisely trued below 0.1 μm runout and 10 nm repeatability or better.

The above conditions for ductile grinding of ceramics can be summarized as: the grinding force less than several 10 mN (per 100 mm^2) and the grinding temperature less than 400°C, which is equivalent to 1/100 of the force and 1/(4–5) of the temperature observable in a conventional grinding process.

This is to say that the criteria for the machine tool to achieve ductile grinding of ceramics is accurate positioning capability and high repeatability to constantly control the grinding condition within $\sigma_p \leq \sigma < \sigma_f$ and $d \leq d_c$ (Figure 1.1).

1.5.2 Key Technologies of a Ductile Microgrinding Machine Tool

As described in several publications,[17] the ultraprecision machine tool must have a structure of high thermal rigidity (or low thermal expansion), at least one digit better than conventional machine tools. However, the dynamic rigidity is less important and still acceptable even if it is one digit lower.

For example, the compliances of $C_r = 0.1$ μm/kg_f in radius direction, $C_a = 0.03$ μm/kg_f in axial direction, and $C_c = 0.1$ μrad/kg m in rotational direction are sufficient for the main spindle whereas the error motions of 50 nm in both radius and axial directions and 0.2 μrad in rotational direction or better are expected. As for X–Y table, the dynamic rigidity should be $k_x \approx 0.1$ kg_f/μm (traverse direction) and $k_y \approx 0.05$ kg_f/μm whereas the thermal rigidity should be as good as that of the main spindle. The temperature of the environment is normally maintained at room temperature ± 0.1°C.

Between the wheel and workpiece, the contact rigidity $k_v \approx 5$ kg_f/μm with a standard deviation of 0.5 kg_f/μm in the normal direction (perpendicular to the grinding direction) and the dynamic rigidity $k_{vd} \approx 10$ kg_f/μm with a standard deviation of 2 kg_f/μm. These values indicate that the rigidity is one digit smaller than that of conventional machine tools. Futhermore, the tangential dynamic rigidity is about $k_{dt} \approx 10$ kg_f/μm (standard deviation 0.2 kg_f/μm) and $k_w \approx 2$ kg_f/μm is quite standard for the workpiece mounting table. The value listed above is designed for the aerostatic bearing and the table guideway. An aerostatic system fulfills the design criteria for the ductile microgrinding machine.

In the subsequent sections, the actuators and sensors are exemplified as the key technology to realize the ductile microgrinding.

[Example I]

Figure 1.18 is the state-of-art machine tool newly developed for microgrinding. The key technology used in the system is Giant Magnetostrictive Actuator (GMA) for a wide range positioning of 100 μm–10 nm that is hybridized with a PZT actuator. The advantages of GMA include large displacement

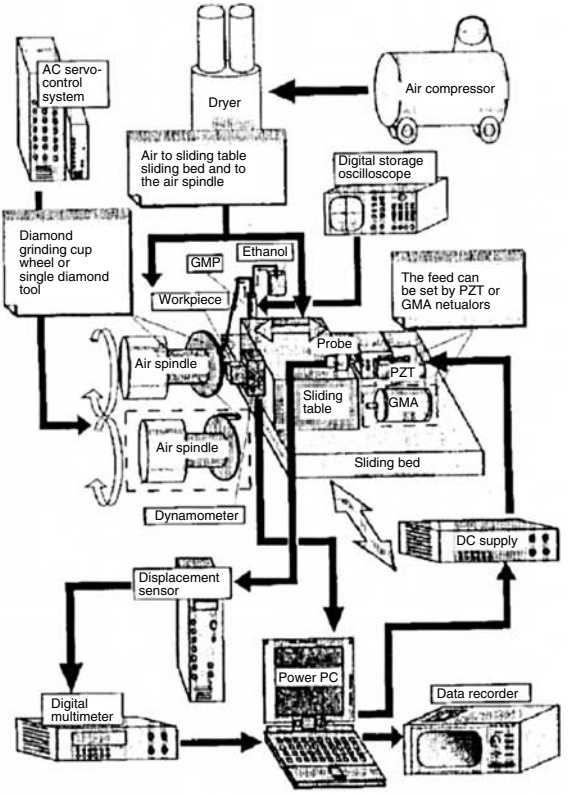

Schematic of the MUPMT (Multipurpose Ultraprecision Machine Tool)

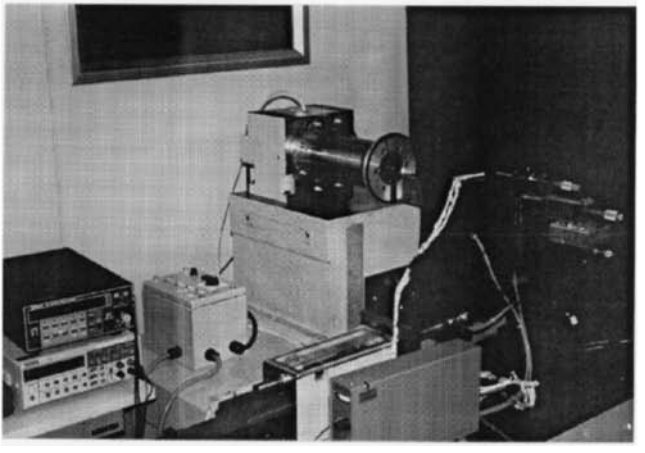

FIGURE 1.18
Whole view of the MUPMT.

(upto 2000 ppm), big power output (elastic energy 14 MJ/m^3, several ten times bigger than PZT) and high response speed (μsec–nsec). Making a full use of these advantages, GMA is able to execute from roughing (μm order) to finishing (several nm order). For more precise finishing at subnanometer scale, the PZT actuator is the alternative.

In the range where the grinding force is relatively bigger, GMA can provide a better performance in rigidity because it requires no magnifier element to get necessary displacement or power. Contrary to GMA, PZT actuator normally demands a power supply with high voltage and a magnifier element to enlarge the displacement. This hybrid actuator proposes a solution to use two different kinds of actuators fully. It does not, however, mean that the GMA is unable to achieve nm positioning without the assistance of PZT.

Figure 1.19 shows the grinding force and the relative displacement between the wheel and workpiece, by the grinding wheel of SD12000R100B at wet grinding with the conditions of 10 nm depth-of-cut, 1550 m/min grinding speed and 100 nm/rev feed rate. The results show that both the normal and tangential grinding forces are constantly below 10 mN. The surface roughness measured by Zygo is $R_a = 0.32$ nm and $R_y = 2.42$ nm (0.2×0.2 mm^2) whereas $R_a = 1.28$ nm and $R_y = 1.59$ nm (0.363×0.363 mm^2) by AFM.

The key component, as shown in Figure 1.20, has a GMA structure.[19] The position is constantly monitored by an electrostatic gap sensor. The feedback control selectively drives the AC servomotor for a large infeed or the GMA for a fine infeed.

[Example II]

The key technologies for microgrinding machine tools also include rapid response speed and extremely smooth movements in the *X*–*Y*–*Z* axis, the main spindle, and the fine infeed. Therefore, the driving resistance and the intermittent motion such as stick-slip must be avoided. As shown in Figure 1.21, the current trend in movements for *X*–*Y*–*Z* axis and the main spindle is to replace the friction of solid–solid contact with pneumatic or hydraulic friction.[20–22]

Since the convention ball screws possess a large spring constant, the energy generated by the rotational movement is often converted into the vibration circuit of the feed elements, resulting in an error motion.

In microgrinding, the vibration induced by the disturbance from the feed device is much bigger than that granted by the grinding process itself. Instead of increasing the rigidity of the whole machine tool, therefore, efforts are made to shut noises out from the tool holder and workpiece-mounting table by using media that has a small spring constant. The feed device developed from such a viewpoint is a built-in unit comprising of an aerostatic ball screw, a rotary encoder, and a backlash-free aerostatic bearing connected to a servomotor. As the solid friction is free, it is able to

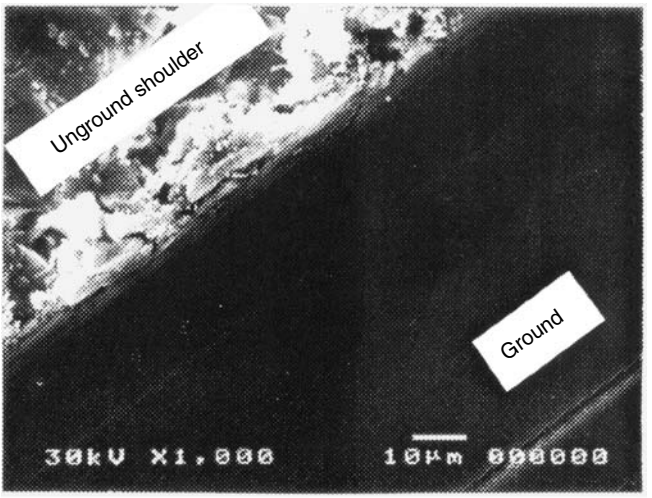

SEM micrograph of ductile grinding on glass BK7

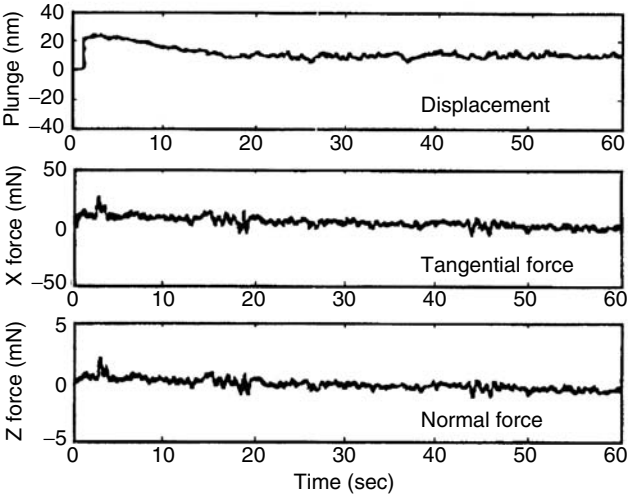

FIGURE 1.19
Experimentally measured normal and tangential force during grinding test on glass BK7.

achieve the power consumption <0.5 W, the temperature rise <0.1°C, the encoder resolution of 64 million pulse/rev and the infeed of 1 nm/step.

Figure 1.22 shows the workpiece-mounting table B and the feed unit for *Y*-axis. These two units can be incorporated together or used separately. The built-in friction free air balance in the *Y*-axis guarantees the level of B table to be ± 0.04 μm/ϕ200 mm, as the *Y*-axis moves up and down. The accuracy has currently been improved upto nanometers.

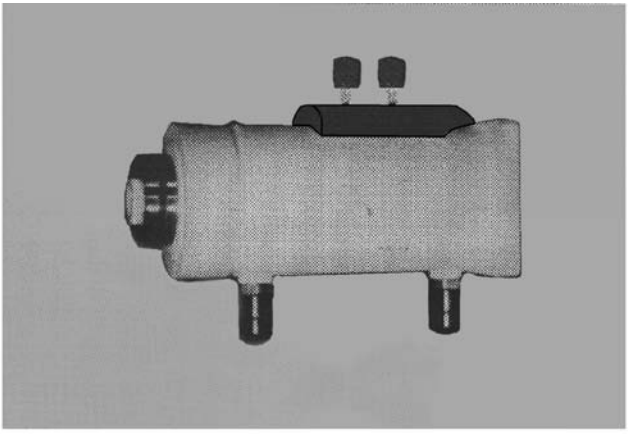

External view of the GMA

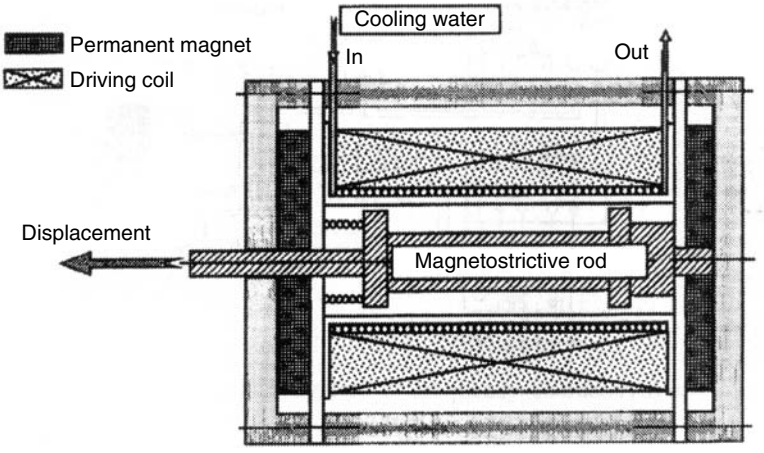

FIGURE 1.20
Schematic of the GMA.

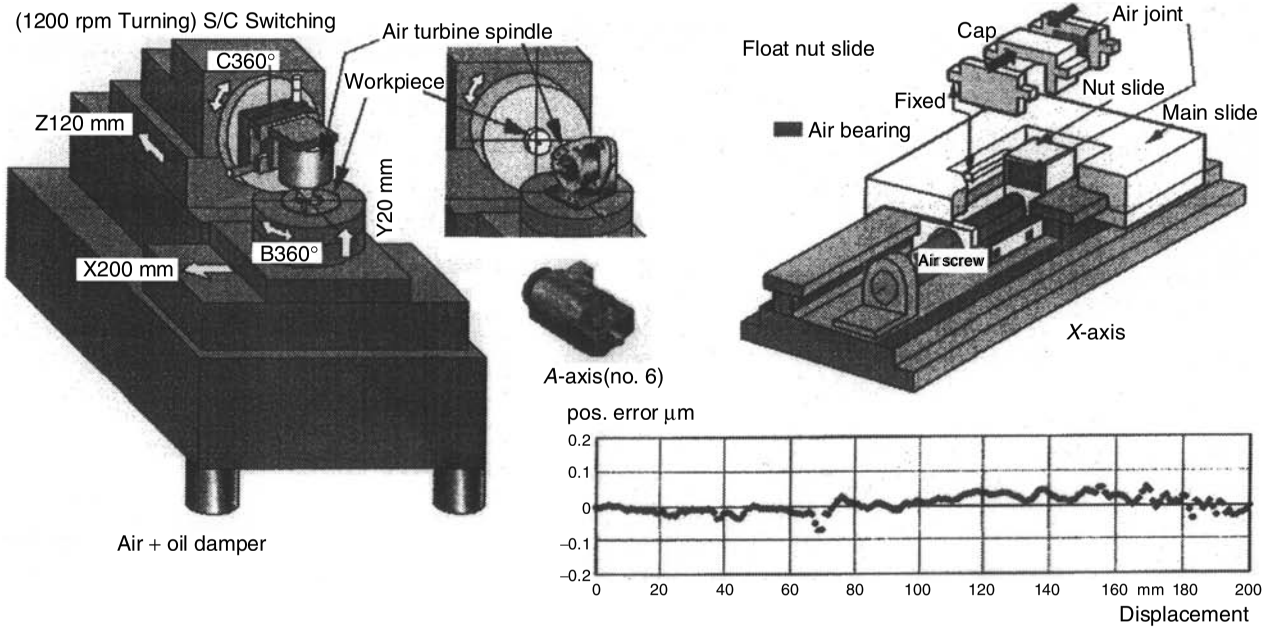

FIGURE 1.21
Schematic of the ultraprecision machining center developed by Y. Takeuchi et al. (From Takeuchi et al., *Annu CIRP*, 45, 1 (1996) 401.)

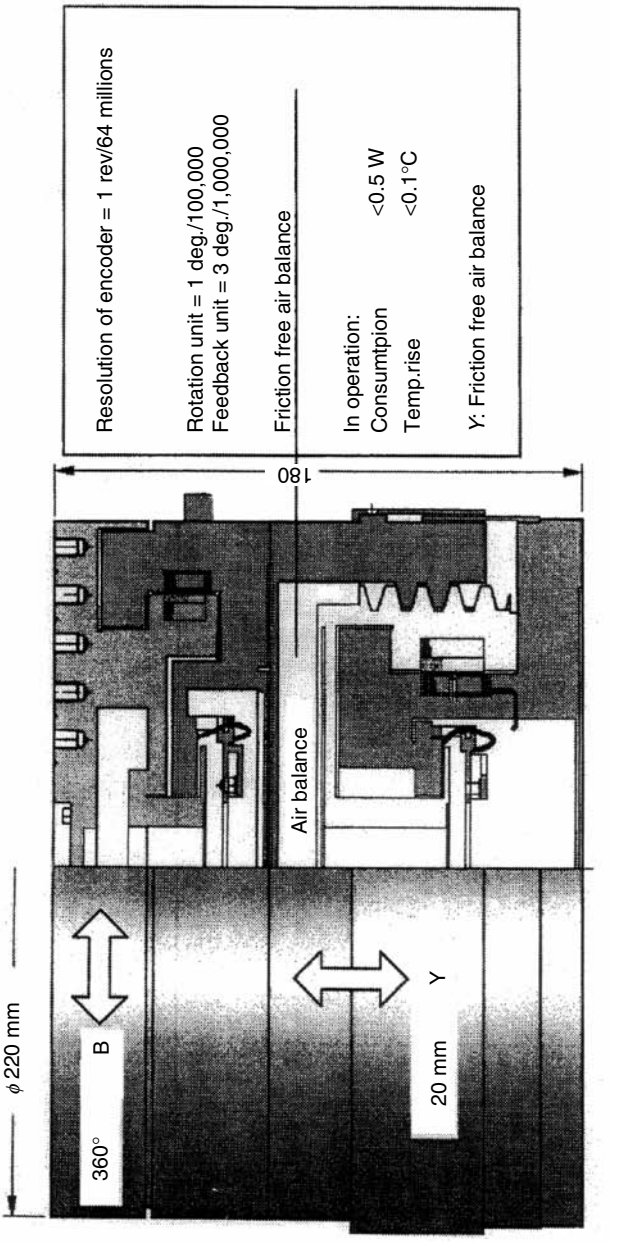

FIGURE 1.22
Intelligent ultraprecision unit with rotary table B ($\pm$0.04 μm/ϕ200 mm) and up-down feed Y-axis unit.

References

1. Eda, H. et al., *Principle of Production Process*, Edited by JSME, Published by Nikankogyo-shinbun (1998, 1) 36.
2. Yoshikawa, H., Brittle–ductile behavior of crystal surface in finishing, *J JSPE*, 35, 2 (1969) 662.
3. Taniguchi, N., *Basics and Applications of Nanotechnology*, Published by Kogyo-chosakai (1988) 45, 257.
4. Mcmahon, C.J., Jr., *Microplasticity*, Interscience Publishers (1968) 46.
5. Bifano, T.G., Ductile-regime grinding of brittle materials, PhD dissertation, NCSU (1988) 153.
6. Inamura, T. et al., Renormalized molecular dynamics simulation of crack initiation process in machining defectless monocrystal silicon, *Bull JSPE*, 63.1 (1998) 86.
7. Tanaka, Y. and Ueguchi, T., Grinding process in vacuum atmosphere, *J JSPE* (in Japanese), 35, 3 (1969) 189.
8. Chouanine, L., Eda, H., and Shimizu, J., Analytical study on ductile-regime scratching of glass using sharply pointed tip diamond indenter, *Int JSPE*, 31.2 (1997) 109.
9. Syn, C.K. and Taylor, J.S., Ductile–brittle transition of cutting mode in diamond of single crystal silicon and glass, Poster session 1989 ASPE/IPES conference, Monterey (1989).
10. Blackley, W.S. and Scattergood, R.O., Ductile-regime machining mode for diamond turning of brittle materials, *Prec Engg*, 13, 2 (1991) 95.
11. Bifano, T.G. and Fawcett, S.C., Specific grinding energy as an in process control variable for ductile-regime grinding, *Prec Engg*, 13, 4 (1991) 256.
12. Sagawa, K. and Eda, H., Investigation of the ductile-mode grinding of ceramics, *Bull JSME* (in Japanese) (1991).
13. Eda, H. et al., Development of multi-purpose ductile-regime machining system for ceramics and glasses, *J JSPE* (in Japanese), 62, 2 (1996) 236.
14. Chouanine, L., Eda, H., and Shimizu, J., Development of key-technology on the state-of-art machine tool and generalization of grinding forces under ductile mode grinding experiments, *Int J JSPE*, 32, 2 (1998) 98.
15. Tomita, Y. and Eda, H., Development of new bonding materials for fixed abrasive of grinding stone instead of free abrasives processing, *Bull JSPE* (in Japanese), 61, 10 (1995) 1428.
16. Lawn, B.R. and Swain, M.V., Microfracture beneath point indentations in brittle solids, *J Mater Sci*, 10 (1975) 113.
17. Eda, H. Ed., *Design and Manufacture of Ultra Precision Machine Tool*, Kogyo-chosakai Press Co (in Japanese) (1993) 75.
18. Chouanine, L. and Eda, H., Sub-nanometer precision grinding of optical and electron glasses under ductile-regime conditions, *Proc 4th Int Conf UME*, Braunschweig (1997, 5) 351.
19. Eda, H. et al., Study on giant magnetostriction actuator—Development of device with high power and ultra precision positioning, *Bull JSPE* (in Japanese), 57, 3 (1991) 532.
20. Takeuchi, Y., Sawada, K., and Sata, T., Ultra-precision 3-D micromachining of glass, *Annu CIRP*, 45, 1 (1996) 401.
21. Takeuchi, Y. and Sawada, K., Three dimensional micromachining by means of ultraprecision milling, *Proc 4th Int Conf UME*, Braunschweig (1997, 5) 596.
22. Sawada, K. and Takeuchi, Y., *Ultraprecision Machining Center and Micromachining*, Published by Nikkan-kogyo-shinbun (in Japanese) (1998).

2

Ductile-Mode Ultra-Smoothness Grinding of Fine Ceramics with Coarse-Grain-Size Diamond Wheels

H. Yasui

CONTENTS

2.1 Introduction

Fine ceramics have recently been used increasingly as structural and functional components such as high-quality components of equipments and machines because of their excellent mechanical, electrical, and optical properties. To make use of such properties as value-added elements, they should be machined with high surface smoothness and quality.

Grinding operation is one of the most effective methods used for high smoothness machining of fine ceramics. It is difficult, however, to achieve crack-free high smoothness surfaces by ductile-mode grinding because of their mechanical properties of high brittleness [1]. Therefore, it is necessary

to select suitable grinding conditions for ductile-mode grinding. Some researchers [2,3] report ductile-mode grinding with a wheel of grain size finer than #1500-mesh (about 10 μm in grain diameter). The truing and dressing techniques for the fine grain-sized wheel, however, are difficult. In addition, the depth of cut and table speed are also limited to a certain small range because the active grain is thrown off easily from the wheel surface by small grinding force. Therefore, the problems of poor productivity and high grinding costs still remain. If a coarse-grain-size wheel like the #140 mesh wheel (about 100 μm in grain diameter) is used in ductile-mode grinding of fine ceramics, significant improvement in productivity and high reduction in grinding cost can be expected for high smoothness grinding.

This chapter introduces that the coarse #140-mesh diamond wheel can be used for ultra-smoothness grinding of fine ceramics. First of all, we discuss that ductile-mode grinding of fine ceramics with the coarse #140-mesh metal-bonded diamond wheel is possible because of the experimental relationship between the table speed and the ground workpiece surface. Second, the influence of the speed of the wheel and the workpiece material on ductile-mode grinding is explained. Finally, the newly developed ductile-mode ultra-smoothness grinding method with coarse-grain-size wheel, in which the resultant surface roughness is below about 10 nm (P-V) and 1 nm (RMS), is introduced.

2.2 Ductile-Mode Grinding with #140 Mesh Wheel

2.2.1 Experimental Procedure

Experiments were conducted by plunge grinding with a conventional surface grinder (Figure 2.1). The experimental conditions are summarized in Table 2.1. The metal-bonded diamond wheels of coarse grain size of #140 mesh and #800 mesh are used for examining the possibility of ductile-mode grinding of fine ceramics with the coarse-grain-size wheel. The concentration of wheels used is 50, which is considerably lower than that employed in usual grinding operations. The table speed and the wheel speed range from 0.05 mm/sec to 150 mm/sec and from 20 m/sec to 85 m/sec, respectively. The fine ceramics used are hot pressed silicon carbide (HPSC), normally sintered silicon carbide (SSC), hot isostatic pressed silicon nitride (HIPSN), and normally sintered silicon nitride (SSN).

In the experiments, the working surface of the wheel is controlled so as to hold the wheel surface constant, by slightly truing and dressing of the wheel or grinding of the workpiece. The Nomarski differential interference microscope and stylus profilometer are set up on the grinder head as shown in Figure 2.2 for observing the abrasive grains on the wheel surface and

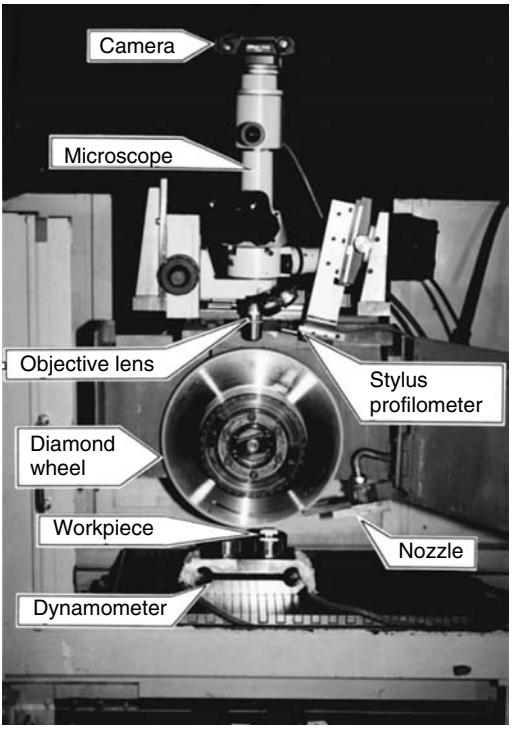

FIGURE 2.1
View of surface grinder.

measuring the topography of the wheel surface, respectively. The rotary encoder and the position scale are also assembled additionally to the wheel spindle and wheel cover to measure the same wheel surface. Hence, stable grinding is maintained by the measuring system. The ground workpiece surface is observed by the Nomarski microscope and the scanning electron

TABLE 2.1

Experimental Conditions

Wheel	SD140Q50M SD800Q50M
Workpiece	SSN (HV:1600) HIPSN (HV:2400) HPSC (HV:3300) SSC (HV:2500)
Wheel speed	$V_g = 20$–85 m/sec
Table speed	$v_w = 0.05$–150 mm/sec
Depth of cut	$t_t = 5$ μm
Coolant	Soluble (1/50) Flow rate: 12 L/min

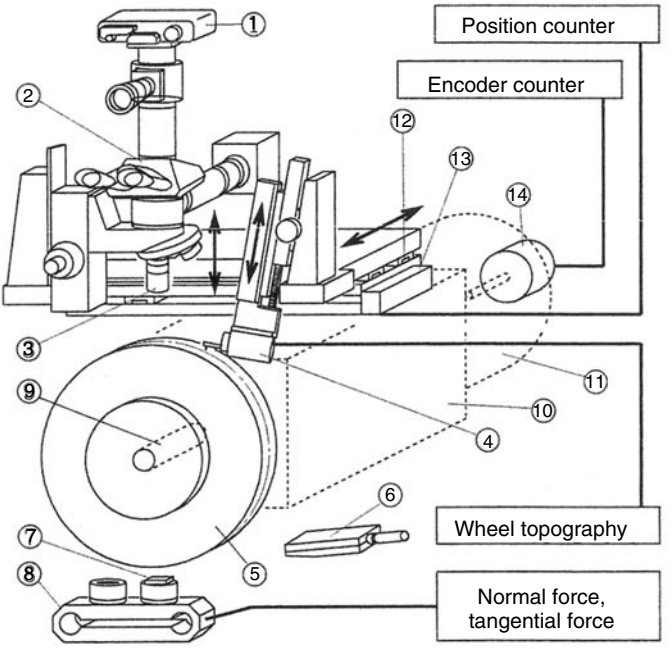

1. Camera 2. Microscope 3. Objective lens 4. Stylus profilometer
5. Grinding wheel 6. Nozzle 7. Workpiece 8. Dynamometer 9. Spindle
10. Head 11. Motor 12. Cross roller guide 13. Position scale
14. Rotary encoder

FIGURE 2.2
Experimental arrangement.

microscope (SEM). The surface roughness of the ground workpiece is measured with the ordinal stylus profilometer, the three-dimensional surface interferometer (WYKO TOPO-3D), and the atomic force microscope (AFM). In the case of profilometry, the measuring area is monitored by a CCD camera as shown in Figure 2.3 so that the relation between the stylus scanning direction and grinding direction is correctly adjusted [4].

2.2.2 Influence of the Table Speed

Figure 2.4 shows the microscopic and SEM photographs of the HPSC surface ground at $v_w = 0.05$ mm/sec, 0.5 mm/sec, and 5 mm/sec under a wheel speed of $V_g = 20$ m/sec with the #140-mesh wheel. From the figure, the grinding cracks are observed on the workpiece surfaces ground at $v_w = 5$ mm/sec and $v_w = 0.5$ mm/sec though the ductile-mode grinding area is

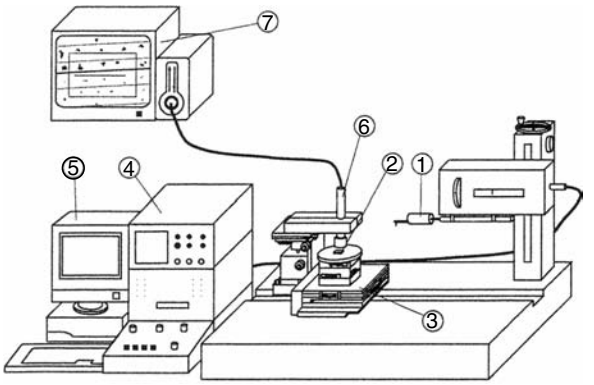

1. Stylus 2. Specimen 3. XTθ – stage 4. Profilometer
5. Personal computer 6. CCD camera 7. Monitor

FIGURE 2.3
Stylus profilometer.

also observed on both workpiece surfaces. The ductile-mode ground area at $v_w = 0.5$ mm/sec is much more than $v_w = 5$ mm/sec. At the slowest table speed of 0.05 mm/sec in the experiment, the smooth ductile-mode ground surface without grinding cracks, on the other hand, is obtained all over the entire observed workpiece area. The whole ground workpiece area of 10 mm^2, which is furthermore observed widely, however, is also found to be ductile-mode ground surface. Therefore, the grinding cracks are considered to decrease with the decrease in table speed.

A WYKO 3D image of 256 μm^2 of HPSC surface ground at $v_w = 0.05$ mm/sec is shown in Figure 2.5. From the figure, it is found that the ground workpiece surface consists of regular grinding grooves parallel to the grinding direction. The height and pitch of the grinding groove are about 200 nm (P-V) and below about 100 μm, respectively. The surface roughness in the 3D image is about 200 nm (P-V), 40 nm (RMS), and 30 nm (R_a). Therefore, the maximum 3D surface roughness formed by plunge ductile-mode grinding is considered to be mainly related to the height of grinding grooves.

Figure 2.6 shows an AFM 3D image and 2D profile of 50 μm^2 of HPSC surface ground at $v_w = 0.05$ mm/sec. The 2D profile is an example of surface roughness parallel to grinding direction, including the large microhole. In the 3D image, the surface is depicted inversely so that the concave on the surface is displayed the convex upside down to observe clearly the microhole formed on the ground workpiece surface. From the figure, it is clear in the measurement of AFM accuracy order that the observed workpiece area consists of almost ductile-mode ground surface though there are some microholes of the size 1–3 μm and below the depth of about 50 nm. The microholes are estimated to be pores in the workpiece itself or fracture traces of fragile portions inside the workpiece material.

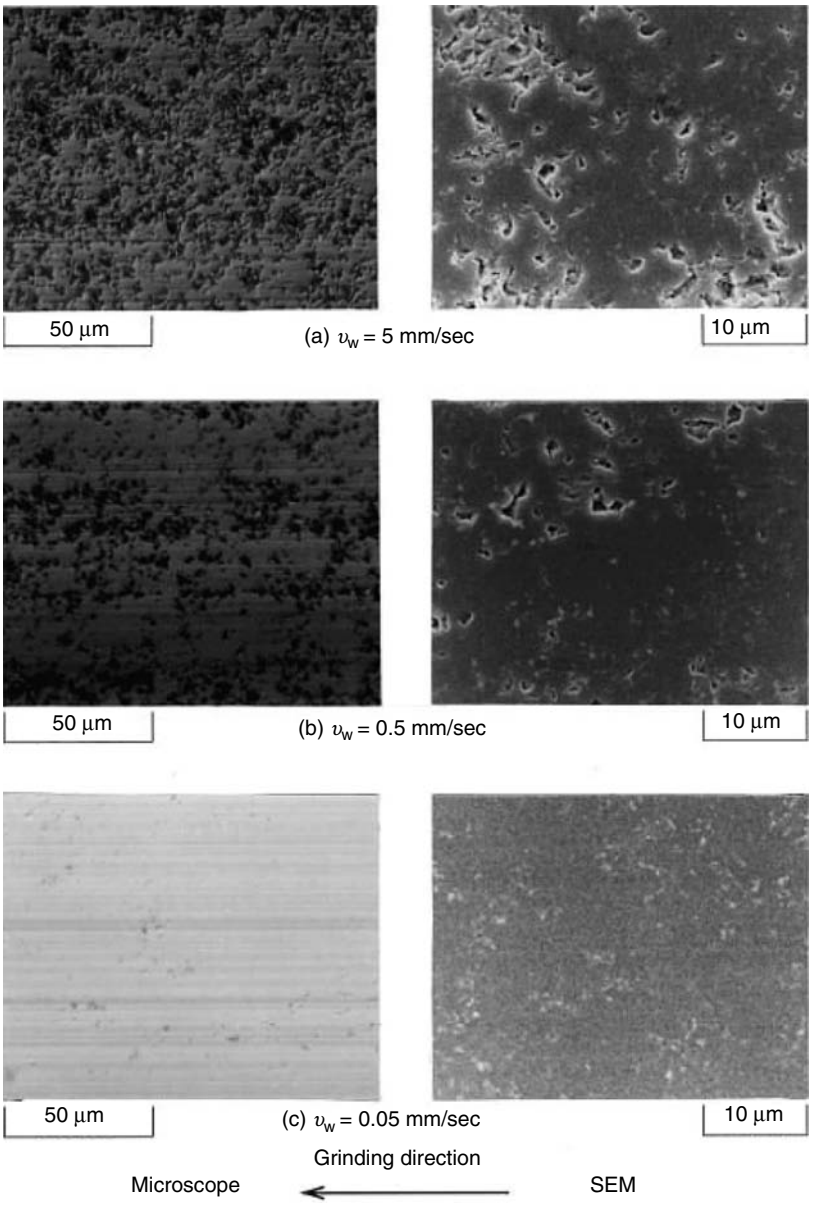

FIGURE 2.4
Microscopic and SEM photographs of the HPSC surfaces ground at three kinds of table speeds with the #140-mesh wheel [SD140Q50M, $V_g = 20$ m/sec, $t_t = 5$ μm, Soluble (1/50)].

Considering the results mentioned above, ductile-mode grinding with the #140-mesh wheel of low concentration of 50 is possible in the plunge grinding of HPSC ceramic with a conventional surface grinder. Nevertheless,

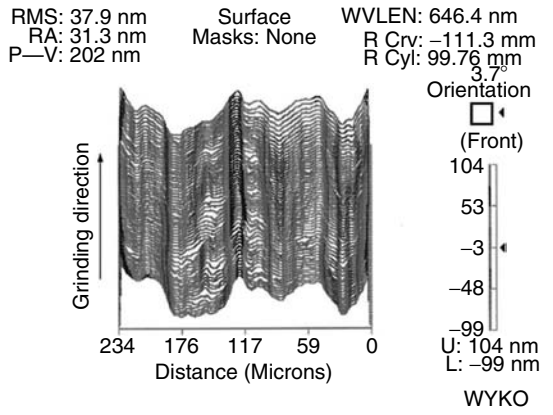

FIGURE 2.5
A WYKO 3D image of the HPSC surface ground at $\nu_w = 0.05$ mm/sec with the #140-mesh wheel [SD140Q50M, $V_g = 20$ m/sec, $t_t = 5$ μm, Soluble (1/50)].

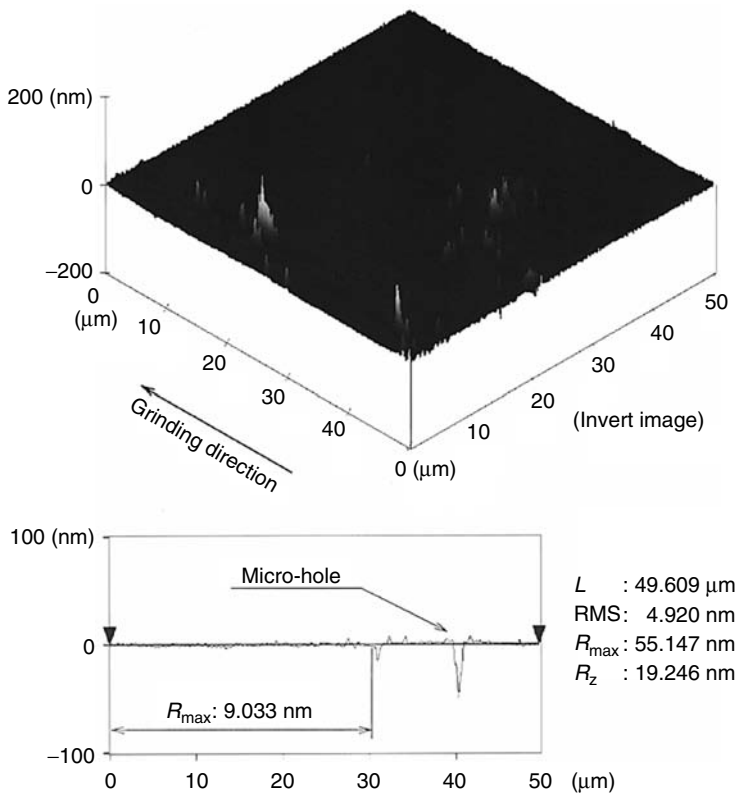

FIGURE 2.6
An WYKO 3D image of the HPSC surface ground at $\nu_w = 0.05$ mm/sec with the #140-mesh wheel [SD140Q50M, $V_g = 20$ m/sec, $t_t = 5$ μm, Soluble (1/50)].

it is generally assumed that a coarse-grain-size diamond wheel like the #140-mesh wheel cannot be used for ductile-mode grinding of fine ceramics.

The microscopic and SEM photographs of the HPSC surface ground at $v_w = 0.05$ mm/sec and 5 mm/sec with the #800-mesh wheel are shown in Figure 2.7. It is obvious from the figure that in the case of the #800-mesh wheel as well as the #140-mesh wheel as shown in Figure 2.4, the smooth ductile-mode ground area is more for a slower table speed. Compared with the workpiece surface ground with the #140-mesh wheel as shown in Figure 2.4, however, more grinding cracks caused by brittle fracture are observed on both workpiece surfaces ground at $v_w = 0.05$ mm/sec and 5 mm/sec.

Figure 2.8 shows randomly sampled parts of the same circumferential surface profiles of the #140-mesh and #800-mesh wheels before and after grinding. Those #140-mesh and #800-mesh wheels are the same wheels used for obtaining the results as shown in Figure 2.4 and Figure 2.7. It should be noted that the horizontal scale for the #140-mesh wheel is expressed four

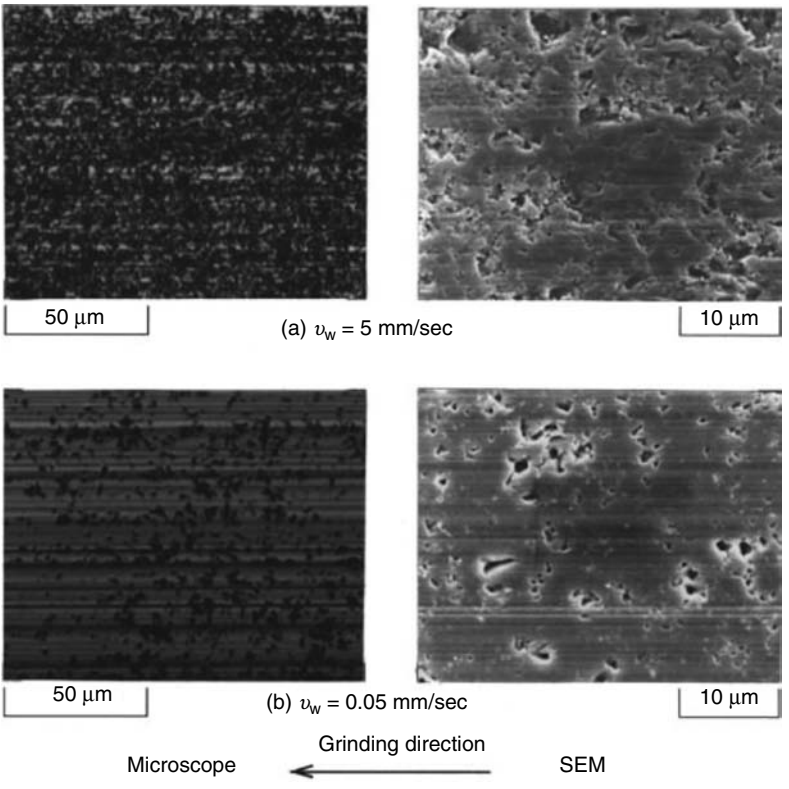

FIGURE 2.7
Microscopic and SEM photographs of the HPSC surfaces ground at $\nu_w = 0.05$ mm/sec and 5 mm/sec with the #800-mesh wheel [SD800Q50M, $V_g = 20$ m/sec, $t_t = 5$ μm, Soluble (1/50)].

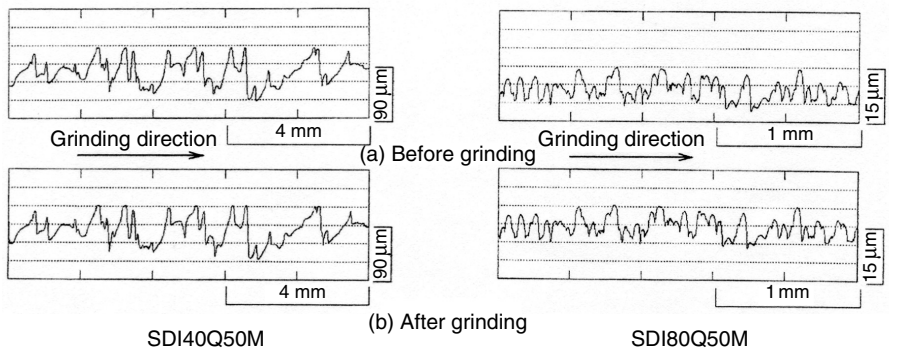

FIGURE 2.8
Comparison of the surface profile of the #140-mesh wheel with #800-mesh wheel before and after grinding.

times as long as that of the #800-mesh wheel. From the figure, profiles of the #140-mesh and #800-mesh wheels are not found to change with grinding; therefore, stable grinding seems to be maintained. The cutting edge distribution of the #800-mesh wheel is much closer than that of the #140-mesh wheel. Therefore, the grain depth of cut of the #140-mesh wheel becomes geometrically deeper than that of the #140-mesh wheel. The reason why the smooth ductile-mode ground surface is obtained more easily with the coarse #140-mesh wheel than the fine #800-mesh wheel cannot be explained on the basis of a consideration of grain depth of cut because ductile-mode grinding is considered more difficult for deeper grain depth of cut.

Typical microscopic images of the cutting edges on the #140-mesh and #800-mesh wheel surfaces are represented in Figure 2.9. Compared with the

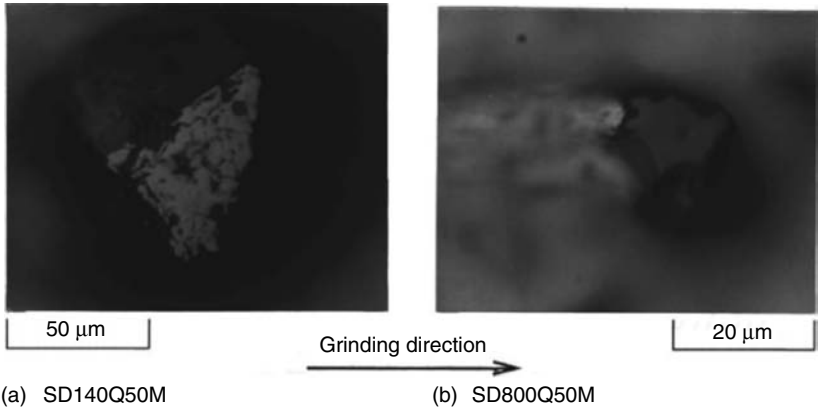

FIGURE 2.9
Typical microscopic appearances of the wear land of cutting edges on the #140-mesh and #800-mesh wheel surfaces.

#800-mesh wheel, the cutting edge of the #140-mesh wheel has large wear land of 50 μm width. It may be reasonable to say that the thermal aspect depending on the wear land of cutting edge has a considerable effect on the ductile-mode grindability of HPSC ceramic. In other words, large grain can have a large flat wear land to raise the grinding temperature higher near the grain-work interference zone due to the sliding and plowing action. Therefore, it is inferred that softening or relaxation of brittleness of the material takes place and the ductile flow occurs easily.

Figure 2.10 shows the relationship between Vickers hardness HV of the ground HPSC surface and the table speed for the #140-mesh and #800-mesh wheels. In the figure, the hardness after lapping is also expressed for comparison. The measurement, however, is carried out for the ductile-mode ground surface. In the measurement of the Vickers hardness, the indentation load is set 200 g so that no cracks are generated by loading. In Figure 2.10, the depth of indentation is about 1.5 μm. It can be seen from the figure that the surface hardness for the #800-mesh wheel after grinding is almost the same as that after lapping, whereas the hardness for the #140-mesh wheel decreases largely for a slower table speed. Considering the results as shown in Figure 2.4, Figure 2.7, and Figure 2.10, it is inferred that the material in the grinding zone is more or less softened and plastically deformed due to the grinding heat generated by the cutting edges of large wear land on the #140-mesh wheel surface.

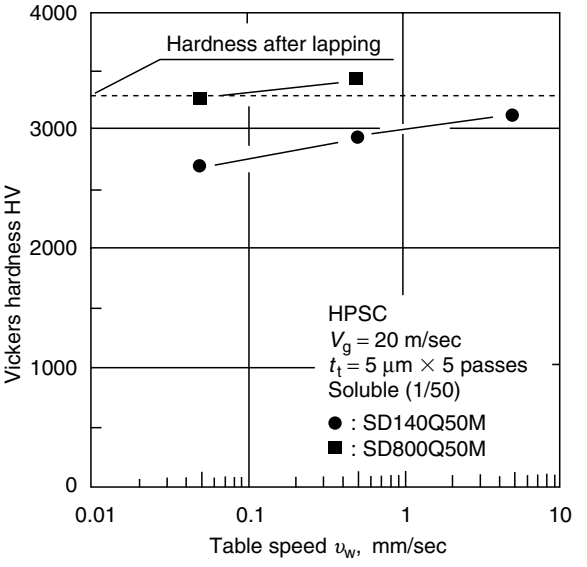

FIGURE 2.10
Relationship between the ground HPSC surface hardness and the table speed.

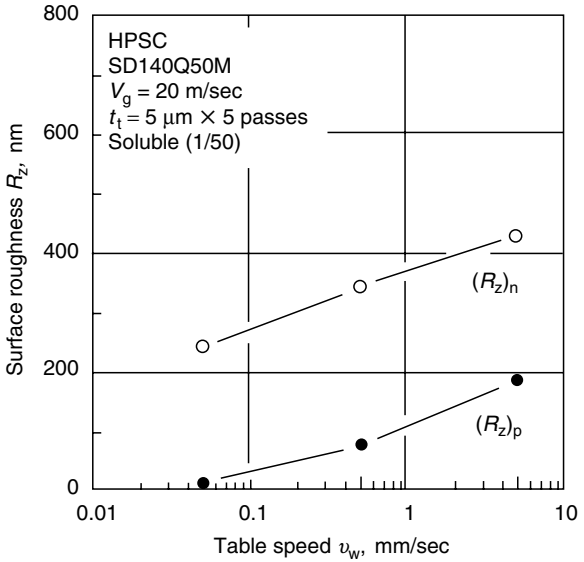

FIGURE 2.11
Relationship between the ground HPSC surface roughness and the table speed.

The relationship between the surface roughness R_z and the table speed v_w for the #140-mesh wheel is shown in Figure 2.11. Here, $(R_z)_p$ and $(R_z)_n$ in the figure denote the surface roughness parallel and normal to the grinding direction, measured with the stylus profilometer, respectively. The reference lengths of $(R_z)_p$ and $(R_z)_n$ are 250 μm and 800 μm, respectively. The plotted data are average values of 10 points. It is obvious from the figure that the values of $(R_z)_n$ are considerably larger than those of $(R_z)_p$ in the whole range of table speed because of the formation of relatively high grinding grooves, as shown in Figure 2.4. The height of the grinding groove is determined to some degree by the cutting edge distribution on the wheel surface in the case of ductile-mode grinding, so $(R_z)_n$ tends to be limited to a certain value. On the whole, $(R_z)_n$ decreases from about 500 nm to 200 nm in this experiment as the table speed decreases from $v_w = 5$ mm/sec to 0.05 mm/sec. $(R_z)_p$, on the other hand, decreases from about 200 nm to 20 nm. In any case, $(R_z)_p$ below 20 nm is easily obtainable at extremely slow table speed for grinding of HPSC ceramic with the #140-mesh wheel.

2.2.3 Influence of the Wheel Speed

The HPSC surfaces ground at four kinds of table speeds of $v_w = 0.05$ mm/sec, 0.5 mm/sec, 5 mm/sec, and 50 mm/sec for the wheel speed of $V_g = 20$ m/sec and 85 m/sec are compared photographically in Figure 2.12. It is clear from

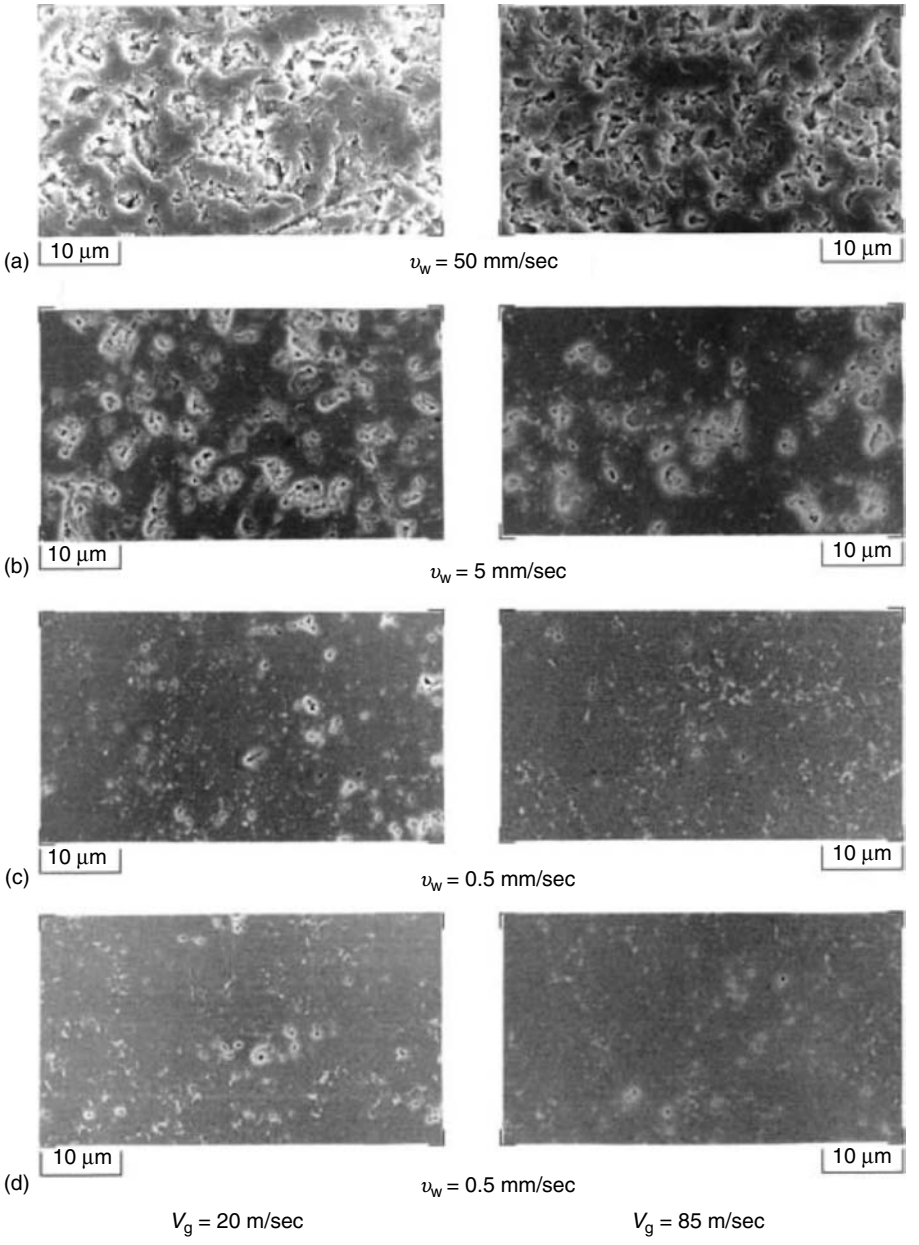

FIGURE 2.12
SEM photographs of the HPSC surfaces ground at $V_g = 20$ m/sec and $V_g = 85$ m/sec with the #140-mesh wheel [SD140Q50M, $t_t = 5$ μm, Soluble (1/50)].

the figure that in the case of both wheel speeds, the grinding cracks decrease as the table speed decreases. The smooth ductile-mode ground surface without grinding cracks over the entire observed workpiece area is obtained at the table speed of $v_w = 0.5$ mm/sec and 0.05 mm/sec under $V_g = 85$ m/sec, whereas only $v_w = 0.05$ mm/sec under $V_g = 20$ m/sec. The critical table speed at which the whole workpiece surface is formed by ductile-mode grinding is much faster for $V_g = 85$ m/sec than for $V_g = 20$ m/sec. This means that the occurrence of more grinding heat at $V_g = 85$ m/sec influences easier ductile-mode grinding.

Figure 2.13 shows a WYKO 3D image and 2D profile of HPSC surface ground at $v_w = 0.05$ mm/sec under $V_g = 85$ m/sec. The 2D profile is for a

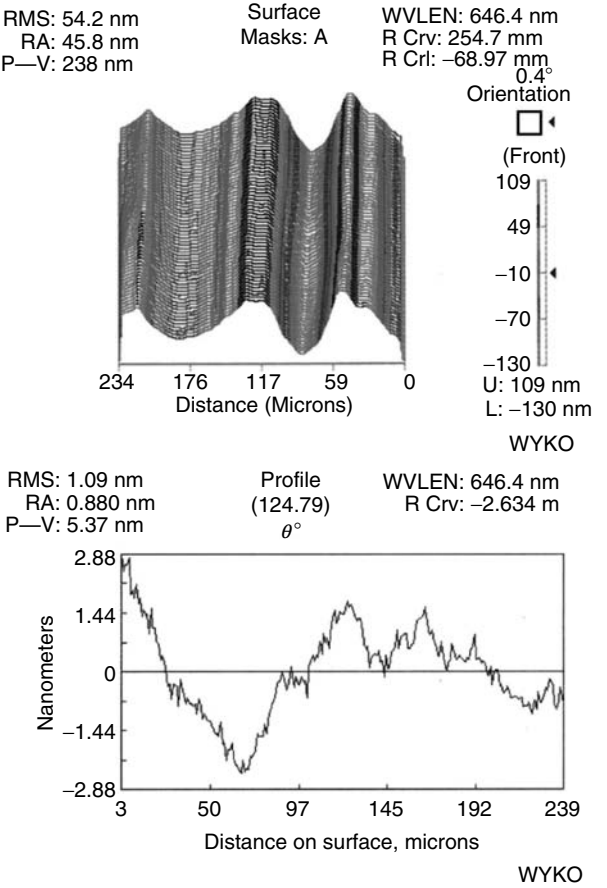

FIGURE 2.13
A WYKO 3D image and 2D profile of the HSPC surface ground at $\nu_w = 0.05$ mm/sec under $V_g = 85$ m/sec with the #140-mesh wheel [SD140Q50M, $V_g = 20$ m/sec, $t_t = 5$ μm, Soluble (1/50)].

sample of the surface roughness parallel to the grinding direction. From the 3D image, it is clear that the ground surface under $V_g = 85$ m/sec as well as $V_g = 20$ m/sec, as shown in Figure 2.5, consists of grinding grooves parallel to the grinding direction. The height and pitch of grinding grooves are almost the same as $V_g = 20$ m/sec; that is, about 200 nm (P-V) and below about 100 μm, respectively. The surface roughness in the 3D image is about 200 nm (P-V). From the 2D profile, on the other hand, it is found that the parallel surface roughness is about 5 nm (P-V), 1 nm (RMS), and 0.9 nm (R_a), corresponding to the ultra-smoothness surface roughness.

Figure 2.14 shows the relationship between the surface roughness and the table speed for wheel speeds of $V_g = 20$ m/sec, 50 m/sec, and 85 m/sec. From the figure, the relationship between normal roughness $(R_z)_n$ and the table speed is found to be almost the same for the three wheel speeds. This means that wheel speed has little influence on the height of the grinding groove.

As for the parallel roughness $(R_z)_p$, on the other hand, the quantitative relationship between the $(R_z)_p$ and the table speed is different with the wheel speed though the $(R_z)_p$ in each wheel speed decreases qualitatively as the table speed decreases. $(R_z)_p$ at the same table speed is smaller for a higher wheel speed. In particular, the difference in $(R_z)_p$ between the wheel speeds is remarkable at slower table speeds. In the case of $V_g = 85$ m/sec, $(R_z)_p$ attains about 10 nm (R_z) at $v_w = 0.5$ mm/sec of the measuring limit of the profilometer. The attainable table speed is faster than that in the case of lower wheel speeds of $V_g = 20$ m/sec and 50 m/sec.

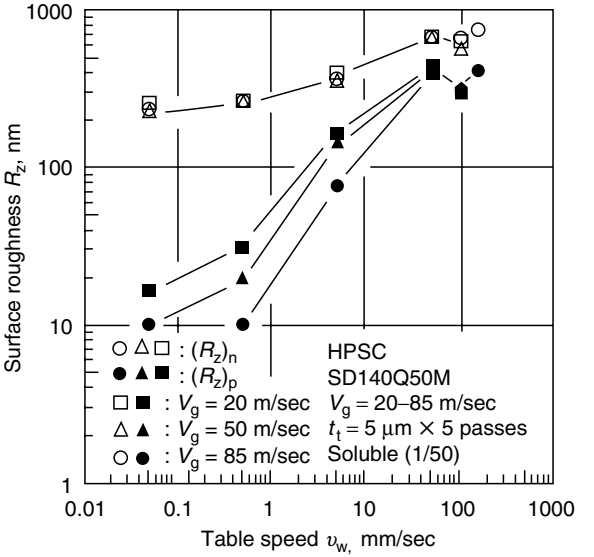

FIGURE 2.14
Influence of the wheel speed on the surface roughness.

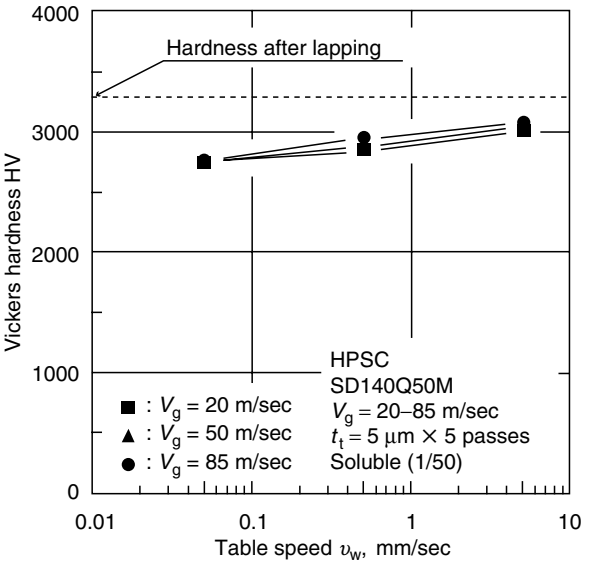

FIGURE 2.15
Influence of the ground workpiece hardness on the wheel speed.

Figure 2.15 shows the relationship between the hardness of the ductile-mode ground HPSC surface layer and the table speed for the wheel speed of $V_g = 20$ m/sec, 50 m/sec, and 80 m/sec. As shown in the figure, the wheel speed has little influence on the hardness of the ductile-mode ground surface.

2.2.4 Influence of the Workpiece Material

The surface roughness and quality of ground ceramics depend not only on the material properties of the powder but also on the sintering methods. The SEM photographs of the SSC and HPSC surfaces ground at $v_w = 0.05$ mm/sec, 0.5 mm/sec, 5 mm/sec, and 50 mm/sec under the wheel speed of 20 m/sec with the #140-mesh wheel are shown in Figure 2.16. It is found from the figure that grinding cracks in the case of the SSC ceramic decrease in the same manner as in the case of the HPSC ceramic, with the decrease in table speed. However, many more grinding cracks are observed than in the case of HPSC ceramic. Especially, even at $v_w = 0.05$ mm/sec, SSC ceramic has many grinding cracks whereas HPSC ceramic has few cracks. In the case of HPSC ceramic, the relatively good surface is considered to be obtained because of its closed crystallite structure and its high strength. SSC ceramic, on the other hand, has a few pores in itself; therefore, macroscopic brittle fracture occurs. This porosity of SSC ceramic also causes the deterioration of the ground surface smoothness.

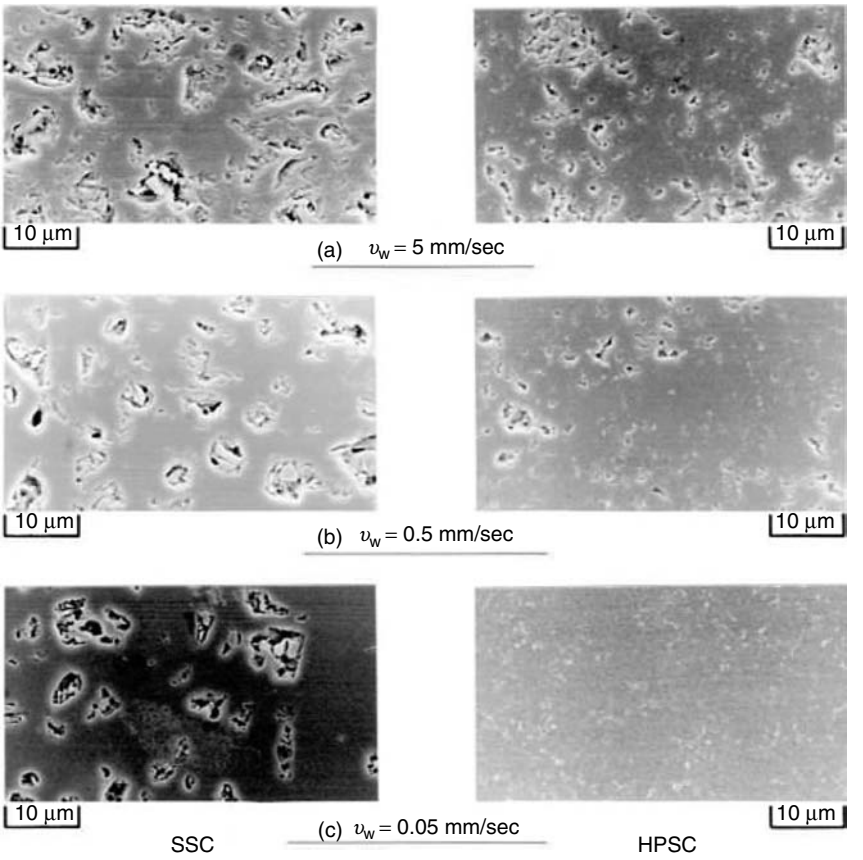

FIGURE 2.16
Comparison of the SSC surface with the HPSC surface ground with the #140-mesh wheel [SD140Q50M, $V_g = 20$ m/sec, $t_t = 5$ μm, Soluble (1/50)].

Figure 2.17 shows the relationship between the surface roughness and the table speed for HPSC and SSC ceramics. From the figure, it is obvious that the surface roughness of both ceramics decreases as the table speed decreases. Compared with HPSC ceramic, the surface roughness of SSC ceramic is considerably high because of the grinding cracks, as shown in Figure 2.16.

Figure 2.18 shows the SEM photographs of the HIPSN surface ground at $v_w = 0.05$ mm/sec, 0.5 mm/sec, and 5 mm/sec under $V_g = 20$ m/sec with the #140-mesh and #800-mesh wheels. As shown in the figure, at the higher table speed of 5 mm/sec, grinding grooves with several grinding cracks are found on the workpiece surfaces ground with both #140-mesh and #800-mesh wheels. At the table speed of below 0.5 m/sec, however, few grinding grooves are observed on the surface, whereas a flat area or grinding cracks are observed. This means that the grooves of HIPSN ceramic are not

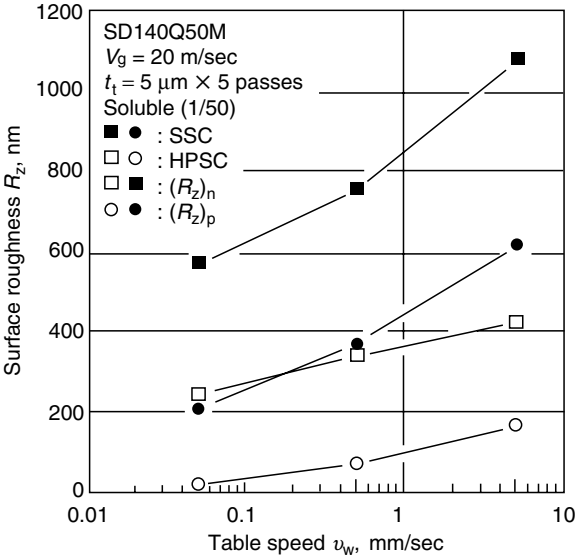

FIGURE 2.17
Difference between the surface roughnesses of the HPSC and SSC ceramic ground with the #140-mesh wheel.

formed at slow table speed because of little pile-up of the workpiece material. The grinding cracks and the ductile-mode ground area are less and more for slower table speed, respectively. At $v_w = 0.5$ mm/sec and 5 mm/sec, fewer grinding cracks are found with the #140-mesh wheel than with the #800-mesh wheel. At the slowest table speed of $v_w = 0.05$ mm/sec, with the #140-mesh wheel, the smooth ductile-mode ground surface without grinding cracks is obtained over the observed workpiece area. In the case of the #800-mesh wheel, on the contrary, numerous grinding cracks are observed at the slowest table speed of $v_w = 0.05$ mm/sec. According to the results mentioned above, a smooth ductile-mode ground HIPSN surface is obtained more easily with the coarse #140-mesh wheel than the fine #800-mesh wheel.

A WYKO 3D image and 2D profile of the crack-free HIPSN surface in Figure 2.18 ($v_w = 0.05$ mm/sec, #140 wheel) are shown in Figure 2.19. The 2D profile is for a sample of surface roughness parallel to the grinding direction. It is found from the figure that the 3D surface roughness is about 190 nm whereas the 2D surface roughness parallel to the grinding direction is below 10 nm (P-V) corresponding to the ultra-smoothness surface roughness.

Figure 2.20 represents a closeup AFM 3D image and 2D profile of 50 μm^2 of the HIPSN surface ground at the same grinding condition as shown in Figure 2.19. The 2D profile is for a sample of surface roughness parallel to the grinding direction, including a large microhole of several μm diameter, which is also seen in HPSC ceramic. The microroughness excluding the

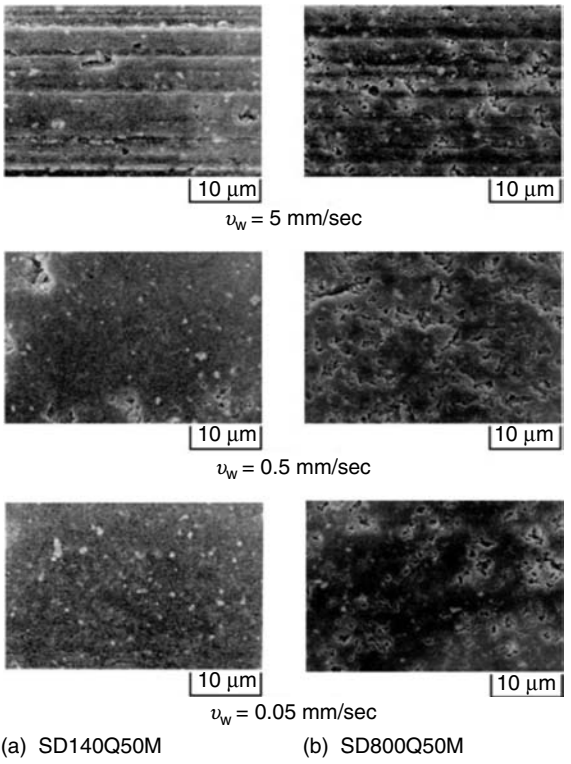

FIGURE 2.18
Influence of the table speed and wheel grain size on the ground HIPSN surface [$V_g = 20$ m/sec, $t_t = 5$ μm, Soluble (1/50)].

microholes, which are considered to be pores in HIPSN itself or fracture traces of fragile portions inside HIPSN, becomes very smooth.

Thus, a smooth ductile-mode ground surface can also be obtained with plunge grinding of HIPSN ceramic with the coarse #140-mesh wheel.

2.3 Ultra-smoothness Grinding

2.3.1 Ultra-smoothness Grinding Method

As stated above, ductile-mode grinding of fine ceramics is possible with plunge grinding with the coarse #140-mesh grain-size diamond wheel. The 3D surface roughness in ductile-mode plunge grinding, however, is limited

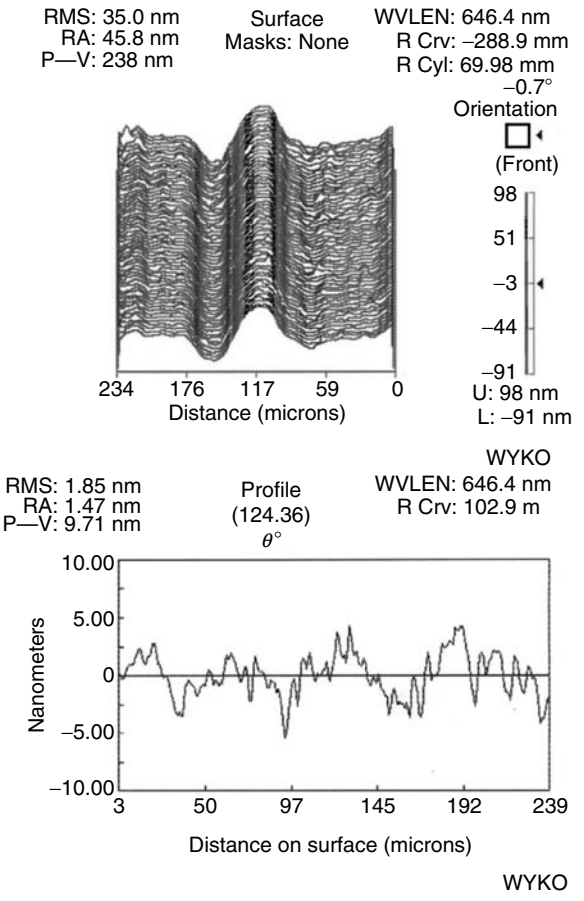

FIGURE 2.19
A WYKO 3D image and 2D profile of the HIPSN surface ground at $\nu_w = 0.05$ mm/sec with the #140-mesh wheel [SD140Q50M, $V_g = 20$ m/sec, $t_t = 5$ μm, Soluble (1/50)].

to about 200 nm (R_{max}) in the above-mentioned experiments because of the formation of grinding grooves. The 3D surface roughness of 200 nm (R_{max}) is much better than the well-known data obtained in the usual grinding operation. However, the ultrasmooth roughness below 10 nm (R_{max}), which is almost the same as that after lapping, could not be obtained in plunge grinding. To obtain ultra-smoothness roughness with the coarse-grain-size wheel, it is necessary to diminish and remove the grinding grooves.

Now, the ultra-smoothness grinding method has been newly devised [5,6]. The schematic of the new method is shown in Figure 2.21. In the method, the workpiece is fed simultaneously toward the directions normal and parallel to the grinding direction. The method is different from the usual traverse surface grinding in which the crossfeed normal to the grinding direction is

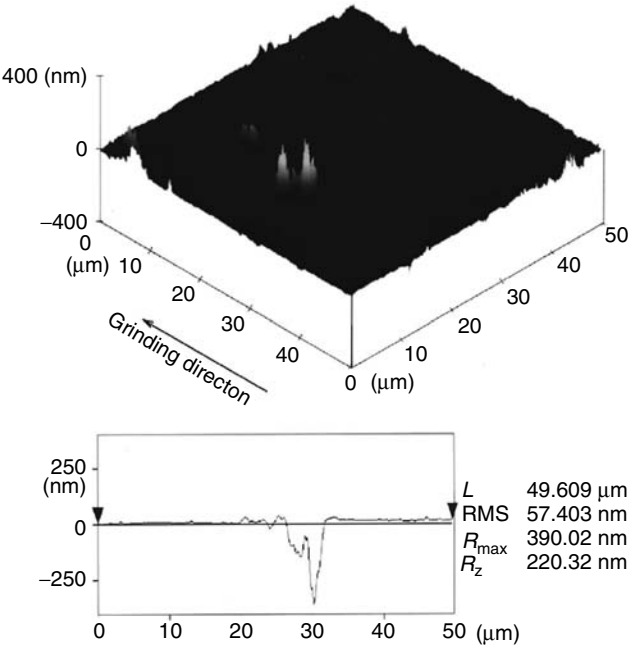

FIGURE 2.20
A closeup AFM 3D image and 2D profile of the HIPSN surface ground at $v_w = 0.05$ mm/sec with the #140-mesh wheel [SD140Q50M, $V_g = 20$ m/sec, $t_t = 5$ μm, Soluble (1/50)].

done after grinding the whole width of the workpiece in a pass or stroke of the table. In the method, the crossfeed $(v_w)_n$ normal to the grinding direction is faster than the plunge feed $(v_w)_p$ parallel to the grinding direction. The experiments are carried out with the NC grinding machine as shown schematically and photographically in Figure 2.22 and Figure 2.23, respectively.

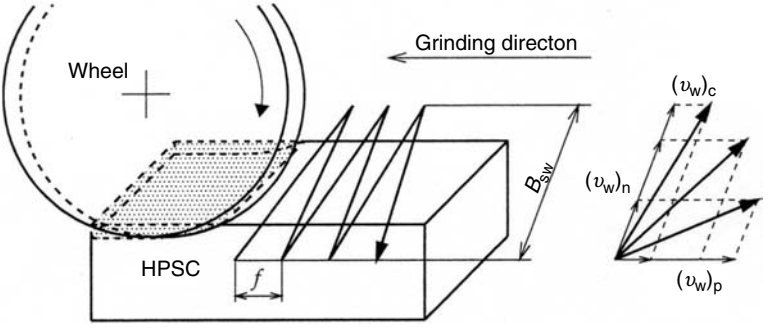

FIGURE 2.21
Ultra-smoothness grinding method.

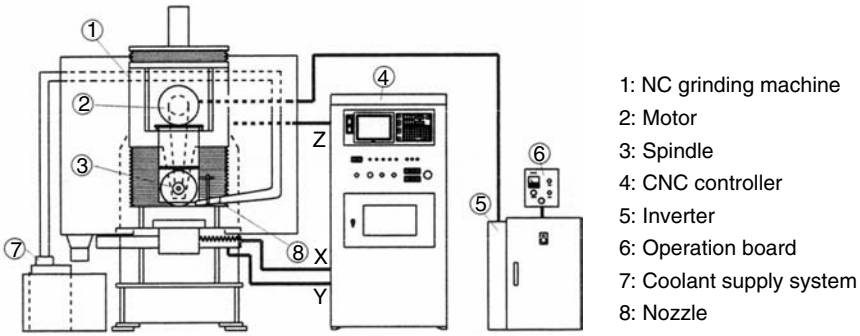

FIGURE 2.22
Schematic diagram of NC grinding machine.

In the experiments, $(v_w)_n$ and $(v_w)_p$ are set by determining the resultant feed $(v_w)_c = \{(v_w)_n + (v_w)_p\}^{\frac{1}{2}}$, crossfeed width B_{sw} and feed width f. The machine is reconstructed with a conventional NC equipment, which has an accuracy of 1 μm for each movement of the X, Y, and Z directions. The experimental conditions are summarized in Table 2.2.

2.3.2 Ultra-smoothness Grinding Results

Figure 2.24 shows the microscopic photographs of the HPSC surface ground at $(v_w)_c = 3.33$ mm/sec with the #140-mesh wheel. From the figure, it is

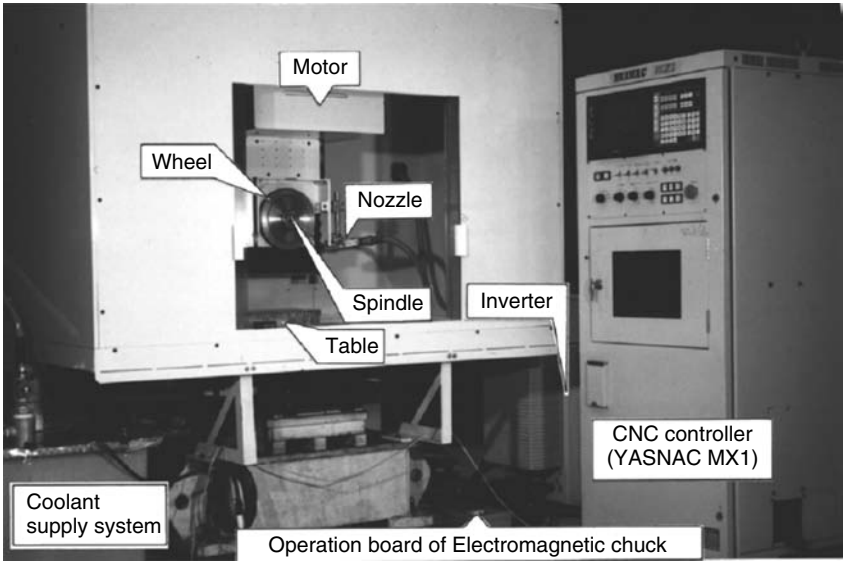

FIGURE 2.23
Appearance of NC grinding machine.

TABLE 2.2

Ultra-smooth Grinding Experimental Conditions

Grinding Method	Ultra-smoothness
Wheel	SD140Q50M
Workpiece	HPSC (HV:3300)
Wheel speed	$V_g = 20$ m/sec
Resultant feed	$(v_w)_c = 3.33$ mm/sec
Crossfeed width	$B_{sw} = 18$ mm
Plunge feed	$f = 20$ μm/stroke
Depth of cut	$t_t = 2$ μm
Coolant	Soluble (1/50)
	Flow rate: 12 L/min

obvious that no grinding cracks and no grinding grooves are found over the observed workpiece area.

Figure 2.25 shows a WYKO 3D image of 256 μm^2 of HPSC surface ground at $(v_w)_c = 3.33$ mm/sec. From the figure, it is found that the workpiece surface is not formed by continuous regular grooves as shown in Figure 2.5 but by some discontinuous short grinding grooves. The 3D surface roughness is about 26 nm (P-V), 3.7 nm (RMS), and 3 nm (R_a), corresponding to near ultra-smoothness surface roughness. The height of the grinding groove is considered to be below about 26 nm (P-V), which is much lower than that in the plunge ductile-mode grinding as shown in Figure 2.5. The pitch of the grinding groove is also not regular as observed

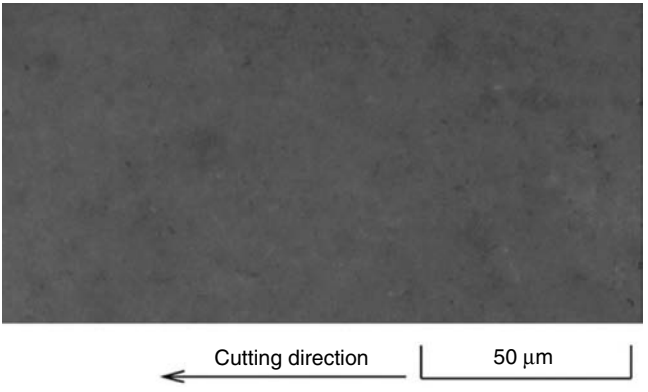

FIGURE 2.24
Microscopic photograph of the HPSC surface ground at $(v_w)_c = 3.33$ mm/sec with the #140-mesh wheel by ultra-smoothness grinding method [SD140Q50M, $V_g = 20$ m/sec, $t_t = 5$ μm, Soluble (1/50)].

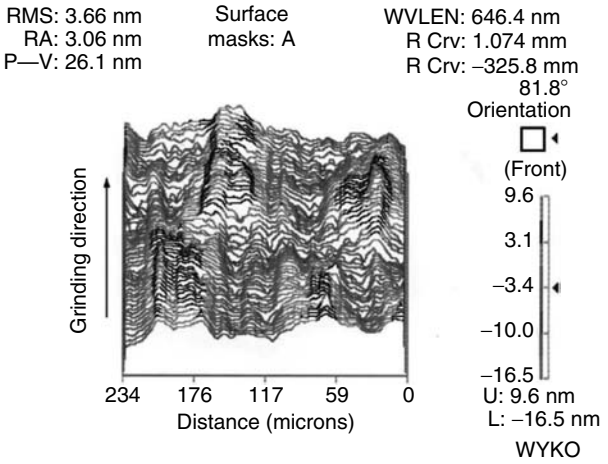

FIGURE 2.25
A WYKO 3D image of the HPSC surface ground at $(\upsilon_w)_c = 3.33$ mm/sec with the #140-mesh wheel by ultra-smoothness grinding method [SD140Q50M, $V_g = 20$ m/sec, $t_t = 5$ μm, Soluble (1/50)].

in plunge grinding. Consequently, the grinding grooves are considered to be removed to some extent.

Figure 2.26 shows an AFM 3D image and 2D profiles of 50 μm^2 of HPSC surface ground at $(v_w)_c = 3.33$ mm/sec. The upper and middle 2D profiles parallel to grinding direction are measured at the places excluding and including the microhole, respectively. Obvious microholes can hardly be found on the observed 3D image. From the 2D profiles, the surface roughness values parallel to the grinding direction are about 3 nm (P-V) and 0.8 nm (RMS) excluding microholes and about 9 nm (P-V) and 1 nm (RMS) including microholes, respectively. In addition, the surface roughness normal to the grinding direction is about 8 nm (P-V) and 1.5 nm (RMS). Accordingly, in the measurement of AFM accuracy order, it is reasonable to say that the ground surface with the newly devised method can be ultra-smooth. The entire ground workpiece area of 10 mm^2, which is further observed widely, however, also consists of the ultrasmooth surface formed by the low height of grooves with no grinding cracks.

2.4 Conclusion

Ductile-mode grinding of fine ceramics with the coarse #140-mesh metal-bonded diamond wheel has been shown to be possible in plunge surface grinding. It is estimated that the thermal effect due to the large wear land of the cutting edge on the #140-mesh wheel surface has considerable effect on

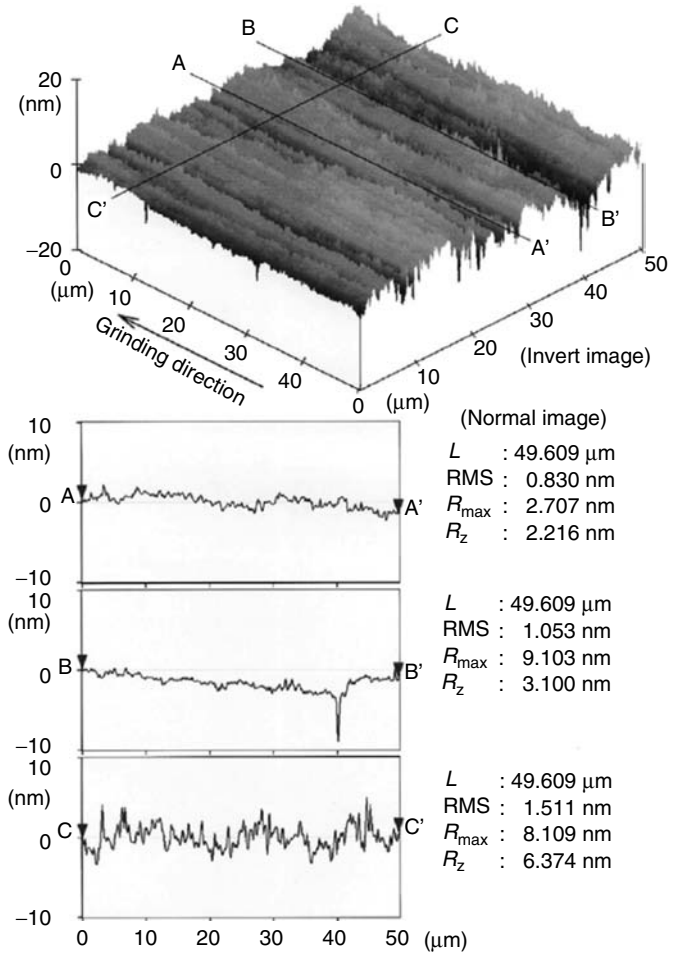

FIGURE 2.26
An AFM 3D image and 2D profiles of the HPSC surface ground at $(v_w)_c = 3.33$ mm/sec with the #140-mesh wheel by ultra-smoothness grinding method [SD140Q50M, $V_g = 20$ m/sec, $t_t = 5$ μm, Soluble (1/50)].

ductile-mode grindability. The various kinds of grinding parameters, that is, table speed, wheel speed, workpiece material property, and so on, influence ductile-mode grindability. As a result, optimum grinding conditions should be selected for ductile-mode grinding. Based on the result obtained in plunge surface grinding, ultra-smoothness grinding method has been newly devised for obtaining the ultra-smoothness roughness below 10 nm (R_{max}), which is almost the same as that after lapping. According to the experimental investigation using the new ultra-smoothness grinding method, the surface roughness of the ground HPSC ceramic surface of 50 μm^2 measured with

AFM is as smooth as about 9 nm (P-V) and 1.5 nm (RMS). Therefore, in the measurement of AFM accuracy order, it is reasonable to say that the ground surface with the newly devised method can be ultrasmooth. The entire ground workpiece surface of 10 mm^2, however, is also ultrasmooth.

The new method is inadequate for productive ultra-smoothness grinding of fine ceramics. When the method is used after the rough grinding of fine ceramics with the same coarse-grain-size grinding wheel, this may be obtained. Nevertheless, it is considered important that the method is improved toward high productivity due to the investigation of the optimum grinding condition [7–10].

References

1. Yoshioka, J., Hashimoto, F., Miyashita, M., Kanai, A., Abo, A., and Daito, M., Ultraprecision grinding technology for brittle materials. ASME, Shaw, M.C., Grinding Symposium PED, Vol. 16, 1985, 255.
2. Namba, Y., Yamada, Y., Tsuboi, A., Unno, K., and Nakao, H., Surface structure of Mn–Zn ferrite single crystals ground by an ultra-precision surface grinder with various diamond wheels. *Annals of the CIRP*, Vol. 41, No. 1, 1992, 347.
3. Ichida, Y. et al., Mirror finish grinding of silicon nitride ceramics. Proceedings 1st International Conference on New Manufacturing Technology, 1990, 317.
4. Yasui, H., Arino, Y., and Matsunaga, K., Ductile-mode high smoothness grinding of fine ceramics by diamond wheel of coarse grain size (1st Report), *Journal of the Japan Society for Precision Engineering,* Vol. 63, No. 9, 1997, 1270.
5. Yasui, H., Yamazaki, G., Hiraki, Y., Sakamoto, S., Sakata, M., Saeki, M., and Hosokawa, A., Ultra-smoothness grinding of fine ceramics with #140-mesh grain size diamond wheel, Proceedings of 14th American Society for Precision Engineering, Annual Meeting, 1999, 125.
6. Yasui, H. and Yamazaki, G., Possibility of ultra-smoothness grinding of fine ceramics using a coarse grain size diamond wheel, *Journal of the Japan Society for Precision Engineering,* Vol. 69, No. 1, 2003, 115.
7. Yasui, H., Development of polishingless ultra-smoothness grinding method (1st Report), *Journal of the Japan Society for Precision Engineering,* Vol. 69, No. 12, 2003, 1713.
8. Yasui, H. and Sawa, T., Effect of grinding fluid supply on ultra-smoothness grinding of fine ceramics, Proceedings of the ASPE 18th Annual Meeting, 2003, 447.
9. Yasui, H. and Sawa, T., Influence of fluid supply on ultra-smoothness grinding of silicon nitride ceramic with #140 metal bond diamond wheel, Proceedings of the ASPE 19th Annual Meeting, 2003, 565.
10. Yasui, H. and Sawa, T., Ultra-smoothness grinding of a glass with #140 metal bond diamond wheel, ICPMT2004, 2004.

3

Mechanisms for Grinding of Ceramics

S. Malkin and T.W. Hwang

CONTENTS

3.1 Introduction

Despite the development of advanced ceramic materials possessing enhanced properties, the widespread use of these materials for structural applications has been limited mainly because of the high cost of machining by grinding. In the manufacture of ceramic components, grinding can comprise up to 80% of the total cost [1]. Efficient grinding requires selecting

operating parameters to maximize the removal rate while controlling surface integrity [2,3]. Lowering grinding costs by using faster removal rates is constrained mainly by surface damage to the ceramic workpiece, which causes strength degradation. Any attempts to optimize the grinding parameters should take into account the prevailing grinding mechanisms and their influence on the resulting surface damage and mechanical properties.

The present chapter is concerned with what happens during grinding as abrasive grits interact with the ceramic workpiece. Most past research on grinding mechanisms for ceramics has followed either the ''indentation fracture mechanics'' approach or the ''machining'' approach [2]. The indentation fracture mechanics approach models abrasive–workpiece interactions with the idealized deformation and crack systems produced by an indentor. The machining approach typically involves measurement of forces for single-point and multipoint cutting coupled with microscopic observations of surface morphology and grinding debris. Both of these approaches provide important insights into the nature of the grinding process for ceramics.

3.2 Indentation Fracture Mechanics Approach

The indentation fracture mechanics approach likens abrasive–workpiece interactions for grinding of ceramics to small-scale indentation events. The deformation and fracture patterns observed for normal contact with a Vickers pyramidal indentor under an applied load P are illustrated in Figure 3.1. A zone of plastic deformation is found directly under the indentor. Two principal crack systems emanate from the plastic zone: median/radial and lateral cracks. Median/radial cracks are usually associated with strength degradation and lateral cracks with material removal.

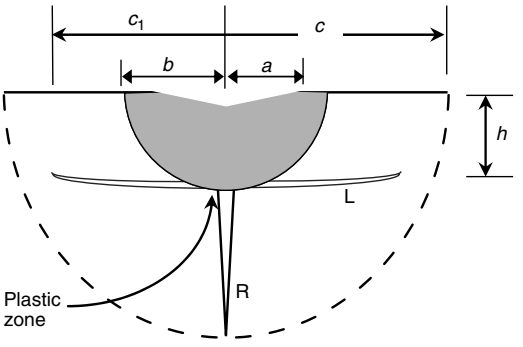

FIGURE 3.1
Plastic zone, median/radial cracks (R), and lateral cracks (L) for Vickers indentation. (From Lawn, B.R. and Swain, M.V., *J. Mater. Sci.*, 10, 113, 1975. With permission.)

Though originally developed for static normal loading, this approach has also been extended to include the effect of a tangential load (moving indentor).

3.2.1 Median/Radial Cracks: Static Indentor

Now let us consider how median/radial cracks can affect the strength degradation due to grinding. For this purpose, the normal applied load P on the indentor (abrasive grit) is considered to cause a median/radial crack of dimension c, as shown in Figure 3.1, which in turn leads to a reduction in the fracture strength. Larger cracks due to more severe grinding conditions and bigger forces should cause a greater reduction in the fracture strength after grinding.

Investigations of median/radial cracks using fracture mechanics started in the 1970s [4–11]. In one of the first studies, the median crack size was predicted using the Boussinesq solution for the elastic stress field due to point loading normal to the surface [4]. The stress intensity factor obtained by integrating the stress field around a median crack was used to predict the relationship between the applied load P and crack size c. Because elasticity predicts infinite stress at the contact point, the observed size of the deformation zone was taken as a lower limit on the integration. A proportional relationship was predicted between the load and crack length ($P \propto c$), which is consistent with experimental results for soda-lime glass [4]. However, in subsequent work [7], median crack extension was observed to occur not only during loading but also during unloading. This was attributed to nonuniform plastic deformation beneath the indentor, which causes residual stresses. Lateral cracking also occurred during unloading.

Many researchers have investigated the influence of plastic deformation and residual stresses on median/radial and lateral cracks [10–17]. An early study focused on resolving median crack propagation into two parts, an elastic component and an irreversible (residual) component [10,11]. The results suggest that the elastic component initiates the median crack and causes it to extend downward during loading, whereas the residual component provides continued crack extension, as the indentor is withdrawn. By modeling the indentation under the indentor as an expanding plastic zone surrounded by an elastic matrix, the stable crack size c (Figure 3.1) for a sharp pyramidal indentor after loading with force P and then unloading was obtained as [12]:

$$P/c^{3/2} = K_c \Big/ \left\{ \xi (\cot \psi)^{2/3} (E/H)^{1/2} \right\}, \tag{3.1}$$

where H is the hardness, E the elastic modulus, K_c the fracture toughness, 2ψ the included angle between opposite indentor edges, and ξ a constant. The relationship between load and crack size in Equation 3.1, $P \propto c^{3/2}$, fits the

experimental results quite well for many materials [12]. This relationship would apply only above a minimum threshold load P^* below which median cracks should not be initiated [9]:

$$P^* = 54.5(\alpha/\eta^2\gamma^4)(K_c^4/H^3), \tag{3.2}$$

where α, η, and γ are constants ($\alpha = 2/\pi$ for a Vickers indentor, $\eta \approx 1$, and $\gamma \approx 0.2$).

Although originally developed for a pyramidal indentor, a similar fracture mechanics analysis has also been developed for other indentor shapes. Assuming that the residual stress component is the main source of crack extension, the stress intensity factor for a penny-like crack was obtained as [17]:

$$K_r = \chi E(\delta V/V)^{1/3}(\delta V)^{2/3}/c^{3/2}, \tag{3.3}$$

where χ is a constant, V the plastic zone volume, and δV the indentation volume. To predict the relationship between load and crack size, it is necessary to relate δV and $\delta V/V$ to the applied load for different indentor shapes. The problem becomes greatly simplified by assuming the hardness to be independent of indentor shape, which is consistent with measurements for several brittle materials [13,18,19]. The hardness (indentation pressure) can be written as

$$H = P/\alpha_0 a^2, \tag{3.4}$$

where α_0 is a geometrical constant and a is a characteristic dimension of the indentation. The ratio $\delta V/V$ was also found to be independent of indentor shape and to follow a relationship of the form

$$\delta V/V \propto (H/E)^{3/2}. \tag{3.5}$$

For stable crack growth, combining Equation 3.3 and Equation 3.5 and equating K_r to K_c leads to

$$K_c = \chi(EH)^{1/2}(\delta V)^{2/3}/c^{3/2}. \tag{3.6}$$

For a pyramidal indentor, the indentation volume is

$$\delta V = (2/3)\, a^3 \cot\psi, \tag{3.7}$$

where a is half the diagonal length (Figure 3.1). Combining Equation 3.4, Equation 3.6, and Equation 3.7 would give the same load/crack length relationship as Equation 3.1 with $\xi = \{(2/3)^{2/3}/\alpha_0\}\chi$. For a spherical indentor of radius R,

$$(\delta V)^{2/3} = (\pi/4)^{2/3}R^2(a/R)^{8/3}, \tag{3.8}$$

where a is now the indentation radius. In this case, the load/crack length relationship becomes

$$P^{4/3}/c^{3/2} = (4\pi/R)^{2/3}\chi^{-1}(K_c E^{-1/2} H^{5/6}). \tag{3.9}$$

Therefore, the load/crack length relations in Equation 3.1 and Equation 3.9 predict $P \propto c^{3/2}$ for a pyramidal indentor and $P \propto c^{9/8}$ for a spherical indentor. This agrees quite well with experimental results in Figure 3.2 for ZnS.

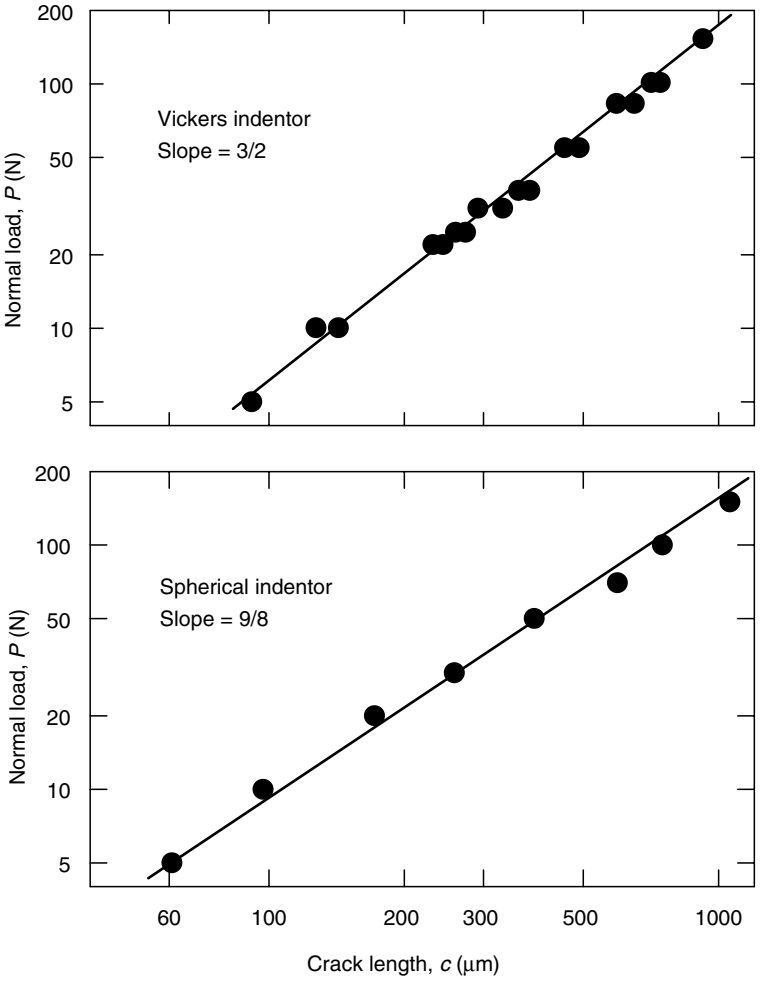

FIGURE 3.2
Load/crack length data for ZnS. (From Marshall, D.B., *J. Am. Ceram. Soc.*, 67, 57, 1984. With permission.)

As stated above, strength degradation is usually attributed to median/radial cracks and the influence of residual stresses on their extension [11,20–22]. The residual stress distribution for static indentation has been predicted [13] by superimposing the Boussinesq elastic stress field with the elastic/plastic solution for a spherical cavity under an internal pressure. The results indicate residual compressive stresses near the contact surface with a steep transition to tensile stresses reaching 0.1 to 0.15 H at the elastic/plastic boundary in the subsurface. Similar residual stress distributions have been reported for silicon nitride ceramics after grinding [23–25], but the peak residual tensile stresses are much smaller. For example, the peak residual tensile stress in Figure 3.3 is only about 0.007 H after grinding of hot-pressed silicon nitride (HPSN) [25]. Such small s tresses may not cause significant strength degradation. However, critical stress intensity factors evaluated from measurements of cracks produced by sharp indentors were about 30% less than those determined by double cantilever or double torsion tests [26,27], which suggests that the residual stresses due to indentation caused a 30% strength reduction.

According to fracture mechanics, the effect of crack size c on fracture strength σ_f can be written as

$$\sigma_f = K_{ic}/Yc^{1/2}, \tag{3.10}$$

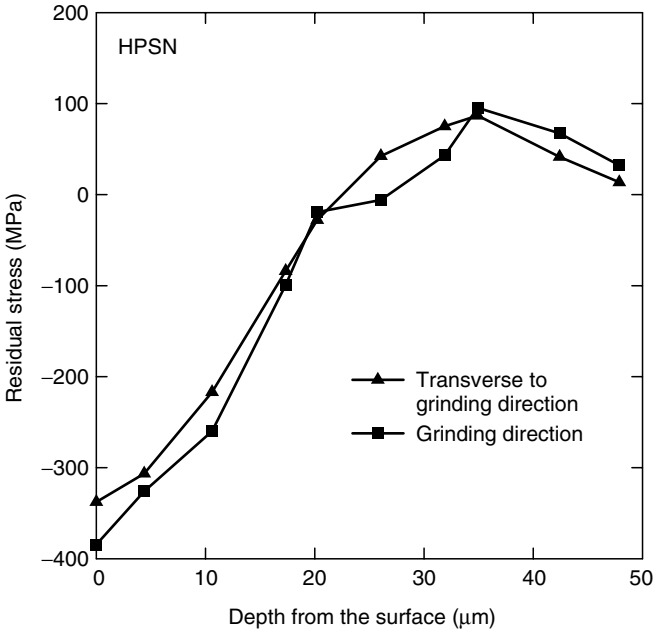

FIGURE 3.3
Residual stress versus depth for HPSN. (From Hakulinen, M., *J. Mater. Sci.*, 20, 1049, 1985. With permission.)

where K_{ic} is the fracture toughness and Y a constant that depends on crack geometry and orientation. When combined with the effect of load on crack size (Equation 3.1 and Equation 3.9), the influence of applied normal force on strength after indentation becomes

$$\sigma_f = A_p(H/E)^{1/6}(K_c^4/P)^{1/3} \tag{3.11}$$

for a pyramidal indentor ($A_p \equiv 1/\{Y(\xi)^{1/3}(\cot\psi)^{2/9}\}$) [20] and

$$\sigma_f = A_s(H^5/E^3)^{1/18}(K_c^3/P)^{4/9} \tag{3.12}$$

for a spherical indentor ($A_s \equiv (4\pi/R)^{2/9}/\{Y(\chi)^{1/3}\}$). Experimental results for a pyramidal indentor appear to correlate fairly well with Equation 3.11 for various ceramics and glasses [20].

By analogy with indentation, the formation of median cracks during grinding should result in a fracture strength relationship of the form [28]:

$$\sigma_f = \eta f_n^{-m}, \tag{3.13}$$

where f_n is the normal grinding force per grit analogous to the applied indentation load P. Experimental results for silicon nitride in Figure 3.4

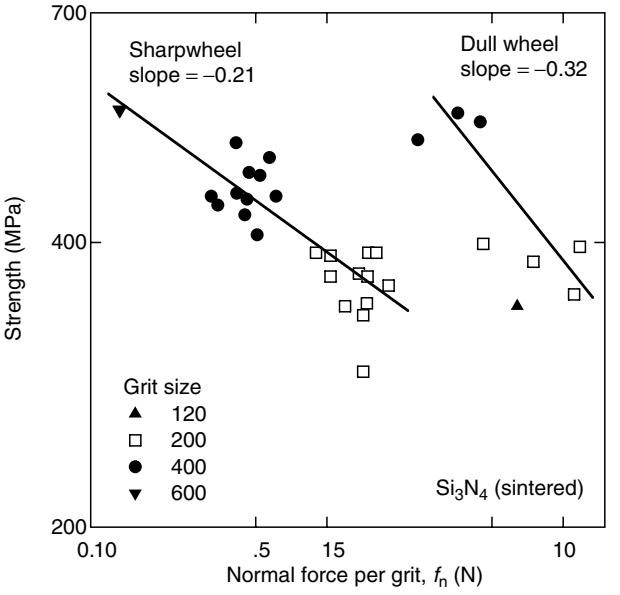

FIGURE 3.4
Flexural strength versus normal force per grit. (From Ota, M. and Miyahara, K., *4th Int. Grinding Conf.*, SME Technical Paper MR90–537, 1990. With permission.)

follow Equation 3.13 quite well with exponents $m = 0.21$ for a sharp wheel and $m = 0.32$ for a dull wheel, as compared with expected values of $m = 1/3$ for a pyramidal (sharp) indentor (Equation 3.11) and $m = 4/9$ for a spherical (dull) indentor (Equation 3.12). It should be noted that the forces per grit in Figure 3.4 are average values obtained by dividing the normal grinding force by the estimated number of active grits. Strength degradation should be dictated by the largest force per grit, which could be much bigger than the average. According to Equation 3.2, the threshold load for median crack formation with a pyramidal indentor for this material is approximately 3 N, which is probably smaller than the largest force per grit for most conditions in Figure 3.4.

3.2.2 Median/Radial Cracks: Moving Indentor

An active abrasive grit is subject not only to a normal load as in static indentation, but also to a tangential load in the direction of motion [29–32]. Analogous to the Boussinesq solution, the elastic stress field due to both a normal force component P and tangential component P' acting at a point on the surface has been modeled using the Michell solution [29]:

$$\sigma_{ij} = \left(\frac{P}{\pi r^2}\right)\left[f_{ij}(\theta,\phi)\right]_{\lambda,\mu} + \left(\frac{P'}{\pi r^2}\right)\left[g_{ij}(\theta,\phi)\right]_{\lambda,\mu}, \tag{3.14}$$

where λ and μ are Lame's constants and r, θ, and ϕ are polar coordinates. The tangential force tends to intensify the tensile stresses normal to the direction of motion ahead of the contact point. This would favor median crack propagation in the plane of motion [29], which could explain why test bars often exhibit more strength degradation when ground transversely than longitudinally. For example, results in Figure 3.5 [33] show strength degradation for transversely ground test bars above a critical uncut chip thickness (grit depth of cut) of about 0.16 μm, but not for longitudinally ground test bars. Similar strength anisotropy has also been reported for many other materials [34–42].

As with static indentation, the moving indentor also causes localized plastic deformation. Unlike static indentation, however, the normal contact pressure depends on the contact configuration and indentor geometry [30]. The median crack length has been predicted using an approximate plane strain plasticity analysis, which estimates the transverse crack-opening force perpendicular to the plane of motion. Although the average normal pressure is sensitive to indentor geometry, the predicted ratio of the transverse to normal force is approximately 0.35 for various indentors. The resulting load/crack size relationship is of the form $P \propto c^{3/2}$ [30], which is consistent with experimental results for glass [31], but not for other materials. For HPSN, the results in Figure 3.6 show approximately $P \propto c$ at

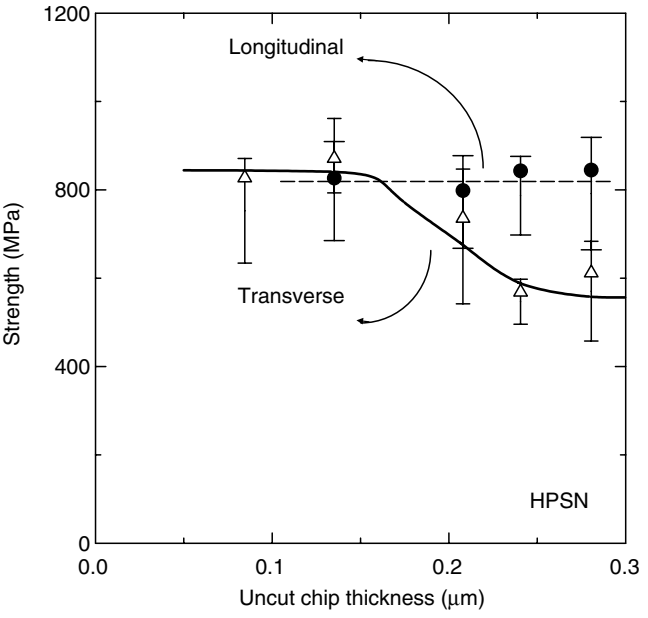

FIGURE 3.5
Transverse rupture strength versus uncut chip thickness for longitudinal and transverse grinding. (From Mayer, J.E., Jr. and Fang, G.P., *NIST SP* 847, 205, 1993. With permission.)

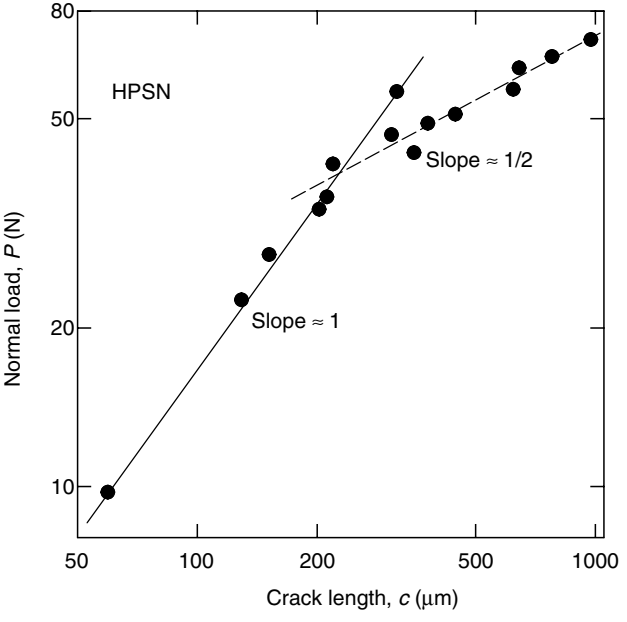

FIGURE 3.6
Normal load versus crack length. (From Kirchner, H.P., *J. Am. Ceram. Soc.*, 67, 127, 1984. With permission.)

low normal loads and $P \propto c^{1/2}$ at high loads [32]. The proportional relationship at low loads is consistent with the elastic solution for static indentation [4], so the influence of residual stress may be insignificant in this regime. However, at high loads, the residual stresses for a moving indentor could become the dominant factor. Analogous to static indentation with a spherical tool [17], the crack opening force determined from the residual stress field was related to the stress intensity factor. This elastic–plastic analysis for the moving indentor yields a load/crack length relationship $P \propto c^{1/2}$ [32]. Data in Figure 3.7 for both single-point and multipoint grinding suggest $P \propto c^{6/5}$ [31]. However, crack depths for multipoint grinding are only about half as big as for single-point grinding at the same normal loads. The indentor used in the scratching test is probably sharper than a typical abrasive grit, which might account for this difference. Another possible factor is the interactions between cracks from adjacent scratches in multipoint grinding, which could reduce the stress intensity factor [43,44].

Strength degradation resulting from single-point and multipoint grinding is associated with failures, which initiate from extended fracture origins induced by these events [31]. For an edge-notch crack, the predicted fracture strength would be given by Equation 3.10 with $Y = 1.99$. Experimental measurements of crack size and fracture strength for both single-point and multipoint grinding tests follow this behavior [31]. Analogous to the case of

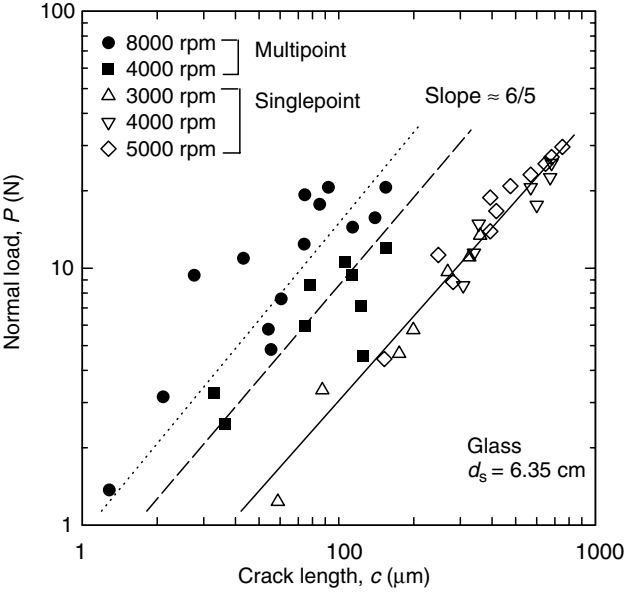

FIGURE 3.7
Normal load versus crack length. (From Kirchner, H.P., *J. Am. Ceram. Soc.*, 67, 347, With permission.)

static indentation, the fracture strength can be related in turn to the normal load if the load/crack size relationship is given. The load/crack size relationships for a moving indentor (scratching) and multipoint grinding are again of the form $P \propto c^{n}$ where $1/2 < n < 3/2$, which combined with Equation 3.13 yields a relation between fracture strength and normal load $\sigma_f \propto P^{-m}$ where $1/3 < m < 1$.

3.2.3 Lateral Cracking and Crushing

Whereas median/radial cracks are associated with strength degradation, lateral cracks may lead to material removal. Lateral cracks (Figure 3.1) initiate during unloading near the bottom of the plastic zone, and then propagate laterally on a plane nearly parallel to the specimen surface [6–8, 15]. Deflection of the crack toward the free surface can cause material removal by fracture (chipping). The effect of the applied load P on the lateral crack length c_ℓ has been estimated using simple plate theory [15]. If h is the distance from the free surface to the crack plane, the crack size for $c_\ell \gg h$ becomes [15]:

$$c_\ell = c^{L}\left[1 - (P_o/P)^{1/4}\right]^{1/2}, \tag{3.15}$$

where

$$P_o \equiv (\zeta_o/A^2)(\cot\psi)^{-2/3}(K_c^4/H^3)(E/H), \tag{3.16}$$

$$c^{L} \equiv \left\{\zeta_L \cot\psi^{5/6}\ A^{-1/2}(K_c H)^{-1}E^{3/4}\right\}^{1/2} P^{5/8}, \tag{3.17}$$

and ζ_o, ζ_L, and A are constants. At large contact loads ($P \gg P_o$), Equation 3.15 reduces to $P \propto c_\ell^{8/5}$, which is similar to the form for median/radial cracks.

An expression for the minimum threshold load for lateral cracking, P_ℓ^*, has been derived as [14,45]:

$$P_\ell^* = \zeta(K_c^4/H^3)f(E/H), \tag{3.18}$$

where ζ is a dimensionless constant and $f(E/H)$ is a weak function such that $\zeta f(E/H) \approx 2\times10^5$. Values for P_ℓ^* can be compared with average normal loads per grit to predict whether a lateral fracture mechanism or ductile removal mechanism might prevail [45]. For example, the normal force per grit for grinding of sintered silicon nitride (Figure 3.4) is less than the estimated critical threshold load of about 30 N, which would suggest ductile flow rather than lateral cracking. However, the predicted threshold load for median cracks (3 N for silicon nitride [9]) is much less than for lateral cracks,

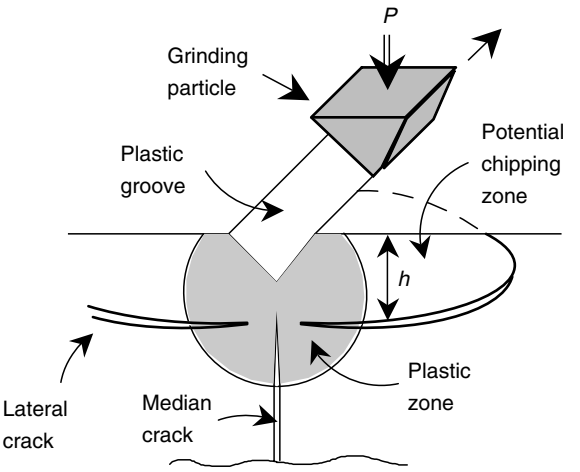

FIGURE 3.8
Plastic zone, median/radial, and lateral cracks for moving indentor. (From Evans, A.G. and Marshall, D.B., in *Fundamentals of Friction and Wear of Materials*, Rigney, D.A., Ed., ASME, 439, 1981. With permission.)

which would suggest that ductile grinding may produce median cracks and strength degradation.

The size of the lateral crack can be used to estimate abrasion (grinding) rates [45]. Assuming that the volume removed by a grit under a normal load P in Figure 3.8 is proportional to the lateral crack size and length of travel ℓ, the total volumetric removal V_ℓ is

$$V_\ell = \alpha_L (P^{9/8}/K_c^{1/2}H^{5/8})(E/H)^{4/5}\ell, \tag{3.19}$$

where α_L is a constant. This expression correlates fairly well with some limited data for grinding of ceramics only at extremely small removal rates [45,46]. Evidence of material removal by lateral cracking is often observed on scratched grooves.

In addition to lateral cracking, material removal by fracture has also been related to crushing [32,47–49]. Crushing ahead of and beneath the contact has been attributed to mixed mode fracture resulting from the distribution of in-plane hoop stresses and shear stresses [29]. The crushed zone boundary beneath a moving indentor has been estimated by assuming that crushing occurs by fractures originating at distributed preexisting flaws where the elastic strain energy density exceeds a critical value [48]. A somewhat more comprehensive model was subsequently developed which attributes crushing to sequential crack branching under a moving indentor [49]. This latter model successfully predicted crushing depths for single-point grinding of glass, but over predicted crushing depths for HPSN [49].

These differences may be related to the assumption of a purely elastic stress field. Localized plastic deformation, which should be more significant for the silicon nitride, would reduce the stress intensity and crushing depth.

3.3 Machining Approach

The machining approach typically involves measurement of cutting forces and energy together with microscopic observations of grinding debris and surface morphology. Although microscopic observations provide important evidence about the prevailing grinding mechanisms, any plausible physical model of abrasive–workpiece interactions must be able to quantitatively account for the magnitude of the grinding energy and its dependence on the operating conditions.

3.3.1 Grinding Debris

Examination of grinding debris for various brittle materials [33,50–53] suggests material removal mainly by brittle fracture. For example, SEM micrographs of grinding debris collected for reaction bonded silicon nitride (RBSN) ground with a 400 grit diamond wheel are shown in Figure 3.9. The debris consists mostly of relatively large plate-like particles (Figure 3.9a) which appear to have fractured from the workpiece by lateral cracking, and much finer particles (Figure 3.9b) which may have been generated by crushing. The plate-like particles typically have grinding striations on one side as seen in Figure 3.9a. The striations may have been generated either immediately before the particle fractured from the workpiece or during the preceding grinding pass.

Grinding debris generation has also been studied in-process using a camera equipped with a micro-flash [50]. Many fine particles were observed flying off both ahead of and just behind the grit, which suggests material dislodged by lateral cracking crushed into smaller particles. Crushing (pulverization) may also be responsible for much finer particles (powder) beneath the scratched groove [54,55]. Aside from brittle fracture particles, continuous flow-type chips are also occasionally observed at high grinding speeds and shallow depths of cut [50,56], which would indicate ductile flow.

3.3.2 Microscopy of Scratches and Ground Surfaces

A detailed picture of the prevailing mechanisms has been developed from microscopic observations of scratches produced by single-point diamond

(a)

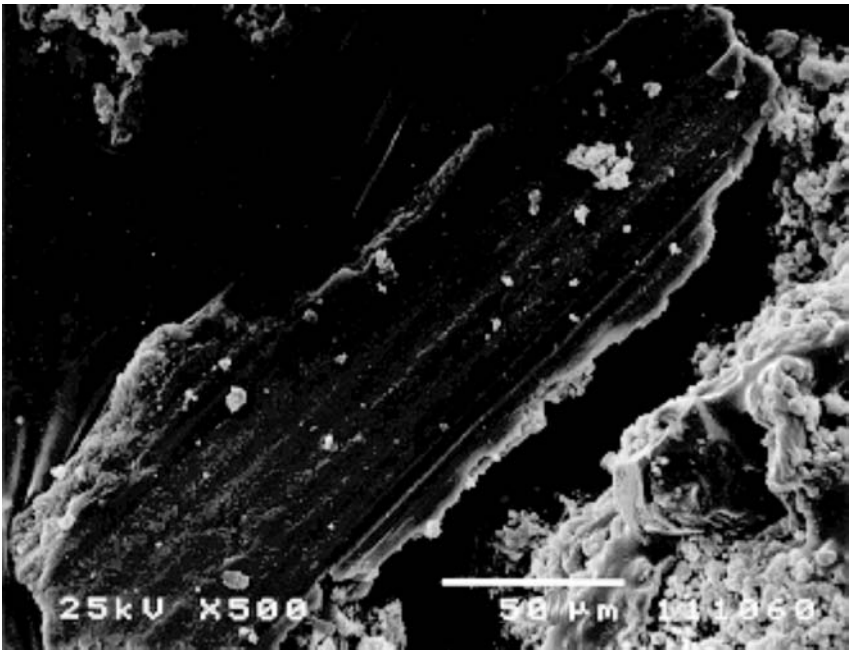

(b)

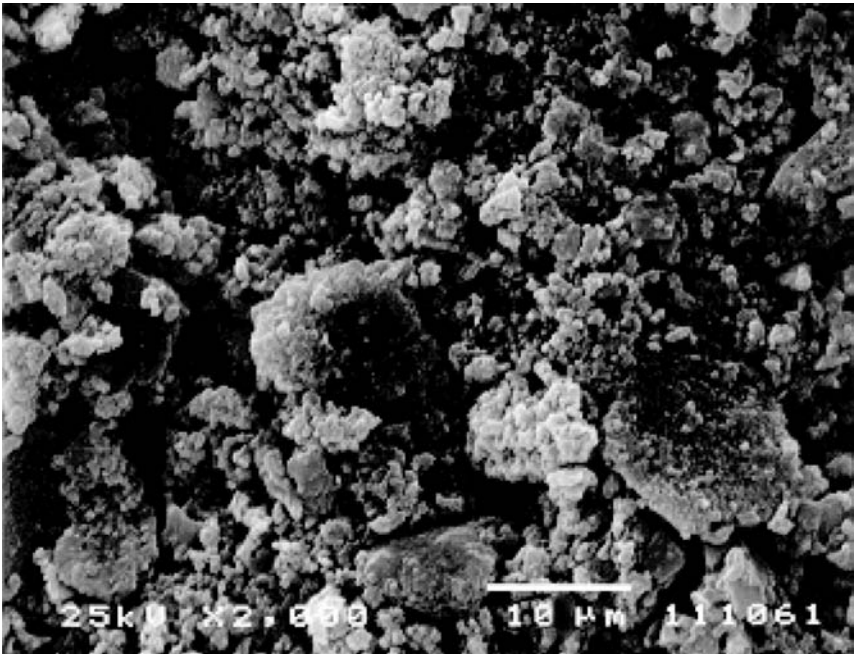

FIGURE 3.9
Grinding debris, RBSN (Coors/Eaton), 400 grit wheel (Norton) [65]: (a) $a = 38$ µm, $v_w = 200$ mm/sec, $v_s = 10$ m/sec; (b) $a = 22$ µm, $v_w = 100$ mm/sec, $v_s = 32$ m/sec.

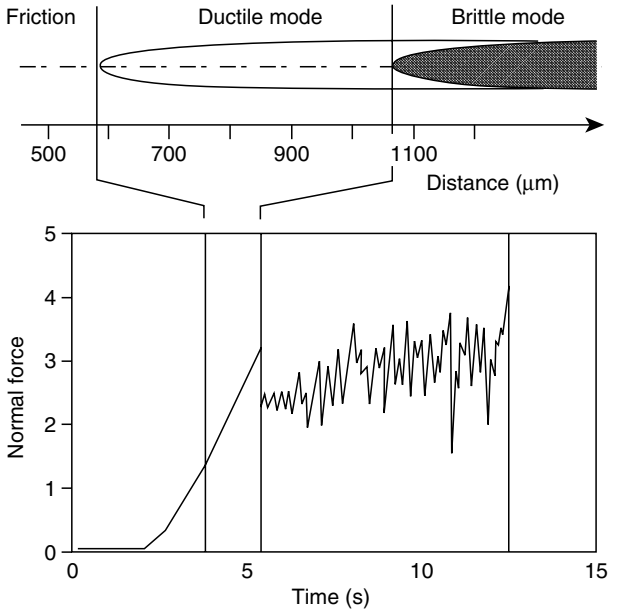

FIGURE 3.10
Cutting regimes for silicon. (From Brinksmeier, E., Preub, W., and Riemer, O., *Proc. 8th Int. Prec. Eng. Sem.*, 335, 1995. With permission.)

tools [31,32,47,54,57–63]. Scratching experiments performed with fixed depths of cut on silicon nitride [32] and alumina [58] show evidence of ductile flow, lateral cracking and chipping along the groove, and crushing beneath and ahead of tool with an increased depth. However, in most actual grinding processes, the depth of cut progressively increases as the abrasive grit passes through the grinding zone. This behavior has been simulated with single-point cutting by inclining the workpiece in the cutting direction. For inclined single-point cutting of silicon and germanium [61], initial ductile flow progressively changed to brittle fracture after a critical depth of cut was reached (Figure 3.10). The normal force increased linearly with distance (depth of cut) in the ductile regime, and then fluctuated about a lower value as brittle fracture occurred.

Grinding involves a multitude of scratches and interactions between adjacent scratches. The effect of interactions between adjacent scratches on stock removal has been investigated for hot-pressed alumina by making a series of parallel scratches with separation distances from 0 to 250 μm [64]. The results in Figure 3.11 show a strong dependence on the separation distance, as well as the load. Either when the separation is so large that the scratches do not interact or small enough to overlap, material removal is

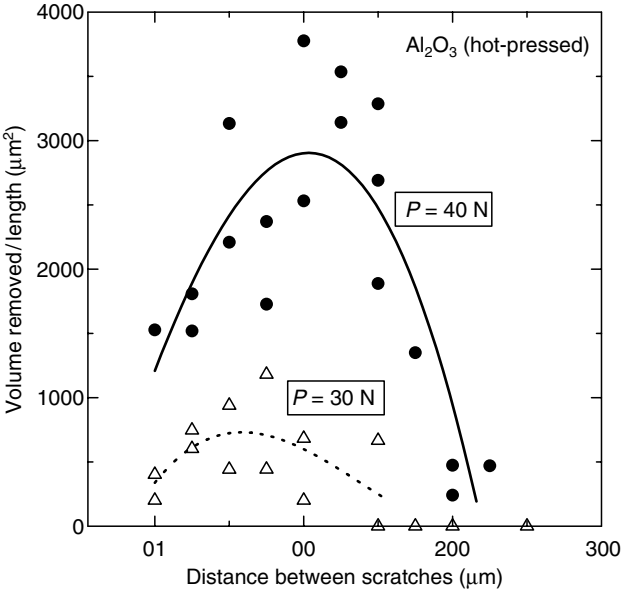

FIGURE 3.11
Material removed per unit length versus distance between scratches. (From Xu, H.H.K., Jahanmir, S., and Wang, Y., *J. Am. Ceram. Soc.*, 78, 881, 1995. With permission.)

relatively small. At intermediate distances, the removal becomes much bigger.

SEM micrographs in Figure 3.12 show HPSN surfaces ground with a 180 grit diamond wheel before etching (Figure 3.12a) and after etching (Figure 3.12b) with hydrofluoric acid [65]. Although some fractured areas can be seen, the as-ground surface exhibits mainly ductile flow associated with plowing along the grinding direction. However, after etching, many of the finer striations disappear whereas grooves generated by abrasive grits can still be seen. Etching of the ground silicon nitride surfaces with hydrofluoric acid appears to have removed a smeared glassy layer. The formation of glassy material on silicon nitride surfaces during sliding can be attributed to the oxidation reaction [66]:

$$Si_3N_4 + 3O_2 \rightarrow 3SiO_2 + 2N_2. \tag{3.20}$$

Silicon oxide glassy layers have also been recently identified on ground silicon surfaces [67] using energy dispersive spectroscopy.

3.3.3 Grinding Energy and Mechanisms

A fundamental parameter derived from the grinding forces and machining conditions is the specific grinding energy, which is defined as the energy

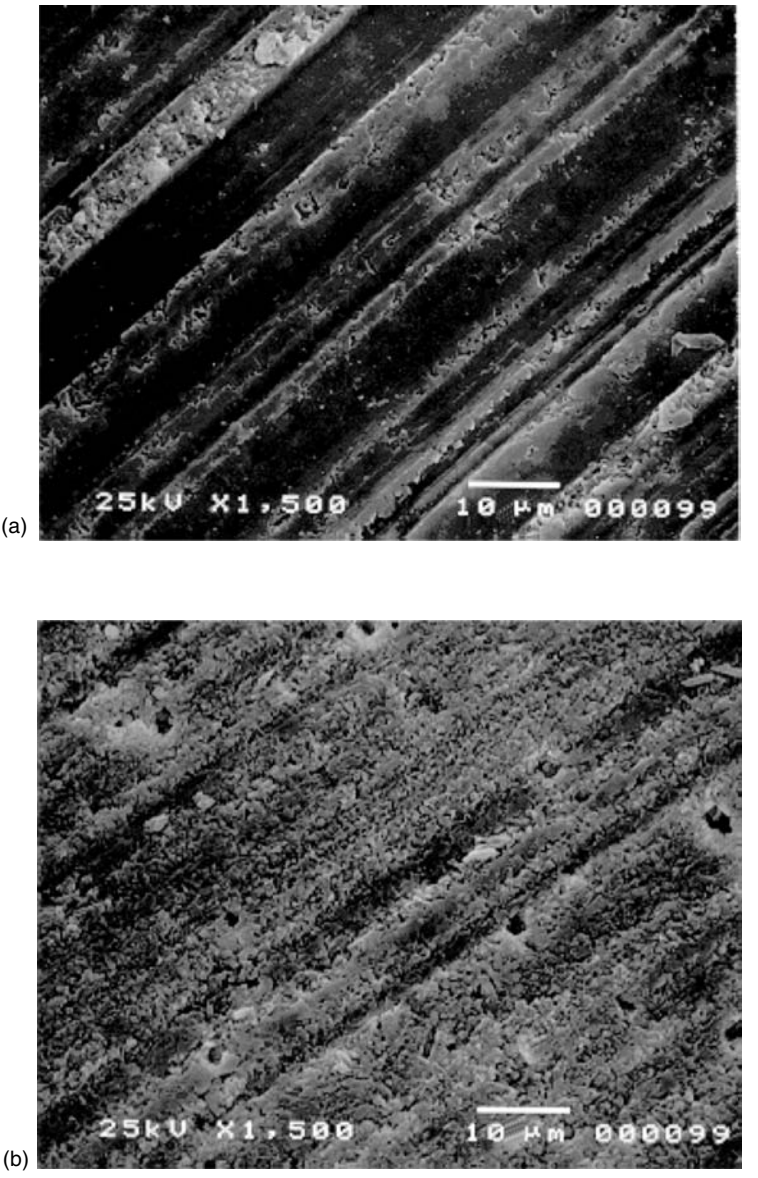

FIGURE 3.12
Ground surfaces, HPSN (Kyocera SN220), 180 grit wheel Norton ($a = 38$ µm, $v_w = 100$ mm/sec, $v_s = 32$ m/sec) (a) as ground; (b) after etching. (From Hwang, T.W. and Malkin S., *ASME J. Manuf. Sci. Eng.*, 121, 623. With permission.)

per unit volume of material removal. The specific energy is obtained from the relationship [68]:

$$u = \frac{F_t v_s}{Q_w} = \frac{P_m}{Q_w}, \tag{3.21}$$

where F_t is the tangential grinding force, v_s the wheel velocity, P_m the net grinding power, and Q_w is the volumetric removal rate. For metallic workpiece materials, the total specific grinding energy can be modeled as the sum of chip formation, plowing, and sliding components [68]. For ceramics and other brittle materials, the relationship between the grinding mechanisms and specific energy is complicated by the occurrence of both brittle fracture and ductile flow.

3.3.3.1 Specific Grinding Energy

Force and grinding energy data have been obtained for various ceramics over a wide range of conditions [69–75]. For straight surface grinding of HPSN, specific energies have been reported ranging from about 10 J/mm^3 at very high removal rates to about 800 J/mm^3 at very low removal rates [65,69–71]. A simple explanation for this type of behavior is that a decrease in removal rate results in a smaller undeformed (uncut) chip size, causing more flow and less brittle fracture. Results for specific grinding energy versus average uncut chip cross-sectional area in Figure 3.13 for aluminum oxide and silicon nitride show two distinct regimes [72]. Below an average uncut chip area of about 0.05 μm^2, which would correspond to a maximum undeformed chip thickness of about 0.35 μm (see Equation 3.23), the specific energy increases steeply with smaller chip size. Above the transition, the specific energy decreases more slowly as the chip size increases. The undeformed chip thickness at the transition may correspond to the critical threshold depth of cut, d_c corresponding to the critical load (Equation 3.18) below which fracture should not occur [76]:

$$d_c = \beta(E/H)(K_c/H)^2, \tag{3.22}$$

where β is a constant. Although the maximum undeformed chip thickness of 0.35 μm at the transition is somewhat bigger than the value computed from Equation 3.22 with $\beta = 0.15$, these results suggest material removal mainly by ductile flow below the transition and brittle fracture above the transition.

The magnitude of the specific grinding energy and its dependence on the operating parameters is a direct consequence of the prevailing grinding mechanisms. One parameter, which has been used to analyze specific grinding energy data, is the maximum undeformed (uncut) chip thickness taken by an individual cutting point (grit depth of cut) which can be written as [68]:

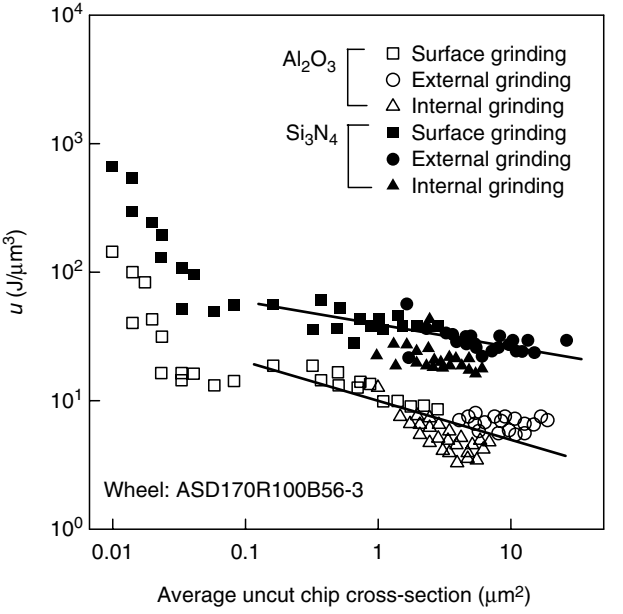

FIGURE 3.13
Specific energy versus average uncut chip cross-sectional area. (From Chen, C., Jung, Y., and Inasaki, I., in *Grinding Fundamentals and Applications*, Malkin, S. and Kovach, J.A., Eds., 39, 201, 1989. With permission.)

$$h_m = \left[\frac{3}{C\tan\theta}\left(\frac{v_w}{v_s}\right)\left(\frac{a}{d_s}\right)^{1/2}\right]^{1/2}, \tag{3.23}$$

where C is the active cutting point density, v_w the workpiece velocity, a the wheel depth of cut, d_s the wheel diameter, and θ is the semiincluded angle for the undeformed chip cross-section assumed to be triangular as illustrated in Figure 3.14. Experimental results for the specific energy obtained from various ceramics and a glass as listed in Table 3.1 are plotted versus h_m in Figure 3.15 for a 400 grit resin-bonded diamond wheel and in Figure 3.16 for a 180 grit wheel [77]. Results for the various workpiece materials with both wheels showed the same type of inverse behavior, a decrease in specific energy with h_m at a diminishing rate toward a minimum value. Each set of results in Figure 3.15 and Figure 3.16 was statistically fitted by least squares to an equation of the form:

$$u = \frac{A_s}{h_m} + B_s, \tag{3.24}$$

where A_s and B_s are constants. Values of A_s and B_s obtained by least square fitting are included in Table 3.1. The fitted curves shown in Figure 3.15 and

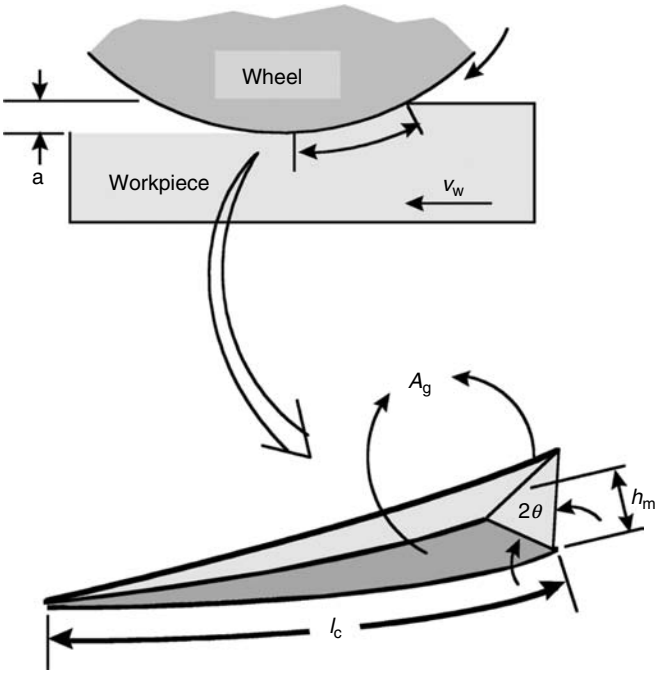

FIGURE 3.14
Illustration of undeformed chip geometry. (From Hwang, T.W. and Malkin, S., *ASME J. Manuf. Sci. Eng.*, 121, 623. With permission.)

Figure 3.16 represent the grinding behavior quite well except perhaps for the RBSN workpiece. The correlation coefficients for least square fitting were all in excess of 0.9 except for the RBSN. It can be seen in Table 3.1 that both A_s and B_s values for the 400 grit wheel are bigger than those for the 180 grit wheel on the same HPSN (Norton NC132), workpiece material. For the RBSN in Figure 3.15b, a better fit may be obtained using a stronger inverse relationship with h_m.

3.3.3.2 Brittle Fracture Energy

The relationship between the specific grinding energy and the undeformed chip thickness as described above should be related to the grinding mechanisms. It has been suggested that removal mechanisms at small values of h_m are dominated by high energy ductile flow (ductile regime) because the force acting on each grit is less than the critical load for lateral cracking to occur. The lower specific energy and bigger forces per grit at large values of h_m might indicate material removal by brittle fracture.

This explanation for the influence of h_m on the specific energy would imply that the minimum specific energy B_s should be comparable to the

TABLE 3.1

Experimental Grinding Conditions, Workpiece Properties, Fitted Values of A_s and B_s for Plots of Specific Energy Versus h_m, and Estimated Plowed Surface Energies Per Unit Area J_s and Correlation Coefficients r

Wheel	C (mm^{-2}) d_g (μm)	Grinding Parameters	Workpiece Material	E (GPa)	H (GPa)	K_c (MPa $m^{1/2}$)	$G_c/2$ (J/m^2)	A_s (10^3 J/m^2)	B_s (J/mm^3)	J_s (J/m^2)	r
DN400-	$C = 107$	$a = 5 \sim 38$ μm	S/RBSN	297	15.0	6.6	73.3	11.4	32.9	15,300 ± 1,520	0.83
N100B-1/4	$d_g = 38$	$v_w = 5 \sim 200$ mm/sec	RBSN*	165	10.0	3.6	39.3	35.3	0.0	4,700 ± 245	0.94
			HPSN[1]	325	19.6	5.0	38.5	15.4	28.7	18,000 ± 705	0.96
		$v_s = 10 \sim 40$	Al_2O_3	380	13.3	4.5	26.6	9.1	10.5	7,900 ± 255	0.97
DN180-	$C = 21$	$a = 5 \sim 76$ μm	HPSN[1]	325	19.6	5.0	58.9	9.1	16.7	14,200 ± 585	0.95
N100B-1/4	$d_g = 84$	$v_w = 5 \sim 200$ mm/sec	HPSN[2]	276	18.2	5.7	38.5	4.9	16.6	15,900 ± 365	0.98
			SiC[1]	410	27.4	3.5	14.9	6.4	7.4	10,000 ± 400	0.96
		$v_s = 10 \sim 40$ m/sec	SiC[2]	427	27.0	3.0	10.5	5.5	7.0	9,100 ± 590	0.91
			Glass**	70	5.5	0.75	4.0	2.0	1.0	1,800 ± 85	0.95

HPSN[1]—Norton NC132, HPSN[2]—Kyocera SN220, SiC[1]—Carborundum, Hexoloy SA, SiC[2]—Norton, Glass—Soda-lime Glass, S/RBSN—Coors/Eaton, RBSN—Coors/Eaton, Al_2O_3—Wesgo, Al995.

Source: *From Hwang, T.W., 1997, Grinding energy and mechanisms for ceramics, PhD Thesis, University of Massachusetts.

**From Lawn, B.R. and Evans, A.G., 1980, *J. Am. Ceram. Soc.*, Vol. 63, pp. 574–581.

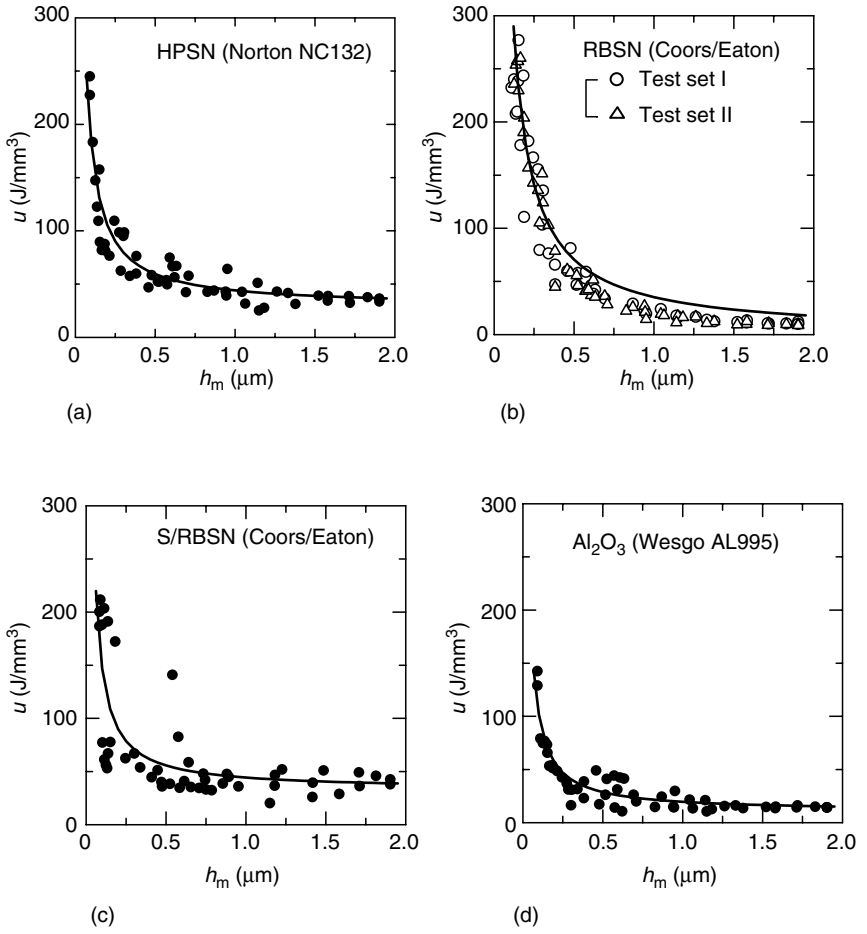

FIGURE 3.15
Specific grinding energy versus undeformed chip thickness (Norton 400 grit diamond wheel).

energy for material removal by brittle fracture. That portion of the grinding energy associated with brittle fracture can be estimated as the product of the surface area generated by fracture and the material's fracture energy per unit area [51]. For simplicity, the particles removed by grinding can be assumed small cubes of dimension b_f. In this case, the total surface area produced per unit volume of material removed, a_f, is equal to the total surface area of a cube divided by its volume:

$$a_f = \frac{6b_f^2}{b_f^3} = \frac{6}{b_f}. \tag{3.25}$$

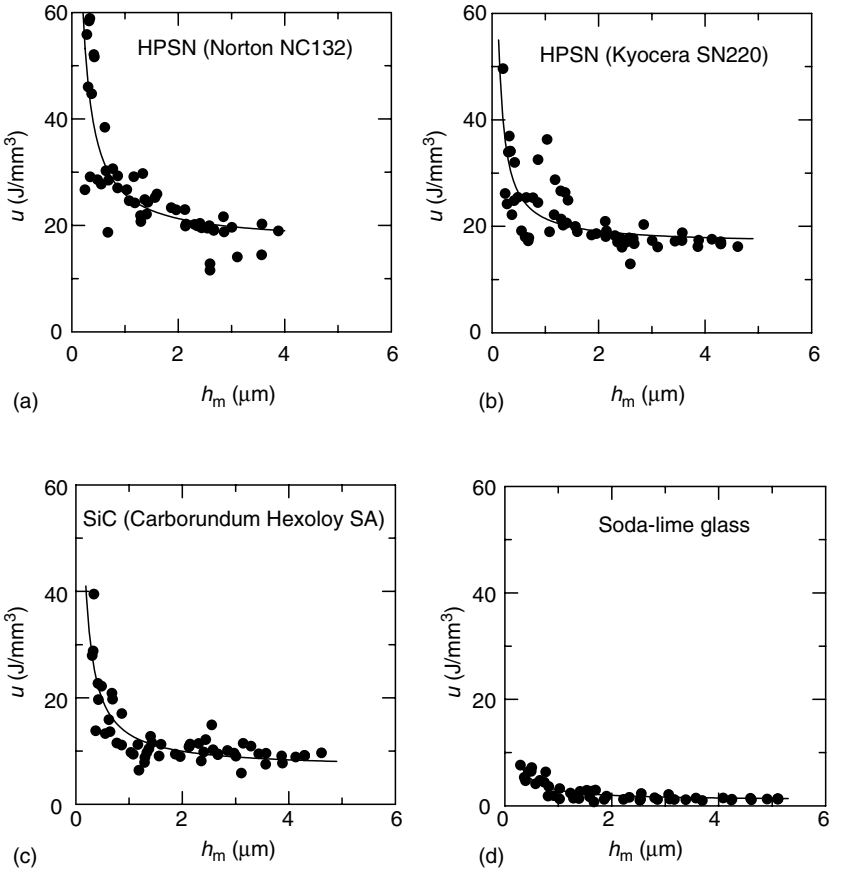

FIGURE 3.16
Specific grinding energy versus undeformed chip thickness (Norton 180 grit diamond wheel).

Approximating the fracture surface energy as half the critical energy release rate G_c ($G_c = {K_c}^2/E$) for crack formation (two surfaces), the specific energy due to fracture becomes

$$u_f = \left(\frac{G_c}{2}\right) a_f = \frac{3G_c}{b_f}. \tag{3.26}$$

The smallest particles removed by grinding are approximately 1 μm in size, although many are much larger. For HPSN, $G_c \approx 80\ \mathrm{J/m^2}$. Using these values for b_f and G_c leads to a specific fracture energy $u_f \approx 0.24\ \mathrm{J/mm^3}$, which is only a negligible portion of the extrapolated minimum grinding energy for

HPSN. This same argument would also apply to all the other workpiece materials as listed in Table 3.1 with the possible exception of RBSN. Therefore, most of the grinding energy must be expended by ductile flow, even though material removal is mainly by brittle fracture.

3.3.3.3 Plowed Surface Area Analysis

SEM observations reveal characteristic grooves and a heavily deformed layer on the ground surface. The generation of this deformed surface layer is apparently related to plowing by numerous abrasive points passing through the grinding zone, thereby leading to surfaces with multiple overlapping scratches and grooves. Therefore, it might also be worthwhile to analyze the grinding energy in terms of the plowed area generated on the workpiece by the active abrasive cutting points.

For the purpose of estimating the plowed surface area, again consider the plowing geometry for a single undeformed chip with a triangular cross-section of semiincluded angle θ as shown in Figure 3.14. Assuming that the active cutting points per unit area C are uniformly distributed on the wheel surface, the undeformed chip thickness h_m is given by Equation 3.23 [68]. For each undeformed chip as shown in Figure 3.14, the corresponding plowed surface area A_g generated at the sides of the groove is given by

$$A_g = \frac{h_m l_c}{\cos\theta}. \tag{3.27}$$

Multiplying by the number of cutting points per unit time per unit width of grinding leads to an expression for the overall rate of plowed surface area generated per unit width [65]:

$$S'_w = C v_s A_g. \tag{3.28}$$

Substituting for h_m from Equation 3.23 and noting that $l_c = (a d_s)^{1/2}$ results in

$$S'_w = \left(\frac{6C}{\sin 2\theta}\right)^{1/2} (v_w v_s)^{1/2} (a)^{3/4} (d_s)^{1/4}. \tag{3.29}$$

A plot of the measured power per unit width for HPSN (Norton NC132) ground with both a 400 grit wheel ($C = 107\ \text{mm}^{-2}$) and 180 grit wheel ($C = 21\ \text{mm}^{-2}$) versus the corresponding values of S'_w with $\theta = 60$ degrees is presented in Figure 3.17. A nearly proportional relationship is obtained between power per unit width and S'_w. Similar behavior was found with all the other wheel/workpiece combinations listed in Table 3.1. Each plot of the measured power per unit width versus the rate of plowed surface area generated per unit width was fitted to a linear relationship of the form:

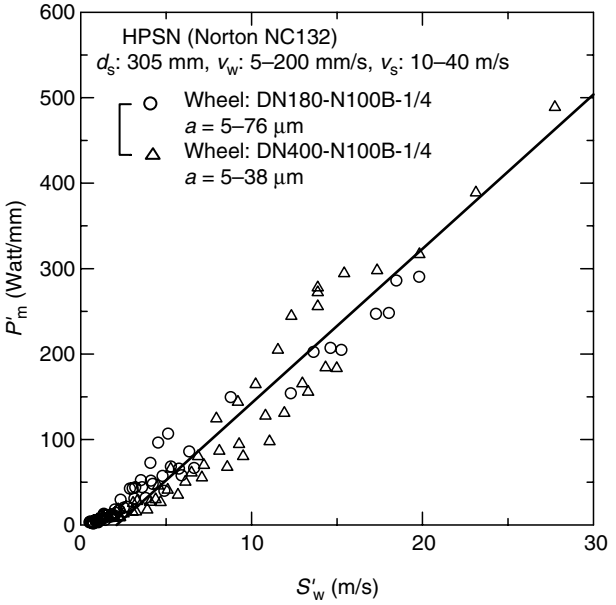

FIGURE 3.17
Power per unit width versus rate of plowed surface area generated per unit width.

$$P'_m = J_s S'_w + B_p, \tag{3.30}$$

where J_s and B_p are constants. Assuming that the total grinding energy is associated only with plowing and neglecting the influence of the intercept B_p, the slope J_s would correspond to the average energy per unit area of plowed surface generated. The slopes J_s obtained for various workpiece materials together with their standard errors and correlation coefficients r for least square fitting of the data are included in Table 3.1. The values of J_s are typically about two orders of magnitude bigger than the corresponding fracture surface energies ($G_c/2$ in Table 3.1), which is a further indication that most of the energy dissipation is associated with ductile flow.

3.3.3.4 Plowed Surface Energy and Workpiece Properties

According to the analysis presented above, J_s represents the surface energy per unit area generated by plowing. Estimated values for J_s in Table 3.1 are nearly constant for a given workpiece material regardless of the grinding conditions and grit size. Therefore J_s might be considered to be a ''characteristic'' material property which depends on the mechanical properties of the workpiece (E, H, and K_c) included in Table 3.1.

A number of attempts were made to correlate J_s with E, H, and K_c [65]. J_s generally tends to increase with H, and K_c, but no satisfactory correlation was found with any one of these three mechanical properties. Therefore, correl-

ations were attempted with combinations of material properties. From indentation fracture mechanics, the volumetric material removal per unit length of travel by scratching with a pyramidal tool has been theoretically related to the lateral crack size and the mechanical properties [8,45]. For a given volumetric removal per unit length of travel, this leads to a relationship between the normal load P and the mechanical properties, which can be written as [8]:

$$(P)^{5/4} \propto (K_c^{3/4} H^{1/2}) \tag{3.31}$$

or using a modified analysis [45]:

$$(P)^{9/8} \propto (K_c^{1/2} H^{5/8}). \tag{3.32}$$

Therefore J_s for a given volume removal per unit length might be related to the combined mechanical properties on the right hand side of Equation 3.31 and Equation 3.32, namely $K_c{}^{3/4}H^{1/2}$ and $K_c{}^{1/2}H^{5/8}$. A plot of J_s versus $K_c{}^{3/4}H^{1/2}$ presented in Figure 3.18 yields quite a good correlation, with J_s proportional to $(K_c{}^{3/2}H^{1/2})^2$. A proportional relationship between J_s and $(K_c{}^{1/2}H^{5/8})^{9/5}$ in Figure 3.19 shows somewhat more deviation, especially for silicon carbide ceramics.

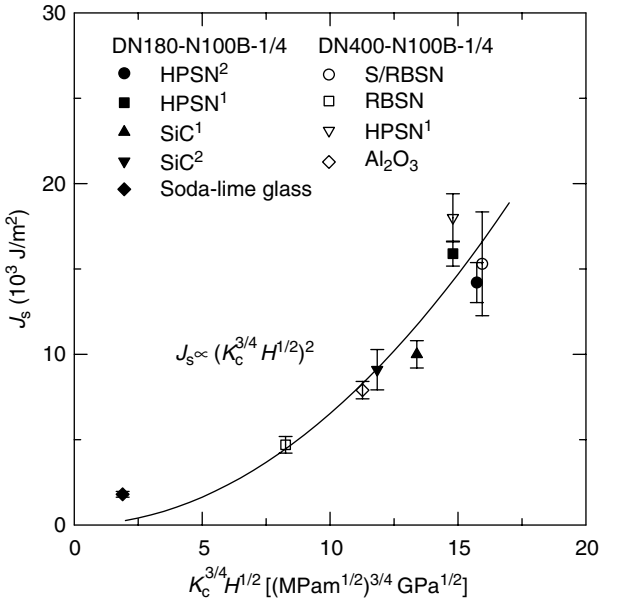

FIGURE 3.18
Plowed surface energy per unit area versus $K_c{}^{3/2}H^{1/2}$. (From Hwang, T.W. and Malkin, S., *ASME J. Manuf. Sci. Eng.*, 121, 623. With permision.)

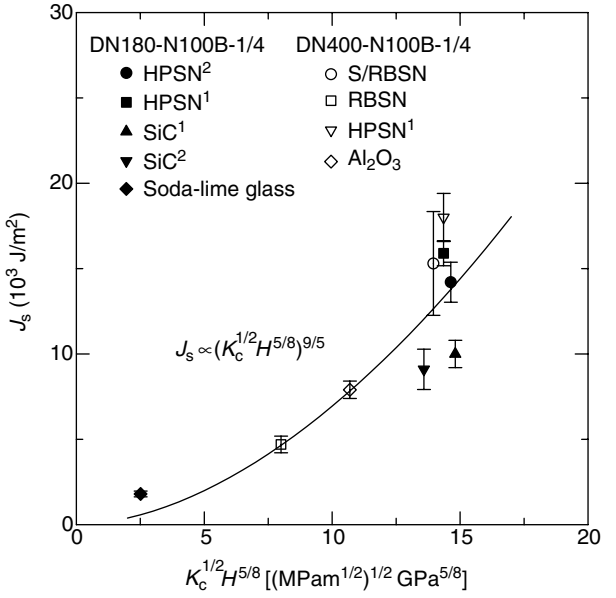

FIGURE 3.19
Plowed surface energy per unit area versus $K_c^{1/2}H^{5/8}$. (From Hwang, T.W. and Malkin, S., *ASME J. Manuf. Sci. Eng.*, 121, 623. With permission.)

The results in Figure 3.18 would indicate that $J_s \propto K_c^{3/2}H$. Therefore, the grinding power per unit width should be proportional to the product of $K_c^{3/2}H$ and the rate of plowed area generated per unit width. Indeed all the results in Figure 3.20 (540 data points as indicated in Table 3.1) of P_m' versus $K_c^{3/2}HS_w'$ tend to fall close to the same straight line. For all the materials ground over a wide range of conditions, the net grinding power per unit width can be approximated as:

$$P_m' = MK_c^{3/2}HS_w', \tag{3.33}$$

where $M \approx 6.4\times10^{-20}\ \mathrm{N^{-3/2}m^{13/4}}$.

3.4 Concluding Remarks

Most past research on grinding mechanisms for ceramics has followed either the ''indentation fracture mechanics'' approach or ''machining'' approach. The indentation fracture mechanics approach would seem to offer the possibility of describing both the material removal process and its influence on strength degradation in terms of the force or depth of cut at an

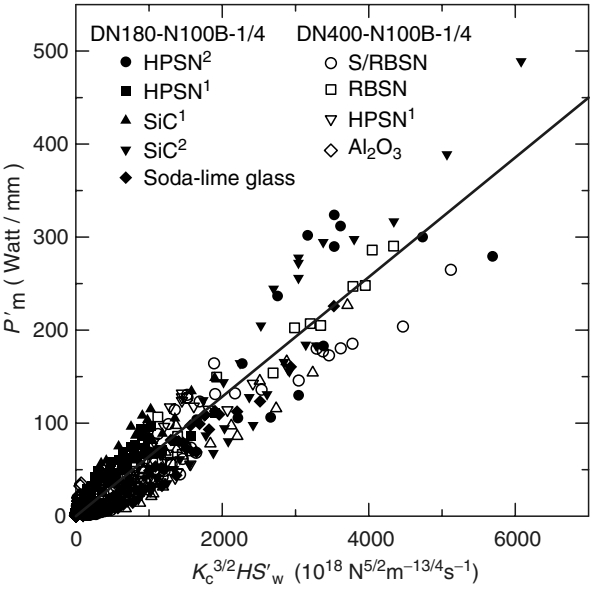

FIGURE 3.20
Grinding power per unit width versus $K_c^{3/2} HS'_w$. (From Hwang, T.W. and Malkin, S., *ASME J. Manuf. Sci. Eng.*, 121, 623. With permission.)

individual cutting point. Furthermore, it predicts the possibility of ductile regime grinding at extremely low removal rates where the force or depth of cut per grit is below a critical value. While providing some important insights into what may occur during abrasive–workpiece interactions, this approach has had limited quantitative application to realistic grinding operations. Its application is complicated by the grit geometry, interactions between grinding scratches, and elevated temperatures at the grinding zone.

From the machining approach, it has become evident that material removal for grinding of ceramics occurs mainly by brittle fracture, although most of the grinding energy is associated with ductile flow due to plowing. A new plowing model has been developed which quantitatively accounts for the grinding energy by relating the grinding power to the rate of plowed surface area generated. Over a wide range of grinding conditions, the power was found to be nearly proportional to the rate of plowed surface area generated, which suggests a nearly constant energy per unit area of plowed surface J_s. Values for J_s are much bigger than the corresponding fracture surface energies and are proportional to $K_c^{3/2}H$. Much additional research is needed to evaluate the general validity of this plowing model and its applicability to different types of grinding operations.

References

1. Kovach, J.A., Blau, P.J., Malkin, S., Srinivasan, S., Bandyopadhyay, B., and Ziegler, K., 1993, A feasibility investigation of high speed, low damage grinding process for advanced ceramics, *5th Int. Grinding Conf.*, Vol. I, SME.
2. Malkin, S. and Hwang, T.W., 1996, Grinding mechanisms for ceramics, *Ann. CIRP*, Vol. 45/2, pp. 569–580.
3. Verlemann, E., 1993, Technologies and strategies for the machining of ceramic components, *Ceramic Monographs*, No. 1.8.3.1, Varley Schmid GmbH.
4. Lawn, B.R. and Swain, M.V., 1975, Microfracture beneath point indentations in brittle solids, *J. Mater. Sci.*, Vol. 10, pp. 113–122.
5. Hockey, B.J., 1971, Plastic deformation of aluminum oxide by indentation and abrasion, *J. Am. Ceram. Soc.*, Vol. 54, pp. 223–231.
6. Lawn, B.R. and Wilshaw, T.R., 1975, Indentation fracture: principles and applications, *J. Mater. Sci.*, Vol. 10, pp. 1049–1081.
7. Lawn, B.R. and Fuller, E.R., 1975, Equilibrium penny like cracks in indentation fracture, *J. Mater. Sci.*, Vol. 10, pp. 2016–2024.
8. Evans, A.G. and Wilshaw, T.R., 1976, Quasi-static solid particle damage in brittle materials: I, *Acta Metall.*, Vol. 24, pp. 939–956.
9. Lawn, B.R. and Evans, A.G., 1977, A model of crack initiation in elastic/plastic indentation fields, *J. Mater. Sci.*, Vol. 12, pp. 2195–2199.
10. Marshall, D.B. and Lawn, B.R., 1979, Residual stress effects in sharp contact cracking: part 1: indentation fracture mechanics, *J. Mater. Sci.*, Vol. 14, pp. 2001–2012.
11. Marshall, D.B., Lawn, B.R., and Chantikul, P., 1979, Residual stress effects in sharp contact cracking: part 2: strength degradation, *J. Mater. Sci.*, Vol. 14, pp. 2225–2235.
12. Lawn, B.R. and Evans, A.G., 1980, Elastic/plastic indentation damage in ceramics: the median/radial crack system, *J. Am. Ceram. Soc.*, Vol. 63, pp. 574–581.
13. Chiang, S.S., Marshall, D.B., and Evans, A.G., 1982, The response of solids to elastic/plastic indentation. I. Stresses and residual stresses, *J. Appl. Phys.*, Vol. 53(1), pp. 298–311.
14. Chiang, S.S., Marshall, D.B., and Evans, A.G., 1982, The response of solids to elastic/plastic indentation. II. Fracture initiation, *J. Appl. Phys.*, Vol. 53(1), pp. 312–317.
15. Marshall, D.B., Lawn, B.R., and Evans, A.G., 1982, Elastic/plastic indentation damage in ceramics: the lateral crack system, *J. Am. Ceram. Soc.*, Vol. 65, pp. 561–566.
16. Marshall, D.B., 1983, Controlled flaws in ceramics: a comparison of Knoop and Vickers indentation, *J. Am. Ceram. Soc.*, Vol. 66, pp. 127–131.
17. Marshall, D.B., 1984, Geometric effects in elastic/plastic indentation, *J. Am. Ceram. Soc.*, Vol. 67, pp. 57–60.
18. Samuels, L.E. and Mulhearn, T.O., 1957, An experimental investigation of the deformed zone associated with indentation hardness impressions, *J. Mech. Phys. Solids*, Vol. 5, p. 125.
19. Van Der Zwaag, S., Hagan, J.T., and Field, J.E., 1980, Studies of contact damage in polycrystalline zinc sulphide, *J. Mater. Sci.*, Vol. 15, pp. 2965–2972.

20. Marshall, D.B., 1983, Surface damage in ceramics: implications for strength degradation, erosion and wear, *Nitrogen Ceramics*, Riley, F.L., Ed., Nijhoff, The Hague, p. 635.
21. Marshall, D.B., Evans, A.G., Yakub Khuri, B.T., Tien, J.W., and Kimo, G.S., 1983, The nature of machining damage in brittle materials, *Proc. Roy. Soc. London*, Vol. A835, p. 461.
22. Lawn, B.R., Hockey, B.J., and Ritcher, H., 1983, Indentation analysis: applications in the strength in wear of brittle materials, *J. Microscopy*., Vol. 130, Pt. 3, p. 259.
23. Samuel, R. and Chandrasekar, S., 1989, Effect of residual stresses on the fracture of ground ceramics, *J. Am. Ceram. Soc*., Vol. 72, pp. 1960–1966.
24. Ahn, Y., Chandrasekar, S., and Farris, T.N., 1993, Measurement of residual stresses in machined ceramic using the indentation technique, *NIST SP* 847, pp. 135–146.
25. Hakulinen, M., 1985, Residual strength of ground hot isostatically pressed silicon nitride, *J. Mater. Sci*., Vol. 20, pp. 1049–1060.
26. Petrovic, J.J., Dirks, R.A., Jacobson, L.A., and Mendiratta, M.G., 1976, Effects of residual stresses on fracture from controlled surface flaws, *J. Am. Ceram. Soc*., Vol. 59, pp. 177–178.
27. Swain, M.V., 1976, A note on the residual stress about a pointed indentation impression in a brittle solid, *J. Mater. Sci*., Vol. 11, pp. 2345–2347.
28. Ota, M. and Miyahara, K., 1990, The influence of grinding on the flexural strength of ceramics, *4th Int. Grinding Conf*., SME Technical Paper MR90–537.
29. Conway, J.C., Jr. and Kirchner, H.P., 1980, The mechanics of crack initiation and propagation beneath a moving sharp indentor, *J. Mater. Sci*., Vol. 15, pp. 2879–2883.
30. Cheng, W., Ling, E., and Finnie, I., 1990, Median cracking of brittle solids due to scribing with sharp indentors, *J. Am. Ceram. Soc*., Vol. 73, pp. 580–586.
31. Kirchner, H.P., 1984, Comparison of single-point and multipoint grinding damage in glass, *J. Am. Ceram. Soc*., Vol. 67, pp. 347–353.
32. Kirchner, H.P., 1984, Damage penetration at elongated machining grooves in hot pressed Si_3N_4, *J. Am. Ceram. Soc*., Vol. 67, pp. 127–132.
33. Mayer, J.E., Jr. and Fang, G.P., 1993, Diamond grinding of silicon nitride, *NIST SP* 847, pp. 205–222.
34. Mecholsky, J.J., Freiman, S.W., and Rice, R.W., 1977, Effect of surface finish on strength of fracture of glass, *11th Int. Congress on Glass*, Prague, Czechoslovakia.
35. Thomas, M.B., West, R.D., and West, W.E., 1987, A study of selected grinding parameters on the surface finish and strength of hot pressed silicon nitride, *Intersociety Symp. on Machining of Adv. Ceramic Mater. and Components*, American Ceramic Society, pp. 218–234.
36. Miyasato, H., Okamoto, H., Usui, S., Miyamoto, A., and Ueno, Y., 1989, The effect of grinding on strength of hot-pressed silicon nitride, *ISIJ Int*., Vol. 29(9), pp. 726–733.
37. Andersson, C.A. and Bratton, R.J., 1979, Effect of surface finish on the strength of hot pressed silicon nitride, in *The Science of Ceramic Machining and Surface Finishing* II, *NBS Special Publication* 562, pp. 463–476.
38. Unno, K. and Imai, T., 1987, Performance of diamond wheel in grinding ceramics, *Proc. 6th Int. Conf. on Prod. Eng*., Osaka, pp. 26–32.
39. Kawamura, H., 1991, Study of grinding process and strength for ceramic heat insulated engine, *Superabrasives 91*, SME, pp. 9–1 to 9–7.
40. Spur, G. and Tio, T.H., 1988, Surface layer damage in grinding of advanced engineering ceramics, *Trans. NAMRC/SME* XVI, pp. 224–231.

41. Matsuo, Y., Ogasawara, T., and Kimura, S., 1987, Statistical analysis of the effect of surface grinding on the strength of alumina using Weibull's multi-modal function, *J. Mater. Sci.*, Vol. 22, pp. 1482–1488.
42. Hawman, M.W., Cohen, P.H., Conway, J.C., and Paangborn, R.N., 1985, The effect of grinding on the flexural strength of a sialon ceramic, *J. Mater. Sci.*, Vol. 20, pp. 482–490.
43. Kachanov, M. and Montagut, E., 1986, Interaction of a crack with certain micro-crack arrays, *Eng. Frac. Mech.*, Vol. 25, pp. 625–636.
44. Hu, K.X. and Chandra, A., 1993, A fracture mechanics approach to modeling strength degradation in ceramic grinding processes, *ASME J. Eng. Ind.*, Vol. 115, pp. 73–84.
45. Evans, A.G. and Marshall, D.B., 1981, Wear mechanisms in ceramics, *Fundamentals of Friction and Wear of Materials*, Rigney, D.A., Ed., ASME, pp. 439–452.
46. Koepke, B.G. and Strokes, R.J., 1979, Effect of workpiece properties on grinding forces in polycrystalline ceramics, in *The Science of Ceramic Machining and Surface Finishing* II, *NBS Special publication* 562, p. 75.
47. Kirchner, H.P. and Conway, J.C., 1985, Mechanisms of material removal and damage penetration during single point grinding of ceramics, *Machining of Ceramic Materials and Components*, ASME, New York, Vol. 17, pp. 53–61.
48. Larchuk T.J. Conway, J.C., Jr., and Kirchner, H.P., 1985, Crushing as a mechanism of material removal during abrasive machining, *J. Am. Ceram. Soc.*, Vol. 68, pp. 209–215.
49. Conway, J.C., Jr. and Kirchner, H.P., 1986, Crack branching as a mechanism of crushing during grinding, *J. Am. Ceram. Soc.*, Vol. 69, pp. 603–607.
50. Imanaka, A., Fujino, S., and Maneta, S., 1972, Direct observation of material removal process during grinding of ceramics by micro-flash technique, in *The Science of Ceramic Machining and Surface finishing*, *NBS Special Publication* 348, p. 37.
51. Huerta, M. and Malkin, S., 1976, Grinding of glass: the mechanics of the process, *ASME J. Eng. Ind.*, pp. 459–467.
52. Huerta, M. and Malkin, S., 1976, Grinding of glass: surface structure and fracture strength, *ASME J. Eng. Ind.*, pp. 468–473.
53. Pai, D.M., Ratterman, E., and Shaw, M.C., 1989, Grinding swarf, *Wear*, Vol. 131, pp. 329–339.
54. Zhang, B. and Howes, T.D., 1994, Material-removal mechanisms in grinding ceramics, *Ann. CIRP*, Vol. 43/1, pp. 305–308.
55. Zhang, B. and Howes, T.D., 1995, Subsurface evaluation of ground ceramics, *Ann. CIRP*, Vol. 44/1, pp. 263–266.
56. Toh, S.B. and McPherson, R., 1986, Fine scale abrasive wear of ceramics by a plastic cutting process, in *Science of Hard Materials, Inst. Phys. Conf.* Serf. No. 75, Chap. 9, Adam Higler, Ltd., Rhode, pp. 865–871.
57. Yoshikawa, M., Bi, Z., and Tokura, H., 1987, Observations of ceramic surface cracks by newly proposed methods, *J. Ceram. Soc., Jpn. Int. Ed.*, Vol. 95, pp. 911–918.
58. Zhang, B., Tokura, H., and Yoshikawa, M., 1988, Study on surface cracking of alumina scratched by single-point diamonds, *J. Mater. Sci.*, Vol. 23, pp. 3214–3224.
59. Johansson, S. and Schweitz, J., 1988, Contact damage in single-crystalline silicon investigated by cross-sectional transmission electron microscopy, *J. Am. Ceram. Soc.*, Vol. 71, pp. 617–623.

60. Tönshoff, H.K., Telle, R., and Roth, P., 1990, Chip formation and material removal in grinding of ceramics, *4th Int. Grinding Conf.*, SME Technical Paper MR90–539.
61. Brinksmeier, E., Preub, W., and Riemer, O., 1995, From friction to chip removal: an experimental investigation of micro cutting process. Part II: Ductile to brittle transition in monocrystalline silicon and germanium, *Proc. 8th Int. Prec. Eng. Sem.*, pp. 335–338, Compiegne, France.
62. Nakajima, T., Uno, Y., and Fujiwara, Y., 1989, Cutting mechanism of fine ceramics with a single point diamond, *Prec. Eng.*, Vol. 11, pp. 19–25.
63. Matsuo, T., Toyoura, S., Oshima, E., and Ohbuchi, Y., 1989, Effect of grain shape on cutting forces in superabrasive single-grit tests, *Ann. CIRP*, Vol. 38/1, pp. 323–326.
64. Xu, H.H.K., Jahanmir, S., and Wang, Y., 1995, Effect of grain size on scratch interactions and material removal in alumina, *J. Am. Ceram. Soc.*, Vol. 78, pp. 881–891.
65. Hwang, T.W. and Malkin S., 1999, Grinding mechanisms and energy balance for ceramics, *ASME J. Manuf. Sci. Eng.*, Vol. 121, pp. 623–631.
66. Singhal, S.C., 1976, Effect of water vapor on the oxidation of hot pressed silicon nitride and silicon carbide, *J. Am. Ceram. Soc.*, Vol. 59, pp. 81–82.
67. Zarudi, I. and Zhang, L.C., 1997, Subsurface structure change of silicon after ultra-precision grinding, *Advances in Abrasive Technology*, Zhang, L.C. and Yasunaga, N., Eds., World Scientific, Singapore, pp. 33–37.
68. Malkin, S., 1989, *Grinding Technology: Theory and Application of Machining with Abrasives*, John Wiley & Sons, New York. Reprinted by SME.
69. Spur, G., Stark, C., and Tio, T.H., 1985, Grinding of non-oxide ceramics using diamond grinding wheels, *Machining of Ceramic Materials and Components*, Subramanian, K. and Komanduri, R., Eds., PED-Vol. 17, ASME, p. 33.
70. Subramanian, K. and Keat, P.P., 1985, Parametric study on grindability of structural and electronic ceramics. Part I: *Machining of Ceramic Materials and Components*, Subramanian, K. and Komanduri, R., Eds., PED-Vol. 17, ASME, p. 25.
71. Inasaki, I. and Nakayama, K., 1986, High-efficiency grinding of advanced ceramics, *Ann. CIRP*, Vol. 35/1, pp. 211–214.
72. Chen, C., Jung Y., and Inasaki, I., 1989, Surface, cylindrical and internal grinding of advanced ceramics, *Grinding Fundamentals and Applications*, Malkin, S. and Kovach, J.A., Eds., PED-Vol. 39, ASME, pp. 201–211.
73. Kitajima, K., Kai, G.Q., Kumagai, N., Tanaka, Y., and Zheng, H.W., 1992, Study on mechanism of ceramics grinding, *Ann. CIRP*, Vol. 41/1, pp. 367–371.
74. Roth, P. and Tönshoff, H.K., 1993, Influence of microstructure on grindability of alumina ceramics, *NIST SP* 847, pp. 247–261.
75. Zhang, L.C., 1994, Grindability of some metallic and ceramic materials in CFG regimes, *Int. J. Mach. Tools Manufact.*, Vol. 34, No. 8, pp. 1045–1057.
76. Bifano, T.G., Dow, T.A., and Scattergood, R.O., 1991, Ductile regime grinding: a new technology for machining brittle materials, *ASME J. Eng. Ind.*, Vol. 113, pp. 184–189.
77. Hwang, T.W., 1997, Grinding energy and mechanisms for ceramics, PhD Thesis, University of Massachusetts.

4

Grinding of Ceramics with Attention to Strength and Depth of Grinding Damage

J.E. Mayer Jr.

CONTENTS

ABSTRACT Experimental grinding research has led to information regarding ground strength of the ceramic and depth of damage in the ceramic caused by grinding. Diamond wheel grit size and machine parameters of wheel depth of cut, workspeed, and wheelspeed in surface grinding were investigated. The investigated ceramic materials are hot-pressed silicon nitride, reaction-bonded silicon nitride, aluminum oxide, and silicon carbide. Results provide methodology to achieve maximum ground strength and to use damage depth information to minimize grinding time.

4.1 Introduction

Advanced engineering structural ceramics are in demand for various applications, especially for the automotive industry due to their outstanding high-temperature capacity, wear resistance, chemical resistance, and lower weight-to-strength ratio than metals. The high-temperature capacity of a ceramic engine allows fuel to be burned at higher temperature, which gives a better fuel efficiency. The better strength-to-weight ratio of ceramic material can reduce the weight of the engine and further enhance the fuel efficiency by reducing the overall weight of the vehicle. The excellent wear resistance of advanced engineering ceramic materials makes them the best candidates for applications such as industrial seals and bearings. Table 4.1 lists some applications of advanced structural ceramic materials. Recently, a diesel engine manufacturer reported the production of ceramic fuel injection pins, and an auxiliary turbine manufacturer is producing ceramic seals for its gas turbine engines.

Some of the most common advanced structural ceramics include aluminum oxide (alumina), silicon nitride, silicon carbide (SiC), and zirconium oxide (zirconia). Table 4.2 shows the sales distribution of major advanced ceramic items [1]. This table indicates that structural ceramics account for one-third of the $20 billion market, and this market is growing. Since advanced structural ceramics are the hardest among all the materials and some of them such as aluminum oxide and SiC are the most broadly used materials for making abrasives and conventional grinding wheels for grinding metals, it is therefore very difficult to machine these materials. By far, the grinding process with diamond grinding wheels is the only effective way of final shaping the advanced structural ceramics [2]. As a result of this, the machining cost can be from 70% to 90% of the total component cost [3]. In addition, the brittleness of the ceramic material makes it extremely vulnerable to incur microcracks during the grinding process, which can result in a highly inhomogeneous distribution in structural strength of the machined component [4].

TABLE 4.1

Applications of Advanced Structural Ceramic Materials

Applications of Advanced Structural Ceramics					
Textile machine parts	Bearings	Catalyst supports	Filters	Nozzles	Rolling jigs
Laboratory equipment	Burners	Cutting tools	Heaters	Port liners	Thermal insulators
Wear resistant parts	Casting dies	Drawing dies	Medical implants	Protection tubes Fuel injection pins	
Turbo charger wheels	Coil forms	Extrusion dies	Membranes	Pump parts	Seals
	Potential Applications				
	Engine Components		**Gas Turbine Parts**		
Bearings	Glow plugs	Diesel particulate traps	Bearings	Heat exchanger	Shrouds
Cylinder liners	Manifolds	Piston caps and rings	Blades	Housing	Stators
Prechamber	Tappets	Valves and seats	Heat shields	Rotor and shaft	

It is well known that the material removal mechanism in the grinding of ceramics is mainly a brittle fracturing process and grinding induced damage in terms of microcracks has been observed in various ceramics. Ceramic materials are very sensitive to cracks due to their low fracture toughness. The principal induced crack systems are the lateral cracks and the median cracks. The lateral cracks are parallel to the ground surface, and the median

TABLE 4.2

World Wide Advanced Ceramic Industry Sales

Major Items (Percentage Numbers in Parentheses are Based on 1994 Data)	**1993 (in Billions)**	**1994 (in Billions)**
Engineering structural ceramics (32%) Electrical and electronic ceramics (21%) Capacitors, substrates, and packages (20%) Electrical porcelain (5%) Bioceramics (1%) Others (21%)	$18.3 Total	$20.2 Total

cracks are perpendicular to the surface. The lateral cracks have been used to explain the material removal process and the median cracks to explain strength degradation [5,6].

This paper describes experimental grinding research, which has led to information regarding the ground strength of the ceramic and the depth of damage in the ceramic caused by grinding. Results provide methodology to achieve maximum ground strength and to use damage depth information to minimize grinding time.

4.2 Ceramic Materials

The ceramic materials investigated in this paper are hot-pressed silicon nitride (HPSN), reaction-bonded silicon nitride (RBSN), zirconia-toughened alumina (Al_2O_3), and porous SiC. The available material properties for these ceramics are given in Table 4.3. The HPSN and zirconia-toughened alumina ceramics were in the shape of flexural strength test bars cut from billets. The RBSN ceramic was molded into bars of the shape of flexural test specimens. The porous SiC ceramic was provided in the shape of flexural test specimens.

4.3 Experimental Procedure

4.3.1 Grinding

Surface grinding was employed to determine the ground strength of the ceramics and the depth of damage caused by the grinding process. Two

TABLE 4.3

Ceramic Material Properties

	HPSN	RBSN	Zirconia-Toughened Al_2O_3	Porous SiC
Grain size (μm)	—	1–2	1	—
Density (g/cm^3)	3.2	2.36	4.38	—
Porosity	<1%	20%	<0.5%	19.5%
Elastic modulus, E (GPa)	310	200	340	—
Vickers Hardness, H (GPa)	17.9	6.8	16.5	—
Flexural strength (MPa)	800	205	925	145
Fracture Toughness, K_{IC} (MPa m$^{\frac{1}{2}}$)	4.7	2.5	4.5	—
Brittleness, H/K_{IC} (m$^{-\frac{1}{2}}$)	3808	2720	3667	—

commercial surface grinders were used, one with microprocessor control on the wheel depth of cut which could be controlled at a unit of 1.27 microns. The other had computer numerical control (CNC) on all axes where the wheel depth of cut could be controlled at a unit of 0.254 microns. A water miscible synthetic grinding fluid was used with a concentration ratio of 1:30.

Resinoid-bonded diamond grinding wheels with 152.4 mm outer diameter and with different grit sizes were employed. The grit surface density was measured in this work by means of an optical microscope sighting on the grit flats after wheel truing and dressing. The grinding wheels were trued with a commercial diamond roll truing device and were dressed with aluminum oxide dressing sticks. Truing and dressing procedures were standardized and were as those recommended by the diamond grinding wheel supplier. For the truing process, each wheel is mounted on its own hub, which is not removed during the life of the wheel. The wheel is adjusted in the hub to make it concentric with the grinder spindle using a dial indicator, the outer surface of the wheel is coated with a permanent ink marker, and the wheel is trued until all the ink markings have been removed. By this truing process, the grinding wheel is expected to run quite precisely. The effect of wheel runout on the depth of cut that each grit takes has been estimated at about 2%–4%, or less, for the test conditions employed.

4.3.2 Grit Depth of Cut

The value of grit depth of cut, h_{max}, depends on both machine and wheel parameters. Equation 4.1 was used to compute the value of h_{max} in this research. This expression for h_{max} was proposed by Shaw, Reichenbach, and Mayer [7,8,9]. Figure 4.1 illustrates

$$h_{max} = \sqrt{\frac{4v_w}{v_c C r}} \sqrt{\frac{a_e}{d_s}}, \tag{4.1}$$

where h_{max} is the grit depth of cut (maximum undeformed chip thickness), C is the number of active cutting points per unit area of the wheel periphery (grit surface density), r is the ratio of chip width to average undeformed chip thickness, v_c is the wheel peripheral speed, v_w is the workpiece speed (table speed), a_e is the wheel depth of cut, and d_s is the wheel diameter.

The value of r is reported to be in the range of 10–20 [7]; but in this paper, r was assumed to be 10.

4.3.3 Strength Testing

Flexural strength tests were performed in accordance with MIL-STD-1942 (MR) [10,11] on all bars that are ground in this research. For HPSN ceramic,

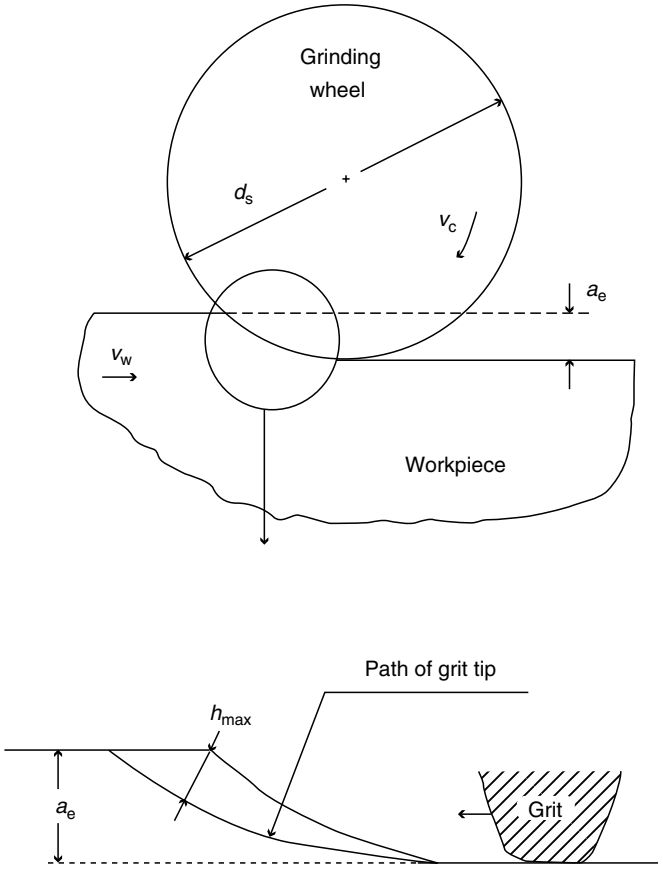

FIGURE 4.1
Illustration of the surface grinding process showing various process variables.

a total of five bars were tested for each grinding condition to establish the flexural strength. For the other ceramic materials, 10 bars were tested for each grinding condition to establish the flexural strength. The Weibull characteristic strength was used to present the results in this investigation.

4.3.4 Lapping

Ceramic workpieces, which have been ground under conditions that degrade the strength, can be brought back up to maximum strength by removing the damaged surface layer. The damaged layer can be removed by the lapping process, which is a low-stress process and imposes no further damage as it removes layers of surface. Diamond lapping was employed in this research to establish the depth of damage as a function of grinding grit depth of cut.

A lapping system equipped with a 15 in. copper lap plate and an electronically controlled diamond slurry dispenser was used in this research. A 3 μm diamond slurry was employed, which produced higher and more stable material removal rate than a 1 μm diamond slurry. The slurry was applied at a rate of 3 sec of spray every 30 sec. The lapping pressure on each ceramic test bar was 35,700 Pa. A sample carrier accommodated five test bars arranged around the outer perimeter of the carrier.

Only one lapping station (ring) was employed at a time because that gave better control over a consistent lapping process than using all three stations. Using these lapping conditions, a consistent depth removal rate of 0.01 mm in 20 min was achieved lapping the alumina ceramic. The copper lap plate needed reconditioning after every 20 min of use to reproduce a rough surface texture to entrap and embed diamond grits to perform the cutting action. A 140- or 170-mesh diamond-conditioning ring was employed, which gave higher material removal rate than a 120- or 140-mesh diamond-conditioning ring. The reconditioning time employed was 1–2 min.

4.3.5 Grinding Procedure for Determining Ground Strength

For investigating ground strength of HPSN and RBSN ceramics, the grit sizes of the wheels employed are shown in Table 4.4. The wheels have a concentration of 150 and an uncoated diamond. The width and thickness of the diamond layer are 3.17 mm.

For grinding of HPSN ceramic, the test conditions employed for finish grinding are shown in Table 4.5. The machine parameter of width of grind was held constant at $b_b = 1.59$ mm, and the wheel speed, v_c, was held constant at 24.7 m/sec. For test condition numbers 1, 2, 6, 7, and 8, five bars were ground with the grind direction longitudinal to the length of the bar, and another set of five bars were ground transverse to the bar length. For the other test conditions, the grind direction was either longitudinal or transverse (see Table 4.5).

For the grinding of RBSN ceramic, the test conditions employed for finish grinding are shown in Table 4.6. The machine parameter of width of grind was held constant at $b_b = 1.59$ mm. For test condition number 2 through

TABLE 4.4

Grit Size of Diamond Grinding Wheels

Wheel	Grit Mesh Size	Mean Grit Size (μm)	Grit Surface Density (#/mm^2)
D4/8MIC-R150	1200	5.1	49.91
SDG320-R150	320	50.8	27.59
SDG180-R150	180	87.5	11.66
SDG110-R150	110	152	8.324
SDG100-R150	100	249	6.402

TABLE 4.5

Test Conditions for HPSN Ceramic

Test Condition	HPSN Batch	Wheel Grit Size d_k (μm)	Table Feed v_w (mm/sec)	Depth of Cut a_e (mm)	Grind Direction	Grit Depth of Cut h_{max} (μm)
1	A	5.1	7.62	0.0013	L and T	0.0845
2	A	50.8	7.62	0.0025	L and T	0.1351
3	B	50.8	7.62	0.0025	L	0.1351
4	B	152	1.02	0.0254	T	0.1600
5	B	152	4.56	0.0013	T	0.1600
6	A	87.5	7.62	0.0025	L and T	0.2079
7	A	152	7.62	0.0025	L and T	0.2460
8	A	249	7.62	0.0025	L and T	0.2850
9	B	152	4.56	0.0254	T	0.3380
10	B	152	25.4	0.0508	T	0.95
11	B	152	80.43	0.0051	T	0.95
12	B	152	127.0	0.1270	T	2.67

Note: L represents longitudinal and T represents transverse.

number 8, ten bars were ground with the grind direction longitudinal to the length of the bar, and another set of ten bars were ground transverse to the bar length. For test condition number 1, the grinding direction was transverse. A similar procedure was employed to determine the ground strength of zirconia-toughened Al_2O_3 and porous SiC ceramics.

4.3.6 Grinding Procedure for Determining Damage Depth

For determining the depth of damage caused by the grinding of RBSN and zirconia-toughened alumina, the ceramic materials were first ground under a range of grit depth of cut conditions and then lapped to establish the depth

TABLE 4.6

Test Conditions for RBSN Ceramic

Test Condition	Wheel Grit Size d_k (μm)	Wheel Speed v_c (m/sec)	Table Feed v_w (mm/sec)	Depth of Cut a_e (mm)	Grit Depth of Cut h_{max} (μm)
1	50.8	47.1	2.00	0.0025	0.0500
2	50.8	39.9	6.73	0.0025	0.1000
3	50.8	24.7	7.62	0.0025	0.1351
4	87.5	24.7	7.62	0.0025	0.2079
5	152	24.7	7.62	0.0025	0.2460
6	249	24.7	7.62	0.0025	0.2805
7	152	31.9	36.4	0.0508	1.000
8	152	31.9	119.4	0.0762	2.000

TABLE 4.7

Grit Sizes of Diamond Grinding Wheels

Wheel	Grit Mesh Size	Mean Grit Size (μm)	Grit Surface Density (#/mm^2)
SD320-R100	320	50.8	29.07
SD110-R100	110	152	6.13

of grinding damage. Resinoid-bonded diamond wheels with a concentration of 100 were employed for the grinding phase. Table 4.7 shows the two different diamond grit sizes used. The wheel diameter was 152.4 mm.

The grinding conditions used for finish grinding in this research are shown in Table 4.8 and Table 4.9. Table 4.8 is for the grinding conditions for RBSN ceramic and Table 4.9 is for the alumina ceramic. The grind directions were perpendicular to the direction of the tensile stress in the subsequent flexural strength test, which is ground transverse to the length of the bar.

The procedure employed for determining the depth of damage caused by grinding is as follows. Large samples of 40 or more test workpieces are ground at each grinding test condition. The test workpieces ground at a given test condition are then subdivided into groups of five. The first group of five is flexural strength tested as ground. The Weibull characteristic strength is computed and is used as the strength of that group. The second group is lapped to a depth removed of either 0.0127 mm or 0.0254 mm as a starting point and strength tested. The depth removed by lapping is measured with a digital micrometer. The subsequent groups are lapped to incrementally increasing depths of material removal and then strength tested. A plot of flexural strength versus depth of material removed by lapping is made, and the lapped depth at which maximum strength is reached is taken as the effective damage depth for that particular grinding test condition. This lapping and strength testing procedure is then repeated for each test condition. This lapping and strength testing approach for experimentally determining the depth of damage induced in ceramics by the grinding process was previously employed by Spur [4] and Inasaki [12].

TABLE 4.8

Grinding Test Conditions for RBSN Ceramic

Test Condition No.	Wheel Grit Size d_k (μm)	Wheel Speed v_c (m/sec)	Table Feed v_w (mm/sec)	Depth of Cut a_e (mm)	Grit Depth of Cut h_{max} (μm)
1	50.8	47.1	2.12	0.0025	0.05
2	50.8	39.9	7.62	0.0025	0.10
3	152	24.7	7.62	0.0025	0.29
4	152	24.7	30.1	0.0508	1.20
5	152	24.7	119.4	0.0762	2.66

TABLE 4.9

Grinding Test Conditions for Zirconia Toughened Alumina Ceramic

Test Condition No.	Wheel Grit Size d_k (μm)	Wheel Speed v_c (m/sec)	Table Feed v_w (mm/sec)	Depth of Cut a_e (mm)	Grit Depth of Cut h_{max} (μm)
1	152	47.9	7.5	0.0025	0.23
2	152	39.9	14	0.0025	0.35
3	152	39.9	30	0.0051	0.61
4	152	31.9	80	0.0127	1.4
5	152	27.9	140	0.0381	2.6

4.4 Results and Discussion

4.4.1 Ground Strength

4.4.1.1 HPSN Ceramic

The flexural strength test results for HPSN ceramic for all the test conditions (test condition number 1 through number 12) are shown plotted against h_{max} in Figure 4.2 and Figure 4.3. Two curves are shown, one for longitudinal grinding and the other for transverse grinding. For longitudinal grinding, the flexural tensile stress was applied parallel to the grinding direction. For transverse grinding, the flexural stress was applied perpendicular to the grinding direction. The data point symbols, which are circles (either open or

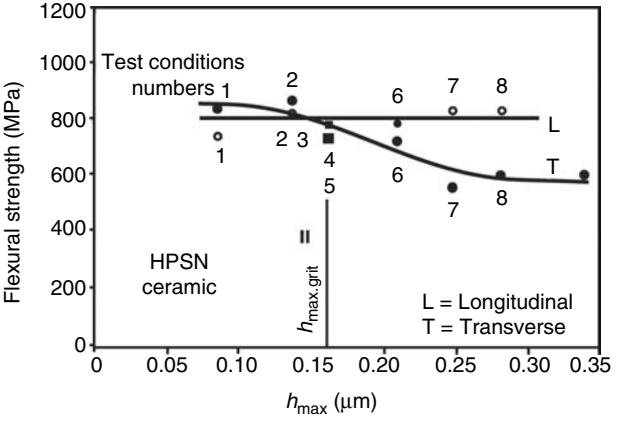

FIGURE 4.2

Flexural strength as a function of grit depth of cut, h_{max} (test condition number 1 through number 9), for HPSN ceramic.

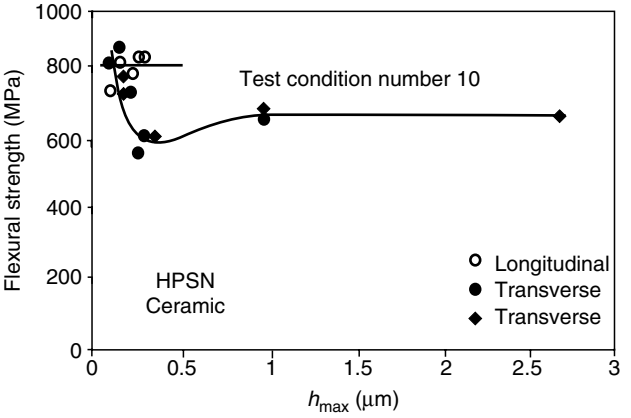

FIGURE 4.3
Flexural strength as a function of grit depth of cut, h_{max} (test condition number 1 through number 12), for HPSN ceramic.

solid circles), are for test conditions where only the wheel grit size was varied. The other data point symbols are for test conditions where only the machine parameters of workpiece speed and wheel depth of cut were varied. The data shown in Figure 4.2 were previously published by Mayer and Fang [13].

From Figure 4.2 and Figure 4.3, it can be seen that for grinding in the longitudinal direction there is little or no loss of strength as h_{max} increases for the range that is investigated. However, for transverse grinding, there is a decrease in strength as h_{max} increases beyond a critical value of h_{max} of about 0.160 μm. Figure 4.2 identifies this critical value of h_{max}.

It is concluded from Figure 4.2 and Figure 4.3 that the controlling factors regarding flexural strength are grind direction and wheel grit depth of cut, h_{max}. Additionally, a critical h_{max} value exists for maximum ground strength, and for HPSN this critical h_{max} value is about 0.160 μm.

4.4.1.2 RBSN Ceramic

Flexural strength test results for RBSN ceramic for test condition numbers. 1–8 are shown plotted against h_{max} in Figure 4.4 and Figure 4.5. Two curves are shown in these figures, one for longitudinal grinding and the other for transverse grinding. The data point symbols, which are circles (either open or solid), are for test conditions where only the wheel grit size was varied (test condition numbers 3 through number 6). The other data point symbols are for test conditions where only the machine parameters were varied.

Since h_{max} is solely a geometric factor, there might be concerns that thermal effects could also be a controlling factor. It should be observed that test condition number 1 is operating at near the maximum safe wheel speed for the resinoid-bonded grinding wheel employed in this research.

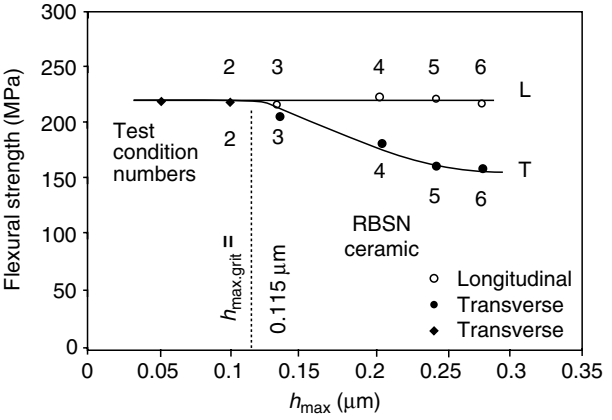

FIGURE 4.4
Flexural strength as a function of grit depth of cut, h_{max} (test condition number 1 through number 6), for RBSN ceramic.

From Figure 4.4 and Figure 4.5, it can be seen that for grinding in the longitudinal direction there is little or no loss of strength as h_{max} increases for the range that is investigated. For transverse grinding, there is a decrease in strength as h_{max} increases beyond a critical value of h_{max} of about 0.115 μm. Figure 4.4 identifies this critical value of h_{max}. The data in Figure 4.4 and Figure 4.5 were previously reported by Mayer and Fang [14].

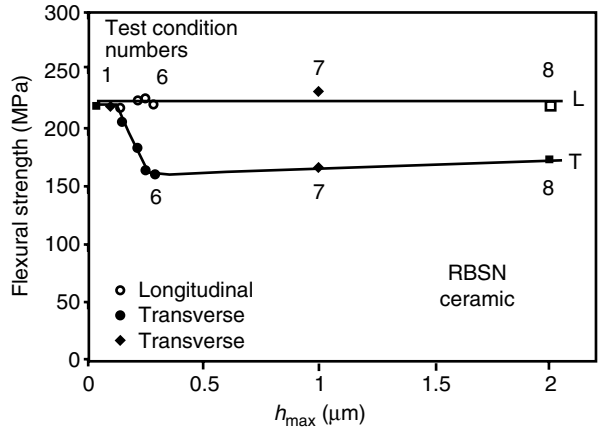

FIGURE 4.5
Flexural strength as a function of grit depth of cut, h_{max} (test condition number 1 through number 8), for RBSN ceramic.

Test condition numbers 2, 7, and 8 are also operating at elevated wheel speeds. Since the flexural strength data points for test condition numbers 1, 2, 7, and 8 fall along the same curves as for the lower wheel speed conditions (test condition number 1 through number 6), it appears that a thermal effect is not related to flexural strength for normal grinding conditions with ceramics.

It is concluded from Figure 4.4 and Figure 4.5 that the controlling factors regarding flexural strength are grind direction and wheel grit depth of cut, h_{max}, for the range of test conditions employed. Additionally, a critical h_{max} value exists for maximum ground strength, and for RBSN this critical h_{max} value is about 0.115 μm.

By comparing Figure 4.2 through Figure 4.5, it is seen that both ceramic materials have similar trends regarding flexural strength versus h_{max}. The higher inherent strength of HPSN is reflected in the higher maximum flexural strength for HPSN than that of RBSN. Note that each of these ceramic materials has its own value for critical grit depth of cut.

4.4.1.3 Other Ceramics

Grinding investigations have been conducted on other ceramics, namely zirconia-toughened alumina and porous SiC (19.5% porous), which further confirm the importance of the grit depth of cut, h_{max}, in regard to flexural strength of the ground ceramic. Figure 4.6 and Figure 4.7 show flexural strength versus h_{max} results for zirconia-toughened alumina. Although additional research is necessary, it is quite apparent that the critical h_{max} value is 0.05–0.1 μm or less for this ceramic. Note the substantial reduction in flexural strength as the critical h_{max} value is exceeded. Zirconia-toughened

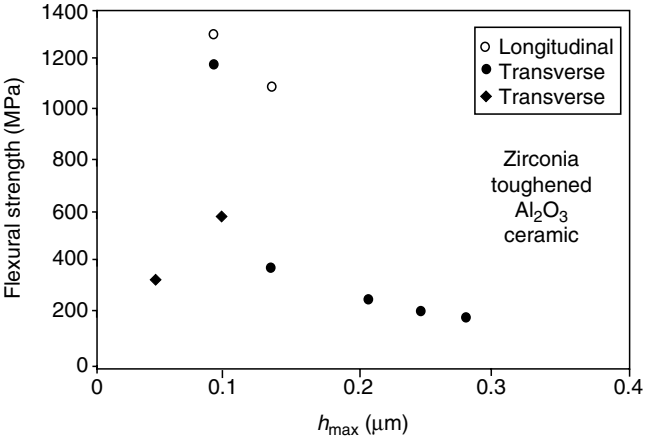

FIGURE 4.6
Flexural strength as a function of grit depth of cut, h_{max} (h_{max} up to 0.28 μm), for zirconia-toughened Al_2O_3 ceramic.

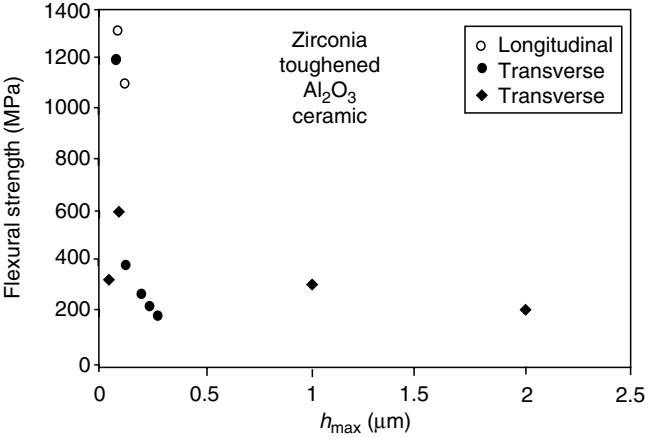

FIGURE 4.7
Flexural strength as a function of grit depth of cut, h_{max} (h_{max} up to 2.0 μm), for zirconia-toughened Al_2O_3 ceramic.

alumina can have high flexural strength; however, to achieve this it must be ground at an h_{max} value equal to or less than the critical value.

Results for the porous SiC are shown in Figure 4.8. It is seen from this figure that the flexural strength has not dropped off even at rather high h_{max} values. Figure 4.8 indicates that the critical h_{max} value for this ceramic is greater than 3.5 μm. This porous SiC has low, but very consistent strength regardless of the h_{max} value within normal grinding conditions.

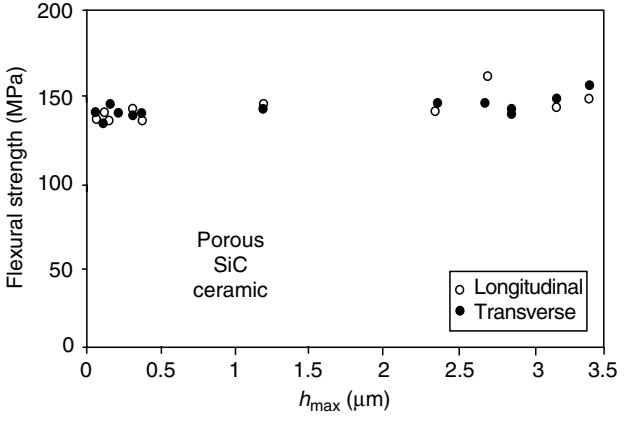

FIGURE 4.8
Flexural strength as a function of grit depth of cut, h_{max}, for porous SiC ceramic.

4.4.1.4 Guidelines for Efficient High-Strength Finish Grinding

Guidelines for efficient high-strength finish grinding of ceramics were previously published by Mayer and Fang [15]. The guidelines are developed using the data in Figure 4.2 through Figure 4.8, Equation 4.1, and the concept that it is best to employ the highest value of h_{max} to achieve higher grinding removal rates. This concept for maximum strength grinding means that

$$h_{max} = h_{max.grit}, \tag{4.2}$$

where $h_{max.grit}$ is the largest h_{max} value for which maximum strength occurs.

4.4.1.5 Physical Meaning of Critical Grit Depth of Cut

The physical interpretation of flexural strength versus h_{max} curves in Figure 4.2 through Figure 4.8 is that when h_{max} becomes small enough to cause the cracks induced by the grinding process to diminish in size equal to or smaller than those inherent in the ceramic material; then no reduction in strength will occur. In that case, maximum strength will occur.

As the size of the induced cracks is related to the stress imposed by each grinding grit, which is in turn related to the grit depth of cut, it is expected that the critical grit depth of cut should be controlled by fracture mechanics principles. Key material properties in fracture mechanics analysis as reported by Kirchner and Larchuk [16], Ota and Miyahara [17], and Veldkamp et al. [18] are fracture toughness (K_{IC}), hardness (H), and elastic modulus (E). Note also the large difference in porosity in these materials, which must also play a role. Only by a comprehensive fracture mechanics analysis can an analytical model for critical h_{max} regarding flexural strength be developed.

4.4.2 Depth of Damage

4.4.2.1 RBSN Ceramic

Figure 4.9a through Figure 4.9e show plots of flexural strength versus depth of material removed by lapping for RBSN ceramic for the grinding test conditions of h_{max} of 0.05, 0.10, 0.29, 1.20, and 2.66 μm, respectively. Note that when the grinding damage is removed, the strength reaches a rather consistent maximum value with further lapping depth removed. From Figure 4.9a through Figure 4.9e the effective grinding damage depth can be read. Figure 4.4 and Figure 4.5 show that the maximum strength for RBSN ceramic is 220 MPa. Figure 4.9a through Figure 4.9b are at maximum strength and therefore lapping is not expected to change the strength, and thus for h_{max} of 0.05 and 0.10 μm, the effective grinding damage depth is taken as 0 μm. Figure 4.9c through Figure 4.9e increase asymptotically to maximum strength.

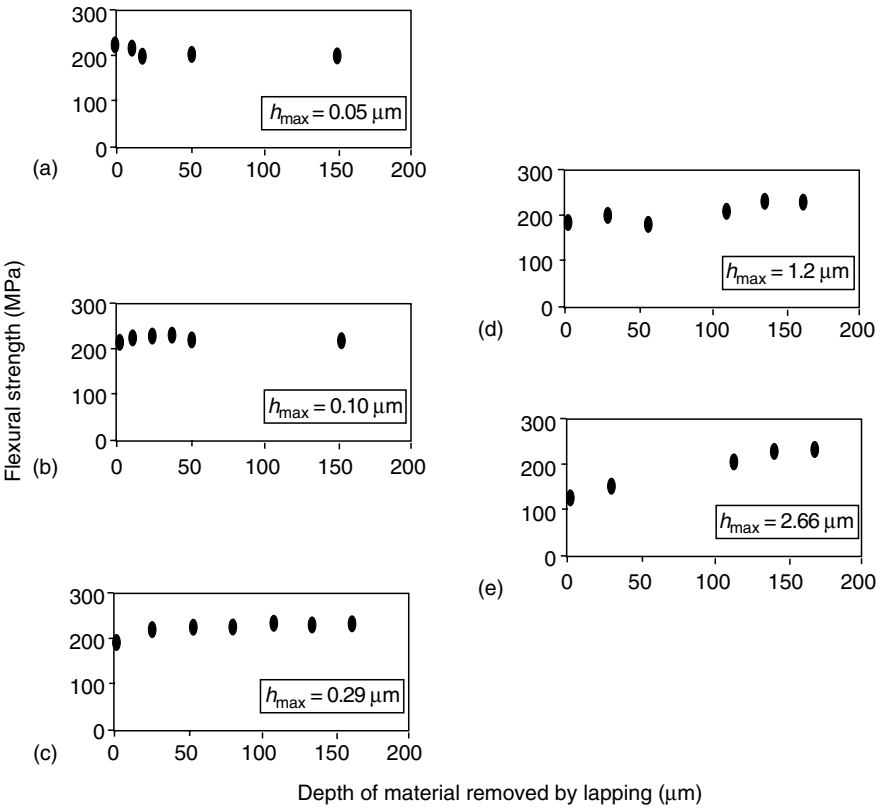

FIGURE 4.9
Flexural strength vs. depth of material removed by lapping for RBSN ceramic with original surface ground at (a) $h_{max} = 0.05$ μm, (b) $h_{max} = 0.10$ μm, (c) $h_{max} = 0.29$ μm, (d) $h_{max} = 1.20$ μm, and (e) $h_{max} = 2.26$ μm.

The grinding depth of damage is shown plotted against the grinding test conditions, h_{max}, in Figure 4.10 for RBSN ceramic as determined from Figure 4.9a through Figure 4.9e. The depth of damage shown in Figure 4.10, determined by the lapping method, is an effective depth of damage because it is based on flexural strength rather than on a direct measurement of the damage depth. From Figure 4.10, the effective grinding damage depth for RBSN ceramic appears to be 100–125 μm. The authors do not have a good explanation for the constant depth of damage at the larger grit depths of cut; perhaps residual stresses might be a factor.

4.4.2.2 Zirconia-Toughened Alumina Ceramic

Flexural strength versus depth of material removed by lapping results for zirconia-toughened alumina ceramic are shown in Figure 4.11a through

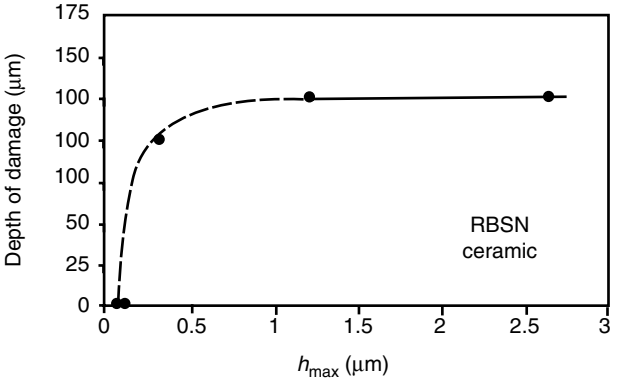

FIGURE 4.10
Depth of damage determined by the lapping method for RBSN ceramic.

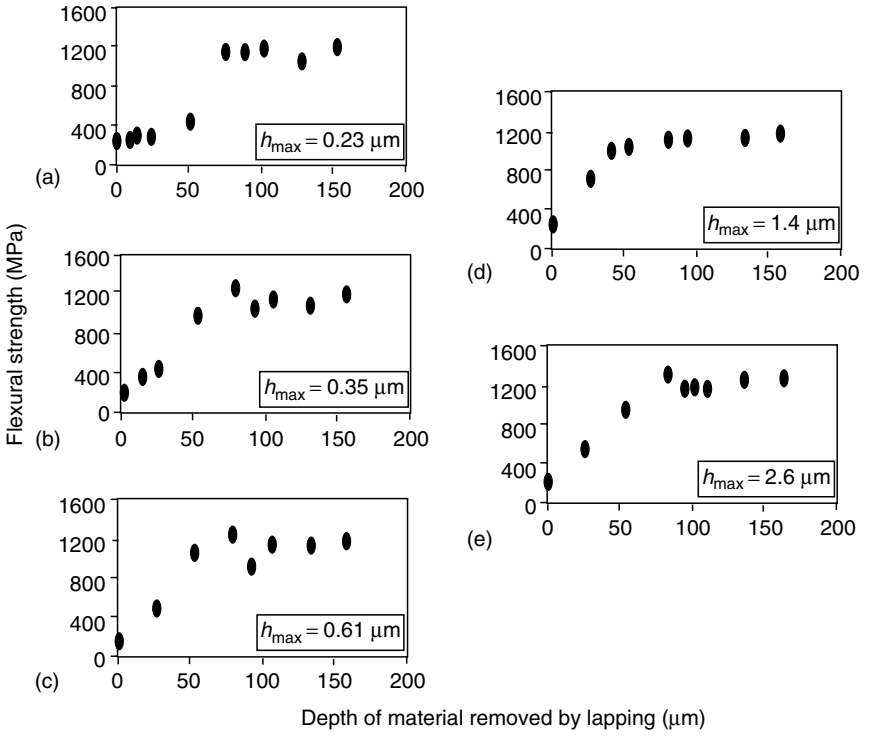

FIGURE 4.11
Flexural strength vs. depth of material removed by lapping for RBSN ceramic with original surface ground at (a) $h_{max} = 0.23$ μm, (b) $h_{max} = 0.35$ μm, (c) $h_{max} = 0.61$ μm, (d) $h_{max} = 1.4$ μm, and (e) $h_{max} = 2.6$ μm.

Figure 4.11e for the grinding test conditions of h_{max} of 0.23, 0.35, 0.61, 1.4, and 2.6 μm, respectively. Again, when the grinding damage is removed, the strength reaches a rather consistent maximum value with further lapping depth removed. From Figure 4.11a through Figure 4.11e the effective grinding damage depth was read.

The grinding depth of damage versus the grinding test conditions, h_{max}, results are shown in Figure 4.12 for zirconia-toughened alumina ceramic as determined from Figure 4.11a through Figure 4.11e. The effective depth of damage at h_{max} of about 0.1 μm, i.e., the critical h_{max} where maximum strength is reached during grinding is assumed to be 0 μm. From Figure 4.12, the effective grinding damage depth for zirconia-toughened alumina ceramic appears to be 75 μm.

The depth of damage was also computed based on the measured as-ground flexural strength and fracture mechanics [19]. The computed values for depth of damage are 165, 291, 271, 127, and 201 μm, respectively for the h_{max} values of 0.23, 0.35, 0.61, 1.4, and 2.6 μm. Although the computed values are of the right order of magnitude, it is concluded that the computed depth of damage is not as reliable as the depth of damage determined by the lap and strength test method.

Zhang and Howes [20] made direct measurements of the depth of grinding damage by an inspection process using SEM combined with an etching technique. They investigated other ceramics, namely, HPSN, hot-pressed alumina, and sintered SiC. Their results indicate that the damage depth increases exponentially with increases in grit depth of cut, h_{max}. They reported that the depth of damage for h_{max} of about 1 μm is 16 μm for SiC, 32 μm for alumina, and 42 μm for silicon nitride. The Zhang and Howes results are not based on strength data, whereas the results in this paper are effective depths of damage based on flexural strength.

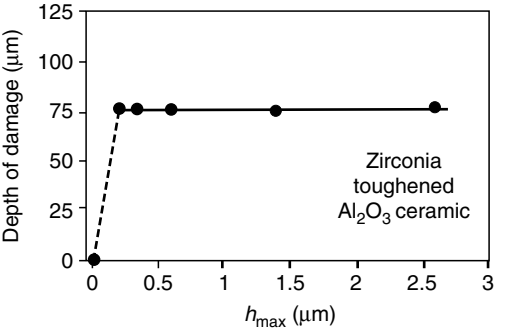

FIGURE 4.12
Depth of damage determined by the lapping method for zirconia-toughened alumina ceramic.

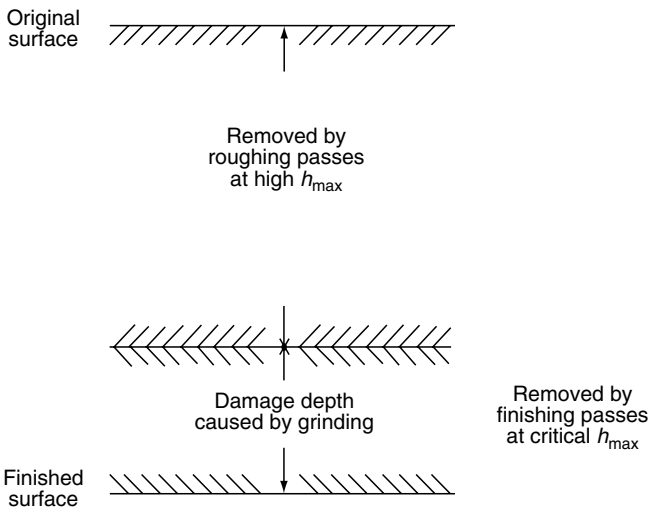

FIGURE 4.13
Strategy for minimum grinding time.

4.4.2.3 Strategy for Minimum Grinding Time

The plots of depth of damage versus h_{max} in Figure 4.10 and Figure 4.12 suggest a strategy for high removal rate grinding while achieving maximum strength. This strategy is rough grind at high h_{max} leaving an amount of finish stock equal to the damage imposed by the rough grinding, then finish grind at the critical h_{max} to remove the roughing damage and to achieve maximum strength. Figure 4.13 illustrates this strategy. By rough grinding at the highest h_{max} available on the grinding equipment, maximum removal rate is achieved for roughing. By finish grinding at the critical h_{max} value, maximum removal rate for finish grinding is achieved. Therefore, the shortest (or minimum) grinding time for completing both the roughing and finishing operations is achieved. To apply this strategy, the depth of damage needs to be established by means of an experimental method such as the lapping approach. Fortunately, the depth of damage appears to be a constant with increasing h_{max} values.

4.5 Conclusions

From the results of this research, the following conclusions regarding the grinding of ceramics can be drawn:

1. The controlling factors influencing flexural strength of ground ceramics appear to be grind direction and wheel grit depth of cut, h_{max}.

2. For longitudinal grinding, i.e., when the grinding direction is parallel to the applied tensile stress, the wheel grit depth of cut, h_{max}, has no effect on the flexural strength.
3. For transverse grinding, i.e., when the grinding direction is perpendicular to the applied tensile stress, the flexural strength drops off when the wheel grit depth of cut, h_{max}, is increased beyond a critical value.
4. Each ceramic material appears to have its own critical h_{max} value.
5. The lapping and strength testing approach can be used to experimentally determine the effective depth of damage caused by grinding of ceramics.
6. With the knowledge of the depth of damage, a strategy is proposed for high removal rate grinding including both roughing and finishing while still achieving maximum strength.

References

1. Ceramic Industry 1994, 1995.
2. McEachron, R.W. and Lorence, S.C., Superabrasives and structural ceramics in creep-feed grinding, *Ceramic Bulletin*, Vol. 67, No. 6, 1988, pp. 1031–1036.
3. Spur, G., Creep Feed Grinding of Advanced Engineering Ceramics, Note FER 08c, Production Technology Center Berlin, Pascalstrabe 8–9, D-1000 Berlin 10, 1990.
4. Konig, W., Cronjager, L., Spur, G., Tonshoff, H.-K., Vigneau, M., and Zdeblick, W.J., Machining of New Materials, *Annals of the CIRP*, Vol. 39/2, 1990, pp. 673–681.
5. Lawn, B.R. and Marshall, D.B., Indentation fracture and strength degradation in ceramics, *Fracture Mechanics of Ceramics, Vol. 3: Flaws and Testing*, Bradt, R.C., Hasselman, D.P.H. and Lange, F.F., Eds., Plenum Press, 1978.
6. Malkin, S. and Ritter, J.E., Grinding mechanisms and strength degradation for ceramics, *Intersociety Symposium on Machining of Advanced Ceramic Materials and Components*, ASME, 1988, pp. 57–72.
7. Kalpakjian, S., *Manufacturing Engineering and Technology*, Addision-Wesley Publishing Co., Reading, MA, 1989.
8. Reichenbach, G.S., Mayer, J.E., Kalpakcioglu, S., and Shaw, M.C., The role of chip thickness in grinding, *Trans. ASME*, Vol. 18, 1956, pp. 847–850.
9. Tonshoff, H.K., Peters, J., Inasaki, I., and Paul, T., Modelling and simulation of grinding processes, *Annals of the CIRP*, Vol. 41/2, 1992, pp. 677–688.
10. MIL-STD-1942(MR), Flexural Strength of High Performance Ceramics at Ambient Temperature, Department of the Army, Washington, DC, 1983.
11. Quinn, G.D., Baratta, F.I., and Conway, J.A., Commentary on U.S. Army Standard Test Method for Flexural Strength of High Performance Ceramics at Ambient Temperature, AD-A160 873, AMMRC 85-21, Army Material and Mechanics Research Center, Watertown, MA 02172-0001, 1985.

12. Inasaki, I., Grinding of hard and brittle materials, *Annals of the CIRP*, Vol. 36/2, 1987, pp. 463–471.
13. Mayer, J.E. Jr. and Fang, G.-P., Effect of grit depth of cut on strength of ground ceramics, *Annals of the CIRP*, Vol. 43/1, 1994, pp. 309–312.
14. Mayer, J.E. Jr., Fang, G.-P., and Edler, J.P., Grinding of reaction bonded silicon nitride (RBSN) ceramic, *Manufacturing Science and Engineering*, MED-Vol. 4, ASME, 1996, pp. 267–271.
15. Mayer, J.E. Jr. and Fang, G.-P., Efficient improved strength grinding of ceramics, *5th International Grinding Conference*, SME, 1993.
16. Kirchner, H.P. and Larchuk, T.J., Fracture mechanics investigation of grinding of ceramics, *Project Final Report*, Contract No. DE-AC01-83ER80015, U.S. Department of Energy, 1984.
17. Ota, M. and Miyahara, K., The influence of grinding on the flexural strength of ceramics, *SME Technical Paper*, MR90-538, 1990.
18. Veldkamp, J.D.B., Hattu, N., and Snijders, V.A.C., Crack formation during scratching of brittle materials, *Fracture Mechanics of Ceramics, Vol. 3: Flaws and Testing*, R.C. Bradt et al., Plenum Press, 1978.
19. Boettger, J.M., Ker, M.K., Shore, P., and Stephenson, D.J., Influence of ductile mode grinding on the strength of silicon based ceramics, *Proceedings of the International Conference on Machining of Advanced Materials*, NIST Special Publication 847, 1993, pp. 353–358.
20. Zhang, B. and Howes, T.D., Subsurface evaluation of ground ceramics, *Annals of the CIRP*, Vol. 44/1, 1995, pp. 263–266.

5

Highly Efficient and Ultraprecision Fabrication of Structural Ceramic Parts with the Application of Electrolytic In-Process Dressing Grinding

B.P. Bandyopadhyay, H. Ohmori, and A. Makinouchi

CONTENTS

SUMMARY In manufacturing parts from structural ceramics, grinding costs can constitute up to 80% of the total manufacturing costs; this has been well documented. The high cost of manufacturing is attributed to: (a) the low material removal rates (MRR) and (b) the high wear of the superabrasive wheels. By maximizing the MMR, grinding costs can be reduced significantly. However, high MRR leads to increased wear of the grinding wheel, which requires frequently redressing the grinding wheel by stopping the process. One of the authors of this paper, Dr. Ohmori, has pioneered a novel grinding technology, known as electrolytic in-process dressing (ELID), which incorporates ''in-process dressing'' of metal-bonded grinding wheels. This technology provides dressing of the metal-bonded wheels during the grinding process, while maintaining continuous protrudent abrasive from the superabrasive wheels. With ELID grinding applied to various structural ceramic materials for high MRR, successful grinding operations were accomplished using coarse grit-sized wheels. ELID grinding provided stable operations and achieved high MRR in conventional grinding machines. Both the principle and the characteristics of ELID grinding, with emphasis on their importance in industrial applications in the manufacture of ceramic components, will be addressed in this paper.

Two types of silicon nitride-based ceramics were ground using different grit-sized wheels and ELID technology. With the application of ELID, a mirror finish was realized with a #4000 mesh-size wheel (average grain size $= 4$ μm). Variations in ground surface topography caused by wheel grain size were analyzed using scanning electron microscopy (SEM) and atomic force microscopy (AFM). The SEM and AFM studies revealed that material was predominantly removed in the ductile mode when ELID grinding was performed using a #4000 grit-size wheel or finer.

The effects of finish ELID grinding on the flexural strength of silicon nitride specimens were studied. Kyocera's silicon nitride SN 235, in the form of modulus of rupture (MOR) specimens, was ground with a #6000 grit-sized cast iron-bonded diamond (CIB-D) grinding wheel. As a result of ductile mode grinding, with the application of finish ELID grinding, a significant improvement was noted in the strength of the Si_3N_4 specimens. ELID grinding, and an additional method to improve the flexural strength of silicon nitride specimens, will be addressed in this paper.

KEY WORDS *ELID (electrolytic in-process dressing), structural ceramics, electrodischarge truing (ED truing), metal-bonded diamond grinding wheels, cast iron fiber-bonded diamond grinding wheel, dynamometer, efficient grinding, grinding ratio, mirror finish grinding, ductile-mode grinding, brittle-mode grinding, scanning electron micrograph, atomic force micrograph, modulus of rupture.*

5.1 Introduction

Interest in advanced structural ceramics has increased significantly in recent years as a result of their unique physical properties and the significant improvement in their mechanical properties and reliability. The advantages of ceramics over other materials include: (a) high hardness and strength and their retention at elevated temperatures, (b) chemical stability, and (c) superior wear resistance. The advanced ceramic industry in the US consists of approximately 100 companies with sales equal to or greater than $14 billion per year with a yearly growth rate of about 8% [1]. Structural ceramics are categorized as one of the most difficult materials to machine effectively. However, this material is performing an important role in the advancement of industries such as aerospace, automobile, computer, fine mechanics, medical utility, and optical telecommunication. Time-consuming machining processes such as roughing, shaping, finishing, and polishing are inevitable for the commercialization of structural ceramics. Grinding costs can account for up to 80% of the component costs for ceramics, compared with 5% to 15% for metallic components [2]. This problem has forced manufacturers to strive for near net-shape processes, e.g., casting, cold compacting, injection molding, hot pressing, hot isostatic pressing, and so on. However, these processes are incapable of producing a part to precise dimensional tolerances with a high surface finish. Final machining is still commonly required.

Ceramic materials are generally machined by superabrasive wheels, most commonly diamond grinding wheels. The primary cost drivers in grinding structural ceramics are low efficiency due to low removal rates, high superabrasive wheel wear rates, and long wheel dressing time. Manufacturing engineers have tried solving the problem in traditional ways, using highly rigid grinding machines and tough metal-bonded superabrasive wheels. This research has led to the successful development of CIB-D grinding wheels. These wheels are manufactured by mixing diamond abrasive, cast iron powder or fibers, and a small amount of carbonyl powder. The wheels are compacted to a desired form under 6 to 8 ton/cm^2 pressure and sintering in an ammonia atmosphere. These wheels possess very high grinding ratio and can be used for high MRR. The comparison of the grinding ratio between the CIB-D wheel and resinoid-bonded wheel is shown in Figure 5.1 [3,4].

Although these wheels possess a high grinding ratio and can be used for high-MRR grinding of ceramics, they are not suitable for long-term continuous grinding for the following reasons:

1. Tougher metal-bonded wheels exhibit poor dressing ability; therefore, efficient and stable grinding will be difficult to achieve simultaneously.

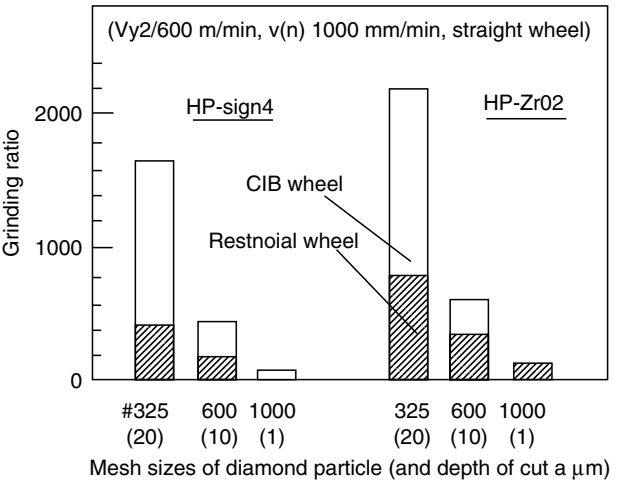

FIGURE 5.1
Comparison of grinding ratio between cast iron-bonded diamond (CIB-D) wheel and resinoid wheel.

2. High-MRR grinding will promote wear of the abrasive grains; therefore, more frequent redressing of the wheel will be required by stopping the grinding process.
3. While machining metals such as steel, wheel loading (embedment of swarf) will be caused.

Dr. Ohmori pioneered a novel grinding technology that incorporates in-process dressing of metal-bonded superabrasive wheels known as electrolytic in-process dressing (ELID), Japanese Patent No. 1,947,329 [5]. This technology provides in-process dressing to metal-bonded wheels, during the grinding process, for continuous protrudent abrasive from superabrasive wheels. The authors applied this technology in the grinding of representative structural ceramic materials such as silicon nitride (Kyocera's SN235), SiAlON, and tungsten carbide. Both conventional (non-ELID) and ELID high-MRR grinding were performed using rough grinding wheels with various bonds. A machining center and a turning center were used for efficient surface grinding and cylindrical grinding, respectively. The principle of ELID grinding technology, as well as the effect of various bonds, the type of power supply on the ELID grinding mechanism (in particular the manner of boundary layer formation on the wheels), and abrasive grit protrusion will be presented later in this paper. The results of high-efficiency grinding, mirror finish grinding, and the effect of finish ELID grinding on the strength of the silicon nitride specimens will also be presented.

5.2 ELID Grinding Principle

The concept of in-process dressing in a crude form was first proposed by Nakagawa and Suzuki [4]. Nakagawa and Suzuki studied the effects of in-process dressing with a dressing stick. The grinding wheel was dressed at the beginning of each stroke, as shown in Figure 5.2. The results of the in-process dressing are shown in Figure 5.3. The steady-state grinding force was significantly lower with in-process dressing than in grinding without in-process dressing. Because of these encouraging results, more progressive dressing methods using electric power have been developed. Dressing methods using electric power are not new, in fact the principle of ELID is based on ''electrochemical grinding'' (ECG) [5–6]. The grinding wheel is dressed because of the electrolysis process between the grinding wheel, which is made the anode, and the fixed copper electrode, which is made the cathode. The main difference between the ECG and ELID is that the purpose of ECG is to remove material from the work piece, whereas in ELID, the wheel is dressed by removing a small amount of material in the order of a few microns. This is achieved by using low current density during ELID. A bronze-bonded (BB) diamond grinding wheel was dressed using this technology [7]. However, the authors used a sodium chloride solution as an electrolyte, which is harmful to machine tools.

In-process dressing of grinding wheels, based on the electrodischarge principle is commercially available. The system uses an electro-conductive grinding wheel energized with a small amount of pulse current. Current flows from the wheel to the chuck through the coolant. The flow of ions creates hydrogen bubbles in the coolant, creating an electric potential across the wheel and coolant. When the potential becomes critical, a spark jumps across the bubble. These sparks melt the material as it begins to clog the wheel and thus provide in-process dressing [8]. This method does not provide continuous protrudent grains from the superabrasive wheels. Therefore, it is not suitable for ultrafine grinding of materials, particularly when using a micrograin-sized grinding wheel.

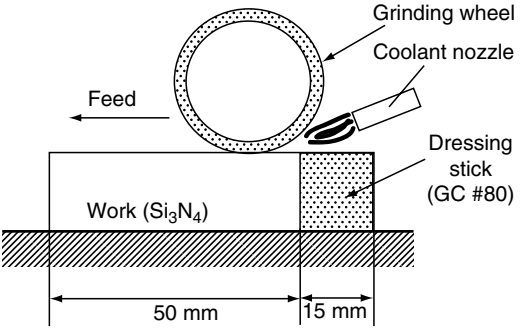

FIGURE 5.2
Schematic diagram of in-process dressing method with a dressing stick.

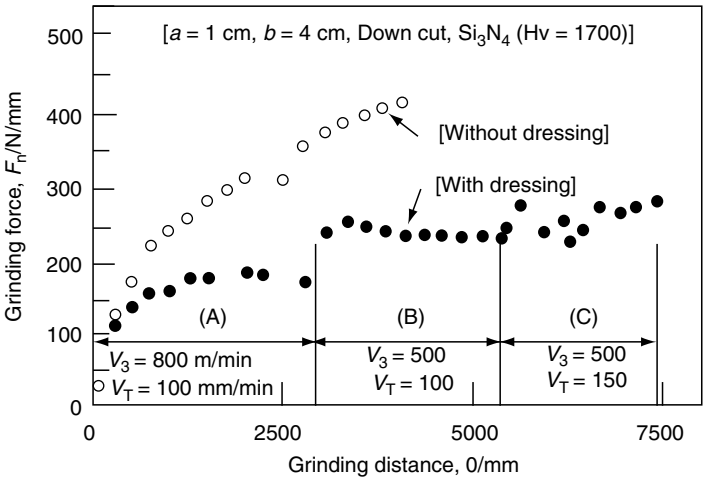

FIGURE 5.3
Grinding force with in-process and without in-process dressing.

ELID grinding was first proposed in 1988; a number of papers describing the advantages of the process have been published [9–11]. The basic construction of the ELID grinding system is shown in Figure 5.4. The ELID system's essential elements are as follows: (a) a metal-bonded grinding wheel, (b) an electric power source, and (c) an electrolytic coolant. The most important feature is that a special machine is not required. The principle of ELID grinding is shown in Figure 5.5 [12]. The metal-bonded grinding wheel is connected to the positive terminal of a power supply with a smooth brush contact, and a fixed electrode is made negative. The electrode is made from copper that has 1/6 of the wheel periphery length and a width of 2 mm more than the rim thickness of the wheel. The gap between the wheel and the electrode can be

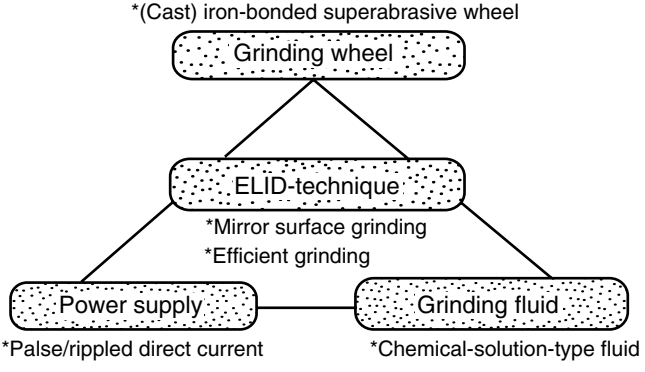

FIGURE 5.4
The ELID grinding technique.

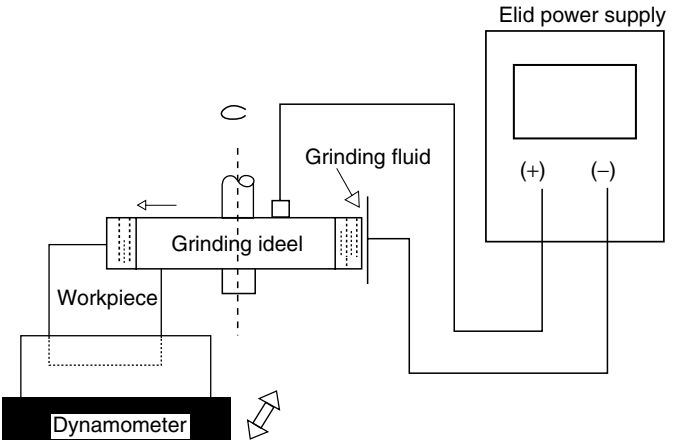

FIGURE 5.5
The principles of ELID grinding.

adjusted by mechanical means. A clearance of approximately 0.1 mm was kept between the positive and negative poles.

ELID grinding consists of the following steps:

1. Truing is required to reduce the initial eccentricity. In this investigation, the truing was performed with a SiC wheel of grit size #100. The operation was performed at 300 rpm.
2. Mechanical dressing is performed with an aluminum oxide stick of grit size #400, also at 300 rpm. The truing of tough metal-bonded wheels is very difficult and time consuming for coarse grit sized wheels of larger diameter. A new efficient electrodischarge truing (ED truing) has been developed and is discussed in Section 5.2.1.
3. Predressing of the wheel by electrolysis: predressing (also known as ELID dressing) was performed at 300 rpm for 30 min.
4. Grinding with ELID was carried out at the recommended cutting speed. The condition of electrolysis of the last two processes differs due to wheel surface condition during electrolysis.

5.2.1 Electrodischarge Truing Technique

Before beginning the grinding process, the grinding wheel is trued and dressed. This is required to reduce the wheel's eccentricity as a result of mounting it on the spindle. Truing is also carried out to provide a desired shape on a wheel or to correct a dulled profile. Truing of conventional wheels is easily performed with a diamond dresser. Although metal-bonded superabrasive wheels have many good features, such as high grinding ratios,

they are difficult to true. A significant amount of research has involved the areas of truing and dressing. The majority of these investigations were performed to study the effect of diamond dressing on surface roughness [13–15]. Some studies have focused on the mechanics of dressing [16] and the development of a mathematical model to characterize the wheel's topography [17]. In one investigation, authors [18] have measured the protrusion height of abrasive grains after truing and dressing. However, these studies have not produced an efficient method of truing of metal-bonded superabrasive wheels. The metal-bonded diamond grinding wheels can be efficiently trued using a newly developed method known as ED truing. The concept of ED truing was first introduced by the authors [19]. ED truing offers the following advantages: (a) applicable to all metal-bonded wheels and electrically conductive resinoid-bonded wheels, (b) precise truing due to on-machine application, (c) applicable to small wheels and thin wheels due to small applied force, (d) ED truing has a high efficiency, and (e) it can be applied for producing certain type of profile or shape. Because of the above mentioned advantages, ED truing has been applied for truing by other investigators [20,21].

In the ED truing system, the grinding wheel was rotated at a slower speed and while the cathode was turned and moved toward and along the axis of the grinding wheel. The same external power source was used for ED truing and ELID grinding. The ED truing system is shown in Figure 5.6. A copper tungsten electrode was selected for ED truing due to its excellent wear characteristics. Truing of the wheel was performed by varying both the voltage and current. To maintain insulation of the electrodes, a small amount of grinding fluid was added between them. During ED truing, the

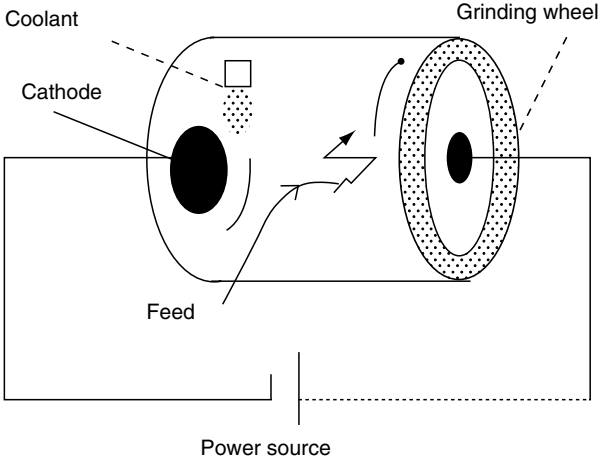

FIGURE 5.6
Electrodischarge truing system.

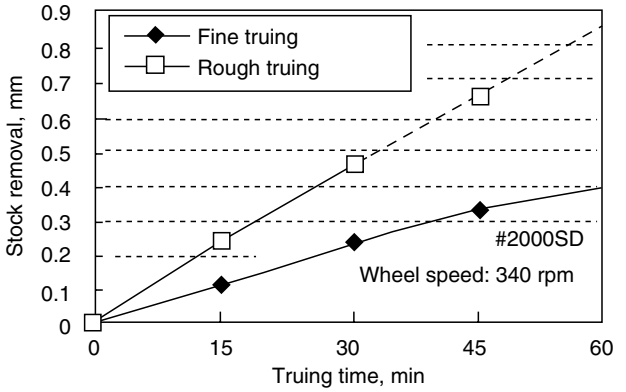

FIGURE 5.7
Change in stock removal in wheel diameter with truing time.

bonded material was melted and easily removed due to the spark between the wheel and the cathode. Figure 5.7 shows the relationship between the truing conditions and the decrease in wheel diameter. The rough truing efficiency was 0.2 mm of material removal in 15 min in the wheel diameter and the fine truing efficiency was about half of that (ED truing was applied on a bronze and iron-bonded hybrid wheel). The following electrodischarge conditions were used in this experiment: (a) wheel speed 340 rpm, (b) cathode speed 3090 rpm, (c) feed speed 100 mm/min, (d) depth of cut 2 μm/pass; electrical conditions: (a) for rough truing 150 V, 60 A and (b) for fine truing 120 V, 48 A, $\tau_{on/off}$: 12/3 μsec. The wheel, trued by the application of electrical discharge, has a straightness of 6 μm/W50 mm and a roundness of 2 μm/150 mm diameter, indicating a high profile accuracy.

5.2.2 Electrical Behavior during Predressing

The relationship between electric current, voltage, and time during electrical dressing is shown in Figure 5.8. When predressing starts (point 1), the surface of the trued wheel has good electrical conductivity. Therefore, the current is high as set in the power source, and the voltage between the wheel and the electrode is low. After several minutes the cast iron bond material, which is mostly ionized Fe^{+2}, is removed by electrolysis. The ionized Fe reacts to form $Fe(OH)_2$ and $Fe(OH)_3$ according to the following:

$$Fe \rightarrow Fe^{+2} + 2e^{-} \tag{5.1}$$

$$Fe^{+2} \rightarrow Fe^{+3} + e^{-} \tag{5.2}$$

$$H_2O \rightarrow H^{+} + OH^{-} \tag{5.3}$$

$$Fe^{+2} + 2OH^{-} \rightarrow Fe(OH)_2 \tag{5.4}$$

$$Fe^{+3} + 3OH^{-} \rightarrow Fe(OH)_3 \tag{5.5}$$

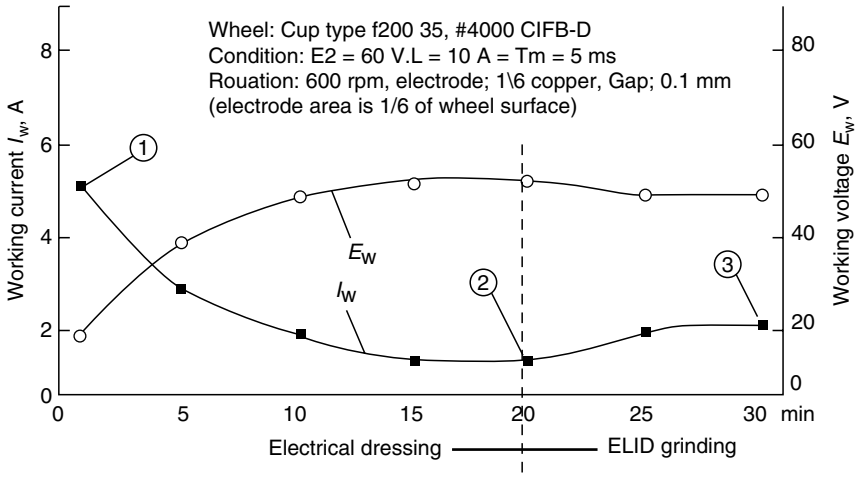

FIGURE 5.8
Electrical behavior during electrolytic dressing.

These hydroxides further change into oxides (e.g., Fe_2O_3) during electrolysis. After these reactions have occurred and insulating oxide layers grow on the wheel, its electrical conductivity will be reduced. The current decreases and the working voltage becomes as high as originally set in the open circuit voltage (denoted by 2).

5.2.3 ELID Grinding Mechanism

The various stages of ELID grinding are shown in Figure 5.9. At the beginning, grinding is performed with a predressed wheel and the protrudent grains grind the work piece. With time, the grains and the oxide layer begin to wear. The wear of the oxide layer causes an increase in the electroconductivity of the wheel surface, thus the electrolysis increases (denoted by 3 in Figure 5.8) and the oxide layer is recovered. The protrusion of the grains remains constant. For high-efficiency ELID grinding, a thinner insulating layer on the wheel surface is required. However, for a mirror finish ELID grinding a relatively thick oxide layer is preferred [22]. The ideal wheel condition is shown in Figure 5.10.

5.3 Experimental Setup

Most of the high-efficiency grinding experiments were conducted on a vertical machining center. A straight metal-bonded diamond grinding wheel was inserted into the machine spindle. The electrolysis occurs on

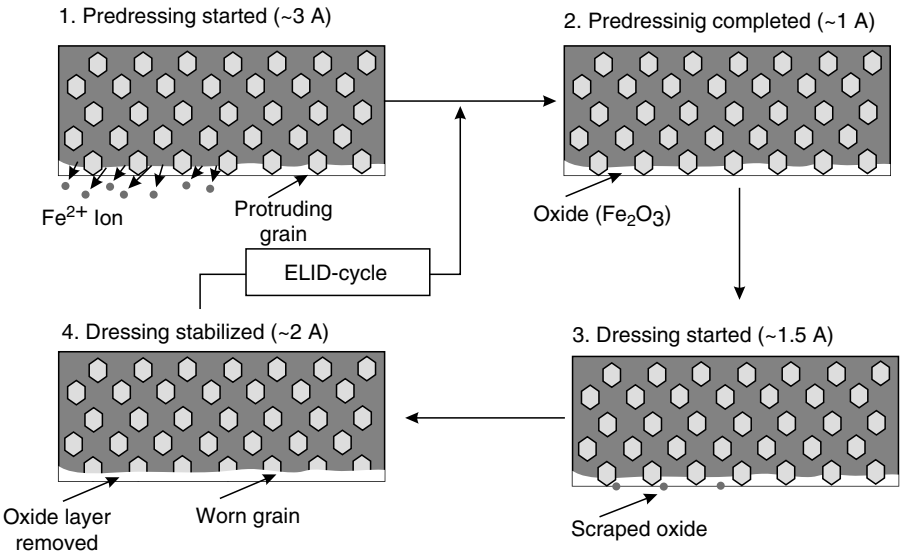

FIGURE 5.9
Mechanism of ELID grinding.

supplying a suitable grinding fluid and an electric current between the grinding wheel and the fixed electrode. The silicon nitride (Kyocera's SN235) was clamped to a vice that was firmly fixed to the base of a strain gage dynamometer. The dynamometer was clamped to the machining

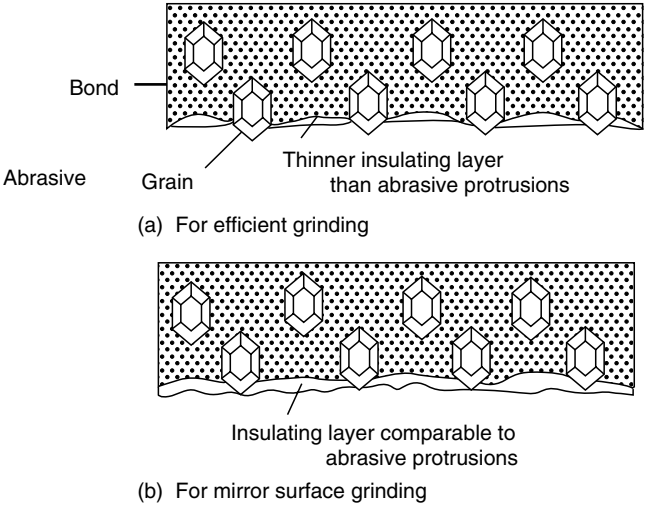

FIGURE 5.10
Ideal wheel condition for (a) efficient grinding and (b) mirror surface grinding.

center table and the reciprocating grinding operation was performed. The output from the dynamometer was recorded through a data acquisition system and the normal component of the force was monitored.

A vertical rotary surface grinder with a 5.5 kW motor was used for the ultraprecision grinding of ceramics. The spindle speed was regulated by means of an invertor. The spindle of the machine was mounted on hydrostatic oil bearings and the table feed was controlled by a direct current (DC) tachometer generator connected to a reduction motor, allowing for continuous feed adjustment. To study the effect of finish ELID grinding on the flexural strength of silicon nitride specimens, a Kuroda Precision Industries surface grinder model CS-CHF with a 2.2 kW spindle was used.

5.3.1 Grinding Wheels

Straight metal-bonded wheels were used in the high-MRR experiments. The specifications of the wheels are as follows:

1. Cast iron fiber-bonded (CIFB), cobalt-bonded (CB), bronze-bonded, cast iron powder-bonded wheels, and steel-bonded wheels with different diamond friabilities such as MBG-600, RVG, MBG-660
2. Straight wheels
3. Wheel diameter = 150 mm
4. Wheel width = 10 mm
5. Grit sizes = #140 (average grain size = 96 μm) and #170 (average grain size = 80 μm)
6. Concentration = 100

Cup type, CIFB diamond grinding wheels of 200 mm diameter and of different grit sizes were used in the ultraprecision ELID grinding experiment. In this series of investigations, the effect of grit size on the surface finish was studied. A straight, #6000 grit size (average grain size = 3.15 μm), SD cast iron-bonded wheel was used to study the effect of finish ELID grinding on the strength of ground silicon nitride specimens. The specimens were rough-ground using a #140 grit-size BB diamond wheel.

5.3.2 Grinding Fluid

Noritake AGF-M grinding fluid diluted to 1:50 was used in the experiments; the fluid rate was 20 to 30 L/min.

5.3.3 Power Supply

A direct pulse generator was used as a power supply. This is a modified power source from a conventional eletrodischarge machine. The power supply is capable of supplying different output voltages, current settings, and pulse on- and off-time settings. Fuji Elider in Tokyo markets power supplies of various capacities for ELID grinding [5]. These power supplies have the following advantages:

1. Very stable, powerful, high-frequency DC pulse current is available for a long period of time.
2. The generated high-frequency DC pulse current consists of high-quality square wave containing less harmonics or noises, which may interfere with other electronic devices nearby, such as computers or NC controllers.
3. The circuit is designed with enough marginal capacity to withstand any abuse handling such as short circuit of the output lines.

5.3.4 Materials

Silicon nitride material (Kyocera's SN 235) in the form of a rectangular block was used in these high-efficiency grinding experiments. The dimension of the work piece material was 50 $\times$ 50 $\times$ 20 mm. For the ultraprecision grinding experiments, two silicon nitride materials, a sintered reaction-bonded silicon nitride (SRBSN), and a cast and sintered silicon nitride (Si_3N_4) obtained from a commercial vendor were used. The microstructure of the two materials was studied using SEM on polished specimens. The backscattered electron mode of imaging was used to reveal the grains of silicon nitride. The grain size of the silicon nitride phase in SRBSN was between 0.3 μm and 0.4 μm, while the Si_3N_4 had a grain size between 0.6 and 0.8 μm. The effects of finish ELID grinding on the strength Kyocera's silicon nitride SN 235, in the form of MOR specimens, were studied. The size of the specimen was 3 $\times$ 10 $\times$ 50 mm.

5.3.5 Measuring Instrument Used

The surface finish was measured by a Mitutoyo 501 surface roughness measuring instrument using a 5 μm diamond stylus. A multicomponent strain gage dynamometer from Advanced Mechanical Technology, Inc., MC-12 Series was used for the measurement of force. Surface topography was analyzed using SEM and AFM. An Instron-type universal tester was used for the bending tests.

5.4 Results and Discussions

5.4.1 Influence of Bond Material

In this series of investigations, the effects of the three types of metal-bonded wheels, CIFB, CB, and BB, were studied. Figure 5.11 shows the effect of bonded material on the dressing current. A CIFB wheel has the type of electrical behavior that indicates easy isolation of the wheel surface, i.e., the working current easily decreases. In contrast, a CB wheel showed a relatively constant current during dressing, and a BB wheel showed almost constant current [23]. Figure 5.12 shows the change in the wheel diameter before and after dressing. A CIFB wheel has a thick insulating layer consisting of the oxides and hydroxides generated on the wheel surface. The thickness is checked by measuring the wheel diameter before and after dressing. A BB wheel has a thin insulating layer and a CB wheel has an insulating layer between these extremes. With a CB wheel, cobalt hydroxide or oxide will be formed, whereas with a BB wheel, copper hydroxide or oxide will be formed during the ELID dressing similar to the chemical reaction shown in the Equation 5.1 through Equation 5.5. Therefore, the wheel color after the ELID dressing will be different as shown in Figure 5.12. The thickness of the oxide layer will depend on the following factors: (a) the different rates of chemical reaction and (b) the stability of the oxides. With Fe_2O_3 as the most stable oxide, the oxide layer thickness in the CIFB wheel was found to be maximum [24].

For high-efficiency grinding, a thin insulating layer is preferred. This condition will provide a high dressing rate and high abrasive protrusion.

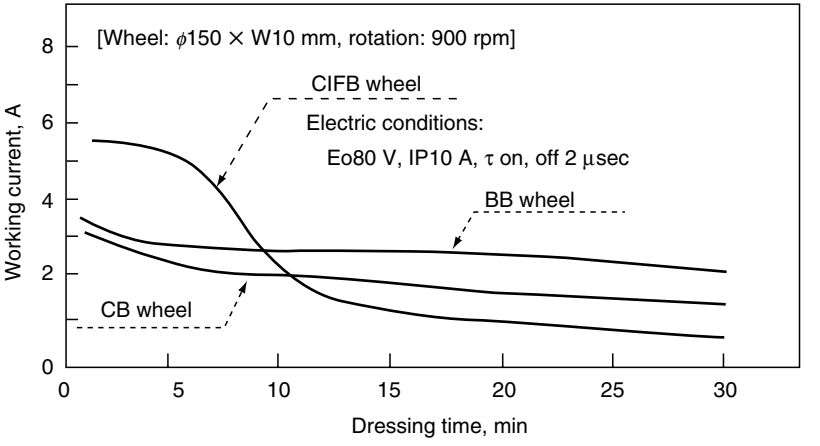

FIGURE 5.11
Difference in dressing current due to wheel bond material.

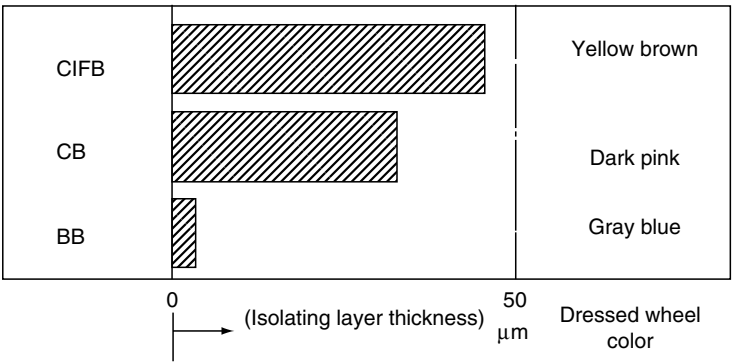

FIGURE 5.12
Difference in wheel diameter before and after predressing.

Therefore, BB wheels are recommended for rough grinding. The CIFB wheels that have a thick insulating layer should be used for mirror finish grinding. However, our investigations have shown that CIFB can be used for rough as well as mirror finish grinding.

After 30 min of predressing, each wheel (#140 metal-bonded CBN wheel) was tested for grinding steel and a plunge grinding operation was performed. Figure 5.13 shows the difference in the normal grinding force for the three bond materials. It is clear from the figure that a wheel with a thinner insulating layer has a lower grinding resistance (e.g., the BB wheel). The grinding force was maximum for the CIFB wheel.

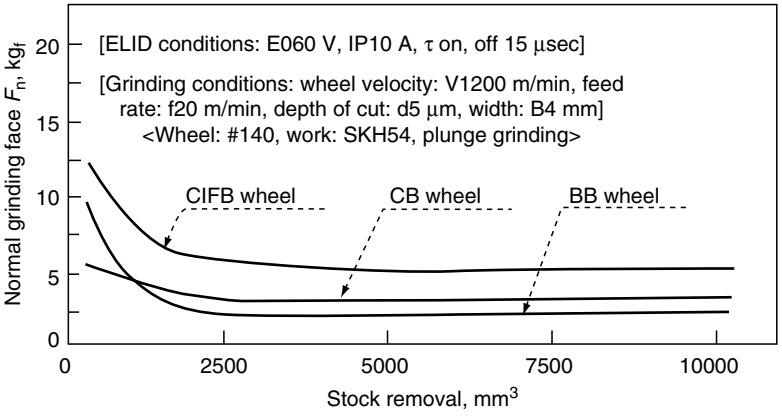

FIGURE 5.13
Difference in grinding force due to wheel bond material.

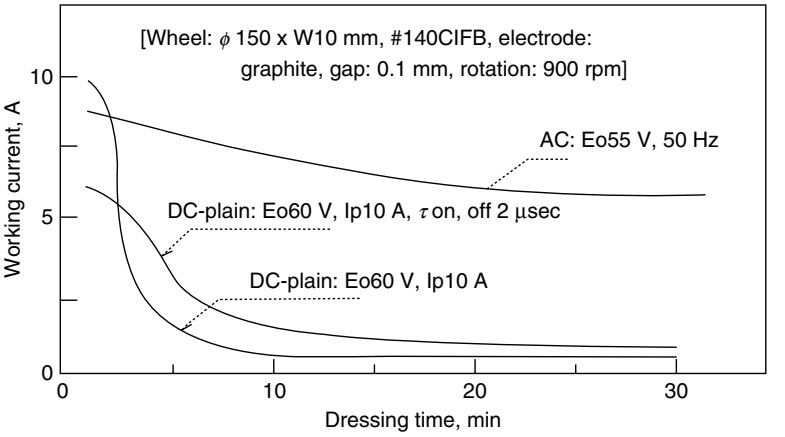

FIGURE 5.14
Difference in dressing current due to power source.

5.4.2 Influence of Power Source

The effects of using three types of power sources were studied on a CIFB-D grinding wheel: one using a DC-pulse, one using DC-plain (constant voltage) and one using alternate voltage (AC). Figure 5.14 shows the difference in dressing current depending on the type of the power source. The DC-plain produced the sharpest decrease in the dressing current, while AC caused the smallest decrease.

Figure 5.15 shows the difference in insulating layer and the etched layer thickness during the initial period of dressing. DC-plain caused the maximum thickness, and AC the least. The etched layer was obtained by

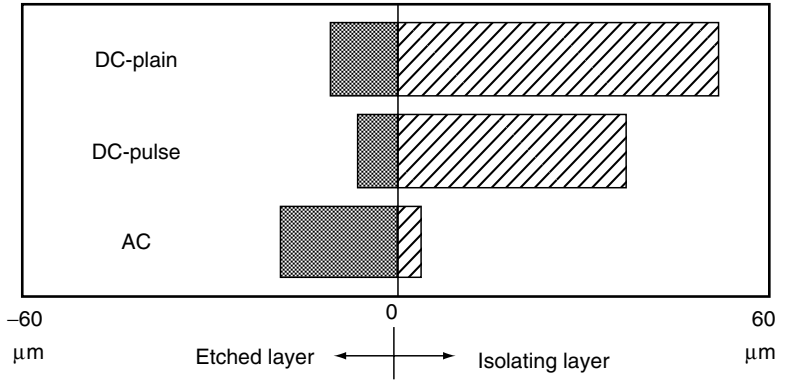

FIGURE 5.15
Difference in isolating layer and etched layer thickness due to power source.

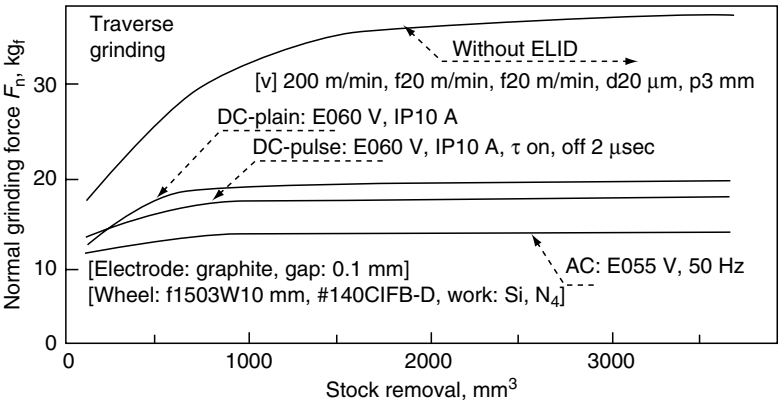

FIGURE 5.16
Difference in grinding force due to power source.

measuring the change in wheel diameter after dressing and scrapping the insulating layer. Figure 5.16 shows the effects of the power source on the normal component of the grinding force. The DC-plain source exhibited the highest grinding force because the thick oxide layer reduced the effectiveness of the cutting action. If a DC-plain source is applied to a CB or BB wheel, it should be effective because the wheels do not generate much of an insulating layer (see Figure 5.12).

5.4.3 Comparison between Conventional and ELID Grinding

Conventional and ELID grinding were performed with a CIFB-diamond grinding wheel. All the grinding wheels were trued and dressed before grinding, as described earlier, ensuring the same wheel condition for conventional and ELID grinding. This series of experiments was conducted under the following conditions: cutting speed = 1200 m/min, table feed rate = 5000 mm/min, depth of cut = 0.01 mm, and the width of cut = 5 mm; a CIFB-D wheel with grit size #170 was used. The MRR under this condition is 250 mm^3/min. The relationship between the total volume of material removed and the normal grinding force in conventional grinding is shown in Figure 5.17. During this process, there is a continuous increase in the grinding force. The grinding force reached around 38 kg_f (373 N) when the total volume of material removed was 6000 mm^3. The relationship between the normal grinding force during ELID grinding is shown in Figure 5.18. Both ELID dressing and ELID grinding were performed at 60 V, I_p = 16 A, and with 4 μsec as the on-time and off-time. The outer surface of the wheel became yellow after the ELID dressing, owing to the formation of iron oxides. Compared with Figure 5.17, the grinding force was less during ELID grinding. The

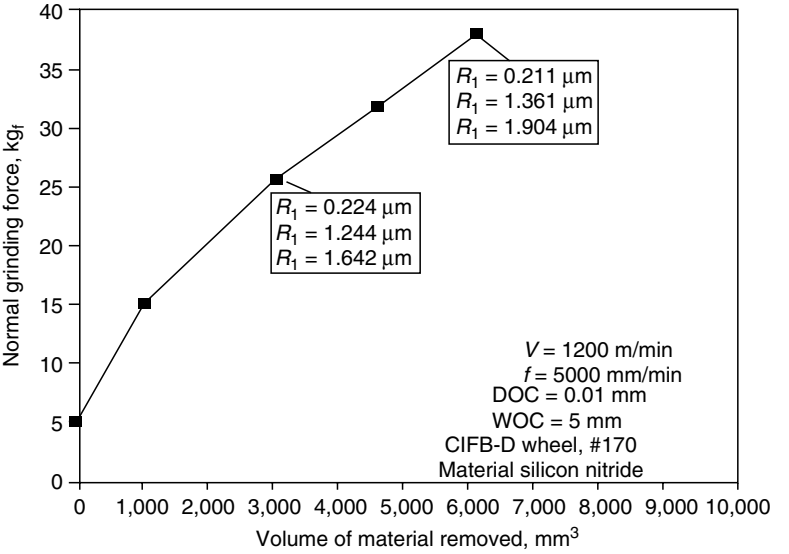

FIGURE 5.17
Relationship between the volume of material removed and the normal grinding force, conventional grinding; 1 kg_f = 9.81 N.

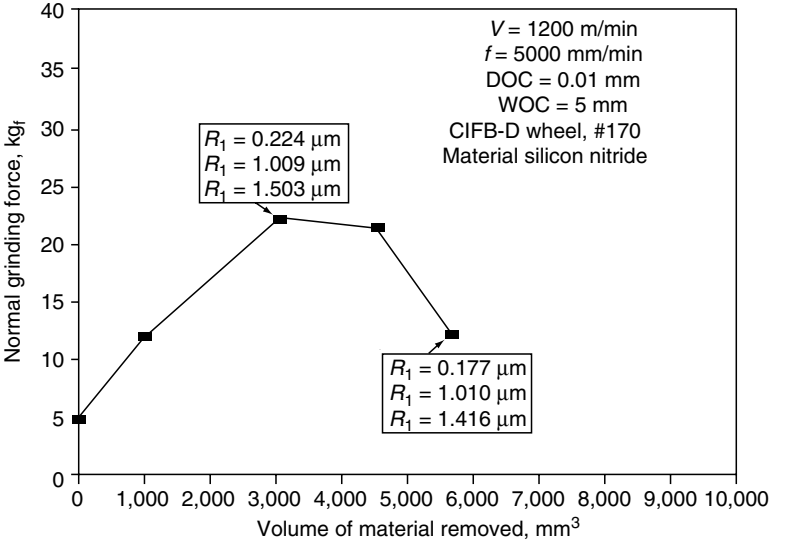

FIGURE 5.18
Relationship between the volume of material removed and the normal grinding force (ELID) grinding.

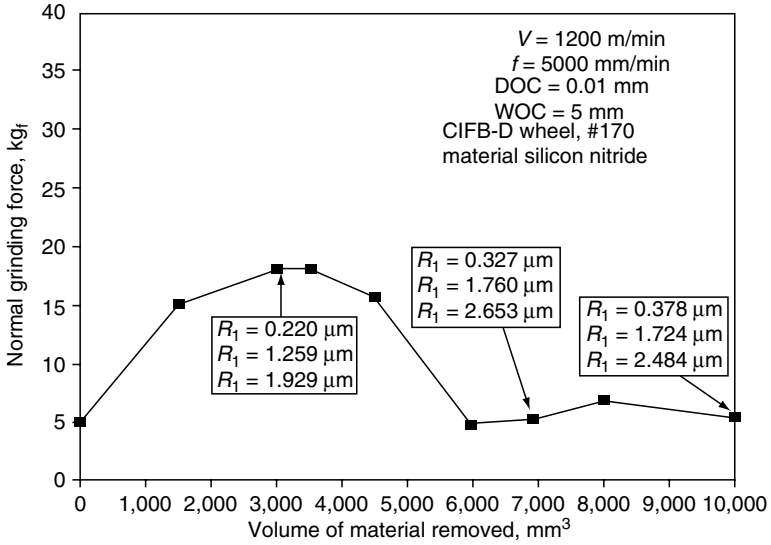

FIGURE 5.19
Relationship between the volume of material removed and the normal grinding force (ELID) grinding; $V = 90$ V; $I_p = 24$ A; $\tau_{on} = \tau_{off} = 4$ μsec.

effect is more visible after 4500 mm^3 of material removal, i.e., after 18 min of grinding. The effects of ELID grinding were studied by performing ELID grinding with the increased voltage such as 90 V and $I_p = 24$ A; the results are presented in Figure 5.19. The grinding force is less than that in conventional grinding (Figure 5.17) and ELID grinding with 60 V (Figure 5.18). The significant reduction in grinding force took place after 4500 mm^3 of material removal. The grinding force stabilized after 6000 mm^3 of material removal (24 min of grinding) and remained constant to only 5 kg_f (49 N). Therefore, the full potential of ELID grinding with low and stable grinding force can be used only after 6000 mm^3 of material removal. This can be achieved by using a ''dummy'' work piece in the beginning for a certain period of time (24 min under these cutting conditions), followed by ELID grinding of the actual ceramic parts. The other alternative will be to use modified ELID dressing, which will be discussed later.

Three surface finish parameters, center line average R_a, ten point height of the roughness profile R_z, and the maximum peak to valley height of the profile R_t, were measured after a particular interval. The results of these measurements are shown in Figure 5.17 through Figure 5.19. ELID and conventional grinding produced almost the same surface finish in rough grinding.

5.4.4 Modified ELID Dressing Grinding

Conventional grinding and ELID grinding were performed with CIFB-D grinding wheels of grit size #170 under different grinding conditions such

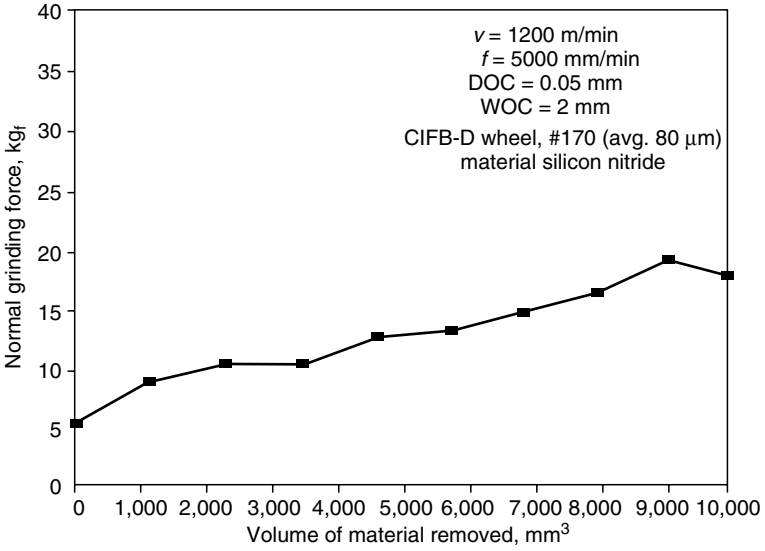

FIGURE 5.20
Relationship between the volume of material removed and the normal grinding force, conventional grinding.

as, a cutting speed of 1200 m/min, a feed rate of 5000 mm/min, depth of cut of 0.05 mm, and a width of cut of 2 mm. This will provide an MRR of 500 mm^3/min. ELID dressing was performed at 90 V for 30 min and ELID grinding was performed at 60 V; the results are presented in Figure 5.20 and Figure 5.21. Compared with conventional grinding, a lower grinding force was noted in the case of ELID grinding. As pointed out earlier, a stable grinding force was established after approximately 6000 mm^3 of material had been removed, i.e., 12 min of grinding. On comparing Figure 5.17 and Figure 5.20, it is found that the grinding force is less in Figure 5.20, but the MRR in this case is double that of the grinding shown in Figure 5.17. This is probably because the material is removed predominantly by brittle fracture [2,24]; therefore, less energy is required for the removal of the material.

The relationship between the volume of material removed and the grinding force with modified ELID dressing is shown in Figure 5.22. The modified ELID dressing was performed in two stages before ELID grinding. In the first stage, the ELID dressing was performed at 90 V for 30 min. The oxide layer formed during ELID dressing was removed mechanically by an aluminum oxide stick of grit size #400 at 300 rpm. Then, the second stage of ELID dressing was performed also at 90 V for 30 min. The electrical behavior during the modified ELID dressing is shown in Figure 5.23. ELID

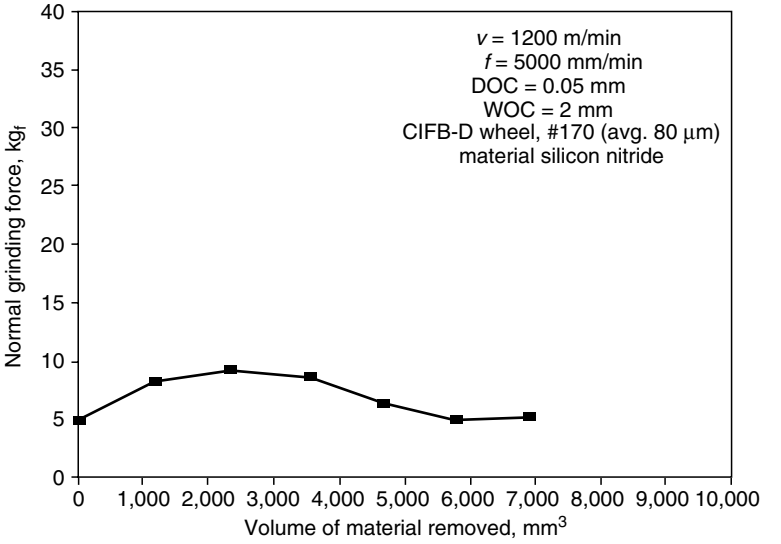

FIGURE 5.21
Relationship between the volume of material removed and the normal grinding force (ELID) grinding; $V = 60$ V; $I_p = 16$ A; $\tau_{on} = \tau_{off} = 4$ μsec, ELID dressed for 30 min with 90 V.

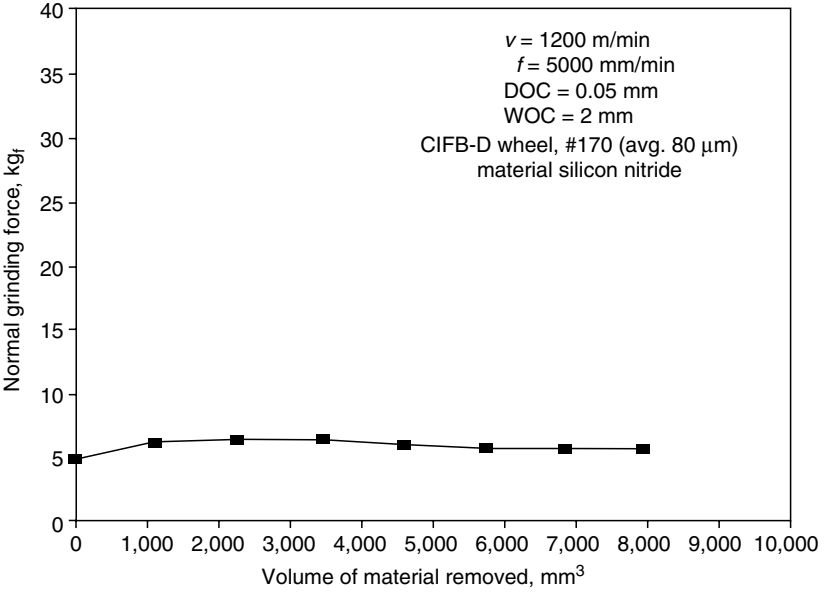

FIGURE 5.22
Relationship between the volume of material removed and the normal grinding force (ELID) grinding; $V = 60$ V; $I_p = 16$ A; $\tau_{on} = \tau_{off} = 4$ μsec, ELID dressed in two stages.

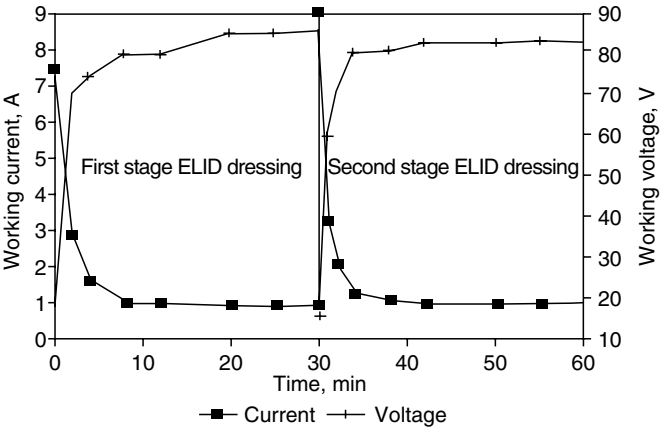

FIGURE 5.23
Electrical behavior of modified ELID dressing.

grinding was then performed with a 60 V supply. The grinding force remained low and almost constant from the beginning (Figure 5.22). Therefore, by applying modified ELID dressing as explained above, a stable and low grinding force can be achieved from the beginning.

5.4.5 Grinding with Bronze and Cobalt-Bonded Wheels

The relationship between the volume of material removed and the grinding force for the BB wheel is shown in Figure 5.24 and Figure 5.25. The same relationship for the CB wheel is shown in Figure 5.26 and Figure 5.27. With all these wheels, a significant reduction of grinding force was noticed when ELID grinding was performed. The stable grinding was achieved with the CIFB wheel after 12 min of grinding. However, for the both CB and BB wheels the stable grinding force was noticed almost immediately.

5.4.6 Investigation of Grinding Ratio

The grinding characteristics for silicon nitride ceramics under different grinding conditions were investigated with and without ELID. Figure 5.28 shows the change in the normal grinding force under the following conditions: depth of cut (d), 50 μm; feed rate (f), 5 m/min; grinding width (B), 3 mm; and the wheel velocity (V), 1500 m/min. A CIB-D grinding wheel was used in each of these experiments. When conventional grinding was performed, the normal grinding force changed severely and sparks were observed at the peaks of the normal grinding force. This phenomenon was caused by the extreme frictional heat generation between the wheel bond

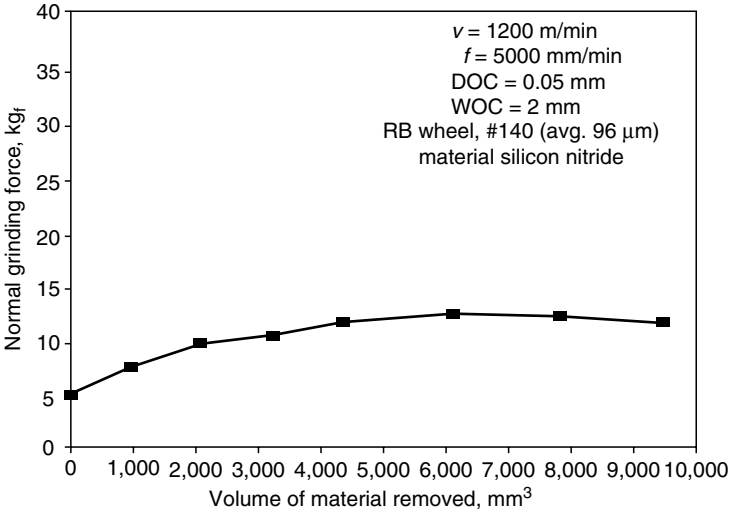

FIGURE 5.24
Relationship between the volume of material removed and the normal grinding force (conventional grinding).

surface and the work surface [24]. On the other hand, the grinding force with ELID showed little change from the start of the operation and stabilized at a lower value than the minimum value without ELID. Figure 5.29 shows the changes in the normal grinding force for tungsten carbide, with

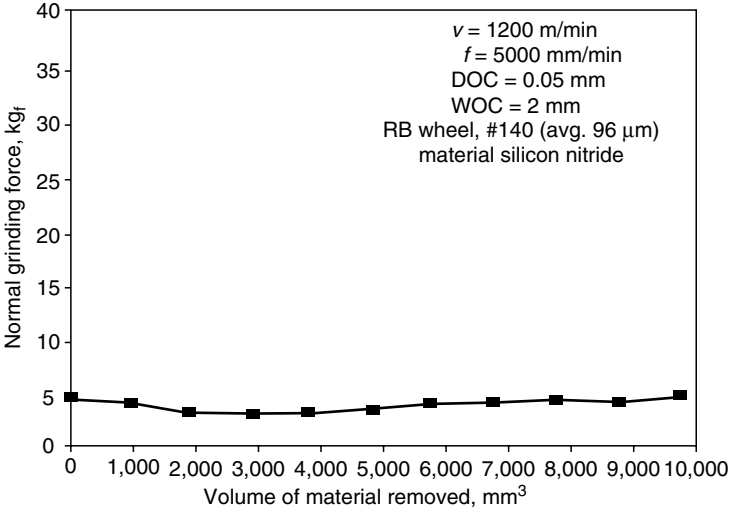

FIGURE 5.25
Relationship between the volume of material removed and the grinding force (ELID) grinding; $V = 60$ V, $I_p = 16$ A, $\tau_{on} = \tau_{off} = 4$ μsec, ELID dressed for 30 min with 60 V.

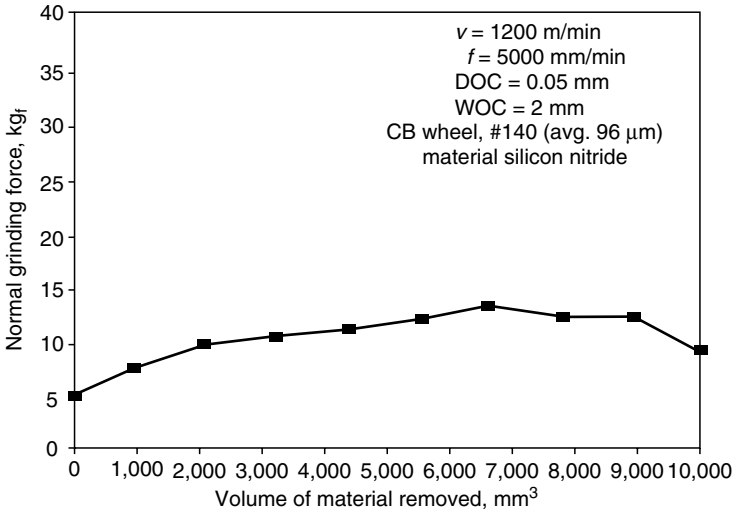

FIGURE 5.26
Relationship between the volume of material removed and the normal grinding force (conventional grinding).

or without ELID. Although the grinding force without ELID stabilized after rapid increase, ELID grinding produced a resistance that was several times lower. The grinding ratio (G-Ratio) was also determined as indicated in Figure 5.28 and Figure 5.29. In the case of silicon nitride, a reduction in

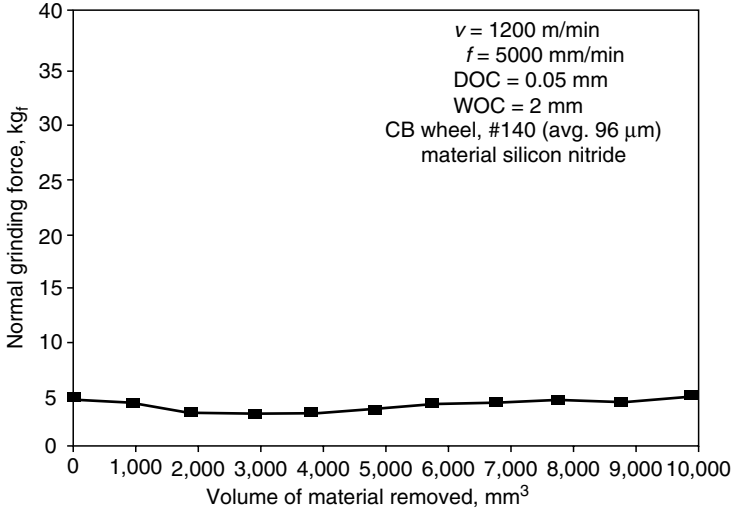

FIGURE 5.27
Relationship between the volume of material removed and the normal grinding force (ELID) grinding; $V = 60$ V, $I_p = 16$ A, $\tau_{on} = \tau_{off} = 4$ μsec, ELID dressed for 30 min with 60 V.

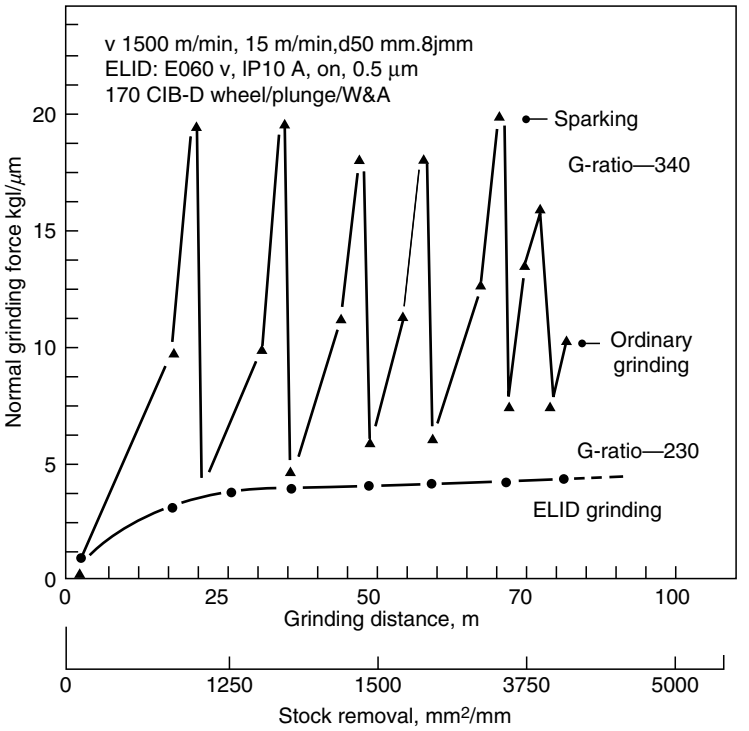

FIGURE 5.28
Effect of ELID on Si_3N_4 grinding.

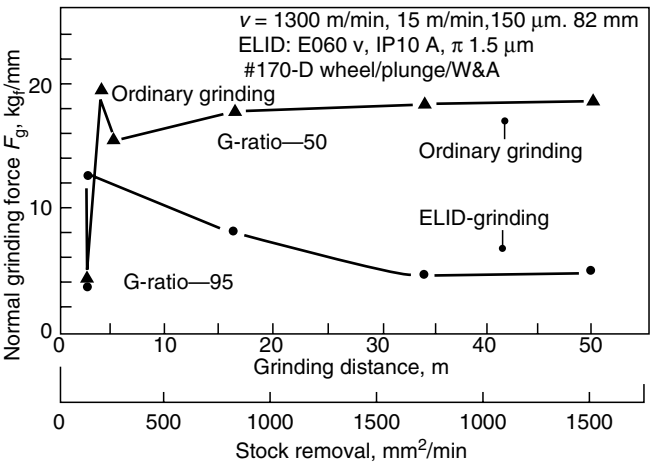

FIGURE 5.29
Effect of ELID on WC-Co grinding.

TABLE 5.1

G-Ratio

Wheel Type	Conventional Grinding	ELID Grinding
MBG-600	131	87
RVG	175	105
MBG-660	134	66
C.I. Powder Bonded	174	58

RBG: most friable, MBG-660: least friable, steel-bonded wheels.
Cutting conditions: $V = 1200$ m/min, $f = 5000$ mm/min, DOC = 0.05 mm, WOC = 2 mm, Grit size = #140, material: silicon nitride.

grinding ratio from 340 to 230 was noticed when ELID was performed. However, in the case of WC-Co, an improvement from 50 to 95 was observed when ELID was performed together with a lower stabilized force.

The next series of experiments were performed using diamond grinding wheels with a range of abrasive friability. Diamond grinding wheels with MBG 660, RVG, and MBG 600 diamonds were employed. RVG diamond is the most friable and MBG 660 the least friable. The bond material for all the wheels was steel. The grinding ratio for all these wheels and the cast iron powder-bonded wheels was determined for ELID grinding and for conventional grinding. The results are presented in Table 5.1.

There was a reduction in G-ratio when grinding using ELID. However, it should be noted that for high MRR using conventional grinding, frequent wheel dressing is required. This is a nonproductive time and for a metal-bonded wheel it may be quite high. Dressing will also remove some of the diamond layer from the wheel [25]. In ELID grinding however, the force remains lower and almost constant. Therefore, the grinding can be performed for a long time producing parts cost effectively.

5.4.7 Efficient Cylindrical Grinding on a Turning Center

As stated earlier in Section 5.2, no special machine is required for ELID grinding. A turning center was modified for cylindrical grinding with ELID. This machine realizes efficient cylindrical grinding with a traverse tool path shown in Figure 5.30. Efficient cylindrical grinding operation was performed with SiAlON. Figure 5.31 shows the changes in the grinding spindle load with ELID and without ELID. The changes with ELID were smaller than those without ELID and the load with ELID more or less stabilized at much lower values than without ELID. The following grinding conditions were used: depth of cut (d), 100 μm per diameter; traverse speed (f), 150 mm/min; work velocity (v), 30 m/min; and the wheel velocity (V), 1413 m/min.

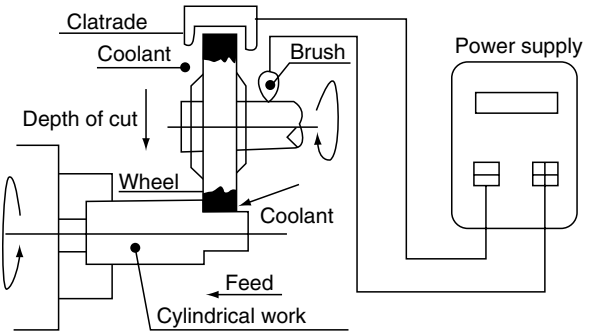

FIGURE 5.30
Schematic of ELID grinding for cylindrical grinding method.

5.4.8 Ultraprecision Grinding with ELID

Experiments were conducted to study the effects of mesh size on the surface finish of the work piece. The surface grinding operation was performed on a vertical rotary surface grinder. Cup type CIFB diamond grinding wheels of 200 mm diameter were used in the experiment. Grinding wheels of various grit sizes were used in the experiments (see Table 5.2). A DC pulse generator was used as a power supply, with an open voltage of 60 V (square wave) and a peak current of 10 A. The pulse width can be adjusted in the experiments and set to 5 μsec on-time and off-time. The following cutting conditions were used in the experiments: cutting speed, 21.5 m/sec; work piece feed rate, 80 mm/min; and the depth of cut, 1μm/pass. The results of ELID grinding are presented in Figure 5.32 and Figure 5.33 [26,27]. Three surface

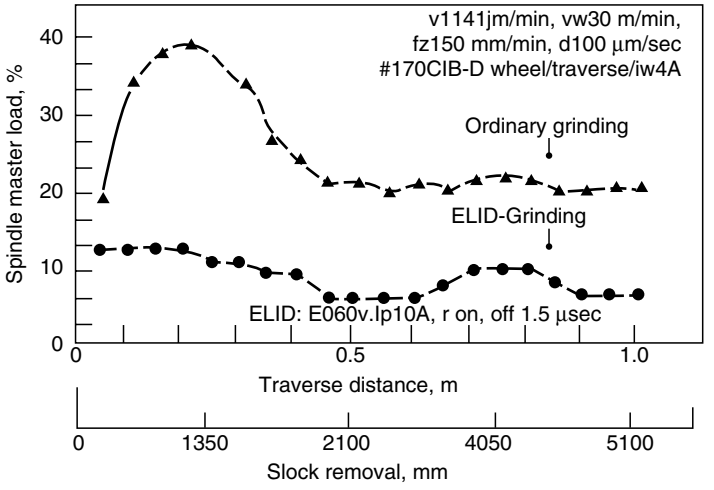

FIGURE 5.31
Effect of ELID in SiA1ON grinding (cylindrical grinding on a turning center).

TABLE 5.2

Grain Size of Used Diamond Grinding Wheels

Mesh Size	Grain Size (mm)	Average Grain Size (mm)
#325	40–90	63.0
#600	20–30	25.5
#1200	8–16	11.6
#2000	5–10	6.88
#4000	2–6	4.06
#6000	1.5–4	3.15
#8000	0.5–3	1.76

finish parameters R_a, R_z, and R_{max} were measured after the grinding operations. A mirror finish surface was obtained when ELID grinding was performed with a #4000 mesh-size wheel or finer. Figure 5.32 and Figure 5.33 show a significant improvement in surface finish when grinding using a #4000 mesh wheel compared with #2000 mesh wheel. Better surface finish was obtained with the SRBSN material than Si_3N_4, especially when using rougher wheels. However, with finer wheels (#4000) almost the same surface finish was obtained with both materials. The results are shown in Figure 5.34 [27]. To produce a mirror surface finish by ELID grinding, a three-step operation was required. The silicon nitride specimens were first ground with a #325 mesh-size wheel. These specimens were further ground

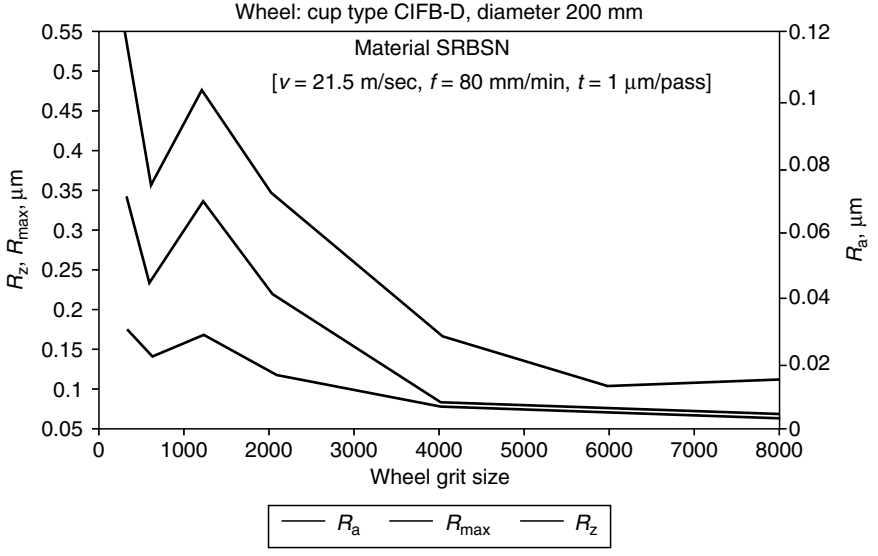

FIGURE 5.32
The effect of wheel grit size on surface finish.

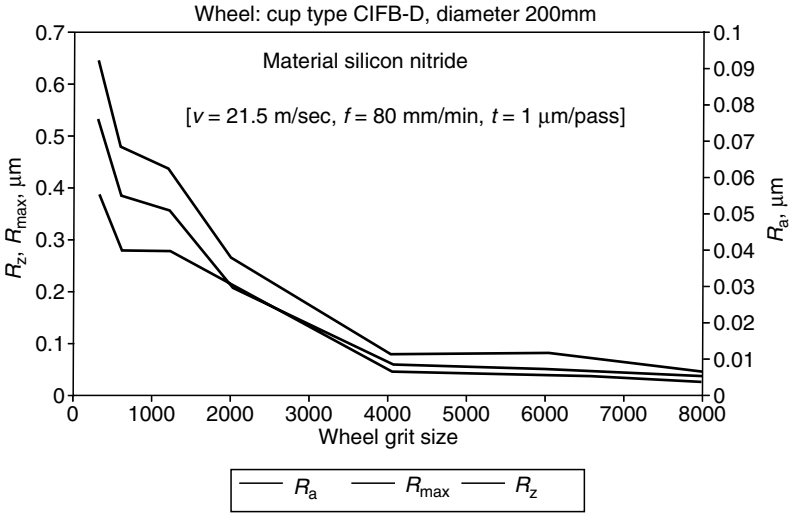

FIGURE 5.33
The effect of wheel grit size on surface finish.

with a #600 grit-size wheel and finally ground with a #4000 mesh-size wheel. The mechanism of material removal in ceramic grinding is a combination of microbrittle fracture and micro- or quasiplastic cutting mechanism [28,29]. The quasiplastic cutting mechanism, typically referred

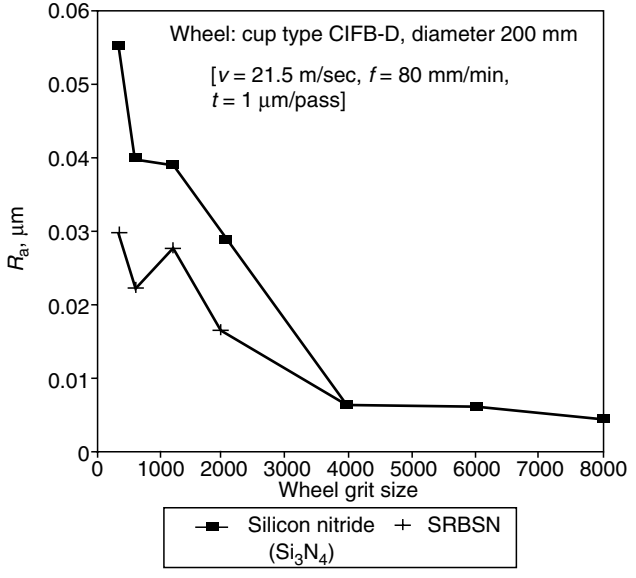

FIGURE 5.34
The effect of wheel grit size on surface finish.

to as ductile-mode grinding, results in grooves on the surface that are relatively smooth in appearance. By a careful choice of grinding parameters and control of the process, ceramics can be ground predominantly in this mode [30,31]. On the other hand, the microbrittle fracture mechanism results in surface fracture and fragmentation. Ductile-regime grinding is preferred since no grinding flaws are introduced if the machining is performed in this mode. Surfaces ground in the brittle fracture mode will have significant amounts of surface fragmentation. On the other hand, a surface produced by the ductile mode will contain little or no surface fragmentation. These two modes can be easily differentiated by observing the surfaces under SEM and AFM.

5.4.8.1 SEM and AFM Studies

The ground surface topography was analyzed by SEM and AFM to determine the brittle- to ductile-mode transition. The specimens were sputter coated with Au–Pd to enable easier SEM imaging. The brittle fracture portion of the work piece will be represented by a ''white frosted'' area in the SEM micrograph. Specimens ground with a #325 grit wheel showed a significant white frosted area confirming that the material was predominantly removed by brittle fracture. The SEM micrographs also showed that with increasing grit size (finer grain size), the amount of surface fragmentation decreases. When ELID grinding was performed with a #4000 grit-size wheel or a finer, SEM micrographs did not show any surface fragmentation. This shows that under the material is ground in the ductile mode [27].

Ground surfaces were also observed under AFM. The observed surface area was $18 \times 18\ \mu m^2$. The change in surface topography can be observed using AFM. The AFM surface topography also shows that the material was predominantly removed in the ductile mode when ELID grinding was done using a #4000 mesh wheel or finer. The surface finish obtained from the AFM study is presented in Table 5.3 [27].

TABLE 5.3

Surface Roughness of Si_3N_4 by AFM

Wheel Mesh	R_a (nm)	R_{max} (nm)	R_{rms} (nm)	R_z (nm)
#325	112.7	1164.7	147.8	832.7
#600	126.5	1533.3	173.3	786.3
#1200	79.54	950.8	108.6	666.0
#2000	41.34	756.5	61.48	456.7
#4000	7.474	334.7	14.34	138.3
#6000	3.734	180.0	5.8	108.3
#8000	3.177	187.9	5.119	102.9

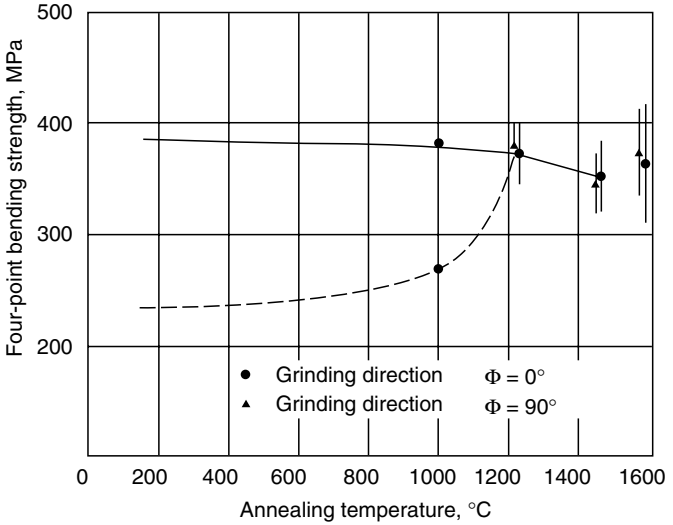

FIGURE 5.35
Effects of annealing on four-point bending strength.

5.4.9 Flexural Strength of Silicon Nitride

Significant research has been conducted to study the effect of grinding parameters on the strength of ground ceramic specimens. Various investigators have also studied the effect of grinding direction on the strength of ceramics. Figure 5.35 shows the relationship between the annealing temperature and bending strength of alumina ceramics at room temperature. The results show that before annealing specimens ground in the transverse direction have a bending strength 60% lower than that of the specimens ground longitudinally. The bending strength of the specimens ground in the transverse direction increased with the annealing temperature. At about 1200°C, the strength was approximately equal to that of the specimens ground in the longitudinal direction [32]. The effects of annealing temperature on the strength of ground silicon nitride specimen have not been studied. Therefore, experiments were conducted to study the effect of annealing and ELID finish grinding on the bending strength of silicon nitride specimens.

The material used in the experiment was silicon nitride SN235 manufactured by Kyocera. The size of the specimens was $3 \times 10 \times 50$. This is the recommended size for the four-point bending test. A large number of Si_3N_4 specimens were fixed on a plate with wax and mounted on the table of the surface grinding machine. Specimens were ground in longitudinal (PG) and in transverse (TG) direction using a #140 grit-size BB diamond wheel. The following grinding conditions were used: (a) wheel velocity, 1200 m/min, (b) table speed, 20 m/min; (c) traverse pitch, 1 mm, (d) depth of cut, 5 μm, and (e) spark out, 3 passes. The total depth of cut was around 70 μm.

Four-point bend tests were performed at room temperature and at 1400°C. All bending tests had an upper span of 10 mm and a lower span of 30 mm. An Instron-type universal tester was used for bending tests, with a constant cross head of 0.2 mm/min. Figure 5.36 shows the dimensions and coordinate system of the beam specimen with ground surface in a four-point bend test.

Bending test results are presented in Figure 5.37. A significant reduction in bending strength was noticed when specimens were transversely ground compared with those ground longitudinally. PG and TG specimens were annealed at 1200°C for 2 h and the bending strength was determined. The strength of the heat-treated TG specimens increased significantly as shown in Figure 5.37 [33]. There was no significant change in the strength of the PG ground specimens after the annealing process. As the TG specimens have the lowest strength, it was decided to study the effect of ELID finish

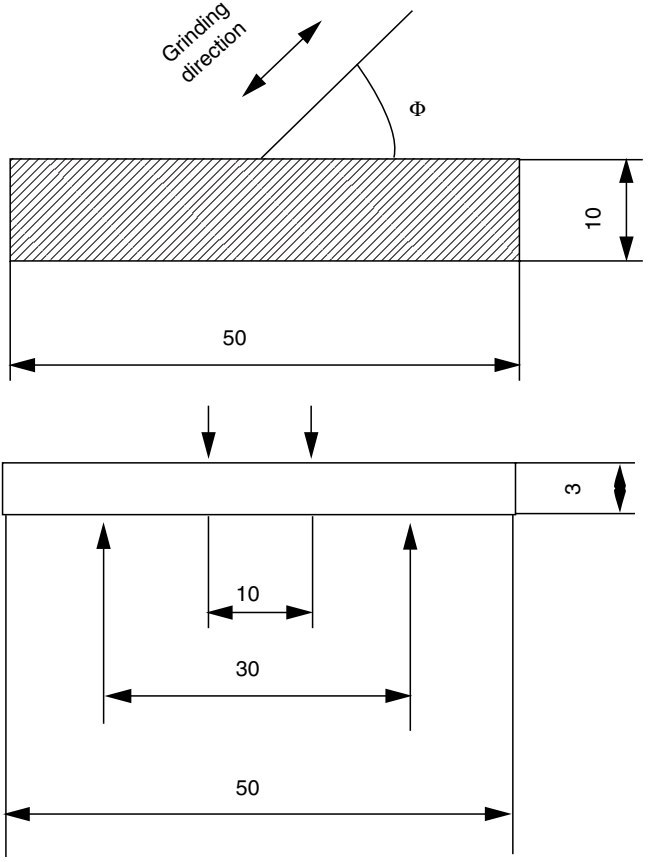

FIGURE 5.36
Dimensions and coordinate system of the beam specimen with the ground surface in a four-point test.

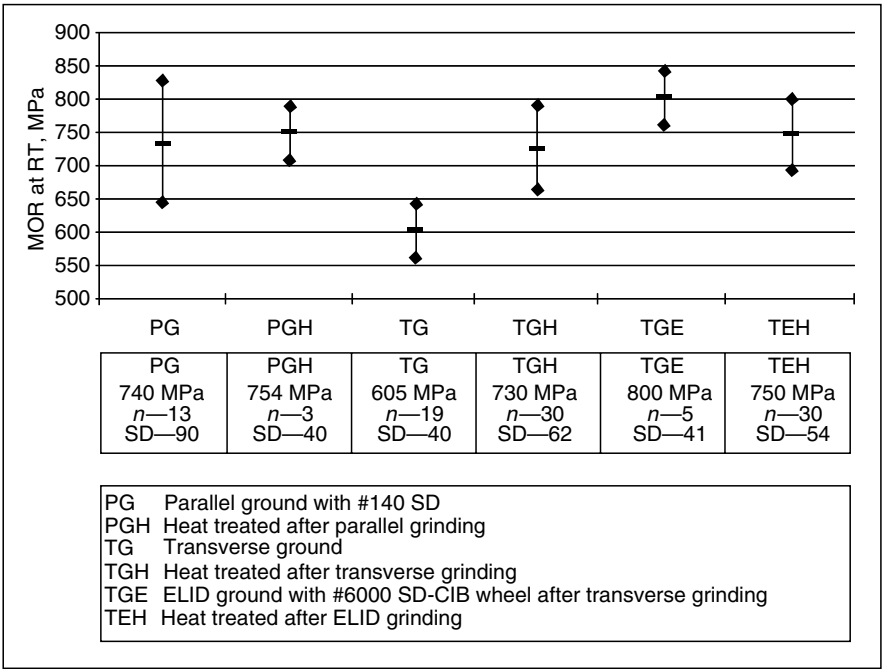

FIGURE 5.37
The effect of ELID grinding on the strength of Si_3N_4.

grinding on the bending strength of TG ground specimens. These specimens were ground using ELID grinding and a #6000 grit-size (average grain size $= 3.15$ μm) SD cast iron-bonded wheel. The diameter of the wheel was 150 mm and the width was 10 mm. The following grinding conditions were used: wheel speed, 1200 m/min; table speed, 20 m/min; traverse pitch, 0.6 mm; depth of cut, 0.5 μm; and total depth of cut, 40 μm.

The power supply used in the experiment was EPD-10 A, with a capacity of 90 V, 10 A. The following ELID conditions were used: E_o, 60 V; I_p, 10 A; on-time and off-time, 2 μsec [square wave]. Noritake AFG-M grinding fluid with 2% of water was used in the experiment. The bending strength of the ELID ground specimens was determined (TGE). These ELID ground specimens were annealed and the bending strength of these specimens was also determined. The results are presented in Figure 5.37. A significant improvement in the bending strength of Si_3N_4 specimens was achieved when ELID grinding was applied. The bending strength of the specimens was determined at 1400°C. The results are presented in Figure 5.38. The maximum bending strength at the elevated temperature was found with the TGE specimens [33].

Previous investigations have shown that during grinding of ceramics two sets of flaws are introduced. One set is parallel to the grinding direction,

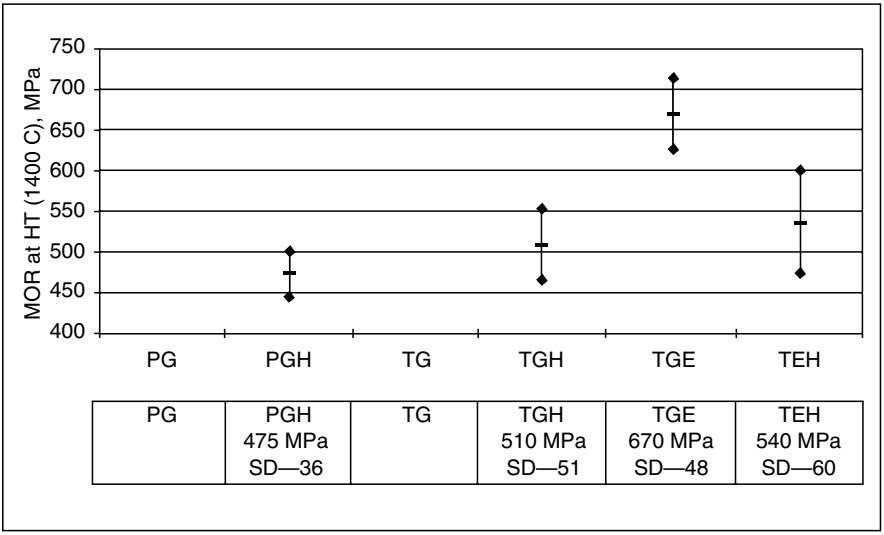

FIGURE 5.38
The effect of ELID grinding on the strength of Si_3N_4 (at elevated temperature).

which is fairly elongated, while the second is perpendicular to the grinding direction and smaller in size [34]. This has resulted in a significant reduction in the strength of the silicon nitride ceramic when ground in the transverse direction. As explained earlier, ductile-mode grinding was performed with the application of fine ELID grinding. When TG work pieces were finish ELID ground with a #6000 grit-sized wheel, the grinding mode was ductile. The flaws produced by initial grinding were removed by the fine ELID grinding. The TGE specimens therefore do not contain any significant microcracks. This may be the reason for the significant improvement in the bending strength of the TGE specimens.

5.5 Conclusions

In this paper, the application of ELID grinding for effective and precision grinding of various structural ceramic materials is described. ELID technology has been successfully applied for surface grinding using a machining center, a horizontal surface grinder, a vertical rotary surface grinder, and for cylindrical grinding on a turning center. The results are as follows:

1. Compared with conventional grinding, there is a significant reduction in normal grinding force with ELID grinding. Therefore, ELID grinding is recommended for heavy material removal grinding, low-rigidity machines, and low-rigidity work pieces.

2. The full potential of ELID grinding, that is, reduced grinding force, can be used only after it has been stabilized. However, the newly proposed modified ELID dressing can provide reduced and almost constant grinding force immediately at the start of grinding.
3. Compared with conventional grinding, a reduction in G-ratio was found when ELID grinding was performed. The G-ratio can be improved by optimizing the ELID current.
4. A mirror surface was achieved on silicon nitride materials when ELID grinding was performed using a #4000 grit-size wheel. The finish ELID technology will find wide application in the optical and semiconductor industries such as mirror finishing of silicon wafers, many kinds of ceramics, ferrite, and glass.
5. SEM and AFM studies reveal that the work piece was predominantly ground in the ductile mode when ELID grinding was performed with a #4000 grit-sized wheel or finer.
6. The bending strength of transversely ground Si_3N_4 specimens can be improved by annealing at 1200°C.
7. A significant improvement in the bending strength of Si_3N_4 was achieved when finish ELID grinding was performed.

5.6 Acknowledgments

The authors express their sincere thanks to the industrial members of the ELID research project for their financial support. Part of the research project was supported by the U.S. Department of Energy. Special thanks to Fuji Die Co. Ltd., Toyko, Japan, for supplying grinding wheels and Ikegami Mold of America and RIKEN authorities for their financial support. The authors also thank Ms. Joyce Medalen for preparing the manuscript.

References

1. Jahanmir, S., Ives, L.K., Ruff, A.W., and Peterson, M.B., ''Ceramic Machining: Assessment of Current Practice and Research Needs in the United States,'' NIST special publication 834, Gaithersburg, MD, 1992.
2. Malkin, S. and Hwang, T.W., ''Grinding Mechanisms for Ceramics,'' *Annals of the CIRP*, Vol. 45, No. 2, 1996, pp. 569–580.
3. Nakagawa, T., Suzuki, K., and Uematsu, T., ''Three Dimensional Creep Feed Grinding of Ceramics by Machining Center,'' *Proceedings ASME, WAM, PED*, 17, 1985, pp. 1–7.

4. Nakagawa, T. and Suzuki, K., ''Highly Efficient Grinding of Ceramics and Hard Metals on Machining Center,'' *Annals of CIRP*, Vol. 35, No. 1, 1986, pp. 205–210.
5. Fuji ELIDer, Catalog from Fuji Die Co. Ltd., Tokyo, Japan, 1996.
6. McGeough, J.A., *Principles of Electro Chemical Machining*, Chapman and Hall, 1974, pp. 162–195.
7. Welch, E., Yi, Y., and Bifano, T., ''Electro Chemical Dressing of Bronze Bonded Diamond Grinding Wheels,'' *Proceedings of the International Conference on Machining of Advanced Materials*, NIST publication 847, 1993, pp. 333–340.
8. NICCO Creep Feed Grinders: Catalog from Carl Citron Inc., NJ.
9. Ohmori, H. and Nakagawa, T., ''Mirror Surface Grinding of Silicon Wafers with Electrolytic In-Process Dressing,'' *Annals of CIRP*, Vol. 39, No. 1, 1990, pp. 329–332.
10. Ohmori, H., ''Electrolytic In-Process Dressing (ELID) Grinding Technique for Ultra Precision Mirror Surface Machining,'' *International Journal of JSPE*, Vol. 26, No. 4, 1992, pp. 273–278.
11. Ohmori, H. and Takahashi, I., ''Efficient Grinding of Sintered Diamond and CBN Materials Utilizing Electrolytic In-Process Dressing (ELID),'' *Proceedings of the 1st International Abrasive Technology Conference*, Seoul, Korea, 1993.
12. Bandyopadhyay, B.P., Ohmori, H., and Takahashi, I, ''Efficient and Stable Grinding of Ceramics by Electrolytic In-Process Dressing (ELID),'' *Journal of Materials Processing Technology*, Elsevier, Vol. 66, 1997, pp. 18–24.
13. Vickerstaff, T.J., ''Diamond Dressing—Its Effect on Work Surface Roughness,'' *Industrial Diamond Review*, Vol. 30, 1970, pp. 260–267.
14. Davis, C.E., ''The Dependence of Grinding Wheel Performance on Dressing Procedure,'' *International Journal of Machine Tool Design Research*, Vol. 14, 1974, pp. 33–52.
15. Konig, W. and Meyen, H.P., ''AE in Grinding and Dressing: Accuracy and Process Reliability,'' *SME*, 1990, MR, pp. 90–526.
16. Malkin, S. and Murray, T., ''Mechanics of Rotary Dressing of Grinding Wheels,'' *Journal of Engineering for Industry, ASME*, Vol. 100, 1978, pp. 95–102.
17. Koshy, P., Jain, V.K., and Lal, G.K., ''A Model for the Topography of Diamond Grinding Wheels,'' *Wear*, Vol. 169, 1993, pp. 237–242.
18. Syoji, K., Zhou, L., and Mitsui, S., ''Studies on Truing and Dressing of Grinding Wheels, 1st Report,'' *Bulletin of the Japan Society of Precision Engineering*, Vol. 24, No. 2, 1990, pp. 124–129.
19. Suzuki, K., Uematsu, T., Yanase, T., and Nakagawa, T., ''On-Machine Electrodischarge Truing for Metal Bond Diamond Grinding Wheels for Ceramics,'' *Proceedings of the International Conference on Machining of Advanced Materials*, NIST 847, July 1993, pp. 83–88.
20. Wang, X., Ying, B., and Liu, W., ''EDM Dressing of Fine Grain Super Abrasive Grinding Wheel,'' *Journal of Materials Processing Technology*, Elsevier, Vol. 62, 1996, pp. 299–302.
21. Piscoty, M.A., Davis, P.J., Saito, T.T., Blaedel, K.L., and Griffith, L., ''Use of In-Process EDM Truing to Generate Complex Contours on Metal Bond Superabrasive Grinding Wheels for Precision Grinding Structural Ceramics,'' *Proceeding of International Conference on Precision Engineering*, Taipei, Taiwan, 1997, pp. 559–564.
22. Ohmori, H., Takahashi, I., and Bandyopadhyay, B.P., ''Ultra Precision Grinding of Structural Ceramics by Electrolytic In-Process Dressing (ELID) Grinding,'' *Journal of Materials Processing Technology*, Elsevier, Vol. 57, 1996, pp. 272–277.

23. Ohmori, H., Takahashi, I., and Bandyopadhyay, B.P., ''Highly Efficient Grinding of Ceramic Parts by Electrolytic In-Process Dressing (ELID) Grinding,'' *Materials and Manufacturing Processes*, Marcel Dekker, Vol. 11, No. 1, 1996, pp. 31–44.
24. Bandyopadhyay, B.P., Ohmori, H., and Makinouchi, A., ''Efficient and Precision Grinding Characteristics of Structural Ceramics by Electrolytic In-Process Dressing (ELID) Grinding,'' *Proceedings of 1998 Japan–U.S.A. Symposium on Flexible Automation*, Otsu, Japan, July 1998, pp. 305–311.
25. Bandyopadhyay, B.P., ''Application of Electrolytic In-Process Dressing for High Efficiency Grinding of Ceramic Parts: Research Activities 1995–1996,'' ORNL/SUB/96-SV716/1 Report, February 1997.
26. Ohmori, H., Takahashi, I., and Bandyopadhyay, B.P., ''Ultra-precision Grinding of Structural Ceramics by Electrolytic In-Process Dressing (ELID) Grinding,'' *Journal of Materials Processing Technology*, Elsevier, Vol. 57, 1996, pp. 272–277
27. Bandyopadhyay, B.P., Ohmori, H., and Takahashi, I., ''Ductile Regime Mirror-Finish Grinding of Ceramics with Electrolytic In-Process Dressing (ELID) Grinding,'' *Materials and Manufacturing Processes Journal*, Marcel Dekker, Vol. 11, No. 5, 1996, pp. 789–802.
28. Inasaki, I., ''High Efficiency Grinding of Advanced Ceramics,'' *Annals of CIRP*, Vol. 35, No. 1, 1986, pp. 211–214.
29. Inasaki, I., ''Speed Stroke Grinding of Advanced Ceramics,'' *Annals of CIRP*, Vol. 37, No. 1, 1988, pp. 299–302.
30. Ohmori, H. and Nakagawa, T., ''Analysis of Mirror Surface Generation of Hard and Brittle Materials by ELID (Electrolytic In-Process Dressing) Grinding with Superfine Grain Metallic Bond Wheels,'' *Annals of CIRP*, Vol. 41, No. 1, 1995, pp. 287–290.
31. Namba, Y., Yamada, Y., Tsuboi, A., Unno, K., and Nakao, H., ''Surface Structure of Mn–Zn Ferrite Single Crystals Ground by an Ultra Precision Surface Grinder with Various Diamond Wheels,'' *Annals of CIRP*, Vol. 41, No. 1, 1992, pp. 347–351.
32. Matsuo, Y., Ogasawara, T., Kimura, S., Sato, S., and Yasuda, Y., ''The Effects of Annealing on Surface Machining Damage of Alumina Ceramics,'' *Journal of the Ceramic Society of Japan*, (Intl. Edition), Vol. 99, No. 5, 1991, pp. 371–376.
33. Bandyopadhyay, B.P. and Ohmori, H., ''The Effect of ELID Grinding on the Flexural Strength of Silicon Nitride,'' to be published in the *International Journal of Machine Tools and Manufacture*, Pergamon press.
34. Rice, R.W. and Mecholowsky, J.J., ''The Nature and Strength Controlling Machining Flaws in Ceramics,'' *Symposium on the Science of Ceramic Machining and Surface Finishing II*, NBS Publication 562, 1979, pp. 351–378.

6

Electrolytic In-Process Dressing Grinding of Ceramic Materials

H. Ohmori and K. Katahira

CONTENTS

ABSTRACT Efficient precision grinding techniques for ceramics are required in order to mass-produce ceramic parts. New grinding techniques for ceramics that employ fine bonded superabrasive wheels and high-stiffness grinding machines have been designed in order to achieve high grinding efficiency and produce high-quality ceramic parts. Ceramics are extremely hard to machine using conventional methods. Mirror finishing of these hard, brittle materials requires the use of diamond abrasives. Grinding in particular, compared with lapping and polishing, can be used to efficiently produce various geometric forms. A novel grinding technology, known as electrolytic in-process dressing (ELID) that incorporates in-process dressing of metal-bonded grinding wheels, provides dressing of the metal-bonded wheels during the grinding process, while maintaining continuous protrudent abrasive from superabrasive wheels. This paper describes the highly efficient and precise ELID grinding method and discusses the ELID grinding process and the grinding characteristics of ceramic materials.

KEY WORDS *ELID, electrolytic in-process dressing, ceramics, electro-discharge truing (ED truing), metal-bonded diamond grinding wheels, cast-iron-bonded diamond grinding wheel, efficient grinding, mirror finish grinding, ductile mode grinding, brittle mode grinding, surface modification.*

6.1 Introduction

Interest in advanced ceramics has increased significantly in recent years due to its unique physical properties and the significant improvement in the mechanical properties and reliability. The advantages of ceramics over other materials include: (a) high hardness and strength, the retention thereof at elevated temperatures, (b) chemical stability, and (c) superior wear resistance. Until now, mirror surface machining of ceramics has been performed mainly by polishing or lapping. However, such machining techniques cannot always be described as highly efficient or productive, and the adverse effects of scattered abrasive particles on equipment, the treatment of waste liquids, and other problems remain to be investigated.

On the other hand, grinding in particular, compared to lapping and polishing, can be used to efficiently produce geometric forms. New ceramic grinding techniques that employ fine bonded superabrasive wheels and high-stiffness grinding machines have been designed to achieve high grinding efficiency and high-quality ceramic parts. Dr. Ohmori pioneered a novel grinding technique that incorporates in-process dressing of metal-bonded superabrasive wheels known as ELID [1–8], Japanese Patent No. 1,947,329 [9].

This technique provides in-process dressing of metal-bonded wheels, during the grinding process, for continuous protrudent abrasive from superabrasive wheels. Moreover, ELID grinding has recently been found to bring about improvements in the surface characteristics of the workpiece being processed [10–14], and this technique produces superior resistance to corrosion and wear, as well as other advantages. The present chapter describes the basics of the ELID grinding technique and presents a discussion on the ELID grinding process and the grinding characteristics of ceramic materials.

6.2 ELID Grinding Technique

6.2.1 The Concept of ELID

ELID grinding was first proposed in 1988, and a number of reports describing the advantages of this process have been published [1–14]. The basic construction of the ELID grinding system is shown in Figure 6.1. The essential elements of the ELID system include: (a) a metal-bonded grinding wheel, (b) an electric power source, and (c) an electrolytic coolant. The most important feature is that there is no requirement for a special machine.

The principle of ELID grinding is shown in Figure 6.2. The wheel serves as the positive electrode. The negative electrode is installed opposite the grinding surface of the wheel. The clearance between these two electrodes is set at 0.1–0.3 mm. DC-pulse voltage is supplied between the two electrodes in order to electrolytically remove only the metal bond of the wheel, allowing efficient and automatic dressing of the wheel. This dressing is continued even during the grinding work in order to prevent reduced wheel sharpness from wear, thereby realizing highly efficient mirror surface grinding.

ELID grinding consists of the following steps:

1. Truing, for example, using a SiC wheel of grit size #100 or an aluminum oxide stick is required in order to reduce the initial eccentricity.
2. The truing of tough metal-bonded wheels is very difficult and time consuming for coarse-grit wheels of larger diameter. A new efficient electrodischarge truing (ED truing) has been developed and is discussed in Section 6.2.2.
3. Predressing (also known as ELID dressing) is performed for 15–30 min by electrolysis.
4. Grinding with ELID is carried out at the recommended cutting speed.

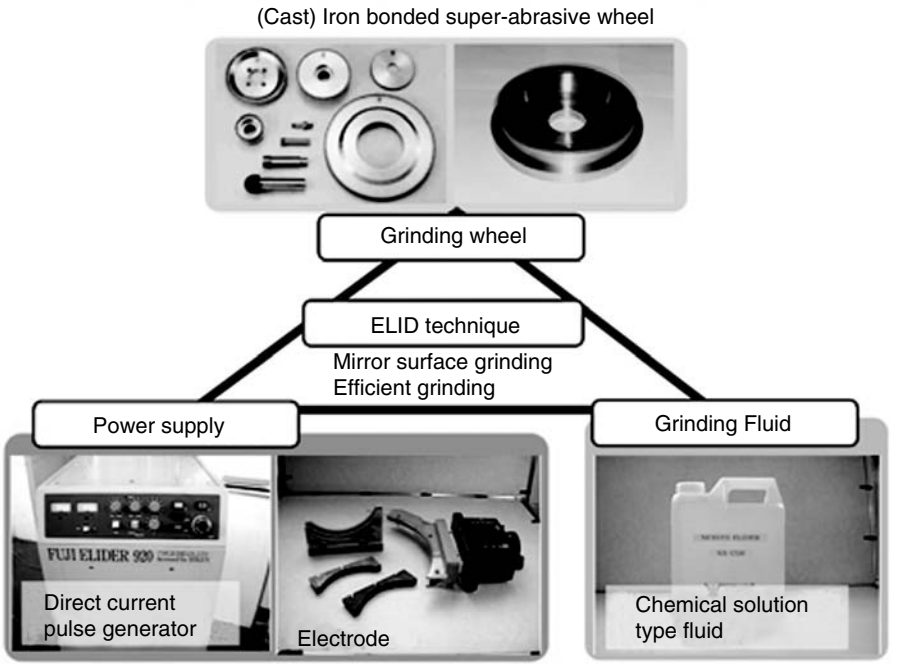

FIGURE 6.1
The ELID grinding technique.

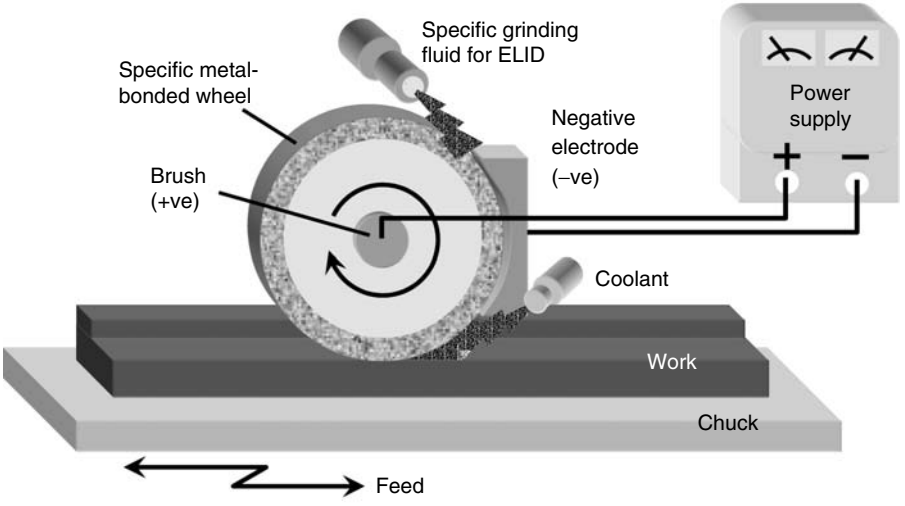

FIGURE 6.2
The principle of ELID grinding.

6.2.2 ED Truing Technique

Before beginning the grinding process, the grinding wheel is trued and dressed. This is done in order to reduce the eccentricity of the wheel resulting from mounting the wheel on the spindle. Truing is also carried out in order to create a wheel having a desired shape or to correct a dulled profile. Truing of conventional wheels is easily performed with a diamond dresser. Although metal-bonded superabrasive wheels have many good features, such as higher rigidity, they are difficult to true. Several studies have examined areas of truing and dressing. The majority of these investigations examined the effect of diamond dressing on surface roughness [15–17]. A number of studies have focused on the mechanics of dressing [18] and the development of a mathematical model to characterize the topography of the wheel [19]. In one investigation, the present authors [20] measured the protrusion height of abrasive grains after truing and dressing. However, an efficient method for the truing of metal-bonded superabrasive wheels has not yet been reported. Metal-bonded diamond grinding wheels can be efficiently trued using a newly developed method known as ED truing, which was first introduced by the present authors [21]. ED truing offers the following advantages: (a) applicability to all metal-bonded wheels and electrically conductive resinoid-bonded wheels, (b) precise truing due to on-machine application, (c) applicability to small wheels and thin wheels due to a small applied force, (d) high efficiency, and (e) can be used to produce various profiles or shapes. The above-mentioned advantages have resulted in the application of ED truing in a number of studies [22,23].

In the ED truing system, the grinding wheel is rotated comparatively slowly, whereas the cathode is turned and moved toward and along the axis of the grinding wheel. The same external power source is used for ED truing and ELID grinding. The ED truing system in Figure 6.3 and Figure 6.4 shows a view of machine set with ED truer. A copper tungsten electrode was selected for ED truing due to its excellent wear characteristics. Truing of the wheel was performed by varying both voltage and current. In order to maintain insulation of the electrodes, a small amount of grinding fluid was added between the wheel and the electrode.

During ED truing, the bonded material is melted and is easily removed by the sparks between the wheel and the cathode. Figure 6.5 shows the relationship between the truing conditions and the decrease in the grinding wheel diameter. The rough truing efficiency was 0.2 mm for a 15 min period of material removal in the wheel diameter and the fine truing efficiency was approximately half of that (ED truing was applied on a bronze-and-iron-bonded hybrid wheel).

6.2.3 Electrical Behavior during Predressing

The relationship among electric current, voltage, and time during electrical dressing is shown in Figure 6.6. When predressing starts (point 1),

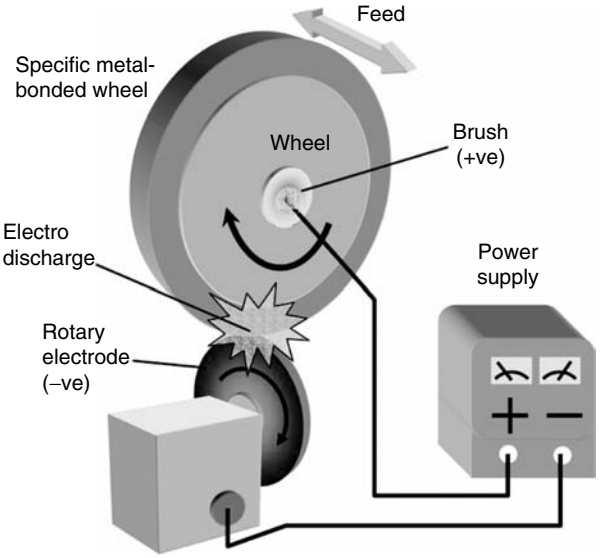

FIGURE 6.3
Overview of machine setup with electrodischarge truer. The ED truing system.

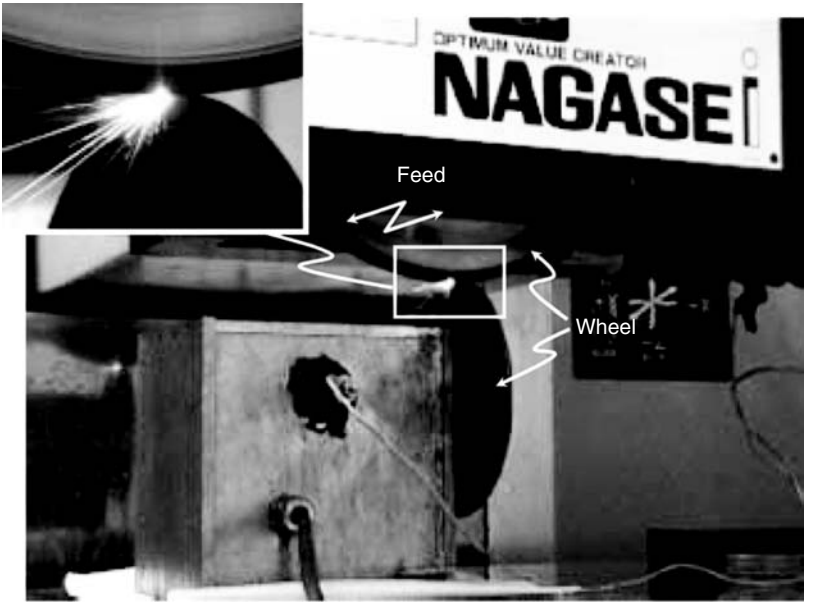

FIGURE 6.4
Overview of machine setup with ED truer.

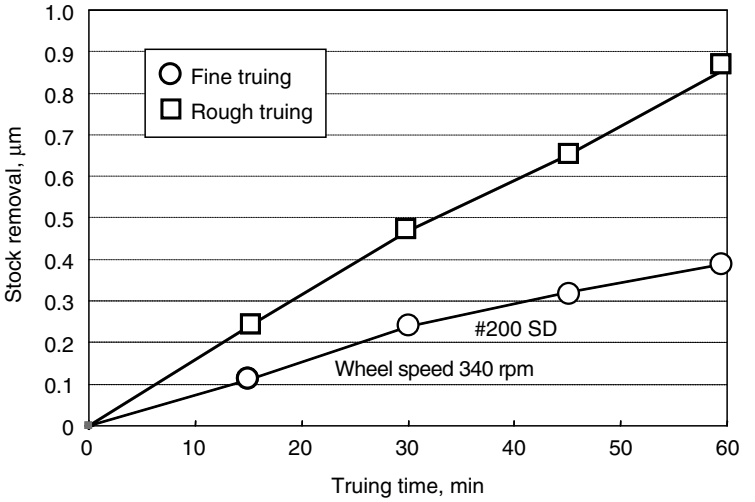

FIGURE 6.5
Change in stock removal in wheel diameter with truing time.

the surface of the trued wheel has good electrical conductivity. Therefore, the current is high, as set in the power source, and the voltage between the wheel and the electrode is low. After several minutes the cast-iron-bonded material, which is mostly ionized Fe^{+2}, is removed by electrolysis. The ionized Fe reacts to form $Fe(OH)_2$ and $Fe(OH)_3$ according to the following equations:

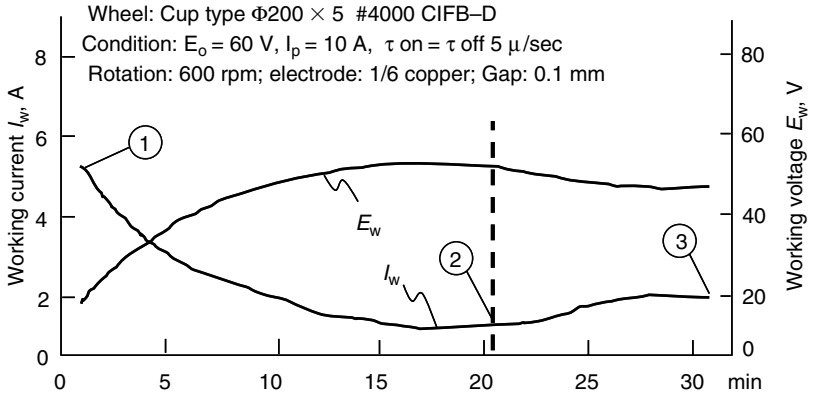

FIGURE 6.6
Electrical behavior during electrolytic dressing.

$$Fe \rightarrow Fe^{+2} + 2e^{-} \tag{6.1}$$

$$Fe^{+2} \rightarrow Fe^{+3} + e^{-} \tag{6.2}$$

$$H_2O \rightarrow H^{+} + OH^{-} \tag{6.3}$$

$$Fe^{+2} + 2OH^{-} \rightarrow Fe(OH)_2 \tag{6.4}$$

$$Fe^{+3} + 3OH^{-} \rightarrow Fe(OH)_3 \tag{6.5}$$

These hydroxides are further changed into oxides (e.g., Fe_2O_3) during electrolysis. After these reactions have occurred and insulating oxide layers have grown on the wheel, its electrical conductivity will be reduced. The current decreases and the working voltage becomes as high the original open circuit voltage (denoted by 2).

6.2.4 The ELID Grinding Mechanism

The various stages of ELID grinding are shown in Figure 6.7. At the beginning, grinding is performed with a predressed wheel and the protrudent grains grind the workpiece. With the passage of time, the grains and the oxide layer begin to wear. The wearing of the oxide layer causes an increase in the electroconductivity of the wheel surface, thus the electrolysis increases (denoted by 3 in Figure 6.6) and the oxide layer is recovered.

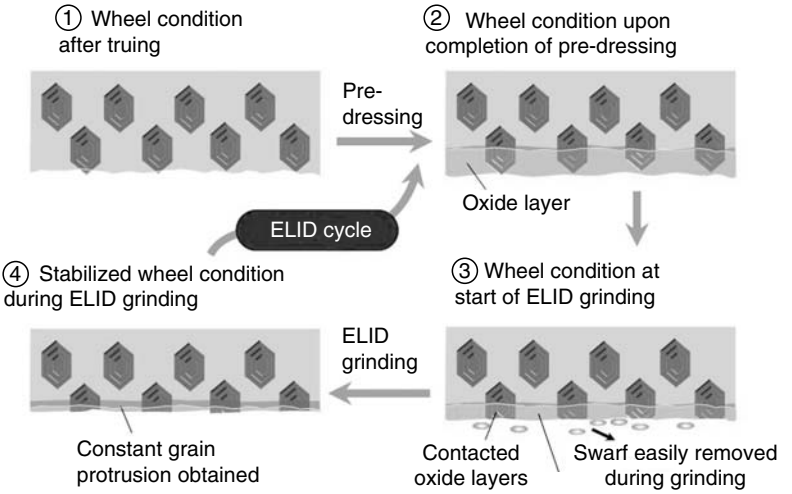

FIGURE 6.7
Mechanism of ELID grinding method.

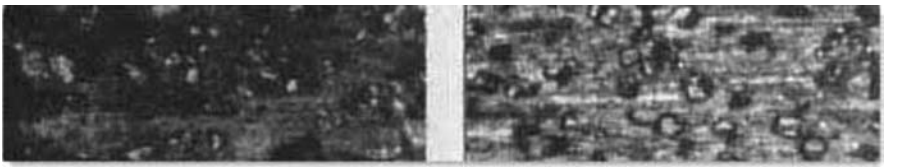

FIGURE 6.8
Microscopic photographs of the wheel surface after grinding with ELID (left) and without ELID (right).

The protrusion of the grains remains constant. The mechanism of ELID grinding shown in Figure 6.7 is explained in detail as follows: (1) First, the wheel bond is electrolyzed, which causes the abrasives to protrude appropriately. (2) At the same time, this process produces nonconductive oxidized iron that accumulates to form a layer of coating on the wheel surface, automatically reducing the electrolysis current, at which point the initial dressing is complete. (3) When the actual grinding work is started in this state, the nonconductive oxide layer on the wheel surface comes into contact with the surface of the workpiece, and is removed by friction. When this takes places, the abrasives start grinding the workpiece, and consequently the wheel begins to wear. This reduces the insulation of the wheel surface, allowing the electrolytic current to flow again. (4) As a result, the entire process starts again with the electrolysis of the wheel bond where the nonconductive oxide coating between the worn out abrasives has become thin, allowing the abrasives to protrude again (process returns to (2)). This is how the ELID cycle functions. The ELID cycle varies according to the type of metal bond of the wheel used, the electrolytic conditions, the workpiece, and the grinding conditions; all these can be optimized for practical performance.

Figure 6.8 compares microscopic photographs of the wheel surface after grinding with ELID (left) and without ELID (right) in order to demonstrate the effectiveness of ELID. As shown in the figure, for grinding without ELID (right-hand photograph), the abrasives are worn out, scratch marks caused by the workpiece are observed on the bond surface, and the sharpness is poor, whereas for the grinding with ELID (left-hand photograph), the bond surface maintains abrasive protrusion by electrolysis.

6.3 Efficient and Precision ELID Centerless Grinding of Zirconia Ceramics

6.3.1 Experimental Setup for ELID Centerless Grinding of Zirconia Ceramics

In this section, microfabrication grinding with ELID centerless grinding is proposed. In an experiment, we conducted efficient, high-precision grinding

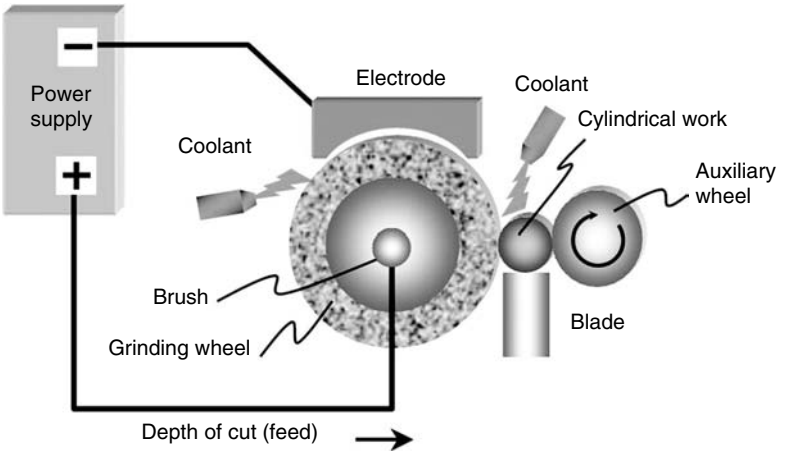

FIGURE 6.9
ELID centerless grinder.

of zirconia ceramics using the ELID centerless grinder shown in Figure 6.9. Cast-iron-bonded diamond wheels of mesh size #170 for coarse grinding, #1200 for intermediate grinding, and #4000 or #8000 for finish grinding were used. The average grit size of the #4000 and #8000 wheels were approximately 4 and 2 μm, respectively. A chemical-solution-type grinding fluid was used as the medium for ELID. A specific pulse generator for ELID was used.

In order to achieve efficient and precise ELID grinding, the ELID centerless grinding process should be performed according to the following steps:

1. Precision truing of metal-bonded wheels to the required shape by ED truing
2. Predressing of wheels by electrolytic process
3. Grinding process with ELID

Precision truing was carried out by the ED truing method. The state of the ED truing is shown in Figure 6.10. The bonded materials were melted and removed efficiently during the discharge between the wheel and cathode made from CuW alloy. A very accurate wheel with a straightness of 4 μm per 50 mm width and a roundness of 1 μm per 150 mm diameter was attained. When a wider grinding wheel (50 mm) was used, a higher current and voltage was used for initial electrolytic dressing. A longer dressing time (approximately 40 min) was also required. Cylindrical grinding experiments for ceramics were performed on a centerless grinder for in-feed and through-feed grinding. As a result of the advantages of the ELID technique,

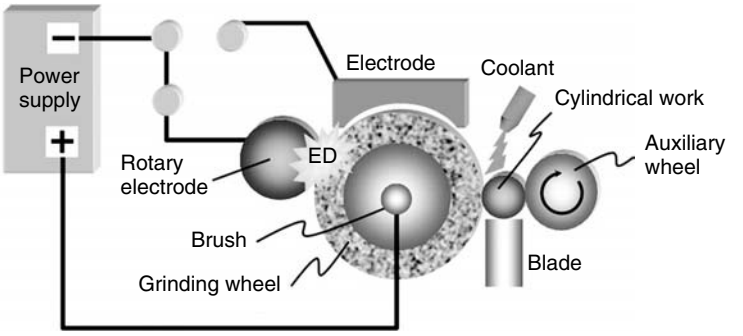

FIGURE 6.10
ED truing for ELID centerless grinder.

ground surface roughness was successfully improved by a factor of approximately two.

6.3.2 Results of ELID Centerless Grinding of Zirconia Ceramics

Figure 6.11 shows the relationship between in-feed speed and surface roughness in R_z using #2000 and #4000 wheels for the in-feed grinding of Si_3N_4 and ZrO_2 ceramics. Better results for ZrO_2 were obtained with the #4000 wheel at a lower in-feed speed of 0.04 mm/min. As higher in-feed speeds result in higher productivity, efficient centerless grinding was achieved with ELID.

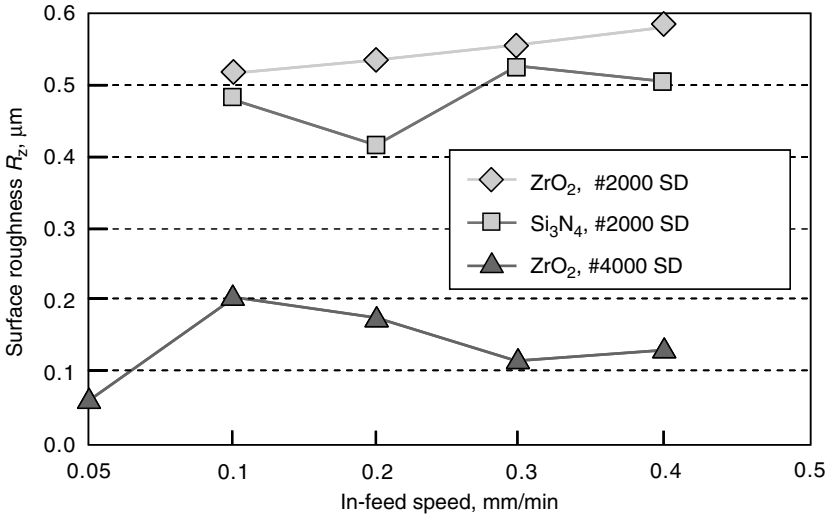

FIGURE 6.11
Relation between surface roughness and in-feed speed.

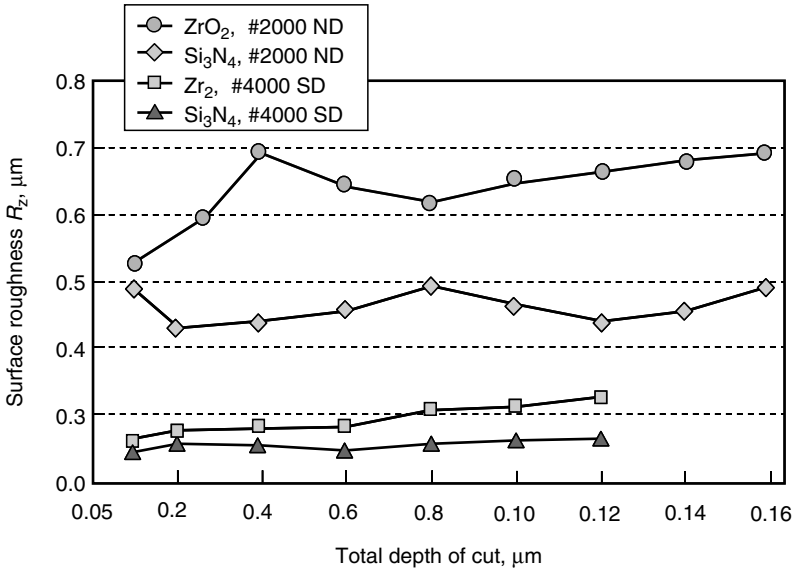

FIGURE 6.12
Relationship between surface roughness and total depth of cut.

Figure 6.12 shows the relationship between the total depth of cut and the surface roughness in the grinding of Si_3N_4 and ZrO_2 ceramics. The surface roughness remains approximately constant during the ELID grinding of both the ceramics after a total grinding depth of 40 μm. A better surface

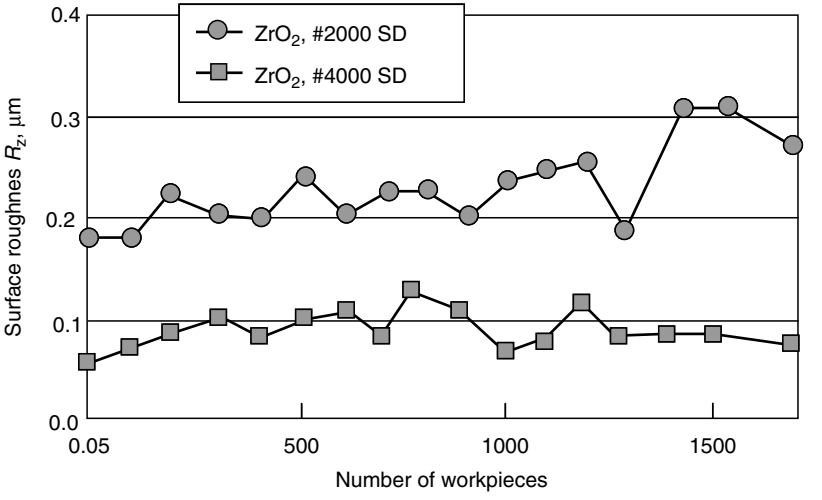

FIGURE 6.13
Change of surface roughness for grinding number of ZrO_2 optical fiber ferrule.

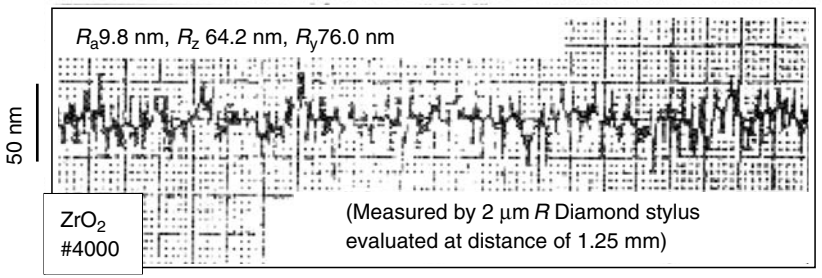

FIGURE 6.14
Example of surface profile produced by #4000 wheel and ELID technique.

finish was obtained using the #4000 wheel for the grinding of the Si_3N_4 ceramic workpieces.

Figure 6.13 shows the changes in the ground surface roughness obtained using the #2000 and #4000 wheels during ELID grinding of ZrO_2 by through-feed grinding. The ground surface roughness did not change noticeably due to continuous electrolytic dressing for any of the workpiece. A smooth surface roughness, approximately equal to that obtained using loose abrasive processes, such as polishing or buffing, was obtained using the #4000 wheel. The grinding contact time was very short, approximately 5 sec, for each workpiece.

Figure 6.14 shows an example of surface profile obtained using the #4000 wheel for ZrO_2 ferrules. A very smooth surface can be achieved. Figure 6.15 presents examples of ZrO_2 optical fiber ferrules finished by ELID centerless through-feed grinding. Table 6.1 shows R_z and surface straightness (R_q) obtained for different wheel grits. A significant improvement in the surface roughness and straightness was achieved by fine-grit wheels using the ELID technique.

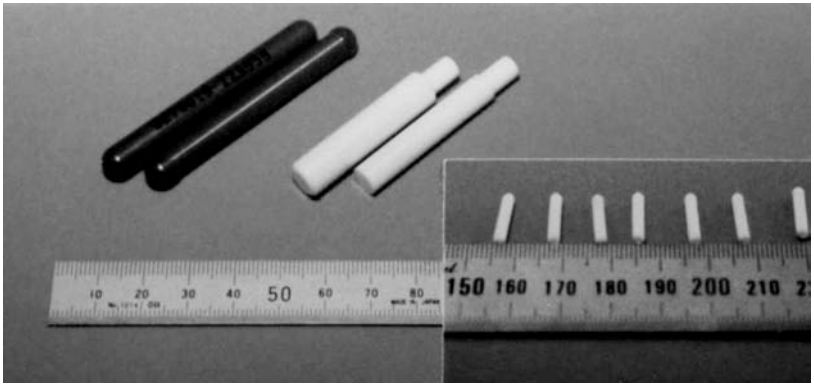

FIGURE 6.15
Samples of ZrO_2 ferrules produced by ELID centerless grinding.

TABLE 6.1

ELID Centerless Grinding Results (μm) by Through-Feed for ZrO2 Ferrules

	#800	#2000	#4000	#8000
R_z	0.90	0.26	0.066	0.072
R_q	0.040	0.26	0.032	0.054

The ELID process enabled the maintenance of protruding fine grains that realized stable and efficient grinding performance with high quality and accuracy, with respect to roundness and straightness.

The following conclusions are based on the above-mentioned experimental results:

1. Stable, efficient, and precise grinding of ceramic components has been achieved by mirror grinding using the ELID technique.
2. Efficient and precise truing can be attained by the electrodischarge method for metal-bonded grinding wheels using centerless grinding.
3. Good ground surface roughness and accuracy are achieved using the #4000 metal-bonded grinding wheel in through-feed grinding for ZrO_2 optical fiber ferrules.
4. Good ground surface roughness can be obtained using the #4000 metal-bonded wheel in microfabrication grinding.
5. A micropin core with a very high aspect ratio can be ground efficiently.

6.4 ELID Grinding Characteristics for the Machining of Optical Surface Quality for Ceramic Spherical Lens Molds

6.4.1 Mechanism of ELID CG-Grinding

We have performed efficient, high-precision grinding of SiC and Si_3N_4 ceramic spherical lens molds with cup wheels by the ELID process (henceforth called ELID CG-grinding) and have investigated the ground surface characteristics in detail.

Similar to the conventional ELID grinding system, ELID CG-grinding is essentially composed of the following elements: (1) a cup metal-bonded diamond wheel, (2) an ELID DC-pulse power source, (3) a specific grinding fluid (which serves as an electrolytic agent), and (4) a fixed copper electrode. Figure 6.16 shows a schematic diagram of the ELID CG-grinding process.

The generating mechanism of the spherical surface ground with cup wheels was first introduced in 1920 by W. Taylor, an English scholar. As shown in Figure 6.17, the workpiece is mounted on a work spindle, and the inclination angle α between the axis of rotation of the workpiece and that of the wheel spindle is properly adjusted. Theoretically, the radius of curvature of the lenses that are produced can be calculated using the following equations:

$$R = \mathrm{Dsi}/(2^{*}\sin \mathrm{a}) \quad \text{(for convex lens)} \tag{6.6}$$

$$R = \mathrm{Dso}/(2^{*}\sin \mathrm{a}) \quad \text{(for concave lens)} \tag{6.7}$$

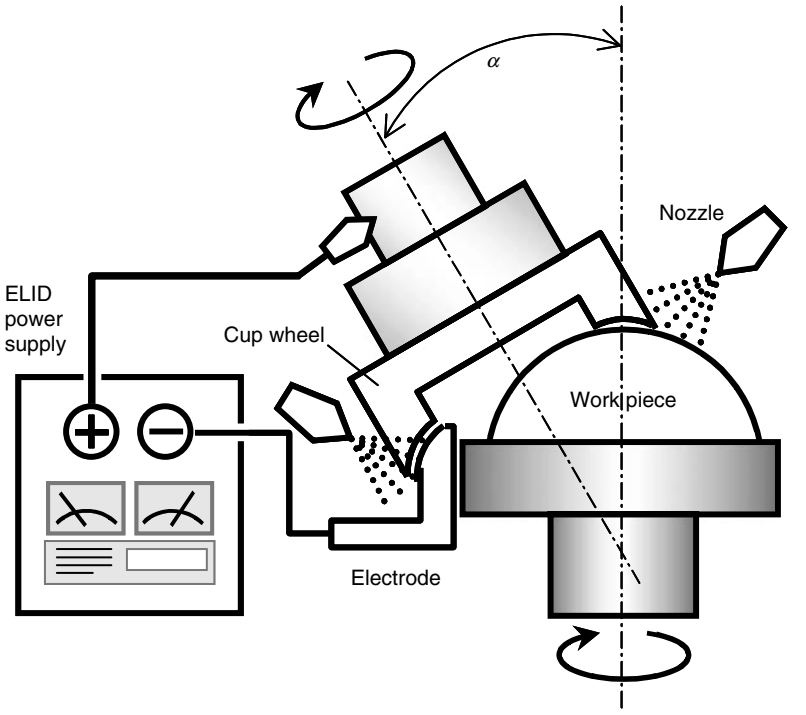

FIGURE 6.16
Schematic of ELID CG-grinding.

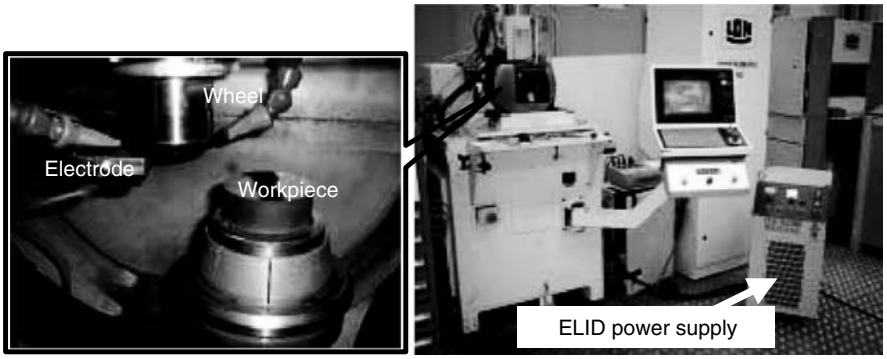

FIGURE 6.17
Overview of experimental setup.

where R is the radius of curvature of the lenses, Dsi is the internal diameter of the grinding wheel, Dso is the external diameter of the grinding wheel, and α is the inclination angle of the axes of rotation between the workpiece and the wheel.

From a geometrical point of view, the parameters of dimensional error and shape accuracy in ELID CG-grinding consist mainly of the following: (1) inclination deviation of the workpiece axis from the wheel axis, (2) position deviation of the wheel-workpiece contact point from the workpiece rotation center in the α plane, and (3) position deviation of the wheel axis from the α plane. Among these, (1) and (2) affect the dimensional error of the lenses, and (3) influences the shape accuracy of the lenses. In contrast, wheel wear has no impact on the shape accuracy of the lenses that are produced.

6.4.2 Experimental Setup for ELID CG-Grinding

Experiments were conducted on a specific LOH machine. Two cup-cast-iron-bonded diamond wheels were used. The mesh size of the wheels was #325 for coarse grinding and #4000 for finish grinding. NEXSYS was used as an ELID coolant. A DC-pulse generator was used as the ELID power supply, with adjustable output voltages, currents, and duty factors. An open voltage of 90 V with a current of 20 A was set for these experiments. SiC and Si_3N_4 ceramics were tested. Figure 6.17 shows an overview of the experimental setup.

6.4.3 ELID CG-Grinding of Ceramic Spherical Lens Molds

Figure 6.18 shows the surface roughness and topography of the SiC spherical lens mold produced using ELID. Experimental conditions were a wheel speed of 5000 rpm, a workpiece rotation rate of 500 rpm, a feed rate of

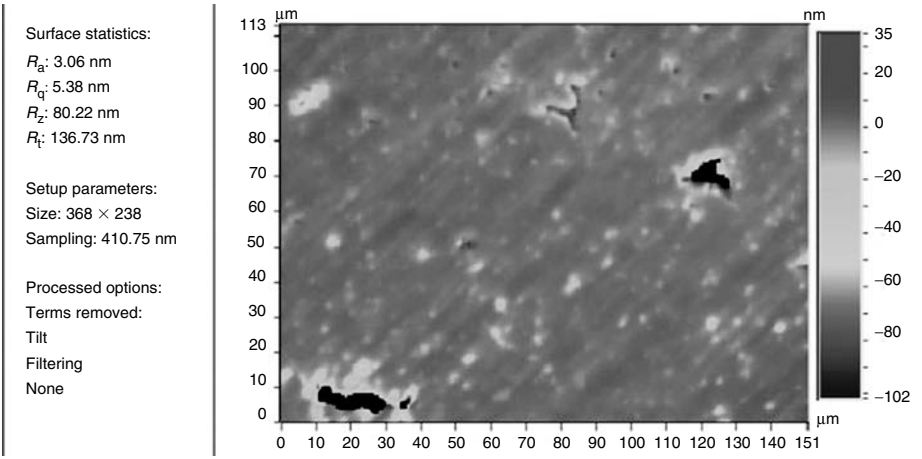

FIGURE 6.18
Surface roughness and topography.

30–50 μm/min for #325 and 4–6 μm/min for #4000, and a spark-out time of 60 sec. Although some initial defects appear on the surface, the ELID process achieves an improved surface finish, with a surface roughness similar to that obtained by loose abrasive processes such as polishing or lapping. In this case, the finished roughness was approximately $R_y = 73$ nm and $R_a = 3$ nm, which demonstrates that ELID with extremely fine abrasives can produce highly smooth surfaces. This technique is also characterized by high precision and efficiency, attributable to the metal bonding of the abrasive. Finished examples are shown in Figure 6.19. A mirror-like mold could be finished in approximately 3–5 min.

In addition, other optics and mold materials, including Si_3N_4, Tungsten carbide (WC), Zirconia (ZrO_2), Silicon hardened steel (X38CrMoV5.1), and Zerodur were fabricated in order to demonstrate the effectiveness of the proposed method. We obtained the surface roughness of the following materials:

$$\begin{aligned} Si_3N_4\ R_a &= 8\text{–}12 \text{ nm (\#4000 SD)} \\ WC\ R_a &= 2\text{–}3 \text{ nm (\#4000 SD)} \\ ZrO_2\ R_a &= 1\text{–}2 \text{ nm (\#8000 SD)} \\ Si\ R_a &= 6\text{–}8 \text{ nm (\#4000 SD)} \\ Steel\ R_a &= 5\text{–}8 \text{ nm (\#4000 SD)} \\ Zerodur\ R_a &= 7\text{–}8 \text{ nm (\#4000 SD) } 0.5\text{–}1.5 \text{ nm (\#8000 SD)} \end{aligned}$$

Based on the above-mentioned experimental results, extremely smooth surfaces were successfully achieved. These results also indicate that ELID CG-grinding can be successfully used to fabricate spherical lenses and molds with a more stable process, at higher efficiency and of better surface quality, compared to conventional grinding.

FIGURE 6.19
ELID ground lens mold.

Efficient and precise grinding of spherical lens molds with cup wheels using the ELID process was proposed and tested in the present study. Our investigations revealed that ELID CG-grinding can be used to successfully achieve better surface roughness.

6.5 ELID Grinding Characteristics and Surface Modifying Effects of Aluminum Nitride Ceramics

6.5.1 Experimental Setup for ELID Grinding of AlN Ceramics

Aluminum nitride (AlN) ceramics have excellent electrical insulation and dielectric properties, a high thermal conductivity that is approximately 10 times than that of alumina, as well as a thermal expansion coefficient that is close to that of Si. As such, AlN ceramics are anticipated to be used in semiconductor mounting boards, heat-dispersing substrates for power modules, and other heat-sink materials in a variety of high-value-added applications [24,25]. In this section, we report the efficient, high-precision grinding of sintered AlN ceramics using the ELID process and describe the ground surface modifying characteristics in detail.

TABLE 6.2

ELID Grinding Conditions

Workpiece	**Aluminum Nitride (AlN) Ceramics**
Grinding machine	Precision rotational grinder
Grinding wheel	Cast-iron-bonded diamond wheel (#325, #600, #1200, #2000, #4000, #8000, and #30000)
Grinding conditions	Wheel rotation: 2000 rev/min Work rotation: 3000 rev/min Depth of cut: 2 μm/min, 1 m/min
Grinding fluid	Chemical solution type grinding fluid (5% dilution to water), density: 1.07 g/cm^3, Ph (50×): 10.0, conductivity (50×): 123 μsec/cm
Electrical conditions	Open voltage: 90 V, peak current: 10 A, pulse timing (on/off): 2/2 μsec, pulse wave: square

Table 6.2 lists the experimental conditions for ELID grinding. A precision rotational grinder was used for external grinding. The wheels used in this experiment were #325, #600, and #1200 for rough grinding, #2000 and #4000 for intermediate grinding, and #8000 and #30000 for finishing. The #30000 wheel had an average grit size of approximately 0.3 μm. In addition, surface evaluation and testing, as described in Table 6.3, were carried out on AlN, in which ELID grinding was performed in order to examine the surface properties and surface modifying effects. In this experiment, ELID grinding was performed on test specimens that are referred to as the ELID series. For the purpose of comparison, another set of test samples were polished using emery paper and then finished by buff polishing using alumina abrasive grains (average grain diameter: 0.3 μm) (referred to as the polished series).

Figure 6.20 shows the results of surface roughness measurements for AlN subjected to ELID grinding. The obtained results indicate that finer the grain size of the grinding wheel, greater the improvement in the surface roughness.

TABLE 6.3

Methods Used for Surface Evaluation and Testing

Surface roughness	SURFTEST-701 (Mitutoyo Co. Ltd)
Surface observation	JSM-5600LV (Scanning Electron Microscopy; SEM) (JEOL Ltd)
Surface hardness test	Nano hardness tester (CSM Instruments)
Surface tribology test	Reciprocating sliding test system (HEIDEN Co. Ltd)
Surface elemental analysis	ESCALAB MK II (x-ray Photoelectron Spectroscopy; XPS) (Thermo VG), Microlab350 (Auger Electron Spectroscopy; AES) (thermo VG)

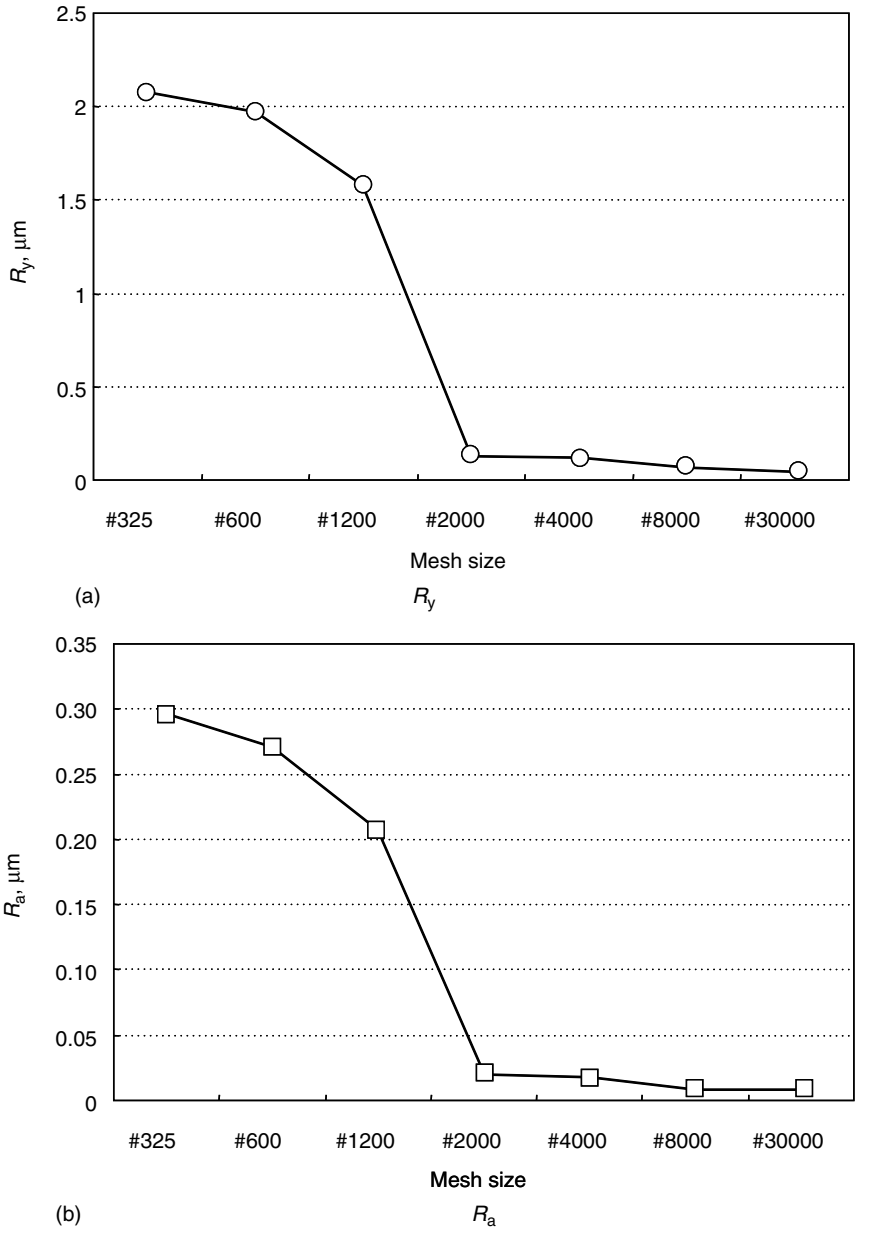

FIGURE 6.20
Relation between mesh size and surface roughness.

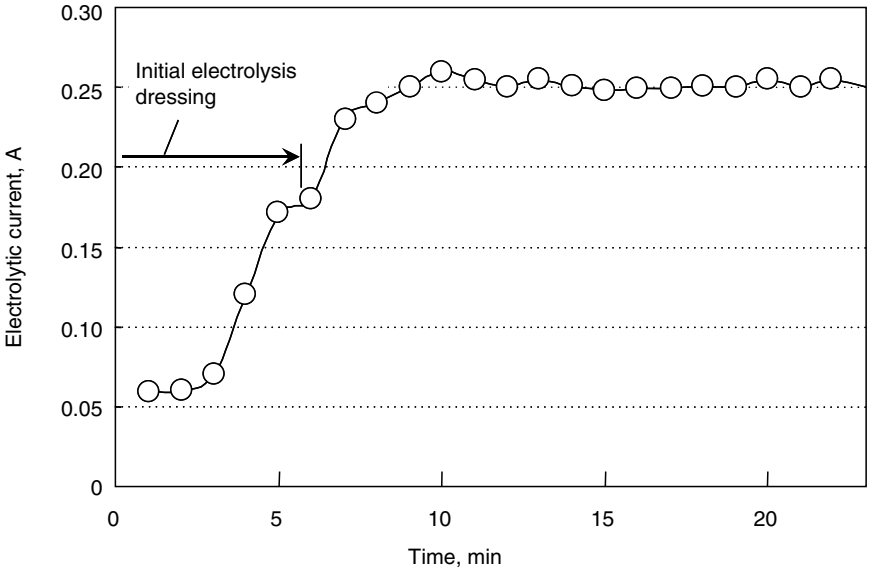

FIGURE 6.21
Behavior of the electrolytic current for processing using a #4000 grinding wheel.

A dramatic improvement in the roughness of ground surface was confirmed between #600 and #2000 wheels. This is attributed to changes in the material removal mechanism between the two grains. By final-finish machining using #30000 abrasive, a satisfactory surface roughness of 0.008 μm R_a was obtained.

Significant improvement in surface roughness and form accuracy was successfully achieved by fine-grit wheels using the ELID technique. Figure 6.21 shows the behavior of the electrolytic current for processing using a #4000 grinding wheel. The current is low at the initial electrolysis stage and increases after the wheel comes in contact with the workpiece. There is no subsequent variation with processing time, and the current remains constant at approximately 0.25 A, indicating that the ELID conditions are appropriate and that stable processing occurs from beginning till the end. This trend in current values was confirmed for all of the other wheels, in addition to the #4000 wheel. A finished example is shown in Figure 6.22.

6.5.2 Observation of the ELID Ground Surface

Figure 6.23 shows the results of SEM observations of the ground surfaces obtained with #325 to #30000 grinding wheels. The surfaces ground with the #325 and #600 wheels demonstrate a rough processed state with the material removed by the breakdown of the grain boundary. On the surface, ground with the #1200 wheel, small areas in which the material was removed by

FIGURE 6.22
ELID ground AlN.

means other than the breakdown of the grain boundary were confirmed. However, in the same way as the surface ground with the #325 wheel, most of the areas were removed in the brittle failure mode, in which the breakdown of the grain boundary is the principle mechanism.

Conversely, the surfaces ground with the #2000, #8000, and #30000 wheels were processed to a smooth surface, with almost no breakdown in the grain boundary. SEM observations of machined surfaces confirmed that between rough machining with #1200 abrasive and intermediate finishing with #2000 abrasive, there exists a brittle–ductile transition point for aluminum nitride. In order to create a high-quality machined surface, the use of fine abrasive particles of at least #2000 is essential. Figure 6.24 summarizes the relationship between the wheel mesh size and the removal mechanism when ELID grinding is used. These results demonstrate that ELID with extremely fine abrasives can produce highly smooth surfaces. This technique is also characterized by high precision and efficiency that are attributable to the metal bonding of the abrasive.

6.5.3 Surface Modifying Effect by ELID Grinding

In order to verify the surface modifying effect at the top of the substrates on which ELID grinding was applied, the hardness was tested using a

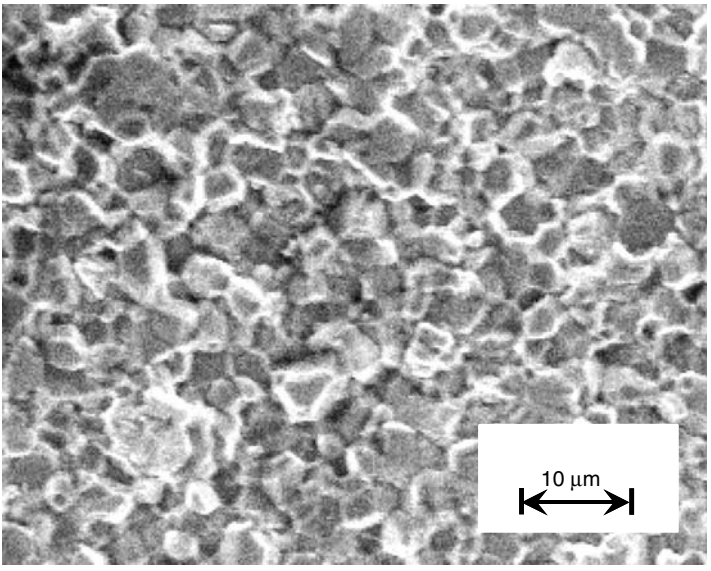

(a) #325

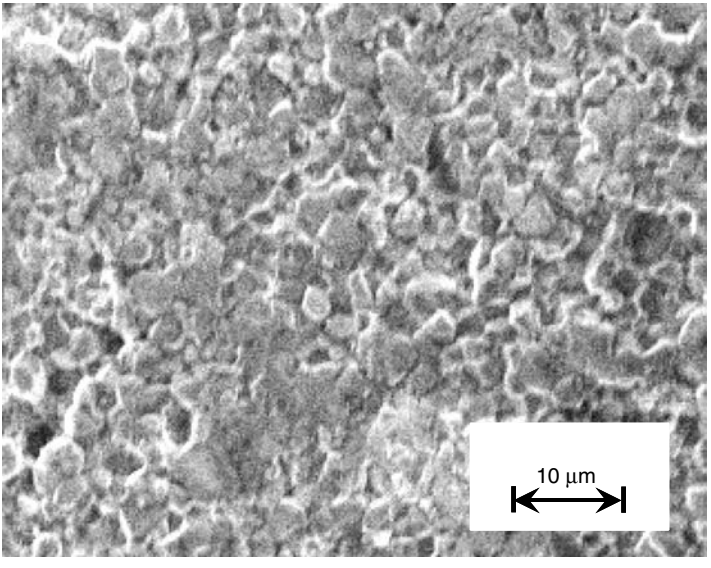

(b) #600

FIGURE 6.23
SEM images of ground surface by ELID.

(continued)

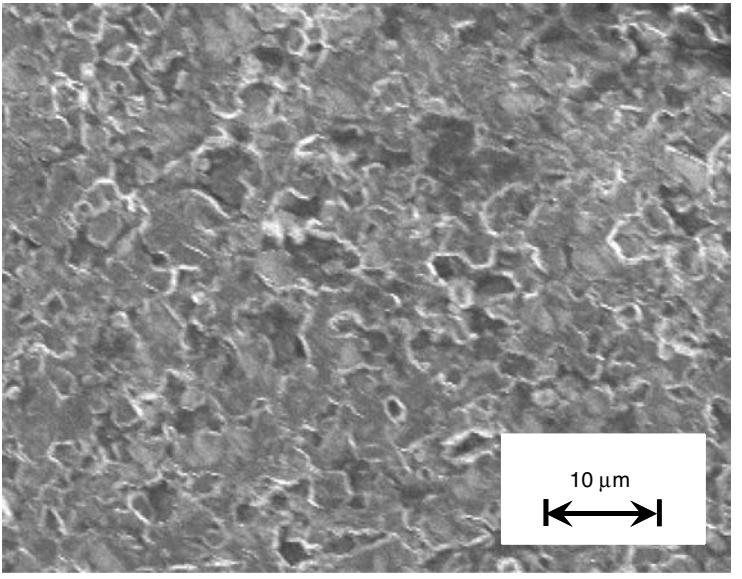

(c) #1200

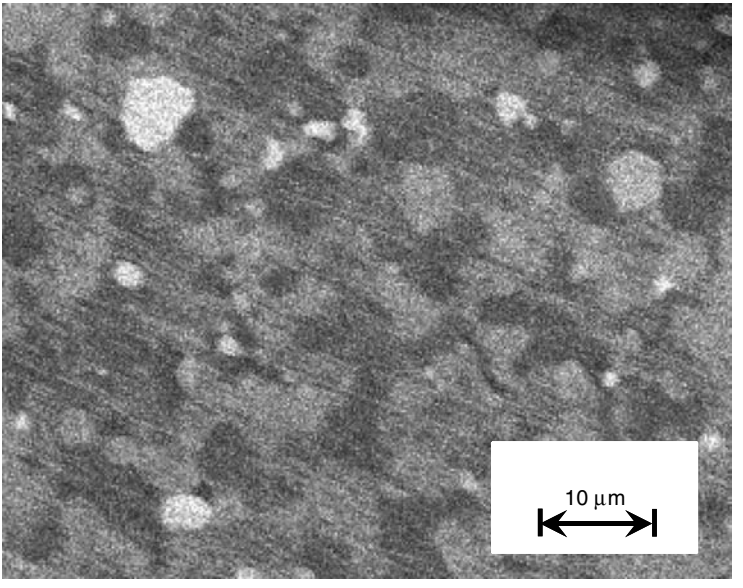

(d) #2000

FIGURE 6.23 (continued)

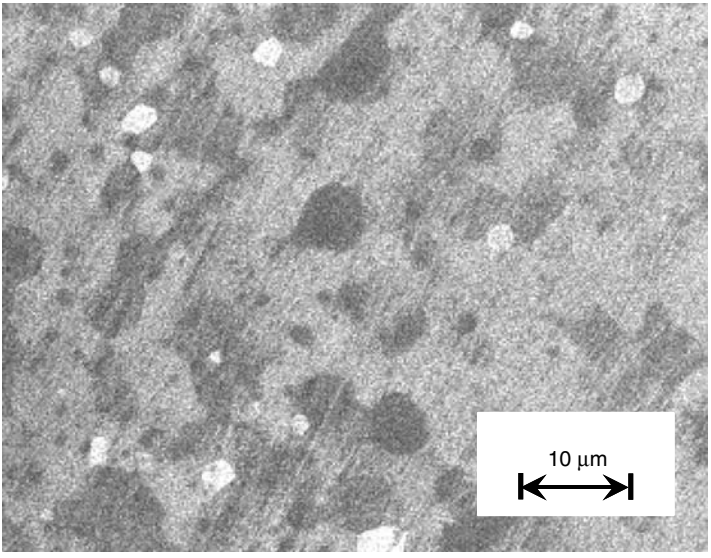

(e) #4000

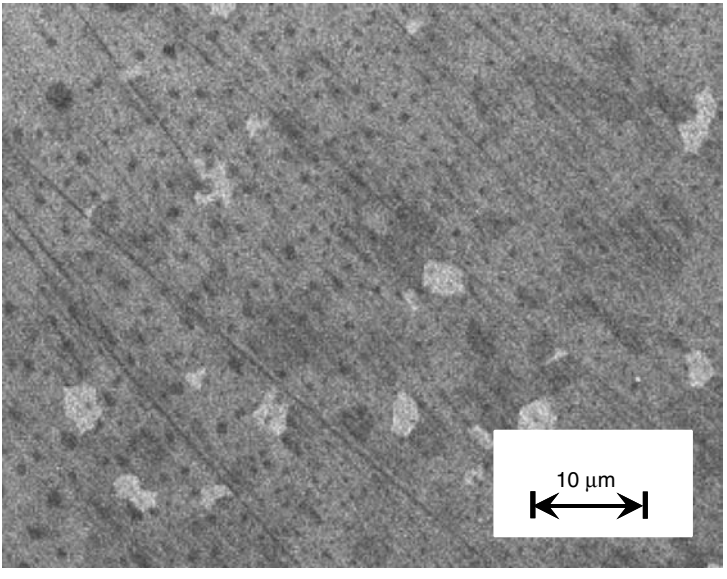

(f) #8000

FIGURE 6.23 (continued)

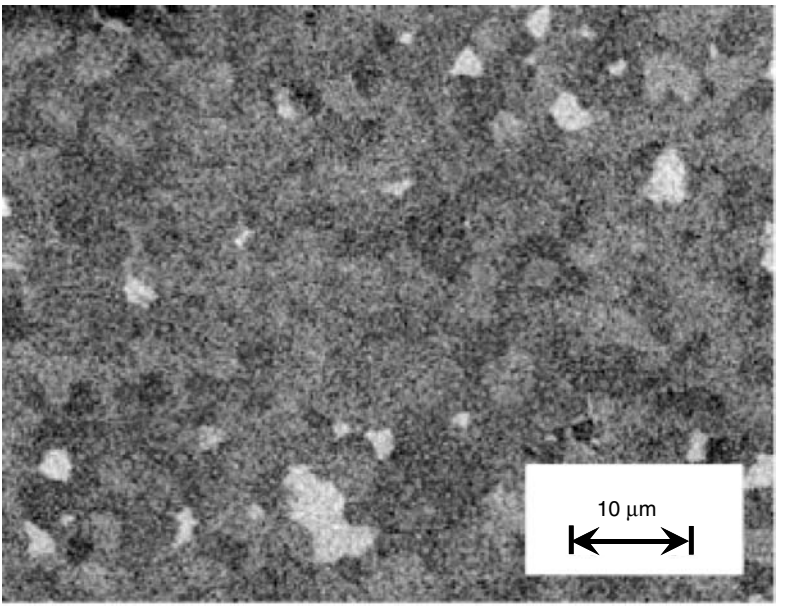

FIGURE 6.23 (continued)

nanoindenter. The maximum indentation load was set to 2 mN. Figure 6.25 shows the results of calculating the Vickers hardness of the top surface, from the relationship between the indentation load and the indentation depth. The resulting value indicates that the hardness of the ELID series is approximately 400 HV higher than that of the polished series. Consequently, it was found that

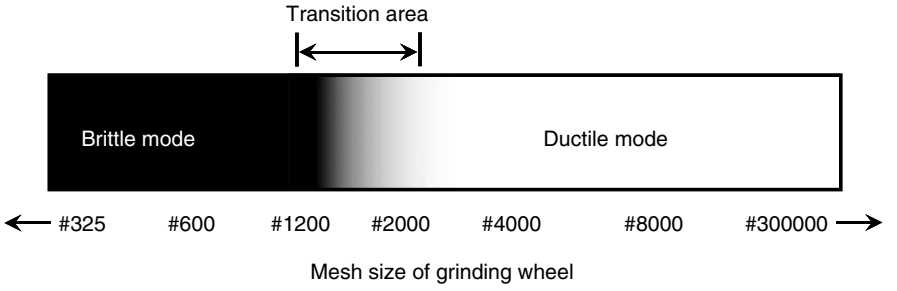

FIGURE 6.24
Relation between wheel mesh size and removal mechanism.

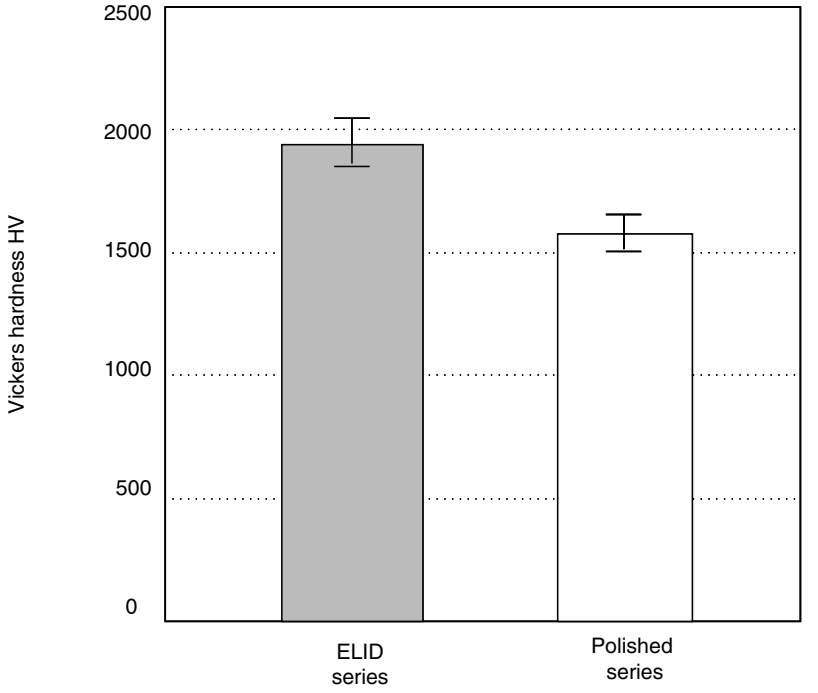

FIGURE 6.25
Results of hardness measurements using a nanoindenter.

implementing ELID grinding on AlN produces a surface modifying effect that enhances the hardness of the top surface of the workpiece.

Figure 6.26 shows the relationship between the frictional coefficient μ and the number of sliding cycles, with respect to the results of the friction and wear testing. The testing conditions were as follows:

- Load: 200 g
- Diameter of opposite material (alumina ball): 3.175 mm
- Sliding distance: 10 mm
- Testing speed: 5 mm/sec
- Number of tests: 100 times

The results indicate that the frictional coefficient μ of the ELID series is lower than that of the polished series. The high-quality surface hardness, as shown in Figure 6.25, obtained as a result of the surface modifying effect due to ELID grinding may be one of the reasons why the sliding characteristics are improved.

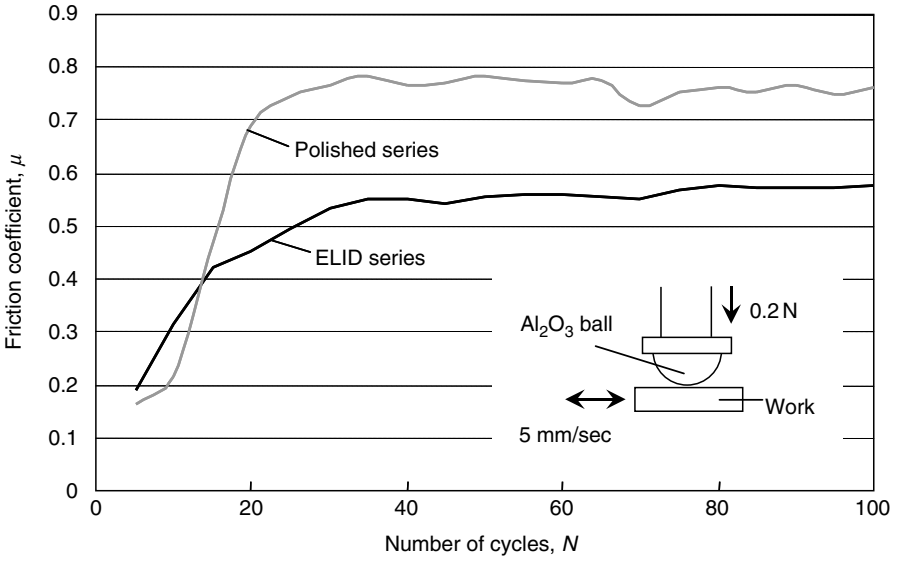

FIGURE 6.26
Relation between the frictional coefficient μ and the number of sliding cycles.

6.5.4 Analysis of the Modified Surface

The properties of the machined AlN surface were analyzed by chemical element analysis using Auger electron spectroscopy. Figure 6.27 shows the results of this analysis. With respect to the intensity of oxygen atoms, the peaks of the ELID series are sharper than those of the polished series. Figure 6.28 shows the results of elemental analysis in the depth direction for various test material surfaces using x-ray photoelectron spectroscopy (XPS). The etching rate was set at 5 nm/min. With respect to the state of diffusion in the depth direction of the oxygen element, the ELID series maintains a higher peak than the polished series, suggesting that the increase in surface hardness shown in Figure 6.25 is caused by the oxygen diffusion phenomenon demonstrated here. As shown in Figure 6.26, ELID grinding yields superior tribological properties in the early stage of tribology testing, by virtue of not only the highly smooth surface attained, but also the resulting oxygen element diffusion layer. The ELID grinding method can be used to fabricate machined surfaces exhibiting desirable characteristics for hard AlN ceramics.

Further experiments are planned in order to clarify the details of the diffusion mechanism of the oxygen element and determine the optimum processing conditions for ELID, such as the type of abrasive, the feed rate, and the machining fluid.

According to the above-mentioned experimental results, the final finishing using a #30000 wheel produced an extremely smooth ground surface

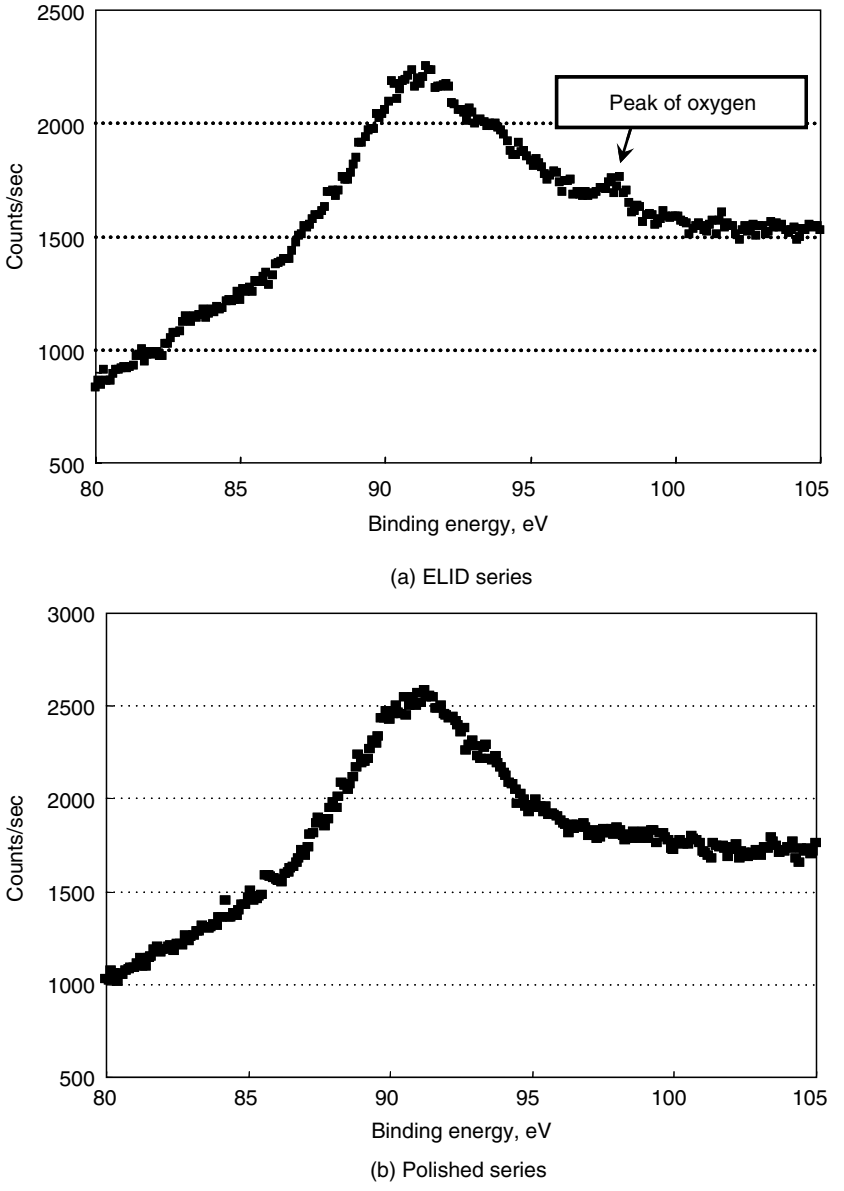

FIGURE 6.27
Results of analysis via Auger electron spectroscopy.

roughness of 0.008 μm R_a. In addition, the ELID series demonstrated surface hardness and sliding characteristics that were superior to those of the polished series. These advantages may be attributable to the diffusion phenomenon of the oxygen element produced by the ELID grinding.

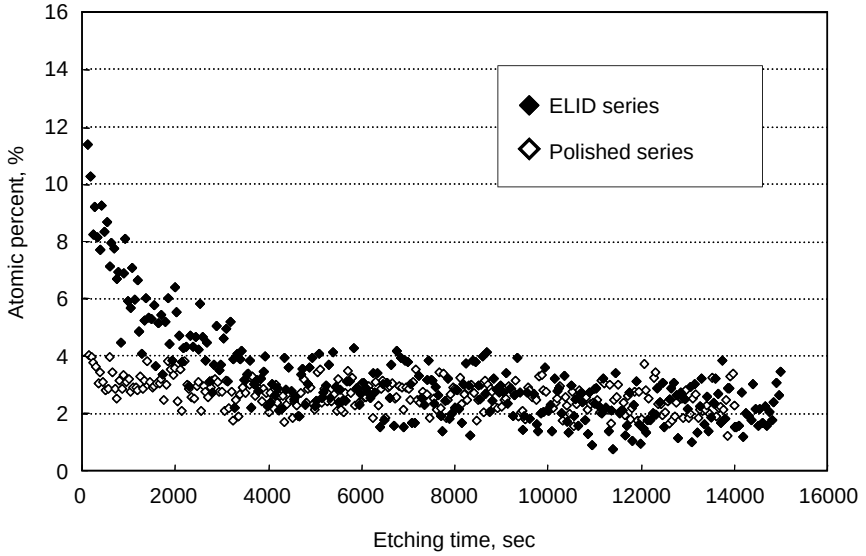

FIGURE 6.28
Results of elemental analysis carried out using XPS.

Acknowledgments

The authors would like to express their sincere thanks to the industrial members of the ELID research project for their financial support. In addition, special thanks are due to NEXSYS Corporation and the AD&S center of RIKEN for their assistance in testing.

References

1. Ohmori, H. and Nakagawa, T., Mirror surface grinding of silicon wafers with electrolytic in-process dressing, *Annals of the CIRP*, Vol. 39, No. 1, 1990, pp. 329–332.
2. Ohmori, H., Electrolytic in-process dressing (ELID) grinding technique for ultra precision mirror surface machining, *International Journal of JSPE*, Vol. 26, No. 4, 1992, pp. 273–278.
3. Ohmori, H. and Takahashi, I., Efficient grinding of sintered diamond and CBN materials utilizing electrolytic in-process dressing (ELID), *Proceedings of the 1st International Abrasive Technology Conference*, Seoul, Korea, 1993.
4. Ohmori, H. and Nakagawa, T., Analysis of mirror surface generation of hard and brittle materials by ELID (electrolytic in-process dressing) grinding with superfine grain metallic bond wheels, *Annals of the CIRP*, Vol. 41, No. 1, 1995, pp. 287–290.

5. Ohmori, H., Takahashi, I., and Bandyopadhyay, B.P., Ultra precision grinding of structural ceramics by electrolytic in-process dressing (ELID) grinding, *Journal of Materials Processing Technology*, Elsevier, Vol. 57, 1996, pp. 272–277.
6. Ohmori, H., Takahashi, I., and Bandyopadhyay, B.P., Highly efficient grinding of ceramic parts by electrolytic in-process dressing (ELID) grinding, *Materials and Manufacturing Processes*, Marcel Dekker, Vol. 11, No. 1, 1996, pp. 31–44.
7. Ohmori, H. and Nakagawa, T., Utilization of nonlinear conditions in precision grinding with ELID (electrolytic in-process dressing) for fabrication of hard material components, *Annals of the CIRP*, Vol. 46, No. 1, 1997, pp. 261–264.
8. Ohmori, H. and Marinescu, I.D., Super-smooth surfaces with ELID technique, *Abrasives*, Vol. 8, No. 9, 1998.
9. Fuji ELIDER, catalog from Fuji Die Co. Ltd., Tokyo, Japan, 1996.
10. Ohmori, H., Katahira, K., Nagata, J., Mizutani, M., and Komotori, J., Improvement of corrosion resistance in metallic biomaterials by a new electrical grinding technique, *Annals of the CIRP*, Vol. 51, No. 1, 2002, pp. 491–494.
11. Ohmori, H., Katahira, K., Uehara, Y., and Lin, W., ELID-grinding of microtool and applications to fabrication of microcomponents, *International Journal of Materials and Product Technology*, Vol. 18, No. 4/5/6, 2003, pp. 498–508.
12. Katahira, K., Watanabe, Y., Ohmori, H., and Kato, T., ELID grinding and tribological characteristics of TiAlN film, *International Journal of Machine Tools and Manufacture*, Vol. 42, 2002, pp. 1307–1313.
13. Ohmori, H., Katahira, K., Uehara, Y., Watanabe, Y., and Lin, W., Improvement of mechanical strength of micro tools by controlling surface characteristics, *Annals of the CIRP*, Vol. 52, No. 1, 2003, pp. 467–470.
14. Ohmori, H., Katahira, K., Mizutani, M., and Komotori, J., Investigation on color-finishing process conditions for titanium alloy applying a new electrical grinding process, *Annals of the CIRP*, Vol. 53, No. 1, 2004, pp. 455–458.
15. Vickerstaff, T.J., Diamond dressing—its effect on work surface roughness, *Industrial Diamond Review*, Vol. 30, 1970, pp. 260–267.
16. Davis, C.E., The dependence of grinding wheel performance on dressing procedure, *International Journal of Machine Tool Design Research*, Vol. 14, 1974, pp. 33–52.
17. Konig, W. and Meyen, H.P., AE in grinding and dressing: accuracy and process reliability, *SME*, 1990, MR 90–526.
18. Malkin, S. and Murray, T., Mechanics of rotary dressing of grinding wheels, *Journal of Engineering for Industry*, *ASME*, Vol. 100, 1978, pp. 95–102.
19. Koshy, P., Jain, V.K., and Lal, G.K., *A Model for the Topography of Diamond Grinding Wheels*, Wear, Vol. 169, 1993, pp. 237–242.
20. Syoji, K., Zhou, L., and Mitsui, S., Studies on truing and dressing of grinding wheels, 1st Report, *Bulletin of the Japan Society of Precision Engineering,* Vol. 24, No. 2, 1990, pp. 124–129.
21. Suzuki, K., Uematsu, T., Yanase, T., and Nakagawa, T., On-machine electrodischarge truing for metal bond diamond grinding wheels for ceramics, *Proceedings of the International Conference on Machining of Advanced Materials*, NIST 847, July 1993, pp. 83–88.
22. Wang, X., Ying, B., and Liu, W., EDM dressing of fine grain super abrasive grinding wheel, *Journal of Materials Processing Technology*, Elsevier, Vol. 62, 1996, pp. 299–302.
23. Piscoty, M.A., Davis, P.J., Saito, T.T., Blaedel, K.L., and Griffith, L., Use of in-process EDM truing to generate complex contours on metal bond superabrasive

grinding wheels for precision grinding structural ceramics, *Proceedings of the International Conference on Precision Engineering*, Taipei, Taiwan, 1997, pp. 559–564.
24. Kämpfe, A., Eigenmann, B., and Löhe, D., Advanced X-ray analysis of grinding residual stresses in AlN and Al_2O_3, *Proceedings of European Conference on Residual Stresses*, Vol. 6, No. 2, 1999, pp. 27–28.
25. Hoshina, T., Tatami J., Meguro T., Komeya, K., Tsuge, A., Kuibira, A., and Nakata, H., Effect of coarser grains on sintering of AlN, *Key Engineering Materials*, Vol. 247, 2003, pp. 87–90.

7

High-Efficiency Belt Centerless Grinding of Ceramic Materials and Hardened Tool Steel

G. Dontu, D. Wu, and I.D. Marinescu

CONTENTS

7.1 Introduction

This chapter is focused on belt centerless grinding applied to hard-to-machine materials. The initial objective is to assess the feasibility of high stock removal on ceramics while maintaining a good control on the process. Attempts in this area have been few and not highly successful, hence there are few or no literature on this subject.

The use of coated abrasives has been proven to be more economical and faster than alternative stock removal procedures. Coated abrasives have been transformed from simple ''sand paper'' through technological advances in backings, adhesive bonds, abrasive grains, and joint designs. Coated abrasives are used for dimensioning to close tolerances in a variety of materials ranging from wood, metal, ceramics, and glass.

High-speed stock removal is made possible through technological advances of the three main raw materials that comprise the coated abrasive belts. Minerals, backings, and adhesive bonds are the three raw materials that encompass the manufacture of coated abrasives. Minerals perform the actual job of grinding, finishing, and polishing. Emery and garnet, two natural minerals, are supplemented with six synthetic materials: aluminum oxide, silicon carbide, alumina-zirconia, ceramic aluminum oxide, diamond, and recently CBN. The base, or carrier, for the abrasive mineral is the backing material. To optimize the flexibility, rigidity, or toughness required for the application, the proper weight, thickness, and type of material needs to be selected. Four backing materials that are generally used are paper, cloth, fiber (a combination of paper and cloth), and polyester film.

The machines that use the abrasive belt technology are more powerful and efficient than past machinery. Through the combination of multiple machine heads, excellent surface quality can be achieved in a single pass. The configuration of rough grinding, semi-finishing, and final finishing machine heads can achieve a surface finish of 0.26 μm or less. Improved machinery can achieve high levels of accuracy going down to ± 0.25 μm.

The process of centerless grinding is used for continuous grinding of cylindrical surfaces. The workpiece is supported by a rest blade in contrast to cylindrical grinding where the workpiece is supported by its centers. The grinding head is responsible for the removal of material. A contact wheel, an idler roll, and the abrasive belt are the three main components of the grinding head. The regulating wheel ensures the contact between the workpiece and the grinding head. The regulating wheel is a rubber-bonded wheel that is tilted to generate axial feed. It rotates at approximately one twentieth the surface speed of the contact wheel. The cutting forces exerted by the grinding head hold the workpiece against the work-rest blade (through feed support). The workpiece rotates at the same surface speed as the regulating wheel (Figure 7.1).

Centerless grinding has several important advantages:

- The process is rapid, as through-feed centerless grinding is almost continuous.
- The operator requires very little skill.
- The process can be easily automated.
- The workpiece is fully supported by the work rest and the regulating wheel in the cutting zone. This allows more intense cutting without the fear of distortion.
- Accurate size control is achievable because there is no distortion of the workpiece.

Abrasive belt centerless grinding offers some additional advantages:

- Stock removal time is decreased.
- Belts require much lower unit forces.

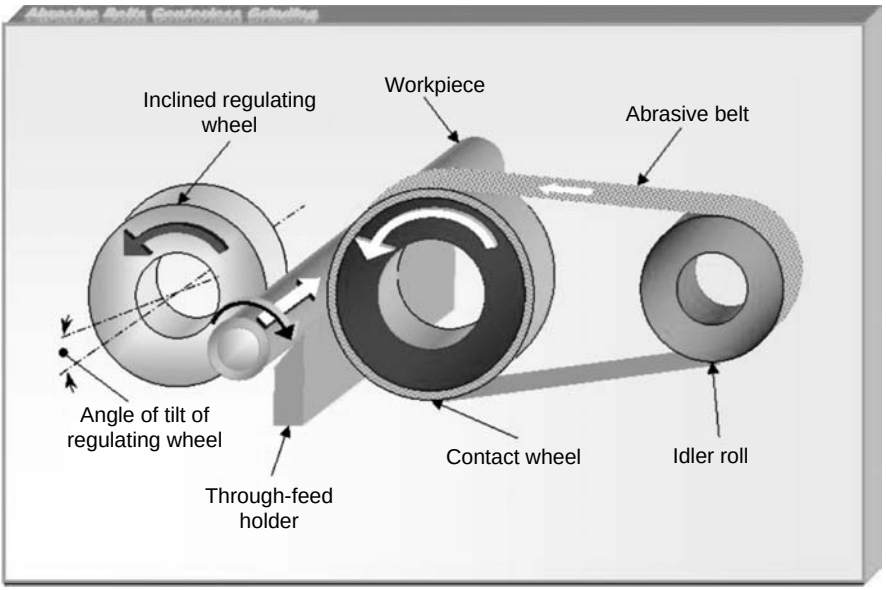

FIGURE 7.1
Abrasive belt centerless grinding setup.

- Higher feed rates are attainable.
- There is no need for dressing or truing of a wheel.
- Setup times are reduced.
- Constant surface speed can be maintained.
- Cooler operation.
- Belts can be used in multiple-head configurations.

Surface quality also depends on a number of variables. Specification of machine rigidity, the contact wheel, the abrasive belt and the parameters for the workpiece surface speed, belt speed, and production through-feed rate are just a few examples of these variables.

7.2 Definition of the Problem

Ceramic materials are difficult-to-machine materials. To obtain a good quality machined surface, it is necessary to use a very small depth of cut, usually at the submicron level, which keeps the process to very low productivity and efficiency. Most of the highly industrialized countries

invested very heavily in the development of ceramic materials in the last 15–20 years. Even though there are a number of good results obtained using ceramic materials, the rate of increase in the number of applications for these materials in industry is still very slow. Due to their excellent wear resistance and tolerance of high temperature, ceramics are the desired materials for many applications in the automotive, aerospace, and bearing industry. The barrier is the high cost and difficulty of machining these materials.

Hardened tool steel is another kind of difficult-to-machine material that is studied in this chapter. M7 is molybdenum-type high-speed steel designed with higher carbon and vanadium to provide high hardness (up to HRC 65–67) and good wear resistance.

The first issue to be addressed in belt centerless grinding of ceramics is dimensional control. Centerless grinding, in both its fixed abrasive and coated abrasive variants, uses a rubber-regulating wheel to ensure the contact between the cutting tool (wheel or belt) and the workpiece. Thus, the introduction of an elastic element in the dimensional chain renders the adjustment of the depth of cut difficult. In the specific case of belt centerless grinding, there are two more elastic components that intervene on the dimensional chain. The cutting action of the abrasive belt is insured by the contact roll, which has a much higher elasticity coefficient than bonded abrasive wheels. The second additional elastic component is the backing of the abrasive belt. The variability introduced by these factors also affects the influence of the work parameters, surface speed, and feed, on the material removal. As in any other cutting process, the part itself will influence the dimensional precision of the process through its material characteristics and tolerance heredity.

7.3 Objectives

- To establish the necessary characteristics for the abrasive belts and the machine tools, using them such that high stock removal can be achieved on ceramic materials while maintaining good output precision and surface quality.
- To optimize the process parameters for belt centerless grinding of ceramic materials and hardened tool steel. Our preliminary trials focused on the relationship between process parameters, belt speed and through-feed, and several output parameters: depth of cut, stock removal, material removal rate (MRR), and surface roughness.

7.4 Experiments for Ceramic Materials

Experiments have been performed on an ACME Model 47 Belt Centerless Grinder. The machine tool has been modified by the manufacturer to meet the needs of our research better. The main modifications were focused on increasing the variability of the main adjustable parameters: belt speed, feed, and part diameter. In this respect, the machine was equipped with smart drives for both the main drive and the regulating wheel. Thus, the contact wheel rpm can be continuously varied between 0 and 5000 rpm while the regulating wheel covers the 0–115 rpm range. The tilt angle of the regulating wheel can be varied between 0 and 10 degrees. The regulating wheel diameter is 152.4 mm, for which the maximum through feed (for maximum regulating wheel rpm and maximum tilt angle) is 1066.8 cm/min. The 70 durometer rubber-covered contact wheel has a 203.2 mm diameter and 101.4 mm width.

The abrasive belt used for these tests was a 3M Flex diamond belt with 125 μm grit size. The length of the belt is 2133.6 mm and the width is 101.4. The test samples were extruded aluminum oxide 96%, cylindrical shaped, with an average length $L_{ave} = 101.25$ mm (Figure 7.2). The sample material density is $\rho = 3.702\ g/cm^3$. Taking into account that these were preliminary tests and that there is very limited data on this type of process, we opted for a full factorial design of the experiments. Thus, the variable process parameters were

- Belt speed (m/sec), with 5 levels: 30.48, 35.56, 39.62, 44.19, and 48.26.
- Through feed (cm/min), with 5 levels: 149.1, 174.0, 198.9, 223.5, and 248.4.

The fixed parameters were

- Regulating Wheel tilt angle: 3°
- Set depth of cut: 30 μm

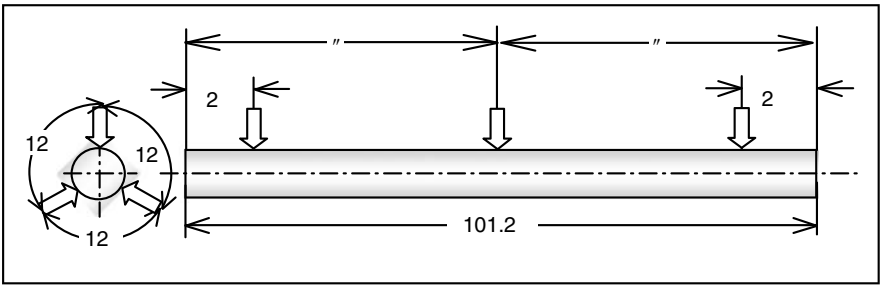

FIGURE 7.2
Al_2O_3 sample, showing the location of the six points where the diameter was measured.

Thus, the experiments matrix had a 5×5 size with 25 set points. For each set point, the experiments were repeated four times. The sample set was $5 \times 5 \times 4 = 100$ samples. The measured sample input parameters were

- Initial average diameter for each sample, D_i (mm) (the measurements were performed on three diameters and on three locations on the sample's length).
- Initial sample weight, W_i (grams).
- Initial sample roughness, R_{ai} (μm).

The sample average for the input parameters were $D_{i\,ave} = 6.903$ mm; $W_{i\,ave} = 14.231$ g; and $R_{ai\,ave} = 0.58$ μm. The measured output parameters were

- Sample final diameter, D_f (mm) (average in six points)
- Sample final weight, W_f (g)
- Sample final roughness, R_{af} (μm)

The computed output parameters were

- Actual depth of cut, DOC $= D_i - D_f$ (mm)
- Stock removal, SR $= (W_i - W_f) \times \rho^{-1} \times L_{ave}{}^{-1}$ (cm^3/cm)
- Material removal rate, MRR $=$ SR $\times$ Feed (cm^3/min)

The tests were performed using high-flow 5% water-based coolant.

7.5 Results

After the samples were machined and measured, the data were first analyzed as a pure sample set, considering all 100 samples. Using this approach, we can obtain initial information on the consistency of the tests. Figure 7.3 through Figure 7.5 show the measured parameters, sample diameter, sample weight, and surface roughness for all 100 samples. Each set of 20 samples was machined with a constant belt speed while the feed was increased. A very good correlation can be observed for sample diameter (Figure 7.3) and sample weight (Figure 7.4). The sample roughness (Figure 7.5) displayed an acceptable correlation coefficient and maintained its values in a predictable range for the belt grit size.

In addition, from this data we can observe a relatively high heridity of the parameters. This behavior is typical for machining processes where the dimensional chain includes elastic elements, allowing variations that occur

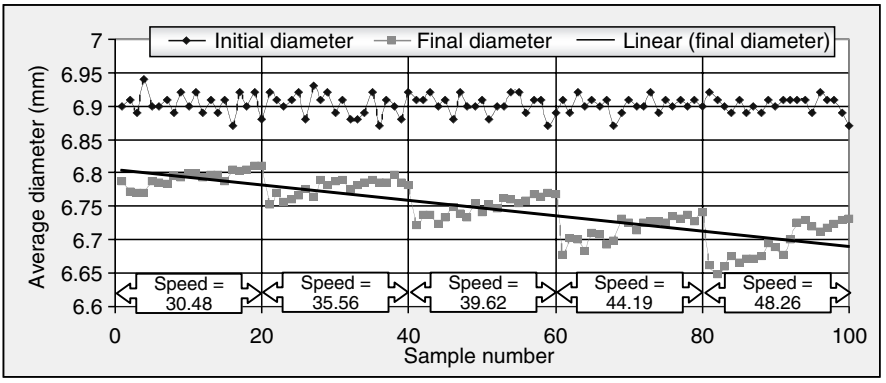

FIGURE 7.3
Measured initial and final sample diameter for a 100 sample set.

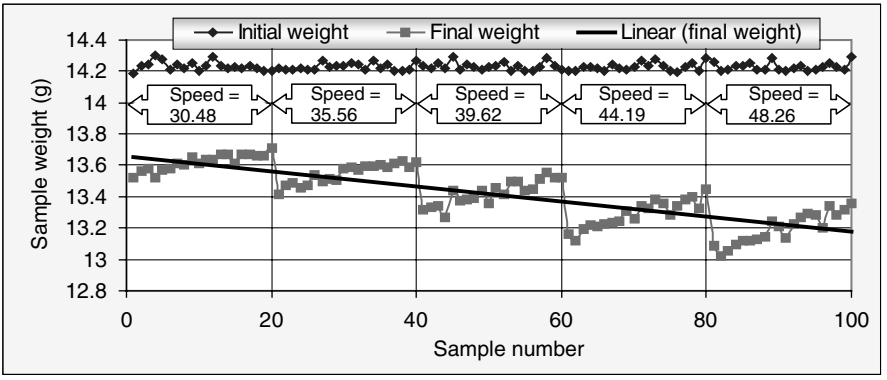

FIGURE 7.4
Measured initial and final sample weight for a 100 sample set.

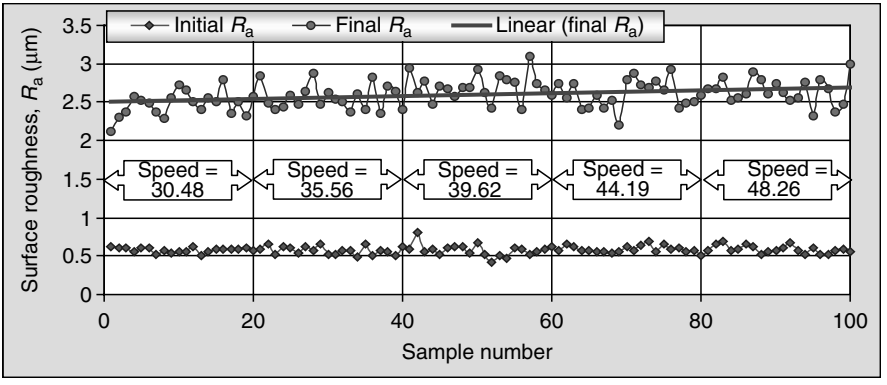

FIGURE 7.5
Measured initial and final sample surface roughness, R_a, for 100 samples.

in the initial state to propagate, with a certain dampening coefficient, to the postmachining state.

The second step of our analysis is to treat the sample set as a multiple observation one. Thus, we computed the average on the four samples that were machined in the same set points. The average values obtained for each set point were then plotted in four ways: 3D surface, contour bands, which are obtained by intersecting the obtained surface with XY planes, and 2D scatter graphs for feed and belt speed, respectively. The analyzed parameters are depth of cut (Figure 7.6a through Figure 7.6d), stock removal (Figure 7.7a through Figure 7.7d), MRR (Figure 7.8a through 7.8d), and surface roughness (Figure 7.9a through Figure 7.9d).

From Figure 7.6a through Figure 7.6d, it can be observed that the depth of cut has a typical variation of the centerless grinding process, that is, it decreases with the increase in the through feed and increases with the

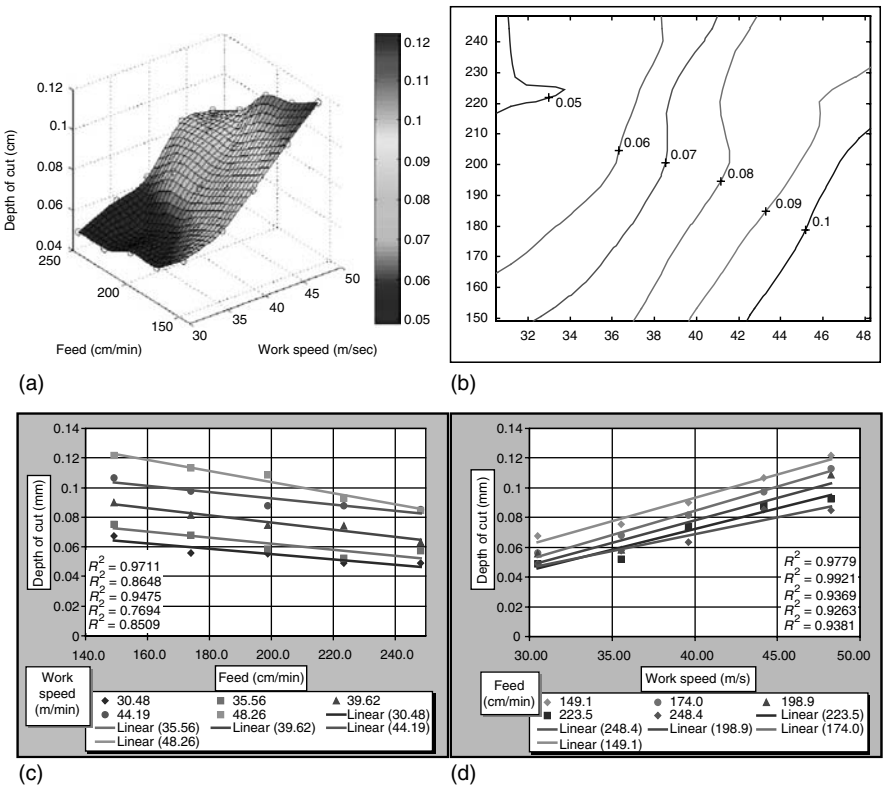

FIGURE 7.6

(a) Depth of cut vs. feed and belt speed. (b) Contour bands for several values of the depth of cut. (c) Depth of cut vs. feed for each of the used belt speeds. The sample coefficient of determination, R^2, is also shown. (d) Depth of cut vs. belt speed for each of the used feeds. The sample coefficient of determination, R^2, is also shown.

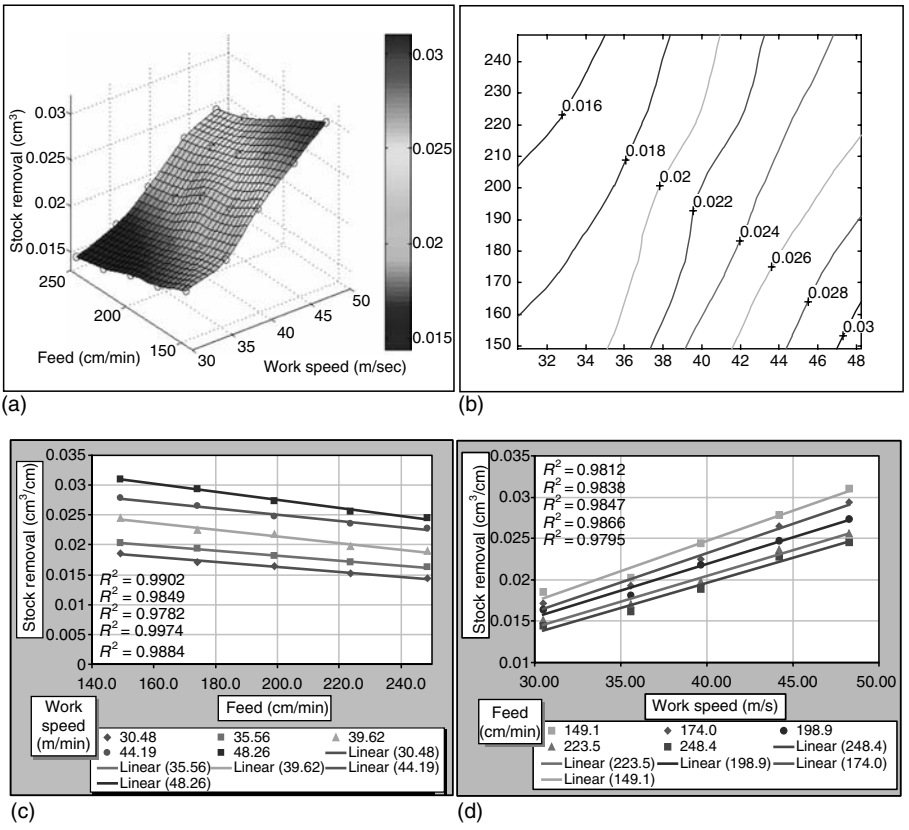

FIGURE 7.7
(a) Stock removal vs. feed and belt speed. (b) Contour bands for several values of stock removal. (c) Stock removal vs. feed for each of the used belt speeds. The sample coefficient of determination, R^2, is also shown. (d) Stock removal vs. belt speed for each of the used feeds. The sample coefficient of determination, R^2, is also shown.

increase in the belt speed. The high values obtained for the sample coefficient of dependency indicate a very good linear relationship among the process parameters and the output ones. The somehow unexpected result was the range obtained for the depth of cut. As previously mentioned, the set depth of cut was 30 μm. The measured depth of cut ranges from 49 to 121 μm. A possible explanation for the difference between the set depth of cut and the measured one is that the reference coordinate is set when first contact between the abrasive belt and the sample takes place. Keeping in mind that the dimensional chain contains three elastic elements, this first contact translates, in fact, into a pressure applied on the sample by the contact wheel and the regulating wheel. When adjusting the regulating wheel for the set depth of cut, we increase this pressure. The resulting depth of cut is, therefore, a combination of the work parameters (speed and feed),

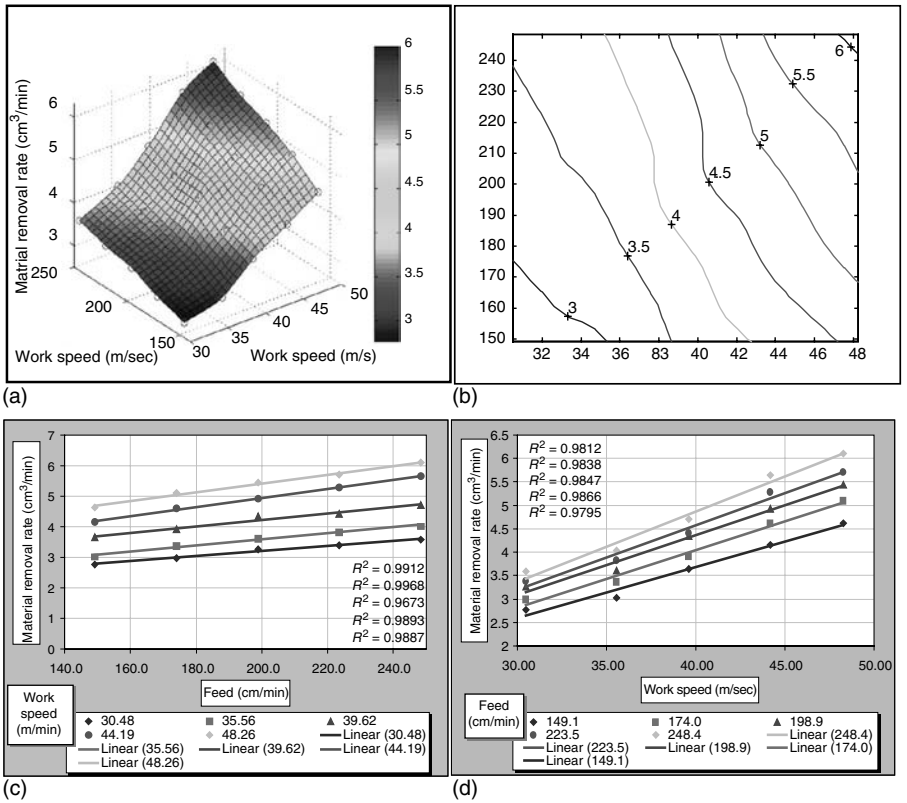

FIGURE 7.8

(a) Material removal rate vs. feed and belt speed. (b) Contour bands for several values of material removal rate. (c) Material removal rate vs. feed for each of the used belt speeds. The sample coefficient of determination, R^2, is also shown. (d) Material removal rate vs. belt speed for each of the used feeds. The sample coefficient of determination, R^2, is also shown.

the cutting capacity of the belt, and the contact pressure. Thus, the good linear dependency, shown in Figure 7.6c and Figure 7.6d, offers a good opportunity for controlling the process. Useful in this respect are diagrams such as the one presented in Figure 7.6b. The contour bands are obtained by intersecting a surface such as the one presented in Figure 7.6a by XY horizontal planes. The vertical offset of these planes represents the value of the analyzed parameter, which in this case is the depth of cut. Each point on a contour band corresponds to the same depth of cut, thus offering the possibility of optimizing the process parameters. The values obtained are atypical for grinding ceramics and are related, to a high degree, with the cutting capacity of the diamond belt.

The next analyzed parameter is the stock removal, and the corresponding graphs are presented in Figure 7.7a, through Figure 7.7d. Theoretically, the stock removal is directly proportional with the depth of cut. To confirm

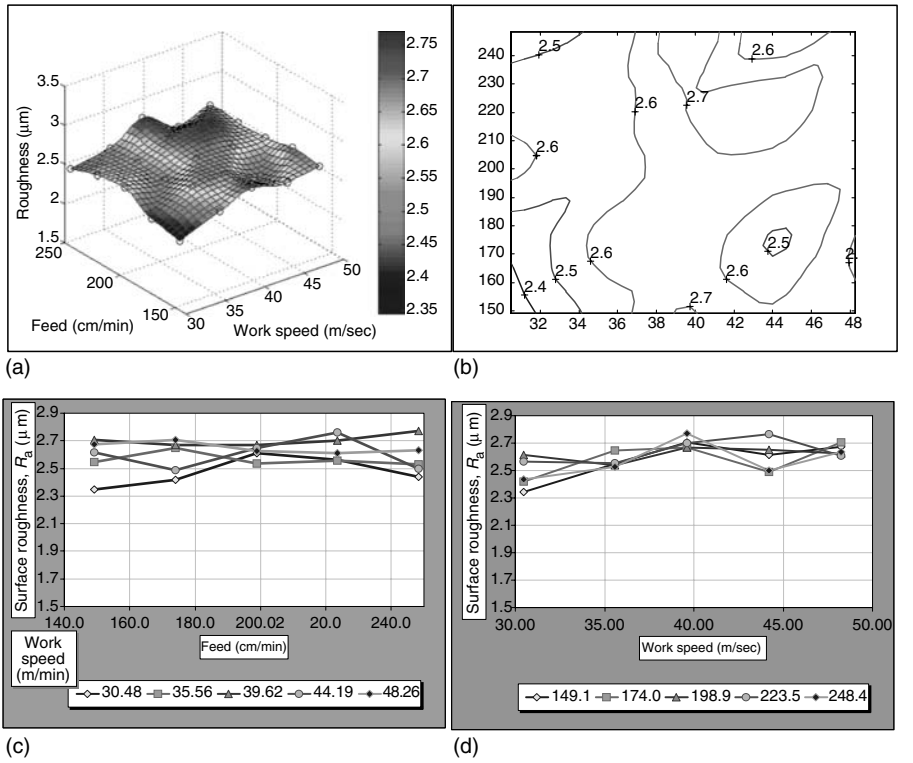

FIGURE 7.9
(a) Surface roughness vs. feed and belt speed. (b) Contour bars for several surface roughness values. (c) Surface Roughness vs. feed for each of the used belt speeds. Surface roughness vs. work speed for each of the used belts. (d) Surface roughness vs. work speed for each of the used belts.

the results obtained by measuring the depth of cut, the stock removal was computed using the weight variation of the samples. Figure 7.7a through Figure 7.7d display the same type of variation as for depth of cut, maintaining the high values for the linear correlation, confirming this way the consistency of the experiments. This parameter also has high values as compared with previously known values for stock removal in the case of grinding ceramic materials.

Combining the values for stock removal with the ones of the through feed, we computed the MRR, which is a very good indicator of the process productivity. The graphs showing the variation of this parameter are presented in Figure 7.8a through Figure 7.8d. As shown in Figure 7.8c, the MRR increases with the increase in the through feed, the higher depth of cut at lower feeds not compensating for the increase in feed. Thus, when optimizing the process for a certain depth of cut, both variations should be taken into account. As expected, the linear correlation is very good.

The final parameter analyzed is the surface roughness, R_a. The graphs obtained are presented in Figure 7.9a through Figure 7.9d.

The data obtained for the surface roughness do not show the same consistency and correlation as the other analyzed parameters. The sample determination coefficients are between 0.3 and 0.4. The obtained roughness range, between 2.3 and 2.8 μm, is not uncommon for the grit size and depths of cut used in these experiments. From Figure 7.5 and Figure 7.9a, we can observe a slight increasing trend toward higher values of belt speed and feed.

7.6 Preliminary Conclusions

- The preliminary tests presented in this chapter strongly indicate that high removal rates can be obtained by belt centerless grinding of alumina using diamond belts, and thus establishing a solid starting base for further studying and developing this application of belt centerless grinding.
- The process showed very good consistency.
- The linear relationships between the work parameters (belt speed and through feed) and the depth of cut, stock removal, and MRR are very strong with an average sample coefficient of determination above 0.96. This aids in controlling the process well.
- Based on the established correlation, the process can be easily optimized.
- No inference can be made yet on the resulting surface roughness.

7.7 Experimental Plan for M7 Hardened Tool Steel Drill Bar

To conduct the experiments, the initial measurements (including diameter, weight, and roughness of 400 samples) have been finished. The grinder has been adjusted initially. The contact wheel and regulating wheel have been dressed. The contact wheel is a 90 durometer rubber covered contact wheel with 203.2 mm diameter and 101.6 mm width.

The abrasive belt used for these tests are:

- 3M Flex diamond belt with 125 μm grit size, 2133.6 mm length, and 101.6 mm width.
- 3M Flex CBN belt with 125 μm grit size, 1371.6 mm length, and 101.6 mm width.

The test samples were M7 hardened tool steel drill bar, cylindrical shaped, with an average length $L_{ave} = 98.425$ mm and 118° point angle.

The variable process parameters were

- Belt speed (m/sec), with five levels: 35.56, 40.64, 45.72, 50.8, and 55.88.
- Through feed (cm/min), with five levels: 208.53, 250.24, 291.95, 333.66, and 375.36.

The fixed parameters were

- Regulating wheel tilt angle: 5°
- Set depth of cut: 0.254 mm

Thus, the experiments matrix had a 5×5 size with 25 set points. For each set point, the experiments were repeated five times. The sample set was $5 \times 5 \times 5 = 125$ samples. Considering the use of both diamond belt and CBN belt, 250 samples are needed. The measured sample input parameters, the measured output parameters, and the computed output parameters are the same as those in the experiments for ceramic materials. The tests were performed using a high-flow 5% water-based coolant, which is designed to operate at very high fluid pressures and volumes and primarily for machining and grinding exotics and highly alloyed steels.

7.8 The Problem Encountered and Possible Reasons

In preliminary testing of the samples, a taper shape of the workpiece was observed after grinding. The taper shape existed in the samples before grinding and, in theory, grinding should be able to remove it. However, after grinding, the taper tended to increase even after dressing the contact wheel and the regulating wheel. Possible reasons could be that hardened tool steel has a higher hardness than ceramics and was machined with a larger depth of cut, for which the flex belt was not rigid enough to keep the workpiece going forward in a straight line. This resulted in the deviation in the workpiece, which led to the taper shape.

7.9 Remaining Work

For ceramic materials, future experiments will be performed using smaller grit sizes for the diamond belts, concentrating more on the surface quality.

In addition, by using a load cell on the regulating wheel's slide, we expect to better control the first contact between belt and part, thus minimizing the initial contact pressure. For hardened tool steel, the reasons for taper shape need further investigation and factorial experiments need to be conducted.

7.10 Benefits to Companies

Owing to the results of this research project, belt manufacturers will have the necessary information to modify their products to achieve better efficiency in the grinding of ceramic materials. Machine tools manufacturers could use the data to adapt their machines to the specific conditions of high-efficiency grinding of hard and brittle materials.

7.11 Related Work Outside AMMC

Koes, R.W., Coated abrasive centerless grinding offers both stock removal and quality manufacturing advantages, ACME Manufacturing Company, Technical Report.

Mayer, J.E., Fang G.P., Effect of grinding parameters on surface finish of ground ceramics, *Annals of the CIRP*, Vol. 44, No.1, 1995.

7.12 Related Work Inside AMMC

Marinescu, I.D., Dontu, G., Abrasive belt centerless grinding, *Abrasives Magazine*, February/March, 1999.

8

AE Monitoring of the Lapping Process

M. Pruteanu, R. Coman, and I.D. Marinescu

CONTENTS

8.1 Introduction

Acoustic emission (AE) has been widely used in many fields such as material behavior detecting, nondestructive testing, investigating friction and wear processes, monitoring engineering structures, and mechanical machining processes since the late 1960s.

Lapping with diamond abrasive slurry is one of the most used processes for very hard and brittle materials. Previous research on lapping and free abrasive wear indicated that brittle fracture plays an important role in the material removal mechanism, especially when the abrasive size is big and normal pressure is high. Cracks generated in the lapping process reduce material strength. A key problem in industry is the controlling and monitoring of the surface damage and integrity of ceramics in-process. AE technology has been recognized internationally as one of the most promising in-process abrasive machining damage detection and monitoring method.

The lapping process is a very complex three-body abrasion. During friction and wear processes, many AE signals could be generated because of the interactions, impact, dislocation, deformation, and removal of materials. In the area of tribology, AE was used to characterize wear mechanisms, discern plastic deformation and fracture, and to monitor active friction and wear processes. AE signals were related to friction coefficient, abrasive grit size, and wear rate.

Until now, a little attention has been paid to research of lapping using AE. K. Phillips has used this method to determine the active number of abrasive particles in a specific unit of area during lapping of glass and fused silica. Another researcher, Dornfeld, investigated the glass-lapping process using AE and he focused on distinguishing between two-body and three-body abrasions and between the ductile and brittle material removal mechanisms.

By supporting the study regarding the monitoring of machining processes using AE signals, the industry will be able to apply the results efficiently. This will improve its manufacturing processes in terms of quality of parts and machining productivity. The study of the AE signals emitted during certain operations can lead to a better understanding of the phenomena that take place in the machining area and thus create the possibility of conducting the processes according to the desired goal.

8.2 Related Work

8.2.1 Within University of Toledo

1. Marinescu, I., Webster, J.A., Brittle/ductile grinding regime for brittle materials, Diamond and CBN Ultrahard Materials Symposium 93, Ontario, Canada, Sept. 29–30, 1993.
2. Ruiling, Zeng, Acoustic emission investigation of ceramic lapping process, MS Thesis, Kansas State University, Manhattan, Kansas, 1998.
3. Webster, J.A., Marinescu, I.D., Benett, R.J., Acoustic emission for process control and monitoring of surface integrity during grinding, *Annals of CIRP*, Vol. 43, 1994, pp. 299–304.

8.2.2 Outside AMMC

1. Ivanov, V., Application of the acoustic emission method for nondestructive monitoring and investigation of materials, *Defektoscopiya*, No. 5, May, 1980, pp. 65–84.

2. Kishi, Cozo, Investigation of scratching ceramics using acoustic emission, *International Journal of Japan Society of Precision Engineering*, Vol. 22, 1988.
3. Tonshoff, H.K., Wulfsbeerg, J.P., Kals, H.J.J., Developments and trends in monitoring and control of machining process, *Annals of CIRP*, Vol. 37, 1988, pp. 611–622.

8.3 Methodology

The key problem is the picking up of an AE signal effectively. A monitoring system based on recording and processing of the AE signals was developed to study the accuracy and sensitivity of this type of sensor to any change in the state of the lapping process. The equipment should be able to recognize any modification or malfunction in the process. These could be generated by wrong selection of the machining parameters or by unpredictable malfunctions or damages of workpieces or the lapping machine.

The experimental equipment used in this research is listed as follows:

- Lapmaster lapping machine, model 12C, variable speed 90 VDC, 7.5 amp motor (0–60 rpm) with 12'' grooved cast-iron plate, 5'' cast-iron conditioning rings, and a magnetic stirrer
- Cole-Parmer peristaltic pump, 7021–24 pump head and 13 mm diameter Masterflex Tygon special tubing

The AE measurement system includes the following:

- AE sensor, model R15 (PAC—Physical Acoustics Corporation), sensitivity scale: 100–1000 kHz
- Preamplifier and filter, model 1220A, gain: 40/60 dB, frequency scale: 100–1200 kHz
- IBM 486 PC with GPIB interface board

Other instruments used

- Roughness meter Hommel tester LV 15

Figure 8.1 shows the schematic of the experimental setup. Three ceramic workpieces touch the lapping plate on their bottom surfaces and the load on their top surfaces. The workpieces are held in place by a slotted disk that is fixed at the bottom of the load using a piece of double stick tape. The AE sensor is installed on an arm and immersed directly in a few drops of oil put in the

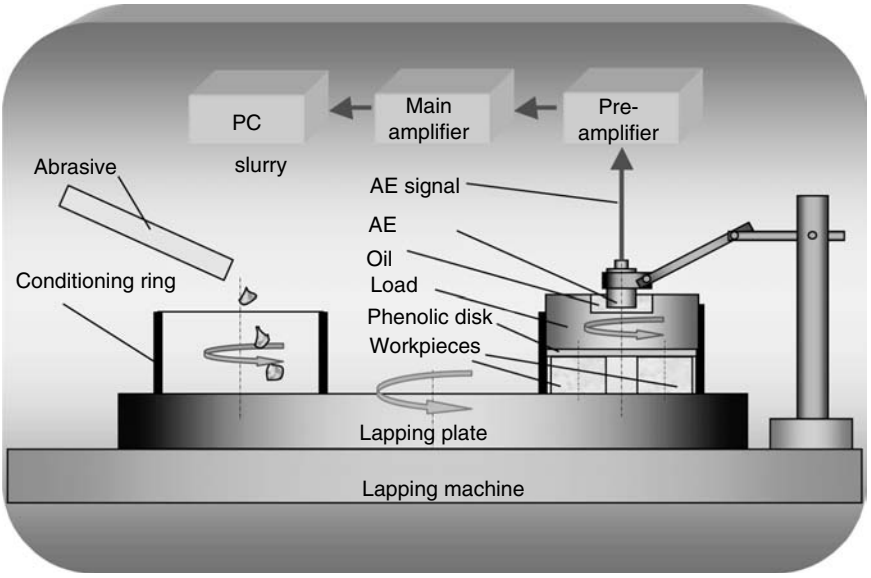

FIGURE 8.1
Setup for the acquisition of the acoustic emission signal in the lapping process.

load (about 0.2 mm from the bottom end of the recess of the load plate). The oil is used to transmit the AE signal from the load to the AE sensor.

The AE signal generated at the workpiece/plate interface is transmitted to the AE sensor via workpieces and the load. After amplifying and filtering, the raw AE signal with frequency between 0.1 and 1 MHz is collected and data are recorded.

Ceramic workpieces (rings with 0.5″ ID, 0.8″ OD and 0.2″ thickness) made of Al_2O_3 (Table 8.1) were lapped with diamond slurry on the single-side lapping machine using a cast-iron plate and two conditioning rings.

TABLE 8.1
Workpiece Material Properties

Material	**Al_2O_3—99.8%**
Physical properties	
Density (g/cm^3)	3.96
Mechanical properties	
Tensile strength (MPa)	310 (at 25°C) 220 (at 1000°C)
Modulus of elasticity (GPa)	366
Poisson ratio	0.22
Compressive strength (MPa)	3790 (at 25°C) 1.929 GPa (at 1000°C)

Diamond abrasive was suspended in a water-based carrier and supplied by a peristaltic pump at a flow rate of 0.75 mL/min. The slurry was based on either monocrystalline or polycrystalline diamond grains with 0.25 μm grit size.

During the lapping experiments, the following parameters were kept constant:

- Flow rate: 0.75 mL/min
- Carrier type: water-based
- Slurry concentration: 1.4 g/500 mL

The following parameters were varied:

- Diamond type: monocrystalline and polycrystalline
- Rotation of the lapping plate: 3, 6, and 9 rpm
- Load: 380, 750, and 1200 g
- Lapping time: 5, 15, 30, and 60 min

8.4 Experimental Results

8.4.1 Experimental Procedure

Three variables were considered in the experiments: (1) type of diamond: monocrystalline (M) and polycrystalline (P); (2) rotation speed of the plate: 3, 6, and 9 rpm; (3) mass of the load: 380, 750, and 1200 g. The experimental conditions are listed in Table 8.2.

In each experiment, AE signals were recorded and three parameters were extracted from the AE signals: hits, counts, and energy. Each lapping experiment lasted 60 min. The AE signals were sampled for about 30 sec at the end of each lapping time: 5, 15, 30, and 60 min. The surface roughness of the workpiece and the material removal rate (MRR) at each sampling stage were measured.

8.4.2 Data Analysis

One objective of the experiments is to find the correlation between the AE signal and surface roughness of workpieces. Counts, hits, and energy are some of the important AE parameters in the AE signal analysis. Experimental data show that counts and hits vary irregularly with machining time. It is not encouraged to try to find the correlation between AE counts, or hits, and surface roughness of workpieces.

TABLE 8.2

Experimental Conditions

Test Number	Type of Diamond	Rotation Speed of Plate (rpm)	Mass of Load (g)
1 (M31)	M	3	380
2 (M61)	M	6	380
3 (M91)	M	9	380
4 (M32)	M	3	750
5 (M62)	M	6	750
6 (M92)	M	9	750
7 (M33)	M	3	1200
8 (M63)	M	6	1200
9 (M93)	M	9	1200
10 (P31)	P	3	380
11 (P61)	P	6	380
12 (P91)	P	9	380
13 (P32)	P	3	750
14 (P62)	P	6	750
15 (P92)	P	9	750
16 (P33)	P	3	1200
17 (P63)	P	6	1200
18 (P93)	P	9	1200

The lapping process can be considered as a process with energy release. A rough surface has high energy and a smooth surface has low energy. It is reasonable to focus on its energy while checking the relationship between the AE signal and surface quality of workpieces.

8.4.2.1 Energy Per Unit Time

Energy per unit time (EPT) can be obtained by dividing the total energy recorded in a period of time by the duration of the recording. From Figure 8.2, it can be observed that the EPT decreases with time, showing the same variation as surface roughness. Similar cases can also be observed in tests carried out with both 6 rpm and 9 rpm. We can say that EPT has some kind of correlation to the surface roughness. In these experiments, we cannot tell if the EPT finally goes to a small constant as the surface roughness does.

One can see that increasing the load leads to higher values of the EPT, which can be explained by higher AE activity since the abrasive grains are pressed more against the workpiece. The same observation can be made for increasing the plate rotation. One can say that an increase in the plate rotation will yield smoother surfaces and higher values for EPT.

Taking into account the ideas mentioned above, one can say that the EPT is a relevant AE parameter for monitoring the lapping process. It is sensitive to the changes of load and plate rotation and can also monitor the roughness

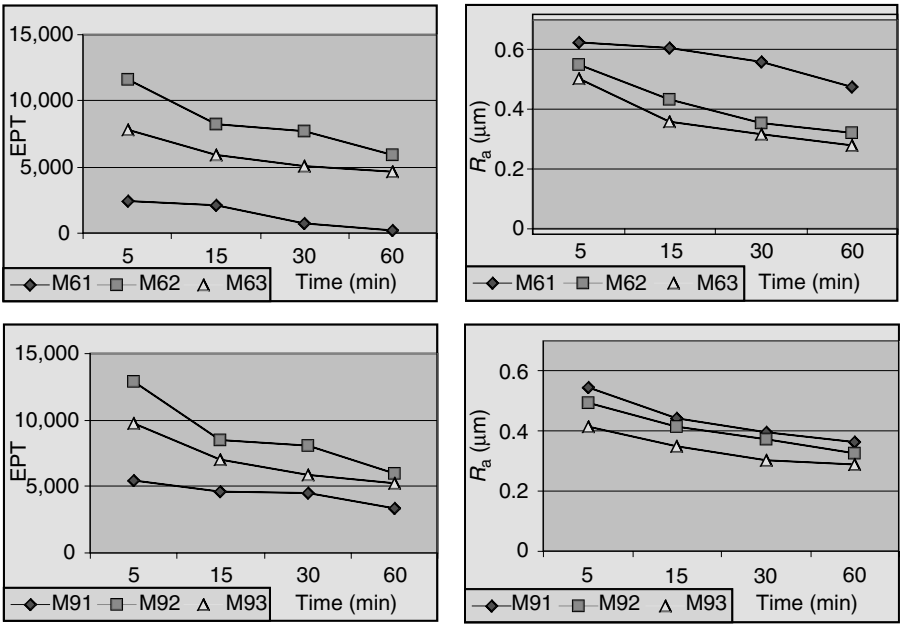

FIGURE 8.2
Energy released per unit time vs. time (left) and surface roughness vs. time (right).

resulting from the process conducted with certain values of the process parameters. This can be explained by the correlation that exists between the input parameters (load and plate rotation) and the output parameters, one of which is the surface roughness. Owing to the above conclusion, the next steps that were taken were focused on studying the relevance of EPT for monitoring other parameters of the lapping process and the correlation between them and this feature of the AE signal.

Figure 8.3 shows the variation in EPT function of the load used for lapping for both monocrystalline and polycrystalline diamond grains. One can draw the conclusion that EPT is sensitive to the type of abrasive that is used for lapping since the values of this AE feature are different for mono- and polycrystalline diamond grains. On the other hand, the different values of EPT function of load can be explained by different mechanisms of material removal. At very low values of load, the prevalent phenomenon that occurs in the machining area is the rolling of abrasive grains on the workpiece surface. This generates AE signals with low energy and is related to low values of MRR. When using a heavier load (750 g) indentation, scratching and plowing of abrasive grains on the workpiece surface occur. All these phenomena generate AE signals with much higher energy because of the friction between the abrasive grain and the workpiece material that is involved in these mechanisms of material removal. By increasing the load

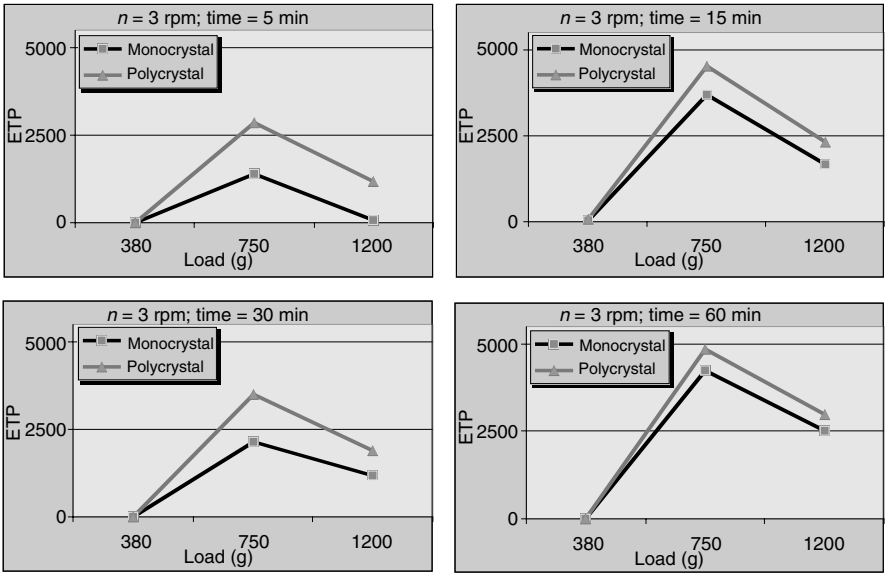

FIGURE 8.3
Energy released per unit time vs. load at various lapping times.

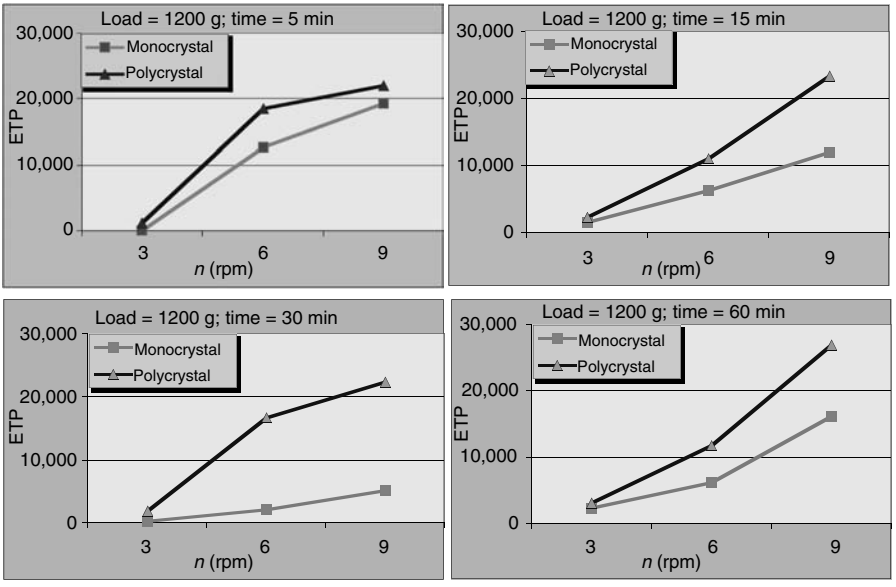

FIGURE 8.4
Energy released per unit time vs. lapping plate rotation for various lapping times.

used for lapping, the material removal mechanism is based mainly on brittle fracture of the ceramic material. This generates AE signals with higher energy than the rolling of the diamond abrasive grains on the workpiece material, but lesser than the friction between them. From Figure 8.3, one can conclude that EPT of the AE signal is sensitive and can be successfully used for monitoring the type of abrasive and the prevalent mechanism of material removal.

Similar conclusions can be drawn from Figure 8.4, which shows the variation in the EPT function of the rotation of the lapping plate. It can also be seen that the energy released is different for the two types of diamond grains (monocrystalline and polycrystalline), as it is always higher for the polycrystalline diamond. EPT is directly proportional with the rotation of the lapping plate because at higher speeds all the phenomena generated by the material removal mechanisms are more intense. One can say that EPT is suitable also for monitoring the rotation of the lapping plate.

8.5 Conclusions

Among multiple features of the AE signal, it was found that the energy per unit time is sensitive to the change in almost all lapping parameters and thus it is suitable for monitoring this machining process. The energy of the AE signal has some kind of correlation with the surface roughness of workpieces, and this can be explained by the correlation between the input and output parameters on one hand and between the input parameters and the AE signal on the other.

8.6 Remaining Work

For the AE system, a high-speed signal acquisition should be used to monitor the lapping process in real time. Many experiments on work parameters and the quality of lapped workpieces should be carried out to confirm the conclusions drawn so far. Based on the experimental results, a practical database can be established and used in real production. Some new programs should be developed to efficiently analyze AE signals and correlate them to surface integrity.

9

Effectiveness of ELID Grinding and Polishing

C.E. Spanu and I.D. Marinescu

CONTENTS

9.1 Introduction

This chapter represents a state-of-the-art process in the domain of electrolytic in-process dressing (ELID) abrasives. The information enclosed represents a considerable effort of analysis and synthesis of more than 50 titles from most relevant research published on this topic in the United States, Japan, and western Europe for the last 10 years. A comprehensive description of the principle and characteristic mechanisms of ELID abrasion are introduced. Specific features of each component of ELID grinding and polishing system are described further. Next, an explanation of the successful and wide application of ELID principles to ceramic grinding is furnished. Most important, 14 applications of ELID principle to modern abrasive processes are documented. The final summary and conclusions represent a handy tool for rapid information on ELID abrasion.

9.1.1 Principle and Mechanism of ELID Grinding

ELID grinding is a grinding process that employs metal-bond-abrasive wheels dressed in-process by the means of an electrolytic process. The procedure continuously exposes new sharp abrasive grains to maintain the material removal rate and continuously improve the surface roughness. A key issue in ELID is to sustain the balance between the removal rate of the bonding metal by electrolysis and the wear rate of diamond abrasive particles (Chen and Li I & II, 2000). Whereas the diamond wearing rate is directly related to grinding force, grinding conditions, and workpiece mechanical properties, the removal rate of the bonding metal depends on ELID conditions such as voltage and current, and the gap between electrodes.

ELID grinding was first proposed by the Japanese researcher Hitoshi Ohmori in 1990 (Ohmori and Nakagawa, 1990). Its most important feature is that no special machine is required. Power sources from conventional electrodischarge or electrochemical machines, as well as ordinary grinding machines can be used for this method. ELID grinding is based on electrochemical grinding (ECG). The grinding wheel is dressed during the electrolysis process, which takes place between the anodic workpiece and the cathodic copper electrode in the presence of the electrolytic fluid. The main

difference between ELID and ECG is that the purpose of ECG is to aid the grinding by removing material from the workpiece, whereas the purpose of ELID is to remove small amounts of material (few microns) from the bond of the wheel.

The chemistry of the process is presented in Figure 9.1, whereas the mechanism of the process is presented in Figure 9.2. The rate of bond metal dissolution is highest at the metal–diamond interface particles; in other words, the tendency of electrolytic dissolution is to expose the diamond particles (Chen and Li I, 2000). In addition, the metal dissolution rate increases with diamond concentration particles (Chen and Li I, 2000).

For a fixed gap and applied voltage, the current density does not change much with the diamond concentration particles (Chen and Li I, 2000). Hence, to maintain a constant rate of metal removal, the applied electric field should be lower for a higher diamond concentration tool and vice versa. This electric field concentration effect is greatly reduced when the diamond particle is half exposed (Chen and Li II, 2000). This effect sharply decreases from its highest value near the diamond–metal boundary to a

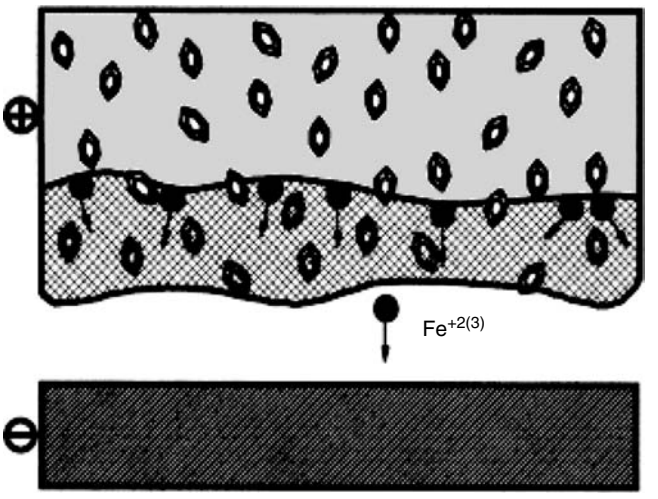

$$Fe - 2e \rightarrow Fe^{+2}$$
$$Fe - 3e \rightarrow Fe^{+3}$$
$$H_2O \rightarrow H^+ + OH^-$$
$$Fe^{+2} + 2OH^- \rightarrow Fe(OH)_2$$
$$Fe^{+3} + 3OH^- \rightarrow Fe(OH)_3\downarrow$$

FIGURE 9.1
Dressing mechanism of ELID grinding. (From Qian, J., Ohmori, H., and Li, W., *Int J Mach Tools Manuf*, 41, 193, 2001. With permission.)

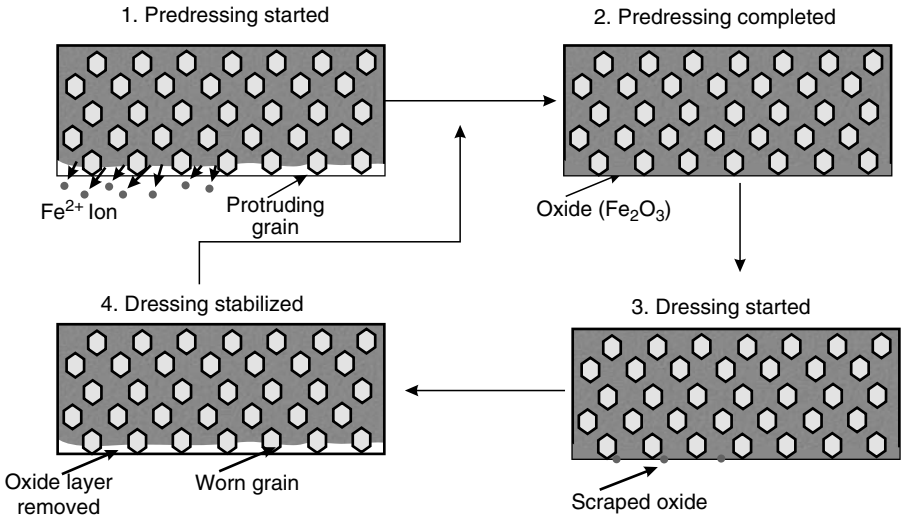

FIGURE 9.2
Mechanism of ELID. (From Stephenson, D.J., Veselovac, D., Manley, S., and Corbett, J., *J Int Soc Prec Eng Nanotechnol*, 25, 336, 2001. With permission.)

small value at a distance of the order of the diamond particle size (Chen and Li II, 2000).

In a conventional grinding operation, the tool face is smooth and has no protrusion of diamond particles after truing (Chen and Li II, 2000). Mechanical dressing opens up the tool face by abrasion with dressing stone, which makes the grits to be exposed in the leading side and supported in the trailing side. Laser and electrodischarge dressing opens up the tool face by thermal damage, producing craters, microcracks, and grooves.

This induces a degradation of the diamonds because the diamond graphitizing temperature is relatively low, about 700°C. In electrochemical dressing, grits are exposed by dissolving the surrounding metal bonds (Chen and Li II, 2000).

9.1.2 Components of ELID Grinding System

The ELID system's essential elements are a metal-bonded grinding wheel, a power source, and an electrolytic coolant.

The metal-bonded grinding wheel is connected to the positive terminal of the power supply with a smooth brush contact, whereas the fixed electrode is connected to the negative pole. The electrode is made from copper that has one-sixth of the wheel peripheral length and a width of 2 mm wider than the wheel rim thickness. The gap between the wheel and the active surface of the electrode is 0.1–0.3 mm and can be adjusted by mechanical

means. The stages of ELID grinding are presented in Figure 9.3; the precision truing of the micrograin wheel up to a runout of 2–4 μm (see Figure 9.4). This is achieved through an electrical discharge method and it is carried out to reduce the initial eccentricity below the average grain size of the wheel and improve wheel straightness, especially when a new wheel is first used or reinstalled.

1. The predressing process of the wheel by electrolytic means. The protrusion of the abrasive grains is sought. The procedure is performed at low speed and takes about 10–30 min.
2. The grinding process with continuous in-process dressing by electrolytic means.

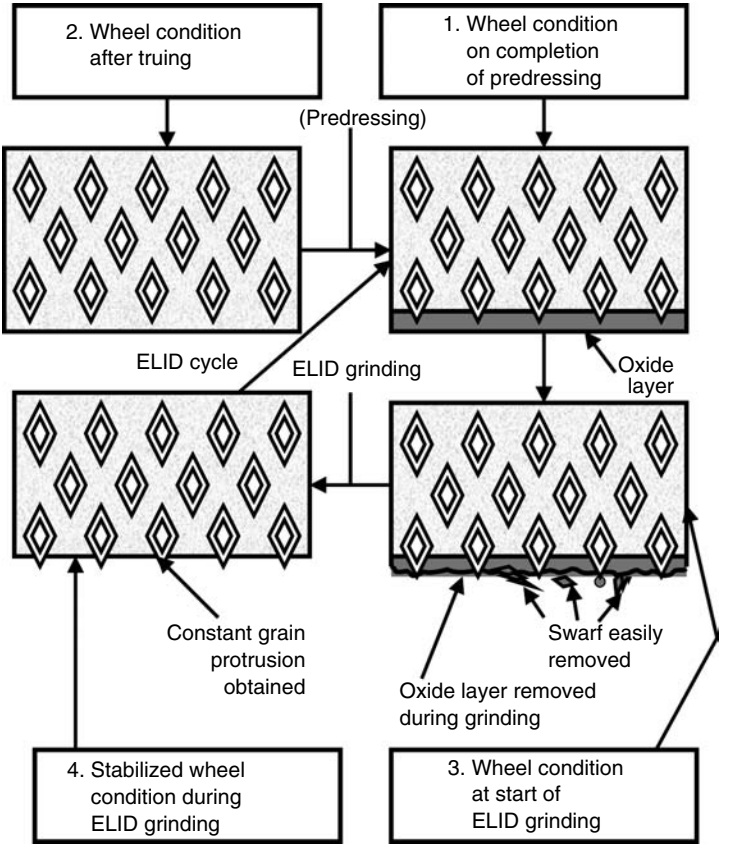

FIGURE 9.3
Stages of ELID grinding. (From Bandyopadhyay, B.P. and Ohmori, H., *Int J Mach Tools Manuf*, 39, 839, 1999. With permission.)

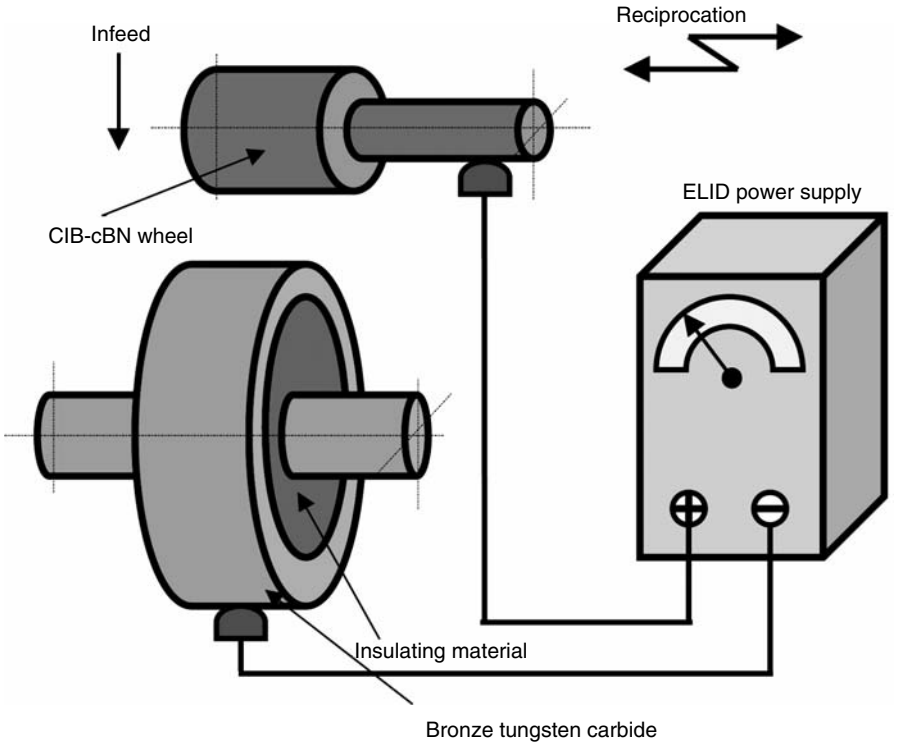

FIGURE 9.4
ELID truing mechanism. (From Qian, J., Ohmori, H., and Li, W., *Int J Mach Tools Manuf*, 41, 193, 2001. With permission.)

The conditions of electrolysis of the last two stages are different (as shown in Figure 9.5 and presented in next paragraph) because of the change in the wheel surface condition.

9.1.3 Electrical Aspects of ELID Grinding

The current characteristics (current value I and voltage E) are not constant during a complete ELID procedure. When the predressing stage starts, the active surface of the wheel has a high electrical conductivity; the current is high while the voltage between the wheel and the electrode is low (vertical line 1, in Figure 9.5). After several minutes, the bond material (cast iron) is removed by electrolysis and transformed into Fe^{2+}. The ionized Fe will form $Fe(OH)_2$ or $Fe(OH)_3$ according to the chemical transformations shown in Figure 9.1.

The hydroxides further change into oxides Fe_2O_3 through electrolysis. This insulating oxide layer (20 μm thick) will reduce the electroconductivity

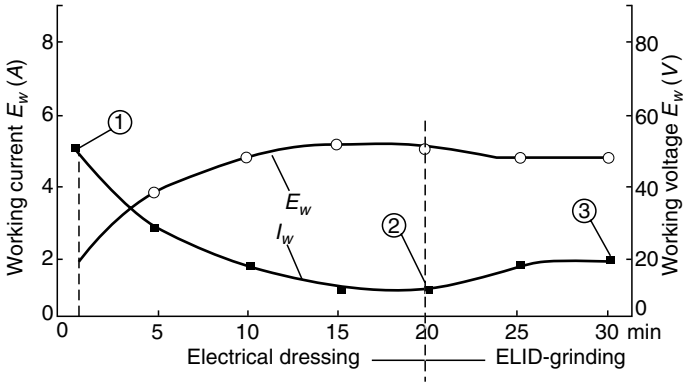

FIGURE 9.5
Current characteristics during ELID grinding. (From Ohmori, H., Takahashi, I., and Bandyopadhyay, B.P., *J Mat Proc Technol*, 57, 272, 1996. With permission.)

of the wheel surface. The current decreases while the voltage increases (vertical line 2, in Figure 9.5). Now, the grinding process can start with the protruding abrasive grains. As the grains are worn, the insulating oxides' layer is also worn. This increases the electroconductivity of the wheel so that the electrolysis intensifies, generating a fresh insulating layer (vertical line 3, in Figure 9.5). The protrusion of the grains remains constant.

The layer of oxide has a larger flexibility and a lower retention characteristic as compared to the bulk bond material (Zhang et al., 2001a). Figure 9.6 depicts the characteristics of the oxide film thickness and different types of grinding operations, rough or finish. For rough grinding, thin insulating layer is required, whereas for mirror-like finish ELID grinding, a relatively thick insulating layer is preferred.

An important aspect is the slight increase in the wheel diameter (or thickness) during ELID grinding (Zhang et al., 2001a) because of the etched and oxide layers' formation. The increase in the relative wheel diameter caused by insulator layer formation for different types of electrolytes is presented in Figure 9.7.

9.1.4 Characteristics of Grinding Wheel in ELID Applications

The wheels for ELID applications are as follows:

Cast-Iron-Bonded Diamond. These wheels are manufactured by mixing diamond abrasive, cast-iron powder or fibers, and a small amount of carbonyl iron powder. The compound is shaped in the desired form under a pressure of 6–8 t/cm^2, and then sintered in an atmosphere of ammonia. These wheels are not suited for continuous grinding for long

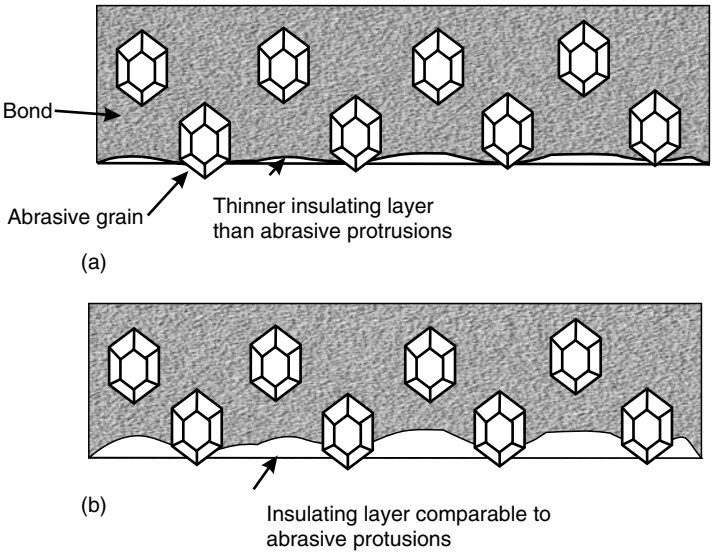

FIGURE 9.6
Ideal wheel conditions for: (a) efficient grinding; (b) mirror-surface finish. (From Bandyopadhyay, B.P., Ohmori, H., and Takahashi, I., *J Mat Proc Technol*, 66, 18, 1997. With permission.)

periods of time because (1) a tougher metal-bonded wheel has poor dressing ability—both efficient and stable grinding cannot be achieved; (2) high material removal rate frequently wears the abrasive imposing frequent redressing procedures; (3) the wheels become embedded with swarf during grinding of steels.

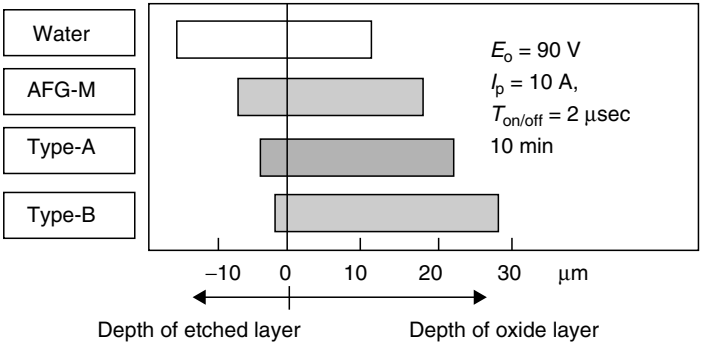

FIGURE 9.7
The depth of etched and oxide layers with different coolants. (From Zhang, C., Ohmori, H., Kato, T., and Morita, N., *Prec Eng J Int Soc Prec Eng Nanotechnol*, 25, 56, 2001a. With permission.)

Cast-Iron Fiber-Bonded Diamond (CIFB-D). These wheels provide high grinding ratio and high material removal rates.

Cubic Boron Nitride (cBN). ELID grinding provides dressing of tough metal-bonded wheels during grinding process. This in-process dressing procedure will control the abrasive protrusions before and during the grinding of ceramics.

9.1.5 Structure and Properties of Ceramics

Today, the U.S. structural ceramics market is estimated at over $3500 million as compared with $20 million in the year 1974, $350 million in 1990, and $865 million in 1995. The application of these materials can be found in tool manufacturing, automotive, aerospace, electrical, electronics industries, communications (fiber optics), medicine, and so on (http://www.acers.org/news/factsheets.asp).

The properties of ceramic materials, like all materials, are dictated by the types of atoms present, the types of bonding between the atoms, and the way the atoms are packed together (also known as the atomic scale structure). Most ceramics are compounded of two or more elements. The atoms in ceramic materials are held together by a chemical bond. The two most common chemical bonds for ceramic materials are covalent and ionic, which are much stronger than in metallic chemical bond. That is why, in general, metals are ductile, and ceramics are brittle.

The atomic structure primarily affects the chemical, physical, thermal, electrical, magnetic, and optical properties. The microstructure can also affect these properties but has its major effect on mechanical properties and on the rate of chemical reaction. For ceramics, the microstructure can be entirely glassy (glasses only), entirely crystalline, or a combination of crystalline and glassy. In the last case, the glassy phase usually surrounds small crystals, bonding them together.

The most important characteristics of ceramic materials are high hardness, resistance to high compressive force, resistance to high temperature, brittleness, chemical inertness, electrical insulator properties, superior electrical properties, high magnetic permeability, special optic and conductive properties, and so forth.

9.1.6 ELID Grinding Applied to Various Materials (Grobsky and Johnson, 1998)

During the last 10 years, a number of publications have addressed the merits of ELID when applied to bound abrasive grinding on brittle materials such as BK-7 glass, silicon, and fused silica using fine mesh superabrasive wheels. Many of these publications report that ELID grinding provides the

ability to produce spectacular finishes on these brittle material surfaces, with surface roughness on the nanometer scale (4–6 nm).

For some applications, this completely eliminates the need for loose abrasive lapping or polishing. The application of ELID grinding to the fabrication of large (150–250 mm in diameter) optical components is also studied. Published data suggest that ELID grinding can be successfully applied to substrates of this size regime.

9.1.7 ELID Grinding Applied to Ceramic Materials

Interest in advanced structural ceramics has increased significantly in recent years because of their unique physical characteristics and significant improvements in their mechanical properties and reliability.

Despite these advantages, the use of structural ceramics in various applications has not increased rapidly in part because of the high machining cost of these materials. The cost of grinding may account for up to 75% of the component cost for ceramics compared to 5%–15% for metallic components (Ohmori et al., 1996).

The primary cost drivers in the grinding of ceramics are (1) low efficiency resulting from the low removal rate; (2) high superabrasive wheel wear rate; (3) long wheel dressing times (Ohmori et al., 1996).

The grinding process often results in surface fracture damage nullifying the benefits of advanced ceramic processing methods (Bandyopadhyay and Ohmori, 1999). These defects can significantly reduce the strength and reliability of the finished component and are sensitive to grinding parameters.

Stock removal rate increases with the increase in the number of passes, higher stock removal rates obtained for stiffer machine tool (Zhang et al., 2000a, b). For similar bond type grinding wheels, a larger stock removal rate was obtained for larger grit sizes of the wheels (Zhang et al., 2000). Cast-iron-bonded wheel has a larger stock removal rate, yet a lower grinding force as compared with a vitrified bonded grinding wheel (Zhang et al., 2000). Machine stiffness has little effect on residual strength of grounded silicon under multipass grinding conditions; this can be attributed to the effect of actual depth of cut of the wheel on workpiece strength (Zhang et al., 2000). As the number of passes increases, the actual depth of cut approaches the set depth of cut, which means that regardless of the machine tool stiffness, the grinding force does not significantly alter the workpiece strength (Zhang et al., 2000). In addition, more compressive residual stress can be induced with a dull grinding wheel or with a grinding wheel of a higher grit size, or with a wheel of stiff and strong bond material (Zhang et al., 2000).

It was proved that a grinding wheel with a larger grit size presents a larger damage depth to the grounded piece (Zhang et al., 2000). As the

number of passes increases, the normal grinding force also increases (Zhang et al., 2000). This increase in force is steeper in the beginning passes and slows down as the number of passes increases, a phenomenon more evident for a high stiffness machine tool (Zhang et al., 2000). Because of machine tool deflection, the normal grinding force was smaller under lower machine stiffness (Zhang et al., 2000). In addition, the normal force approaches a limit value, regardless of the machine stiffness characteristics (Zhang et al., 2000).

Therefore, ELID may not be beneficial to workpiece strength, although it may be good for workpiece accuracy (Zhang et al., 2000). An interesting aspect, yet controversial and not much studied, addresses the pulverization phenomenon, which takes place in the surface layer of a ceramic workpiece during grinding (Zhang and Howes, 1994). Surface pulverization makes ceramic grains much smaller than those in the bulk, and makes the ground surface look smoother.

9.2 Material Removal Mechanisms in Grinding of Ceramics and Glasses

Generally, there are two approaches to investigate the mechanisms of abrasive–workpiece interactions during the grinding of ceramics (Bandyopadhyay et al., 1999):

1. *Indentation–fracture mechanics approach*, which models abrasive–workpiece interactions by the idealized flaw system and deformation produced by an indenter.
2. *The machining approach* involves measurement of forces coupled with scanning electron microscope (SEM) and atomic force microscope (AFM) observation of surface topography and grinding debris.

The mechanism of material removal in ceramic machining is a combination of microbrittle fracture and micro or quasiplastic cutting. The quasiplastic cutting mechanism, typically referred to as ductile-mode grinding (presented in Figure 9.8), results in grooves on the surface that are relatively smooth in appearance. By careful choice of grinding parameters and control of the process, ceramics can be ground predominantly in this model. On the other hand, the microbrittle fracture mechanism (shown in Figure 9.9) results in surface fracture and surface fragmentation. Ductile regime grinding of ceramics is preferred as no grinding flaws are introduced when the machining is performed in this mode.

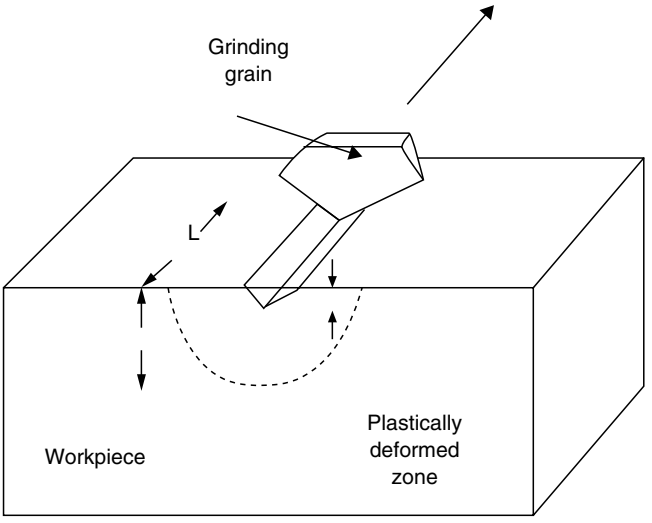

FIGURE 9.8
A close-up view of the schematic of an abrasive grain removing material from a brittle workpiece via ductile-regime grinding. (From Bandyopadhyay, B.P. and Ohmori, H., *Int J Mach Tools Manuf*, 39, 839, 1999. With permission)

As shown in Figure 9.8 and Figure 9.9, directly under the grit, a plastically deformed zone can be noticed. Two principal crack systems are generated in the process. These are median/radial cracks and lateral cracks. The brittle mode removal of material is because of the formation and propagation of these lateral cracks.

The specific depth at which a brittle–ductile transition occurs is a function of the intrinsic material properties, such as plasticity and fracture, and is given by (Bandyopadhyay and Ohmori, 1999):

$$\frac{\text{Platic flow energy}}{\text{Fracture energy}} \approx \frac{E_{\text{p}}}{E_{\text{f}}} \approx d \tag{9.1}$$

where d is the critical depth of cut.

Although it is not easy to observe these microcracks produced by grinding, the depth of the median crack can be determined using the formula (Inaski, 1988):

$$I_{\text{mc}} = [0.034(\text{cotan}\,\psi)^{2/3}\{(E/H)^{1/2}/Kc\}]^{2/3}F^{2/3} \tag{9.2}$$

where ψ is the indenter angle and F is the indentation load, E is the modulus of elasticity, and Kc is the fracture toughness of the material. Therefore, the

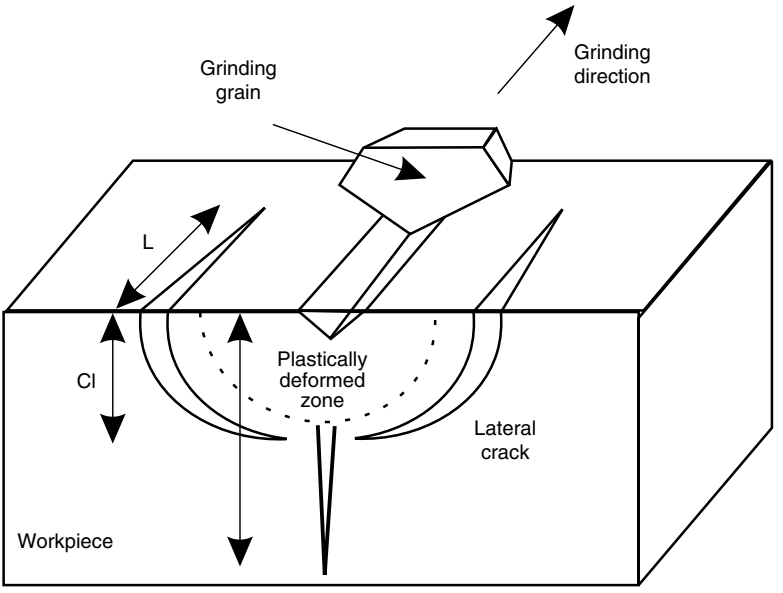

FIGURE 9.9
Schematic of an abrasive grain removing material from a brittle workpiece via brittle-regime grinding. (From Bandyopadhyay, B.P. and Ohmori, H., *Int J Mach Tools Manuf*, 39, 839, 1999. With permission.)

depth of the median crack depends on the material properties, force, and grinding grit shape. Indentation load (F) is determined by dividing the grinding force with the number of active cutting edges on the contact area between the grinding wheel and the workpiece.

This relationship would apply only above a threshold load of F^*. The critical load F^* that will initiate crack can be determined by

$$F^* = \frac{\alpha \mathrm{Kc}^4}{H^3} \tag{9.3}$$

where α is the coefficient that depends on the indenter geometry.

In conclusion, crack size can be estimated theoretically by Equation 9.2 when the load exceeds a certain critical value, which can be determined by Equation 9.3. The important parameters for the critical loads to propagate subsurface damage are presented in Table 9.1 (Bandyopadhyay et al., 1999). In achieving the plastic deformation process, the grain load for SiC and Si_3N_4 should be less than 0.2 N and 0.7 N, respectively. SEM and AFM techniques permit to evaluate the surface and subsurface fracture damage.

TABLE 9.1

Critical Loads Required to Propagate Subsurface Damage

Materials	H [GPa]	E [GPa]	K_c [MN/m$^{3/2}$]	F* [N]
SiC	24.5	392	3.4	0.2
Si_3N_4	14	294	3.1	0.73

Source: From Bandyopadhyay, B.P., Ohmori, H., and Takahashi, I., *Journal of Materials Processing Technology*, Vol. 66, 1997, pp. 18–24.

The micrographs look like in Figure 9.10 and Figure 9.11. From SEM and AFM micrographs, one can assess the difference between the material removal mechanism of brittle fracture and the ductile mode.

9.3 ELID Technique as Compared to Other Grinding Techniques

9.3.1 Summary of ELID Technology

The ELID technology can provide in-process dressing of tough metal-bonded superabrasive grinding wheels. With the application of this technology, the metal-bonded wheels will be electrolytically dressed during the grinding process. This in-process dressing will control the abrasive protrusion before and during the grinding process. Significant reduction of grinding force has been reported with the application of ELID. The specimens were ground both in longitudinal and transverse directions. The basic construction of the ELID grinding system for surface grinding is shown in Figure 9.12.

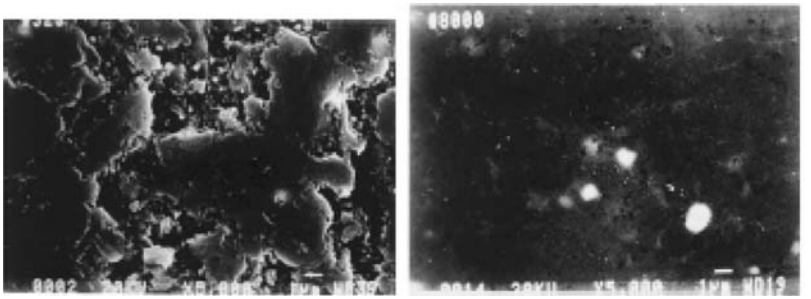

FIGURE 9.10
SEM micrographs: (a) #325; (b) #8000. (From Bandyopadhyay, B.P. and Ohmori, H., *Int J Mach Tools Manuf*, 39, 839, 1999. With permission.)

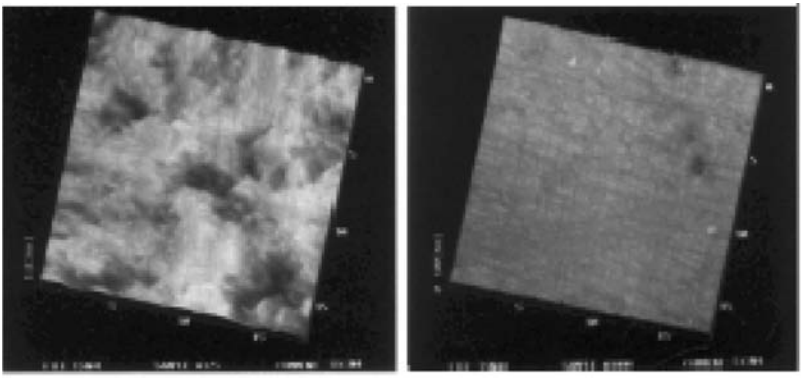

FIGURE 9.11
AFM micrographs: (a) #325; (b) #8000. (From Bandyopadhyay, B.P. and Ohmori, H., *Int J Mach Tools Manuf*, 39, 839, 1999. With permission.)

The ELID essential elements include a metal-bonded grinding wheel, electrolytic power source, and electrolytic coolant. The most important feature is that no special machine is required. The metal-bonded wheel is connected to the positive terminal of a power supply with a smooth brush contact, and a fixed electrode is made negative. The grinding wheel is dressed because of the electrolysis phenomenon that occurs upon the supply of a suitable grinding fluid and an electric current.

In ELID process, protruding grains abrade the workpiece. As a result, the grains and the oxide layer wear down. The wear of the oxide layer increases the wheel's electroconductivity. The current in the circuit will increase,

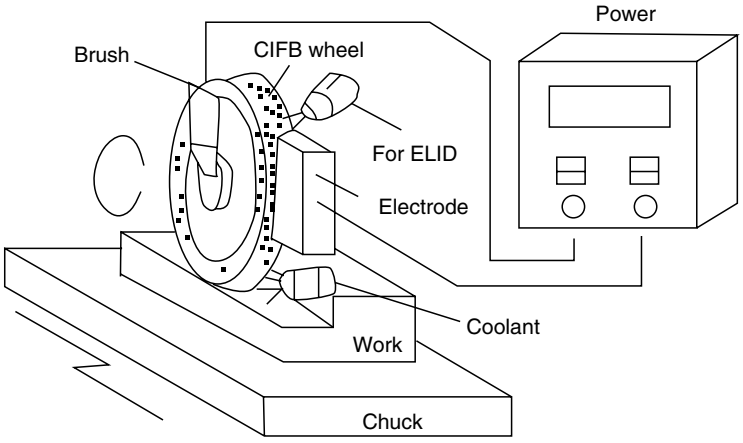

FIGURE 9.12
Construction of ELID grinding system. (From Qian, J., Li, W., and Ohmori, H., *Prec Eng*, 24, 153, 2000a; Qian, J., Li, W., and Ohmori, H., *J Mat Proc Technol*, 105, 80, 2000b. With permission.)

increasing the electrolysis as a result. Therefore, abrasive grains protrude and the oxide layer is recovered. The electrical behavior is nonlinear because of the formation of this insulating oxide layer.

9.3.2 Other In-Process Dressing Technologies

The concept of in-process dressing was promoted in its crude form by Nakagawa (Nakagawa and Suzuki, 1986). The effects of in-process dressing using a dressing stick were studied. The wheel is dressed at the beginning of each stroke. Higher material removal rates were reported. An application of this procedure to side grinding is difficult.

The concept of ECG was introduced by McGeough (1974). The electrolytically conductive metal-bonded wheel is the anode and a fixed graphite stick is the cathode. The dressing process is an electrolytic phenomenon. Wlech et al. (1993) employed this principle but they used sodium chloride solution as the electrolyte, which is harmful for machine tools.

Another technique is based on electrical discharge phenomenon. The electroconductive grinding wheel is energized with a small pulse current. The flow of ions creates hydrogen bubbles in the coolant, creating an increasing electric potential that, when becomes critical, generates a spark that melts the material that clogs the wheel. This procedure does not provide protruding abrasive grains continuously, and is unsuitable for ultrafine grinding of materials, especially with a micrograined-size grinding wheel.

Other nonconventional machining processes based on electrochemical metal removal are electrochemical machining, ECG, electrochemical polishing, and so on.

9.4 Applications of ELID Technique

ELID grinding was employed to process several types of materials like ceramics, hard steels, ceramic glass, ceramic coatings, and so forth, with various shapes (plane, cylindrical external and internal, spherical and aspherical lenses, etc.) and dimensions. Various ELID applications and their reference literature are listed here:

- ELID-side grinding (Zhang et al., 2000, 2001a); ELID double-side grinding (Ohmori et al., 1996)
- ELID-lap grinding (Itoh and Ohmori, 1996; Itoh et al., 1998)
- ELID grinding of ceramics on vertical rotary surface grinder (Ohmori et al., 1996)
- ELID grinding of ceramics on vertical grinding center (Bandyopadhyay et al., 1997)

- ELID grinding of bearing steels (Qian et al., 2000b)
- ELID grinding of ceramic coatings (Zhang et al., 2001a)
- ELID ultraprecision grinding of aspheric mirror (Moriyasu et al., 2000)
- ELID grinding of microspherical lenses (Ohmori et al., 2001)
- ELID grinding of large optical glass substrates (Grobsky and Johnson, 1998)
- ELID precision internal grinding (Qian et al., 2000, 2001)
- ELID grinding of hard steels (Stephenson et al., 2001)
- ELID mirror-like grinding of carbon fiber reinforced plastics (CFRP) (Park et al., 1995)
- ELID grinding of chemical vapor deposited silicon carbide (CVD-SiC) (Zhang et al., 2001a)

9.4.1 ELID-Side Grinding (Zhang et al., 2000, 2001a)

ELID-side grinding setup is presented in Figure 9.13. ELID grinding was compared with a conventional grinding operation applied to same workpieces in similar conditions. The oxide layer obtained during ELID grinding changed the contact status between wheel and workpiece; practically, it was a new bond wheel with a large-flexibility and contractile-ability bonded

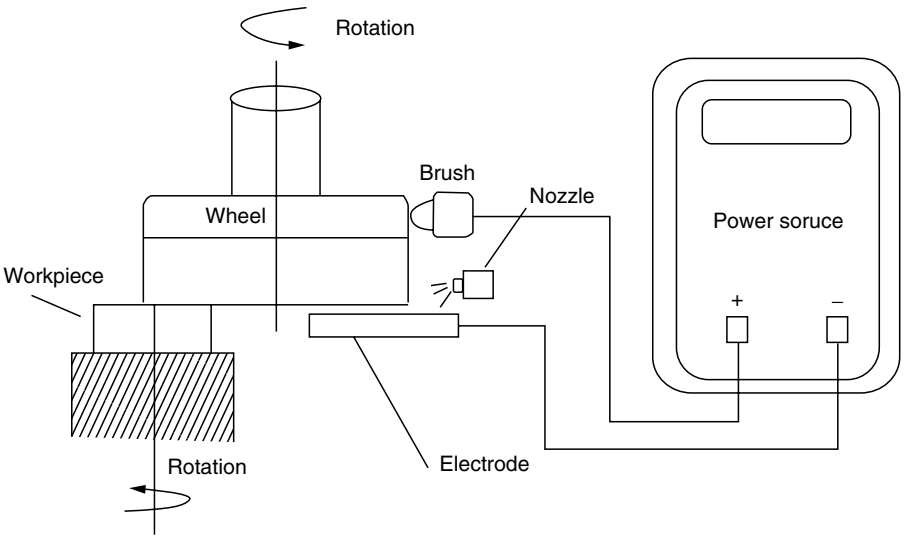

FIGURE 9.13
Principle of ELID face grinding. (From Zhang, C., Kato, T., Li, W., and Ohmori, H., *Int J Mach Tools Manuf*, 40, 527, 2000b. With permission.)

wheel in place of the hard and high-retentive cast-iron bond. The conclusions of the study were as follows:

- ELID double-side grinding can be employed to produce mirror-like surface finish.
- Surface finish of the workpiece ground with ELID was better than that of the workpiece ground conventionally.
- The material removal mechanism for ELID double-side grinding was brittle-fracture mode for coarser wheels and ductile mode for finer wheels.
- The material removal rate for ELID double-side grinding was slightly higher as compared to conventional grinding.
- ELID grinding is highly recommended in precision grinding of hard-brittle materials on conventional machine tools.

9.4.2 ELID Double-Side Grinding (Ohmori et al., 1996)

ELID double-side grinding setup is presented in Figure 9.14. A close-up view of the same is given in Figure 9.15. The conclusions of the study were presented in the following list:

- ELID grinding can be employed to produce mirror-like surface finish.
- Surface finish of the workpiece ground with ELID was slightly better than that of the workpiece ground conventionally.
- Microscopic characteristics showed that the surface of the workpiece ELID ground has fewer pits and sticking-outs, ductile-mode removal was the main removal mechanism.

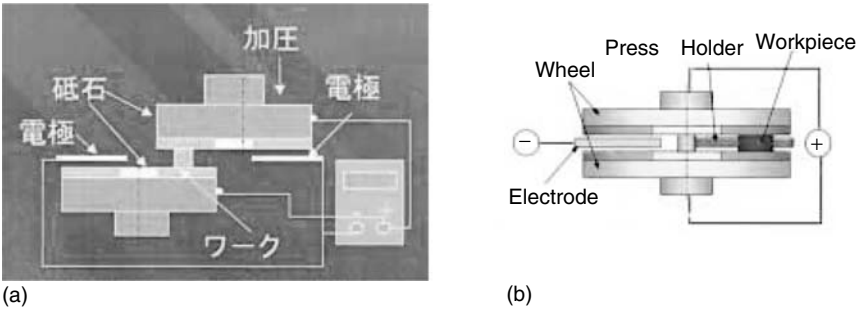

FIGURE 9.14
Setup for ELID double-side grinding: (a) eccentric wheels; (b) concentric wheels. (From Ohmori, H., Takahashi, I., and Bandyopadhyay, B.P., *J Mat Proc Technol*, 57, 272, 1996. With permission.)

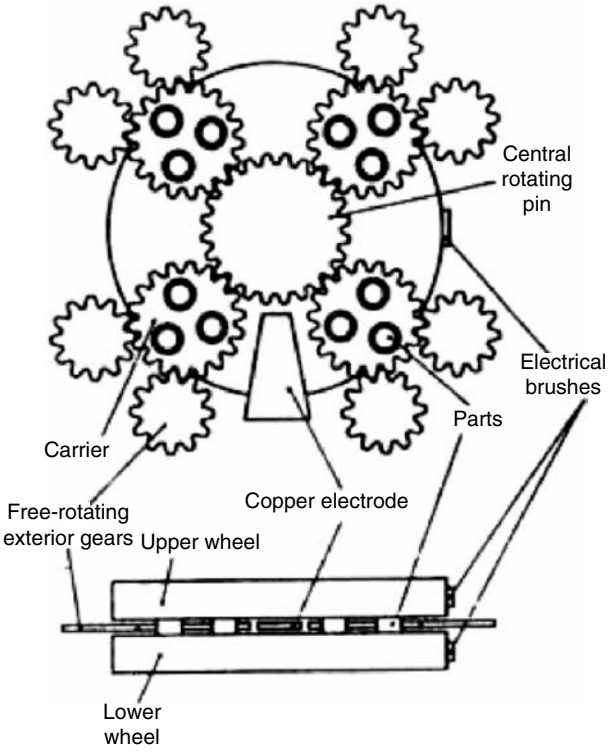

FIGURE 9.15
ELID double-side grinding schematics and close-up view.

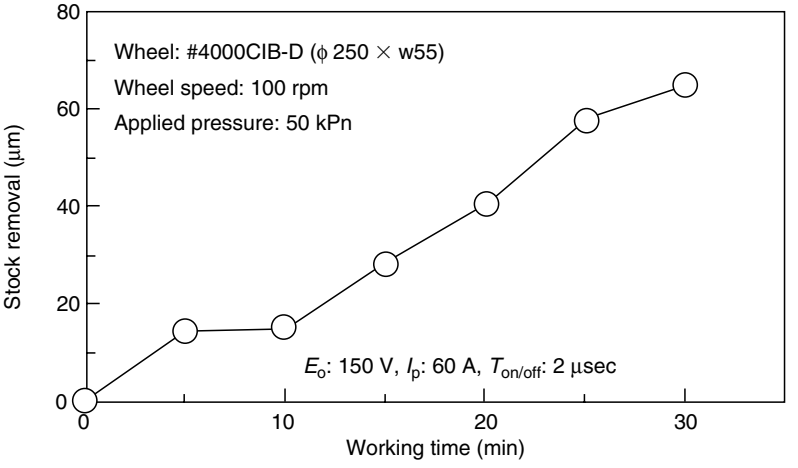

FIGURE 9.16
Stock removal vs. ELID grinding.

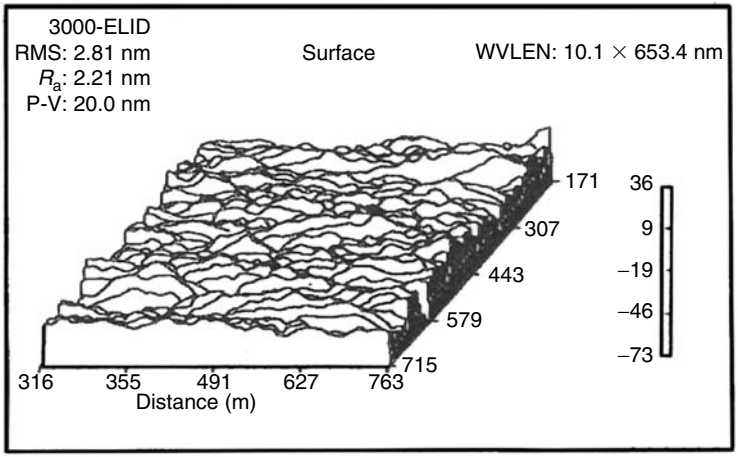

(a)

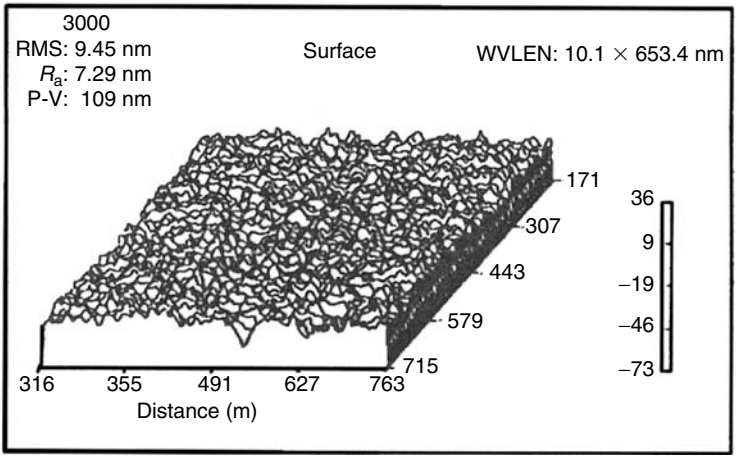

(b)

FIGURE 9.17
Surface aspect of ground workpiece: (a) with ELID; (b) without ELID.

– ELID grinding is highly recommended in precision grinding of hard-brittle materials on conventional machine tools with low rigidity.

9.4.3 ELID-Lap Grinding (Itoh and Ohmori, 1996; Itoh et al., 1998)

ELID-lap grinding is a machining process that employs constant pressure and uses metal-bonded abrasive wheel with ELID. It produces better results for both surface roughness and flatness as compared to other grinding

system. In this research, conventional lap-grinding and ELID-lap grinding operations were compared. This method is applied for the following purposes:

- Grinding materials for which mirror-like finish cannot be obtained through constant feed grinding
- Grinding with metal-bonded wheels finer than JIS #10,000
- By employing a simple setup to be mounted on an existing lapping machine

The principle is presented in Figure 9.18:

The workpiece (made out of silicon and tungsten carbide) is pressed against the lapping wheel. The lapping wheel is connected to positive pole, by means of a fine brush that smoothly touches the wheel surface, while the electrode is connected to the negative pole. The gap between electrodes is of 0.3 mm. The conclusions were listed as follows:

ELID-lap grinding of silicon with JIS #4000 wheel outputs a mirror-like finish at roughness of 3.8 nm, as compared with 7.4 nm roughness outputted by a conventional lap-grinding.

ELID-lap grinding of tungsten with JIS #4000 wheel is more stable than conventional lap-grinding from the viewpoint of the stability of the removal rate value (for an 80 min period).

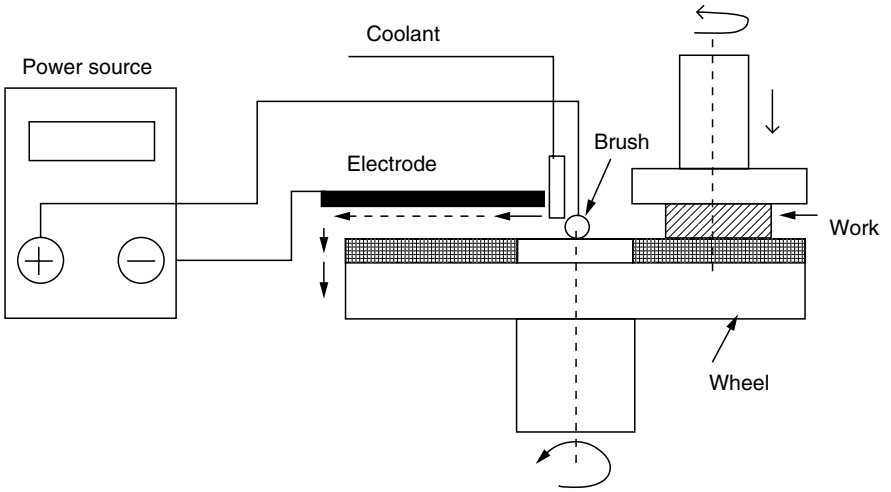

FIGURE 9.18
Principle of ELID-lap grinding. (From Itoh, N., Ohmori, H., Moryiasu, S., Kasai, T., Karaky-Doy, T., and Bandyopadhyay, B.P., *Int J Mach Tools Manuf,* 38, 747, 1998. With permission.)

ELID-lap grinding of silicon was achieved in a brittle-fracture mode for JIS #1200 and down and in a ductile mode for JIS #4000 and up.

When silicon was ground together with tungsten carbide, the surface roughness improved when compared with grinding the silicon alone; brittle-to-ductile transition was observed for JIS #4000 mesh size wheel. In a later study (Itoh et al., 1998), silicon and glass (BK7) were ELID lapped with metal resin diamond-bonded wheels of grit sizes of JIS #8000, JIS #120,000, and JIS #3,000,000.

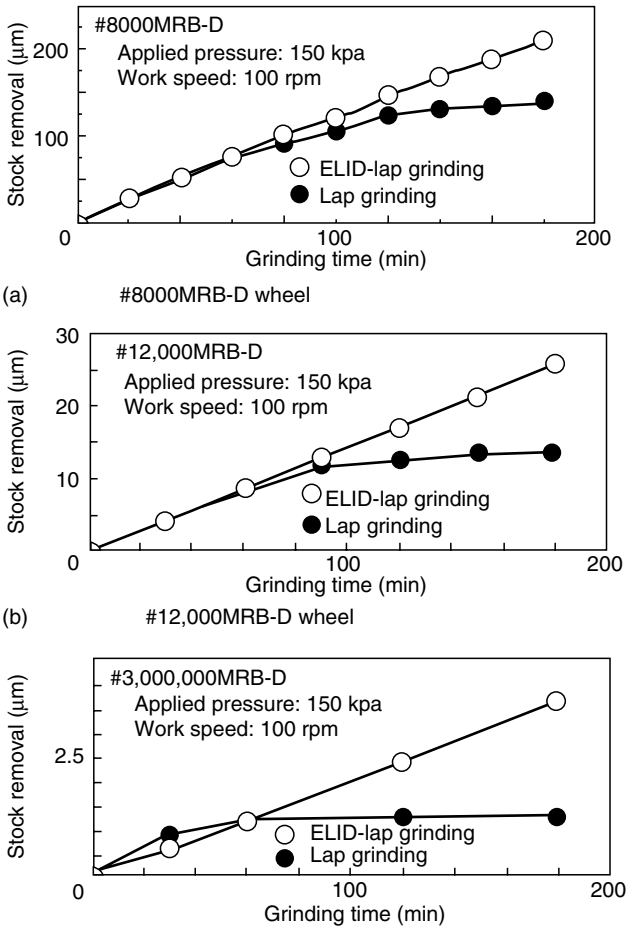

FIGURE 9.19

Grinding efficiency vs. time. (From Itoh, N. and Ohmori, H., *J Mat Proc Technol*, 62, 315, 1996; Itoh, N., Ohmori, H., Moryiasu, S., Kasai, T., Karaky-Doy, T., and Bandyopadhyay, B.P., *Int J Mach Tools Manuf*, 38, 747, 1998. With permission.)

Material removal rate results are presented in Figure 9.19. ELID-lap grinding using the JIS #3,000,000 metal resin bond wheel produced very good ground surfaces of PV 2.8 nm for silicon and PV 2.5 nm for glass.

9.4.4 ELID Grinding of Ceramics on Vertical Rotary Surface Grinder (Ohmori et al., 1996)

The experiments were conducted on a vertical rotary surface grinder with a 5.5 kW motor spindle. The feed can be continuously adjusted within a range. The workpieces were made from intered sintered reaction-bonded silicon nitride (SRBSN) and cast-and-sintered silicon nitride (Si_3N_4). The grain size was between 0.3 and 0.4 μm for SRBSN and between 0.6 and 0.8 μm for Si_3N_4. Cast-iron fiber-bonded diamond wheels of 200 mm diameter were used. A Noritake AFG-M grinding fluid at a rate of 20–30 L/min was used as electrolytic fluid.

The grain size of diamond grinding wheel has the characteristics presented in Table 9.2.

The most significant conclusions of this study are listed below:

- Mirror-like surface finish was obtained after grinding with #4000 mesh size wheel (see Figure 9.16 and Figure 9.17).
- The cutting speed has no significant effect on the surface finish of the workpiece.
- Feed rate has no significant effect on the surface finish, especially for mesh size wheels finer than JIS #325.
- Better surface finish characterizes SRBSN when compared with Si_3N_4, especially with rougher wheels.
- Similar surface finish characterizes SRBSN and Si_3N_4 when finer wheels were used.

TABLE 9.2

Characteristics of Diamond Grinding Wheel

Mesh Size	Grain size (μm)	Average grain size (μm)
170	88–84	110
325	40–90	63.0
600	20–30	25.5
1200	8–16	11.6
2000	5–10	6.88
4000	2–6	4.06
6000	1.5–4	3.15
8000	0.5–3	1.76

Source: From Itoh, N. and Ohmori, H., *Journal of Materials Processing Technology*, Vol. 62, 1996, pp. 315–320.

9.4.5 ELID Grinding of Ceramics on Vertical Grinding Center (Bandyopadhyay et al., 1997)

The experiments were carried out on a vertical machining center. The silicon nitride workpieces were clamped to a vice firmly fixed onto the base of a strain gauge dynamometer. The dynamometer was clamped onto the machining center table and the reciprocating grinding operation was performed.

A direct-current pulse generator was used as a power supply. The square-wave voltage was of 60–90 V with a peak current of 16–24 A. The pulse width was adjusted to 4 μsec on-time and off-time. Different values for the depth of cut and for the width of cut were explored. Material removal rates of 250 mm^3/min up to 8000 mm^3/min were obtained. A comparison between the results obtained after an ordinary grinding operation and the results obtained after an ELID grinding operation was carried out. A modified ELID dressing procedure was also studied. The modified ELID dressing was performed in two stages: (a) at 90 V for 30 min; the insulating oxide layer was mechanically removed by an aluminum oxide stick of #400 grit size at 300 rpm; (b) another dressing stage at 90 V for 30 min. (Figure 9.20, Figure 9.21, Figure 9.22, and Figure 9.23) The conclusions of the study were as follows (see also Figure 9.24):

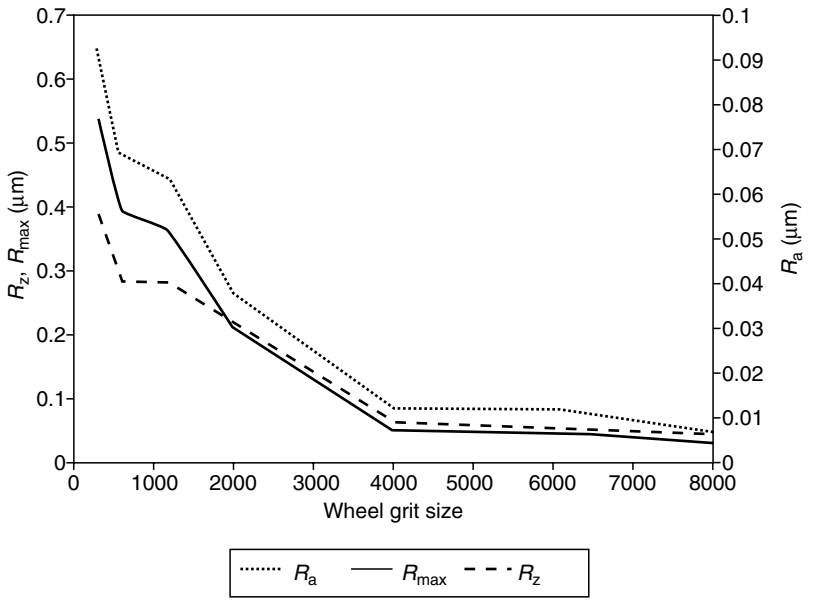

FIGURE 9.20
Effect of grit size on surface-roughness patterns.

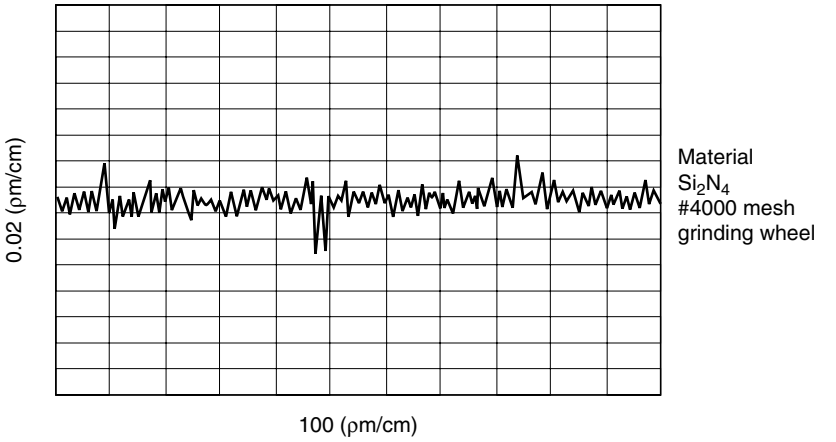

FIGURE 9.21
Typical surface-roughness patterns for #4000 mesh size wheel.

- ELID grinding can achieve high material removal rates.
- ELID grinding is recommended for low-rigidity machine tools and low-rigidity workpieces.
- The grinding force increases continuously during ordinary grinding.

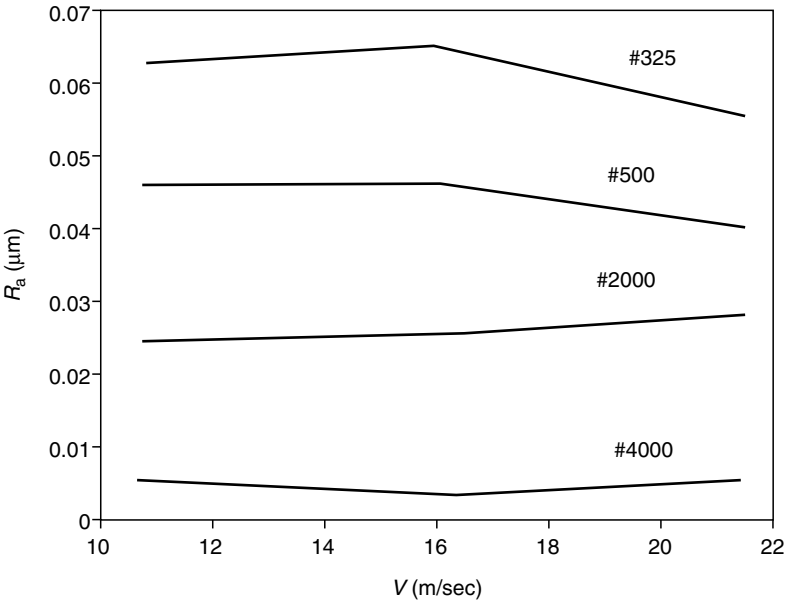

FIGURE 9.22
Effect of cutting speed on surface roughness. (From Ohmori, H., Takahashi, I., and Bandyopadhyay, B.P., *J Mat Proc Technol*, 57, 272, 1996. With permission.)

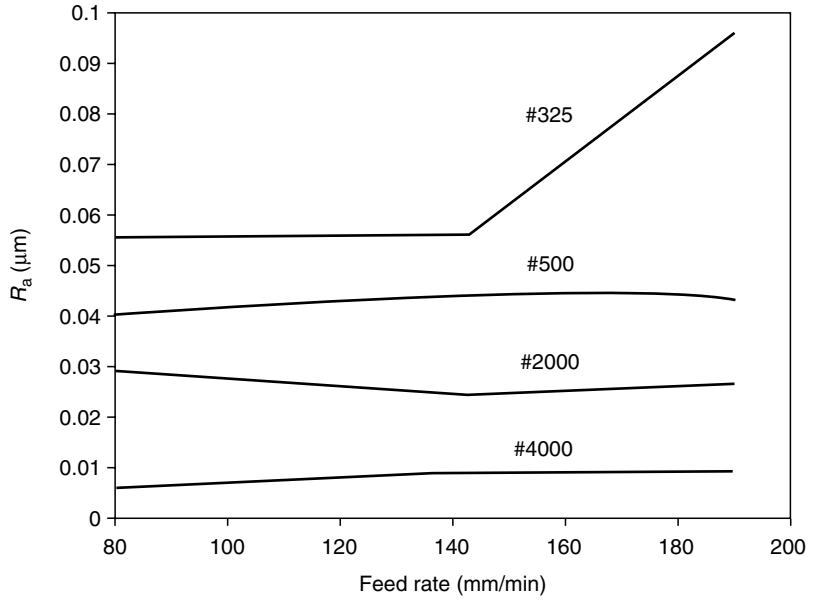

FIGURE 9.23
Effect of feed rate on surface roughness. (From Ohmori, H., Takahashi, I., and Bandyopadhyay, B.P., *J Mat Proc Technol*, 57, 272, 1996. With permission.)

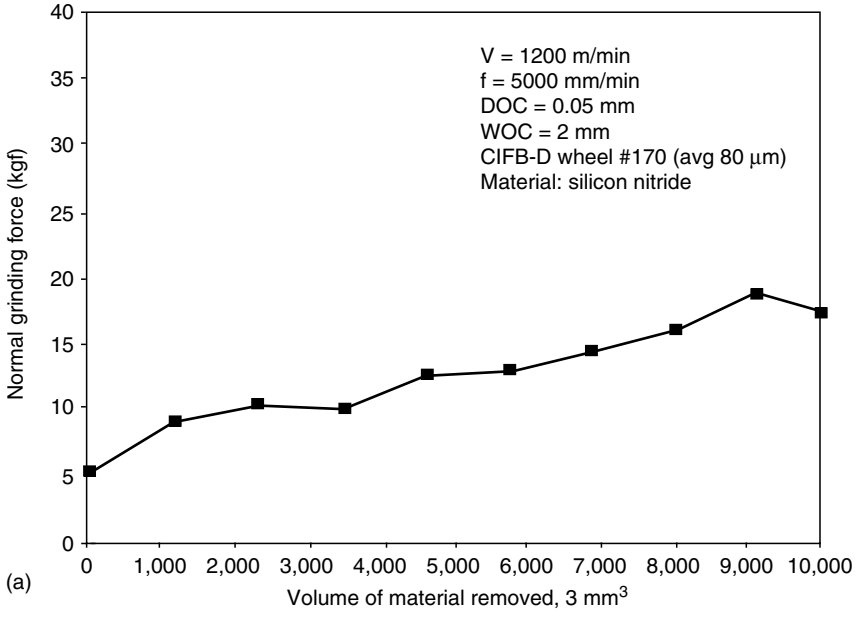

FIGURE 9.24
Relationship between the volume of material removed and the grinding force for: (a) conventional grinding (From Bandyopadhyay, B.P., Ohmori, H., and Takahashi, I., *J Mat Proc Technol*, 66, 18, 1997. With permission.)

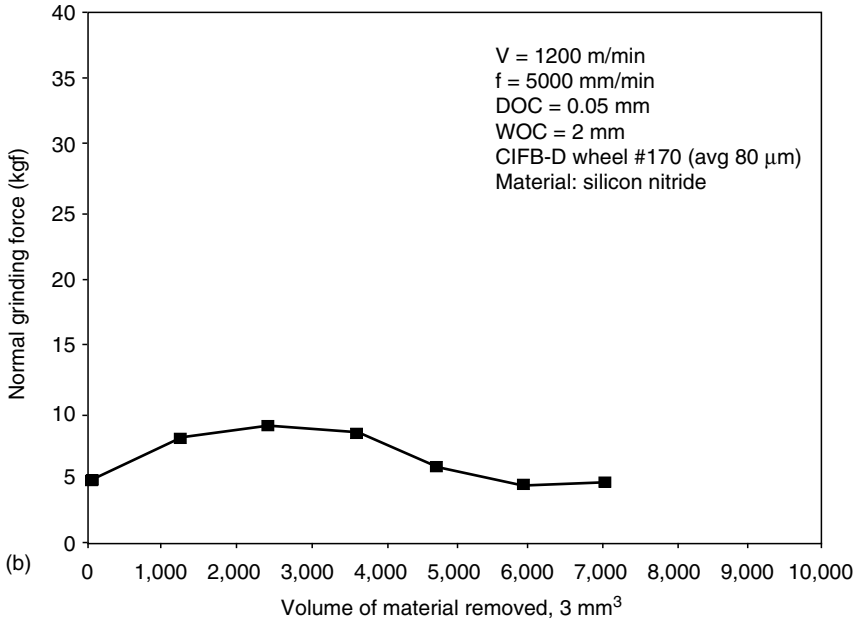

(b)

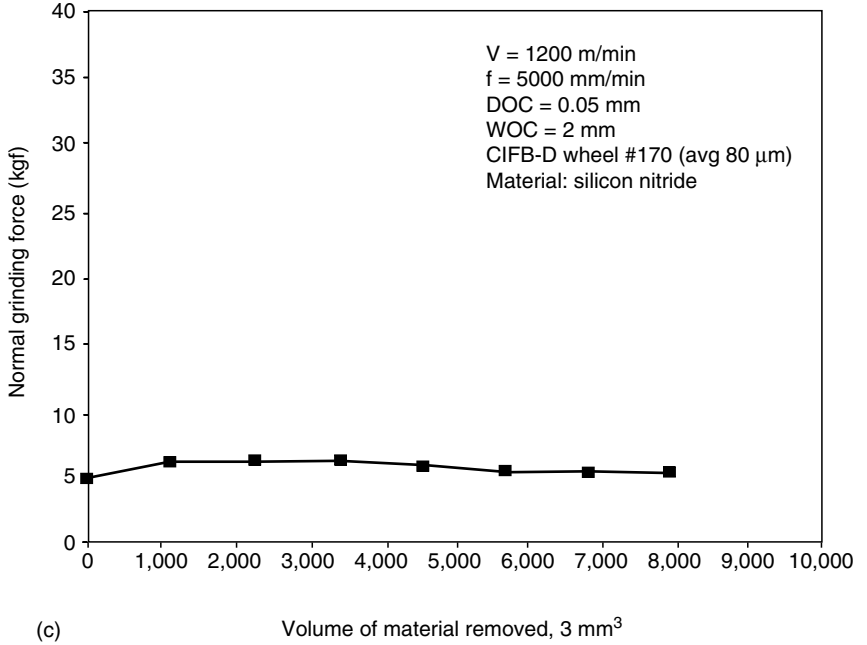

(c)

FIGURE 9.24 (continued)
(b) ELID grinding after ELID dressing; (c) ELID grinding after modified ELID dressing.

- Grinding force is lesser during ELID grinding when compared with conventional grinding; this effect became more visible after 18 min of grinding.
- An increase in the voltage value during ELID grinding will reduce the value of the grinding force even more; this effect became more visible after 18 min of grinding.
- Full potential of ELID grinding can be achieved only after 24 min of grinding when the grinding force stabilizes at a low value.
- ELID and conventional grinding produced almost the same surface finish in rough grinding.
- The grinding force was constant and low after the modified ELID dressing procedure was applied to the wheel.

9.4.6 ELID Grinding of Bearing Steels (Qian et al., 2000)

In this research, ELID as a superfinishing technique for steel bearing components was studied. The experiments were conducted in both traverse and plunge in feed modes. The wheels utilized were cast-iron-bonded using CBN as abrasive. The experiments were carried out on a common cylindrical grinder with a 3.7 kW motor spindle. The negative electrode was made out of stainless steel. A Noritake AFG-M grinding fluid diluted to 1:50 at a rate of 20–30 L/min was used as electrolytic fluid. A direct-current pulse generator was used as a power supply. The square-wave voltage was of 60–150 V with a peak current of 100 A. The pulse width was adjusted to 4 μsec on-time and off-time. Three types of experiments were conducted:

1. Traverse and plunge ELID grinding for evaluating the effects of the grinding wheel mesh size and grinding method on surface roughness and waviness value.
2. Traverse grinding with different mesh size wheels to assess the influence of the mesh size of the wheel over the surface finish and material removal rate.
3. ELID grinding with #4000 mesh size wheel was compared with honing and electric finish methods.

The conclusions were as follows:

- ELID grinding as compared to conventional grinding offered a better surface finish ($R_a = 0.02$ μm for #4000 wheel).
- Plunge ELID grinding outputted poorer surface finish than traverse ELID grinding, especially for coarser grit abrasive wheels (see Figure 9.25).
- Waviness of ground surface improves with the increase in wheel mesh size (Figure 9.26).

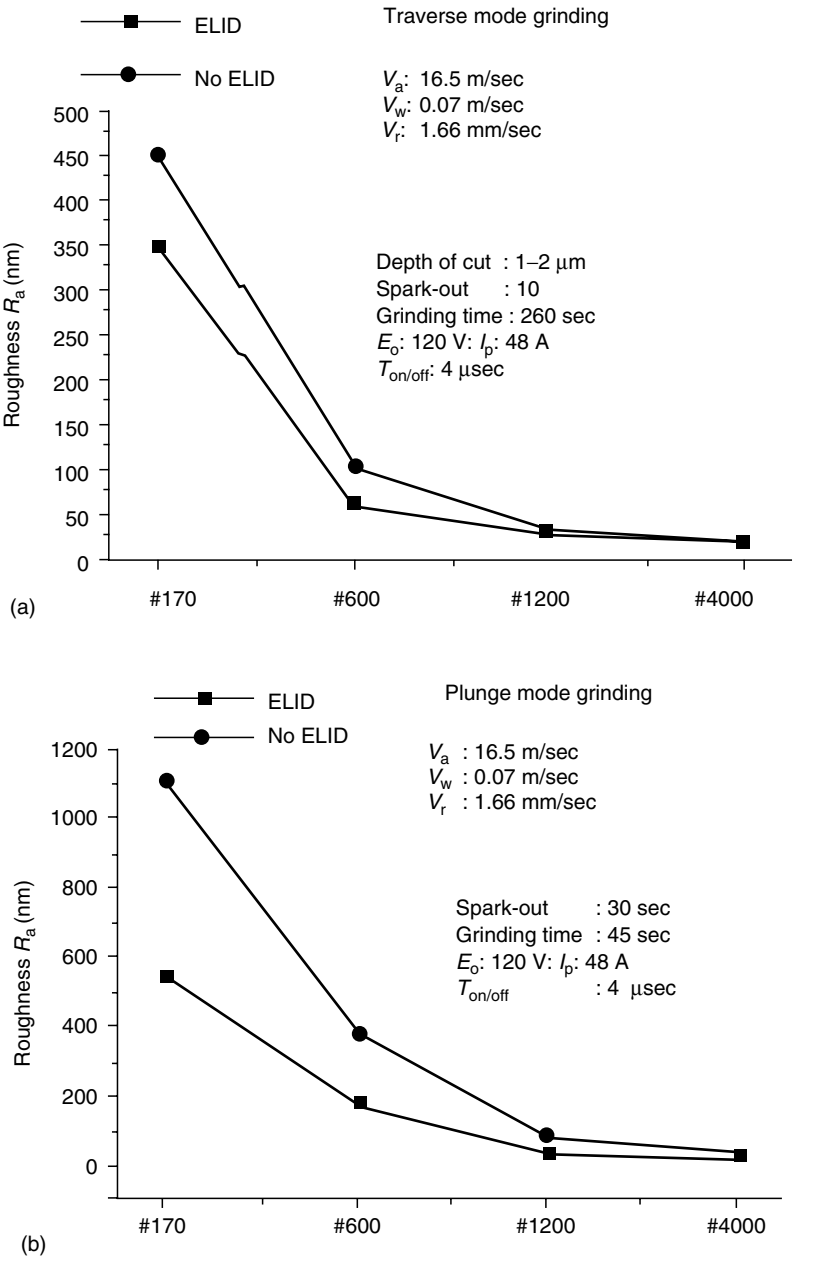

FIGURE 9.25
Comparison of roughness: (a) traverse; (b) plunge.

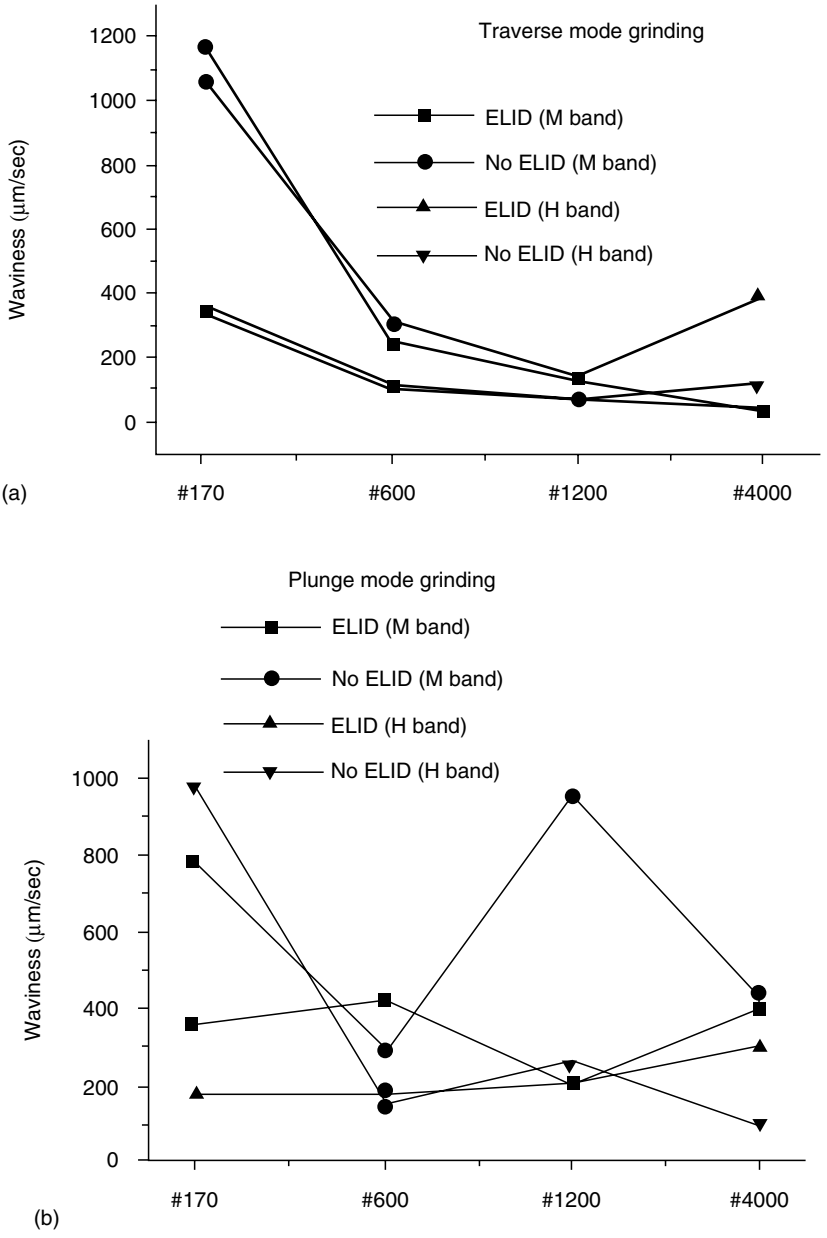

FIGURE 9.26
Comparison of waviness: (a) traverse; (b) plunge.

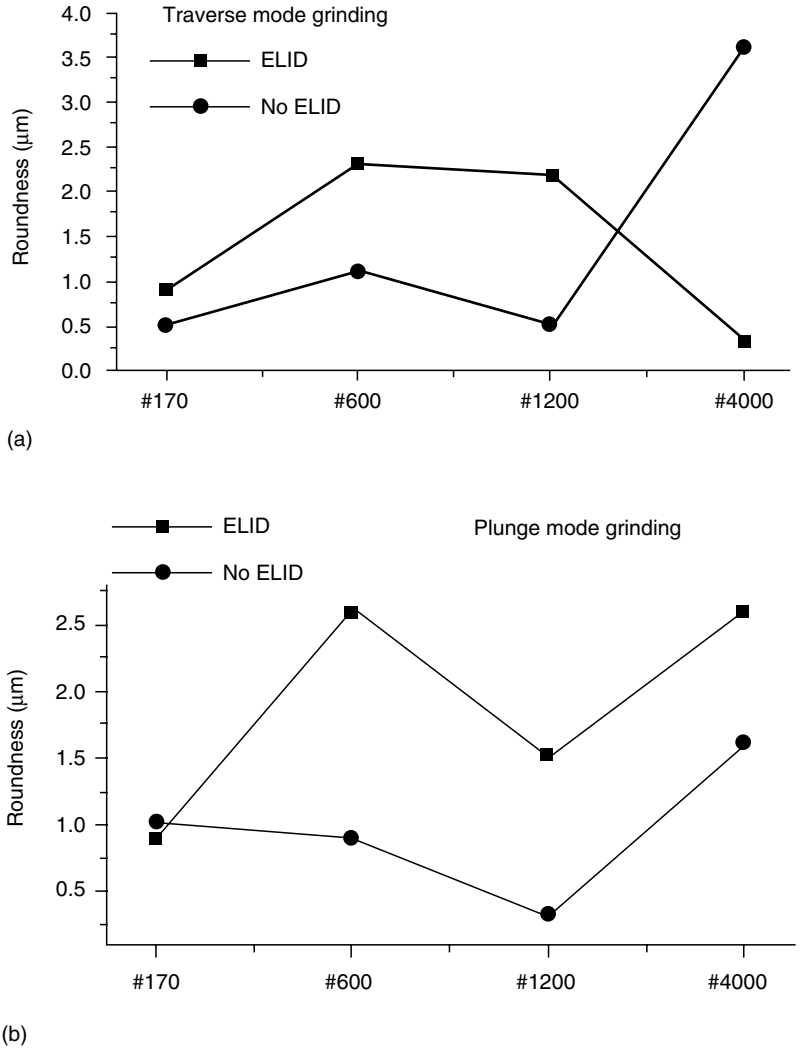

FIGURE 9.27
Comparison of roundness: (a) traverse; (b) plunge.

- ELID process is stable for traverse mode grinding and not so stable for plunge mode grinding (see Figure 9.27).
- Roundness of the ground surface increases with the mesh size of the used wheel.
- Out-of-roundness can be negatively affected by the stiffness of the machine tool, not only as a result of the grinding operation.
- ELID traverse grinding tends to offer a more promising potential than plunge mode grinding.

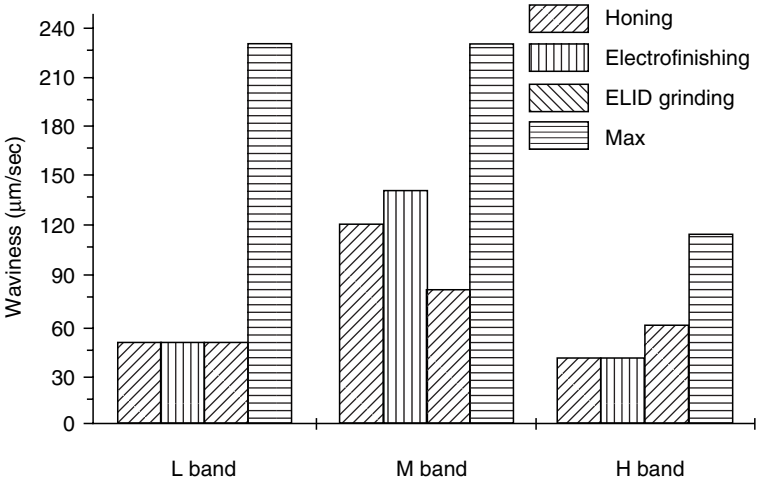

FIGURE 9.28
Surface waviness with different processes.

- A number of three to four spark-out passes will improve the precision (waviness and roundness) of the ground surface.
- Effects of grinding parameters on surface roughness for ELID grinding and conventional grinding are comparable.
- Increased depth of cut and increased traverse rate worsen the surface finish.
- ELID grinding offers better results than both honing and electric polishing (see Figure 9.28).
- Smooth ELID ground surfaces have poorer high band waviness than honed ones, explained by the tool performance because of the smaller contact zone.
- ELID grinding technique induces compressive surface stress of about 150–400 MPa, with a smaller peak than that outputted by a honing process of 600–800 MPa.
- The depth of the compressive layer produced by ELID operation (10 μm) is half the one produced by a honing operation (15–20 μm).
- The cycle time of ELID grinding is twice as large as the one that characterizes the honing and the electric polishing operations; but better roughness and higher removal rate achieved through ELID grinding by a coarser wheel and higher traverse speed prove ELID grinding more cost-effective for small batch production situations.

9.4.7 ELID Grinding of Ceramic Coatings (Zhang et al., 2001a)

Ceramic coatings include a large group of subspecies, such as CVD-SiC, plasma spray deposited aluminum oxide, and plasma spray deposited

chromium oxide. The efficient machining and the required quality of these ceramic coatings have not been mastered yet. In this research, a comparative study of diamond grinding of ceramic coatings on a vertical grinder was done. Two types of dressing procedures as applied to cast-iron-bonded diamond wheel, with #4000 mesh size—alumina rotary dressing and ELID dressing and grinding—were compared. The conclusions can be synthesized as follows:

- There is a critical current value for each electrolytic dressing system; when the current is smaller the thickness of the insulating oxide layer increases with the value of the current; otherwise, it decreases.
- Thickness and depth of oxide layer largely depends on the coolant type.
- A small increase in the wheel diameter or thickness after electrolytic dressing is noticed, conversely as in the rotary and other mechanical methods of dressing.
- Roughness for the rotary dressing decreases sharper than ELID method in the first 3 min; after 3 min, the roughness decreased constantly for ELID grinding but showed a wavelike model for the dressing method.
- The wear of abrasive grains will produce an instability of the grinding performance for dressing technique, while it remains constant for ELID technique.
- Surface roughness depends on material properties in both methods.
- All ceramic coatings except sintered SiC presented a better roughness after ELID dressing than after rotary dressing.
- Plasma spray deposited chromium oxide is difficult to grind to an extremely fine roughness.
- For both dressing methods, the micrographs prove that the material removal mechanism presents both brittle-fracture and ductile modes; for the ELID dressing, more ductile mode than the brittle-fracture mode was present, except for sintered SiC; whereas for the rotary dressing more brittle-fracture mode than the ductile mode was present.
- Ductile-mode grinding can be implemented even on a common grinder, by controlling the wheel topography.
- For the ELID method, the interaction between the abrasive grain and the workpiece surface is accomplished through a spring-damper system (because of the existence of the oxide layer), whereas for rotary dressing, the contact is rigid and stiff (see Figure 9.29); oxide layer absorbs vibrations and reduces the actual exposed cutting edge of the abrasive grain.

9.4.8 ELID Ultraprecision Grinding of Aspheric Mirror (Moriyasu et al., 2000; see also Figure 9.30)

The quality of soft x-ray silicon carbide mirrors influences the performance of modern optical systems. To accomplish the high precision of these

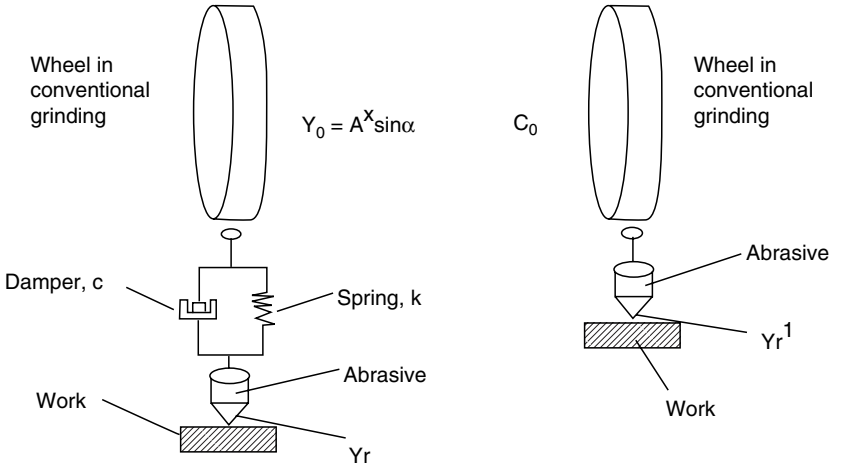

FIGURE 9.29
Wheel–work interface models for ELID and conventional grinding. (From Zhang, C., Ohmori, H., Marinescu, I., and Kato, T., *Int J Adv Manuf Technol*, 18, 545, 2001b. With permission.)

aspheric mirrors, an ELID grinding system was employed. A #1000 cast-iron grinding wheel was mechanically trued and predressed using electrical methods. The workpiece surfaces were concave spherical with a curvature of 2 m. After grinding, the form was measured and the data were compared with the planned data by the mean of the least squares method. A form error

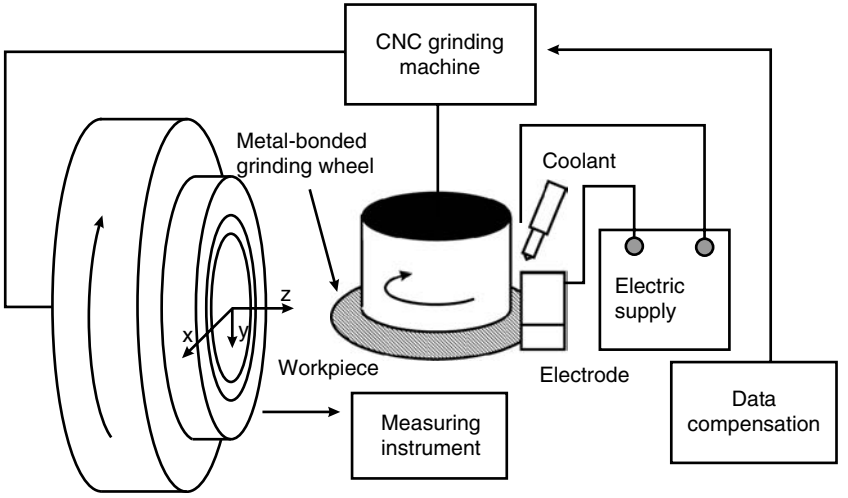

FIGURE 9.30
Aspherical form control system. (Moryiasu, S., Ohmori, H., Kato J., Koga H., Ohmae, M., Ultraprecision form control of aspheric mirror with ELID grinding, 2000.)

was calculated and compensation data were generated. Accordingly, a new form was ground. This procedure was applied five times to exponentially decrease the errors from 2.6 to 0.38 μm. Analyzing the repeatability of the system, the achieved data are considerably accurate.

9.4.9 ELID Grinding of Microspherical Lenses (Ohmori et al., 2001)

The ductile-mode grinding of brittle optical parts is studied in this research. The implementation of ductile-mode cutting requires expensive items like ultraprecision vibration-free rigid machine tools, high-resolution feeding motion control, submicron grit wheels, clean work environment, and so on. The conclusions of this study are as follows:

- ELID grinding is stable, efficient, and economical.
- Low grinding speed, insufficient work-wheel fixture, instability on using ultrafine abrasive and small-size wheels, difficulty in achieving precise and efficient truing and dressing of the wheels, trouble in obtaining precise and effective fixtures are some problems connected with implementing the ductile or semiductile-mode grinding of micro optical components.
- Coarse grit size wheels (#325) do not show any difference in the final roughness when ELID is applied.
- #4000 wheels, however, showed a better surface finish when ELID was employed.
- ELID high-precision grinding of microspherical wheels with cup wheels (ELID-CG grinding) has the potential to achieve high spherical accuracy and finish R_a 20 nm.
- ELID-CG grinding can be successfully used to fabricate microspherical lenses with a more stable process, higher efficiency, and better surface quality than conventional grinding.

9.4.10 ELID Grinding of Large Optical Glass Substrates (Grobsky and Johnson, 1998)

The ability of ELID grinding using fine mesh superabrasive wheels to produce spectacular finishes (R_a 4–6 nm) on brittle surfaces of BK-7 glass, silicon, and fused silica was proved. For some applications, ELID grinding eliminated polishing or lapping operations. In this research, ELID grinding was employed to grind optical components of 150–250 mm diameter.

9.4.11 ELID Precision Internal Grinding (Qian et al., 2000, 2001)

Few researches have reported on mirror-surface internal grinding because of the limitation of the abrasive grit size applicable to nonmetallic bond

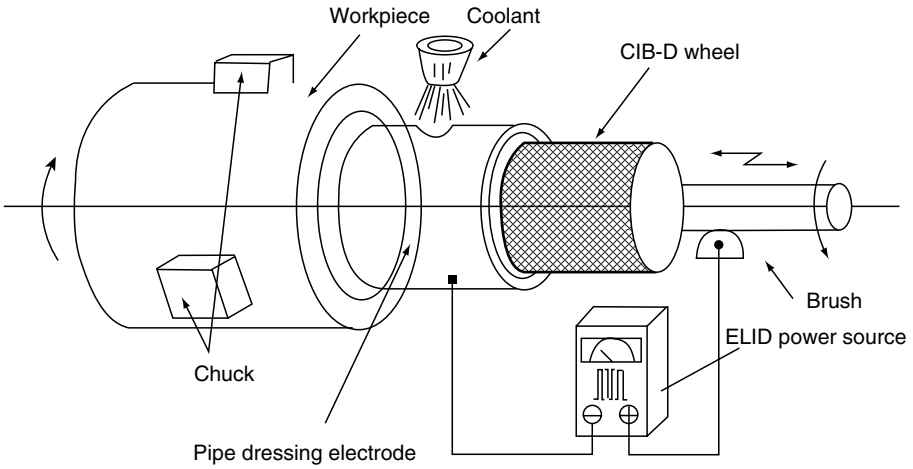

FIGURE 9.31
Schematic of interval ELID grinding. (Qian et al., 2000b)

grinding wheels. A novel method to carry out ELID grinding of internal cylindrical surfaces on an ordinary grinding tool, named interval ELID, is presented (see Figure 9.31). The wheel is dressed at intervals and the abrasive grains remain protruding. After predressing operation, the insulating oxide layer is 30 μm thick, increasing, therefore, the external diameter of the grinding wheel. The current characteristics for interval ELID grinding are shown in Figure 9.32. In internal grinding, the abrasive wear occurs

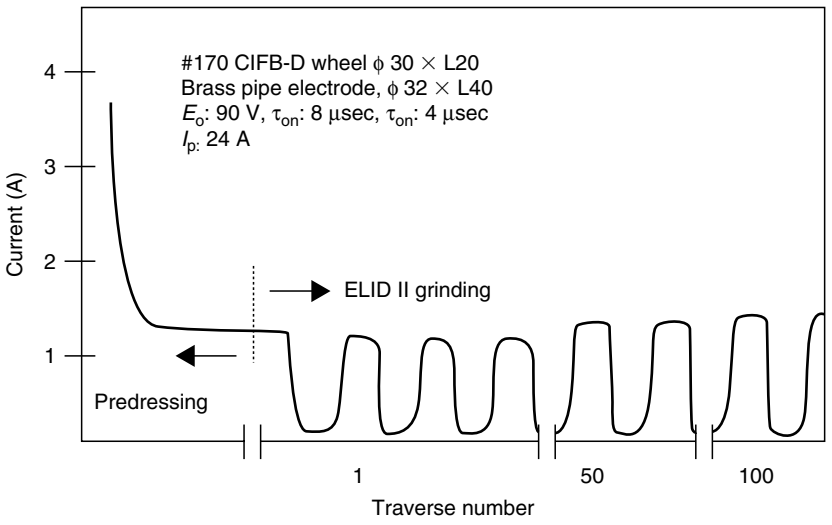

FIGURE 9.32
Current fluctuation in interval ELID grinding. (Qian et al., 2000b)

rapidly because of the smaller diameter of the wheel. The conclusions of the study are presented briefly here:

- Because of the limitation of the wheel diameter, the wheel speed can be adjusted only within a small range; the effect of speed on work results is not significant.
- The higher the speed (within the limited range), the better the internal surface finish.
- Effects of grinding parameters during interval ELID grinding are similar to those obtained after conventional internal grinding.
- Ground surface quality increases with the increasing mesh size value of the wheel; fine abrasive wheels can, therefore, be used to fabricate smooth surfaces, without the risk of losing the stability of the surface roughness.
- Internal mirror-surface finish was possible for pieces made of bearing steel, alumina. Later studies (Qian et al., 2001) added some new conclusions that are presented here.
- Pipe dressing electrodes are superior to other shape electrodes.
- Another ELID technique, ELID III, is introduced (see Figure 9.33).
- It is possible to achieve mirror-like surface with an appropriate coarse grinding wheel; the roughness obtained after ELID III grinding with #2000 grit size is almost the same with the roughness obtained after ELID with #4000 with cBN.
- A combination of ELID II and ELID III can be used for finishing processes especially when small diameters are applicable.
- Both rough and finish grinding can be achieved on the same machine tool using ELID II and ELID III procedures.

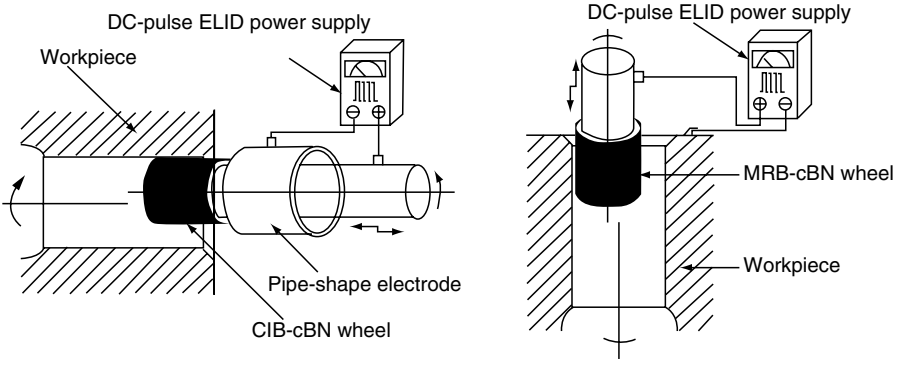

FIGURE 9.33
ELID II and ELID III internal grinding processes. (From Qian, J., Ohmori, H., and Li, W., *Int J Mach Tools Manuf*, 41, 193, 2001. With permission.)

9.4.12 ELID Grinding of Hard Steels (Stephenson et al., 2001)

Hardened bearing steels like M50 was ultraprecision ground to produce an optical quality surface ($R_a < 10$ nm), using a 76 μm cBN grit and 500 μm depth of cut. The final surface finish is enhanced by the burnishing action of the worn cBN grits. ELID technique was employed to improve the surface finish by maintaining the protrusion and sharpness of the cBN grits and avoid the pullout of the carbides in the secondary finishing zone phenomenon.

Another grinding technique used to minimize microcracking, surface burn, and phase transformation is low stress grinding (LSG). However, special demands of machine tool stiffness, low and controllable vibration state, low wheel speed, and frequent wheel dressing operations should be addressed in this case. The LSG is characterized by lower removal rates, lower grinding ratios, and significant increasing of production costs, while some localized surface damage and surface finish in the range of R_a 100–200 nm are to be obtained.

Other studies (Onchi et al., 1995) reported an R_a 30 nm roughness after grinding SAE52100 with a porous cBN wheel, but with relatively low removal rates and very fine cBN wheels, or up to R_a 60 nm (Puthanangady et al., 1995) after superfinishing hardened steel pieces with #500 grit size fused alumina stones.

This study employed cBN grinding wheels with the grit size of 30 μm for roughing, 2 μm for medium finish, and 0.7 μm for final mirror-like finish. The following conditions were used: 100 mm diameter D151 electroplated diamond wheel at 3000 rpm, traverse rate of 5 mm per rev and an *n*-feed of 1–4 μm per pass. The following parameters were used for the current work such as: voltage 60 V, peak current 10 A, on-time 6 μs, off-time 2 μs, and square pulse wave.

Some of the most important conclusions of the study are presented here (see also Figure 9.34 and Figure 9.35):

- A repeatable surface finish less than R_a 10 nm can be ultraprecision grounded with 75 μm cBN grit and 500 μm depth of cut.

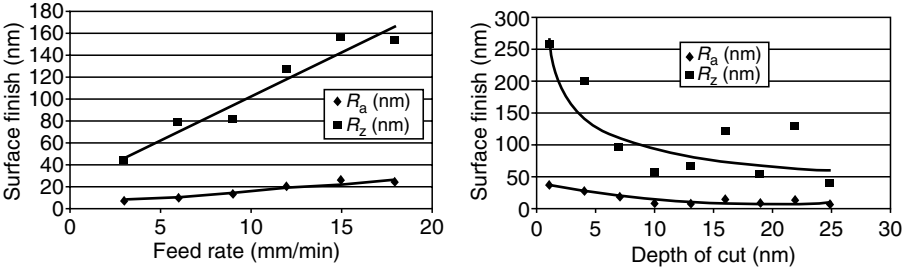

FIGURE 9.34
Surface finish vs. feed rate and depth of cut. (From Stephenson, D.J., Veselovac, D., Manley, S., and Corbett, J., *J Int Soc Prec Eng Nanotechnol*, 25, 336, 2001. With permission.)

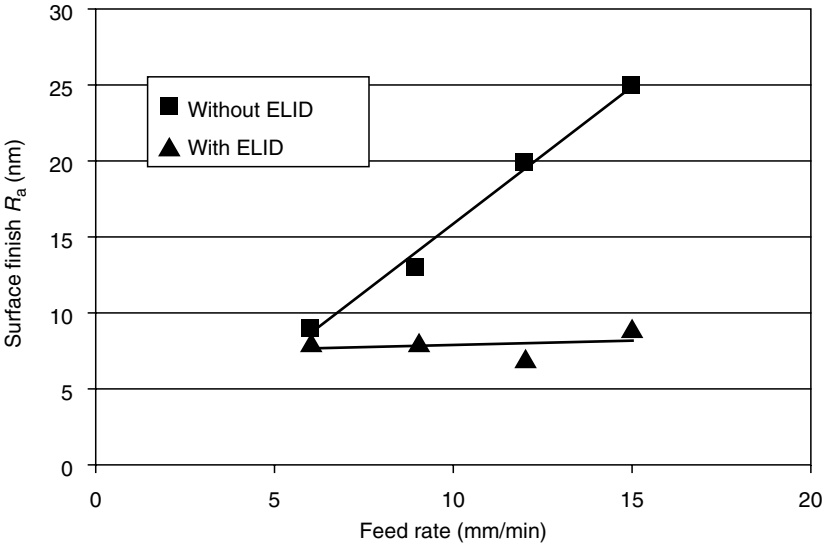

FIGURE 9.35
Surface finish vs. feed rate for ELID and non-ELID grinding. (From Stephenson, D.J., Veselovac, D., Manley, S., and Corbett, J., *J Int Soc Prec Eng Nanotechnol*, 25, 336, 2001. With permission.)

- Best surface finish of R_a 2.3 nm was obtained with a 200 μm depth of cut.
- The order of chip thickness is 1–10 nm.
- Carbide pullout of the cBN grits can be avoided by employing ELID dressing technique.
- Development of optical quality surfaces can be considered in terms of the processes occurring in the primary and secondary finishing zones of the cup wheel, with the final surface finish enhanced by the burnishing action of worn cBN grits.

9.4.13 ELID Mirror-Like Grinding of Carbon Fiber Reinforced Plastics (Park et al., 1995)

CFRPs are used in aircraft and spacecraft industries, machine tool spindles, power-transmission shafts, and robotic arms. The conclusions of this study are listed as follows:

- Surface roughness of the CFRP improved substantially for diamond wheels with mesh number below #4000.
- For diamond wheels with mesh number finer than #4000 wheel, the roughness did not improve noticeably.

- The higher limit of the surface roughness for a #6000 wheel was R_{max} 0.65 μm.
- CFRP surface roughness is better than that of brittle materials grounded in similar ELID conditions because of the elastic deformation of this material.
- Mirror-like surface finish is strongly dependent on the grinding direction; the grinding at 90°C with respect to fiber direction permits the best results.
- The spark-out effect on the roughness was noticeable for rapid feed-grinding but small for creep feed grinding.
- Mirror-like finish is accompanied by a homogenization mechanism by grinding heat and chip smearing.

9.4.14 ELID Grinding of Chemical Vapor Deposited Silicon Carbide (Zhang et al., 2001a)

Chemical vapor deposited silicon carbide (CVD-SiC) is the second most ideal material for deflection mirrors used in short wavelength laser system, next only to crystalline diamond. Conventional polishing techniques were found insufficient to produce CVD-SiC mirrors. The conclusions drawn in this study are as follows:

- ELID grinding has a strong potential to achieve extremely smooth surfaces.
- The surface roughness reduced with the grain size.
- In ELID grinding exist fewer pits and sticking-outs produced during brittle fracture when the abrasive grains crush and plow the surface of the workpiece, as compared to other dressing techniques; the number of pits and sticking-outs reduces with the decreasing of the grain size.
- The ratio of the ductile vs. brittle-fracture mechanisms is higher for ELID grinding than for conventional dressing procedure; the ratio increases with the decreasing of grain size.
- It is possible for ELID to realize ductile-mode removal even on a conventional, not-so-stiff, and precise grinder, by properly controlling the depth and composition of the insulating oxide layer.

9.5 Summary and Conclusions

ELID grinding is a grinding process that employs metal bond-abrasive wheels continuously *in situ* dressed via an electrolytic process. The procedure

exposes new sharp abrasive grains by dissolving the surrounding metal bonds to maintain constant the material removal rate and continuously improve the surface roughness.

ELID grinding was first proposed by the Japanese researcher Hitoshi Ohmori in 1990 (Ohmori and Nakagawa, 1990). Its most important feature is that no special machine is required. ELID uses a square-wave voltage of 10–100 V with a peak current of 5–50 A. The pulse width is commonly adjusted to 2–7 μsec on-time and off-time. The ELID system's essential elements are a metal-bonded grinding wheel, an electrolytic power source, and an electrolytic coolant.

The metal-bonded grinding wheel, connected to the positive terminal of the power supply with a smooth brush contact, is dressed during the electrolysis process by the fixed copper electrode, connected to the negative pole, in the presence of the electrolytic fluid. The copper electrode has one-sixth of the wheel peripheral length and a width 2 mm wider than the wheel rim thickness. The 0.1–0.3 mm gap between the wheel and the active surface of the electrode can be adjusted by mechanical means. A special high pH grinding fluid at a rate of 20–30 L/min is used as electrolytic fluid. The stages of ELID grinding are as follows: (1) the precision truing of the micrograin wheel; (2) the predressing process of the wheel via electrolysis, performed at low speed for about 10–30 min; (3) the grinding process with continuous wheel in-process dressing by electrolytic means.

A controlled insulating oxide layer (approx. 20 μm thick) is obtained. The layer of oxide has a larger flexibility and a lower retention characteristic as compared to the bulk bond material. Thickness and depth of oxide layer largely depends on the coolant type. As the grains wear during the grinding process, the insulating oxide layer is also worn. This increases the electro-conductivity of the wheel so the electrolysis will intensify, generating a fresh insulating layer. The protrusion of the grains remains constant. For rough grinding, thin insulating layer is required, whereas for mirror-like finish, ELID grinding a relatively thick insulating layer is preferred. A slight increase in the wheel diameter (or thickness) during ELID grinding is noticed because of the oxide layers formation, conversely as in the rotary and other mechanical methods of dressing.

During the last 10 years, a number of publications have addressed the merits of ELID when applied to abrasive grinding on brittle materials such as BK-7 glass and fused silica, ceramics, hard steels, ceramic coatings, and so on, with various shapes (plane, cylindrical external and internal, spherical and aspherical lenses, and so on.) and dimensions. For some applications, ELID grinding eliminated polishing or lapping operations.

ELID grinding provides the ability to produce spectacular finishes on brittle material surfaces, with surface roughness on the nanometer scale (4–6 nm). Coarse grit size wheels (JIS #325 and coarser) show only slight differences in the final roughness when ELID is applied as compared to conventional grinding. However, for finer wheels (JIS #4000 and finer),

ELID showed a better surface finish when it was employed as compared to conventional grinding in similar conditions.

ELID grinding is more stable than conventional grinding from the removal rate value viewpoint. Material removal rates of 250 mm^3/min up to 8000 mm^3/min were reported. The chip thickness is of an order of 1–10 nm. Stock removal rate increases with the increase in the number of passes, stiffness of machine tool, and larger grit sizes of the wheels. Cast-iron-bonded wheels have a larger stock removal rate yet a lower grinding force as compared to a vitrified bonded grinding wheel.

ELID grinding can be accomplished through brittle-fracture mode for coarse wheels and in a ductile mode for finer (JIS #4000, . . . , #20,000, FEPA #1200, and finer) wheels. By careful choice of grinding parameters and control of the process, ceramics can be ground predominantly in ductile mode and this results in grooves on the surface that are relatively smooth in appearance. Ductile-mode grinding can be implemented even on a common grinder, by controlling the wheel topography.

SEM and AFM techniques permit to evaluate the surface and subsurface fracture damage to assess the difference between the material removal mechanism of brittle-fracture and the ductile mode. Both the cutting speed and the feed rate have no significant effect on the surface finish of the workpiece.

ELID grinding can be used for low-rigidity machine tools and low-rigidity workpieces. Grinding force is lower during ELID grinding as compared to ordinary grinding. Grinding force was constant and low after the first ELID dressing complete procedure. ELID grinding technique induces compressive surface stress of about 150–400 MPa. The depth of the compressive layer produced by ELID operation (10 μm) is half the one produced by a honing operation (15–20 μm), for instance.

Hardened bearing steels like M50 can be ultraprecision ground to produce an optical quality surface ($R_a < 10$ nm). The final surface finish is enhanced by the burnishing action of the worn grits. A surface roughness of R_a 30 nm can be attained after SAE52100 grinding with porous cBN grinding wheels, but with relatively low removal rates and very fine cBN wheels.

References

Bandyopadhyay, B.P. and Ohmori, H., The effect of ELID grinding on the flexural strength of silicon nitride, *International Journal of Machine Tools and Manufacturing*, Vol. 39, 1999, pp. 839–853.

Bandyopadhyay, B.P., Ohmori, H., and Takahashi, I., Efficient and stable grinding of ceramics by electrolytic in-process dressing (ELID), *Journal of Materials Processing Technology*, Vol. 66, 1997, pp. 18–24.

Chen, H. and Li, J.C.M., Anodic metal matrix removal rate in electrolytic in-process dressing I: two dimensional modeling; protrusion effect and three-dimensional modeling, *Journal of Applied Physics*, Vol. 87, no. 6, 2000, pp. 3151–3164.

Chen, H. and Li, J.C.M., Anodic metal matrix removal rate in electrolytic in-process dressing II: protrusion effect and three-dimensional modeling, *Journal of Applied Physics,* Vol. 87, no. 6, 2000, pp. 3159–3164.

Grobsky, K. and Johnson, D., ELID Grinding of Large Optical (Glass Substrates), Report of Zygo Corporation, 1998.

Inaski, I., Speed-stroke grinding of advance ceramics, *Annals of the CIRP*, Vol. 37, no. 1, 1988, p. 299.

Itoh, N. and Ohmori, H., Grinding characteristics of hard and brittle materials by fine grain lapping wheels with ELID, *Journal of Materials Processing Technology*, Vol. 62, 1996, pp. 315–320.

Itoh, N., Ohmori, H., Moryiasu, S., Kasai, T., Karaky-Doy, T., and Bandyopadhyay, B.P., Finishing characteristics of brittle materials by ELID-lap grinding using metal-resin bonded wheels, *International Journal of Machine Tools and Manufacturing,* Vol. 38, 1998, pp. 747–762.

McGeough, J.A., *Principles of Electrochemical Machining*, Chapman and Hall Publishing House, London, 1974.

Moriyasu, S., Ohmori, H., Kato, J., Koga H., and Ohmae, M., Ultraprecision form control of aspheric mirror with ELID grinding, *Annual Report of Japan Synchrotron Radiation Research Institute (JASRI)* 1996, pp. 218–219.

Nakagawa, T. and Suzuki, K., Highly efficiency grinding of ceramics and hard metals on grinding center, *Annals of CIRP*, Vol. 35, no. 1, 1986, pp. 205–210.

Ohmori, H. and Nakagawa, T., Mirror surface grinding of silicon wafers with electrolytic in-process dressing, *Annals of CIRP*, Vol. 39, no. 1, 1990, pp. 329–332.

Ohmori, H., Takahashi, I., and Bandyopadhyay, B.P., Ultra-precision grinding of structural ceramics by electrolytic in-process dressing (ELID) grinding, *Journal of Materials Processing Technology*, Vol. 57, 1996, pp. 272–277.

Ohmori, H., Lin, W., Moriyasu, S., and Yamagata, Y., Advances on micro-mechanical fabrication techniques: microspherical lens fabrication by cup grinding wheels applying ELID grinding, RIKEN Review, no. 34, April 2001.

Onchi, Y., Matsumori, N., Ikawa, N., and Shimada, S., Porous fine CBN stones for high removal rate superfinishing, *Annals of CIRP*, Vol. 44, no. 1, 1995, pp. 291–294.

Park, K.Y., Lee, D.G., and Nakagawa, T., Mirror surface grinding characteristics and mechanism of carbon fiber reinforced plastics, *Journal of Materials Processing Technology*, Vol. 52, 1995, pp. 386–398.

Puthanangady, T.K. and Malkin, S., Experimental investigation of the superfinishing process, *Wear*, Vol. 185, 1995, pp. 173–182.

Qian, J., Li, W., and Ohmori, H., Cylindrical grinding of bearing steel with electrolytic in-process dressing, *Precision Engineering*, Vol. 24, 2000a, pp. 153–159.

Qian, J., Li, W., and Ohmori, H., Precision internal grinding with metal-bonded diamond grinding wheel, *Journal of Materials Processing Technology*, Vol. 105, 2000b, pp. 80–86.

Qian, J., Ohmori, H., and Li, W., Internal mirror grinding with a metal/metal–resin bonded abrasive wheel, *International Journal of Machine Tools and Manufacturing*, Vol. 41, 2001, pp. 193–208.

Stephenson, D.J., Veselovac, D., Manley, S., and Corbett, J., Ultra-precision grinding of hard steels, *Journal of International Societies for Precision Engineering and Nanotechnology*, Vol. 25, 2001, pp. 336–345.

Wlech, E., Yi, Y., and Bifano, T., Electrochemical dressing of bronze bonded diamond grinding wheels, Proceedings of International Conference on Machining of Advanced Materials, Gaithersburg, MD, NIST 874, 1993, pp. 333–340.

Zhang, B. and Howes, T.D., Material-removal mechanisms in grinding ceramics, *Annals of CIRP*, Vol. 43, no. 1, 1994, pp. 305–308.

Zhang, B., Yang, F., Wang, J., Zhu, Z., and Monahan, R., Stock removal rate and workpiece strength in multi-pass grinding of ceramics, *Journal of Materials Processing Technology*, Vol. 104, 2000, pp. 178–184.

Zhang, C., Kato, T., Li, W., and Ohmori, H., A comparative study: surface characteristics of CVD-SiC ground with cast iron bond diamond wheel, *International Journal of Machine Tools and Manufacturing*, Vol. 40, 2000, pp. 527–537.

Zhang, C., Ohmori, H., Kato, T., and Morita, N., Evaluation of surface characteristics of ground CVD-SiC using iron bond diamond wheels, *Precision Engineering, Journal of International Societies for Precision Engineering and Nanotechnology*, Vol. 25, 2001a, pp. 56–62.

Zhang, C., Ohmori, H., Marinescu, I., and Kato, T., Grinding of ceramic coatings with cast iron bond diamond wheels. A comparative study: ELID and rotary dresser, *International Journal of Advanced Manufacturing Technology*, Vol. 18, 2001b, pp. 545–552.

10

Mono- Versus Polycrystalline Diamond Lapping of Ceramics

M. Pruteanu, I. Benea, and I.D. Marinescu

CONTENTS

10.1 Introduction

The lapping process has become a widely used procedure to achieve the high tolerances required for today's advanced ceramics. Lapping is a loose-abrasive machining process, which combines abrasive particles within an oil or water-based carrier to form a slurry. The slurry is fed into a rotating lap plate (usually cast iron) to form an abrasive film between the plate and the parts to be lapped. In typical lapping operations, the abrasive is forced into the lap plate, and the parts are lapped with continuously supplied abrasive suspended in a liquid medium. Lapping is an automated, three-body abrasion process used to obtain a superior surface quality: high dimensional accuracy and flatness, good roughness, and minimal subsurface damage. Other benefits of lapping include no clamping or heat distortion due to low cutting forces and speeds, no expensive tooling required, very thin and nonmagnetic parts can be processed, irregular-shaped parts can be easily machined.

During the lapping process, the main actions of the abrasive grains against the workpiece include indentation, rolling, scratching, and plowing. Many researchers have studied the behavior of brittle materials under the action of a diamond indenter. Lateral and median/radial cracks were generated during the indentation process. Material removal mainly results from the propagation of lateral cracks, which commonly takes place in the unloading

stage. The median cracks that extend toward the depth direction play a very significant role in the surface and subsurface damage of material [1]. Buijs et al. [2] investigated the glass lapping process and developed a model based on indentation fracture. The model expresses the material removal rate (MRR), surface roughness, subsurface damage, and load/abrasive particle as a function of particle size, material properties of workpiece and lapping plate, applied pressure and relative velocity between the plate and the workpiece.

As the contracting company (Warren Diamond Co.) is a member company, we can identify it as the primary beneficiary. The project's main goal is to optimize the lapping process, by finding a correlation between the process parameters (of which very important is the type of the slurry) and the final parameters of the ceramic parts (dimensional accuracy and surface roughness). Therefore, a part of the optimization process is concerned with a comparative study of the behavior of polycrystalline versus monocrystalline diamond slurry. The aspects that will be taken into account are the MRR and the grain size distribution.

The final results are important for those who want to apply the lapping process to ceramic parts efficiently. Recommendations concerning the process parameters (rotation of the lapping plate, load per grain, and time) and the slurry (type and size of grains, optimum size distribution, and flow rate) that has to be used will be available to the member companies.

10.2 Experimental Methodology

Lapping experiments were carried out on a Lapmaster International Model 12C lapping machine that has a DC variable speed motor, which spins a 300 mm plate over a range of 0–60 rpm. The experimental setup is illustrated in Figure 10.1. Ceramic workpieces (rings with 0.5″ ID, 0.8″ OD, and 0.2″

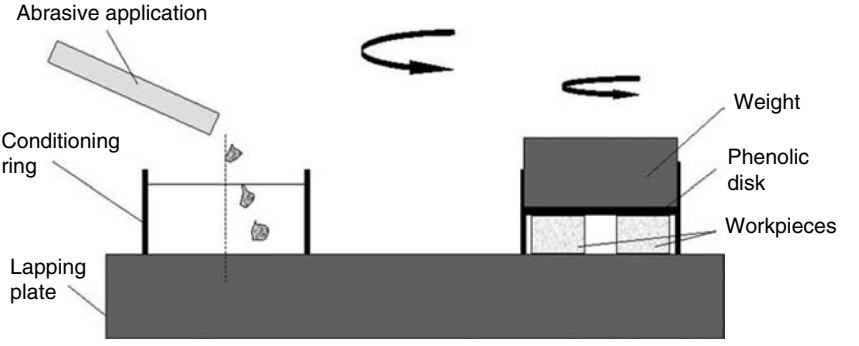

FIGURE 10.1
Lapping setup.

TABLE 10.1

Workpiece Material Properties

Material	**Al_2O_3—99.8%**
Physical properties	
Density (g/cm^3)	3.96
Mechanical properties	
Tensile strength (MPa)	310 (at 25°C) 220 (at 1000°C)
Modulus of elasticity (GPa)	366
Poisson ratio	0.22
Compressive strength (MPa)	3790 (at 25°C) 1.929 GPa (at 1000°C)

thickness) made of Al_2O_3 (Table 10.1) were lapped with diamond slurry on the single-side lapping machine using a cast iron plate and conditioning rings.

Diamond abrasive was suspended in a water-based carrier and supplied by a peristaltic pump at a flow rate of 1.5 mL/min. Three workpieces, fixed at the bottom of a weight with a holder, were lapped simultaneously. The slurry was based on either monocrystalline or polycrystalline diamond grains of four sizes: 25, 15, 3, and 1 μm.

Using 25, 15, 3, and 1 μm grains, the following parameters were kept constant:

- Flow rate, 1.5 mL/min
- Rotation of the lapping plate, 56 rpm
- Slurry concentration, 1.4 g/500 mL (7 ct/500 mL)
- Load/grain, 0.0037 g/grain for 1 and 3 μm grains 0.8404 g/grain for 15 and 25 μm grains

During the experiments, only the machining time was varied: 2, 7, 17, 47, and 107 min, for each grain size, for both monocrystalline and polycrystalline diamond slurry.

For all the workpieces, the following characteristics were measured before and after each experiment: thickness, mass, and surface roughness (measured in four areas). The average initial surface roughness was $R_a = 1.5$ μm.

10.3 Experimental Results

An important component of these lapping tests is the evaluation of the performance of monocrystalline and polycrystalline diamond slurry. In

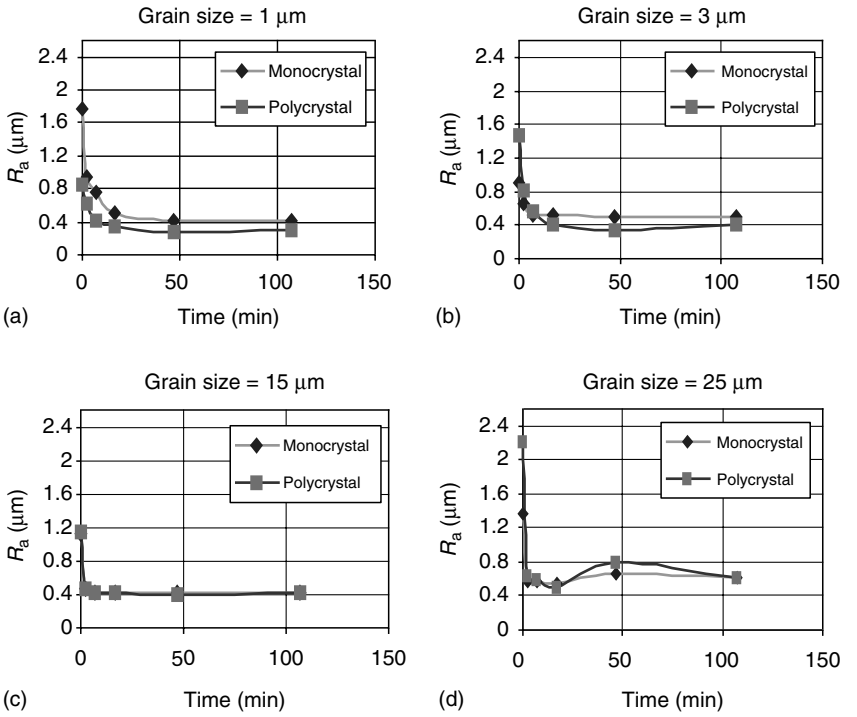

FIGURE 10.2
Roughness versus time.

addition, the experiments aimed to determine the effect of the abrasive size and machining time on the surface roughness and MRR. Figure 10.2 and Figure 10.3 are diagrams of the surface roughness data obtained for both monocrystalline and polycrystalline slurry.

As shown in Figure 10.2, the surface roughness decreases more rapidly with time at the beginning of machining. After approximately 15 min the surface roughness does not decrease significantly or even increases. After 15 minutes it is not recommended to continue the lapping process.

Results from lapping with the smallest abrasive (1 μm) showed the polycrystalline diamond producing a better surface than the monocrystalline diamond whereas for the 3 μm grains the latter yields better results from the roughness point of view. The best roughness values were obtained with the 15 μm grain size (Figure 10.3) for both monocrystalline and polycrystalline diamonds in all the studied ranges of the lapping time. For larger grain sizes, the influence of the diamond type is insignificant.

Figure 10.4 through Figure 10.6 illustrate the influence of the lapping time and grain size on the MRR. For 1 μm grain size, the monocrystalline diamond leads to higher MRR after a short machining time. The 15 μm

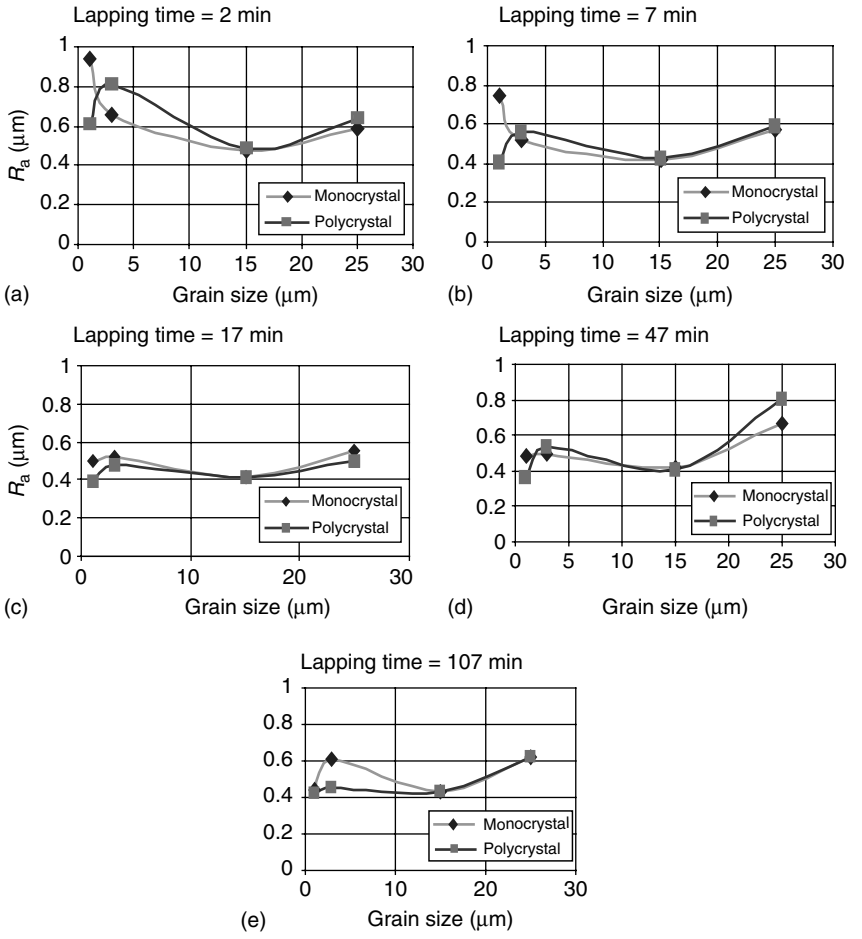

FIGURE 10.3
Roughness versus grain size.

abrasive gives better results than any other size and the polycrystalline diamond outperforms the monocrystalline one.

With the 1, 3, and 15 μm abrasive sizes, it can be considered that the polycrystalline diamond is effective in improving the surface finish whereas the monocrystalline diamond generates a better MRR. This is possible because of the different abrasive action of each type of diamond and its behavior determined by its physical properties.

The monocrystalline diamond behaves differently from the polycrystalline one only because of larger grain size. This could be due to the breakage of larger polycrystalline grains (25 μm) into much smaller particles than those resulted after the breakage of monocrystalline diamond. One can see

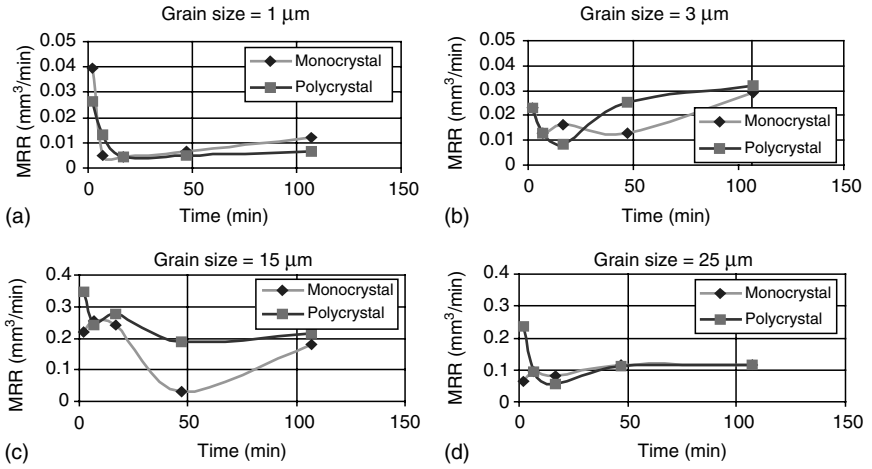

FIGURE 10.4
Material removal rate versus time.

this aspect illustrated in Figure 10.7 and Figure 10.8 in which the grain size distribution for both monocrystalline (Figure 10.7) and polycrystalline (Figure 10.8) diamonds are shown before and after lapping. The final grain size distribution is shown for the slurry that was collected after the total lapping time (107 min).

As can be seen, even if the initial grain size distribution is almost identical for both types of diamonds, after completing the lapping process, the grain size distribution differs in terms of the number of smaller particles. The mean grain size was initially 22.36 μm in the range of 8.482–62.23 μm for polycrystalline and the mean size was 20.54 μm for monocrystalline diamond, spread in the range of 12.00–52.33 μm. At the end of lapping, the grain size was in the range of 0.375–47.98 μm for polycrystalline and 0.53–40.35 μm for monocrystalline diamonds. From the shape of the size distributions one can see that after lapping, the number of larger grains is higher for monocrystalline than for polycrystalline diamonds.

The ideas mentioned here can explain why the MRR for the 25 μm polycrystalline grains is lower than that for the monocrystalline diamond.

Based on the presented research some conclusions can be drawn:

- Lapping of alumina parts with diamond slurry can significantly improve the surface roughness after approximately 15 min, for all grit sizes studied. This will help in the optimization of the lapping cycle.
- Abrasive size is one of the most important factors in the lapping process influencing the MRR and surface roughness.

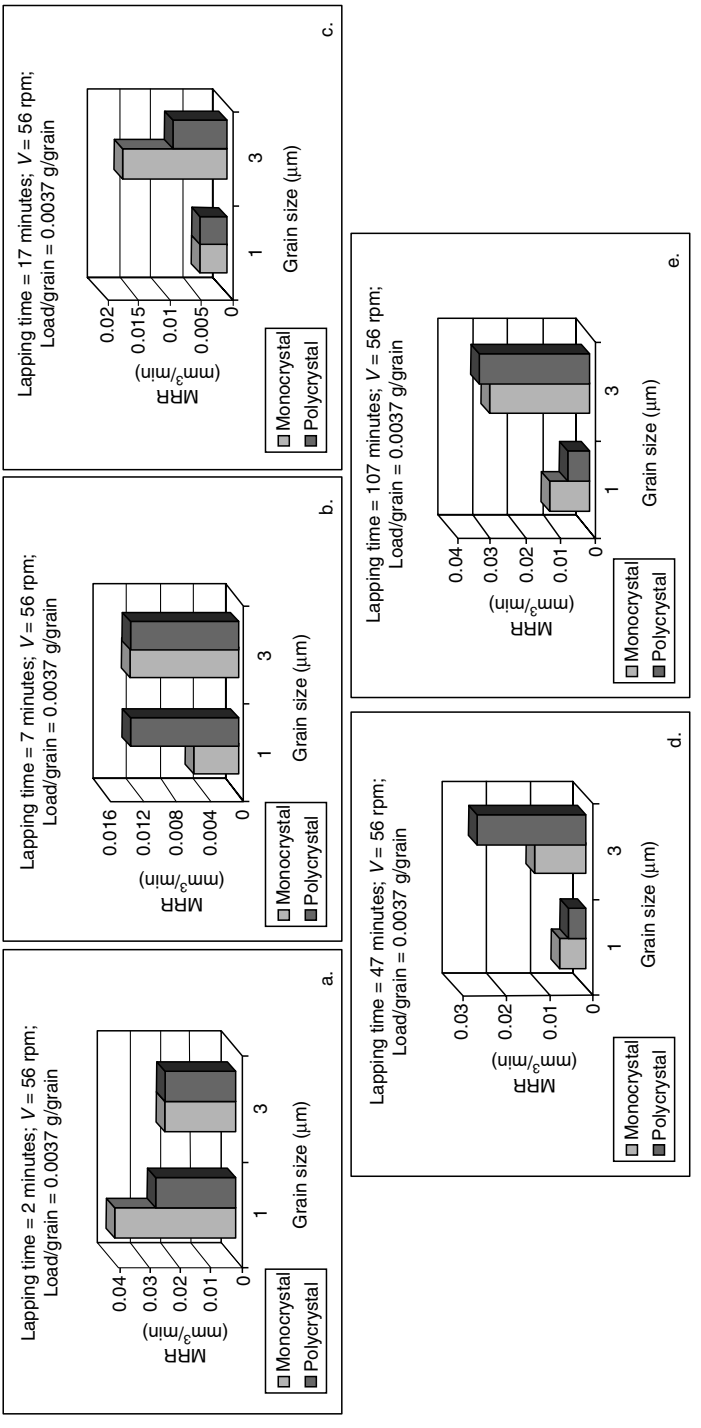

FIGURE 10.5
Material removal rate versus grain size (1 and 3 μm).

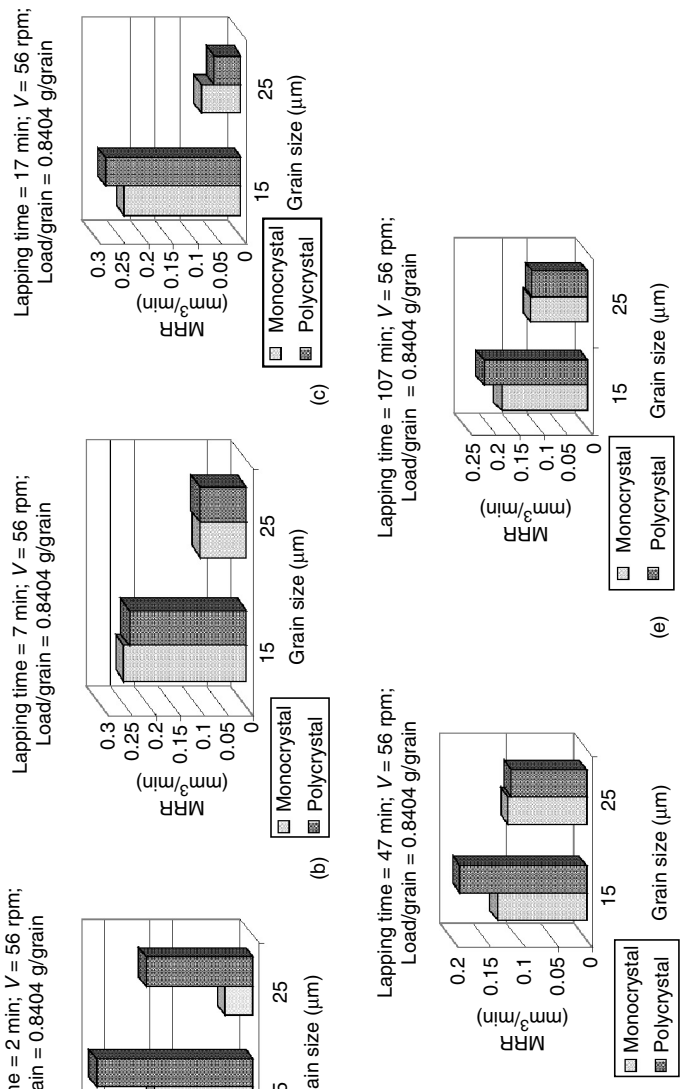

FIGURE 10.6
Material removal rate versus grain size (15 and 25 μm).

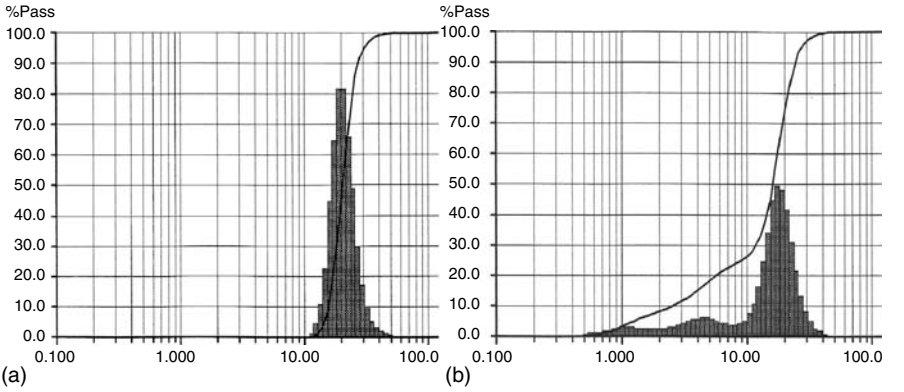

FIGURE 10.7
Grain size distribution for 25 μm monocrystalline diamond: (a) before lapping; (b) after lapping.

- Comparison between the polycrystalline and monocrystalline diamonds suggests using the former for better surface finish and the latter for better MRR.

10.4 Remaining Work

In order to get more relevant results, more values for the rotation of the lapping plate and weights should be considered. Acoustic emission (AE) technique can be used to determine the material removal mechanism in lapping and thus the resulting surface quality. AE signals are very sensitive

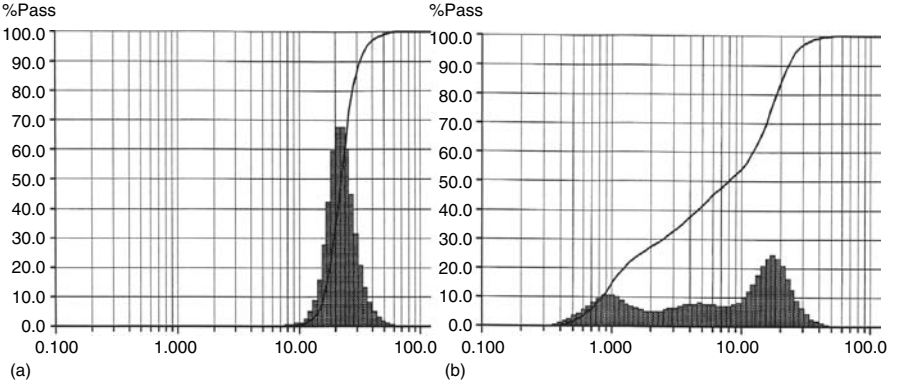

FIGURE 10.8
Grain size distribution for 25 μm polycrystalline diamond: (a) before lapping; (b) after lapping.

to the characteristics of the lapping system such as slurry flow rate, the concentration, and the grit size of the abrasive in slurry. Therefore, this method can be used to optimize the process parameters according to the desired goal.

References

1. Lawn, B.R., and Evans, A.G., Elastic/plastic indentation damage in ceramics: the median radial crack system, *J. Am. Ceram. Soc.*, 1980, 63.
2. Buijs, M., and Korpel-van Houten, K., Three-body abrasion of Brittle materials as studied by lapping, *Wear*, Vol. 166, 1993, pp. 237–245.
3. Chen, C., Sakai, S., and Inasaki, I., Lapping of advanced ceramics. Materials and Manufacturing Processes, Vol. 6, no. 2, 1991, pp. 211–226.
4. Marshall, D.B., Lawn, B.R., and Evans, A.G., Elastic plastic indentation in ceramics: the lateral crack system, *J. Am. Ceram. Soc.*, Vol. 65, 1982.
5. Turco, M., and Marinescu, I.D., Lapping of ceramics, american ceramic society, 97^{th} Annual Meeting, Cincinnati, OH, April 30–May 3, 1995.
6. Benea, I., Micron diamond powder application oriented, Superabrasives & CVD Diamond Theory and Application, Proceedings of the Ultrahard Materials Technical Conference, Windsor, Ontario, Canada, May 28–30, 1998.
7. Benea, I., Micron superabrasives . . . present and future, finer points, Vol. 10, no. 4, 1999.
8. Komanduri, R., Lucca, D.A., and Tani, Y., Technological advances in fine abrasive processes, *Annals of CIRP*, Vol. 46, no. 2, 1997, pp. 545–596.

11

Double Fracture Model in Lapping of Ceramics

I.D. Marinescu

CONTENTS

11.1 Introduction

Advanced ceramic materials offer superior temperature, and tribological and strength characteristics to metals, although the replacement of metal parts with ceramic parts, in many instances, has been hindered by the high cost associated with conversion. Ceramic parts are expensive because of the difficulties in fabrication (20%–30%) and machining (70%–80%). Much of the effort to reduce the cost has been applied to fabrication methods to obtain techniques for near-net shape processing. This goal is much harder to achieve because the required tolerances are tightened every year. Thus, effective and adapted machining methods are required.

The task of machining ceramics differs greatly from metal machining. Metals are more ductile than ceramics, so material removal is primarily done by plastic deformation, which enables us to obtain good surface quality and finish with high dimensional accuracy and with relative ease. However, ceramic material is usually removed through brittle fracture. This mechanism makes it difficult to machine ceramics with good surface quality and integrity. Surface grinding with diamond wheels has been practically applied, but the surface integrity (primarily surface stresses and cracking

damage) suffer because cracks are initiated during grinding, and the resulting surface quality is not sufficient for many applications.

To improve the surface integrity of ceramic materials and to achieve good surface quality, micromachining techniques are used. Lapping, fine-grinding, polishing, honing, and abrasive belt grinding are some of the micromachining methods that are used in achieving this. Material removal is accomplished less aggressively, that is, lesser material removal rates than machining processes and in a more ductile method. Among the processes mentioned, lapping and polishing differ from machining and other micromachining methods in that the abrasive is loose and not bonded to any surface. Lapping and polishing are commonly used to improve the surface of ceramic materials.

11.2 Double Fracture Model

During the lapping process, it is possible to have two types of stock removal mechanism. One of them we named as double fracture mechanism. The fracture is a macrofracture and is the effect of a grain that works like an indenter (Figure 11.1).

At the same time as the fracture, a quantity of energy is transformed in local heat because of the friction and deformation. Unloading fazes the lapping because a small thermal shock, a microfracture, appears on the particles that were just separated by the macrofracture (Figure 11.2).

This mechanism will give us an explanation of what happens in grinding, where the phenomena is more intense because of the dynamics of the process. Even in ductile grinding where the removed material is in a plastic deformed mode because of the thermal shock, the plastic chips suffer a thermal fracture and some of them will be transformed into a powder.

An SEM picture of the collected chips from ductile grinding of alumina oxide shows a spiraled deformed shape like a turning chip (Figure 11.3). Because of this thermal shock, even the ground surface can be affected and some cracks can be observed. To avoid this, some Japanese researchers used a low-power laser to close the cracks after grinding.

These are some hypotheses combined with some evidences regarding this. More detailed research is necessary to elucidate the stock removal mechanism of brittle materials particularly in the case of different types of ceramics.

11.3 Experimental Procedures

11.3.1 Materials

Zirconia-toughened alumina (ZTA) is an aluminum oxide (Al_2O_3) ceramic material in which stabilized zirconia (ZrO_2) is present as a secondary

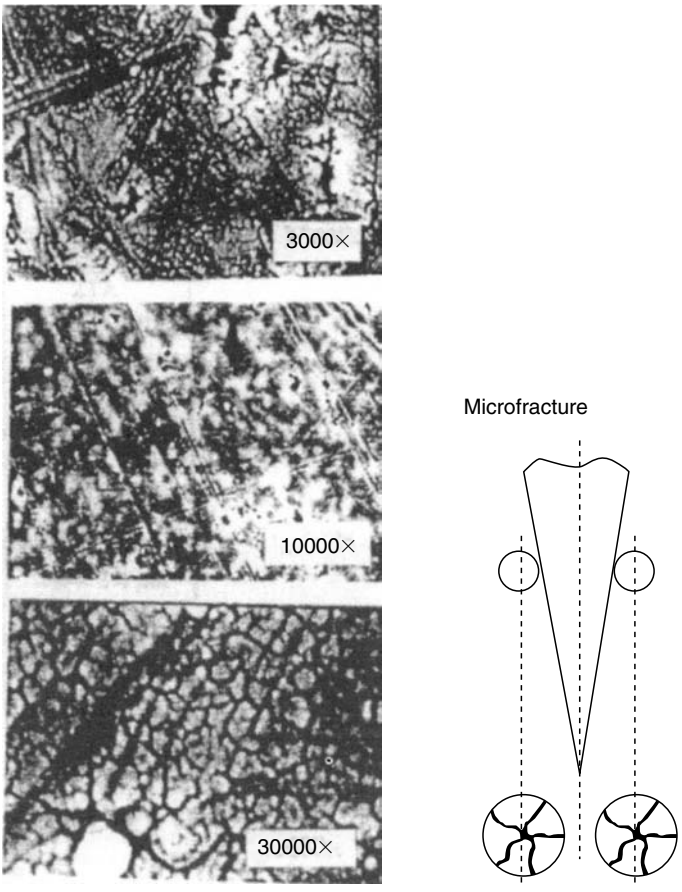

FIGURE 11.1
Microfracture of ceramics.

dispersed phase. It is composed of 80% Al_2O_3 and 20% yttria-stabilized zirconia (15.4% ZrO_2, 4.6% YtO_3). The method of fabrication is hot isostatic pressing (HIP) and then sintering to almost 100% density. The properties are listed in Table 11.1. This material has advantages over single-oxide alumina ceramics because the addition of stabilized zirconia to alumina increases the toughness, strength, and wear resistance while retaining good chemical and heat resistance. The material's tetragonal (metastable) phase to monoclinic (stable) phase transformation provides these enhanced characteristics. ZTA is used for cutting tools and in applications where high abrasion is required.

The material was cut using a diamond saw to obtain dimensions of 1.35 (0.53 in.) × 1.35 cm. The surface to be lapped was surface-ground before lapping. Grinding simulated a machining step that a ceramic part might undergo before lapping. The surface finish was 1.78 μm $R_a \pm 0.89$ μm

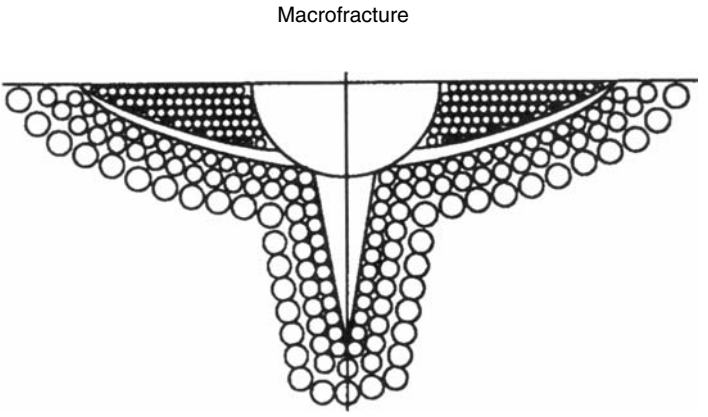

FIGURE 11.2
Macrofracture of ceramics.

(7.0 μin. $R_a \pm 0.5$ μin.). GE man-made standard series diamond powders of sizes 30–40, 10–20, and 2–4 μm were used. The concentration of diamond was kept constant at 7 carats (1.4 g) per 500 mL of carrier.

11.3.2 Apparatus

A Lapmaster 12C, single-side, flat lapping machine was used for experiments. Figure 11.1 and Figure 11.2 illustrate the setup. The 12 in., radially grooved lap plates and conditioning rings were cast iron. The speed of the

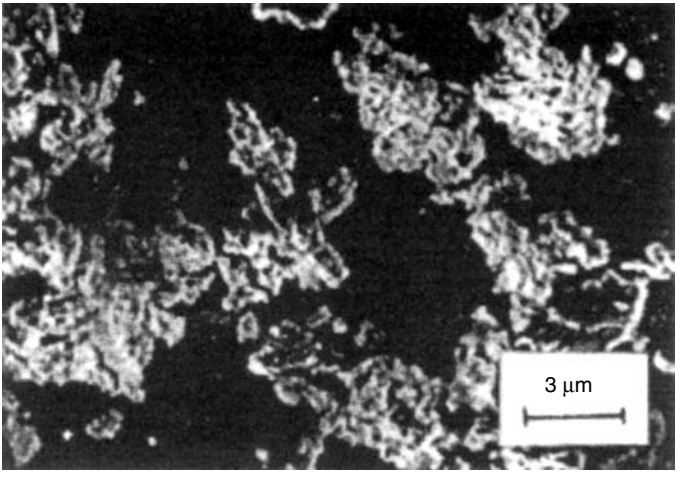

FIGURE 11.3
Ductile ceramic chips.

TABLE 11.1

Properties of Zirconia—Toughened Alumina

Density (g/cm^3)	4.45
Hardness (MPa)	900–1000
Fraction toughness, K_{ic} (MPa $m^{1/2}$)	~7.5
Young modulus (MPa)	2000
Porosity (%)	0.1

lap plate was constant at 56 rpm. Normal force was kept constant at 2.07 kg (4.6 lb). The carrier used was Amplex Corp. type WS/BC (a generic polypropylene glycol carrier). A special carrier type W805 (a new, proprietary carrier) was used in a separate test. A peristatic pump delivered the diamond-carrier slurry at a flow rate of 1.5 mL/min. The lapping power was measured by using a power cell connected to the lap plate drive motor. The surface finish was determined using stylus-type surface analyzer and quantified using the roughness average parameter (R_a). The volume of material removal was calculated by using average thickness values and verified through weight measurements.

11.3.3 Methodology

Lapping experiments were conducted using three abrasives of different size. ZTA workpieces were lapped with all three abrasives in descending order: 30–40, 10–20, and 2–4 μm. Three workpieces were lapped simultaneously. The lap time was 60 min, divided into 4 segments of 15 min each. Surface finish and material removal were measured after each lap segment. Further tests used 10–20 and 2–4 μm abrasive, respectively, to highlight the surface finish performance with respect to time.

11.4 Conclusions

A new model for material removal mechanism was proposed based on the experimental evidences. The ''Double Fracture Model'' was proved in the stock removal mechanism of ceramics lapping.

Based on this model a new technology was developed for laser assisted grinding of ceramics (see chapter 14).

12

Double Side Grinding of Advanced Ceramics with Diamond Wheels

C.E. Spanu, I.D. Marinescu, and M. Hitchiner

CONTENTS

ABSTRACT A double side grinding (DSG) computerized kinematical model accounting for piece rotation inside its slot into the carrier was developed. Trajectories for representative points located on the end faces of the workpiece were simulated. A radial wear gradient of the active surface of the wheel was predicted. Experiments accomplished with different wheel specifications, process parameters, operation duration, and coolant types were carried out. A strong correlation was found between the predicted length of the trajectory of a specific point located on the piece surface and the experimental material removal rate. A radial wear gradient was experimentally confirmed. Conclusions on optimizing the DSG process for advanced ceramics with diamond were drawn.

12.1 Introduction

The cost of abrasive finishing operations applied to ceramic components can count for as much as 75%–80% of the overall manufacturing cost of the part [1], compared with as little as 15%–20% for similar operations applied to conventional metallic components. Lowering this cost by increasing material removal rates is limited by the grinding-induced damage of ceramic component leading to strength degradation [2,3].

The study of abrasive material removal mechanisms of ceramics can be accomplished at two levels: microscopic and macroscopic. The microscopic level involves modeling of the interaction between a single superabrasive grain and the work by a combination of two main mechanisms: brittle fracture—investigated by indentation fracture mechanics [4,5], and plastic deformation—investigated by ductile regime grinding of ceramics at extremely shallow depths of cut [6]. A correlation of the data obtained at the macroscopic level in terms of operation parameters [7,8] with microscopic level interactions is limited by the influence of the random variables that characterize the abrasive operations. Predicting wheel performance is therefore more difficult for abrasive processes than for processes with tools of known geometry.

Abrasive material removal mechanisms of ceramics fall into two main categories: two-body interactions with bonded abrasive (as in grinding), and three-body interactions using loose abrasive (as in lapping and polishing). As shown in previous work [9], one important goal of ceramic abrasion research consists in promoting a highly productive, economical, easy-to-automate, and ecologically friendly grinding process that generates smooth and geometrically precise surfaces with low subsurface damage, and that can successfully replace slower three-body abrasion processes. Extensive studies in double side grinding (DSG) [9–12] modeled the kinematics of the process to analyze the path types, the velocities of workpieces, and the kinematical possibilities of different machine tools. These studies concluded that modifying path types can improve both surface finish and geometry by up to 30% and 40%, respectively, but at a cost of 50% reduction in material removal rate.

According to Uhlmann and Ardelt [9,10], greater changes in performance can be achieved by varying the path type than by varying the grinding pressure or path velocity.

The present research deals with a kinematical model of the DSG operation that, innovatively, accounts for the cylindrical workpiece rotation inside the accommodation slot into the carrier. Trajectories for representative points located on the end surfaces of the workpieces are simulated. Theoretical conclusions on surface finish of the ground components and on wear of active surface of the wheel were drawn.

Experimental studies were conducted to validate the model. DSG experiments were conducted under a range of conditions: with different wheel

specifications, coolants and cooling strategies, and values of process parameters.

A significant correlation between the simulated parameters of the model and the experimental results of the grinding tests validated the model as a useful tool for predicting the DSG operation efficiency.

The predicted radial wear gradient of the active surface of the super-abrasive wheel was also validated.

12.2 Kinematical Model for the Double Side Grinding Operation

During the DSG process, cylindrical workpieces of radius r_p are freely accommodated in specially designed slots into the carriers and moved simultaneously between the two counter-rotating grinding wheels, as shown in Figure 12.1. Three to six carriers follow a planetary motion pattern, led between a fixed external rim and a rotary internal pin.

Technically, this mechanism is a 2K-H internal planetary gear system, in which the sun gear role is played by the internal pin that has z_i teeth and a radius r_i, the planet gear is played by the carriers that each have a number of z_c teeth and a radius r_c, and, finally, the internal gear role is played by the fixed external rim that has z_e teeth.

An eccentric placement of the pieces with respect to the center of the carrier, r_e, offers significant advantages when compared to a circular arrangement [9,10], especially, in preventing the formation of the wear

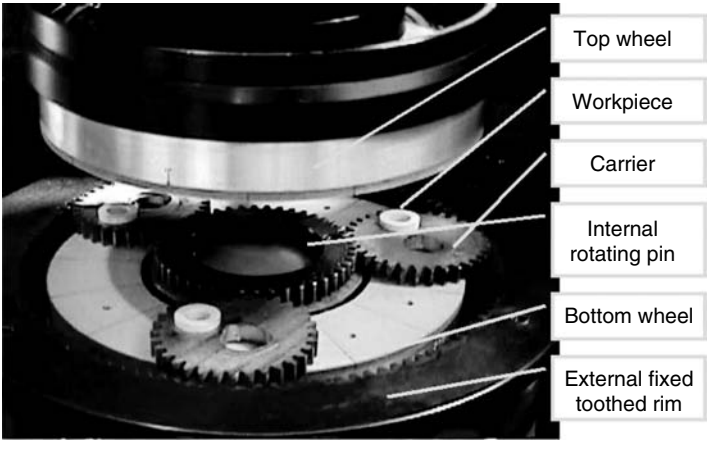

FIGURE 12.1
Components of the double side grinding system.

grooves, a conclusion that will be confirmed and explained further by the present paper, too.

The analytical description of the complex kinematics of the operation is based on three coefficients. The coefficient K_t describes the ratio of the revolving velocity of the carrier's center around the global center, n_q, to the internal pin rotational speed, n_i, and is mathematically described by the relation:

$$K_t = \frac{n_q}{n_i} = \frac{\frac{z_i}{z_e}}{1 + \frac{z_i}{z_e}} = \frac{1}{1 + \frac{z_e}{z_i}}. \tag{12.1}$$

The second coefficient, K_c, describes the ratio of the revolving velocity of the carrier's center to the rotational speed of carrier itself, n_c, and is given by

$$K_c = \frac{n_q}{n_c} = \frac{\frac{z_i}{z_e}}{\frac{z_i}{z_e} - \frac{z_i}{z_c}} = \frac{1}{1 - \frac{z_e}{z_c}}. \tag{12.2}$$

Finally, the speed ratio, K_n, describes the ratio of the revolving velocity of the carrier's center to the rotational speed of the grinding wheel, n_w, ($n_w = n_b$ for bottom wheel and $n_w = -n_u$ for upper wheel), and is given by

$$K_n = \frac{n_q}{n_w} = K_t \cdot \frac{n_i}{n_w} \tag{12.3}$$

Whereas the first two coefficients are constant for a given setup, the last one can vary according to the specific values of the rotational velocities of the wheels.

A fourth coefficient, K, based on the coefficients introduced in Equation 12.1 and Equation 12.3 and one that is very useful in practice, is a multiplication factor that relates two controllable process parameters: the rotational speed of the internal pin and the rotational speed of the bottom and upper grinding wheels, respectively, defined by

$$K = \frac{n_w}{n_i} = \frac{K_t}{K_n} \tag{12.4}$$

According to the geometrical model presented in Figure 12.2, the instantaneous global location vector for the center of the workpiece is given by

$$\bar{r} = \begin{pmatrix} \bar{i} \\ \bar{j} \end{pmatrix}^T \cdot \begin{pmatrix} \cos(\theta_q) & \cos(\theta_c) \\ \sin(\theta_q) & \sin(\theta_c) \end{pmatrix} \cdot \begin{pmatrix} r_i + r_c \\ r_e \end{pmatrix}, \tag{12.5}$$

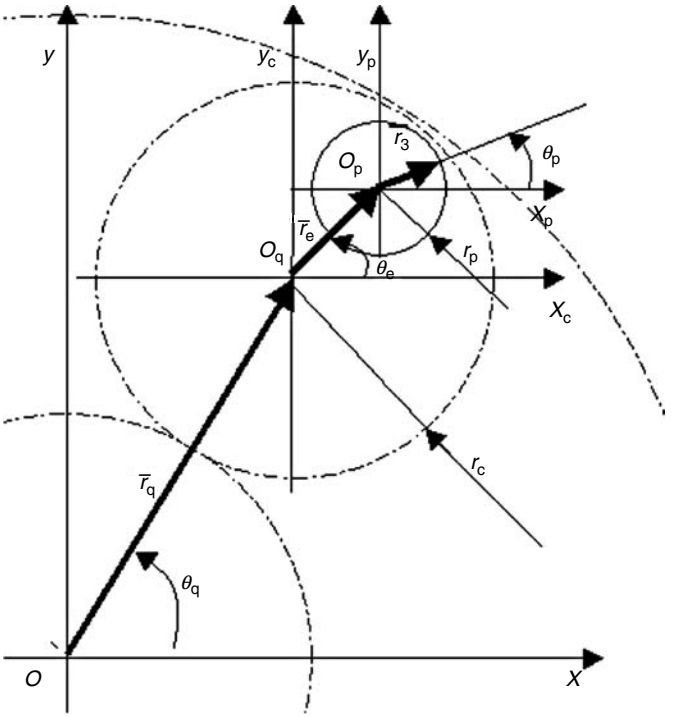

FIGURE 12.2
Geometrical model for double side grinding.

where the instantaneous rotation angle of the internal pin and of the carrier, θ_q and $\theta_{c,}$ are, respectively, calculated in the relations:

$$\theta_q\,[\text{degrees}] = n_q\,[\text{rpm}] \cdot \frac{360}{60} \cdot t\,[\text{sec}]$$
$$\theta_c\,[\text{degrees}] = n_q\,[\text{rpm}] \cdot \frac{1}{K_c} \cdot \frac{360}{60} \cdot t\,[\text{sec}] \tag{12.6}$$

The offset location of the accommodation slot with respect to the center of the carrier can vary between zero and a value defined geometrically in Figure 12.3 and modeled mathematically by the relation:

$$(r_e)_{\max} = \min\{r_c - r_p, (r_{ew} - r_p) - (r_i + r_c), (r_i + r_c) - (r_{iw} + r_p)\}, \tag{12.7}$$

where r_{ew} and r_{iw} are the external and the internal radius of the grinding wheel, respectively.

As the bottom and the upper wheel are counter-rotating with a velocity n_w, the workpiece center describes different trajectories on the active surface of each of the two wheels, trajectories that are altered (stretched or

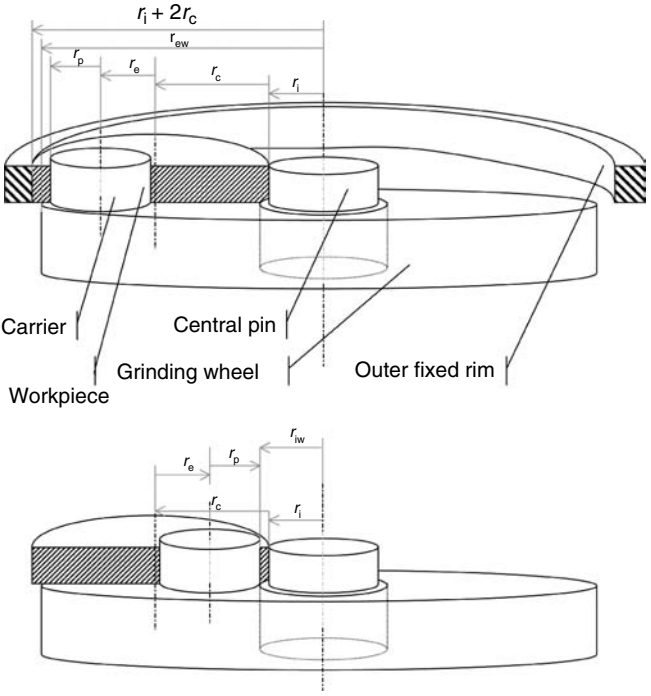

FIGURE 12.3
Dimensional chains for the workpiece offset value with respect to the center of carrier.

compressed) when compared with the global trajectory recorded in a global fixed coordinate system, according to the relation:

$$\bar{\mathbf{r}}_w = \mathcal{R}_{\mathrm{w}} \cdot \bar{\mathbf{r}}, \tag{12.8}$$

where the grinding wheel rotational matrix, $\mathcal{R}_{\mathrm{w}}$, is given by

$$\mathcal{R}_{\mathrm{w}} = \begin{pmatrix} \cos(\theta_{\mathrm{w}}) & \sin(\theta_{\mathrm{w}}) \\ -\sin(\theta_{\mathrm{w}}) & \cos(\theta_{\mathrm{w}}) \end{pmatrix}, \quad \theta_{\mathrm{w}} = n_{\mathrm{w}} \cdot \frac{360}{60} \cdot t \tag{12.9}$$

By employing the global coordinates of center of workpiece from Equation 12.5, the rotational matrix from Equation 12.9, and the expression of the speed ratio coefficient from Equation 12.2 in Equation 12.8, the general expression of the global coordinates of the trajectory of the workpiece center onto the active surface of the wheel can be written as

$$\bar{\mathbf{r}}_w = \begin{pmatrix} \bar{\mathbf{i}} \\ \bar{\mathbf{j}} \end{pmatrix}^{\mathrm{T}} \cdot \begin{pmatrix} \cos(\theta_{\mathrm{q}} - \theta_{\mathrm{w}}) & \cos(\theta_{\mathrm{c}} - \theta_{\mathrm{w}}) \\ \sin(\theta_{\mathrm{q}} - \theta_{\mathrm{w}}) & \sin(\theta_{\mathrm{c}} - \theta_{\mathrm{w}}) \end{pmatrix} \cdot \begin{pmatrix} r_{\mathrm{i}} + r_{\mathrm{c}} \\ r_{\mathrm{e}} \end{pmatrix} \tag{12.10}$$

This expression describes a compressed hypotrochoid on the active surface of the bottom wheel, and an elongated hypocycloid on the active surface of the upper wheel.

To prevent the wear track formation on the active surfaces of the grinding wheels, the trajectory of the workpiece's center in local wheel coordinate systems should avoid resembling a multi-cusp curve. Thus, the rotational speeds to be avoided are calculated accordingly.

The workpiece's center travels on the active surface of the wheel and makes one complete orbit in a time period of:

$$T\ [\text{sec}] = \frac{60}{n_\text{w} - n_\text{q}} = \frac{60}{n_\text{q}} \cdot \frac{K_\text{n}}{1 - K_\text{n}} \tag{12.11}$$

The center of the workpiece will be at the same distance with respect to the center of the wheel as initially was, r_w, after a period of time given by

$$\Delta t\ [\text{sec}] = \frac{360}{6 \cdot n_\text{q}\ [\text{rpm}] \cdot \left(1 - \dfrac{1}{K_\text{c}}\right)} \tag{12.12}$$

When the period defined in Equation 12.11 is formed by an integer number of times, N, of duration time defined in Equation 12.12, the resulting trajectory will be an N-cusped hypotrochoid, a curve that must be avoided, as shown earlier, to prevent the wear track formation. Therefore, for each value of the rotational speed of the internal pin, n_i, the values of the rotational speed of the grinding wheel to be avoided are given by the relation:

$$n_\text{w}^\text{avoid} = n_\text{i} \cdot K_\text{t} \cdot \left(1 + \frac{1 - \dfrac{1}{K_\text{c}}}{N}\right), \quad N \in \boldsymbol{Z}^* \tag{12.13}$$

Negative integer values of N characterize the rotational speeds of the upper wheel that need to be avoided, whereas the positive integer values of the same determine the rotational speeds of the bottom wheel to be avoided to prevent uneven wear of the tool's active surface.

To simulate the trajectory of a point A located on the workpiece's outer diameter at an angle ψ with respect to global abscissa, the friction between the workpiece and the slot was neglected. In these conditions, the workpiece is free to rotate inside the slot with an instantaneous angular velocity, ω_p, determined by the complex interaction between the planetary motion of the carrier around the global center, and the instantaneous rotation of the carrier with respect to its center.

The location vectors of the point A with respect to both global origin and carrier center, $\bar{\text{r}}_{\text{A/O}}$ and $\bar{\text{r}}_{\text{A/O}_c}$, are, respectively, described by the relations:

$$\bar{\mathbf{r}}_{A/O} = \bar{\mathbf{r}} + r_p \cdot \begin{pmatrix} \bar{\mathbf{i}} \\ \bar{\mathbf{j}} \end{pmatrix}^T \cdot \begin{pmatrix} \cos(\psi) \\ \sin(\psi) \end{pmatrix}$$

$$\bar{\mathbf{r}}_{A/O_c} = \begin{pmatrix} \bar{\mathbf{i}} \\ \bar{\mathbf{j}} \end{pmatrix}^T \cdot \left[r_e \cdot \begin{pmatrix} \cos(\theta_c) \\ \sin(\theta_c) \end{pmatrix} + r_p \cdot \begin{pmatrix} \cos(\psi) \\ \sin(\psi) \end{pmatrix} \right] \tag{12.14}$$

Accordingly, the tangential projections of the instantaneous velocity vectors of point A, V_q^{rot} and V_p^{rot}, are, respectively, calculated using the relations:

$$V_q^{rot} = \omega_q \cdot r_{A/O} \cdot \cos(\psi - \delta_q)$$
$$V_p^{rot} = \omega_c \cdot r_{A/O_c} \cdot \cos(\psi - \delta_p) \tag{12.15}$$

The instantaneous angular velocity of the workpiece alone, ω_p, is numerically determined as the resultant of the instantaneous angular velocities of all points located on the outer diameter of the workpiece, as presented in the relation:

$$\omega_p = \begin{cases} M + m, & \text{if } M \times m \leq 0 \\ M, & \text{if } |M| > |m|, \\ m, & \text{if } |M| \leq |m| \end{cases} \tag{12.16}$$

where:

$$M = \max\left\{ \frac{V_q^{rot} + V_p^{rot}}{r_p} \right\}; m = \min\left\{ \frac{V_q^{rot} + V_p^{rot}}{r_p} \right\}. \tag{12.17}$$

In general, the instantaneous global location of a random point R located on the end surface of the workpiece at a distance r_{rand} with respect to the center of the workpiece, is a combination of three rotations: the rotation of the carrier's center around the global origin, the rotation of the carrier itself, and the rotation of the workpiece inside its slot, and it is modeled mathematically by

$$\bar{\mathbf{r}}_r = \begin{pmatrix} \bar{\mathbf{i}} \\ \bar{\mathbf{j}} \end{pmatrix}^T \cdot \begin{pmatrix} x_r \\ y_r \end{pmatrix} = \bar{\mathbf{r}} + r_R \cdot \begin{pmatrix} \bar{\mathbf{i}} \\ \bar{\mathbf{j}} \end{pmatrix}^T \cdot \begin{pmatrix} \cos(\omega_p t) \\ \sin(\omega_p t) \end{pmatrix}, \tag{12.18}$$

where r_R is the distance between the random point R and the center of the workpiece.

As the upper and the bottom wheels are counter-rotating, the trajectories described by the random point R on the active surface of each of the two wheels are altered with respect to the global trajectory presented in Equation 12.18, according to the relation:

$$\bar{\mathbf{r}}_{r/w} = \begin{pmatrix} \bar{\mathbf{i}} \\ \bar{\mathbf{j}} \end{pmatrix}^T \cdot \begin{pmatrix} x_{r/w} \\ y_{r/w} \end{pmatrix} = \mathcal{R}_w \cdot \bar{\mathbf{r}}_r. \tag{12.19}$$

Finally, the length of the trajectory of the random point R, in global coordinates and with respect to the local coordinate system of each grinding wheel are, respectively, calculated for a number, i, of different positions using the relations:

$$l_{\mathrm{r}} = \sum_{i} \sqrt{\left(x_{\mathrm{r}_{(i)}} - x_{\mathrm{r}_{(i-1)}}\right)^2 + \left(y_{\mathrm{r}_{(i)}} - y_{\mathrm{r}_{(i-1)}}\right)^2} \tag{12.20a}$$

$$l_{\mathrm{r/w}} = \sum_{i} \sqrt{\left(x_{\mathrm{r/w}_{(i)}} - x_{\mathrm{r/w}_{(i-1)}}\right)^2 + \left(y_{\mathrm{r/w}_{(i)}} - y_{\mathrm{r/w}_{(i-1)}}\right)^2} \tag{12.20b}$$

12.3 Trajectory Simulation

For the machine tool used during this experimentation, an Italian double-sided grinder SP-3 type 210-3P made by Melchiorre Officina Meccanica SRL, the internal pin has $z_{\mathrm{i}} = 44$ teeth, the carriers have $z_{\mathrm{c}} = 32$ teeth, and the fixed external rim has $z_{\mathrm{e}} = 108$ teeth. The geometrical parameters have the following values: the radius of the internal pin $r_{\mathrm{i}} = 46.8$ mm, the radius of the carrier $r_{\mathrm{c}} = 33.3$ mm, the offset position of the slot $r_{\mathrm{e}} = 11.4$ mm, and the outer radius of the workpiece $r_{\mathrm{p}} = 10.3$ mm.

Accordingly, the constant coefficients have the values of: $K_{\mathrm{t}} = 0.2895$ and $K_{\mathrm{c}} = -0.4211$.

There are several different types of cycloids described on the active surface of the wheels, in function of the value of multiplication factor K. The most representative types of trajectories are shown in Figure 12.4. The resultant instantaneous angular velocity of the piece, ω_{p}, varies between 0 and -2.72 rad/sec, according to the variation function presented in Figure 12.5.

The trajectory of a point fixed on the slot after one revolution of carrier around the global center is represented by the red curve, whereas the trajectory of a point fixed on the outer diameter of the workpiece is represented by the black curve in Figure 12.6 (all the dimensions are in millimeters). The two points coincided initially, when the carrier started its counterclockwise revolution around the center from the 3 o'clock location. The differences occur because of the variation in the instantaneous rotation value of the workpiece inside the slot.

The simulation of the trajectory of a point located on the outer diameter of the piece, for 20 revolutions of the carrier around the global center, is depicted in Figure 12.7. This simulation offers indications of wheel wear

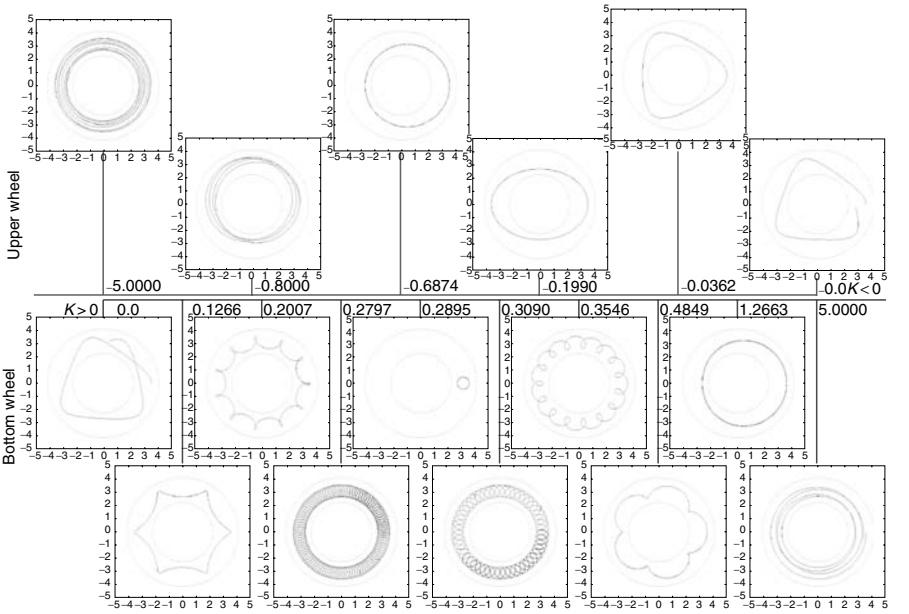

FIGURE 12.4
Type of hypotrochoidal curves generated for different values of the speed ratio coefficient K.

dynamics. As it can be observed, the wear track density decreases from the internal diameter of the wheel toward the outer diameter, generating a radial gradient for the tool wear. This is an inherent result of the process kinematics and is independent of geometrical or process parameters.

The variation of only three input parameters can generate significant variation of the output parameters. These three input parameters are: the slot's eccentricity, the wheel rotational speed, and the value of the K_n coefficient defined in Equation 12.3.

As it can be concluded from Equation 12.20a, the ideal global trajectory of any point fixed on the end surface of the workpiece is not influenced by the kinematical parameters, but only by the geometrical parameters of the planetary gear system, which are fixed for each setup and machine tool utilized. Conversely, the trajectories of the same point on each active surface of the bottom and upper grinding wheels are, respectively, influenced by the wheel rotational speed, but only when the coefficient from Equation 12.3 is variable.

For different values of the slot eccentricity, the trajectory of the workpiece's center, expressed in the global coordinates system, is altered gradually from a circle at $r_e = 0$ to a three-cusp concave curve with accentuated curvature for higher eccentricity values, as it can be observed in Figure 12.8. As it can be observed in Figure 12.9, the trajectories of four points, located at the intersection of the workpiece diameter with inner and

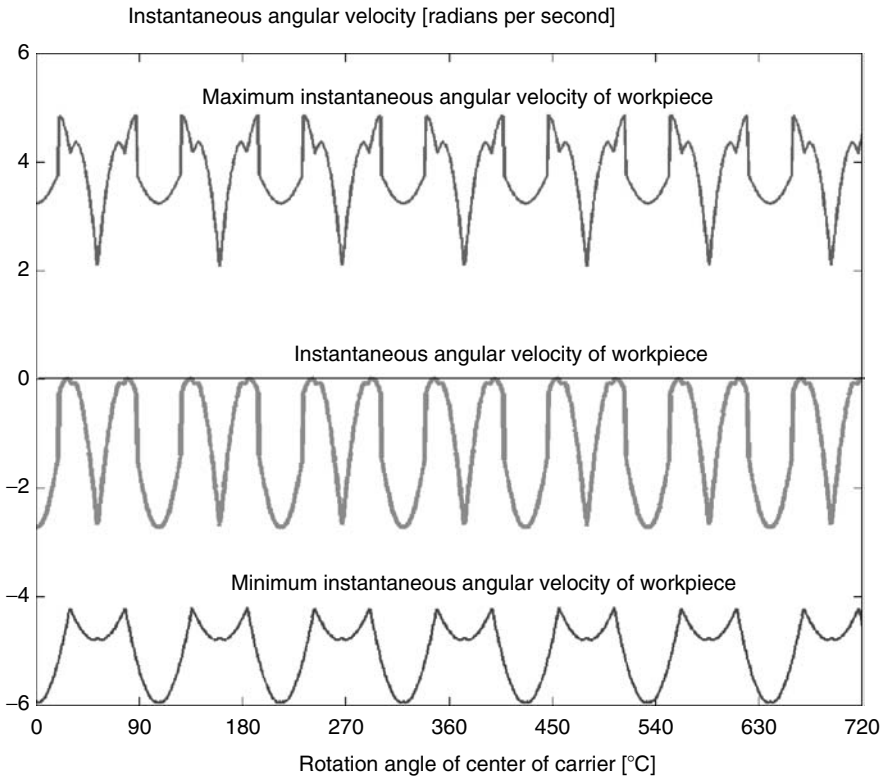

FIGURE 12.5
The variation of the instantaneous angular velocity of the workpiece for two revolutions of the carrier around the global origin.

outer diameters of the piece, described on the active surface of the bottom wheel, tend to have lesser and larger cusps when the value of the eccentricity r_e increases from 0 to 12 mm (the latter value is calculated for the current setup used according to Equation 12.7).

For different rotational speeds of the grinding wheels, limited currently by the machine capabilities between 0 and 250 rev/min, the trajectory of the center of the workpiece is altered, as presented in Figure 12.10, from a multi-cusp curve to a pure circle ($n_w = n_q$), and again to another multi-cusp curve, to end as a planet-orbit-like curve at the highest rotational speeds.

For decreasing values of the K_n coefficient within the feasible interval (from 0 to 1), the trajectory of the workpiece's center on the active surface of the bottom wheel is altered from a circle to a hypotrochoid that has lower number of cusps for lower values of the coefficient, and, finally, to planetary curves with an increased coverage of the active surface of the grinding wheel for lowest values of the speed ratio.

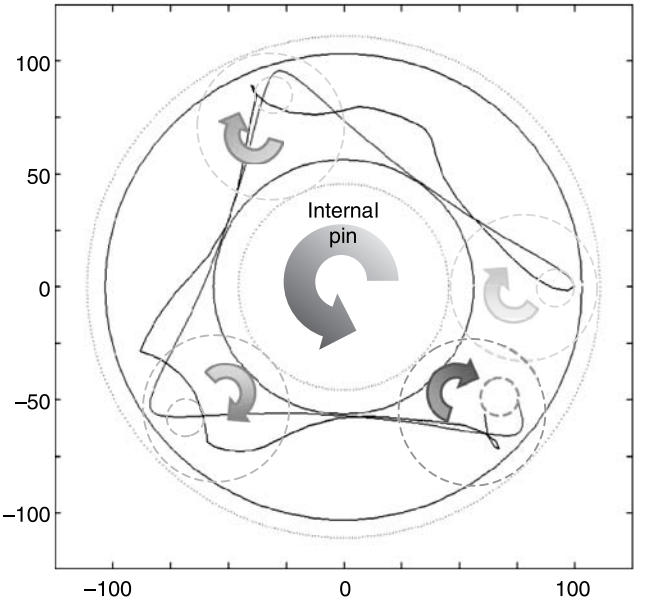

FIGURE 12.6
The trajectory of two points after one revolution of the carrier.

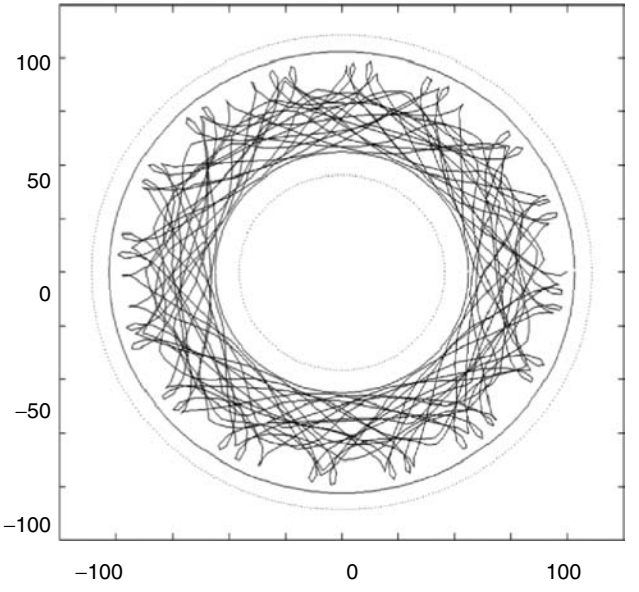

FIGURE 12.7
The trajectory of one point after 20 revolutions of the carrier.

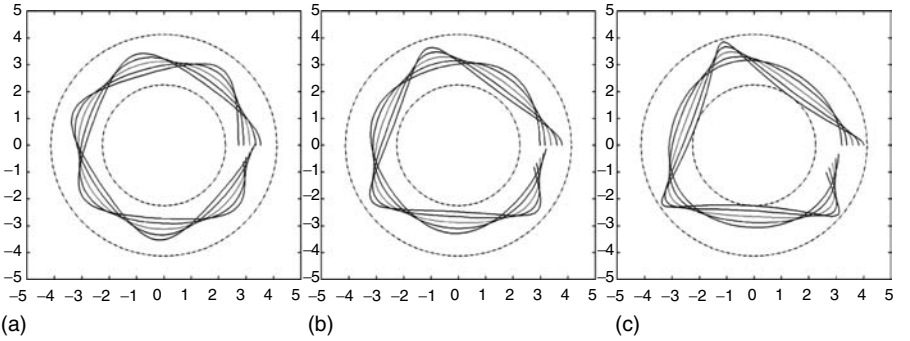

FIGURE 12.8
Trajectories of the workpiece's center and four other representative points located on the work surface, expressed in global coordinates, for offset values r_e of: (a) 0 mm; (b) 6.35 mm; (c) 12 mm.

12.4 Experimental Validation

Factorial experiments of DSG of alumina ceramics with diamond were carried out in the experimental conditions listed in Table 12.1. Before each experiment, the wheels were dressed to a completely restored cutting ability according to the bond type: the vitrified bond wheel was dressed mechanically with silicon carbide superfine dressing sticks, whereas the metal bond wheel was predressed using an electrolytic in-process dressing (ELID) technique.

A complete set of experimental results are presented elsewhere [13,14]. It was reported that wheel speed and specific pressure between the tool and work are significant for the variation of measured parameters, and that the

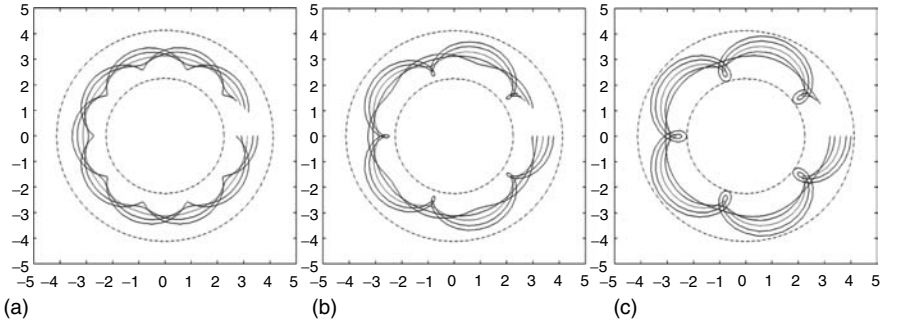

FIGURE 12.9
Trajectories of the workpiece's center and four other representative points located on the work surface, expressed in local coordinates of the bottom grinding wheel, for offset values r_e of: (a) 0 mm; (b) 6.35 mm; (c) 12 mm.

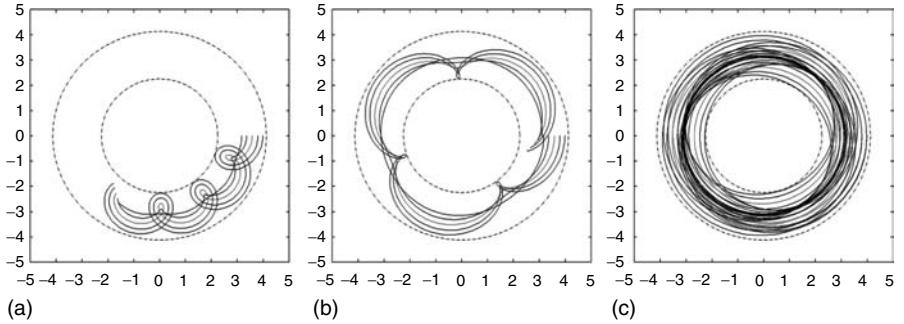

FIGURE 12.10
Trajectories of the workpiece's center and four other representative points located on the work surface, expressed in local coordinates of the bottom grinding wheel, for rotational speed values of the bottom wheel n_b of: (a) 20 rpm; (b) 30 rpm; (c) 100 rpm.

coolant applied under pressure in the grinding zones dramatically improves the tool performance and tool life. In the present report the correlation between the length of the simulated trajectory of the workpiece's center and the operation productivity is quantified.

For each of the three tests, both the values of the trajectory length and the corresponding value of volume of stock removed were used to define the regression model. Each point on the graph is the average of at least six experimental values. The standard deviation was found to spread between 10.2% and 0.6%.

As both the abrasive grain size and the specific pressure influence the real depth of cut at microscopic level, thus influencing the volume of material removed, and as the present model deals with macroscopic level phenomena only, for each value of grain size and specific pressure experimentally explored, specific linear regression equations were written. Noticeably, the dry experiment did not generate consistent data; this aspect is discussed later in this paper.

TABLE 12.1
Values of Parameters for the Test Runs

Grain size [μm]	Concentration	Bond Type	Specific Pressure [MPa]	Coolant Type	Wheel Speed [rpm]	Carrier Speed [rpm]
3.25	50	Metal	0.068	Synthetic	60, 75, 150	7, 12
9	100	Vitrified	0.068	Synthetic	60, 75, 150	7
9	100	Vitrified	0.203	Synthetic	60, 75, 150	7
9	100	Vitrified	0.068	Dry	60, 125, 200	4, 10
9	100	Vitrified	0.203	Dry	60, 125, 200	4, 10

TABLE 12.2

Mathematical Formulation of Regression Models

Grain Size [μm]	Specific Pressure [MPa]	Cooling Strategy	Regression Equation QMR l	R^2	Residuals, Average ± Standard Deviation
3.25	0.068	Coolant	QMR = 0.027 l	0.985	−5.4% ± 15.8%
9	0.068	Under	QMR = 0.855 l	0.991	−7.1% ± 10.1%
9	0.203	Pressure	QMR = 1.695 l	0.994	−3.6% ± 5.1%
9	0.068–0.203	Dry	No correlation	N/A	N/A

For each regression equation, relative predictive power of linear model, R^2, average values, and standard deviation values for the residuals are detailed in Table 12.2.

Figure 12.11 plots the results of the three experiments: the 3.25-μm test, the wet-9-μm test, and the dry-9-μm test, in terms of volume of material removed V_w as a function of the length of the trajectory on the bottom wheel. The high values of R^2 (generally higher than 0.985) indicate a very strong correlation between the volume of material removed and the calculated length of trajectory. Thus, the mathematically formulated model is validated to be used in predicting the volume of material removed as a function of known kinematical parameters.

12.5 Discussion of Results

As presented earlier, the variation of only three factors, specifically, the slot's eccentricity, the wheel rotational speed, and the speed ratio coefficient K_n, leads to different output parameters generation. From these three, the value of the slot's eccentricity is least influential as it causes only slight aspect modifications of the trajectories without significant improvements in the wheel surface coverage.

Conversely, the modification of the speed ratio coefficient K_n is most influential because it causes drastic modifications of the type, aspect, and size of the curve. The simulation shows that better coverage of the active surface of the wheel is obtained for large values of the coefficient, when the trajectories resemble planetary orbits. In the same time, there are values of the coefficient determined in Equation 12.13 that need to be avoided to prevent uneven wear on the active surface of the wheels. In general, better coverage of the active surface of the wheel is obtained for larger values of eccentricity, lower values of speed ratio coefficient, and higher rotational speeds of the wheels.

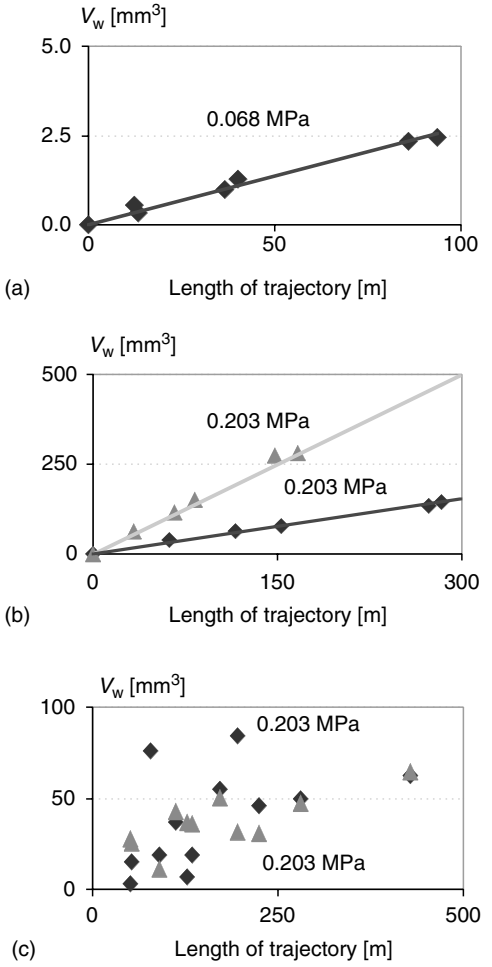

FIGURE 12.11
Volume of material removed vs. length of trajectory for: (a) wet DSG with 3.25 micron grit size wheel; (b) wet DSG with 9 micron grit size wheel, for two values of pressure; and (c) dry DSG with 9 micron grit size wheel, for the same two values of pressure.

The present kinematical model shows that the rotation of the workpiece inside its slot helps in complicating the path along which a random point located on the end surface of the piece travels during the process. This helps to continually alter the grinding direction leading to improved surface finish and geometry.

The real-time process simulation predicts the development of a radial gradient of the wheel wear track density. Regardless of the value of slot eccentricity, and wheel and carrier rotational speed values, the density of

the grinding tracks is higher in circular sections closer to the wheel's internal diameter, and rarer in circular sections closer to the wheel's external diameter, as seen in Figure 12.7. This is an inherent result of the process kinematics and cannot be overcome by controlling the process parameters. This theoretical result is confirmed practically by the uneven erosion during the process of an adherent layer, initially deposited on the active surface of the wheel, as it can be observed in Figure 12.12. The layer is intensively worn in circular sections close to the wheel's inner diameter and barely scratched toward the outer diameter of the wheel.

A strong correlation between the length of the simulated trajectory of the workpiece's center and the operation productivity was experimentally observed. As the grain depth of cut is influenced by microscopic parameters that cannot be accounted for in a macrokinematical model (as grain size and specific pressure), the predictive model must be either calibrated for each value of grain size and specific pressure utilized, or integrated by a wheel

FIGURE 12.12
Radial wear gradient of the diamond wheel.

topographical model with an analytical model that describes the interaction between a single abrasive grain and the work surface. The former solution was adopted for the present paper, whereas the latter is described *in extenso* elsewhere [15].

The experiments revealed that all wet tests consistently generated highly correlated data, whereas the dry test did not. This can be explained by the advantages gained when using an effective grinding fluid and a correctly chosen cooling strategy [13]: the wheel's cleanliness is maintained throughout the process, the real depth of cut is better controlled, the three-body abrasion promoted by the fine diamond breaks is eliminated, the grinding temperature is controlled, etc.

The average grit size has the most dramatic influence over the process productivity, with the 9-μm abrasive size wheel hundred times more efficient in removing material than the 3.25-μm abrasive size wheel in similar conditions. This difference in productivity can be explained mainly by two effects: (1) connection with the grain depth of cut and (2) abrasive concentration, but not by an interaction of these two, as the protrusion height distribution is a function of grain size alone and is independent of the concentration [16]. Thus, the selection of the right grain size and the correct abrasive concentration for each particular application is more important for process productivity and surface finish than the choice of any other process parameters.

A three-time increase in the specific pressure between the wheel and the workpiece generated a two-time more efficient operation. This can be explained by the correlation between an increased depth of cut and the shape, size, and number of active abrasive grains.

12.6 Conclusions

A kinematical model for the DSG operation accounting, first in this research, for workpiece rotation inside the slot into the carrier is described. Trajectories of different points located on the machined surfaces are simulated and dimensionally and geometrically characterized. The correlation between the length of the trajectory of the workpiece's center and the material removing productivity is mathematically modeled. A radial gradient for the wheel wear, with track density values decreasing from the internal diameter of the wheel toward its external diameter, was predicted and experimentally demonstrated.

Significant correlation between the simulated parameters of the model and experimental results qualifies the calibrated model as an accurate predicting tool for the DSG productivity.

References

1. Malkin, S. and Hwang, T.W., Grinding mechanisms of ceramics. *Annals of CIRP*, 1987, 45(2), 569–580.
2. Hwang, T.W., Grinding energy and mechanisms for ceramics. *Ph.D. Dissertation*, 1997, University of Massachusetts, Amherst.
3. Liao, T.W., Flexural strength of creep feed ground ceramics: general pattern, ductile–brittle transition and MLP modeling. *International Journal of Machining Tools Manufacturing*, 1998, 38(4), 257–275.
4. Lawn, B.R., Evans, A.A., and Marshall, D.B., Elastic–plastic indentation damage in ceramics—the median-radial crack system. *Journal of American Ceramic Society*, 1980, 63(9–10), 574–581.
5. Inasaki, I., Grinding of hard and brittle materials. *Annals of CIRP*, 1987, 36(2), 463–471.
6. Bifano, T.A., Dow, T.A., and Scattergood, R.O., Ductile regime grinding: a new technology for machining brittle materials. In Proceedings of the Intersociety Symposium on Machining of Advanced Ceramic Materials and Components, 1988, *ASME,* 113–120.
7. Chen, M.K., Analysis and modeling of creep feed grinding of alumina and zirconia ceramics to optimize parameters for minimum strength degradation. *Ph.D. Dissertation*, 1992, Lehigh University, Pennsylvania.
8. Liao, T.W., Creep feed grinding of alumina with diamond abrasive wheels. *Ph.D. Dissertation*, 1990, Lehigh University, Pennsylvania.
9. Uhlmann, E. and Ardelt, T., Influence of kinematics on the face grinding process on lapping machines. *Annals of CIRP*, 1999, 48(1), 281–284.
10. Uhlmann, E. and Ardelt, T., Kinematics and wheel wear in face grinding on lapping machines. In Progress of Cutting and Grinding—International Academic Publishers, 1998, 251–256.
11. Shanbhag, N., Rajan, M., Manjunathaiah, S., Krishnamurty, S., and Malkin, S., Analysis and simulation of double disc grinding. *Transactions of NAMRI/SME*, 1998, 26, 111–116.
12. Klamecki, B., Material removal asymmetry in the double-side polishing process. *Transactions of NAMRI/SME*, 1998, 26, 177–182.
13. Marinescu, I.D., Spanu, C., Nelson, A., and Hoff, M., Coolants evaluation for diamond double side grinding of ceramic materials. Society of Tribologists and Lubrication Engineers Annual Meeting, New York, section 5D, 2004.
14. Spanu, C., Marinescu, I., Pruteanu, M., and Hitchiner, M., Experimental comparison between two- and three-body-abrasion processes as applied to alumina ceramics. *Transactions of NAMRI/SME XXXI*, 2003, 289–296.
15. Spanu, C.E., Electrolytic in-process dressing applied to double side grinding of ceramic materials. *Ph.D. Dissertation*, 2004, University of Toledo, Ohio.
16. Koshy, P., Jain, V.K., and Lal, G.K., A model for the topography of diamond grinding wheels. *Wear*, 1993, 169, 237–242.

13

Super Polishing of Magnetic Heads

J. Ramírez-Salas and I.D. Marinescu

CONTENTS

13.1 Introduction

Super polishing of magnetic heads is a very important process in the storage media industry. It creates a very flat surface with small surface roughness allowing only a small gap between the head and the storage media (hard disk, floppy disk, tape, etc.). This process can be optimized by making the right decisions in terms of slurry selection (type, amount), plate material, speed (plate and parts), time, and pressure on the parts.

This chapter provides experimental data for the magnetic head material removal rate and surface finish. These two parameters were considered as the important factors for the magnetic head manufacturer as it reflects the needs of the customers. In this step, where we super polish the magnetic heads, we are trying to obtain a direct relationship between slurry type and material removal rate. Other characteristics to be included are particle size, concentration, and amount; more parameters will be included in future experiments.

The main goal of this chapter is to obtain a clear and quantitative difference on the machine parts using polycrystalline and monocrystalline slurries to help the decision-making process. In super polishing, changing the slurry type will modify the machining characteristics and, therefore, different surface finish and material removal rate.

The first approach toward super polishing of magnetic heads attempts to provide qualitative and quantitative analysis of the resulting surfaces of the magnetic heads and the material removal rate of the process. Keeping other parameters as constant as possible and changing only the slurry type, we are able to determine the best choice to cover the customer needs in terms of production volume, economy, and surface quality. This fact will help the related industries to make appropriate suggestions to their customers' needs.

13.2 Related Work

13.2.1 Inside University of Toledo

Extensive work on super polishing of magentic heads was carried out at the University of Toledo's Precision Micro Machining Center. The following are the two active projects:

Mono vs. polycrystalline diamond lapping of ceramics ID # PMMC 1703.
Acoustic emission monitoring of lapping process ID # PMMC 1704.

13.2.2 Outside PMMC

Super polishing of magnetic heads is an important field of research for the superfinishing industry. Some of the results of these research were published:

An ultraprecision lapping on magnetic memory disk substrate of glass by fixed abrasives in newly developed microspherical cell
Yoji Tomita, Tanaka Co. Ltd, Japan and Hiroshi Eda, Ibaraki University, Japan
Japan society of manufacturing engineers
Abrasive micromachining of advanced materials to precision tolerances;
Andrew M. Corsini, Peter Wolters of America Inc.
Ceramic industry manufacturing conference and exposition, Pittsburgh PA, 1995;

Abrasive engineering society
A few nanometers' flatness polishing of NiP plated magnetic disk substrate with alumina abrasives
Heiji Yasui et al., Department of Mechanical Engineering, Kumamoto University, Japan
Ultraprecision in manufacturing engineering conference, Aachen, Germany, 1994
A study on ultrasmoothness polishing of glass magnetic disk substrate
Heiji Yasui et al., Kumamoto University, Japan
Progress in precision engineering and nanotechnology proceedings of the 9th international precision engineering seminar, Braunschweig, Germany, 1997

13.3 Methodology

This research utilizes four types of slurry with the other parameters (plate material, plate surface roughness, time, load, speed, slurry amount) kept as constants. The process starts with the machining of the polishing plate to a roughness of 20–30 μin. and maximum concavity of 25 μm.

The next step is the texturing of the plate using the slurry to be studied, in a higher concentration. Loads of 12 kg are applied to the ceramic ring and machined for about 99 min.

After texturing, the charging process is similar to the texturing but a 5.5 kg load is added to parts and machine for about 99 min. Then the parts are cleaned and measured and loaded into the part holder that locates them at 60° angles using six parts per batch. The batch is then polished for about 12 min, following a cleaning bath with reagent alcohol (<1% of water) and measured again. This way, we obtain the material removed in the cycle. After that, the parts are taken to the atom force microscope (AFM) and then analyzed for roughness and profile of the polished surface.

Figure 13.1 shows the location of the parts in the part holder. The slurry types are monocrystalline diamond 0.25 and 0.125 μm and polycrystalline diamond 0.25 and 0.125 μm. The plate is tin and the polishing speed is 40 rpm.

Notes: During this experiment, the initial roughness of the plate played a very important role in the determination of the material removal rate; also, the material in the part holder (soft or hard) creates a different material removal rate.

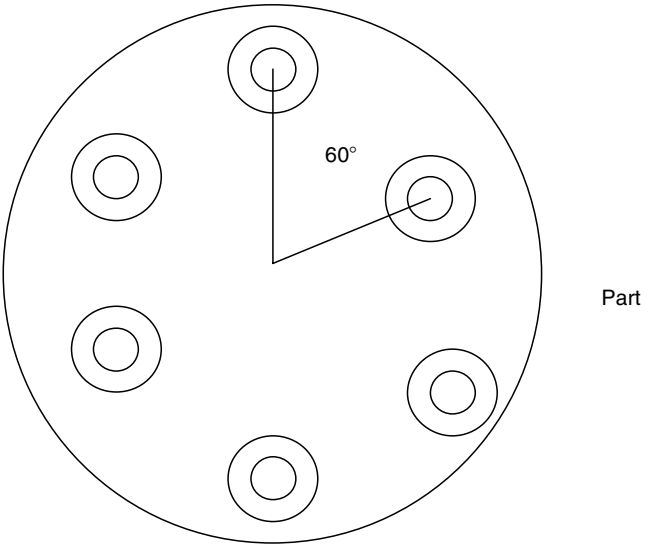

FIGURE 13.1
Part location on the experiments.

13.4 Experimental Results

The main results obtained for the four types of slurries are as follows:

13.4.1 Material Removal

For 0.25 μm monocrystalline diamond, we removed 7.395 μm per 12 min of machining or 0.6163 μm per min. This rate is with a different charging method and is showing lesser efficiency than the one described earlier.

For 0.25 μm polycrystalline diamond, we removed 15.636 μm per 12 min of machining or 1.303 μm per min.

For 0.125 monocrystalline diamond, we removed 3.236 μm per 12 min of machining or 0.2697 μm per min.

For 0.125 polycrystalline diamond, we removed 3.575 μm per 12 min of machining or 0.2979 μm per min.

It can be seen that on the 0.25 μm slurry, the material removal rate for polycrystalline is twice that for monocrystalline, optimizing production volume and time savings.

In the 0.125 μm, the results are quite different; the removal rate is very small (around 9%) compared with the 0.25 μm. In this case, the decision-making process should include other parameters like economy,

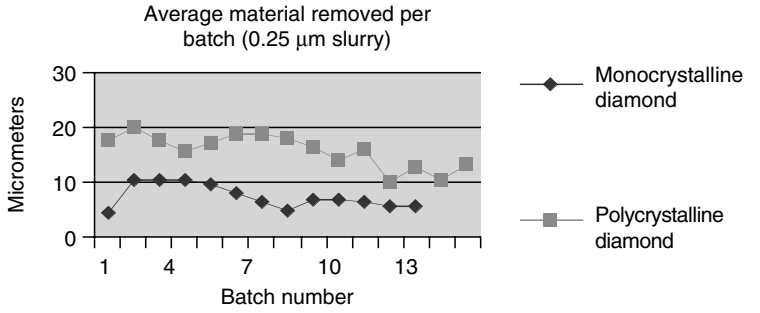

FIGURE 13.2
Average material removed (in μm) per batch of six parts.

availability, and so on. Figure 13.2 shows the graphs for material removed during the experiments.

13.4.2 Roughness and Profile

The preliminary results on the AFM show roughness on some parts of about 2 nm on the lower end of the range. The roughness and profile measurements are in progress because of a heavy volume of work on the AFM and the priorities assigned to it by the department of chemical engineering (owner of the equipment). This fact does not allow more results to be disclosed now that this report is getting printed. Figure 13.3, Figure 13.4, Figure 13.5, and Figure 13.6 are surface roughness images obtained on the AFM for different parts. Figure 13.7, Figure 13.8, and Figure 13.9 are topography images of these parts.

13.5 Remaining Work

The remaining work includes:

- Analysis of the roughness and profile of the parts for the different types of slurries.
- Analysis of the effect on the plate surface roughness, it has proven to be of critical importance in these experiments.
- Analysis of the part holder material (soft or hard) that also showed itself as an important parameter.

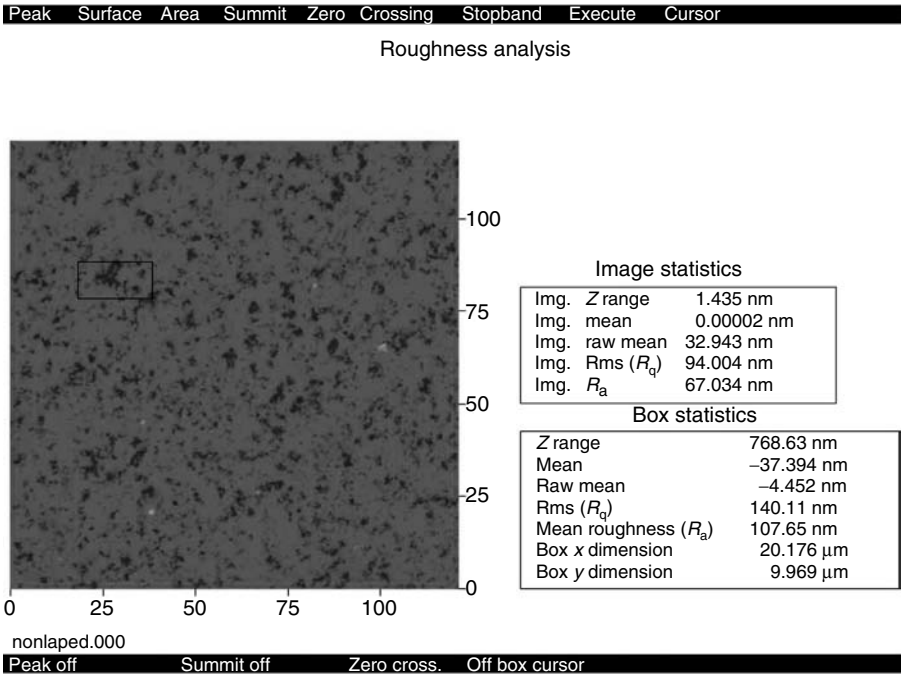

FIGURE 13.3
Image of a nonlapped magnetic head showing the roughness of the full scanned area and the roughness of the small rectangle.

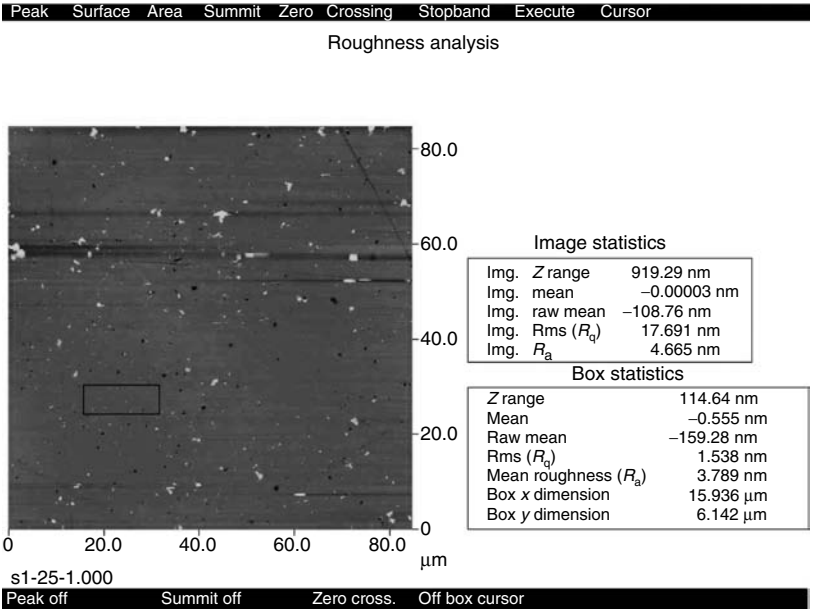

FIGURE 13.4
Image of a lapped magnetic head with 0.25 µm slurry, showing the roughness of the full scanned area and the roughness of the small rectangle.

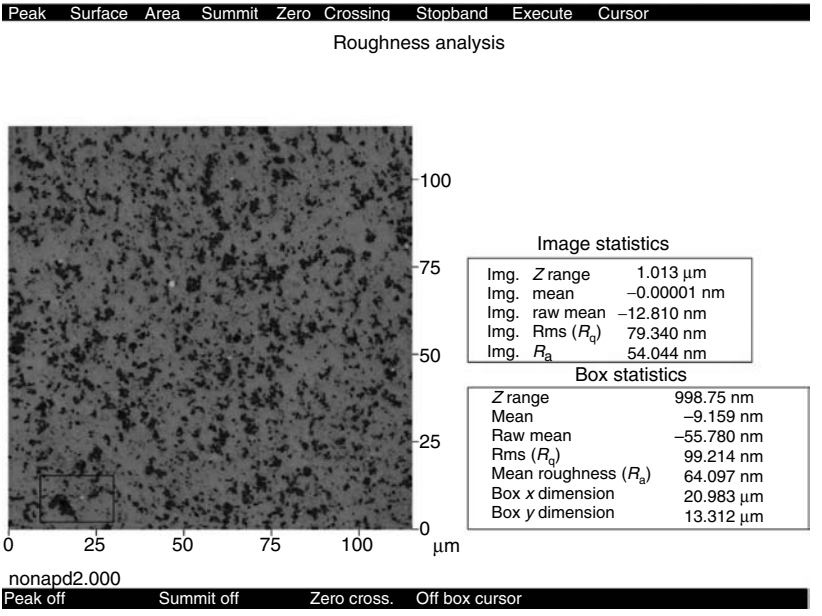

FIGURE 13.5
Image of a nonlapped magnetic head showing the roughness of the full scanned area and the roughness of the small rectangle.

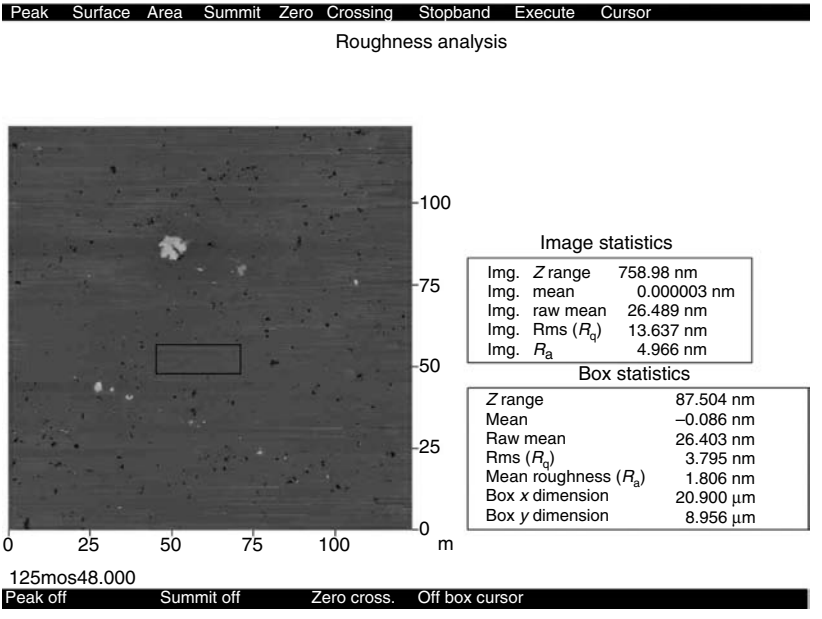

FIGURE 13.6
Image of a lapped magnetic head with 0.125 µm slurry, showing the roughness of the full scanned area and the roughness of the small rectangle.

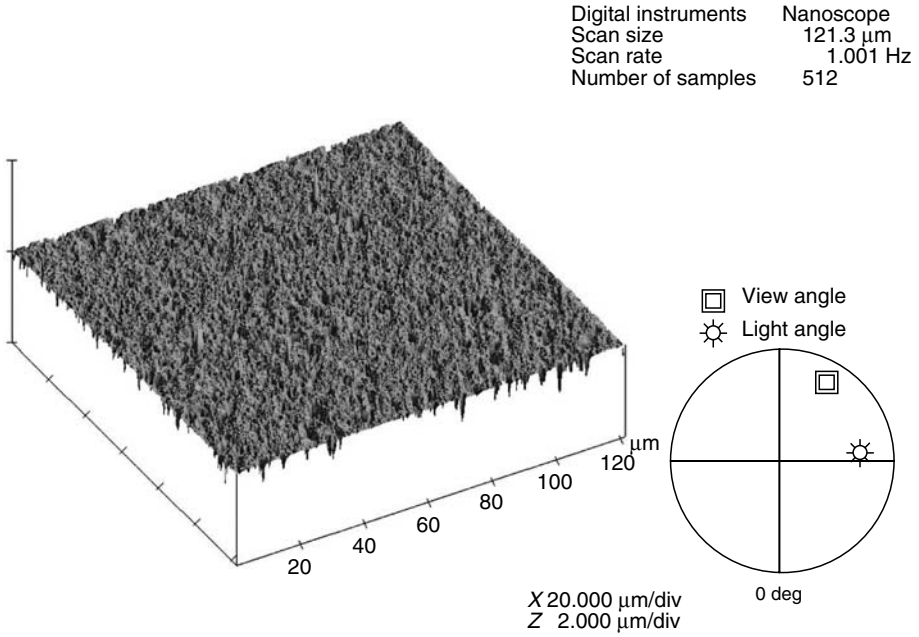

FIGURE 13.7
Image of a nonlapped magnetic head showing the topography of the surface.

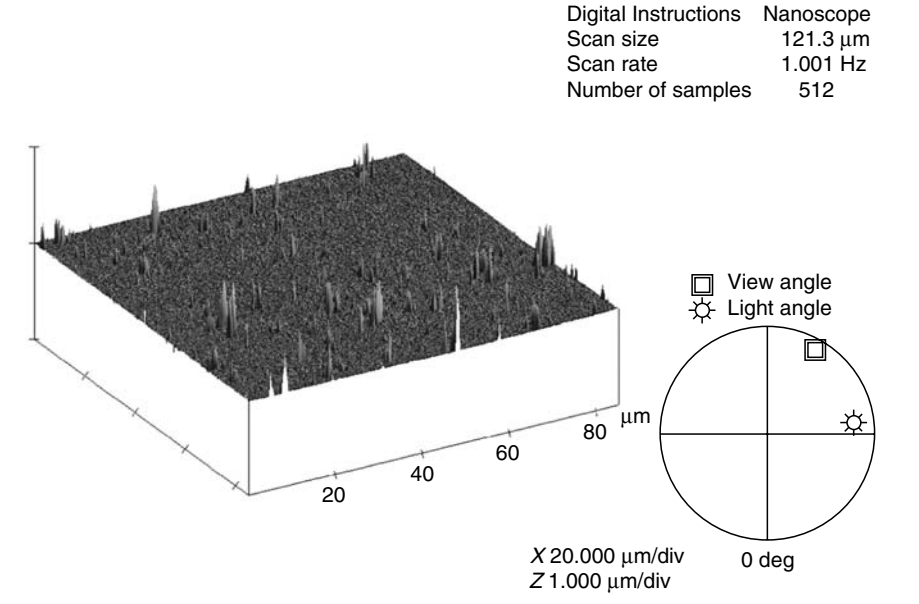

FIGURE 13.8
Image of a lapped magnetic head using 0.25 μm slurry, showing the topography of the surface.

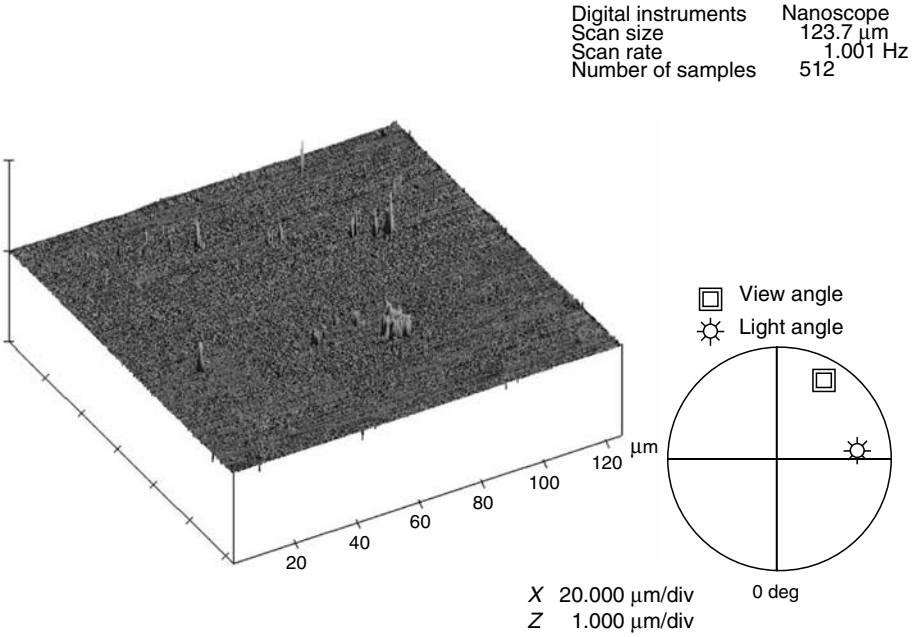

FIGURE 13.9
Image of a lapped magnetic head using 0.125 µm slurry, showing the topography of the surface.

- Other parameter that might be analyzed is the speed (parts and plate) and its effect on the surface roughness.
- The material of the plate is also in the scope of this study.
- Use of acoustic emission techniques for the polishing process analysis.

14

Laser-Assisted Grinding of Ceramics

I.D. Marinescu, T.D. Howes and J. Webster

CONTENTS

14.1 Objectives

The objectives of this chapter are to determine the parameters of a new technology for high productivity, low cost of hot-pressed silicon nitride (HPSN) ceramic materials and to determine if an available grinding wheel system can be used for these applications.

Ceramic materials are commonly brittle materials with varying degrees of brittleness. The aim of this research is to increase the ductility of HPSN ceramic materials by the aid of laser preheating process and in process. With this method, it will be possible to increase the depth of cut (productivity of the process) more than 20 times and at the same time, keep the process in the ductile mode (free of surface and subsurface damages).

This research is unique in that the grinding system will be considered as a thermal-tribo system and the laser energy and friction energy together will provide indications for the necessary energy for increasing the ductility of HPSN ceramic materials.

14.2 Problem Statement

14.2.1 Introduction

Ceramic materials are considered brittle materials and are examples of difficult-to-grind (machine) materials. This is because of the mechanical properties of these materials, most notably hardness, brittleness, and abrasiveness. Previous research showed that the only way to obtain a good quality ground surface is through ductile grinding of ceramics with diamond wheels. But even in this case, the depth of the cut must be less than 1 μm, which makes the process very expensive. Many researchers have tried different solutions and a very successful method was that of high-speed grinding of ceramics, but even in this case the process is very expensive. Ceramic materials are not extensively used in industry because the cost of the machining is very high and represents between 50% and 80% of the cost of the part. We are looking for a solution to reduce the cost through increased productivity.

From the experiments done with high-speed grinding, one can observe the effect of the temperature on the quality of the surface and note that an increase in temperature helps in obtaining a better surface and a better pullout.

14.2.2 Experimental Setup

Based on this observation, an experiment was done at the Center for Grinding Research and Development at the University of Connecticut. A laser was mounted on a surface grinder to preheat the ceramic surface just before it contacts the grinding wheel (see Figure 14.1). A dynamometer and a thermocouple were used together with a data acquisition system. The experiment was done for four types of ceramics (Table 14.1): Al_2O_3, Ferrite, ZrO_2, and Si_3N_3. The aim of the experiment was to show that it is possible to increase the ductility of ceramics through a preheating process and to increase the depth of cut while the material is in the ductile state. The experiment was done in two steps: (1) grinding of ceramic materials and (2) grinding of ceramic materials preheated with laser under the same experimental conditions. During the experiment, the forces and the temperature were measured in process. The experiment parameters were as follows:

- Wheel speed: $Vs = 25$ m/s.
- Depth of cut: $a = 50$ μm.
- Work speed: $vw = 2$ mm/s.
- Wheel type: 1A1, D400, C75, Resin Bond & Friable Diamond, Kt8821YA.

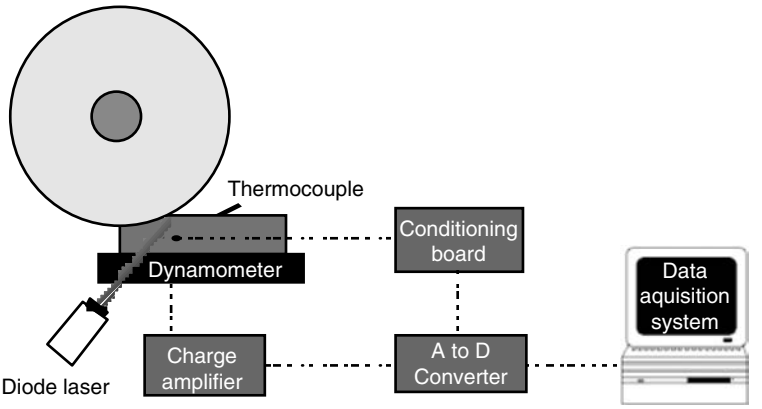

FIGURE 14.1
Experimental setup for tests.

14.2.3 Results and Discussions

The experimental results are presented in Table 14.1. The normal force (F_n) and tangential force (F_z) were generally higher under the laser preheated condition (Figure 14.2 and Figure 14.3). The behavior of silicon nitride is remarkably unusual. From Figure 14.4, one can see that there are two behaviors for the friction coefficient: in one, the friction coefficient decreases when preheating the ceramics (Ferrite, Zr_2O_3), in the other two materials, the coefficient rises slightly in response to laser preheating.

But the most interesting results are shown in Figure 14.5, in which we can see that the roughness of the surface is better for all four types of ceramics when the grinding is done with preheated ceramics.

When we look at SEM photos (Figure 14.6 and Figure 14.7) of surfaces ground with and without heat, we see a tendency toward a ductile surface in the case of grinding with preheating. The structure shows some evidence of melting zones, probably at the asperities of the ceramic materials.

TABLE 14.1

Experimental Results

Workpiece Material	Al_2O_3 w/Heat		Ferrite w/Heat		ZrO_2 w/Heat		Si_3N_4 w/Heat	
F_n [N]	15	9	2.5	2.0	15	25	10	15
F_t [N]	2.5	2.0	0.5	0.25	7	5	5	8
R_a	8.2	12.5	12.3	13.6	5.4	6	3.8	4.5
Force Coefficient	0.167	0.222	0.2	0.125	0.467	0.2	0.5	0.53

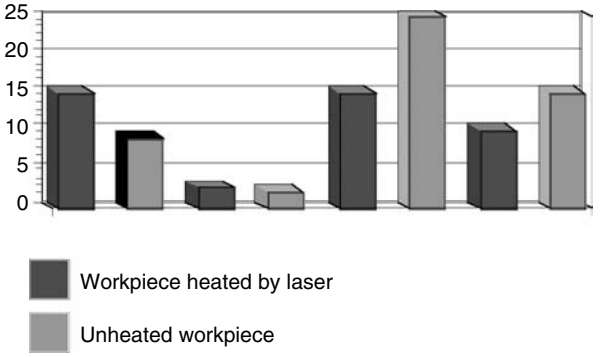

FIGURE 14.2
Normal grinding force.

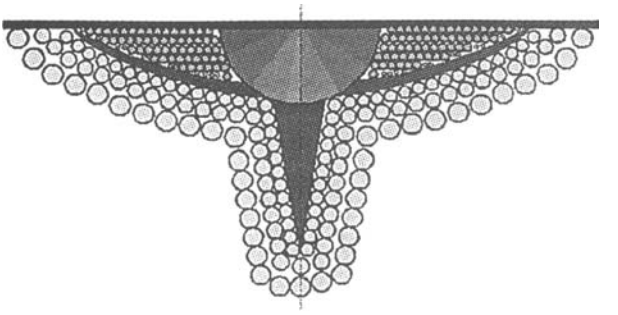

FIGURE 14.3
Macro-fracture.

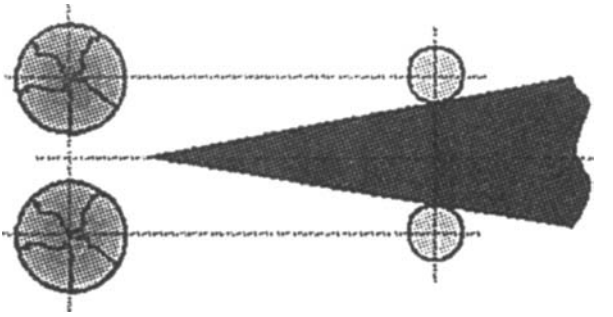

FIGURE 14.4
Micro-fracture.

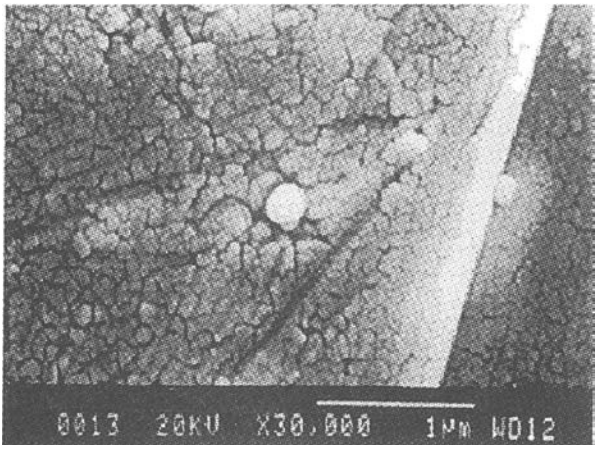

FIGURE 14.5
Workpiece Finish—R_a(μin.).

It is not definite that it is a melting phenomenon, but there is evidence of a thermal phenomenon caused by the preheating and from friction phenomenon between the grinding wheel (diamond and bond) and the ceramic material.

This same trend is signaled by the increase of forces and energy. We know that in the case of ductile grinding, the specific energy is much higher than brittle grinding.

14.3 Stock Removal Mechanism

Many researchers mentioned in their papers the influence of the temperature upon the stock removal mechanism in the case of brittle material, but no one had performed specific research in this area. Even the measurement

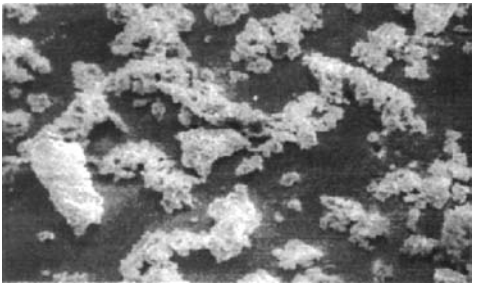

FIGURE 14.6
SEM Image of a ground surface without heat.

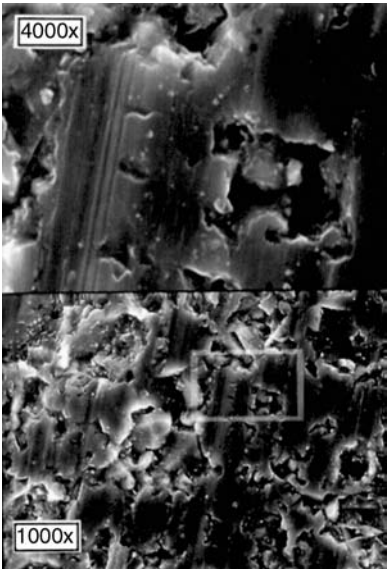

FIGURE 14.7
SEM Image of a ground surface with laser heat.

of the temperature in the grinding contact area is not yet a precise technique and in the case of ceramics there are results between 600°C and 1500°C. Ueda et al. (1995) spent many years of his research work to establish an accurate method and to pick up the temperature at the interface between the abrasive grain and workpiece.

From previous work (Marinescu, I.D., ''*Laser Heating in Grinding of Ceramics*'', CIRP Paris January Meeting, STC-Abrasive Processes, January 26, 1995; Marinescu, I.D., ''*Double Fracture Model in Lapping of Ceramics*'', Proceedings of ASPE, Spring Meeting: Jun 2–4, Annapolis, MD) it had been observed that some of the chips collected have a spiraled plastic deformation shape which does not mean necessarily that the process was ''ductile'' but shows a clear evidence of plastic deformation (Figure 14.6). Based on this observation it is presumed that in the case of ceramics (of the same type) the real phenomenon is a double phenomenon. The removal of material can be by fracture or by plastic deformation (share). This has the effect of a high temperature (higher in the case of a plastic deformed removal mechanism than in the case of a fracture-controlled mechanism). Because of this high temperature and of the contact with the atmosphere immediately after grinding, a thermal shock will produce a thermal fracture in both the ground surface and the chips. In order to avoid this, a method was developed in Japan using a laser to decreed or eliminate the thermal shock as soon as the piece lost contact with the grinding wheel. It is assumed that in the case of ''brittle'' mode there is a double fracture. A macro-fracture which is

responsible for stock removal of the material (Figure 14.3) and a microfracture which is at intragranular level (Figure 14.4) is responsible for some of the surface and subsurface damage.

The presentation of this mechanism is based on evidence (Figure 14.5) and hypothesis, and more research is necessary, especially in order to elucidate the heat transfer during the process.

14.4 Conclusions

(1) Heating ceramic materials before grinding aids the material removal process. In the four ceramic samples, the surface quality was also improved.

(2) With the exception of Si_3N_4 and ZrO_2, the tangential and the normal forces were higher in laser-assisted grinding tests. This indicates a tendency toward a ductile regime grinding mechanism.

(3) Future research will seek to increase the depth of cut while maintaining the ductile grinding model and minimizing surface roughness and subsurface damage.

14.5 Future Directions

(1) Investigation of the tribology of laser-assisted grinding of ceramics: correlation of the friction coefficient and the wear with the temperature of ceramics caused by laser.

(2) Correlation between the melting and softening points of the ceramic and the optimum temperature for obtaining a ductile surface.

(3) Correlation of the ceramic properties with friction and wear phenomena (qualitative and quantitative).

(4) A low-power laser was used for the tests. A more powerful laser will be used in the future tests.

Bibliography

Hoffmeister, H.D., Laser assisted grinding of HPSN with SiC wheels Internal Report, University of Bransbraig, 1995.

Jahanmir, S., Machining of advanced materials, Proceedings of the International Conference on Machining of Advanced Material, NIST Special Publications 847, 1993.

Marinescu, I.D., Laser assisted grinding of ceramics, *CIRP Winter Meeting*, January 22–24, 1995, Paris, France.

Marinescu, I.D., Laser heating in grinding of ceramics, STC-Abrasive Processes, *CIRP Winter Meeting*, January 26, 1995, Paris, France.

Marinescu, I.D., Double fracture model in lapping of ceramics, *Proceedings of ASPE, Spring Meeting*, June 2–4, Annapolis, MD.

Marinescu, I.D., Laser assisted grinding of ceramics, *Journal of Abrasives*, AES, August 1995.

Marinescu, I.D., Hot grinding of ceramics, *Machining and Grinding of Brittle Materials, Ceramic Industry Conference*, 11–13 October 1995.

Ueda, T., Thermal behavior of cutting grain in grinding, *Annals of the CIRP*, Vol. 44 No. 1, 1995.

Ueda, T., Sato, M., Sugita, T., and Nakayama, K., Thermal behavior of cutting grain in grinding, *Annals of the CIRP*, Vol. 44, No.1, 1995.

WestKamper, E., Grinding assisted by Nd: YAG Lasers, *Annals of the CIRP*, Vol. 44 No. 1, 1995.

Wobker, H.G., High efficiency grinding of structural ceramics, *Proceedings of the International Conference on Machining of Advanced Material*, July 20–22, 1993.

Yegenoglu, K., Machines for grinding precision components with high machining performance, Superabrasives 91, *Conference Proceedings*, June 11–13, 1991.

15

Tribological Properties of ELID-Grinding Wheel Based on In-Process Observation Using a CCD Microscope Tribosystem

T. Kato, H. Ohmori, and I.D. Marinescu

CONTENTS

15.1 Introduction

The purpose of this chapter is to present the wear properties of an ELID-grinding wheel based on an in-process observation using a CCD microscope tribosystem. The normal load is changed from 0.049 to 9.8 N. It was noticed that when the surface of the grinding wheel is not covered with an oxide film, powder formation or plowing is observed. The measured wear rate for powder formation or plowing spreads from 9.6×10^{-8} to 5.5×10^{-7} mm^3/mm. When the surface of the grinding wheel is covered with an oxide film, flake formation is observed. The wear rate of flake formation is distributed, in this case, between 6.7×10^{-6} and 2.7×10^{-5} mm^3/mm. During the initial friction stage, the friction coefficient in the presence of an oxide film has a higher value than that without an oxide film. This is because of the fact

that the wear is higher at initial friction stage than that without an oxide film. The friction coefficient at the final friction stage decreases as contact pressure increases.

The electrolytic in-process dressing (ELID) is a grinding technique used to increase surface quality. This innovative method was proposed by one of the authors (Ohmori, 1992; Ohmori and Nakagawa, 1995, 1997). The technology is expected to contribute greatly to precision grinding, especially in the technique of mirror surface finishing of hard and brittle materials. Tribological characteristics of various hard and brittle materials with ELID-grinding have been investigated (Kato et al., 1999, 2000, 2001; Zhang et al., 2000; Ohmori et al., 2001).

The processing mechanism of the ELID-grinding is shown in Figure 15.1. The first position illustrates a cross section of a grinding wheel after truing denoted with stage 1. In the second stage 2, predressing started. The bond material is removed through electrolyze. The goal of this stage is to produce a proper protrusion of grain cutting edge, and to form a layer of oxide on the wheel surface.

The nonconductor oxidation film (Fe_2O_3) is formed on the surface of the grinding wheel as shown in stage 3. Stage 4 of the ELID-grinding can begin when the intensity of the electrolysis phenomenon is controlled by the

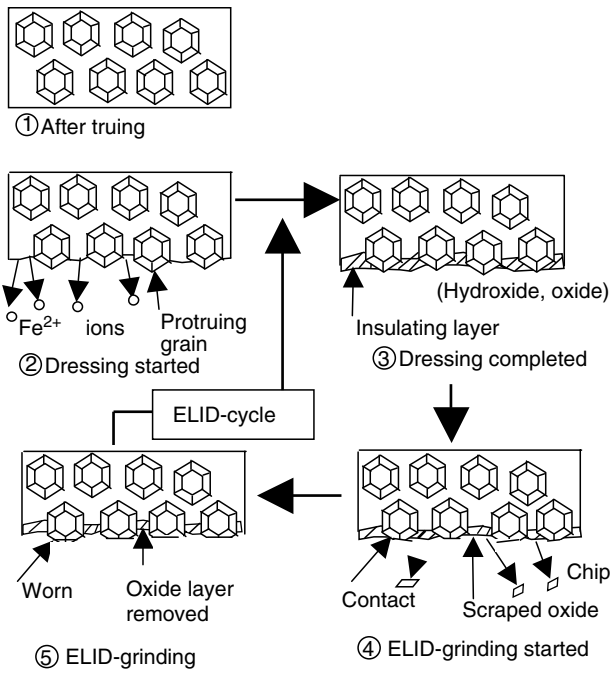

FIGURE 15.1
ELID-grinding mechanisms.

thickness of the sterilized oxidation film. The electrochemistry reactions are as follows:

$$Fe \rightarrow Fe^{2+} + 2e^{-}$$

$$Fe^{2+} \rightarrow Fe^{3+} + e^{-}$$

$$H_2O \rightarrow H^{+} + OH^{-}$$

$$\left.\begin{matrix} Fe^{2+} + 2OH^{-} \rightarrow Fe(OH)_2 \\ Fe^{3+} + 3OH^{-} \rightarrow Fe(OH)_3 \end{matrix}\right\} Fe_2O_3$$

As displayed in the chemical relations, the layer of oxide plays an important role in achieving an excellent ELID-grinding condition. However, the microscopic aspect of oxide layer has not yet been analyzed, and the speed of formation, for example, remains unknown. Moreover, an investigation of the tribological properties of the ELID-grinding wheel has never been accomplished. The purpose of this paper is to investigate wear properties of ELID-grinding wheel under dry grinding conditions.

15.2 Experimental Method

Figure 15.2 shows an outline of the CCD microscope tribosystem. The contact zone was continuously monitored with the CCD microscope during the experiment. The wear process of the wheel was recorded on a video tape recorder. The sapphire pin (radius of pin tip: 1 mm, Hv: 2500) was used as a

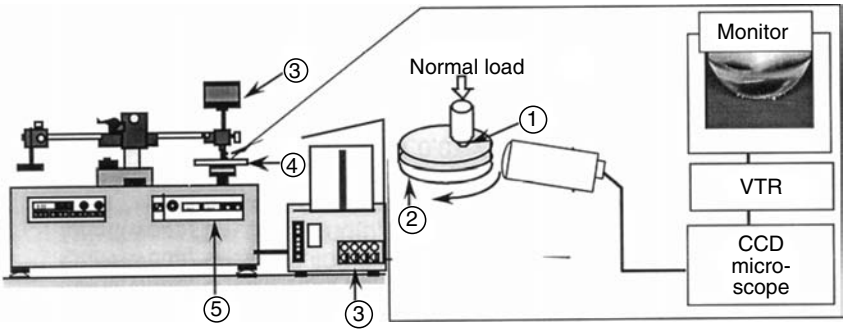

FIGURE 15.2
Schematic diagram of the CCD microscope tribosystem.

specimen. The cast-iron bond diamond wheel of #400 (100 concentration, $\varphi 75 \times 5$ mm, 34.5 mm in the width of the wheelstone, 3 mm in thickness, average grain size: 50 μm) was used for the disk test specimen. The initial electrolysis dressing was applied to the disk specimen with a vertically precise rotary plane grinder after truing. A 30 μm thick oxidation film was then generated. The cast-iron bond diamond-grinding wheel lacking the oxidation film was used. All the specimens were cleaned with acetone using an ultrasonic cleaner.

Wear tests were carried out at room temperature under dry condition. Normal load values of 0.98, 1.96, 2.94, 3.92, and 4.9 N were used. Sliding velocity was fixed at 0.02 m/s, and the sliding distance was 120 mm. Wear of the pin was measured by a gravimetric method using an electronic balance at a 0.0001 g precision. Each worn surface was measured with a profilometer after the wear test to obtain profiles normal to the direction of friction. The profiles were used to calculate the wear rate. The wear rate, w, is defined as $w = V/L$, where V is the wear volume and L is the sliding distance. Each point of the diagrams from the experimental results is an average of five tests and measurements.

15.3 Experimental Result and Discussion

15.3.1 Wear Mode of Abrasive-Grinding Wheel

When surface of the grinding wheel was not covered with an oxide film, either fine powder-like wear particles are formed by the propagation of microcracks (Hokkirigawa, 1991) or no typical wear particle is formed. Such a wear mode is referred to as plowing or powder formation.

When the surface of grinding wheel is covered with an oxide film, wear intensity is caused by a brittle fracture, during which large flake-like wear particles are formed by a surface crack propagation (Kitsubnai et al., 1991). We call this wear mode as flake formation.

Figure 15.3 shows the wear process of the abrasive-grinding wheel. It can be seen in Figure 15.3a that large wear particles were not formed in this case, but powder-like wear particles were observed.

On the other hand, the generation of the powder-like wear particles was observed from the first friction stage, when the surface of grinding wheel is covered with the oxide film as shown in Figure 15.3b. Subsequently, when the sliding distance was increased, the predominant wear mode changed from powder formation to flake formation. As shown in Figure 15.3b the wear of the pin is very high when flake formation is the wear mode.

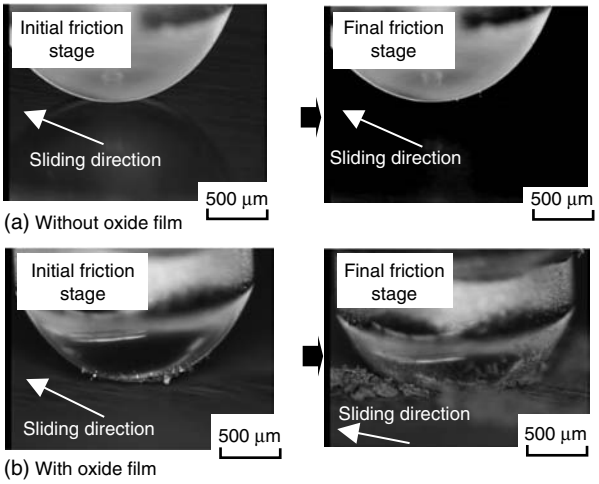

FIGURE 15.3
Wear process of grinding wheel.

15.3.2 Wear Property of Sapphire Pin

Figure 15.4 shows pictures of the pin specimens after wear test.

Figure 15.5 shows the wear of the pin specimen. It can be seen that the wear of sapphire pin, measured as friction paired with the grinding wheel covered with oxide film, is six to seven times greater than that of a sapphire pin measured as a friction pair with a grinding wheel without oxide film. It is considered that the number of active diamond grains, which enable for an excellent pin cutting, increases with the rise of oxide film wear.

From Figure 15.6, it can be observed that after the grinding wear is tested under different conditions, the pin surface roughness presents similar results. It is considered that surface roughness depends only on the size of the diamond grain.

15.3.3 Friction Property

Figures 15.7a and Figure 15.7b show the relationship between the friction coefficient and the normal load at the initial friction stage. It can be seen from Figure 15.7a that initially the friction coefficient has a low value, and subsequently increases sharply for the normal load of 4.9 N. Conversely, from Figure 15.7b, it can be seen that the friction coefficient increases gradually according to the rise in the normal load. The difference between the friction coefficient values corresponding to minimum and maximum thickness of oxide film is larger than that corresponding to the grinding without oxide film, as shown in Figure 15.7. It is also proved that the friction

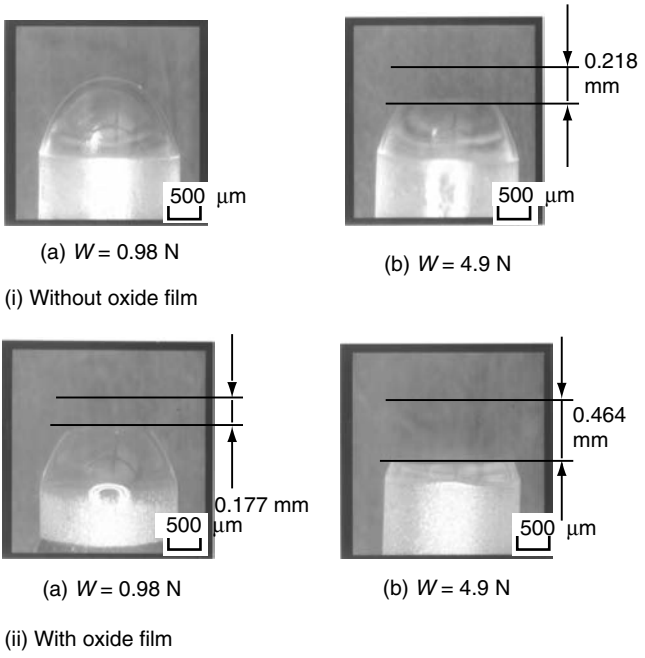

FIGURE 15.4
Weared pin specimens.

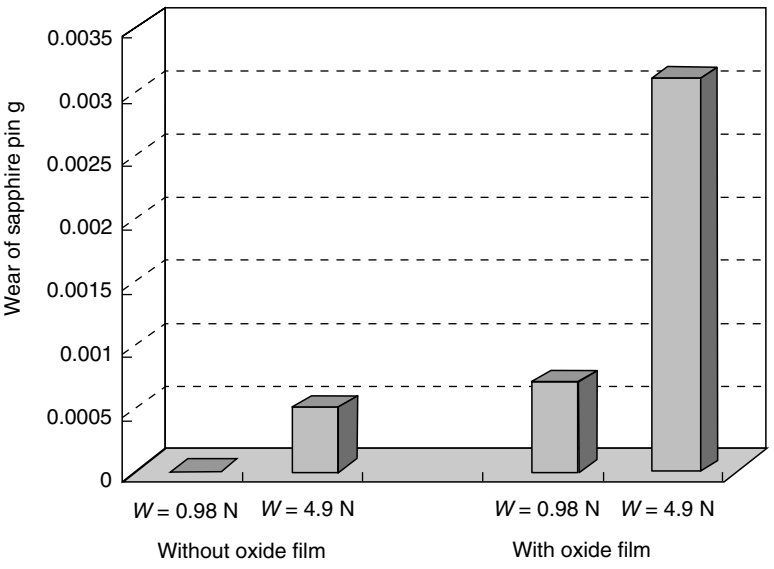

FIGURE 15.5
Wear of pin specimen.

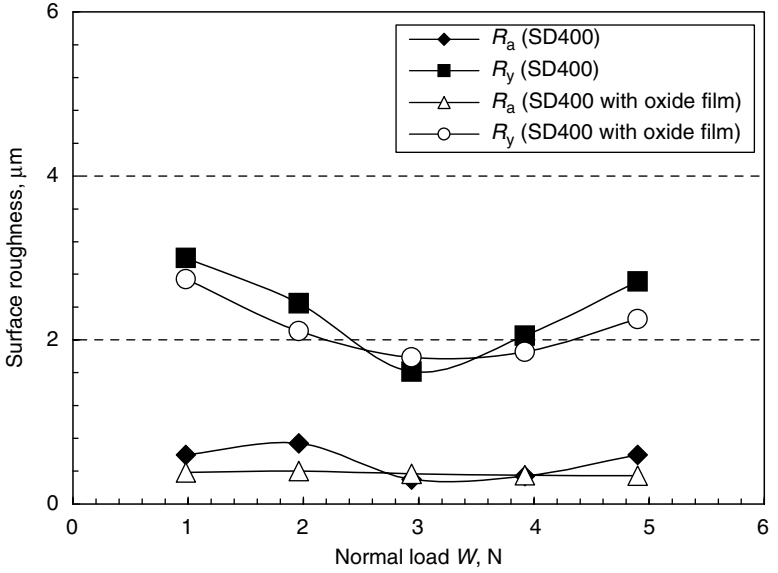

FIGURE 15.6
Surface roughness of the pin.

properties during initial friction stage are closely correlated to wear mode at the initial stage as shown in Figure 15.3.

15.3.4 Wear Property

Figure 15.8 shows the relationship between the wear rate of the grinding wheel and the normal load. It can be seen that the wear rate without oxide film spreads from 9.6×10^{-8} to 5.5×10^{-7} mm^3/mm, whereas the wear rate with oxide film ranges from 6.7×10^{-6} to 2.7×10^{-5} mm^3/mm. The oxide film is likely to wear 12 to 322 times more easily than the cast-iron bonded material under dry conditions. It can also be seen that the wear rate of grinding wheel is independent of the normal load.

15.4 Consideration for ELID-Grinding from the Viewpoint of Tribology

Figure 15.9 shows an example of a grinding based on the relationships from Figure 15.5 and Figure 15.8. The following relation can be drawn:

$$G_2 > G_1,$$

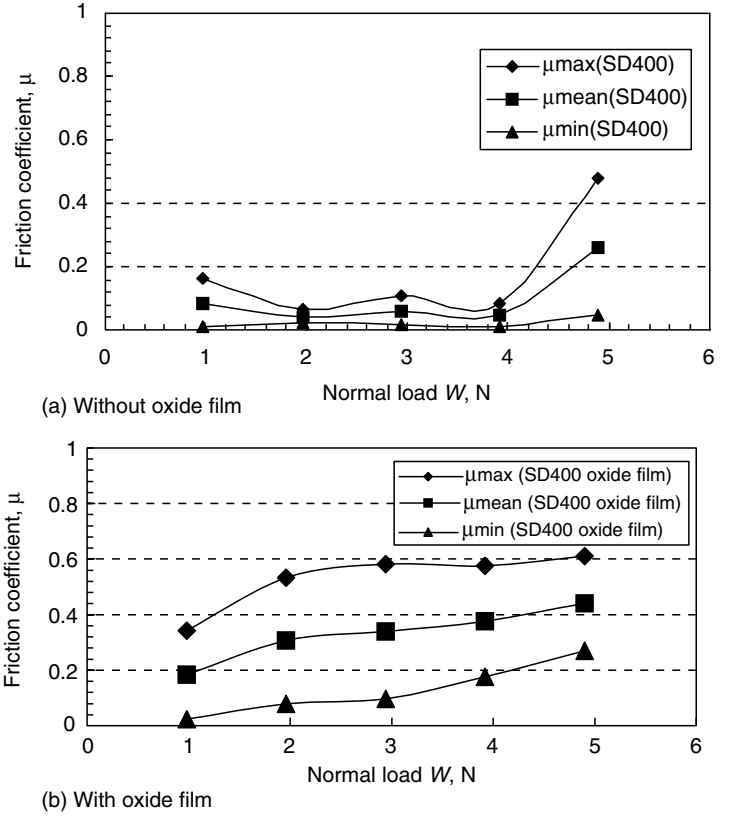

FIGURE 15.7
Relationship between normal load and friction coefficient at initial friction stage.

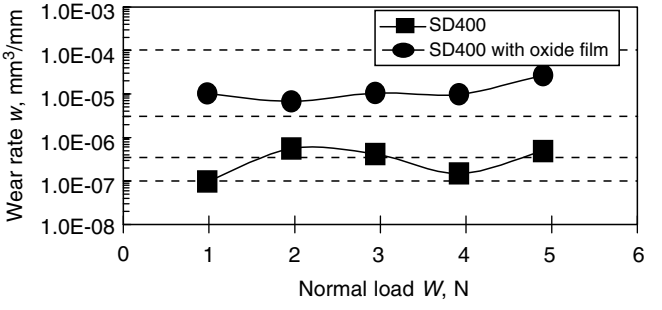

FIGURE 15.8
Relationship between normal load and wear rate of the wheel.

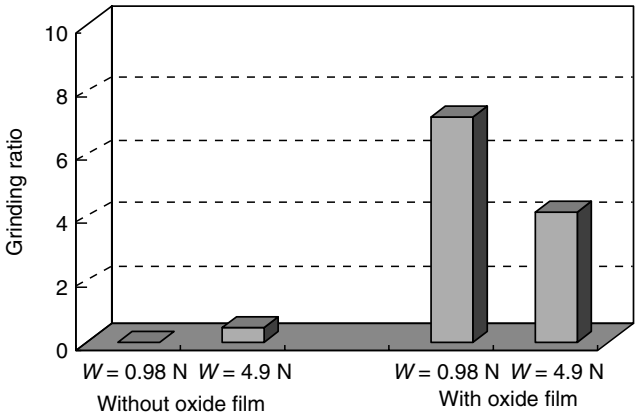

FIGURE 15.9
Example of grinding rate.

where G_1 represents the grinding ratio without oxide film, and G_2 symbolizes the grinding ratio with oxide film.

It can be seen that the wear rate of the grinding wheel covered with oxide film is very large, about 10^{-5} mm^3/mm. However, the grinding ratio value for the wheel with oxide film is larger than that of the wheel without oxide film. It can be concluded that ELID-grinding is an efficient technique whenever high productivity is required.

Figure 15.10 shows the relationship between the contact pressure and the friction coefficient during the final friction stage. The contact pressure is calculated by using the normal load and the contact area of the sapphire pin after the friction test. As seen, the contact pressure with the oxide film is

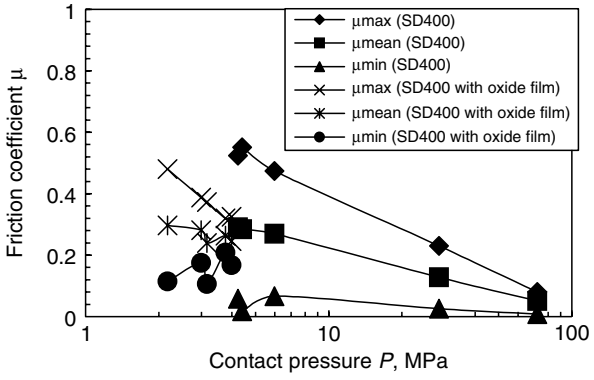

FIGURE 15.10
Relationship between contact pressure and friction coefficient at final friction stage.

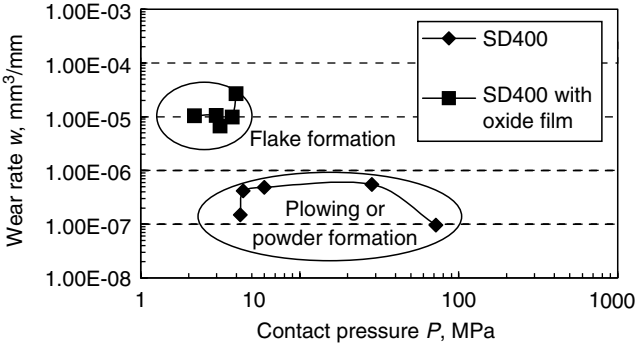

FIGURE 15.11
Relationship between contact pressure and wear rate of grinding wheel.

between 2.2 and 4.0 MPa. The same parameter for wheels without the oxide film spreads from 4.2 to 72 MPa. The friction coefficient values for SD400 with oxide film is very low, about 0.17–0.32 at 4 MPa, whereas the value of the friction coefficient for SD400 without the oxide film is 0.06–0.52 at 4 MPa.

It can also be seen that both values of the friction coefficient are likely to decrease as the average contact pressure increases (Tsuya et al., 1991; Kawayu et al., 2000).

Figure 15.11 exemplifies the relationship between the contact pressure and the grinding wheel's wear rate. Furthermore, it can be seen that in the case of SD400 with oxide film, the wheel's wear rate has high values of 10^{-6} to 10^{-5} mm^3/mm at low pressure because of intense wear such as flake formation of oxide film.

In the case of SD400, the wear rate of the wheel takes a low value of 10^{-7} mm^3/mm at high contact pressure because of mild wear such as plowing or powder formation. Wear rate of the wheel SD400 with oxide film is about 180 times larger than that of SD400 at 4.0 MPa. From Figure 15.9 and Figure 15.11, it can be concluded that even though the grinding wheel covered with oxide film causes an intensified wear rate through flake formation, its grinding rate is higher than that of a grinding wheel without the oxide film.

Figure 15.12 shows the relationship between the friction coefficient and the wear rate of the grinding. From the tribology viewpoint, ELID-grinding is characterized by a high wear rate of the grinding wheel with the oxide film and a relatively low friction coefficient. According to the results, the layer of oxide film enables good grinding with a larger flexibility and low retention.

Conversely, conventional grinding is characterized by a very low wear rate of the grinding wheel; however, it has a high friction coefficient. As

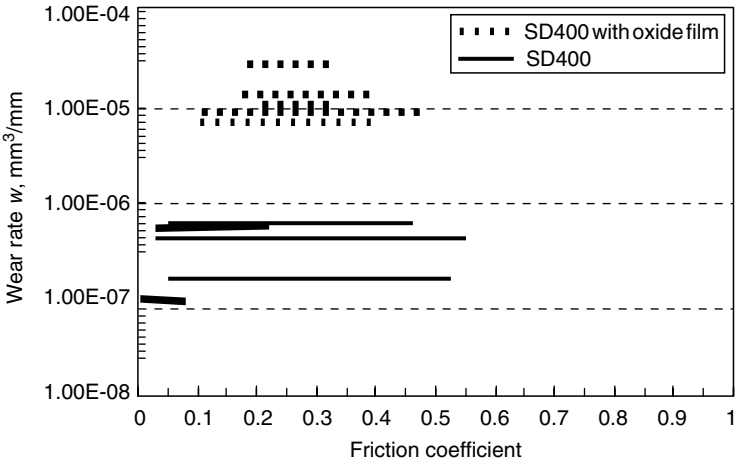

FIGURE 15.12
Relationship between friction coefficient and wear rate at final friction stage.

these results have shown, a high grinding ratio cannot be achieved during conventional grinding.

15.5 Conclusions

The study of wear properties of the ELID-grinding wheel for multipoint contact was based on an in-process observation using a CCD microscope tribosystem. The following conclusions were drawn:

1. When the surface of the grinding wheel is not covered with oxide film, powder formation or plowing were observed and the wheel's wear rate ranges from 9.6×10^{-8} to 5.5×10^{-7} mm^3/mm.
2. If the surface of the grinding wheel is covered with an oxide film, flake formation is observed and the wheel's wear rate ranges from 6.7×10^{-6} to 2.7×10^{-5} mm^3/mm.
3. During initial friction stage, the friction coefficient for the wheel covered with an oxide film has a higher value in contrast to the wheel lacking oxide film. This is because the wear is more intense for the former than for the latter.
4. The oxidation film on the surface of the cast-iron bond of the diamond wheel has a great influence on wear characteristics and friction coefficient.

References

Hokkirigawa, K. Wear mode map of ceramics, *Wear*, 1991, Vol. 151, pp. 219–228.

Kato, T., Ohmori, H., Zhang, C., and Qian, J. Analysis of friction and wear properties of CVD-SiC film with ELID-grinding, Abrasive Technology: *Current Development and Applications I,* [Page No. 8], 1999, pp. 165–172.

Kato, T., Ohmori, H., Zhang, C., Qian, J., Miyakawa, T., Itoh, N., and Hokkirigawa, K. Relationship between surface roughness and friction properties of SiC film finished with ELID-grinding, *Journal of the Society of Grinding Engineering*, 2000, Vol. 44, No. 3, pp. 132–137.

Kato, T., Ohmori, H., Zhang, C., Yamazaki, T., Akune, Y., and Hokkirigawa, K. Improvement of friction and wear properties of CVD-SiC films with new surface finishing method ELID-grinding, *Key Engineering Materials*, 2001, Vol. 196, pp. 91–102.

Kawayu, M., Kato, Y., Itoh, N., Takeich, K., and Uemura, M. Tribology property of spheroidal diamond grain, Proceeding of JAST Tribology Conference, Tokyo, May, 2000, pp. 45–46.

Kitsubnai, H., Tsumaki, N., and Kato, K. Transition of microscopic wear mechanism for Cr_2O_3 ceramic coatings during repeated sliding observed in an sem-tribosystem, Wear, 1991, Vol. 151, pp. 279–289.

Ohmori, H. Electrolytic in-process dressing (ELID) grinding technique for ultraprecision mirror surface machining, *International Journal of the JSPE*, 1992, Vol. 26, No. 4, pp. 273–278.

Ohmori, H. and Nakagawa, T. Analysis of mirror surface generation of hard and brittle materials by ELID-grinding with super fine grain metallic bond wheels, *Annals of CIRP,* 1995, Vol. 44, No. 1, pp. 287–290.

Ohmori, H. and Nakagawa, T. Utilization of electrolyzing non-liniality in precision grinding with ELID for fabrication for hard material components, *Annual of the CIRP*, 1997, Vol. 46, No. 1, p. 261.

Ohmori, H., Kato, T., and Hokkirigawa, K. Tribological characteristics of finished surface with ultraprecision ELID-grinding, *Journal of Japanese Society of Tribologist*, 2001, Vol. 46, No. 8, pp. 632–637.

Tsuya, Y., Nitanai, A., Endo, T., Taki, T., and Umeda, K. Cooperative experiments on evaluation and its data bank construction, *Journal of Japanese Society of Tribologist*, 1991, Vol. 36, No. 2, pp. 83–90.

Zhang, C., Kato, T., Li, W., and Ohmori, H. A comparative study: surface characteristics of CVD-SiC ground with cast-iron bond diamond wheel, *International Journal of Machine Tools and Manufacture*, 2000, Vol. 40, pp. 527–537.

16

Developments in Machining of Ceramic Materials

E. Uhlmann, S.-E. Holl, Th. Ardelt, and J. Laufer

CONTENTS

16.1 Introduction

The function of technical products can be distinctly improved by innovative material applications. Particularly, high-performance ceramic materials have gained a great potential for application in many fields because of their outstanding properties. Examples are hip joint endoprotheses on alumina or zirconia basis, slide bearing and burner components from silicon carbide, as well as ceramic roller bearing components or the frequently

discussed ceramic valves from silicon nitride (Spur, 1989; CeraNews Special, 1996; Pattimore, 1998 ; Popp, 1998; Thiemann, 1998).

Although ceramic parts, as these examples confirm, meet the highest demands on service life and functionality, even today they are only rarely used. The reasons for this lie in the costs accompanying the production of components and in the fact that the respective manufacturing technologies cannot be often used in mass production. On the one hand, high hardness and brittleness of ceramics result in poor machinability and on the other, the same machining produces different charges and machining results deviating from the producer, which complicates automation. At the same time, the innovative application of ceramic materials calls for a far-reaching revision of the production process sequence, particularly in the fields of design, raw part production, machining, and quality control.

Generally, more than 50% of the total production costs arise hereby in finish machining. Using high-precision finishing technologies, however, is usually inevitable, because the quality of production directly influences the functional behavior of the ceramic parts, and the quality of parts after sintering is not sufficient for application. Machine tools for the machining of ceramics must often meet highest demands. In addition to general requirements such as high static and dynamic rigidity as well as highly precise and rigid bearings and ways, suitable clamping systems, special cl devices and cl cleaning equipment, as well as additional devices for the conditioning of diamond tools must be integrated into machine tools. Consequently, the machining process assumes a key position in terms of economy and accuracy.

The high costs of finishing result on the one hand from the relatively low productive power of the generally used machining technologies, which are almost exclusively based on the classic finishing technologies such as grinding, honing, lapping, and polishing, as well as on a few special technologies. Grinding hereby plays the most important role because of the high flexibility, the high attainable material removal rates, and the comparably good automation. On the other hand, there are no adequate strategies for accurate and economical machining of complex geometries such as borings, grooves, spherical surfaces, or sculptured surfaces. A purposeful development of machining technologies apt for ceramic materials based on the conventional methods and the application of efficient systems form the prerequisite to use the application potential of ceramics for real parts more effectively.

The example of the manufacturing process grinding illustrates the complexity of the correlation between process input quantities and the machining result (König, 1980; Spur, 1989; Uhlmann, 1993; Funck, 1994; Brücher, 1996; Liebe, 1996). The spectrum of influencing quantities comprises a ceramic-apt grinding machine and the detailed design of auxiliary processes, especially the conditioning of diamond grinding wheels and the selection of suitable cooling lubrication conditions.

Numerous research studies were conducted during the past few years on finish machining of ceramic materials (Spur, 1989; Uhlmann, 1993; Brücher, 1996; Holl, 1997; Popp, 1998). In addition to the further development of innovative manufacturing technologies such as ultrasonic machining, electrical discharge machining, or laser assisted turning, these studies have also inspired a distinct progress in grinding technology. To illustrate the potential for optimization, this paper will elaborate on some examples of current developments in the field of grinding of ceramic materials.

Although it has become clear in retrospective that the originally predicted growth rates could not be realized, the potential for the application of high-performance ceramics could be further increased based on the comprehensive research results. Parallel to the optimization of innovative technologies, future efforts must therefore focus on transferring the acquired knowledge in sensitively dealing with this material to industrial applications. This implies that fundamental investigations and feasibility studies will concentrate increasingly on industrial projects that focus on quality control, standardization of material and process properties, and the aptitude for mass production. The dialog between research and application, as well as the interdisciplinary exchange of information must therefore be enhanced. One approach, for example, is the Industrial Workshop ''Machining of Ceramic Materials'' (Industriearbeitskreis ''Keramikbearbeitung'') that takes place every six months at the IWF Berlin.

With regard to the future, providing adequate manufacturing technologies for innovative ceramic applications will continue to represent a major field in academic research.

16.2 Honing

16.2.1 General Information

The improvement of the surface topography of tribological functional surfaces has led to a broad application of the honing process to finish machining. Because of high profile bearing ratios in connection with machining traces that cross in a defined way and enhance the absorption of lubricants, honed metallic and ceramic surfaces have good tribological properties particularly during sliding stress, improving the running-in behavior and the service life.

However, suitable honing parameters and optimization approaches determined for metallic materials cannot be applied to the honing of ceramic materials caused by different material removal mechanisms specific for ceramics. Therefore, to supply the fundamental connections required for process optimization, the influence of honing conditions on the course and the result of the honing process must be defined for the various ceramic materials.

16.2.2 Technological Investigations

Extensive investigations on different ceramic materials proved that oxide ceramic materials can be machined with diamond honing stones with wear-resistant bronze bond in the self-sharpening range (Weigmann, 1997). For alumina, the range of ductile material removal can be reached while maintaining the self-sharpening, if small diamond grain sizes in the order of D10 are used at high honing stone pressures. High surface qualities in connection with low residual compressive stresses are reached in this range at the subsurface. An increase in diamond grain size leads to a higher roughness.

For zirconium oxide, in contrast to alumina, a necessary grain normal force was determined for the initiation of the material removal. This initiating power leads to an initiating pressure that increases with decreasing diamond grain size and that has to be overcome to carry out a stationary machining process. The surface formation for the material zirconium oxide is characterized by microplastic deformations. The share of brittle material removal increases with increasing diamond grain size. Figure 16.1 summarizes the fundamental connections determined for the materials alumina and zirconium oxide.

For the material silicon carbide, a stationary material removal is possible only if small diamond grain sizes are used in a wear-resistant metal bond. The surface formation at small diamond grain sizes in the range of D10 is characterized in addition to single brittle chipping areas by plateau areas that resulted from a ductile material removal. The ductile material removal and the low expansion of the brittle fracture areas lead here to the surface qualities of $R_a = 0.05$ μm and lesser. For bigger diamond grain sizes in the order of D20, there are enhanced brittle chippings that cause an increase in surface roughness and a reduction in material strength.

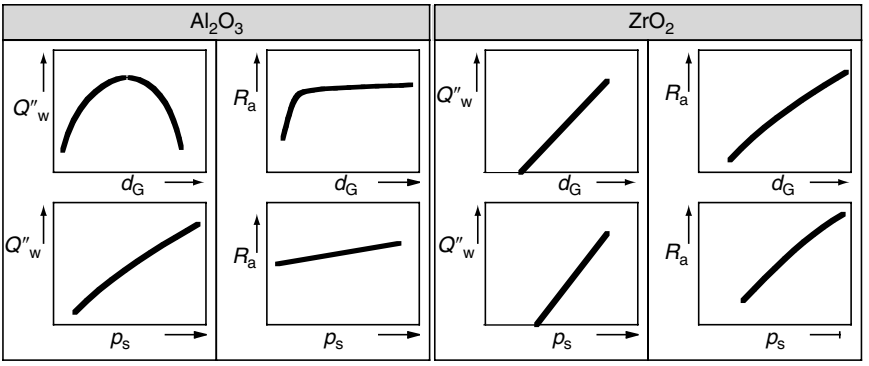

FIGURE 16.1
Material removal rate and roughness in relation to diamond grain size and stone pressure during honing of oxide ceramic materials. (From Weigmann, U-P.: Honen keramischer Werkstoffe. Dissertation TU Berlin, 1997. With permission.)

Silicon nitride can be machined with diamond honing stones with ceramic bonds and with metal bond CBN honing stones. If ceramic bonds are used, honing can be used only as a finishing process due to a high tool wear. Using CBN honing stones leads in connection with a high stone pressure to a stationary machining condition that is characterized by a ductile material removal with brittle chippings in the contact zone of single grains.

Furthermore, it could be shown that the temperature increase of the tool may represent a limiting criterion for the process design particularly at high material removal rates. The amount of heat induced into the material at constant removal mechanisms is hereby not defined by the material removal rate, but by the effect induced into the active zone. If the heat removal is improved or if a higher heat-resistant fixing is used for the honing stones on the tool, it can be presumed that the material removal can be further increased.

16.2.3 Influence of Material and Structural Properties

Material and structural properties exert a great influence on the honing conditions. Thus, a variation of material properties within a material group causes considerable changes in the honing process (Weigmann, 1997). For alumina, for instance, the machining process and the surface formation are highly influenced by the alumina grain size. For zirconium oxide, on the other hand, there is a trend toward an influence of the material hardness on variations of honing parameters. In contrast, different SiC specifications produced almost identical honing results; a correlation between honing process and material properties is not possible here. The Si_3N_4 specification has a great impact on the course of the honing process. The predominant mechanism of surface formation for this material is determined by a ductile material removal. Compared with hot-pressed silicon nitride, sintered and gas pressure sintered material specifications lead to an increase in the share of brittle material removal.

16.3 Grinding with Lapping Kinematics

16.3.1 Process Technology

Surface grinding with lapping kinematics represents an advanced development of plane parallel lapping. The kinematic design of the machine is the same, but instead of lapping wheels and loose grains, bound grinding wheels are used. These mostly consist of silicon carbide or diamond in various bindings. The machining on double-wheel machines allows us to operate a great number of workpieces simultaneously between two horizontal wheels. The parts are fixed in holders that are led between two pin circles. This way,

the characteristic cycloidal path curves are generated between parts and wheels. Corresponding to these path curves, characteristic wear profiles emerge in the process, which require that wheels be conditioned at regular intervals.

In contrast to most of the other grinding methods, not the feed in this double-wheel principle, but the force affecting the upper grinding wheel in the process is defined (Funck, 1994; Spur and Aredlt, 1997; Uhlmann and Ardelt, 1998; Uhlmann, 1998). Using grinding wheels considerably increases the attainable material removal rates in comparison with lapping. As the dirt development is significantly reduced, the process is suitable for automation. Disadvantages compared with lapping include a higher heat development and lower flexibility with respect to cutting tool–workpiece material combinations. Moreover, this method places higher demands on the machine construction in terms of driving powers and dynamic machine rigidities.

Existing lapping machines are only marginally suitable for the application of grinding wheels, because higher cutting forces arise during machining with bound grain, and higher driving powers are required. Because of the increased stress, the grinding process reacts more sensitively to vibrations than does the lapping process. The workpiece holders suffer an increased wear on the tooth flanks and on the sparings due to higher velocities.

16.3.2 Machining Process

Surface grinding with lapping kinematics is less flexible in terms of material combinations of parts and tools than lapping, i.e., the materials and machining parameters must be carefully coordinated. Constant material removal rates can only be reached over a longer period of time, if the grinding wheels operate in the self-sharpening range. Therefore, selecting an appropriate cooling lubricant is also very important.

With respect to evenness and plane parallelism, the attainable accuracies are comparable to those of lapped parts. Ground parts, however, exhibit a surface structure with curved grinding traces superimposing in all directions. Lapped surfaces on the other hand are characterized by a microscopic crater structure that does not reveal any directional dependencies. If surface isotropy is a necessary quality criterion as, e.g., in optical applications, then surface grinding with lapping kinematics cannot be used. The various removal mechanisms and resulting surface patterns are shown in Figure 16.2 for the example of a silicon nitride sample.

16.3.3 Application and Prospect

Today, many different parts are machined by surface grinding with lapping kinematics. Fields of application with the respective part examples are:

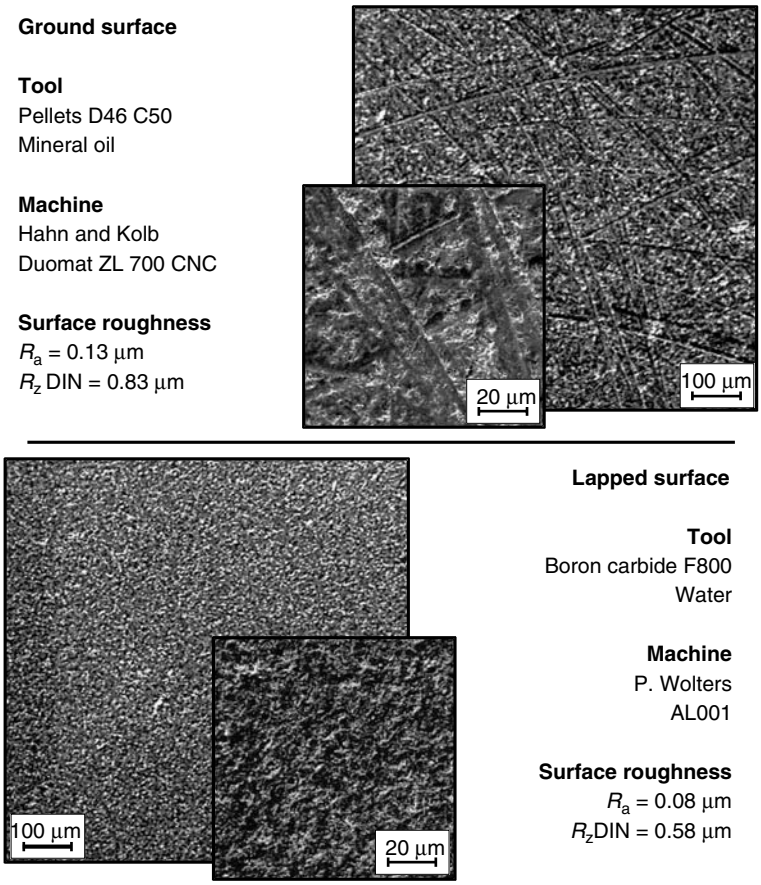

FIGURE 16.2
Silicon nitride samples ground and lapped.

- Bearings: inner and outer rings of bearings, front sides of cylinder rolls
- Pneumatics: faying surfaces on regulating and control elements
- Gaskets and washers: faying surfaces of rotary seals of any kind, gaskets and washers from oxide and nonoxide ceramics, graphite, hard metal, and steel
- Tools: indexable inserts, circles, and revolving blades

In contrast to lapping wheels, profiling of grinding wheels in this range of size is much more difficult. On the one hand, the stiffnesses of the wheel dresser are often not sufficient. On the other hand, the material costs of the used diamond coatings are so high that multiple removal of greater profile

deviations may endanger the economic viability of the process. Profiling causes special problems because of the interrupted cut at pellet grinding surfaces.

The current investigations on surface grinding with lapping kinematics are carried out in cooperation with several industrial partners. Surface grinding with lapping kinematics shall be qualified for the machining of difficult-to-machine materials such as silicon nitride or different hard metals to such an extent that numerous, subsequent lapping operations and following polishing processes can be substituted by one operation to significantly shorten the process sequence in part production.

16.4 Cooling Lubrication in Grinding of Ceramic Materials

16.4.1 General Facts

The task of cooling lubrication in the machining of ceramic materials is to minimize the mechanical, thermal, and chemical stresses arising in the active zone between tool and workpiece. The cooling lubrication serves, on the one hand, to reduce the friction between grain and workpiece and thus to reduce the heat developing in this area. On the other hand, it cools or thermally stabilizes workpiece, tool, and grinding machine by absorbing and removing the developing heat. In addition, the cooling lubrication must wash away the chips from the contact zone or the workroom of the machine (König, 1980; Spur, 1989).

To fulfill the task of cooling lubrication safely, all elements of the cooling lubrication system, i.e., cooling lubricant, circulation system with feeding and cleaning devices, must be effectively designed and coordinated.

16.4.2 Selecting the Cooling Lubricant

16.4.2.1 Technological Aspects of the Selection

The cooling lubricant is of central importance for setting favorable cooling lubrication conditions. Its properties, which are determined by type, oil, additives, concentration, and condition, considerably define the efficiency of the cooling lubrication. Nonwater mixable and water mixable cooling lubricants are available for grinding machines.

16.4.2.1.1 Setting Conditions

The individual cooling lubricants vary in fulfilling the tasks of cooling and lubricating. The different cooling and lubricating capacities of the single media differently affect the process and the work result in relation to

process characteristics such as depth of cut and angle of impact of the cutting edges on the workpiece surface, as well as in relation to characteristics of the active partners, e.g. their ductility, the geometry of the cutting edges, and the existing chip volume.

In connection with an increased chip thickness, a heightened material removal rate leads to a transition from grain flattenings to grain splinterings as predominant wear mechanism because friction processes are reduced and the mechanical stress of the diamond grains increases at the same time. Investigations proved a stationary course of the grinding process that is not significantly influenced by an improved lubricating effect of the cooling lubrication. However, a further increase in related material removal rate already holds the danger that the single grain stresses lead to a splintering of bigger grain fragments and to complete grain chippings for cutting edges that jut out widely. In contrast, reducing the material volume removed per time and the grinding wheel width unit enhances the ductile material behavior during chip formation that is accompanied by intensive friction between grinding grain and material as well as strong grain flattenings.

It is presumed that for these grinding conditions, a good lubricating effect of the cooling lubricant is comparably more important to slow down the wear progress. Starting from an almost comparable initial level, the normal force rose to a clearly higher value in the investigations after a related material removal of $V'_w = 780$ mm^3/mm when using a solution. The measured radial wear confirms the assumption that the grain wear has not yet progressed as much at this process time when using lubricating oil as when using an aqueous solution.

Although using grinding oil offers technological advantages at various material removal rates at low feeds, its application partly faces limits in the range of creep feed grinding. The grinding wheel was strongly thermally damaged after it had been used at a feed of $a_e = 0.7$ mm and with grinding oil. The mineral oil was obviously not able to absorb the amounts of heat generated to a higher extent with the contact length. The problems did not occur when using a solution. Up to a feed value that lay in the investigations at $a_e \approx 0.2$ mm, independent of the material removal rate, the described advantages of a mineral oil as cooling lubricant could nevertheless be confirmed (Brücher, 1996).

16.4.2.1.2 Grinding Wheel Specification and Topography

Irrespective of the used grinding wheel specification, the use of a grinding oil causes a lower increase in process forces. This fact supports the assumption that the statements made with regard to the resin-bonded grinding wheel can well be applied to other specifications. Minimum differences were found for the ceramically bonded grinding wheel. Apparently, the cooling lubricant here has the most minimum effect on the design of the cutting-edge space. Yet, this tool also reveals differences of 50% in the radial

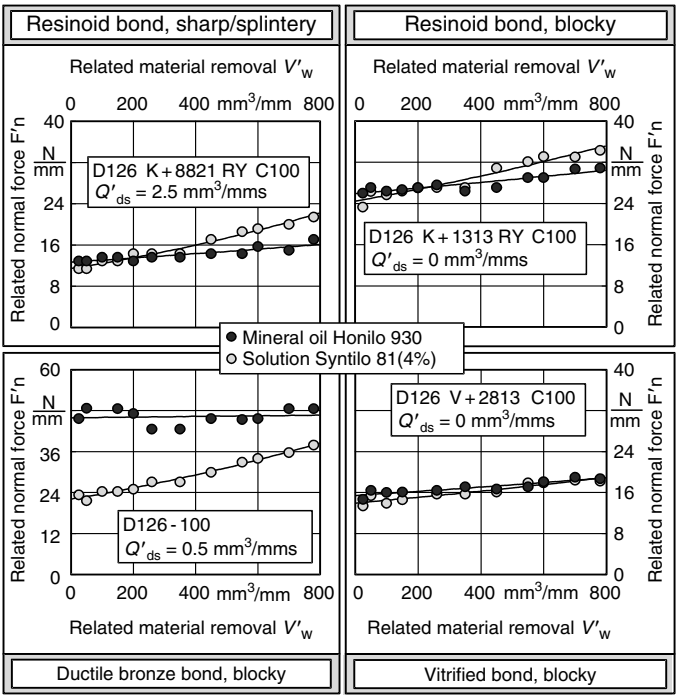

Material:
HPSN

Profiling with SiC-roller
sharpening with
corundum-stick:
v_{cds} = 20 m/s

Grinding parameter:
v_c = 35 m/s
v_{ft} = 10 m/min
Q'_w = 5.0 mm³/mms

Cooling lubrication:
P_{KS} = 2 bar
Q'_{KS} = 3.75 l/min mm
T_{KS} = 20°C

FIGURE 16.3
Normal force as a function of material removal for different grinding wheel specifications and cutting fluids.

wear after a related material removal of $V'_w = 780$ mm³/mms (Brücher, 1996). The increase in grain stress causes an early failure of the brittle–hard bond, which is connected with an increased grain loss and the generation of new cutting edges (Figure 16.3).

The topography of the grinding wheel, which can be defined by the profiling and sharpening conditions, exerts a great influence on the efficiency of the cooling lubrication. On the one hand, it determines the capacity of the tool to transport the cooling lubricant. On the other, it causes a change in the relevant wear mechanisms that are supported or limited by the cooling lubricant. At a small grain protrusion, the grains are firmly enclosed in the bond and therefore exposed over a long period of time to the mechanical and thermal stresses of the grinding process. The grain wear that is characterized primarily by grain microwear, with high portions of flattenings for this grinding wheel specification and the used grinding conditions, is in this range decisive for the course of the grinding process. As there are hardly any grain chippings because the grains are firmly enclosed in the bond, progressing grain flattenings lead to very high numbers of cutting edges at simultaneously high single grain forces and thus, to strong increases in force. Using grinding oil can

hereby reduce the stresses on the grain and hence the degree of grain flattenings, and lead to a more favorable grinding process.

At large grain protrusion, on the contrary, the single grain forces increasing with starting grain wear quickly exceed the critical loads, so that grain chippings occur frequently. This is accompanied by a distinct increase in radial wear of the grinding wheel. The lower stresses on the grinding wheel during grinding with oil, however, continue to result in slower wear speeds, because the wear conditions necessary for exceeding the critical load by the single grain force are generally reached later.

16.4.2.2 Physiological, Ecological, and Economic Aspects

In addition to the technological properties, the physiological and ecological behavior of the cooling lubricant, which due to measures on the part of the legislator is increasingly reflected in economic characteristics, is also decisive in selecting the optimal cooling lubricant.

The purposeful selection is hereby impaired by the large number of technological, economic, ecological, and safety-technological criteria, which must be equally considered. To quantify the aptitude of various cooling lubricants, the selection of cooling lubricants can generally be based on an evaluation of the costs expected for the use of the cooling lubricant. The total costs consist hereby of the specific costs for the cooling lubricant change, the specific costs due to the reduction of cooling lubricant amount by chips, workpiece, etc., as well as specific maintenance and control costs. All these types of cost are massively influenced by the cooling lubricant, so that a cost comparison under constant operation conditions can serve to select the cooling lubricant alternative that presumably has the least cooling lubrication costs. A considerable disadvantage of this procedure, however, is that not all relevant criteria of selection are included in the costs and in the selection process. Above this, there is the problem of giving a sufficiently exact evaluation of some cost shares already before the use of the cooling lubrication in the process.

One possibility to include nonquantifiable criteria in the consideration is presented by an efficiency analysis (Spur and Brücher, 1995; Brücher, 1996). Here, the single objectives are divided as much as possible into subobjectives and then evaluated individually with respect to their potential to fulfill the objective. This can be done by means of concrete characteristic quantities and, if that is not possible, by means of subjective judgments. The individual judgments are afterward combined in consideration of their importance and a total efficiency of the cooling lubricant is defined. The decision of selecting a cooling lubricant affects various departments in a company such as buying, manufacturing, planning, as well as the representative for safety and environment, all of which might have different preferences regarding the selection. To minimize the subjectivity of the decision, experts of these departments should take part in organizing the objective's hierarchy, in

determining the important factors, and in evaluating to what degree the subobjectives are fulfilled.

16.4.3 Design of the Feed System

The feed system realizes the supply of the contact zone with the cooling lubricant. The pressure in the contact zone can hereby serve as a measure for the quality of the supply (Spur et al., 1998). A reduction of the grinding wheel wear can be observed with increasing cooling lubricant pressure. The total grinding forces, which result from cutting forces and cooling lubricant forces increasing with the pressure, rise strongly at an increase in feed pressure when a free jet nozzle is used. If only the pure grinding forces are observed, one can record only a minor increase in force. In the context of a decreasing wear, this can be explained by the fact that the diamond grains can be kept longer in the bond at lower grinding wheel surface temperatures and that they cover longer friction paths under the formation of stronger grain flattenings.

Improved nozzles and nozzle settings form the prerequisite for a reduction of the necessary cooling lubricant volume. A turbulence-free feed of the fluid must be guaranteed to achieve the required jet qualities. In addition to the design of the nozzle, the design of the feed lines from the pump to the nozzle also contributes to the jet quality. Tight radii or sharp edges should hereby be avoided.

Another approach to reduce the circulating cooling lubricant amounts is to use tools with internal cooling to exactly induce the cooling lubricant into the active zone (König et al., 1993). In the extreme case, the cooling lubricant is proportioned in such a way that it is completely used by evaporating. A major advantage of this cooling lubrication technology is that only few amounts of cooling lubricants are required (ca. 10–100 ml/h) and that the cooling lubricant is sprayed only once and does not have to be operated in a cycle.

16.4.4 Design of the Cleaning System

The cleaning of the cooling lubricant assumes a special importance in terms of aspects such as its function and service life. Ceramic chip particles moreover increasingly attack guides and bearings when they circulate in the machine. Therefore, enhanced demands on the cleaning process must be placed when machining ceramic materials.

Processes flotation, filtering, and centrifuging can be used to clean the cooling lubricants used in the machining of ceramic materials. These methods may also be combined in series or parallel connection. A comparative investigation of different cleaning systems revealed advantages for the alluvial filter and the centrifuge with respect to filter fineness and drying degree of the filtrate (Brücher, 1996). A disadvantage of the alluvial filter is that the

relatively large amounts of waste to be disposed arise due to its operation with filter appliances. High-energy costs must be expected on the other hand when using a centrifuge because of the high drum driving power.

References

Brücher, Th.: Kühlschmierung beim Schleifen keramischer Werkstoffe. Dissertation TU Berlin, 1996.

Funck, A.: Planschleifen mit Läppkinematik. Dissertation TU Berlin, 1994.

Holl, S.-E.: Ultraschallunterstütztes Schleifen von Hochleistungswerkstoffen. Vortrag anläßlich der Jahrestagung der Deutschen Keramischen Gesellschaft, München, 13 August 1997.

König, W.: Fertigungsverfahren, Band 2. VDI-Verlag, Düsseldorf, 1980.

König, W. et al.: Kühlschmierstoff-Eine ökologische Herausforderung an die Fertigungstechnik. In: Wettbewerbsfaktor Produktionstechnik, AWK-Sonderausgabe, VDI-Verlag, Düsseldorf, 1993.

Liebe, I.: Auswahl und Konditionierung von Werkzeugen für das Außenrund-Profilschleifen technischer Keramiken. Dissertation TU Berlin, 1996.

N.N.: CeraNews Special. Aktuelle Brancheninformation des Cerasiv-Produktbereichs Medizintechnik, Hrsg.: Cerasiv GmbH, Ausgabe 3, März 1996.

Pattimore, J.: Optimisation of grinding for cylindrical silicon nitride components for mass production. Vortrag und Tagungsband, Informativer Arbeitskreis Keramikbearbeitung, IWF Berlin, 16 March 1998.

Popp, M.: Seriengerechte Herstellung von Bauteilen aus Hochleistungskeramik am Beispiel des Keramikwälzlagers. In: Tagungsband Karlsruher Arbeitsgespräche 1998, BMBF/PFT, Karlsruhe, 12 und 13 March 1998.

Spur, G.: Keramikbearbeitung—Schleifen, Honen, Läppen, Abtragen. Carl Hanser Verlag München Wien, 1989.

Spur, G.; Brücher, Th.: Optimization in the cutting fluids system for grinding of advanced ceramics. Vortrag und Tagungsberichtsband, *First International Machining and Grinding Conference*, Dearborn, USA, 12–14 September 1995.

Spur, G.; Ardelt, Th.: Zylinderläppen und -feinschleifen. ZWF 92, 9, S465–468, 1997.

Spur, G.; Brücher, Th.; and Laufer, J.: Kühlschmierung beim Schleifen keramischer Werkstoffe. In: *11th International Colloquium Tribology, Industrial and Automotive Lubrication*. Stuttgart/Ostfildern, Germany, 13–15 January 1998.

Thiemann, K.-H.: Die Wirkung von Schleiffehlern auf die Festigkeit von Si_3N_4-Keramiken. Vortrag und Tagungsband, Informativer Arbeitskreis Keramikbearbeitung, IWF Berlin, 16 March 1998.

Uhlmann, E.G.: Tiefschleifen hochfester keramischer Werkstoffe. Dissertation TU Berlin, 1993.

Uhlmann, E.G.: Developments in grinding of ceramic materials. *Abrasives Magazine*, July/August 1998.

Uhlmann, E.G.; Ardelt, Th.: Kinematics and wheel wear in face grinding on lapping machines. In: *Progress of Cutting and Grinding*, Chen Dingchang u. a, 1998.

Weigmann, U-P.: Honen keramischer Werkstoffe. Dissertation TU Berlin, 1997.

17

Ultrasonic Machining of Ceramics

G. Spur, E. Uhlmann, S.-E. Holl, and N.-A. Daus

CONTENTS

17.1 Introduction

Ceramic component parts frequently meet the highest demands on long-term guarantee of functional properties. Unfortunately, however, the production

costs are so high that these materials have not yet been totally accepted. A major part of these costs arises in finishing machining and thus, in the classic abrasive processes such as grinding, honing, lapping, and polishing. Moreover, there are still no adequate strategies for accurate and economical machining of complex geometries such as borings, grooves, spherical surfaces, or sculptured surfaces (Uhlmann and Holl, 1998). Ultrasonic lapping and electrical discharge machining are suitable for the production of these flexible geometries, but have some significant disadvantages. Although only conductive materials can be machined with EDM, low material removal rates, high wear of the molds, and mostly insufficient accuracy impose limits on ultrasonic lapping. Therefore, adequate manufacturing technologies for high-precision and economical machining of ceramic materials have been studied and optimized during the past few years.

Based on ultrasonic lapping, in which a tool oscillating with ultrafrequency pushes loose grains into the workpiece surface and thus, removes material, various manufacturing technologies have been combined for some years with ultrasound. Almost all cases produced an improvement in process results (Drozda, 1983; Uematsu et al., 1988; Nankov, 1989; Prabhakar et al., 1992; Pei et al., 1993; Suzuki et al., 1993; Westkämper and Kappmeyer, 1994). Better bore qualities can be reached with difficult to cut materials, if single-pass honing is replaced by high-frequency honing (Westkämper and Kappmeyer, 1995). Warnecke and Zapp (1995) examined the influence of workpiece vibrations directed axially toward the grinding wheel in alternating surface grinding of ceramic materials. In addition to the generation of an improved surface structure, the friction in the active zone and the mechanical stress could be reduced. Cutting with ultrasonic vibrating blades served to reduce the cutting forces while achieving good machining results (Neder, 1990). Ultrasonic lapping successfully produced graphite electrodes for electrical discharge machining (Rhoades, 1985, 1995). Polishing with ultrasonic assistance improved the surface of steel workpieces machined with EDM (Williams and Allen, 1995).

So far, ultrasonic lapping and ultrasonic-assisted grinding have been used in industrial production for the finishing of brittle–hard materials such as ceramics. Because of the high material removal rates obtained in ultrasonic-assisted grinding, along with a high geometrical freedom, a broad field of application can be predicted for this process in the future.

17.2 Ultrasonic Technology

Elastomechanical ultrasonic vibration is generated by the transformation of electric energy in piezoceramic or magnetostrictive sonic converters. A voltage generator serves to convert a low-frequency mains voltage into

a high-frequency electric alternating-current voltage. The generated longitudinal vibrations are periodical elastic deformations of the mechanical vibration system in the micrometer range at supersonic frequencies, that is, higher than 16 kHz (DIN 1320, 1969). The sound generating unit preceding the actual ultrasonic tool or shape-generating counterpart consists of a sonic converter, an amplitude transformer (transforming sections), and sonotrodes (Spur and Krieg, 1995). Figure 17.1 describes the design of a vibration system.

The process of sound generation and transformation should be largely free of losses to obtain high total efficiency of the vibration system. At the same time, it is required to produce a maximum vibrational amplitude at the sonic converter to reach an amplitude at the working surface that

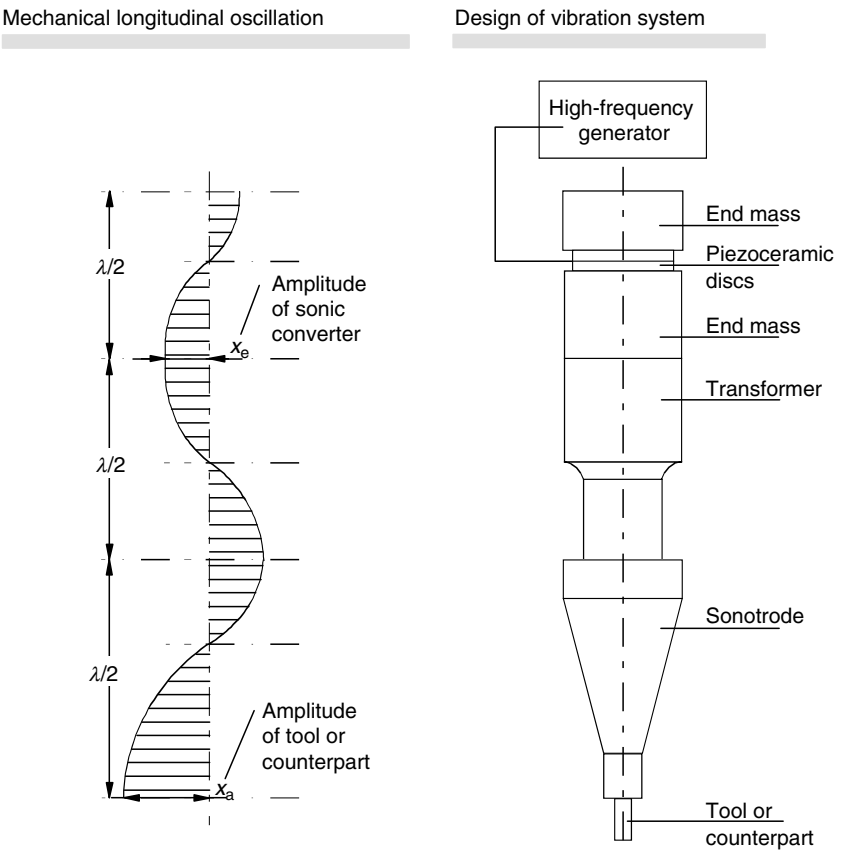

FIGURE 17.1
Design of vibration system and vibration course for the example of ultrasonic lapping. (From Bönsch, C.W., *Dissertation RWTH Aachen*, Germany, 1992; Haas, R., *Dissertation RWTH Aachen*, Germany, 1991.)

corresponds to the machining task. Mainly a loss-free increase in amplitude is guaranteed by means of resonance, that is, a vibration with a frequency that corresponds to that of an eigenfrequency of the system. For the constructive design of the system, this means that the geometrical lengths of the single elements must correspond to half the wavelength of the vibration or an integral multiple.

The amplitude of the converter, however, is generally too low for machining. It can be raised to a value sufficient for machining by a subsequent transformer. The sonotrode serves to take up the tool and also facilitates the resonance-apt adaptation to the entire vibration system. In addition, there is the possibility to design the sonotrode in such a way that it aids in achieving an extra amplitude gain (Haas, 1991). The ultrasonic vibration unit is clamped at the places where vibration nodes occur because acceleration and amplitude are zero at these points and thus, normal force freedom predominates.

Electric energy is converted into mechanical vibrations in modern machinery using the piezoelectric effect. It concerns the reversible property of special ceramic materials to deliver an electric voltage when affected by external forces. This characteristic is used for the generation of ultrasonic vibrations in such a way that the applied voltage is converted into mechanical vibrations. Modern sonic converters usually contain several piezoceramic disks of lead zirconate titanate restricted by two final masses that are mechanically prestressed by a centric screwing.

17.3 Technology of Ultrasonic Lapping

17.3.1 Fundamentals

The manufacturing process of ultrasonic lapping can be assigned according to DIN 8589 part 15 (DIN 8589, 1985) to the special lapping technology, vibration lapping. The geometrically undefined lapping grain distributed loosely in a fluid receives impulses by a shape-generating counterpart vibrating in the ultrasonic range, which enables the grain to carry out material removal (Haas, 1988; Spur, 1989).

Originally, ultrasonic machining was thought to be drilling and sinking by ultrasonic lapping, during which the profile of the shape-generating counterpart is projected onto the workpiece. The machinability of a workpiece by ultrasonics was first described in 1927 by Wood and Loomis (Wood and Loomis, 1927). However, this observation remained largely unnoticed at first, until the British Balamuth requested a patent on a new machining process, nowadays known under the definition vibration lapping, via the law firm Farrer (1948). Extensive scientific investigations were conducted

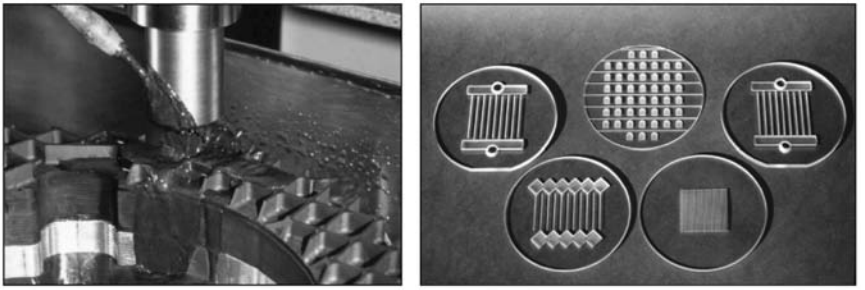

FIGURE 17.2
Process of ultrasonic lapping and machining (Photo from MAFELL Company, Oberndorf, a.n., Germany.)

during the 1950s and 1960s for instance by Shaw (1956) and by Blanck (1961). Moreover, investigations on ultrasonic lapping with additional translatory motion were carried out in the early 1980s (Noelke, 1980).

The increasing application of ceramic materials during the 1980s required the development of suitable manufacturing technologies for hard machining. Ultrasonic lapping is particularly predestined for this purpose. In contrast to conventional manufacturing processes, particularly with geometrically defined cutting edge, ultrasonic lapping serves to machine preferably materials with low fracture toughness K_{IC}. Sinking the shape-generating counterpart into the workpiece enables the generation of any contours, which is not or only partially possible with other processes. Figure 17.3 presents the parameters and limiting quantities determining the work result.

A rotational superposition of the sinking process and a path-determined machining helped to effectively extend the method (Figure 17.4).

In analogy with Spur and Engel (1996) and Engel (1997), who established an exact definition of the term for the tool during lapping, the tool in ultrasonic lapping is described as a combination of the shape-generating counterpart with the lapping grain. In ultrasonic lapping, the loose grain

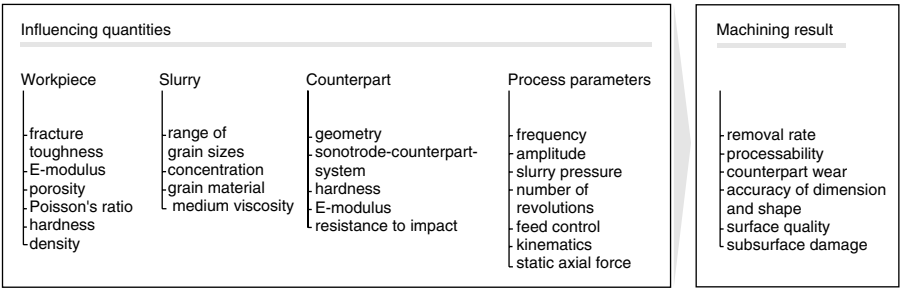

FIGURE 17.3
Influences on machining result during ultrasonic lapping.

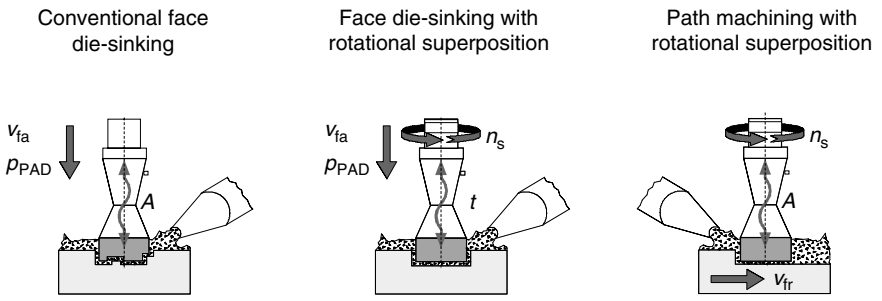

FIGURE 17.4
Process variants of ultrasonic lapping.

deposited in a medium is pushed in the orthogonal direction to the workpiece onto and into the workpiece surface by vibrations of the shape-generating counterpart. The high-frequency cyclic stress affecting the workpiece surface to be machined by a great number of geometrically undefined lapping grains in the working gap leads to material removal. Water is mostly used as the medium, and boron carbide is usually used as the abrasive.

During the rotational motion of the shape-generating counterpart and a path-determined machining, the resulting relative motion between the shape-generating counterpart and the workpiece is supplemented accordingly by additional velocity components. The chip formation and removal mechanisms applying to brittle–hard materials such as ceramics differ distinctly from those of ductile materials such as metals. The term for grain engagement coined by Sabotka (1991) illustrates the subordinate role of plastic processes (penetration) during material removal. Owing to the great number of covalent bonds, material removal is caused by brittle fracture as a result of the mechanical stress in cutting processes. Kinematics in ultrasonic lapping lead to a multitude of microscopic engagement results in the workpiece surface, which is in sum form the macroscopic material removal. Each grain engaging into the workpiece surface causes deformations and induces microcracks into the subsurface. If the stress is relieved, lateral cracks are formed at the edge of the plastically deformed zone and eventually, particle chippings occur (Lawn, 1993; Engel, 1997; Hilleke, 1998).

The material removal mechanism during ultrasonic lapping has not yet been clarified completely. During the process, the inaccessible active zone hinders direct scientific investigations of these mechanisms, so only analogy tests can contribute to the clarification of the active correlations. However, one can proceed from the assumption that the kinetic energy transferred to the grains by the shape-generating counterpart leads to microscopic material removal when striking the workpiece surface.

There are different removal mechanisms listed for ultrasonic lapping in literature that rate the various identified mechanisms partially according to

their effect, and partially treat them equally. The following principles have been determined so far (Spur, 1989; Bönsch, 1992; König et al., 1993; Spur and Krieg, 1995; Hilleke, 1998):

- Direct impact

Material removal is caused by the stress applied to the workpiece surface by the lapping grain, with a brief direct contact between the shape-generating counterpart, the grain, and the workpiece. The kinematic prerequisite for this is that the minimum working gap is smaller or equal to the maximum grain diameter. It is agreed that the direct impact is mostly significant for the achievement of high removal rates. The process is primarily designed in a way that supports this active mechanism.

- Indirect impact

Transfer of energy is necessary for material removal from the shape-generating counterpart to at least two lapping grains to the workpiece surface, under the condition of a force-locking contact between the shape-generating counterpart, lapping grains, and the workpiece, and a working gap height higher than the maximum grain diameter. The distribution of the impact impulse on several grains leads to a reduction in the material removal when compared with the direct impact.

- Grain spinning-on

The mechanism of *grain spinning-on* includes the acceleration of the lapping grain because of the contact with the moving shape-generating counterpart. The grain transfers the energy necessary for material removal to the workpiece surface without a simultaneous contact between the shape-generating counterpart, lapping grain, and the workpiece.

- Rolling motion of grains

This mechanism was found for the superficies of the shape-generating counterpart owing to a lack of transverse vibrations. The grains roll off between the shape-generating counterpart surface and the workpiece surface and engage with the cutters in the material, causing material particle chippings.

- Cavitation

Because of the vibrations of the shape-generating counterpart during the process, the substrate material of the lapping grain, mostly water, is cyclically compressed and expanded. When the water is expanded,

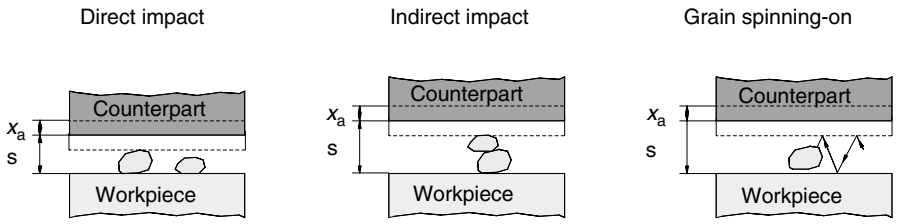

FIGURE 17.5
Predominant removal mechanisms according to Hilleke. (From Hilleke. M., *Dissertation RWTH Aachen*, Germany, 1998.)

steam bubbles may be formed that can cause mass accelerations during subsequent compression and thus contribute to the material removal.

Figure 17.5 presents the predominant mechanisms of material removal during ultrasonic lapping.

Recent investigations (Hilleke, 1998) confirm the statement that direct and indirect impacts as well as grain spinning-on onto the workpiece surface represent the predominant mechanisms of material removal during ultrasonic lapping. The contribution of cavitation phenomena is considered to be trivial (Rozenberg et al., 1964).

17.3.2 Machinability of Ceramic Materials

According to Spur (1989), the machinability of a material is defined as the material behavior during a defined machining. Statements regarding the coefficient of difficulty of material separation are included in this contemplation. Criteria for the analysis and assessment of machinability are given by the attainable material removal rate, the realizable accuracy of dimension and shape, as well as the surface quality. Moreover, subsurface damages caused by the machining process and the resulting subsurface properties are taken into consideration when assessing ceramic materials.

The attainable material removal rate during ultrasonic lapping of ceramic materials depends first on the fracture toughness K_{IC} of the materials. Ceramics with a low fracture toughness as for instance Al_2O_3, RBSN, and SiC can be machined with a high material removal rate, whereas the attainable material removal decreases considerably with increasing fracture toughness (HPSN or ZrO_2) (Spur, 1989; Cartsburg, 1993). These findings can also be transferred to reinforced ceramic materials (Grathwohl et al., 1988; Cartsburg, 1993).

The pronounced connection between the fracture toughness of the material to be machined and the attainable material removal rate can be explained by the described mechanisms of material removal and the related surface formation. Materials with a low resistance to cracks are characterized by the

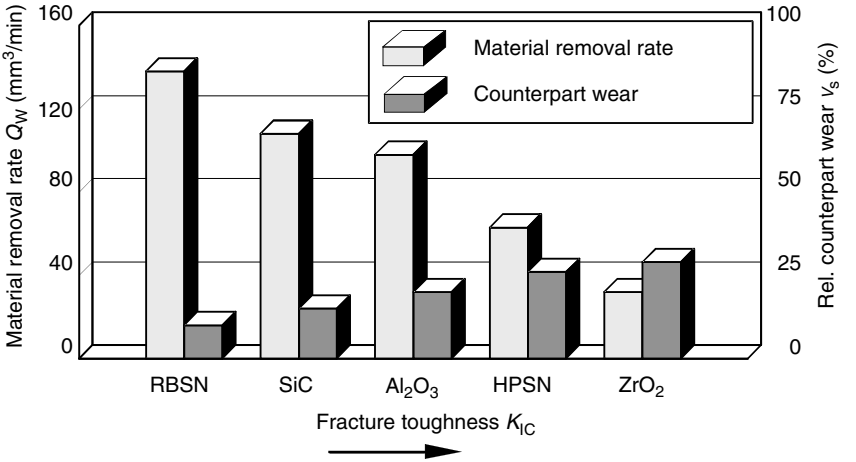

FIGURE 17.6
Material removal rate and shape-generating counterpart wear in relation to fracture toughness of the ceramic to be machined. (From König, W., Vortragsband zur VDI-Fachtagung Neue Werkstoffe erfordern neue Bearbeitungsverfahren, Düsseldorf, Germany, 1988.)

fact that they are hardly able to reduce mechanical stresses by local plastic deformation. Instead, they tend to form and spread cracks. If these cracks extend to the surface, larger material areas are removed (Weigmann, 1997).

Figure 17.6 shows the realizable material removal rates and the resulting shape-generating counterpart wear on the counterpart face during ultrasonic lapping of different ceramics in relation to the fracture toughness. The long machining times in ultrasonic lapping of ceramic materials with high fracture toughness cause an enhanced wear in the form of a reduction in length of the shape-generating counterpart. The reproducibility of material removal rates and counterpart wear is still very limited. Sometimes the high scattering of results can be attributed to the constantly changing machining conditions in the working gap.

17.3.3 Conventional Face Die-Sinking

If the feed motion of a shape-generating counterpart in axial direction is parallel to the ultrasonic vibration, the process is called conventional face die-sinking. The process can be used purely for drilling or for the generation of profiles in the workpiece. In this case, a profiled shape-generating counterpart is used, whose negative shape is projected onto the workpiece (Figure 17.4a).

The machining process is generally designed by first selecting the mean grain size considering the desired removal rate and the resulting surface

quality. Afterward, the related reaction force and the vibrational amplitude are determined in relation to the grain size. The feed required for the die-sinking motion can be realized both with a compulsory feed at constant die-sinking speed and with a force-controlled feed with constant contact pressure. As a rule, the machining is carried out with a force-controlled feed. The supply and removal of the abrasive is carried out by means of an abrasive dressing equipment, which keeps the grains equally distributed in the medium.

Among the process parameters, lapping pressure and feeding power, as well as the vibrational amplitude exert the greatest influence on the work result. In contrast, additional parameters such as the connection between the shape-generating counterpart and sonotrode, abrasive pressure, and so on, have only minor impacts and thus minor significance (Bönsch, 1992). Both parameters significantly define the size of the working gap and also the primarily occurring removal mechanism and the flushing conditions in the working gap.

17.3.3.1 Vibrational Amplitude

Setting the vibrational amplitude at the shape-generating counterpart determines the maximum height of the working gap during the process and the attainable impulse when the shape-generating counterpart strikes the individual lapping grain in the working gap. In principle, it can be confirmed that an increase in vibrational amplitude leads to an increase in material removal rate. On the other hand, statements regarding the relation of the surface quality to the vibrational amplitude differ. Although Haas (1988) observed a clear surface deterioration with increasing vibrational amplitude and explained it by the increasing share of larger grains in the working gap, other authors concluded that there is no crucial connection between surface roughness and vibrational amplitude (Bönsch, 1992; Vogel, 1992).

In addition to a relation of the average peak-to-valley height and the vibrational amplitude, there is also a relation to the material to be machined (Haas, 1988). Hilleke (1998) assumes here an influence of the structural properties grain size and grain boundary strength.

If the vibrational amplitude is too small, the grains are not pressed deeply enough into the workpiece surface, leading to a reduction in material removal rate. Increasing the vibrational amplitude serves to increase the material removal rate to a critical value. If the parameter is further increased, the material removal rate decreases, because the idle path of the shape-generating counterpart, during which hardly any impulses are transferred to the workpiece, increases (Spur, 1989).

Bönsch (1992) found that the optimum vibrational amplitude corresponds roughly to half the mean diameter of the used grain. If the working gap is enlarged further, increased single grain stress occurs due to the high feeding power that may lead to grain fracture. As a result, the number of grains

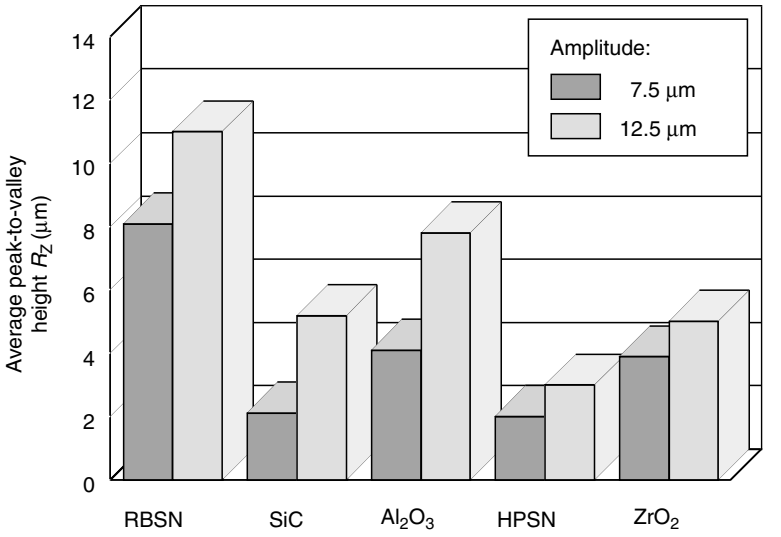

FIGURE 17.7
Relation of surface quality and amplitude of shape-generating counterpart (abrasive: B_4C F320, 50 Vol.%). (From Haas, R., Verfahren zur dreidimensionalen Bearbeitung keramischer Werkstoffe. Werkstoffe and Konstruktion 2, 2, Germany, S127–133, 1988.)

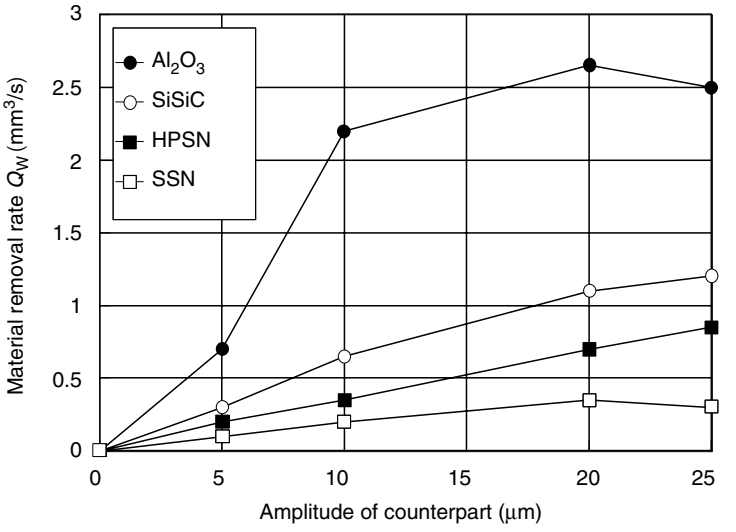

FIGURE 17.8
Relation of material removal rate and amplitude of shape-generating counterpart (abrasive: B_4C F280). (From Grathwohl, G. et al., *Materialwissenschaft und Werkstofftechnik*, Vol. 19, Germany, S81–86, 1988.)

existing in the working gap increases. The probability that the indirect impact mechanism occurs in contrast to direct impact rises due to the high grain density. This distribution of the impact impulse on several grains reduces the material removal rate.

17.3.3.2 Lapping Pressure

Although the selection of the vibrational amplitude influences the attainable removal rate and the surface quality, the lapping pressure affects only the removal rate. The set lapping pressure determines the stress applied to the grains in the working gap. Increasing the lapping pressure therefore leads to an increase in impact impulse and therefore to an increase in material removal rate. If the lapping pressure is too high, however, the grains in the working gap splinter and the impact impulse affecting the workpiece is reduced (König, 1988).

17.3.3.3 Abrasive

The geometrically undefined lapping grains represent the crucial part of the shape-generating counterpart in ultrasonic lapping because of the direct contact with the workpiece surface. When selecting the lapping grain, it must be considered that the hardness of the grain is higher than that of the material to be machined and that there is a sufficient compressive strength to the rising stress caused by the process. Boron carbide is preferably used as the abrasive because it exhibits a higher resistance to fracture than silicon carbide and is less expensive than diamond. A grain size of 40–50 μm is used in industrial practice, representing a sensible compromise between a high material removal rate and a high surface quality (Hilleke, 1998).

> Basically, it can be stated that increasing grain diameters lead to an increase in material removal rate (Noelke, 1980; Grathwohl et al., 1988; Haas, 1991). Contradictory statements exist on the influence of the grain size on the attainable surface quality. Earlier studies describe a linear connection between surface roughness and grain size (Blanck, 1961; Youssef, 1967). Cartsburg (1993) on the other hand concludes that reducing the grain size barely improves the surface qualities, but considerably increases the machining times. The counterpart wear is influenced by the grain size in such a way that selecting a more coarse grain produces an enhanced wear at the face (Noelke, 1980).

The main tasks of the substrate fluid are transporting the grains to the working gap, removing the chips and worn grains afterward, and cooling the shape-generating counterpart (Haas, 1991). Continuously renewing and removing the abrasive secures the process stability. A central bore in the shape-generating counterpart serves to suck off the used abrasive and facilitates the supply of fresh abrasive simultaneously to the working gap by the generated lower pressure. Such a compulsory flushing is particularly indispensable if the machining depth

increases. Investigations on the influence of the mixing ratio on the cutting process showed that there is an optimum percentage distribution of grain and abrasive. Deviations from this optimum distribution lead to a deteriorated process behavior (Haas, 1991).

17.3.3.4 Wear of the Shape-Generating Counterpart

Since the material removal during ultrasonic lapping is based, as described, on the embrittlement of increasingly stressed material areas, materials with a distinctive elastic–plastic behavior are used as counterpart materials. The wear, however, cannot be avoided despite a specific material selection; therefore, the following effects on the process result emerge (Noelke, 1980; Bönsch, 1992):

- Insufficient accuracies of dimension and shape
- Low counterpart times and frequent counterpart exchange
- Shift in resonance frequencies to unfavorable ranges due to length changes in the shape-generating counterpart and the generation of inadvertent flexural and torsional vibration

The use of PCD counterparts could significantly reduce the wear and distinctly improve the reproducibility of the accuracies of shape and dimension (Noelke, 1980; König and Bönsch, 1991). Owing to the high material costs, however, PCD counterparts have not been accepted for ultrasonic lapping.

On the other hand, there is a relation between counterpart wear and fracture toughness of the used workpiece materials (Figure 17.9). The wear of the counterpart increases with increasing fracture toughness of the workpiece. The reason for this is the rising machining time for more viscous materials because the stress applied by impacting grains can be balanced increasingly by elastic–plastic deformations. Materials with a low fracture toughness have a greater tendency to form and spread cracks and thus lead to higher material removal rates.

17.3.4 Conventional Face Die-Sinking with Rotational Superposition

To carry out a drilling without die-sinking a defined profile into the workpiece, the counterpart can be superimposed by an additional rotational motion. This superposition causes an increase in the material removal rate and of the accuracies of dimension and shape (Cartsburg, 1993). Besides, an improved reproducibility of the results can be determined. Because of the rotation of the shape-generating counterpart, the grains are equally distributed in the working gap, leading to a more stable process behavior. Profiling

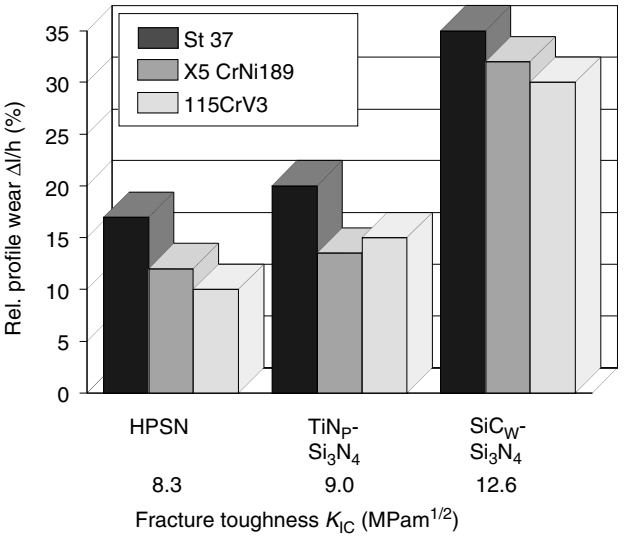

FIGURE 17.9
Wear of shape-generating counterpart in relation to the machined material. (From Spur, G. et al., *Production Engineering*, II/2, 1995. With permission.)

here is not reached by forming of the shape-generating counterpart, but by geometrical generation (Noelke, 1980).

Compared to the surface formation during ultrasonic lapping with standing shape-generating counterpart, adding a rotational motion causes changes in the predominating removal mechanisms. The rotation leads to a rolling motion of the grains at the face of the shape-generating counterpart. Above this, grains are embedded in the face, so a scratching engagement into the workpiece occurs. This mechanism superposes the impulse exchange of the direct and indirect impacts and causes a surface formation that is similar to the one of a conventional lapping process (Cartsburg, 1993). Overlapping these mechanisms leads to an increase in material removal rate by up to 40% if contact pressure and rotational speed are considered.

A crucial rotational speed emerges in relation to the contact pressure when the material removal rate cannot be increased any further or decreases (Figure 17.10). The reason for this is the rupture of the lapping film in the working gap and the resulting chatter vibrations (Cartsburg, 1993). Spur and Krieg (1995) could find in this context a change in the wear profile in relation to the rotational speed. High rotational speeds lead to an increased wear at the outer edge of the counterpart. This is owing to the high centrifugal forces that cause the grains to drift outward. The enhanced wear at the edge of the shape-generating counterpart leads to a reduction in material removal rate because of the reduced active surface.

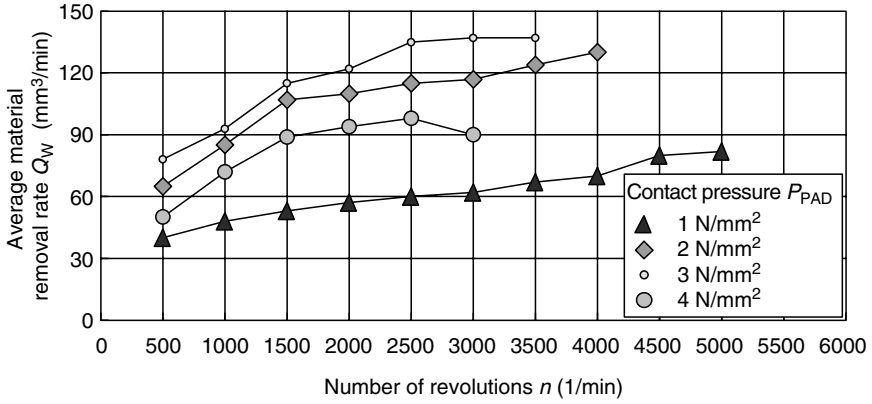

FIGURE 17.10
Material removal rate in relation to contact pressure and rotational speed during ultrasonic lapping of Al_2O_3 with rotating shape-generating counterpart. (From Cartsburg, H., *Dissertation TU Berlin*, 1993. With permission.)

17.3.5 Path Machining

In addition to the generation of bores and the projection of profiles onto the workpiece, according to Figure 17.4c, there is possibility to generate any contours almost independent of the counterpart geometry by superposition of a feeding motion vertical to the die-sinking motion. This is done, for example, in finishing of thin substrates and in the production of fine structures in glass and ceramics (Hilleke, 1998). As Figure 17.11 shows there are two possible machining strategies in path-controlled machining:

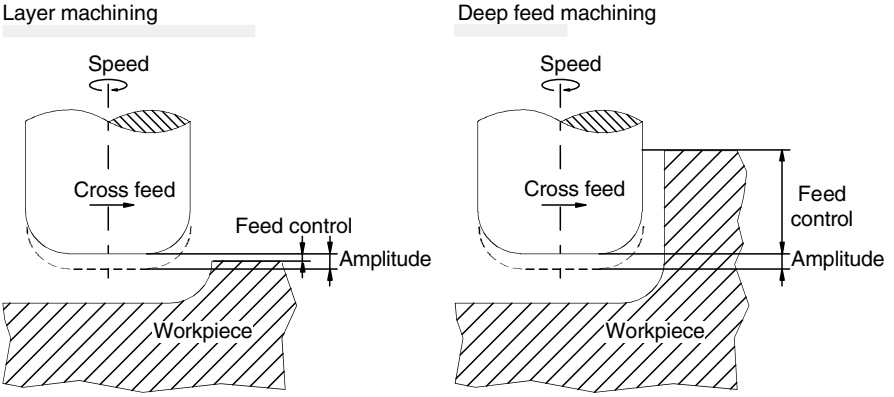

FIGURE 17.11
Layer and deep feed machining during path-controlled ultrasonic lapping. (From Hilleke, M., *Dissertation RWTH Aachen*, 1998. With permission.)

1. Die-sinking the counterpart to desired depth and subsequent running over the required contour (deep feed machining).
2. Slow die-sinking of the counterpart at a high cross-feed speed, so that the counterpart reaches the desired depth of cut in several runs (layer machining) (Noelke, 1980; Hilleke, 1998).

In deep feed machining, the cutting operation is determined by the relative motion between counterpart superficies and workpiece wall and by the rolling motion of the grains. The hammering of grains into the workpiece surface typical for ultrasonic machining is almost omitted; therefore, only low machining speeds can be realized with this machining strategy. High feeds, moreover, increase the danger of clod-like macroscopic chippings that considerably reduce the part quality (Hilleke, 1998).

Layer machining leads to a cutting process carried out by the face of the shape-generating counterpart that corresponds to that of ultrasonic-assisted die-sinking and thus, to comparable machining speeds. Due to missing cross vibrations vertical to the counterpart axis, a real three-dimensional machining is not possible with path-controlled ultrasonic lapping. A respective design of the sonotrodes, however, may serve to induce not only longitudinal vibrations, but also lateral vibrations into the process. This helps to remove material at the workpiece surface directed to the superficies at simultaneous rotation. This kinematic extension of ultrasonic lapping to ultrasonic form machining serves, on the one hand, to generate and machine complex spatial structures and, on the other, to attain a path-controlled deep feed machining at higher material removal rates (Dieter Hansen, 1990).

17.4 Ultrasonic-Assisted Grinding

17.4.1 Fundamentals

Ultrasonic-assisted grinding can be seen as a technological development of ultrasonic lapping with a rotating tool using bound grains. It represents an economical alternative to this method. So far, comparatively less knowledge exists regarding machining parameters, tool specification, and work results. Ultrasonic-assisted grinding has, nevertheless, already been used in industrial practice.

First investigations of ultrasonic-assisted grinding with corundum grinding wheels date from 1956 (Colwell). Vibrating the workpiece with a frequency between 10 and 18 kHz as well as a vibrational amplitude helped to achieve better surface roughnesses and to reduce the process temperature during surface grinding of steel materials. Scientific investigations of the process during the 1970s dealt with the influence of the grinding kinematics

on the result of steel machining (Yano et al., 1970) as well as with the application of diamond grinding wheels to the machining of titanium alloys, hard metal, and alloy steels (Nerubai, 1977). Material removal rates could be increased in all existing investigations as compared with conventional grinding, whereas clear statements concerning machining times and attainable surface qualities could not be derived. Ultrasonic-assisted grinding has been used for the machining of brittle–hard materials since the 1970s and 1980s (NN, 1977; Uematsu et al., 1988). Comprehensive scientific studies of this process, however, appeared only in the 1990s (Bönsch, 1992; Prabhakar et al., 1992; Pei et al., 1993; Suzuki et al., 1993; Spur et al., 1995; Warnecke and Zapp, 1995; Spur and Engel, 1996; Holl, 1997; Spur and Holl, 1997).

During ultrasonic-assisted grinding, the kinematics of the grinding process are superimposed by a longitudinal oscillating active motion. To realize different kinematic variants with respective positions of active partners, tool, and workpiece, ultrasonic vibration can be induced into the contact zone by both the tool and the workpiece. This constructive freedom of design serves to generate varying contours and structures in the workpiece, and to machine any surfaces. Compared with conventional grinding, the mechanisms of surface formation and wear mechanisms are fundamentally altered due to the superposition with ultrasonic vibration (Spur and Holl, 1997). The ultrasonic vibration leads to a temporarily recurring change in direction in active velocity.

The excitation of oscillation is realized by an external voltage generator and a sonic transducer according to the piezoelectric principle. Hereby, an output amplitude of only a few micrometers is reached, which can be increased by means of subsequent sonotrodes up to $A \approx 80\ \mu m$, depending on the respective application.

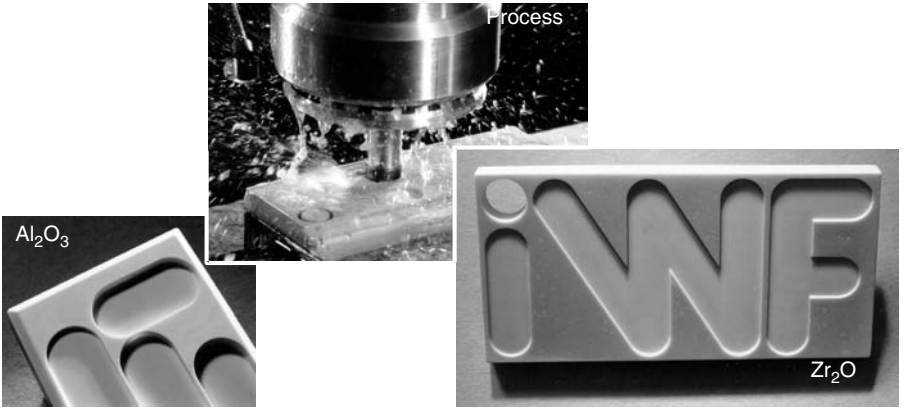

FIGURE 17.12
Process of ultrasonic-assisted cross-peripheral grinding with internal flushing and workpiece example. (From Holl, S.-E., *München*, 1997. With permission.)

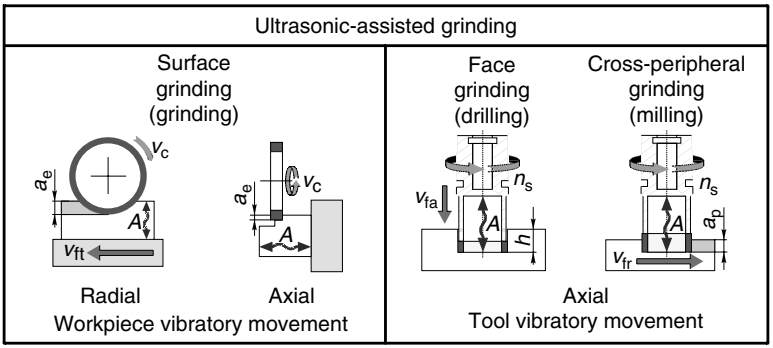

FIGURE 17.13
Process variants of ultrasonic-assisted grinding. (From Holl, S.-E., *München,* 1997. With permission; Uhlmann, E., *Annals of the CIRP*, 47/1, S249, 1998. With permission.)

In relation to the position of the active partners to one another and to the contour to be machined, it can be distinguished between axial and radial oscillating superpositions with respect to the grinding tool. According to DIN 8589, T 11, and Cartsburg (1993), the kinematic modifications depicted in Figure 17.13 result for the used process methods.

Ultrasonics can generally be used for all kinematic modifications. With respect to ceramic materials, however, the machining of complex contours such as borings, grooves, spherical surfaces or sculptured surfaces, and filigree structures is especially interesting. In this context, ultrasonic-assisted grinding offers an effective alternative to previously used, mostly uneconomical, or comparably costly technologies. In addition, ultrasonics allow a purposeful structuring of the workpiece surface, which can for instance be used to avoid directional machining traces.

17.4.2 Machinability of Ceramic Materials

Numerous investigations of ultrasonic lapping asserted that the attainable material removal rate Q_w increases with decreasing tensile strength of the ceramic material. Figure 17.14 illustrates that the removal rate in ultrasonic-assisted face grinding is also strongly related to the material. In addition to the K_{IC}-value, however, strength, hardness, and cutting behaviors also play an important role. Altogether, the resulting material removal rate can be seen as relatively high. Moreover, comparative tests with ultrasonic lapping produced generally better accuracies of shape and clearly higher tool lives.

The critical contact pressure, starting from which process instabilities may arise depending on the equipment, decreases with increasingly difficult machinability (in this example of Al_2O_3 to SiC and ZrO_2 to SSN). This leads to the demand for an application of apt machine components. This refers particularly to the

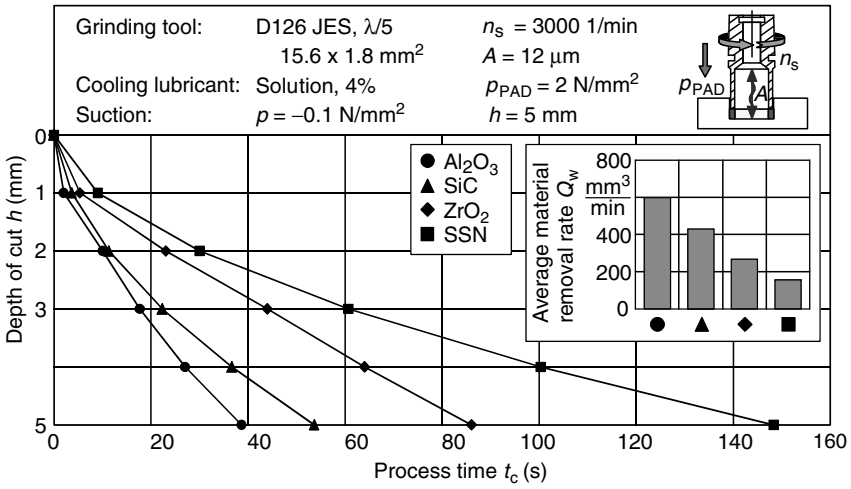

FIGURE 17.14
Depth of cut dependent on the machining time for various ceramic materials.

high forces and moments typical for grinding. Stiffness and settable tool speeds and contact pressures represent important boundary criteria (Spur et al., 1998).

Compared with conventional grinding, ultrasonic-assisted grinding causes higher mechanical and lower thermal stresses. Due to the altered kinematic active motions, the total grinding tool topography engages briefly in relation to the machine setting parameters. The ultrasonic vibration produces steeper angles of engagement as well as shorter cutting lengths and higher depths of engagement, resulting in higher mechanical stresses affecting the tool cutting edges and the material. Using ultrasound considerably reduces the grit flattening and the share of grit fractures. In contrast, however, the share of grit splintering increases, leading to an increase in the number of single cutting edges. The respective wear mechanisms balance each other, so the wear remains generally almost unaltered. It could be proved in this context that the brittle fracture share increases slightly during surface formation, yet without causing a significant change in bending strengths and residual stresses (Spur and Holl, 1997). Tests on pendulum grinding found that the described effect of ultrasonic assistance influences the work result more clearly with increasing contact length (Spur et al., 1995).

17.4.3 Surface Grinding

Surface grinding is divided into two process variants—pendulum grinding and creep feed grinding. In contrast to the pendulum mode, creep feed grinding is characterized by high working engagements a_e at low table feed speeds v_{ft}, resulting in high contact lengths and low chip thicknesses.

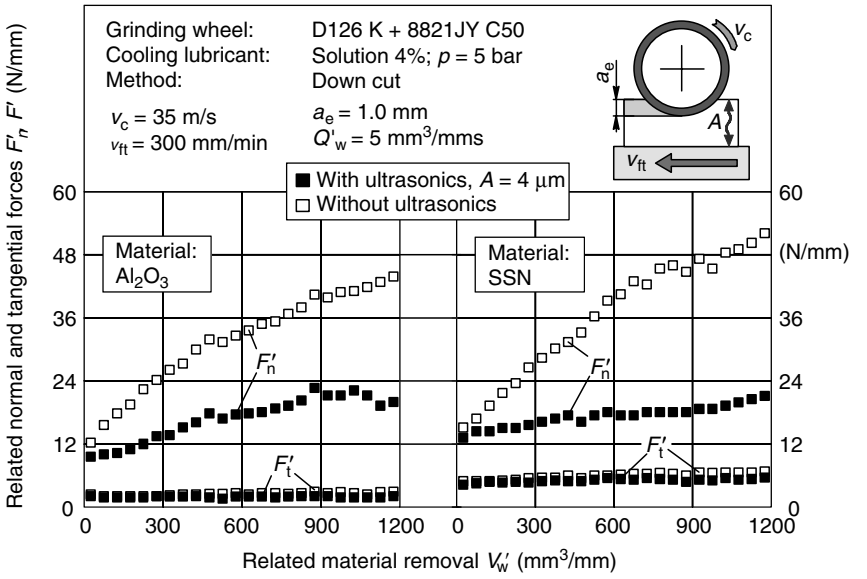

FIGURE 17.15
Related process forces during creep feed grinding with and without ultrasonic assistance.

This leads to low single grain forces, but higher total process forces because more grits engage at the same time.

Figure 17.15 shows the fundamental influence of superimposed radial ultrasonic vibrations in the course of process forces dependent on the grinding time during creep feed grinding of sintered silicon nitride (SSN) and alumina (Al_2O_3). Analogous to Uhlmann (1993) it was found that the forces during conventional conditions increase in degressive fashion at increasing related material removal V_w'. This indicates a fast alteration of the grinding wheel topography. Proceeding from a sharpened tool characterized by a relatively high grain protrusion, an increasing material removal causes a flattening of the diamond grits and an increase in friction effects. At the same time, the forces affecting the grits increase until single diamonds start to splinter or break out when a certain critical load is reached, which leads to diminishing grain protrusion. On the contrary, ultrasonic assistance results in an almost stationary course irrespective of the machined material; hence, force values are distinctly reduced with increasing related material removal V_w'. This contrast is particularly distinct in normal direction, that is, in the direction of the longitudinal workpiece vibration.

17.4.4 Face Grinding

Drilling with face grinding can be carried out with tool-path-controlled or force-controlled feed speed. The machine used plays a decisive role in

selecting the respective feed type. Although ultrasonic lapping machines operate preferably with force control, the application of ultrasonic spindles on face milling machines is usually realized with a tool-path control.

17.4.4.1 Tool-Path-Controlled Feed Speed

To evaluate the machining process, the development of process forces is analyzed for a tool-path-controlled feed speed. Figure 17.16 illustrates that a grinding operation without ultrasonic assistance produces a poor process conduct because rapidly increasing axial forces occur in this case. After a grinding time of $t_c = 22$ sec, the force already reached a value of $F_z = 240$ N that can no longer be tolerated, so the process had to be stopped. The permanent tool–workpiece contact is presumably responsible for a quick blunting of the grinding coating, leading to a strongly reduced cutting ability. This results in an enormous increase in force, if feed speeds are constant. Therefore, an economical production of such contours with conventional methods (grinding without ultrasonics) is not possible.

Using ultrasonic assistance, in contrast, leads only to a minor increase in force and thus results in a stable process during the entire machining time. Ultrasonics produce steeper angles of engagement and a complete meantime lifting of the grinding tool from the workpiece surface. Hereby, a rapid blunting of the tool in connection with a loading of the coating is avoided. Moreover, friction effects are considerably reduced and the contact zone is better supplied with cooling lubricants.

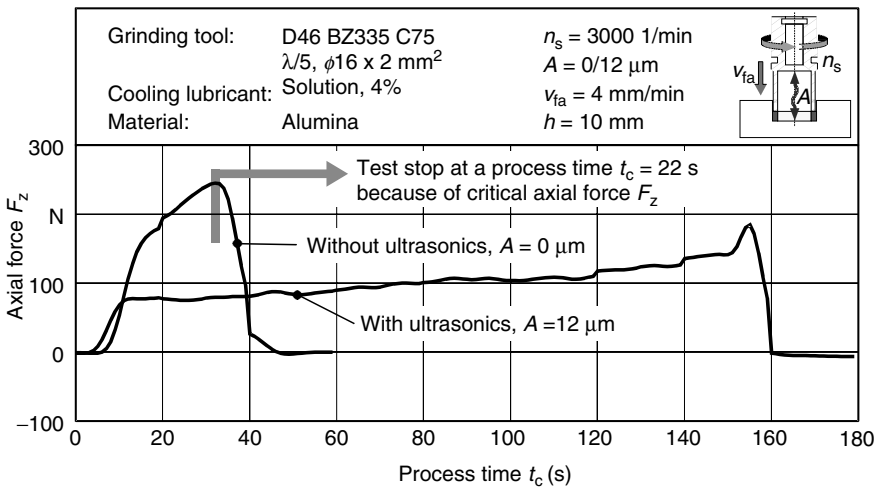

FIGURE 17.16
Comparison between axial forces during tool-path-controlled drilling with and without ultrasonics.

The relatively small grit size (D46) permits good surface qualities and accuracies of shape. The axial wear amounts to about 5–10 μm per 10 mm depth of cut, considering the positioning accuracy of the machine to be used. Projected to a coating width of 5 mm, this leads to a theoretical minimum total tool path of 5 m depth of cut.

17.4.4.2 Force-Controlled Feed Speed

When using a force-controlled feed speed, the grinding tool is sunk with its face into the workpiece under constant bearing pressure p_{PAD}. Without ultrasonic assistance, the axial feed speed was found to be rapidly decreasing toward zero, which can be explained analogous to the previous section by the blunting of the tool. The process comes to a standstill after a few millimeters and can only be reactivated by a meantime sharpening of the coating. However, this would be too costly and therefore uneconomical for real machining tasks. In contrast, ultrasonic assistance produces an almost stationary process course that is also stable at higher depths of cut. The emerging feed speed and thus the material removal rate increase with increasing rotational speeds, bearing pressures, and amplitudes until a machine-technical limit with the result of occurring instabilities is reached.

17.4.5 Cross-Peripheral Grinding

For parts made of advanced ceramics, grooves, radii, sparings, or other sculptured surfaces can be produced before sintering by green or white machining or in the course of finishing, for example, by ultrasonic path lapping (Klocke and Hilleke, 1997) or, for higher dimensions, by coordinate grinding (Mühl and Schumacher, 1994). Conductive ceramics can also be machined by electrical discharge machining. The process results, however, are generally unsatisfactory. Supplementing ultrasonic path lapping with diamond-coated grinding tools leads to ultrasonic-assisted cross-peripheral grinding. This method largely corresponds to the kinematics governing face milling.

Figure 17.12 shows the machining process and contour elements machined from the solid by ultrasonic-assisted cross-peripheral grinding. During machining with tool-path-controlled table feed speed, the resulting grinding forces can be used in relation to the engaging tool area to analyze the machining process and its efficiency. Fundamental technological investigations proved that the resulting process force is dependent on the feed speed v_{fr}, the working engagement a_e, and the back engagement a_p, as well as on the machined material. To analyze the machining of complex geometry elements at one setting, Al_2O_3 was used as an example to finish a ring groove from the solid. The respective tool-path control can be easily realized by the CNC-control of the base machine. Figure 17.17 shows the measured characteristic resultant outputs during machining.

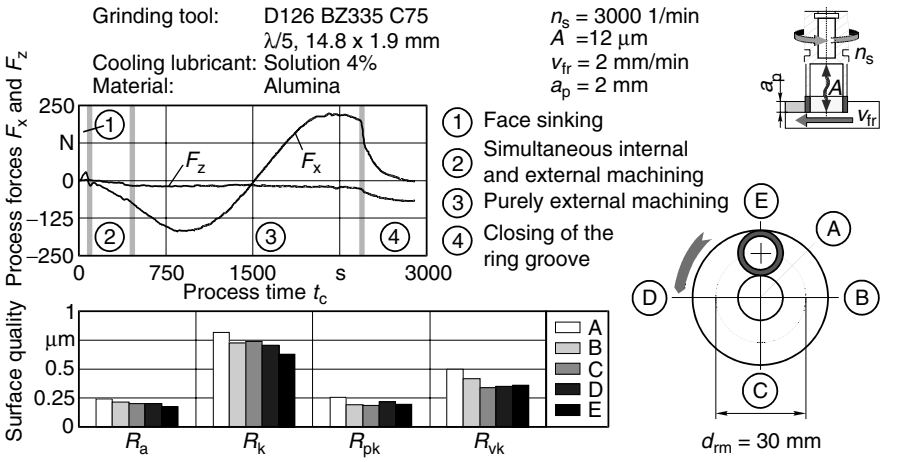

FIGURE 17.17
Milling with ultrasonic-assisted cross-peripheral grinding.

The machining of the ring groove is divided into two working steps and four process phases. In the first step, the tool was sunk with its face into the material to a nominal back engagement $a_p = 2$ mm by means of an ultrasonic-assisted face grinding process. Afterward, it was switched without a break to ultrasonic-assisted cross-peripheral grinding (working step 2). As a result, a simultaneous internal and external machining takes place at first because of the core that remained after the first working step (process phase 2). The width of the groove corresponds to the working engagement, which is in this case the outside diameter of the tool. A purely external machining is realized in the third process phase until the outer circumference of the tool meets again the beginning of the groove. The final process phase serves to close the ring groove. Hereby, the tool engages at the outer circumference, with the contact surface decreasing continuously.

The four process phases of face sinking such as simultaneous internal and external machining, purely external machining, and closing of the groove can be clearly characterized by means of the graph of axial force F_z and table feed force F_x. The force component F_z is important only for the face sinking of the tool. Considering the drifting of the signal accompanying the long process time, F_z can be neglected in the course of working step 2. As had been expected, the stationary force component F_x assumes a sinusoidal curve, which can be explained by the permanent change in direction in connection with the circular path of the tool. The surface quality was measured radial to the ring groove on the five test points A–E (Figure 17.17). The values are very equal, with the arithmetical mean deviation not exceeding $R_a = 0.25$ µm.

Further tests on the materials ZrO_2 and Al_2O_3 partly realized a material removal rate of $Q_w > 10\ mm^3/sec$ at high process stability under variation of back engagement a_p and table feed speed v_{fr} at a working engagement of $a_e = 10$ mm.

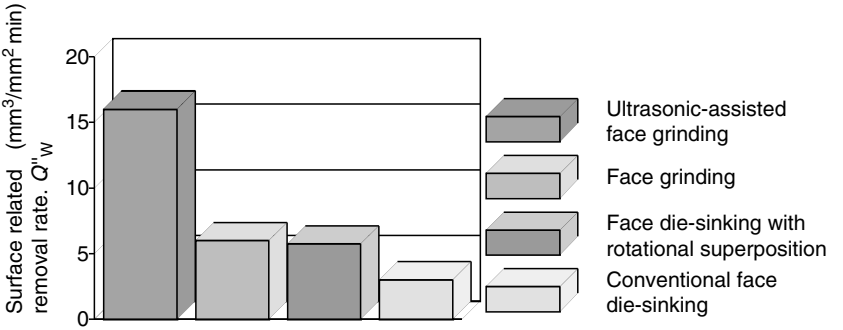

FIGURE 17.18
Process comparison during machining of alumina. (From Cartsburg, H., *Dissertation TU Berlin*, 1993. With permission.)

17.5 Process Comparison

A comparison of the attainable surface-related material removal rates during the application of various processes for drilling in the ceramic material alumina produces the highest values for ultrasonic-assisted face grinding (Figure 17.18). Comparable material removal rates could be determined for conventional face grinding and rotation-superimposed ultrasonic lapping, which however were about two-third lower than those during ultrasonic-assisted grinding. Ultrasonic-assisted conventional face die-sinking in contrast produced by far the lowest material removal rates. The reason for the superiority of ultrasonic-assisted grinding as compared with ultrasonic lapping is that the bound diamond grains completely transfer the impulse energy to the workpiece during grinding. On the contrary, a part of the energy induced into the process is used in ultrasonic lapping by the splintering of the lapping grains. In addition, the scratching grain engagement during grinding proves to be more effective than the impulse-like engagement of the grains in lapping (Cartsburg, 1993).

References

Blanck, D.: Gesetzmäßigkeiten beim Stoßläppen mit Ultraschallfrequenz. *Dissertation TH Braunschweig*, Germany, 1961.

Bönsch, C.W.: Wege zur Prozeßoptimierung beim Ultraschallschwingläppen keramischer Werkstoffe. *Dissertation RWTH Aachen*, Germany, 1992.

Cartsburg, H.: Hartbearbeitung keramischer Verbundwerkstoffe. *Dissertation TU Berlin*, Germany, 1993.

Colwell, L.: The Effects of High-Frequency Vibrations in Grinding. *Transactions of ASME*, May 1956, S124–131.

N.N.: DIN 1320.: Akustik; Grundbegriffe. Beuth-Verlag, Germany, 10.1969.
N.N.: DIN 8589 Teil 15.: Läppen. Beuth-Verlag, Germany, 12. 1985.
Dieter Hansen AG.: Keramikbearbeitung mit Ultraschall—ein Bestandteil der High-Technology. Firmenschrift, Wattwill, Switzerland, 1990.
Drozda, T.J.: Mechanical nontraditional machining processes. *Manufacturing Engineering* 91, 1, S61–64, 1983.
Engel, H.: Läppen von einkristallinem Silicium. *Dissertation TU Berlin*, Germany, 1997.
Farrer, J.O.: Improvements in or relating to cutting, grinding, polishing, cleaning, honing, or the like. *Britisches Patent Patent-Nr*. 602.801, June 3, Great Britain, 1948.
Grathwohl, G.; Iwanek, H.; Thümmler, F.: Hartbearbeitung keramischer Werkstoffe, insbesondere mittels Ultraschallerosion. Materialwissenschaft und Werkstofftechnik, Vol. 19, Germany, S81–86, 1988.
Haas, R.: Ultraschall-Erosion. Verfahren zur dreidimensionalen Bearbeitung keramischer Werkstoffe. Werkstoffe and Konstruktion 2, 2, Germany, S127–133, 1988.
Haas, R.: Technologie zur Leistungssteigerung beim Ultraschallschwingläppen. *Dissertation RWTH Aachen*, Germany, 1991.
Hilleke, M.: Bahngesteuertes Ultraschallschwingläppen sprödharter Werkstoffe. *Dissertation RWTH Aachen*, Germany, 1998.
Holl, S.-E.: Ultraschallunterstütztes Schleifen von Hochleistungswerkstoffen. Vortrag anläßlich der Jahrestagung der Deutschen Keramischen Gesellschaft, München, Germany, 13.10.1997.
Klocke, H.; Hilleke, M.: Bahngesteuertes Ultraschallschwingläppen. Maschinenmarkt, Würzburg 103, 18, Germany, S30–31, 1997.
König, W.: Keramik bearbeiten—aber wie? Vortragsband zur VDI-Fachtagung Neue Werkstoffe erfordern neue Bearbeitungsverfahren, Düsseldorf, Germany, 1988.
König, W; Bönsch, C.: Formzeugverschleiß beim Ultraschallschwingläppen. IDR, 4, Germany, S 226–229, 1991.
König, W.; Bönsch, C.; Hilleke, M.: Ultraschallschwingläppen von CFK—mehr als nur eine Alternative. VDI-Z 135, 7, Germany, S58–62, 1993.
Lawn, B.: *Fracture of Brittle Solids*, 2nd edn, Cambridge: Cambridge University Press, 1993.
Mühl, A.; Schumacher, K.: Prozeß- und Systemverhalten bei der Keramikbearbeitung auf Koordinatenschleifmaschinen. Ergebnispräsentation des BMFT-Verbundprojektes, *Schleifen von Hochleistungskeramik*, Vortragsband zum Symposium, Universität Kaiserslautern, Germany, 19./20.10.1994.
Nankov, M.M.: Supersonic activation or cup-shape diamond disk grinding. ISEM-9, *Proceedings of the Symposium for Electro Machining*. The Japan Society of Electro-Machining Engineers, Nagoya, Japan, S397–399, 1989.
Neder, L.: Technologie des Schneidens von Prepregs mit ultraschallerregten Klingen. *Dissertation RWTH Aachen*, Germany, 1990.
Nerubai, M.: Leistungssteigerung beim Schleifen mit Diamant unter Ultraschall (russisch). Stanki i Instrument, 2, Moskau, UdSS, 1977.
Noelke, H.H.: Spanende Bearbeitung von Siliciumnitrid-Werkstoffen durch Ultraschall-Schwingläppen. *Dissertation TU Hannover*, Germany, 1980.
Pei, Z.J.; Prabhakar, D.; Haselkorn, M.: Mechanistic approach to the prediction of material removal rates in rotary ultrasonic machining. *Manufacturing Science and*

Engineering. American Society of Manufacturing Engineers, Production Engineering Division (Publication) PED vol. 64, ASME, New York, NY, USA, S771–784, 1993.

Prabhakar, D.; Fereira, P.M.; Haselkorn, M.: An experimental investigation or material removal rates in rotary ultrasonic machining. Konferenz-Einzelbericht, *Transactions of the North American Manufacturing Research Institution of SME*, the 20th NAMRC Conference, Washington State University, Pullman, WA, USA, S211–218, 1992.

Rhoades, L.J.: Advances in some specialized grinding processes. *The Winter Annual Meeting of the ASME*, Miami Beach, USA, 17.–22.11.1985, PED-16, 11, S107–139, 1985.

Rhoades, L.J.: Abrasive flow and ultrasonic machining and polishing. Vortrag und und Tagesberichtsband, *First International Machining and Grinding Conference*, Dearborn, USA, S523–541, 12, 14.09.1995.

Rozenberg, L.D.; Kazantsev, V.F.; Makarov, L.O.; Yakhimovich, D.F.: Ultrasonic cutting. Consultans Bureau, New York, USA, 1964.

Sabotka, I.: Planläppen Technischer Keramiken. Dissertation TU Berlin, Germany, 1991.

Shaw, M.C.: Das Schleifen mit Ultraschall. Microtecnic, 10(6) S265–275, 1956.

Spur, G.: Keramikbearbeitung. München; Wien: Hanser Verlag, 1989.

Spur, G.; Engel, H.: Werkzeugeingriff und Oberflächenentstehung beim Läppen spröder Werkstoffe. In: *Jahrbuch Schleifen, Honen, Läppen und Polieren*; Bd. 58; Hrsg.: H.T. Tönshoff, Essen: Vulkan, Germany, 1996.

Spur, G.; Holl, S.-E.: Material removal mechanisms during ultrasonic assisted grinding. *Production Engineering* Vol. IV/2, Germany, S9–14, 1997.

Spur, G.; Krieg, G.H.: The influence of machine tool materials on the wear of profile tools in ultrasonic fine lapping of reinforced high-performance ceramics. *Production Engineering*, Vol. II/2, Germany, 1995.

Spur, G.; Sathyanarayanan, G.; Holl, S.-E.: Ultrasonic assisted grinding of structural ceramics. Vortrag und Tagungsberichtsband, First International Machining and Grinding Conference, Dearborn, USA, 12.–14.09.1995.

Spur, G.; Uhlmann, E.; Holl, S.-E.: Ultrasonic assisted grinding of ceramics. In: Proceedings of the 9th CIMTEC World Ceramic Congress, Florenz, Italy, 14.–19.06.1998.

Suzuki, K.; Tochinai, H.; Uematsu, T.; Nakagawa, T.: New grinding method for ceramics using a biaxially vibrated nonrotational ultrasonic tool. *CIRP Annals*, Vol. 42 No. 1, S375–378, 1993.

Uematsu, T.; Suzuki, K.; Yanase, T.; Nakagawa, T.; Bekrenev, N.: A new complex grinding method for ceramic materials combined with ultrasonic vibration and electrodischarge machining. *The Winter Annual Meeting of the ASME*, Chicago, IL, USA, 1988.

Uhlmann, E.: Tiefschleifen hochfester keramischer Werkstoffe. *Dissertation TU Berlin*, Germany, 1993.

Uhlmann, E.: Surface formation in creep feed grinding of advanced ceramics with and without ultrasonic assistance. *Annals of the CIRP*, Vol. 47/1, S249–252, 1998.

Uhlmann, E.; Holl, S.-E.: Entwicklungen beim Schleifen keramischer Werkstoffe. Vortrag im Rahmen des Seminars, *Moderne Schleiftechnologie*, am 14. Mai 1998 in Furtwangen, Germany.

Vogel, M.: Ultraschallschwingläppen von Siliziumnitrid- und Aluminiumoxidkeramiken. Dissertation TH Karlsruhe, Germany, 1992.

Warnecke, G.; Zapp, M.: Ultrasonic superimposed grinding of advanced ceramics. *First International Machining and Grinding Conference*, Dearborn, Michigan, USA, S1–11, 12–14.09.1995.

Weigmann, U.-P.: Honen keramischer Werkstoffe. *Dissertation TU Berlin, Germany*, 1997.

Westkämper, E.; Kappmeyer, G.: Feiner Abtrag. Anwendungsgerechte Auslegung von Werkzeugen zum Ultraschallhonen. Maschinenmarkt 100, Germany, S28–33, 1994.

Westkämper, E.; Kappmeyer, G.: High frequency honing. *Production Engineering*, Vol. II/2 Germany, S31–36, 1995.

Williams, R.E.; Allen, B.J.: Ultrasonic polishing of EDM workpieces. Vortrag und Tagungsberichtsband, *First International Machining and Grinding Conference*, Dearborn, USA, S523–541, 12.–14.09.1995.

Wood, R.W.; Loomis, A.L.: The physical and biological effects of high-frequency sound-waves of grear intensity. *Philosophical Magazine* 4, 22, Great Britain, S417–436, 1927.

Yano, A.; Shinke, N.; Tanaka, Y.: Untersuchungen über das Ultraschallschwingschleifen. Maschinenmarkt 76, 64, Germany, S1452–1456, 1970.

Youssef, H.: Herstellgenauigkeit beim Stoßläppen mit Ultraschallfrequenz. Dissertation TH Braunschweig, Germany, 1967.

Index

Manufacturing and Industrial Engineering

HANDBOOK OF ADVANCED CERAMICS MACHINING

Ceramics, with their unique properties and diverse applications, hold the potential to revolutionize many industries, including automotive and semiconductors. For many applications, ceramics could replace metals and other materials that are more easily and inexpensively machined. However, current ceramic machining methods remain cost-prohibitive. Fortunately, the current flurry of research will soon yield new and better methods for machining advanced ceramic materials.

Reflecting the life-long dedication of an unsurpassed team of experts from industry and academia, the **Handbook of Advanced Ceramics Machining** explores the latest developments in our understanding of the mechanisms involved in ceramics machining as well as state-of-the-art technologies. Multiple chapters are devoted to various types and aspects of the lapping and grinding processes, such as mechanisms, monitoring techniques, mono- versus polycrystalline abrasives, and tribological properties. Covering methods that offer high-rate material removal and others that provide extremely high-quality surface finish, this book examines conventional, new, and lesser-known methods including ductile grinding, belt centerless grinding, lapping, polishing, double-side grinding, laser-assisted grinding, ultrasonic machining, and the new electrolytic in-process dressing (ELID) grinding method.

Features

- Presents the latest research and technologies for the machining of advanced ceramic materials
- Discusses methods that offer high productivity, high precision, and lower cost
- Includes machining processes other than grinding, such as lapping, ultrasonic machining, and nano-machining
- Provides comprehensive discussion and analysis of the new ELID grinding technology
- Considers the replacement of double lapping with double grinding while using the same kinematics

An indispensable toolkit for opening new avenues of possibility for ceramics applications, the **Handbook of Advanced Ceramics Machining** helps bring cost-effective, high-performance, and high-precision methods into standard practice.

CRC Press
Taylor & Francis Group
an informa business
www.taylorandfrancisgroup.com

6000 Broken Sound Parkway, NW
Suite 300, Boca Raton, FL 33487
270 Madison Avenue
New York, NY 10016
2 Park Square, Milton Park
Abingdon, Oxon OX14 4RN, UK

3837
ISBN 0-8493-3837-9
90000
9 780849 338373

www.crcpress.com